

REPORT DOCUMENTATION PAGE				Form Approved OMB No. 0704-0188	
<p>Public reporting burden for this collection of information is estimated to average 1 hour per response, including the time for reviewing instructions, searching existing data sources, gathering and maintaining the data needed, and completing and reviewing the collection of information. Send comments regarding this burden estimate or any other aspect of this collection of information, including suggestions for reducing the burden, to Department of Defense, Washington Headquarters Services, Directorate for Information Operations and Reports (0704-0188), 1215 Jefferson Davis Highway, Suite 1204, Arlington, VA 22202-4302. Respondents should be aware that notwithstanding any other provision of law, no person shall be subject to any penalty for failing to comply with a collection of information if it does not display a currently valid OMB control number.</p> <p>PLEASE DO NOT RETURN YOUR FORM TO THE ABOVE ADDRESS.</p>					
1. REPORT DATE (DD-MM-YYYY) 12-03-2007		2. REPORT TYPE Final Report		3. DATES COVERED (From – To) 30 May 2003 - 20-Mar-07	
4. TITLE AND SUBTITLE Plasma Assisted Combustion			5a. CONTRACT NUMBER FA8655-03-D-0001, Delivery Order 0003		
			5b. GRANT NUMBER		
			5c. PROGRAM ELEMENT NUMBER		
6. AUTHOR(S) Professor Andrei Y Starikovskii			5d. PROJECT NUMBER		
			5d. TASK NUMBER		
			5e. WORK UNIT NUMBER		
7. PERFORMING ORGANIZATION NAME(S) AND ADDRESS(ES) Moscow Institute of Physics and Technology 9 Institutski Lane Dolgoprudny 141700 Russia			8. PERFORMING ORGANIZATION REPORT NUMBER N/A		
9. SPONSORING/MONITORING AGENCY NAME(S) AND ADDRESS(ES) EOARD PSC 821 BOX 14 FPO AE 09421-0014			10. SPONSOR/MONITOR'S ACRONYM(S)		
			11. SPONSOR/MONITOR'S REPORT NUMBER(S) CRDF 02-9003		
12. DISTRIBUTION/AVAILABILITY STATEMENT Approved for public release; distribution is unlimited.					
13. SUPPLEMENTARY NOTES					
14. ABSTRACT This report results from a contract tasking Moscow Institute of Physics and Technology as follows: The contractor will investigate the use of high voltage, nano-second plasma discharges to ignite and efficiently combust fuel/air mixtures in high speed flows. This strongly non-equilibrium low-temperature plasma has a high mean energy of electrons and will provide a source of reactive atoms, radicals, and excited molecules which has been shown to enhance ignition and combustion. The short duration of the pulses results in relatively low power requirements for generating the discharge. The goal is to demonstrate and understand the physics of energy exchange, ignition and combustion. Also, the use of this type of plasma for aerodynamic flow control will be investigated. Finally, applicability to use this type of discharge to directly initiate a detonation wave will be investigated.					
15. SUBJECT TERMS EOARD, Plasma Physics and Chemistry, ignition, Plasma Combustion					
16. SECURITY CLASSIFICATION OF:			17. LIMITATION OF ABSTRACT UL	18, NUMBER OF PAGES 372	19a. NAME OF RESPONSIBLE PERSON SURYA SURAMPUDI
a. REPORT UNCLAS	b. ABSTRACT UNCLAS	c. THIS PAGE UNCLAS			19b. TELEPHONE NUMBER (Include area code) +44 (0)20 7514 4299

Moscow Institute of Physics and Technology
Physics of Nonequilibrium Systems Laboratory

Plasma Assisted Combustion

EOARD/CRDF Project # RP0-1349-MO-02
Final Report, August 1, 2003 - December 30, 2006

Date Submitted: February 28, 2007



Edited by Dr. Andrei Yu. Starikovskii,
Moscow Institute of Physics and Technology
Physics of Nonequilibrium Systems Laboratory
Institutskii lane, 9, 141700,
Dolgoprudny, 141700, RUSSIA
Phone (+7-495)-408-6347
E-mail astar@neq.mipt.ru
URL <http://neq.mipt.ru>

Declaration of Technical Data Conformity

The Contractor hereby declares that, to the best of its knowledge and belief, the technical data delivered herewith under this contract during the period 08/01/2003 through 12/30/2006 is complete, accurate, and complies with all material requirements of the Contract.

A handwritten signature in black ink, appearing to be 'E.E. Son', written in a cursive style.

Date: 02/26/2007

Name and Title of Authorized Official: Prof. E.E.Son, Vice-Rector, Science

Contents

1	Abstract	7
2	The Study of the Discharges Used for PAI/PAC	13
2.1	The review of discharges used for combustion and ignition control	13
2.1.1	Streamer discharge	15
2.1.2	Dielectric barrier discharge	22
2.1.3	Atmospheric pressure glow discharge	27
2.1.4	Pulsed nanosecond discharges	31
2.1.5	Other discharges	35
2.2	The study of streamer discharge development. Streamer branching and optical control of a streamer head.	38
2.2.1	Experimental study of streamer discharge	38
2.2.2	Single channel measurements	40
2.2.3	Streamer branching	46
2.2.4	Numerical model of streamer discharge	46
2.3	The study of fast ionization wave development at different pressures and plasma production by nanosecond discharge	50
2.3.1	Ionization wave velocity and energy contributed into gas.	50
2.3.2	Spatial uniformity of ionization wave. FIW in a large discharge volume.	52
2.3.3	Electric field and electron density	56
2.4	Experimental investigation of electron density at low gas temperatures . .	59
2.4.1	Experimental setup	59
2.4.2	Electron density decay in molecular nitrogen	63
2.4.3	Electron density decay in molecular oxygen	71
2.4.4	Electron density decay in CO ₂	75
2.4.5	Electron density decay in N ₂ : O ₂ = 4 : 1	79
2.4.6	Electron density decay in water vapor	82
2.5	Modelling of the electron density decay at low gas pressure	83
2.5.1	Modelling of the decay of electron density in molecular nitrogen . .	83
2.5.2	Modelling of the decay of electron density in molecular oxygen . . .	85
2.5.3	Modelling of the decay of electron density in CO ₂	89
2.5.4	Modelling of the decay of electron density in water vapor	90
2.5.5	Experiments and modelling for the high gas temperature	93

3	Experimental and Numerical Investigation of Slow Hydrocarbon Oxidation in Nanosecond Discharge	97
3.1	Experimental setup	98
3.2	Experimental methods	100
3.2.1	Finding of electric current, electric field and energy input	100
3.2.2	Emission spectroscopy. Experimental investigation of optical characteristics of the discharge.	102
3.2.3	Absorption spectroscopy. Methane concentration measurements. . .	105
3.3	Results and discussion	105
3.3.1	Electrodynamic situation of the discharge.	105
3.3.2	Kinetics of alkanes oxidation in the discharge.	110
3.3.3	C ₄ H ₁₀ oxidation in lean mixtures with oxygen under nanosecond discharge	117
3.3.4	C ₁₀ H ₂₂ oxidation in lean mixture with oxygen under nanosecond discharge action	122
3.4	Numerical calculation of C ₂ H ₆ , CH ₄ , H ₂ , C ₂ H ₅ OH oxidation by nanosecond discharge	127
3.4.1	Electron impact processes in the discharge	128
3.4.2	Positive ions kinetics	129
3.4.3	Production of radicals by electron impact	133
3.4.4	Numerical model	134
3.4.5	The results of calculations	135
3.5	Acetone's, acetylene and ethyl alcohol's oxidation under discharge action. Experimental investigation and analysis	138
3.5.1	Results and discussion	139
3.6	Carbon monoxide oxidation in mixtures with oxygen and water. Experimental investigation and analysis	147
3.6.1	Experiment	147
3.6.2	Discussion	148
3.7	Kinetics of neutrals in hydrocarbons (C ₂ H ₆ , CH ₄ , H ₂ , C ₂ H ₅ OH)–oxygen mixtures	150
4	The Experimental and Numerical Study of High-Temperature Kinetic of H₂ and C₁-C₅ PAI	157
4.1	Nanosecond gas discharge ignition of H ₂ -O ₂ -Ar mixtures.	157
4.1.1	Theoretical analysis of ignition efficiency	157
4.1.2	Description of experiment	162
4.1.3	Ignition delay time change in H ₂ -O ₂ mixture by pulsed discharge . .	172
4.2	Ignition delay time change in H ₂ -air mixture by pulsed discharge	178
4.2.1	Experiments in H ₂ : O ₂ : N ₂ : Ar mixture	178
4.2.2	Experiments in H ₂ : O ₂ : N ₂ mixture	181
4.3	Comparison with the computational model	187
4.3.1	Flow model	187
4.3.2	Kinetic model	187
4.4	Ignition delay time measurements in CH ₄ : O ₂ : N ₂ : Ar mixture	191
4.5	Gas discharge and ignition homogeneity measurements	193

4.6	Ignition of homological series of hydrocarbons.	194
4.7	Kinetics of C1-C5 hydrocarbons in gas mixtures for PAI	203
4.7.1	Experimental analysis of the artificial ignition. mixtures with hydrocarbons	208
4.7.2	Simulation of production of atoms and radicals	210
4.7.3	Simulation of autoignition and artificial ignition. Comparison with the experiments	214
5	Experimental and Numerical Analysis of Efficiency of Different Species for Artificial Initiation of Ignition	218
5.1	Experimental study of the efficiency of excited atomic species for artificial ignition	218
5.2	The development of kinetic model to describe the role of the excited species in ignition	225
5.2.1	Experiments in autoignition in N_2O -containing mixtures	226
5.2.2	Other kinetic experiments in N_2O -containing mixtures	227
5.2.3	Analysis of basic reactions in $N_2O-H_2-O_2$ system. Description of numerical model and comparison of calculations and experiments.	228
6	Mechanisms of Flames Control by Means of a Non-Equilibrium Low-Temperature Pulsed Nanosecond Barrier Discharge Plasma	240
6.1	Flame control by pulsed nanosecond barrier discharge	240
6.1.1	Effect of the electric field configuration on the flame	244
6.1.2	Effect of the ionic wind on flame propagation	247
6.1.3	Excitation of particles in a flame	253
6.2	Control of plasma-enhanced combustion using optical diagnostics	265
6.2.1	Role of a nanosecond pulse duration in combustion enhancement	265
6.3	Kinetic mechanisms of plasma-assisted combustion	273
6.3.1	Temperature measurements	274
6.3.2	LIF diagnostic of OH radical in plasma-assisted flame	279
6.3.3	LIF diagnostic of OH radical in streamer discharge and its afterglow	284
7	Liquid Fuel Atomization Using Nanosecond Discharge	293
7.1	The aim of investigations	293
7.2	Experimental setup	294
7.3	The results of experiments	298
8	Supersonic Hydrocarbon-Air Mixtures Ignition and Flame Control by Non-Equilibrium Low-Temperature Plasma.	307
8.1	Hypersonic air plasma flow	307
8.1.1	Electron number density and mean energy in the flow	308
8.1.2	Gas flow rotational temperature measurements	310
8.2	Modelling of the energy exchange processes in the flow	310
8.3	Reacting plasma hypersonic flow	312

9	Detonation Initiation by High-Voltage Pulsed Discharges	317
9.1	Detonation initiation by non-equilibrium nanosecond discharge	318
9.1.1	Experimental setup	318
9.1.2	Nanosecond discharge development	319
9.1.3	Results of detonation initiation experiments	319
9.2	Detonation initiation by microsecond spark discharge	322
9.2.1	Experimental setup	322
9.2.2	Microsecond discharge development	323
9.2.3	Results of detonation initiation experiments	326
9.3	Results discussion	327
10	Conclusions	330
	References	337
	List of figures	353
	List of tables	369

Chapter 1

Abstract

A review was made which discusses different types of the discharges applied for plasma assisted ignition and combustion. Special attention to experimental and theoretical analysis of some plasma parameters was given, such as reduced electric field, electron density and energy branching for different gas discharges. Streamers, pulsed nanosecond discharges, dielectric barrier discharges, radio frequency discharges, atmospheric pressure glow discharges are considered.

Detailed measurements of the parameters of a streamer flash development in the air for the pressure range 90-1300 Torr have been carried out in the plane-to-plane geometry for 20-42 kV positive and negative polarity nanosecond pulses. A numerical model, which successfully predicts such streamer parameters as current, velocity of propagation, and streamer's head diameter in a wide range of pressures and voltages has been developed.

New results have been obtained for spatial control of discharge uniformity at different experimental conditions. LaVision ICCD camera with picosecond resolution was used to obtain discharge images with a gate of 1 ns and subnanosecond delay between frames. We controlled the process of the uniform discharge development from a tip of conical electrode for different pressures and polarities. Development of the discharge in plane-to-plane geometry was investigated for different repetition rates of the pulses.

New technique for the control of electron density with a lower limit of measurements 10^{11} cm^{-3} and temporal resolution up to 100 ns has been adjusted and tested. The technique is based on microwave I/Q interferometry at 94 GHz frequency. The experiments demonstrated the efficiency of the technique in experiments with discharge in repetitive regime. Good correlation between experimental data for electron density obtained from electric current measurements and from microwave interferometry has been demonstrated.

The decay of electron density in the afterglow of a nanosecond pulsed discharge has been investigated for room temperature and for high temperatures (1500–3000 K). The experiments were carried out in N_2 , O_2 , CO_2 , $\text{N}_2 : \text{O}_2 = 4 : 1$, and water vapor for a gas temperature $T=295 \text{ K}$ and high voltage pulse of positive polarity with the amplitude $U=11 \text{ kV}$. Different repetition rates of pulses were tested. The initial electron density practically does not depend upon a gas mixture composition. It is equal to $(1-3) \cdot 10^{12} \text{ cm}^{-3}$ within the pressure range of 1–10 Torr. The plasma decay time decreases with pressure, and corresponds to a few microseconds for N_2 , O_2 , CO_2 , $\text{N}_2 : \text{O}_2 = 4 : 1$. Maximal recombination time ($\tau \approx 1.7 \text{ } \mu\text{s}$, $p=2.5 \text{ Torr}$, $T=295 \text{ K}$) and initial electron density ($n_0 \approx 2.2 \cdot 10^{12} \text{ cm}^{-3}$) have been observed for synthetic air. For water vapor, the recombination

time is significantly lower. The kinetic schemes were proposed for pure gases. Their verification has been made using experimental data. The experiments in a high-temperature range were carried out for $\text{CO}_2\text{:O}_2\text{:N}_2$ mixture with different admixtures of water vapor. It can be concluded from the experiments that water addition decreases significantly the plasma decay time. Typical decay time during high temperature experiments was equal to a few microseconds, and the electron density drops by an order of magnitude during 10 microseconds. Preliminary numerical modelling has been made, the results demonstrate a reasonable agreement with the experiments.

The experimental investigation of processes of alkanes slow oxidation has been performed. We have investigated kinetics of alkanes oxidation from methane to decane in stoichiometric and lean mixtures with oxygen and air at room temperature under the action of uniform high-voltage nanosecond discharge without gas flow. Also we have investigated experimentally kinetics of $\text{C}_2\text{H}_5\text{OH}$, CH_3COCH_3 , C_2H_2 in their mixtures with oxygen and CO:O_2 mixtures with small controlled additives of water vapour.

The discharge was initiated with repetition rate 40 Hz in the discharge screened tube with 5 cm diameter and 20 cm length. The pulses polarity was negative, with 10 kV amplitude and 25 ns duration. Mixtures' initial pressures were varied within 0.8-11 Torr range with the step of 0.8 Torr. The discharge current, electrical field and energy input have been measured with nanosecond time resolution. Emission intensities of the molecular bands such as $\text{NO}(A^2\Sigma \rightarrow X^2\Pi, \delta v = 3)$, $\text{N}_2(C^3\Pi, v' = 1 \rightarrow B^3\Pi, v'' = 7)$, $\text{N}_2(B^3\Pi, v' = 6 \rightarrow A^3\Sigma, v'' = 3)$, $\text{N}_2^+(B^2\Sigma, v' = 0 \rightarrow X^2\Sigma, v'' = 2)$, $\text{CO}_2^+(B^2\Sigma \rightarrow X^2\Pi, \delta v = 0)$, $\text{CH}(A^2\Delta, v' = 0 \rightarrow X^2\Pi, v'' = 0)$, $\text{OH}(A^2\Sigma, v' = 0 \rightarrow X^2\Pi, v'' = 0)$, $\text{CO}(B^1\Sigma, v' = 0 \rightarrow A^1\Pi, v'' = 2)$ have been measured in integral regime (integration time was 2.2 s) and with nanosecond resolution. Methane concentration was measured by absorption of He-Ne laser emission in integral regime. On the base of optical measurements time of the full oxidation of the alkanes was determined.

On the base of experimental data the kinetic scheme was proposed to describe nanosecond discharge action on hydrocarbon-containing mixtures. It was demonstrated that it is possible to describe experimentally obtained dependencies of the oxidation time *vs* gas pressure for different mixtures. The main radicals responsible for oxidation are $\text{O}(^1\text{D})$ and OH . Equal time of oxidation for a set of heavy hydrocarbons is explained by negative reverse back-coupling through stable intermediates, such as H_2O_2 and CO . A good correlation between calculations based on these assumption and experimental data was found.

An analysis of the ignition of H_2 -containing mixtures at high temperatures under the action of a nanosecond high-voltage discharge has been performed numerically and experimentally for a wide range of parameters. A comparison of the equilibrium and nonequilibrium excitation was performed. The model constructed supports the conclusion that nonequilibrium excitation is much more effective than the equilibrium one for ignition control. In particular, the ignition threshold shift in H_2 -Air mixture is about 300 K under the discharge action with the equivalent energy input of 15 K.

The numerical analysis of ignition efficiency allowed to perform experimental investigations of the initiation of the ignition by nanosecond discharge at high temperatures. A novel experimental scheme for the investigation of ignition delay at high temperatures under the action of a high-voltage nanosecond discharge has been developed. Electrical parameters on a nanosecond time scale and the ignition processes on a microsecond

time scale were investigated. Ignition delays for different mixtures, gas pressures and temperatures were obtained experimentally. The dependence of the ignition delay upon temperature, high voltage pulse amplitude, and the energy release into the discharge was determined experimentally for $\text{H}_2\text{-O}_2$ and $\text{H}_2\text{-air}$ mixtures diluted with argon or helium. ICCD camera PicoStar HR12 was used to obtain the discharge images in a hot mixture with high temporal resolution. The wavelength sensitivity of the optical system was 300–800 nm. The homogeneity of the discharge development and the ignition initiation was shown up to the pressure of 2 atmospheres under the discharge excitation. Obtained data were compared with the results of numerical calculations.

We have conducted the experiments and numerical modelling of the ignition of hydrocarbon-containing mixtures under the action of pulsed nanosecond discharge. The experiments were carried out with a set of stoichiometric mixtures $\text{C}_n\text{H}_{2n+2} : \text{O}_2$ (10%) diluted by Ar (90%) for hydrocarbons from CH_4 to C_5H_{12} . The temperature behind the reflected shock wave (T_5) varied from 950 to 2000 K, and the pressure (P_5) was 0.2 to 1.0 atm. For each set of experimental parameters we have compared the ignition by the discharge with autoignition.

A numerical model has been built which takes into account both high-temperature kinetics of the ignition and production of atoms and radicals by a nanosecond discharge. At the first stage, we calculated energy branching in the discharge on the basis of experimentally determined electric field and energy input. Reactions responsible for the energy transfer from electronically excited buffer gas to molecules with subsequent production of atoms and radicals was included into kinetic scheme. At the second stage, we modelled high-temperature kinetics, taking into account atoms and radicals produced at the first step.

Comparison of the results of experiments and numerical modelling gives a reasonable agreement and allows to conclude that, at our experimental conditions, the most important channel of the energy input is dissociation by an electron impact and production of electronically excited atoms and molecules. Additional production of atoms and radicals due to the quenching of electronically excited species in the nearest afterglow does not exceed factor of 2–3. These atoms and radicals (O , H , OH , $\text{C}_n\text{H}_{2n-1}$ etc.) lead to the uniform in space ignition of gas mixtures at temperatures 500–200 K lower than the autoignition temperature.

To elucidate the main channels which are responsible for the ignition under the action of a nanosecond discharge, and separate the role of dissociated species, in part, the role of electronically excited atoms $\text{O}(^1\text{D})$, we performed a set of experiments with specially prepared mixtures of N_2O with hydrogen, diluted by argon. The experiments were carried out behind a reflected shock wave. A radiation of pulsed ArF laser was used instead of the discharge to provoke the ignition. Comparison of ignition by the discharge and by laser flash-photolysis for the same experimental conditions and for gas mixture of special composition has been made.

The kinetics of chemical transformations in $\text{N}_2\text{O-H}_2\text{-O}_2\text{-Ar}$ mixtures have been studied in the temperature range from 1000 to 2700 K and pressures from 0.1 to 10 atm. A shock-tube experiment has been used to obtain data on ignition delay time in mixtures which are diluted with the noble gas (50 to 90% Ar). Based on the data obtained and the data of kinetic experiments in mixtures containing up to 97% Ar, a mechanism to describe the kinetics in the given system has been suggested.

The influence of gas excitation by a pulsed nanosecond atmospheric-pressure barrier discharge (with a high-voltage pulse amplitude up to 25 kV, pulse repetition rate up to 10 kHz, pulse duration is 5–70 ns) on the characteristics of a premixed propane–air and methane–air flames has been investigated within a wide range of the equivalence ratios (0.4–5). It was experimentally found that the flame blow-off velocity increases more than twice with the discharge energy input 0.1% of the burner’s chemical power. The emission profiles of the OH, CH, and C₂ radicals along the flame were studied using emission spectroscopy. An efficient production of active radicals under the action of a barrier discharge has been observed. Based on the data obtained, the increase in the flame propagation velocity is explained by the production of atomic oxygen in a discharge due to the quenching of electronically excited molecular nitrogen N₂ and the electron-impact dissociation of molecular oxygen. A numerical model has been developed that qualitatively describes the influence of a barrier discharge on flame propagation.

It was shown experimentally that results for methane-air flame are similar with propane-air one. The acceleration mechanisms are similar in both cases. Besides proper form of energy input, proper organization of discharge is of great importance. The main characteristics of successful energy input, in this case, is the maximum value of the ratio of flame blow-off velocity with discharge to that one without the discharge (instead of maximum possible flow speed), and the minimal ratio between discharge energy input and chemical power of a burner. The comparison of the effectiveness of plasma-assisted combustion for different types of the discharge, different pulse durations, pulse repetition rates and other parameters, which are responsible for active particles production, was performed. Development of the streamer in different regimes was studied, optimal regimes were found.

It was found that active particles (O and OH primarily), which are produced under the discharge action, play the most significant role in the effect of combustion acceleration. The model of flame acceleration, based on nitrogen quenching on oxygen molecules, with production of O and OH radicals, was confirmed by spectroscopic investigations. Detailed results concerning OH emission and blow-off velocities are represented. For barrier discharge, which was proved to be efficient for flame control, dependence of flame blow-off velocity from pulse amplitude and pulse repetition rate was found.

To prove the suggested mechanism which is responsible for a flame stabilization by the nanosecond barrier discharge we performed measurements of the gas flows (air and propane-air) temperatures in the barrier discharge. The measurements were performed using rotationally-resolved 0-0 band of 2nd positive emission system of a nitrogen molecule. It was found that gas heating in a propane-air mixture is stronger than in a pure air. Basing on the results of numerical modelling we can conclude that additional heating in propane-air mixtures occurs due to atomic oxygen production in the discharge, and the direct thermal heating by the discharge is insufficient to promote a combustion. The main reasons for the temperature growth are the following. The first is an additional energy release in chain reactions, and this effect is important at high temperatures (near the temperature of self-ignition). The second, which is more important at lower temperatures, is the difference in mechanisms of O atoms recombination in air and propane-air: recombination in air proceeds via O-O and O-O₂ collisions, while in propane-containing mixtures the recombination goes with OH radical formation – this process is much more faster. Because the residual time of a mixture portion in the discharge zone is limited by the flow velocity (near 1 ms), such energy release acceleration is important in kinetic processes.

The modelling of gas heating was performed with taking into account O(1D) which is produced in the discharge, good correlation between experimental data and calculations was performed.

Another proof to the mechanism suggested above about the radical's role in the flame control by the barrier discharge is the measurements of OH radical in the flame using laser-induced fluorescence technique. It was demonstrated that additional OH production takes place on the boundary between the discharge and flame zones. Difference between OH density in the flame and the flame supported by the discharge has been observed which is similar to that one for excited OH radicals. The scheme for control of temporal behavior of OH in combustion under the nanosecond discharge influence has been adjusted. The measurements in time-resolved regime with an accuracy about $2\mu\text{s}$ have showed the fast formation of OH radicals near the burner nozzle after the discharge action and their further decrease between pulses. OH maximum corresponds to $1\mu\text{s}$ and corresponds with calculations. These results confirmed the theory about the radical mechanism of the flame stabilization by the nanosecond barrier discharge.

A set-up to study the liquid fuel atomization under the influence of pulsed nanosecond discharge was designed and assembled. The effect of discharge influence was observed during the regime of strongly aerated liquid atomization. Two differences could be mentioned: the optical density of the flow was reduced with the discharge as well as the atomization time. Regimes and electrodes' geometry were found when nanosecond pulsed discharge affects strongly the liquid atomization. With liquid consumption up to 20 g/sec (and discharge power 3kW, which corresponds to 5% vapourization) it's possible to obtain atomization of a flow in the regimes where there is no atomization in the absence of the discharge. It was found that the main mechanism of the discharge influence lies in vapourization of liquid in the breakdown channel with further changes in flow pattern. The maximum liquid consumption for effective atomization is limited by the stable breakdown appearance.

The study of propane-air plasma in the hypersonic flow was performed. The flow regime corresponded to Mach number of 8, gas flow was equal to 0.2 g/s. The pre-chamber was equipped with heater which allowed us to heat the gas up to 700 K before its expansion into the nozzle. The stable diffuse plasma was created by low-pressure aerodynamically stabilized DC discharge between nozzle and high-voltage electrode. Mean electron energy in this type of discharge is rather high and gas excitation includes ionization, dissociation, excitation of electronic and vibrational states, so discharge provides almost no direct heating. Spatial distribution of the different molecular bands emission was measured. The region of gas relaxation and chemical reactions (emission peak of CH radical) was determined. Maximum of CH emission corresponds to the region near the shock wave front, while the maximum of emission intensity of nitrogen molecule corresponds to the near-electrode region. The emission of CH radical rapidly drops down due to fast chemical reactions near the shock wave front in this regime. Thus, we have demonstrated the chemical reactions initiation and ignition zone stabilization in the cold flow by high-voltage gas discharge.

An experimental study of the ignition and detonation initiation by two different kinds of high-voltage pulsed gas discharge has been performed in two smooth detonation tubes. The experiments were carried out at different pressures ranging from 0.15 to 1 bar in various stoichiometric mixtures: $\text{C}_3\text{H}_8 + 5\text{O}_2 + x\text{N}_2$ ($0 \leq x \leq 4$), $\text{C}_3\text{H}_8/\text{C}_4\text{H}_{10} + 5\text{O}_2 +$

$x\text{N}_2$ ($0 \leq x \leq 10$), $0.5\text{C}_6\text{H}_{14} + 4.5\text{O}_2 + x\text{N}_2$ ($0 \leq x \leq 3$), and $\text{C}_3\text{H}_8/\text{C}_4\text{H}_{10} + \text{air}$. In the first setup distributed non-equilibrium nanosecond discharge was used for mixture excitation and ignition. In the second setup localized microsecond spark discharge was used. Electrical parameters of the discharge, ignition delay time, flame front and shock wave velocities were measured in the experiments. Under the experimental conditions, three modes of flame front propagation were observed: deflagration, transient detonation, and Chapman-Jouguet detonation. Essentially higher efficiency of non-equilibrium high-voltage nanosecond discharge as a detonation initiator has been shown: in the setup with distributed non-equilibrium ignition, the length of the deflagration to detonation transition amounted to less than 1 tube diameter in $\text{C}_3\text{H}_8 + 5\text{O}_2$ mixture at initial pressure of 0.3 bar under initiation energy of 70 mJ. Under this kind of initiation, deflagration to detonation transition was also observed at 3 calibers from the discharge chamber in different $\text{C}_3\text{H}_8/\text{C}_4\text{H}_{10} + 5\text{O}_2 + x\text{N}_2$ mixtures with N_2 concentrations up to 38%. The energy input in these cases did not exceed 3 J, the DDT time was less than 1 ms. In the setup with initiation by localized microsecond discharge with stored electrical energy of 14 J, a single spark discharge formed. It ignited the mixture efficiently, but the deflagration to detonation transition length and time increased significantly. Thus it can be concluded that the simultaneous mixture ignition in a large number of discharge cells using non-equilibrium mixture excitation together with Zeldovich's gradient mechanism leads to the rapid formation of a detonation wave.

Chapter 2

The Study of the Discharges Used for PAI/PAC

2.1 The review of discharges used for combustion and ignition control

The ignition of fuel-oxygen and fuel-air mixtures is an important topic in fundamental and applied combustion research. Using relatively simple fuels, we can understand the exact mechanism of combustion initiation, while complex fuel blends more adequately represent the potential end application. As for simple fuel-oxidizer mixtures, ignition delays for autoignition in high-temperature regions were investigated for decades¹⁻³ and can be satisfactorily described numerically by using standard kinetics, such as, for example, a GRI-Mech mechanism.⁴ The ignition delay is the time between start of the process, i.e. heating or the mixing of gases, and the time of an abrupt increase in the temperature, pressure, emission intensity and rate of chemical reactions. The ignition delay depends upon the rate of the dissociation reaction, which is endothermic. The additional production of atoms and radicals at the initial moment can significantly decrease the ignition delay. Presently, various methods of acceleration of ignition are regarded.

A key issue of the ignition studies at strongly non-stationary conditions is the relationship of various mechanisms and processes at the stage of initiation. A relative role of gas vibrational and electron level excitation, ionization and dissociation is being deeply discussed.^{5,6}

Laser methods have some disadvantages, mainly related to the impossibility of providing a high uniformity of ignition initiation in large combustible gas volumes. This is a reason why researchers try to realize multi-point ignition.⁷ Different mechanisms, such as laser induced thermal processes, photoprocesses, laser-induced spark development, and so on,⁸ have to be considered to explain the observed dependence of ignition process upon the system parameters. Experimental analysis has been performed for different wavelengths and for different parameters of the system (gas mixture, pressure, etc.)^{8,9}

A direct comparison of the ignition by three different lasers (ArF, KrF, Nd:YAG) with electric spark was performed for a four-stroke single-cylinder typical high-pressure combustion chamber.¹⁰ It was shown that at comparable total energy consumption (about of 50 mJ), practically the same pressure profile is obtained for both laser and spark ignition. At the same time, the ignition delay of the electric sparks was 4-6 ms longer

than that involving laser sparks.

The spark ignition itself imposes essential restrictions on the system geometry. Spark ignition was mainly investigated in connection with ignition in Otto engines. Detailed 2D modelling of hydrodynamics together with chemical kinetics¹¹ and a comparison with LIF measurements of OH radicals¹² are available in this field.

Ignition by the direct injection of an arc discharge is interesting for hypersonic applications. The most typical geometrical configuration includes a turboblower with a special system of fuel injection and a plasma torch system where one of the electrodes is a metallic nozzle. In this case, ignition limits strongly depend on the system geometry, for example, on the location of the plasma torch in relation to the fuel injectors, on the penetration height of the plasma torch, which is in inverse proportion to flow velocity,¹³ etc.

In spite of the presence of different ignition methods, the problem of a fast and homogeneous ignition of a combustible mixture remains topical. In this paper, the homogeneous ignition method is proposed, which is fast in comparison with the characteristic times of combustion processes and gas dynamics. The method is based on the use of a nanosecond high-voltage discharge in the form of a fast ionization wave (FIW) producing atoms, radicals, and excited molecules. The fast ionization wave originates at very high – hundreds of percent – overvoltage on the electrode system, that is the case where the voltage, at the moment of the discharge initiation, significantly exceeds the threshold of the initiation of a stationary glow discharge. From the point of view of the experiment, this means a high rate of voltage rise – 1 kV/ns and higher. A typical pulse amplitude is tens – hundreds of kV and a duration is 10 – 100 ns. The most distinctive features of this type of discharge are the high propagation velocity (10^9 - 10^{10} cm/s), the good reproducibility of the discharge parameters, and the spatial homogeneity over a large gas volume. These properties may be interesting for different applications, such as hypersonic combustion or the ignition of lean mixtures. A review of our papers concerning the kinetic approach to this discharge and a detailed description of the nanosecond technique of data registration is given in.¹⁴

The high electric field in front and behind the FIW results in an effective gas ionization, dissociation and excitation. At the same time the gas translation temperature does not essentially change. The nonequilibrium energy distribution makes it possible to provide a high efficiency of the FIW as an ignition initiator, at low power input. The discharge produces relatively small amounts of active particles, such as O or H atoms. But even in the case of a low dissociation degree ($10^{-3} - 10^{-5}$) it dramatically influences the kinetics in the high-temperature system.

This chapter discusses plasmas applied for plasma assisted ignition and combustion. Special attention to experimental and theoretical analysis of some plasma parameters, such as reduced electric field, electron density and energy branching for different gas discharges, are given. Streamers, pulsed nanosecond discharges, dielectric barrier discharges, radio frequency discharges, atmospheric pressure glow discharges are considered.

Considering the combustion/ignition problem we are dealing with chemistry at moderate or high gas densities and temperatures typical for ignition and combustion, that is about of 500 – 3000 K. Gas densities mostly important for combustion start from $10^{17} - 10^{18}$ cm⁻³, which corresponds to conditions of hypersonic flight and such densities may be as high as 10^{21} cm³ at conditions of high pressure turbines or in automobile engines. At ambient temperature this corresponds to a pressure range from a few Torr to

tens of bar.

Spark discharge, widely used for ignition in technical systems, arises when high voltage is applied to a discharge gap which is typically about of mm in length. A spark discharge develops as an arc, except for two stages, that is the initial short (1-10 ns at atmospheric pressure) breakdown stage and, possibly, the final stage (milliseconds) caused by hydrodynamic extension of discharge volume that decreases the current.

Atmospheric pressure arc is a most typical and widely spread example of dense low-temperature equilibrium plasma, supported by electric field.¹⁵ This kind of discharge is characterized by sloping down volt-ampere characteristic (that is voltage decrease under current), relatively low voltage drop at the discharge gap (less than hundreds of A), high currents (from parts of A to several kA depending on the impedances of the external circuit), and, that is more important, high gas temperature in the arc (thousands of K). Since this paper is not aimed at an analysis of thermally equilibrium plasma, we will refer to only one of the latest reviews¹⁶ considering main peculiarities of arc plasma as exemplified by numerical modeling.

Actually, a spark discharge developing arc plasma is obtained when a rather long high-voltage pulse is applied to a system of two metallic electrodes divided by a gas layer. Remarkable change of the plasma parameters may be obtained under modifying either the system of electrodes or the shape of high voltage.

2.1.1 Streamer discharge

We observe development of a streamer discharge when high voltage pulse having rather steep front breaks at a time interval comparable with that necessary to cross the discharge gap (a few ns for atmospheric pressure in a few mm, up to cm gap length). Actually, a streamer discharge under atmospheric pressure is an initial stage of a spark breakdown. The existence of two definitely spatially separated regions particularly characterize the streamer. The regions are a streamer head, where high reduced electric field (hundreds of Td) arise and a streamer channel with relatively low electric fields and high conductivity. Formation of a streamer discharge occurs when the electric field in a streamer head is comparable or exceeds the value of the external electric field in the gap (the so-called Mike and Loeb criterion). Streamer velocity, reduced electric field in a streamer head, electron density are defined by the processes in the streamer's head, and the main role of conductive channel is to maintain the head electric potential.

The main production of active species energetically efficient for combustion initiating, which are mainly electronically excited atoms and molecules occurs in a streamer head; this is confirmed by experimental control of the electric field and emission of electronically excited states. Visually the development of a streamer discharge looks like threading of thin filamentary channels between the electrodes, here the branching depends drastically on the gas pressure within the discharge cell.

Sometimes, there appears some kind of misunderstanding in terms that from time to time arises when describing gas discharges. "Filamentary" structures that are optically observed not always mean that streamer plasma has been obtained. For example, when microwave discharge is propagating under atmospheric pressure¹⁷ there is observed definite filamentary spatial structure, that is likely to present thin hot channels of plasma close to equilibrium. Though it is sometimes called "microwave streamers", it does not seem

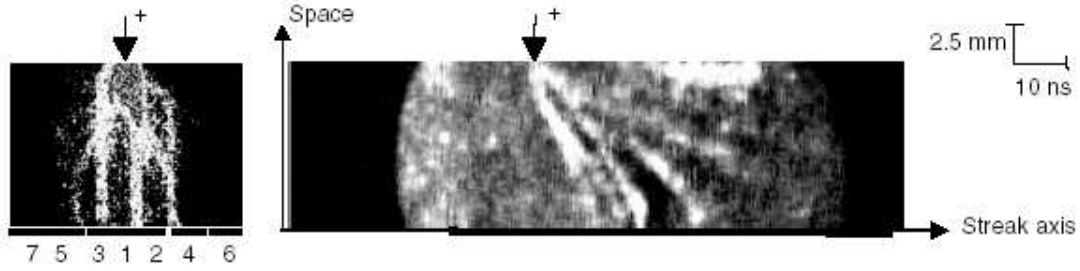


Figure 2.1: Example of still (left) and streak (right) images of a streamer emission²⁸.

to have anything in common with streamer.

A grate number of papers devoted to a streamer discharge describe the main peculiarities of this phenomenon on the basis of either experimental investigations or mathematical modeling. Nowadays a whole set of papers are considered classical. Here it is worth mentioning the papers by Galimberti and co-workers^{18,19} who proposed a model of numerical description of cathode-directed streamer and analysed a possible impact of accumulating vibrationally excited metastable N_2 molecules on the streamer development; by Williams and co-workers,²⁰ who presented the calculations of the streamer in 2D geometry using flux-corrected transport techniques; by Kunhardt and co-workers,²¹ who discussed avalanche-to-streamer transition as a first stage of the streamer development, differences between cathode-directed and anode-directed streamers, the role of photoionization and “run-away” electrons.

The authors of²² considered in detail the processes in streamer channel, particularly they reported that the electron density in the channel is governed by an electron attachment and electron-ion recombination and that the gas heating in streamer channel is not larger than tens of K. The theory of streamer initiation and development was proposed taking into account elementary processes, such as ionization, attachment, recombination, electron diffusion, and photoionization.²³

The authors of²⁴ proposed 2D simulation model to describe the propagation of a negative (that is anode-directed) streamer in plane-to-plane geometry with spatial resolution of $\leq 5 \mu m$ that can be applied to arbitrary shaped electrodes. Practically at the same time a positive streamer in weak uniform electric field was calculated in 2D geometry.²⁵

Calculations of this kind provided a possibility to relate such parameters of a streamer channel as propagation velocity and channel radius to the parameters of the external electric field and the voltage applied. At present the calculations of streamers are being carried out for various gases, for different shapes of supplying voltage,²⁶ for long (more than 10 cm) discharge gaps.²⁷

Streamer branching is extremely important for description of streamer development, starting with several mm discharge gap. This feature has been extensively investigated experimentally.^{28,29} Fig. 2.1 definitely depicts streamer branching in a few mm discharge gap registered in air at atmospheric pressure. The emission corresponds to second positive system of molecular nitrogen. The figure on the left presents an image taken by ICCD – camera with a gate of 100 ns, whereas the one on the right gives a streak-image with a duration of 50 ns.

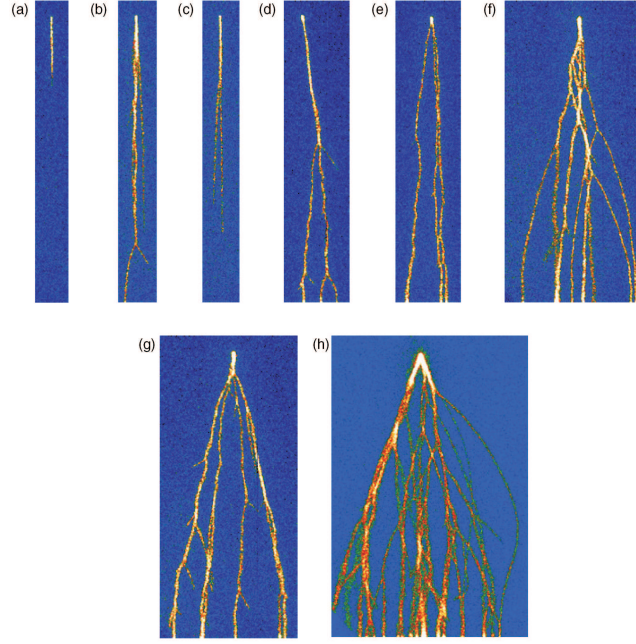


Figure 2.2: CCD photos of a plane-protrusion discharge in air using the semiconductor switch. The applied voltage is (a) 9 kV, (b) and (c) 10kV, (d)(g) 12.5 kV and (h) 15 kV. The optical gate is (a)-(e) $5 \mu s$, and (f)-(h) $50 \mu s$.²⁹

ICCD-images obtained with relatively long gates ($5\text{--}50 \mu s$, see Fig. 2.2) in fact present an integrated picture of discharge development, especially taking into account that long pulse durations (hundreds of ns) are used. This means that their physical interpretation requires more detailed investigation using high temporal resolution. Nevertheless these images provide a brilliant qualitative picture of streamer development in the gap of tens mm.

The image in Fig. 2.3 is taken with high temporal resolution (camera gate is equal to 0.8 ns). It is clearly seen that the emission mainly corresponds to the streamers heads in a streamer flash. This one more testifies that high-energy electronic degrees of freedom are predominantly excited in a streamer head.

Though there have been numerous attempts to describe streamer branching numerically for a few years recently,^{30, 31} there is still some doubt about whether these codes describe real physical instabilities in the streamer front or the observed branching is caused by specific features of the numerical schemes used.

Discharge modification with pressure was studied in.³² The authors reported that the discharges at several atmospheres are widely used for triggering combustion in cars and that their properties are not fully understood since the size and duration of the discharges become very small at high pressures, which makes the experimental approach more difficult. They investigated the discharge development at atmospheric pressure and at 6 bars.

They kept constant Nt value (N is gas density, t is voltage rise time) to obtain similarity in discharge development. Thus, the voltage raised up to 26 kV during $50 \mu s$ at 6 bar, whereas during $300 \mu s$ at 1 atm. Note that they observed a significantly lower (by 6 kV) initiation voltage of the discharge under a steeper voltage, that is at 6 bar.

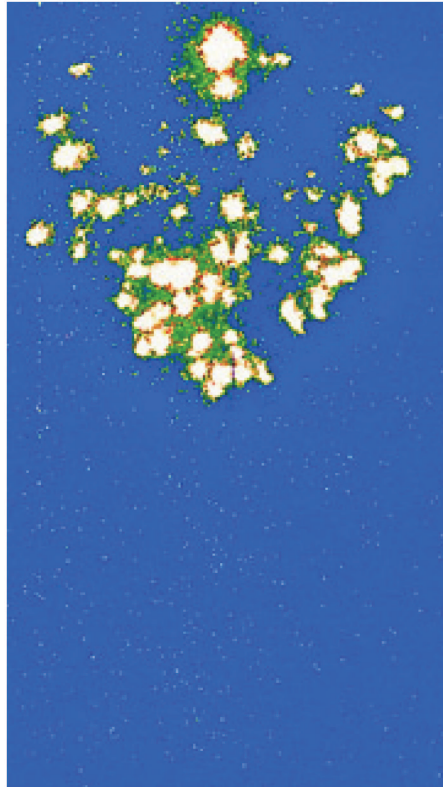


Figure 2.3: Photograph of streamer heads of a point-wire discharge in air taken with the ICCD with 0.8 ns gate. A pulse of 25 kV with a rise time of 20 ns is applied. The photo is taken 31 ns after the start of the pulse. Discharge gap is 25 mm, plane-to-plane geometry²⁹.

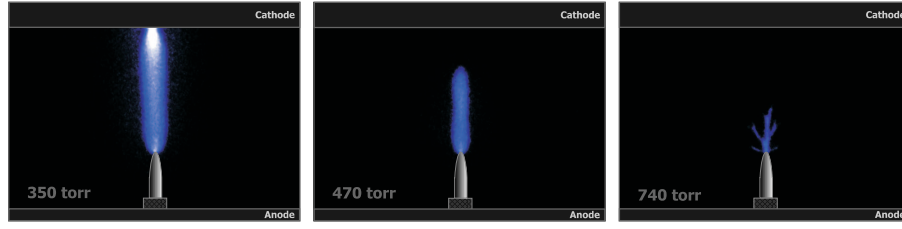


Figure 2.4: ICCD images of streamer in air at different pressures. Interelectrode gap is 30 mm, high voltage amplitude is 20 kV, and pulse duration is 25 ns. According to³⁴.

Having analyzed the results, the authors concluded that the leader channel is formed and thermally equilibrium plasma is produced. This seems questionable since the discharge current remained rather small and did not exceed the values typical for streamers (tens and hundreds of mA).

Another example of streamer modification with pressure is shown in.^{33,34} The authors demonstrated that under decreasing pressure the streamers initiated by a voltage pulse of 22 kV amplitude at high-voltage electrode and 20 ns duration stop branching and propagate as a single channel, whereas the channel diameter increases under decreasing pressure. Fig. 2.4 presents ICCD-images of a streamer emission at different pressures as an illustration.

Investigations of streamers produced by 50 ns pulses with pulsed voltages 10 kV, at pressures from 1 to 10 atm at ambient temperature, show³⁵ that the streamer's diameter decreases, and the number of branches increase with pressure.

As a rule, experimental investigations of streamer discharge are restricted to controlling electrical parameters, such as discharge current, voltage across the gap, and to measuring emission. Emission control with high spatial and temporal resolution makes it possible to determine the streamer's optical diameter and the velocity of propagation.

The papers considering applications of standard measurement techniques to investigate a changing object are of particular interest because such an approach facilitates study of parametrical dependence of different variables. For instance, paper³⁶ described the study of streamer development in preliminary heated gas at constant pressure within the temperature range from ambient to 450 K. It was demonstrated that the diameter of the emitting region increased when density decreased (see Fig. 2.5). Variations of the electric field required for propagation of a streamer in air and streamer propagation velocity were also discussed.

As for plasmachemical applications, such as PAI/PAC, there are a limited number of plasma parameters that are of vital interest. They are electric field value, electron number density, densities of atoms, radicals, and excited species produced in plasma, gas temperature. Regretfully, the experimental information here is rather limited. This is justified by fast development of discharges (typical time scale being nanoseconds), spatial inhomogeneity, as well as changeability of a streamer flash.

A detector based on Pockels effect was used to determine the electric field under streamer-leader transition in air at atmospheric pressure.³⁷ Time response of the detector is determined by temporal resolution of opto-electronic converter, that insures applying it even in picosecond time range. The detector can be relatively small (a few mm in size), it is made of dielectric and that is why it causes weaker distortion than a conductor

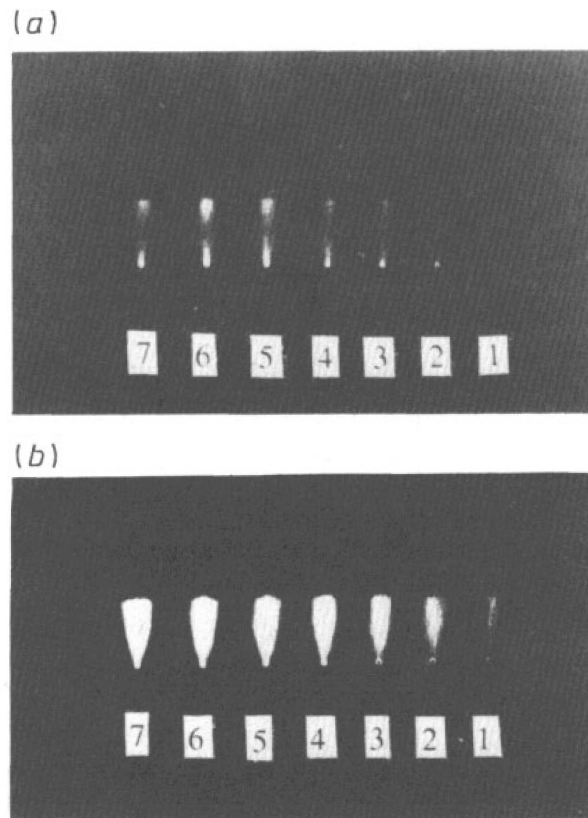


Figure 2.5: The effect of temperature on streamer propagation³⁶. Numbers indicate the number of superimposed shots: a) $T=290$ K and b) $T=373$ K. The applied electric field was 500 kV m^{-1} ; with pulse voltage 4.25 kV and gap length 15 cm .

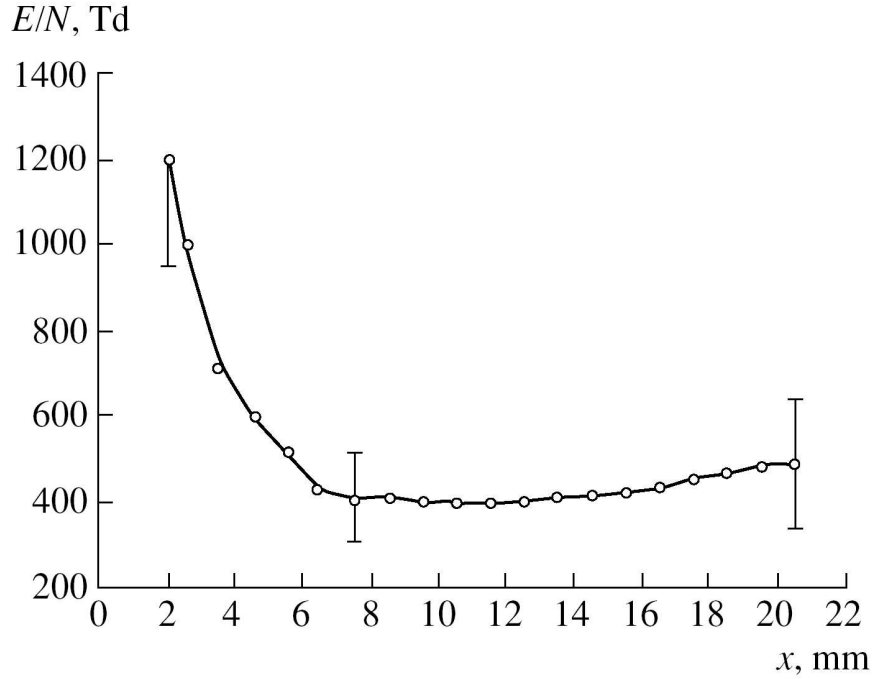


Figure 2.6: Reduced electric field in the streamer head *vs.* the distance from the high-voltage electrode for the interelectrode distance equal to 24 mm⁴⁰.

in plasma. But when electric fields are high, polarization of dielectric leads to local field increase in plasma, that increases the rate of ionization and distort the electric field around the detector.

It is possible to control electric field in the streamer discharge using contactless techniques, for example, controlling the ratio of emission intensities of first negative and second positive systems of molecular nitrogen. Such technique is discussed in.^{38,39} Typical values of the electric field in streamer head reach hundreds of Td. Fig. 2.6⁴⁰ illustrates electric field behaviour in a streamer flash initiated by a high voltage pulse about 20 kV in amplitude (at the high-voltage electrode) and 25 ns duration at repetitive frequency about 1 kHz. The emission was extracted by a narrow slit diaphragm perpendicular to the gap axis. This means that the data are spatially averaged, nevertheless, due to relatively short duration of a high-voltage pulse (75 ns at halfheight), they give a reasonable value of electric field in the streamer head at propagating a slightly branching streamer flash.

This paper also contains linear densities of excited species measured by absolute emission spectroscopy. In particular, when we assume the streamer's diameter to be 1 mm, the density value of the excited nitrogen will be 10^{12} cm^{-3} at the given value of $[\text{N}_2(\text{C}^3\Pi_u)] \approx 10^{10} \text{ cm}^{-1}$ linear density.

Paper⁴¹ can be regarded as one among few examples of direct measurements of radical density. The authors reported measurements of hydroxyl radicals generated by a pulsed corona discharge by laser-induced fluorescence (LIF). The discharge with 35 kV voltage and 100 ns pulse current was initiated between needle and plate electrodes in $\text{H}_2\text{O}:\text{O}_2:\text{N}_2$ mixtures at atmospheric pressure. The OH density is estimated to be about $7 \cdot 10^{14} \text{ cm}^{-3}$ in $\text{H}_2\text{O}(2.4\%):\text{N}_2$ mixture 10 μs after the discharge. Unfortunately, the measurements refer to OH control only in late afterglow of the discharge that hinders analysis of dis-

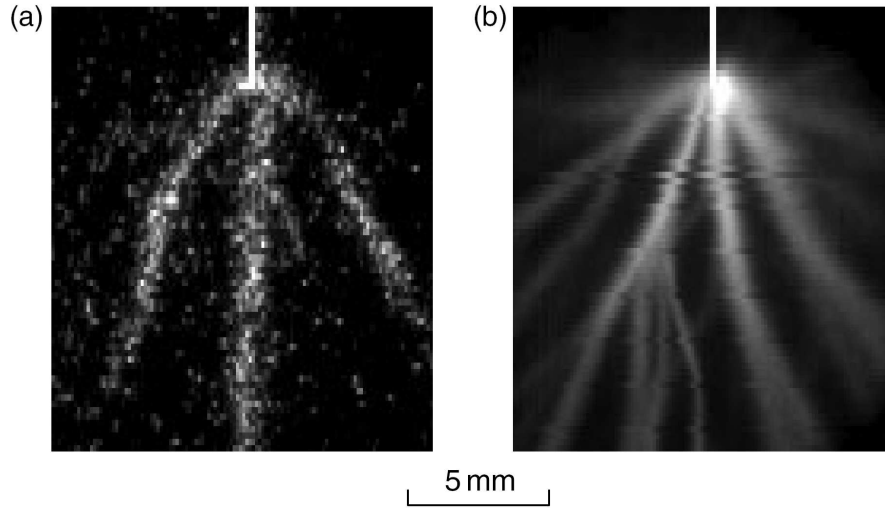


Figure 2.7: (a) Distribution of OH radicals at $5 \mu\text{s}$ observed by the two-dimensional LIF and (b) spontaneous emission of a positive discharge in $\text{H}_2\text{O}(2.4\%):\text{N}_2$ mixture⁴¹. Each image is obtained at a different discharge pulse. The white line represents the needle electrode. Discharge gap is 16 mm.

charge kinetics. On the contrary, spatially resolved absolute measurements of OH density (Fig. 2.7) can be considered as undoubted advantages. The same authors investigated NO production in a similar pulsed discharge in $\text{N}_2:\text{O}_2:\text{Ar}$ gas mixture.⁴²

Thus, it is known that the streamer discharge is a nonequilibrium low temperature plasma with relatively high electric fields in the streamer's head and low fields in the channel. At moderate pressures and when voltage amplitude ranges from units to tens of kV across the discharge gap of a few cm the streamer is developing without branching under condition when the voltage rise is quite fast and the pulse is short to prevent propagation of secondary streamers. The streamer's diameter decreases and branching becomes more pronounced with pressure growing. At present 2D streamer codes are well developed and they support modeling of streamer propagation at gaps up to 10 cm. Nevertheless, the problem of a relative importance of elementary processes responsible for initiation and development of the streamer under different experimental conditions is still being discussed and clarified. Production of electronically excited states able to dissociate mainly occurs in the streamer's head, though some researchers do not deny a possible role of superelastic collisions in the streamer's channel causing additional dissociation at interaction of relatively low energy excited states.

2.1.2 Dielectric barrier discharge

A discharge that occurs in electrode system under condition when at least one electrode is covered by dielectric is called a dielectric barrier discharge (DBD).⁴³ Sometimes it is referred to as either a silent discharge, since it operates noiselessly,⁴⁴ or corona discharge with dielectric⁴⁵ according to physics of process. In case of a pulsed power supply with a short nanosecond rise time and pulse duration of tens-hundreds of nanoseconds the dielectric barrier restricts the current and hinders transition of the discharge to the arc

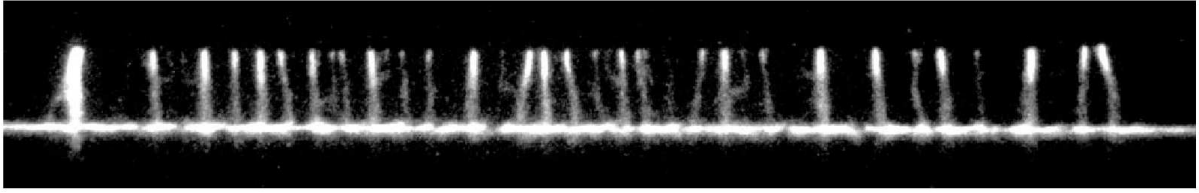


Figure 2.8: Short-time-exposure photographs of a filamentary DBD (anode, top; cathode, bottom) from a single voltage pulse (800 ns exposure time, N_2 , 3 l/min, 1 atm, interelectrode distance 1.7 mm, repetition rate 2000 Hz⁵¹).

form.

In the first place let us turn to a traditional scheme of barrier discharge and discuss some historical points. The barrier discharge has been extensively investigated for nearly 50 years since it is widely used for ozone generation. Until today the process of ozone production by DBD has been studied in detail and has been widely applied in industry. There are papers, for example,^{46,47} that have presented quite exhaustive reviews on ozone synthesis in DBD.

Investigations of electric characteristics of barrier discharge provided determining the main regularities of its development. As a rule, a discharge is generated in either a plane-to-plane or coaxial geometry where one or both electrodes are covered with dielectric. The gap between the electrodes is rather small and is not higher than a few mm. The gas is flowing relatively slow through the system and the electrodes can be additionally cooled. A few kV peak-to-peak sinusoidal high voltage is applied to the electrodes. At this the discharge is initiated twice a period.

The detailed investigation of the discharge structure^{48–49} has demonstrated that the breakdown occurs under certain voltage demonstrating filamentary microdischarge structure. Typical diameter of a microdischarge is a few mm.⁵⁰ The above mentioned means that the development of DBD physically resembles an incomplete streamer breakdown. Fig. 2.8 (⁵¹) presents a typical image of DBD. The reactor used was of knife-to-plate geometry with the length of a knife electrode of 2.5 cm and with the gap distance of 1.7 mm. The grounded plate electrode was covered by a 1 mm thick quartz plate. The image was taken for flowing dry nitrogen (flow speed of 3 l/min) at atmospheric pressure.

When sinusoidal voltage applied to a gap the current pulses are not longer than tens of nanoseconds and in this case their duration is limited by dielectric layer charging. Fig. 2.9 a (⁵²) demonstrates typical current and voltage oscillograms in the barrier discharge in air under atmospheric pressure, whereas Fig. 2.9 b,c present a temporally resolved current pulse of a separate microdischarge and current pulse of a series of microdischarge, respectively. The sinusoidal curve presented in Fig. 2.9 a denotes the voltage shape across the gap with peak-to-peak applied voltage being 13.2 kV. Note that the distance between electrodes varied from 0.5 to 1 mm in these experiments.

It should be mentioned that spatially resolved kinetic measurements of active species in DBD are rather complicated because of sharp spatial inhomogeneity and short inter-electrode distance. Nevertheless, due to general repeatability of the picture, these measurements are still much easier than these in “classical” streamer discharge. This seems to be the reason why greater number of experimental papers are devoted to measurements of electric field, temperature and particles density.

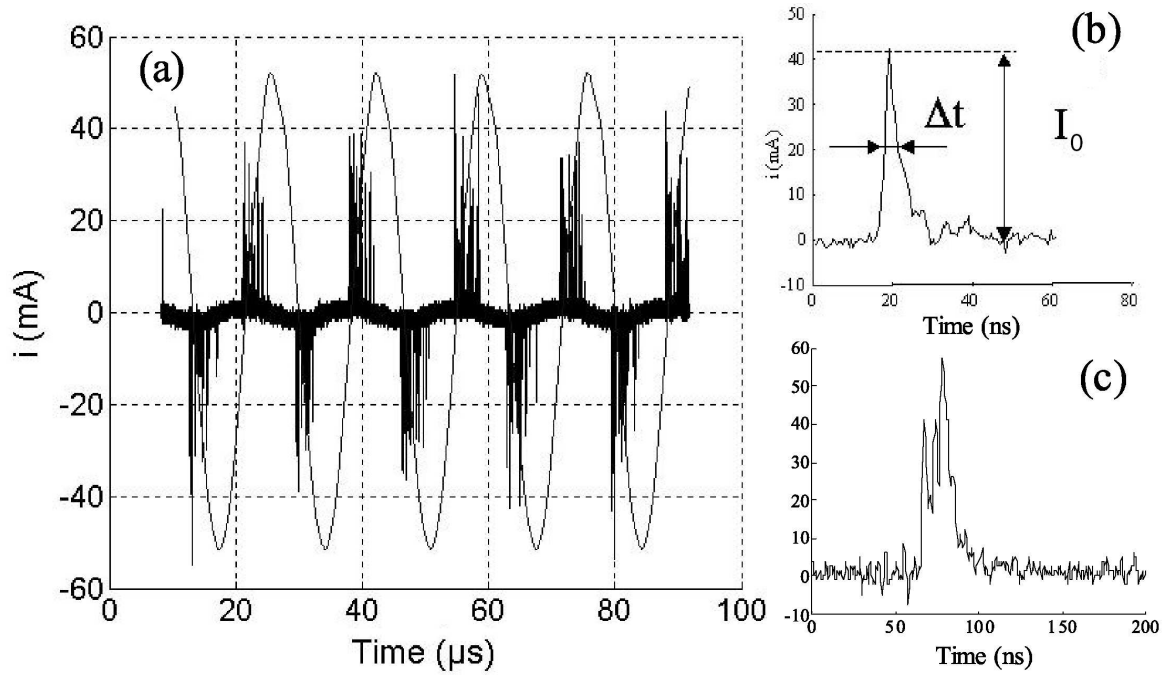


Figure 2.9: (a) Voltage and instantaneous current, (b) single current pulse and (c) series of current pulses, typical for DBD-discharge⁵².

Detailed investigation of the electric field and electron density at a separate microdischarge has been performed in.⁵³ The authors designed a discharge cell (Fig. 2.10 a) so that the discharge consisted of a single and well reproduced microdischarge. Basing on measurements of emission of the second positive and the first negative systems of molecular nitrogen, the authors obtained the values of the electric field in the microdischarge. It is perfectly seen from Fig. 2.10 b that under the microdischarge propagation the field's maximum reaches a few hundreds of Td that is close to the value of the electric field in the streamer's head.

A certain number of charged, excited and dissociated species is produced in the microdischarge when DBD develops in the discharge gap. Papers^{54–55} presents calculations of gas composition after DBD development on the basis of experimental data on electrical parameters in the system.

A more recent paper⁵⁶ gives the results of measurements and detailed calculations of ozone and nitric oxides in DBD discharge in flowing O_2/NO_x and $N_2/O_2/NO_x$ mixtures at typical admixtures of NO_x up to 2000 ppm. They demonstrate that the gas temperature in the discharge does not exceed 440 K, and that the typical O_3 densities are within 10^4 ppm that means that they obtained up to 1% of O_3 which is typical for DBD-type ozonizers.⁴⁷

Direct measurements of dissociated particles in DBD microdischarge are of particular interest. So, in⁵⁷ space and time resolved relative atomic density distributions of nitrogen were measured for the first time at a single filament within a dielectric barrier discharge (DBD) reactor with submillimetre radial dimensions. Two photon absorption laser induced fluorescence (TALIF) spectroscopy using radiation at $\lambda = 206.7$ nm was used for N-atoms mapping. Specially designed multi-pin reactor was taken to carry out

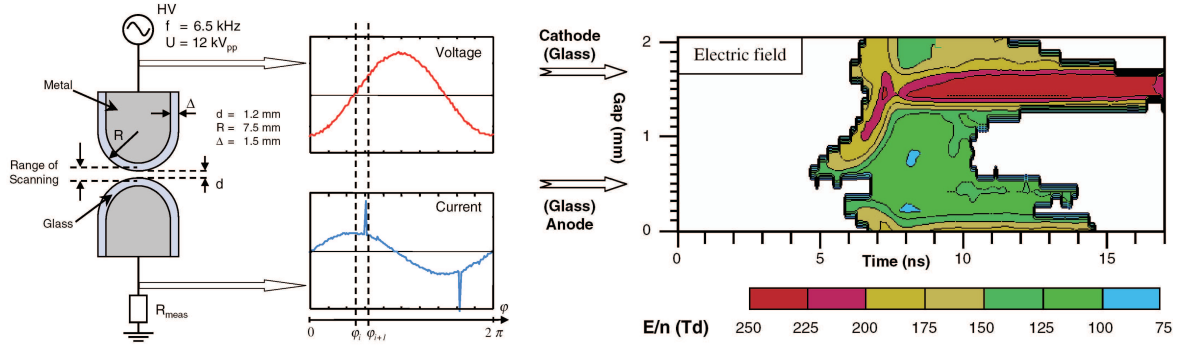


Figure 2.10: (a) Electrode arrangement with the indicated range of axial scanning and a typical example of the oscillograms of voltage and current; (b) Determined distributions of electric field and electron density. The positions of the tips of the electrodes indicated by the arrows on the left⁵³.

2D TALIF measurements moving the discharge cell relative to a laser beam. The authors used high voltage, rising in 90 ns to 15 kV, and the voltage pulse duration was about of 200 ns at half-height. N-atom image from⁵⁷ is reproduced in Fig 2.11. The authors performed numerical modeling that made it possible to compare spatial distribution of nitrogen atoms with the data obtained experimentally. Absolute calculated density values of N-atoms are $(4 - 6) \cdot 10^{14} \text{ cm}^{-3}$ for conditions similar to those in the experiment demonstrating analogous spatial distribution.

Paper⁵⁸ presents the results of TALIF-control (zero-dimensional but time-resolved) of relative densities of atomic oxygen in DBD initiated in point-to-plane geometry in nitrogen-oxygen mixtures under various humidities (from 0 to 2.4%). It was demonstrated that the decay of O-atoms density occurs with different rates on the scale of tens of μs when the production of atomic oxygen is the same and O-densities are equal in the early afterglow (less than 1 μs). Possible chemical reactions causing O-atoms decay at different humidity are discussed.

The gas temperature at the exit of a discharge cell significantly depends on the system itself since when the interelectrode distance is short (units of mm), the heat removal through the electrodes is important. As a rule, gas temperature in a discharge zone is measured using spectroscopy techniques.

The authors of⁵⁹ measured the rotational temperature of the emission of molecular nitrogen ions in order to obtain the gas temperature in the microdischarge areas and in the ambient gas of dielectric barrier discharges in helium/nitrogen mixtures. DBD discharge was initiated by sinusoidal voltage of 19.7 kHz frequency and peak-to-peak amplitude 3500 V. There the current pulses were much longer than the value obtained in filamentary discharges, which typical value is ≈ 10 ns and were comparable with the pulses at atmospheric pressure glow discharges (APGD) in pure helium (about of 1 μs). The authors did not observe a single current pulse, that is typical for uniform APGDs, but a series of pulses. They calculated the rotational spectra of the transition $\text{N}_2^+(\text{B}^2\Sigma_u^+ \rightarrow \text{X}^2\Sigma_g^+)$ using a known reaction scheme for discharges in helium/nitrogen mixtures. The scheme included direct ionization of nitrogen by an electron impact and Penning ionization. As a result, they obtained 400–600 K for a microdischarge region and 300 ± 10 K for ambient gas temperature within the discharge cell.

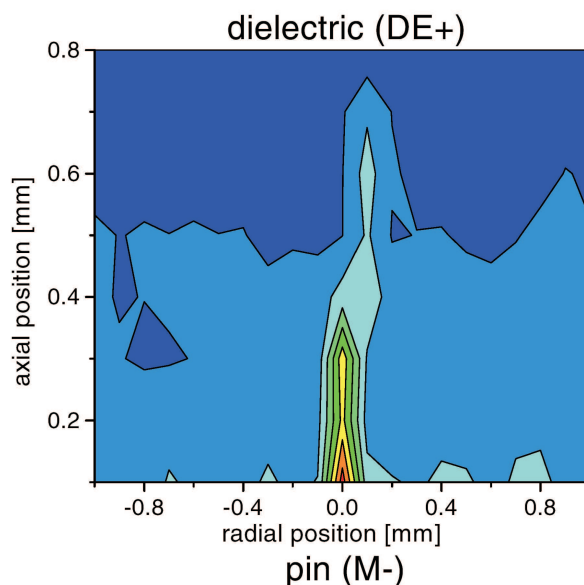


Figure 2.11: Density distribution of atomic nitrogen in a DBD at 950 mbar, containing 90% N₂ and 10% O₂; 8 kV voltage; positive dielectric (DE+); 2 μ s after discharge initiation. Light colours correspond to low densities, dark colours to high densities⁵⁷.

The bulk gas temperature in 30% N₂:70% Ar mixture in short-pulsed (< 15 ns) DBD was reported in.⁶⁰ The temperature was determined using time-resolved diode-laser absorption of metastable Ar 4s' [$\frac{1}{2}$]^o and the rotationally resolved N₂⁺ 1st negative and N₂ 2nd positive systems emission. The gas temperature, derived from the nitrogen emission spectra, was determined from contour analysis of individual vibrational bands, while the temperature under the same conditions was taken from the Doppler width of the metastable Ar absorption spectrum. The gas temperature measured for a low average power DBD at pressures of 10, 30, and 100 Torr and pulse repetition rates of 0.5–30 kHz was found to be 350–400 K and did not vary with pulse repetition rate.

Coherent anti-Stokes Raman scattering (CARS) measurements of gas temperature⁶¹ in DBD with different shapes of electrodes in N₂:O₂:NO mixtures under pressure of 20 and 98 Pa, bipolar high-voltage pulses of 10 kV at a pulse repetition rate of 1 and 2 kHz gave the following values: rotational (gas) temperatures about room temperature and vibrational temperatures of about 800 K at atmospheric pressure and 1400 K at pressure of 20 kPa.

It is interesting to note that as far back as in the 70th of the last century there were scientists who pointed out at increasing of plasmachemical efficiency of DBD under replacing commercial frequency sinusoidal power supply by pulsed nanosecond voltage. Thus, it was demonstrated that using of pulsed nanosecond power supply provides increasing efficiency of ozone synthesis in oxygen from 90 to 130 g/(kWt·h).⁶² Similar results were reported in,⁵¹ where the authors applied low repetition frequency, high-voltage unipolar square pulses with amplitude up to 15 kV, rise and fall times less than 20 ns to drive DBD. According to their experiments, this excitation method of DBDs improves the energy efficiency for ozone synthesis to 8–9 eV per ozone molecule, that is 30% improvement compared with common sinusoidal excitation.

These authors also studied transformation of the discharge into a homogeneous form

under pressure decrease. The experiments were conducted in air at 40 Torr pressure and 4 cm interelectrode distance.

For last 10-20 years the theoretical and experimental investigations of DBDs have been mainly guided by their applications to surface treatment and plasma chemistry including, for example, ozone production and gas cleaning.

Paper⁶³ gives a detailed review of recent work carried out on the numerical modelling of non-thermal gas discharge plasmas in air at atmospheric pressure. The authors described the theory of discharge development for dielectric barrier discharges, techniques and approaches to numerical modelling of low-temperature plasma at atmospheric pressures, including streamers at different electrode configurations (point-to-plane, plane-to-plane) and interelectrode gaps (from mm to units of cm). The importance of the authors' approach is in their underlining the general physical nature of the streamers and DBD microdischarges when they are propagating through the interelectrode gap.

So, the dielectric barrier discharge is a streamer discharge in which the current is restricted by charging of the dielectric layer. In this type of discharge the typical gas temperature is close to ambient temperature, the electric fields that are not higher than hundreds of Td are close to the fields in the streamer, and densities of dissociated and excited species are within the range of $10^{12} - 10^{14} \text{ cm}^{-3}$, according to different papers. Note that the electron density has not yet been measured experimentally either in the streamer or in DBD, whereas typical results of numerical calculations have produced the value of about 10^{12} cm^{-3} for streamers in air under atmospheric pressure.

2.1.3 Atmospheric pressure glow discharge

Ironically enough, two types of discharge investigated at principally different electrode configurations and different power supply by different groups of researches, have been given the same name. Fortunately, this name represents the physical nature of these discharges quite well.

The first one was obtained at sinusoidal power supply and in the configuration of electrode system similar to that of DBD. In 1988 the authors of⁶⁴ observed a stable glow plasma at atmospheric pressure conducting experiments of plasma treatment. They changed the structure of electrodes, the kind of dilute gas, and the frequency of power. On the basis of their experiments they proposed the following requirements for a stable glow discharge in DBD system: (i) helium is to be used as dilute gas; (ii) an insulating plate is to be set on the lower electrode plate; (iii) the brush-style electrode is to be used for the upper high-voltage electrode (in their experiments it consisted of 25 fine wires of stainless steel or tungsten); (iv) the continuous stable discharge is to be created by using high frequency power supply. The authors used radio frequency (RF) power supply with 3000 Hz frequency, while they failed to obtain a stable discharge at frequency of 50 Hz. On the basis of visual direct observation ("transform to arc" or "dark blue, stable") and of the peculiarities of surface treatment for polyethylene terephthalate (PET) film by $\text{O}_2:\text{CF}_4:\text{He}$ mixture they discussed the difference between arc and glow discharge regimes.

Still another paper⁶⁵ reported the experiments on atmospheric pressure glow discharge (APGD) in plane-to-plane electrodes geometry that is more typical for dielectric barrier discharges. The authors pointed out that the atmospheric pressure glow discharge had

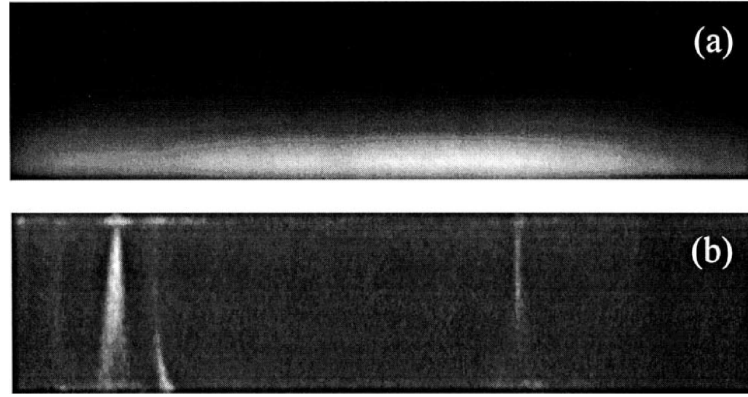


Figure 2.12: Typical 10 ns exposure time photographs of a 4 mm gas gap during (a) an APGD ($V = 11$ kV) and (b) a filamentary discharge ($V = 14$ kV)⁶⁸.

been observed as far back as in the 30th of the last century but in the system of cooled metal electrodes without dielectric barrier and in ambient air. They also noted that development of spatially uniform APGD is accompanied by a single long current pulse in voltage half-period. The current amplitude was about of 10 mA. They concluded that the transition time from glow discharge to arc is extended by adding He gas.

Paper⁶⁶ reported a possibility to sustain spatially homogeneous APGD in plane-to-plane electrode geometry under commercial (50 Hz) frequency of power supply for various gases (air, argon, oxygen and nitrogen). The authors stated that APGD stabilization can be achieved by limiting the current through a separate element of the electrode and proposed to use specially designed wire mesh electrode system. They concluded that referring to paper⁶⁷ which presented current transformation under discharge development from dark Townsend to arc discharge. The authors of⁶⁶ also noted that a single current pulse in voltage half-period corresponded to APGD whereas some irregular number of pulses (typically units-tens) corresponded to filamentary DBD.

Fig. 2.12 given in paper⁶⁸ demonstrates the difference between the views of APGD (upper image) and filamentary DBD (lower image). The images were obtained by ICCD-camera at 10 ns gate.

The following 20 years yielded productive results of extensive research of APGD in configuration similar to DBD configuration. They were proposed complex kinetic models explaining suppression of filamentarisation and transition to the uniform discharge due to accumulation of metastable particles (see, for example,⁶⁸). Electrical and spectroscopical parameters of APGD in plane-to-plane geometry at interelectrode distances up to 1 cm were studied in detail.⁶⁹ As a rule, experimental studies are accompanied by numerical modeling⁷⁰ regarding detailed kinetics including electronically excited particles.⁷¹ A great number of papers consider treatment of different films (organosilicon polymer films,⁷² polypropylene⁷³) by APGD DBD plasma, since using of spatially homogeneous discharge at 1 atm is profitable and technically reliable. The latest conference “Gas Discharges and their Applications” (Toulouse, 5–10 September 2004⁷⁴) highlighted continuous interest to physics of APGD DBD. It is clearly seen from the papers presented for section “Barrier discharges” where 9 of 23 presentations were devoted to atmospheric pressure glow DBD.

The second type of discharge under the same name, as mentioned above, was obtained at DC power supply while cooling the electrodes. In this case gas temperature is much



Figure 2.13: DC glow discharge in air (1.4 kV/cm, 200 mA). Interelectrode distance is 3.5 cm⁷⁹.

higher than in APGD DBD and reaches thousands of K, but still it is much lower than electron temperature, that is the plasma obtained is essentially nonequilibrium. The introduction to paper⁷⁵ contains a brief but physically explicit review evaluating papers concerning investigations of APGD with different power supply including both pioneering studies of the 30-th⁷⁶ and the recent papers.⁷⁷

Papers^{78,79} described DC APGD in nitrogen stabilized by water cooling and gas flow through the discharge cell. The discharge was formed between a pair of platinum pins (separation 0.85 cm) that were vertically mounted on watercooled stainless-steel tubes. Nitrogen passed through the discharge region with a velocity of 20 cm/s. The authors reported electron temperature for obtained plasma being about of $T_e \sim 10000$ K and gas temperature $T_g \sim 2000 - 4000$ K. A typical view of a APGD discharge in air for a 3.5 cm discharge gap is presented in Fig. 2.13.

Spatial profiles of N_2^+ concentration were measured in an atmospheric pressure nitrogen glow discharge by cavity ring-down spectroscopy (CRDS).⁷⁸ At discharge currents about of 100 mA, they reported the radial profiles with radial-half-maximum of about 1 mm. Using a collisional-radiative model they related ion concentrations to electron number densities, and demonstrated a good agreement with spatially integrated electrical measurements. Electron density was within $4 \cdot 10^{11} - 2 \cdot 10^{12} \text{ cm}^{-3}$ at discharge currents in a range of 50–190 A. It is worth noting that the density significantly exceeds (it is 5 times greater at high and tens of thousands times greater at low currents) that obtained using local thermal equilibrium (LTE) approach.⁷⁸

Several optical techniques were presented in⁷⁹ to measure temperature and charged species concentrations in air and nitrogen plasmas. These techniques were applied to both equilibrium and nonequilibrium air or nitrogen plasmas over a wide range of conditions with submillimetre spatial resolution and sub-microsecond temporal resolution. Two kinds of equilibrium plasma (a 50 kW inductively coupled plasma torch flowing at a velocity of 10 m/s and recombining air or nitrogen plasma flowing at a velocity about

Table 2.1: Measured and estimated discharge parameters in APG discharge in air at 0.4 and 10 mA discharge currents. Data are taken from⁷⁵

Parameter	Current is 0.4 mA	Current is 10 mA
Electrode spacing, mm	0.05	0.5
Discharge voltage, V	340	380
Discharge power, W	0.136	3.8
Translational temperature, K	700	1550
Vibrational temperature, K	5000	4500
E/N in positive column, V cm ²	$4.8 \cdot 10^{-16}$	$3 \cdot 10^{-16}$
n_e in negative glow, cm ⁻³	$3 \cdot 10^{13}$	$7.2 \cdot 10^{12}$
n_e in positive column, cm ⁻³	—	$1.3 \cdot 10^{14}$

of 1 km/s through a water-cooled test section) were tested and compared with experiments in a glow discharge generated by a DC electric field in atmospheric pressure air. The gas temperature was controlled using medium-resolution emission spectroscopy of the rotational line structure of selected OH, NO, N₂, and N₂⁺ vibrational bands. Electron densities above approximately $5 \cdot 10^{13}$ cm⁻³ were derived from the Stark-broadened H _{β} lineshape. The concentration of ions was measured by CRDS. Assuming charge neutrality and knowing the ion chemistry, the concentration of N₂⁺ ions was related to the concentration of electrons. The authors reported rotational temperatures equal to 4850 ± 100 K for recombining plasma and 2200 ± 50 K for APGD, while the electron density comprised 10^{15} cm⁻³ for plasma torch and 10^{12} cm⁻³ for APGD.

Paper⁷⁵ analyses in detail DC APGD plasma on the basis of the analogy between APGD and Townsend glow discharge at low pressures. The authors presented a wide picture of the discharge development in air, hydrogen, helium and argon. They analysed rotational and vibrational temperature using registration of emission of the second positive system of molecular nitrogen. They distinguished the APG discharge zones similar to those in the glow discharge both observing them visually (taking photos) and measuring volt-ampere characteristics. The electric field was determined using electrical and spectroscopic experimental data. The electron density was derived from the current. Table 2.1 displays some parameters obtained by the authors. The authors underlined that while comparing of APGD and “common” glow discharge their parameters are to be recalculated not into units of pressure but into units of density. In this case one accounts for changes of density under heating. The measurements are produced as if at “effective pressure” being equal to $P_{eff} = PT_n/T$, where P is the pressure in Torr, T_n is the normal gas temperature (293 K) and T is the actual gas temperature. For example, a reduced electric field for low pressure glow discharges lies typically in the range of 10 – 30 V/(cm·Torr). Using an “effective pressure” P_{eff} , the electric fields at 760 Torr and 1500 K should be in the range of 1.5 – 4.5 kV/cm. These values are in good agreement with those obtained for APGD in.⁷⁵

Analysing the data presented in Table 2.1, one can conclude that, first, the scattering of n_e values may be quite significant and, second, the electric field value ($(3 - 5) \cdot 10^{-16}$ V·cm² = 30–50 Td) is an order of magnitude lower than that in a streamer head and mainly corresponds to excitation of vibrational degrees of freedom.

The authors⁷⁵ concluded that typical features of APGD development in helium, hy-

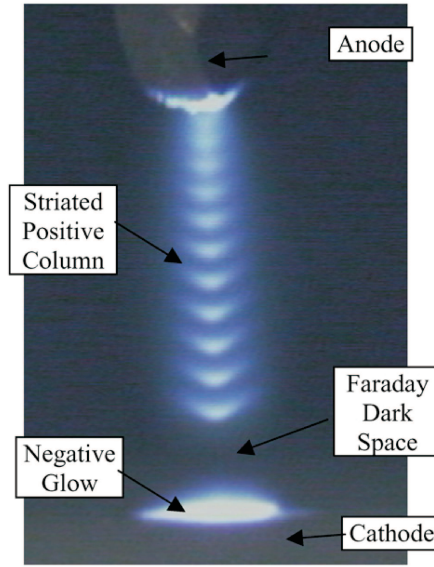


Figure 2.14: Image of the glow discharge in atmospheric pressure hydrogen. Positive column and negative glow are visible; standing striations are visible in the positive column⁷⁵.

drogen and argon resemble to those of glow discharge at low pressures. Thus, (i) each gas has distinct discharge colours and spectral lines corresponding to the species; (ii) in helium the scale of the discharge in every dimension is larger than that for a similar current discharge in air; (iii) in hydrogen the primary column has standing striations under some conditions. An example of APGD in atmospheric pressure hydrogen is given in Fig. 2.14. The regions typical for “common” glow discharges (negative glow, Faraday dark space, and positive column) are clearly seen. As a result, the authors postulated that DC APGD: (a) is a normal glow discharge, (b) is thermally stabilized by its size, that is the electron density is controlled by particle diffusion out of the discharge, namely due to its small radius, (c) leads to relatively low electric fields, that means that the discharge can maintain a high degree of vibrational-translational nonequilibrium.

Thus, APGD is a general name for discharges supporting nonequilibrium plasma at atmospheric pressure, while physical properties of plasma may vary within a wide range of parameters, starting with a plasma close to a streamer type for APGD dielectric barrier discharges to a plasma similar to that of a glow discharge for direct current APGD.

2.1.4 Pulsed nanosecond discharges

As noted above, there can be two kinds of discharge when a high voltage short duration pulse is applied to a gas at atmospheric pressure and ambient temperature. Such a discharge is either a nonequilibrium streamer discharge at short pulse duration (units and tens of ns), or an equilibrium pulsed arc at longer pulses (tens and hundreds of ns). These two kinds are principally nonuniform spatially.

Initiation of the discharge with an abrupt slope of voltage (about of 1 kV/ns) at slightly moderated gas densities is of great interest. Modern high voltage generators (pulse amplitudes of tens and hundreds kV, voltage rise time of units and tens ns, pulse duration of tens and hundreds ns and repetitive frequency up to tens kHz) make it possible

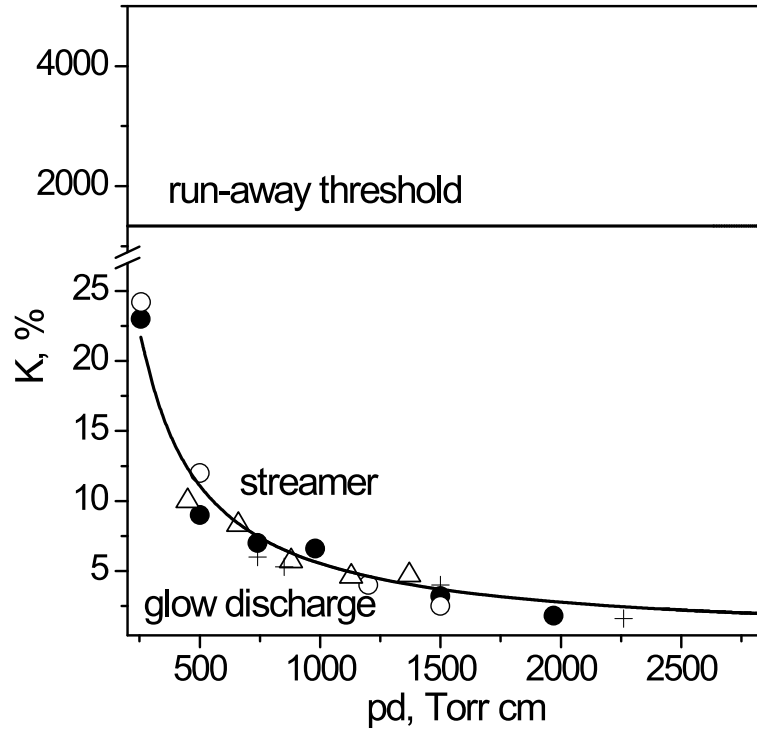


Figure 2.15: Regions of breakdown development per different mechanisms depending upon overvoltage in air¹⁴.

to create a spatially uniform discharge up to gas densities of $(6 - 8) \cdot 10^{18} \text{ cm}^3$,⁸⁰ that corresponds to either temperature about 1000 K and pressure 1 atm, or temperature about 600 K and pressure 0.6 atm. These parameters are particularly important for the problem of fast ignition of combustible mixtures. The discharge can be produced within a big gas volume, reaching, at least, dm^3 .

It is known that when the voltage on a discharge gap is increasing fast, a gas can sustain the voltage exceeding stationary breakdown value.⁸¹ Actually, under these conditions overvoltage $K = U/U_{br}$ (U_{br} is breakdown voltage) as well as pd parameter (p is gas pressure and d is interelectrode distance) define the breakdown mechanism. In case when the overvoltage is about tens of percent, the breakdown is transforming from uniform glow Townsend into a streamer breakdown. On the other hand, when the overvoltage reaches hundreds of percent and more, the breakdown again acquires spatial uniformity. But physical reasons are absolutely different since a part of electrons gains high energy in the breakdown front and transmits to the so called “run-away” regime. They are the electrons that provide uniform preionization in the breakdown front. Here the breakdown is developing from the high-voltage electrode to low-voltage electrode with typical velocity of 10^9 - 10^{10} cm/s . Book⁸¹ gives the curve dividing the regions where either a Townsend or streamer breakdown develops.⁸² This curve is reproduced in Fig.2.15, that also presents the limit for the “run-away” regime of electrons marked by a horizontal line. This can be estimated as a criterion to initiate a uniform discharge.

Pulsed uniform nanosecond gas discharge was first observed more than 100 years ago. It was in 1893 when J.J.Thomson discovered⁸³ that the luminosity wave is propagating along a glass tube (15 m in length and 5 mm in diameter) with a velocity equal, at least,

half-velocity of light in vacuum. Since that time a burst of interest to the subject was observed every other 20-30 years that can be associated with advances in nanosecond technique, both registration and short pulse generation. The paper⁸⁴ reviewed investigations performed from 1970-s to 1990-s discussing the role of “run-away” electrons at breakdown of short overvoltaged gaps. The criterion of transition to “run-away” regime was derived and it was confirmed that “run-away” electrons are important for this kind of breakdown. Following consideration of the problem may be found in the book.⁸⁵

Studies of nanosecond gas breakdown in long tubes carried out in 1980s — 1990s were reviewed in.⁸⁶ The review gave a thorough description of integral electric parameters, such as amplitude and shape of high-voltage pulse, velocity of breakdown front, signal attenuation under discharge propagation along the gap, current including current of fast electrons, delay time of breakdown start, energy input. This type of discharge is assumed to be promising for plasmachemical applications due to efficient gas excitation and ionization caused by high electric fields. This is the review that proposed the name for this type of discharge which is now generally used as “fast ionization wave”.

Review¹⁴ summarised investigations of detailed spatial and temporal structure of high voltage pulsed nanosecond discharge in the form of a fast ionization wave for the last decade of the previous century. The behaviour of electric field, electron and excited state concentrations were analyzed on the basis of experimental data. The analysis based on absolute time-resolved measurements of emission of two molecular bands showed that in the vicinity of the breakdown front the electron energy distribution function (EEDF) should be substantially overpopulated with high-energy electrons. At the same time the conditions when nonstationary and nonlocal nature of EEDF may be neglected can be reached behind the fast ionization wave front. Energy branching in the discharge was analyzed. Possibilities of application of the fast ionization wave as a source of uniform pulsed plasma were suggested and justified.

Let us give a short summary of the present day idea of a homogeneous nanosecond discharge developing in air at moderate densities (up to 0.3-0.4 of density under standard conditions). The discharge is developing from the high-voltage to low-voltage electrode when a high voltage is applied to a discharge gap. The displacement current closes the electric circuit during the discharge propagation along the discharge gap, while the conductive current closes the circuit after the discharge reaches the low-voltage electrode. Spatial uniformity of nanosecond discharge has been proved by numerous imaging with the help of fast CCD cameras. Fig. 2.16 gives an example of a picture of fast ionization wave development in air obtained by the ICCD camera (⁸⁷ by the courtesy of Dr.N.B.Anikin). The discharge was initiated by high voltage positive polarity pulses, where pulse amplitude in cable was 11 kV, duration at half-height was 25 ns, rise time was 5 ns, and repetitive frequency was 40 Hz. The discharge tube diameter was 5 cm, and the distance between the electrodes was 20 cm. Since the spectral sensitivity of the optical system was within 300-800 nm range, emission of the second positive system of molecular nitrogen mostly contributed to the emission. Due to a short radiative lifetime this system reflects adequately discharge spatial development during short intervals. Some maxima are manifested near the electrodes, while on the whole, the discharge is developing uniformly. The velocity of front propagation may be estimated as 2.5 cm/ns that is clearly seen from a succession of images.

The dependence between the velocity of nanosecond discharge and gas pressure, or,

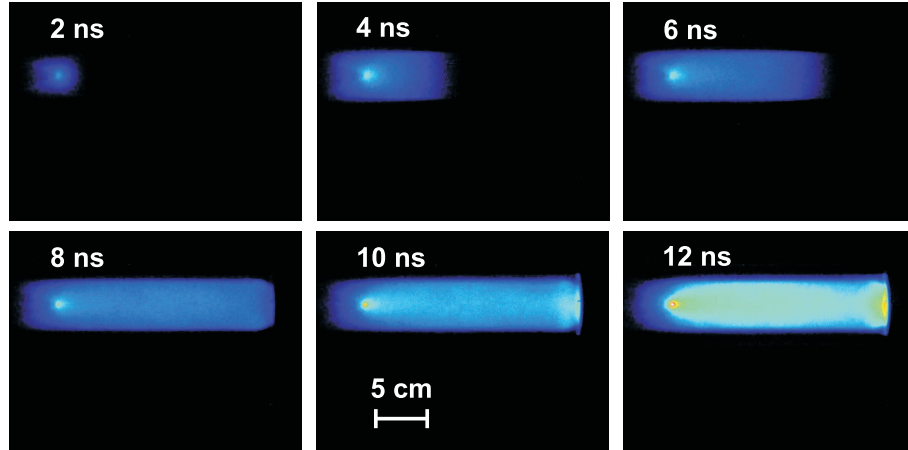


Figure 2.16: Subsequent ICCD images of nanosecond discharge in air. ICCD gate is equal to 1 ns, time moments from the discharge start are indicated⁸⁷. High voltage electrode is on the left hand side.

more physically, gas density, is the one that is mostly often under control during the experiment. Usually it is dome-shaped. It might be noted that a nanosecond discharge can be initiated in different gases, both atomic and molecular, including electronegative ones (for example, SF_6). When all the experimental conditions are kept constant and the high voltage amplitude increases, the dependence of the discharge velocity upon pressure shifts towards more higher gas densities. In case we maintain the constant high voltage pulse amplitude and increase the gas density, the discharge will be transformed into a non-homogeneous streamer form.⁸⁸ On the other hand, there are some evidences that such type of the discharge can be spatially uniform under atmospheric gas density.⁸⁹ The energy input may be as high as 80–95% from the incident pulse.⁹⁰ At the closing stage, the discharge current is rather high and reaches hundreds of A.

The methods of electric field determination were treated in detail in.^{91–93} They were based on the measurements of an electrical potential along the discharge gap or on the control of emission of different molecular bands. The peak of high reduced fields (up to several kTd) is not longer than 2–3 ns in duration. Then the field rapidly decreases to the value of hundreds of Td. It is this narrow peak of high electric fields that is responsible for uniform discharge development in space. High electric fields cause production of electrons with high energies that pre-ionize the gas in the vicinity of the front. The bulk of the required electron concentration and population of upper electronic levels take place behind the FIW front in residual fields. These residual fields are comparable with the fields in a streamer head.

Electron density determined in the drift approximation⁹¹ on the basis of data on charge and field dynamics gave the values of $\sim 10^{12} \text{ cm}^{-3}$. Fig. 2.17 (¹⁴ according to the data taken from^{91,92}) displays typical temporal behaviour of the electric field, electron density and concentration of the electronically excited states.

Energy contributed to the plasma is mainly consumed for excitation of electronic states and the energy balance is shifted towards the high energy level states, including excited states of ions. Fig. 2.18 displays energy branching in air, oxygen and nitrogen under the action of pulsed nanosecond discharge with parameters close to those mentioned in

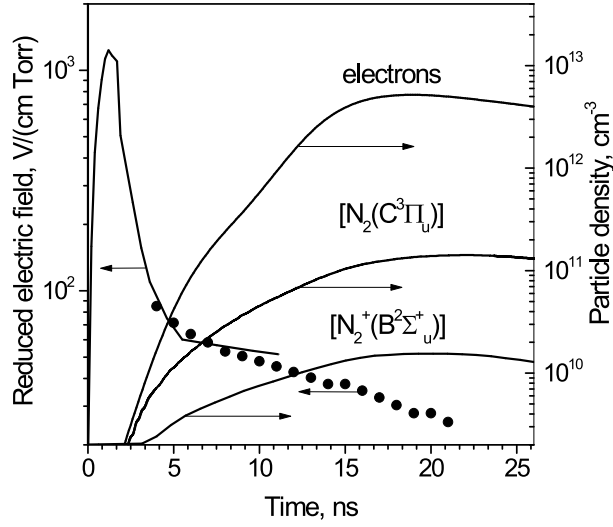


Figure 2.17: Temporal evolution of electric field, $N_2(C^3\Pi_u, v'=0)$ and $N_2^+(B^2\Sigma_u^+, v'=0)$ level densities and electron concentration in nitrogen at a distance 20 cm from the high-voltage electrode. Electric field represented with a solid line is determined from the electrical measurements; represented by symbols – from the spectroscopy. Nitrogen, $P = 4$ Torr, $U = -15.5$ kV¹⁴.

Fig. 2.16. The calculations were made using experimental data on electric field distribution in the framework of two-term approximation of Boltzmann equation for electron energy distribution function. This assumption is valid behind the front of the discharge, when the discharge gap is bridged and there is no sharp gradients of the electric field are absent.⁹⁴ It is clearly seen that under all pressures and all gases the main part of energy is spent on exciting of electronically excited states, that is rather typical for electric field values of hundreds of Td.

Thus, on the one hand, a nanosecond discharge in the form of fast ionization wave is quite interesting for the problem of plasma assisted ignition/combustion, since it: (i) is developing during the times significantly shorter than those typical for ignition, that is control of the discharge and combustion kinetics can be easily separated in time; (ii) is producing a spatially uniform plasma, that is the task can be reduced to 0D geometry; (iii) is generally exciting high-energy levels of molecules causing dissociation at minimal gas heating.

On the other hand, gas density (pressure) limits applications of this discharge at fixed high voltage pulse amplitude. Pressure increase requires either rising amplitude of high voltage pulse that is not always simple technically or designing some special multielectrode systems to initiate discharge quasi-uniformly.

2.1.5 Other discharges

The scope of the report doesn't provide us a chance to consider other types of discharges in detail. Here we will only briefly name the discharges ever used to either initiate or sustain combustion and we will refer to the papers describing corresponding plasmas.

The authors of⁹⁵ in their experiments used radio frequency (RF) discharge to induce combustion of a gas flow at stagnation pressure within the range of 30 Torr to 0.5 atm

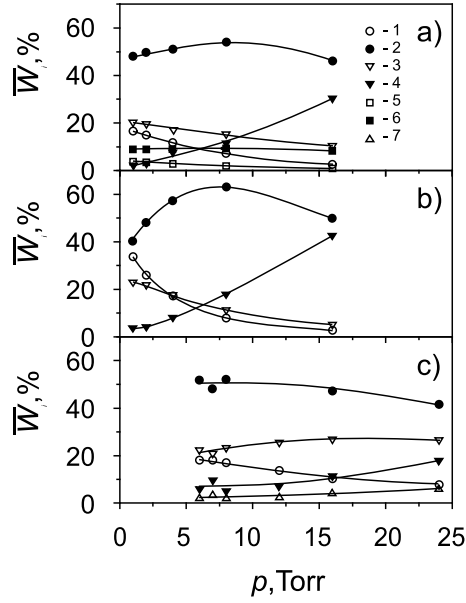


Figure 2.18: Fraction of energy contribution per pulse into inner degrees of freedom for various gases: (a) air (curves 1-4 correspond to N_2 ; 5 and 6 to O_2); (b) nitrogen; (c) hydrogen. Numbers designate: 1 and 5, ionization; 2 and 6, excitation of electronic terms; 3, dissociation; 4, excitation of vibration levels; 7, excitation of rotation levels⁹⁴.

and gas flows up to 70 m/s.

Frequency range within 1 – 100 MHz is commonly used to initiate RF-discharge. RF-discharges are divided into two types depending on the way of their excitation: they may be either inductively or capacitively coupled. When a gas is placed into an inductive coil where an RF-current is initiated then the lines of electric field are closed and the field itself is a vortex electric field. Capacitively coupled discharge means that a gas is placed between the electrodes, the electric field lines connect the electrodes, and the field itself is potential. The book⁹⁶ describes the physics of capacitively coupled RF-discharge, the main processes responsible for discharge development. The book points out that the RF-discharge is mainly applied to excite CO_2 – lasers (pressure range is 1 – 100 Torr) and for surface treatment (pressure range 10^{-3} – 1 Torr).

We will confine ourselves to consideration of higher pressures, where the discharge can be uniform under heat removal either through the electrodes or by gas flow through the discharge cell. When no stabilization by heat exchange is reached the discharge is contracted converging into a bright channel between the electrodes. The visible diameter of the channel is different for different gases. The near-electrode region remains diffusively uniform in case of molecular gases (N_2 , CO_2 , O_2) and filamentarizes in case of atomic gases (Ar, Xe).

In both cases, uniform and contracted, the electron temperature is a few eV, while the other parameters vary greatly. In case of a contracted discharge, gas temperature reaches 3000-4000 K, dissociation degree is 90-95%. Electron temperature is significantly (by one or two orders of magnitude) higher, whereas electric field is lower than in case of uniform RF-discharge. The contracted RF-discharge in its parameters is similar to the arc. Note that an RF torch initiated by powerful RF-signal (hundreds of W, up to kW)

at atmospheric pressure can be promising for applications. When the torch is developing, long (10 cm and longer) hot plasma jets start from a single electrode closing onto ambient space by the displacement current.

At pressures within the range from tens to hundreds Torr and efficient heat removal the RF-discharge generates nonequilibrium plasma similar to plasma of glow discharge. The amplitude of RF voltage is usually hundreds and thousands of Volts. There gas temperature is up to 1000 K, electron number density is about of $n_e \sim 10^{11} \text{ cm}^{-3}$, electric field is within the range of units to hundreds Td. The main energy branching is directed to low energy electronic and vibrational degrees of freedom similar to energy branching in glow discharge.

Some authors⁹⁷ use microwave discharge under moderate gas pressures (up to 300 Torr) to initiate combustion in subsonic and supersonic gas flows. This discharge, when initiated in a free space, has a rather complex spatial structure. It consists of two very typical structures. The first structure is a set of thin bright hot filaments with high conductivity and gas temperature. The second one is a set of the so-called halo structures or “plasmoids”, that surround hot filament. The plasma in halo is nonequilibrium, the electric field is high in comparison with this in the filaments, and the conductivity of this region is rather low. It is exactly this complex structure — “skeleton” made of hot bright filaments surrounded with slightly emitting haloes — that originates as a result of microwave interaction with the gas flow. A detailed description of the physical nature of microwave discharges at moderate pressures can be found, for example, in.^{17,98}

Concluding the review of discharges for PAI/PAC we will present the table that summarizes the author’s ideas concerning typical plasma parameters for discharges mentioned above 2.2. In the table, “vibr.” means vibrational degrees of freedom, and “electr.” means electronic degrees of freedom. It would be wise to note that a wide range of values for MW discharge is caused by a multiplicity of the discharge forms depending upon the experimental conditions.

The given summary is rather indicative and denotes probably the parameters of discharges and plasmas most frequently realized in practice. Changing some of the experimental conditions, the researcher can obtain a significant change of plasmas while preserving the main parameters of the system. For example, varying the frequency or flow rate velocity one can obtain a remarkable change of plasma parameters at unchanged electric pulse.

2.2 The study of streamer discharge development. Streamer branching and optical control of a streamer head.

It is known that self-sustained discharge trends to contraction and transition to the arc. The arc discharge is characterized by low energies of charged particles and by high rate of energy transfer to gas heating, and this is not desirable for efficient plasmachemical applications. Due to this fact, one of the most promising ways to produce strongly nonequilibrium plasma is to organize pulsed discharge with capacitive coupling, for example, barrier discharge and its modifications, when one or both electrodes are covered with dielectric layer. The dielectric layer in this case restricts the discharge which can be transported through the layer.

As a rule, at moderate and high pressures, the barrier discharge develops in two stages: on the first stage the discharge gap bridges by a streamer flash, on the second one we observe non-zero electric current up to charging of the dielectric layer. The main energy input takes place on the second stage of the discharge development, whereas the first stage determines time of the gap closing and uniformity of filamentary structure distribution in the gap. The last point is, undoubtedly, very important for design of the real devices.⁹⁹

There are numerous papers reporting experimental and theoretical study of the streamer corona. Now it is possible to discuss quantitative agreements between theory and experiment for single filament streamers.²⁷

The main processes, which define parameters and typical features of the discharges during their propagation, are quite similar. Among them are preionization of a gas ahead of the discharge front by fast electrons and by ionizing radiation, ionization by an electron impact in relatively strong electric field in the discharge front at relatively weak value of the electric field behind the front.

2.2.1 Experimental study of streamer discharge

A schematic of the experimental setup and diagnostic facility is shown in Fig.2.19,^{100, 33} A thyristor generator PAKM with magnetic pulse compression was used as a pulsed voltage supply. The high-voltage pulses were fed through a 60-m-long RK-50-24-13 cable to the high-voltage connector of the discharge system. A calibrated back-current shunt placed in the break of the braiding of the feeding coaxial cable at a distance of 30 m from the discharge system was used to control the parameters of the pulses. The amplitude of the voltage pulse was 10-21 kV (positive polarity), the FWHM duration was 25 ns, the rise time was 5 ns, and the repetition rate was from 0.5 to 100 Hz.

The discharge section comprises a cube-shape vacuum chamber with 20 mm edge, made of stainless steel. The discharge emission was tested through the optical windows 100 mm in diameter, made of KY-1 quartz. The discharge was organized in a point-plane geometry with interelectrode distances from 20 to 60 mm. High-voltage electrode (cathode) was made of brass and had a disk shape with diameter of 80 mm. Grounded disk-shape anode was made from aluminium and was 100 mm in diameter. To initiate the cathode-directed streamer the needle 0.8 mm in diameter and 8 mm in height was placed in the center of grounded electrode.

Parameter	Arc	Glow	Streamer	DBD	FIW	RF	MW
Pressure	up to 10 – 20 atm	0.01 – 100 Torr	0.1 – 1 atm	1 Torr–1 atm	0.01 – 200 Torr	10^{-3} – 100 Torr	0.1 Torr–1 atm
Current, A	$1 - 10^5$	$10^{-4} - 10^{-1}$	$10^{-4} - 10^{-3}$	$10^{-4} - 10^{-3}$	50 – 200	$10^{-4} - 10^{-1}$	0.1 – 1
Voltage	10 – 100 V	100 – 1000 V	10 – 100 kV	1 – 10 kV	5 – 200 kV	500 – 5000 V	0.1 – 10 kV
E/N or E	1 – 100 V/cm	10 – 50 V/(cm·Torr)	30 – 100 V/(cm·Torr) in a head	30 – 100 V/(cm·Torr)	30 – 100 V/(cm·Torr) behind the front	10 – 100 V/(cm·Torr)	1 – 1000 V/cm
T_g , K	3000 – 10000	300 – 600	300 – 400	300 – 600	300 – 400	300 – 1000	300 – 6000
T_e	5000 – 10000 K	1 – 3 eV	1 – 3 eV	1 – 5 eV	1 – 10 eV	1 – 5 eV	1 – 5 eV
n_e , cm $^{-3}$	$10^{15} - 10^{16}$	$10^{11} - 10^{12}$	$10^{11} - 10^{12}$	$10^{11} - 10^{12}$	$10^{11} - 10^{13}$	10^{11}	from 10^9 to 10^{17}
Uniformity in space	non–uniform	uniform (if not stratified)	non–uniform	non–uniform or uniform (APGD)	uniform	uniform (low pressure) or filamentary (high pressure)	uniform (halo) and filamentary
Main energy input	heating	vibr.	electr.	electr.	electr.	vibr. or electr.	heating, vibr., electr.

Table 2.2: A summary table of the parameters of plasmas used for PAI/PAC

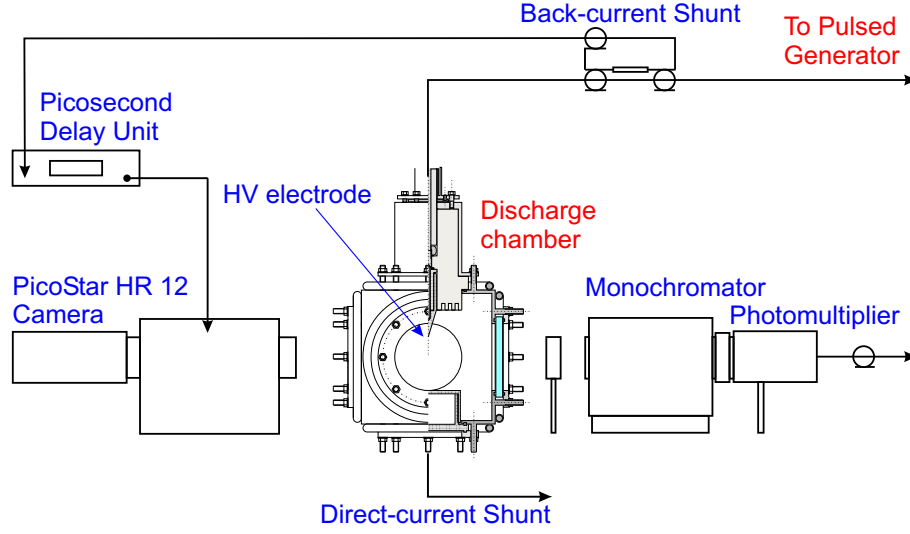


Figure 2.19: Experimental setup for streamer discharge investigations.

Under the action of high voltage pulse of negative polarity the electric field near the needle tip exceeds significantly the value of uniform electric field between the electrodes. Thus, the streamer development from the grounded electrode is induced. Such geometry of electrodes allows to measure directly the current of a streamer flash. To do this, we shunt the needle to earth by 50 Ohm resistor.

The emission spectroscopy technique was used to analyze a cathode-directed streamer discharge. The active particles were detected with an absolute emission spectroscopy. The optical recording facility consisted of condensers, photomultipliers, monochromators, and a set of diaphragms. We used FEU-100 and SNFT-3 photomultipliers (with photocathode sensitivity ranges of 170–830 and 300–800 nm, respectively) and MDR-12-1 and MUM-2 monochromators (with operating ranges of 200–2000 and 200–800 nm, respectively).

To control spatial-temporal characteristics of the discharge we used ICCD camera PicoStar HR12 (LaVision) with a spectral sensitivity range of 200–800 nm and time gate of 200 ps. ICCD camera was focused on the needle of the grounded electrode in a such way that both electrodes were in the frame. Spatial resolution of the images was 0.1 mm. The detection of discharge current and voltage on the gap was made by Tektronix TDS-3054 oscilloscope simultaneously with camera synchropulse. In spite of the periodic regime of the work of generator, in experiments the ICCD camera image, voltage drop and current corresponded to the same streamer flash.

Measurements were performed in N_2-O_2 (4:1) mixture for two lengths of the discharge gap; 30 and 50 mm. At 30 mm gap the pressure in a chamber varied in the range of 320–1300 Torr, at 50 mm gap — in the range of 90–410 Torr. Minimum of pressure for each length was limited by streamer transition to the spark form.

2.2.2 Single channel measurements

At pressures lower than 590 Torr we could registered or branching structure or single streamer channel from experiment to experiment at the same experimental conditions. At pressures lower than 470 Torr we observed a single streamer channel only.

Streamer Discharge At Different Voltage

Development of a streamer channel is defined by a density of seed electrons ahead of the streamer head. These electrons appear due to photoionization and ionization by an electron impact in the region of strong electric fields. Streamer head propagation in space takes place due to its excess electric potential relative to the ambient space. With the streamer motion from the high-voltage electrode to the low voltage one, the streamer channel length and, consequently, voltage drop on it increases. So, the potential of a streamer head decreases.

When the pressure diminishes at constant electric field configuration the reduced electric field increases. The rate of the ionization by an electron impact increase with the reduced electric field, at the same time the photoionization length increases due to decrease of gas density. As a consequence, the velocity of a streamer propagation and diameter of the streamer increase.

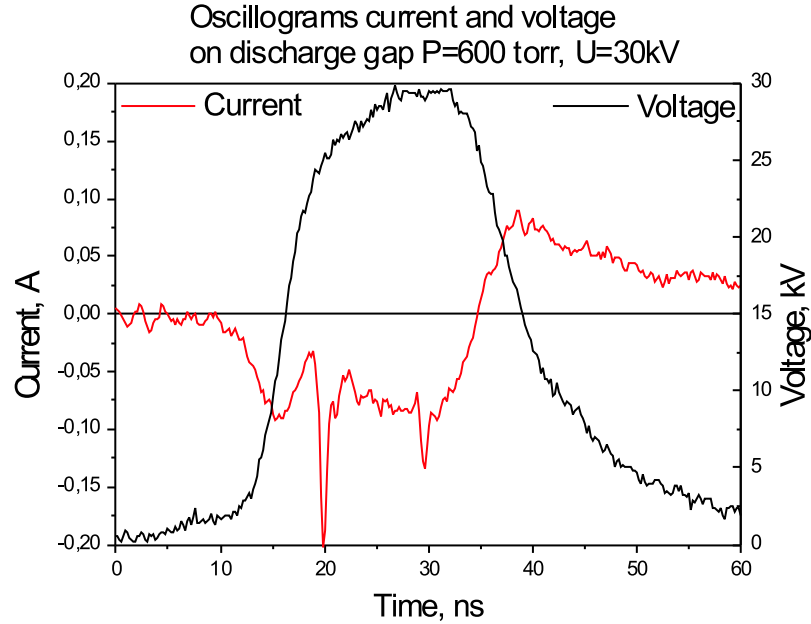


Figure 2.20: Voltage and anode current measurements. 30 mm. Air.

The anode current of a cathode-directed streamer increase with the gas pressure decrease. Anode current profiles are represented in Fig. 2.20 for different pulse voltage in air at the discharge gap length of 30 mm. Velocity of cathode-directed streamer propagation dependence on the voltage applied to the gap is presented on the Figure 2.21. Experimental values of velocity for different pressures are shown with dots, numerical simulation results by curves. The mean value of velocity along the gap for pressures 600 and 740-torr. The values of velocity and current demonstrate good agreement of experiment and calculations. So, now it remains to discuss radius measurements.

The streamer current was measured at the center of plateau of current pulse. Streamer head position is close to the center of the gap at this moment (Fig. 2.22).

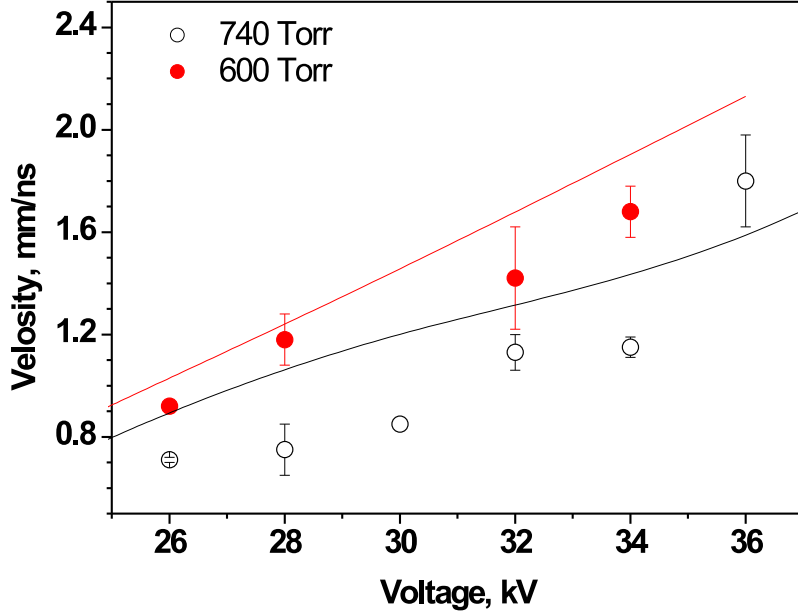


Figure 2.21: Velocity dependence on the voltage. $U = 24$ kV. Discharge gap is 30 mm. Air. Cathode directed streamer. Dots are experimental results, curves are numerical modeling.

In theoretical works when speak about streamer radius usually mean electrodynamic radius, which corresponds to field maximum. But during experiments the streamer radius is determined using image, which is obtained using this or that technique.

In the experiment we measure the emission distribution and emission radius of the streamer. We determine the emission radius on the half-height of the profile. In this picture there is calculated emission distribution of the streamer. The emission radius correspond to this region. The emission radius is differ from the electrodynamic radius. The emission region corresponds to the region of maximal gas excitation, and electrodynamic radius corresponds to the region occupied by plasma. From the point of view of comparison with numerical modeling it is better to determine both parameters. Electrodynamic radius can be determined from the emission distribution in weak tails of the streamer head. So, we have to find the position of maximal intensity in the tails of streamer head. It is impossible to determine this position from integral picture of emission distribution. Thus we should use the instantaneous image of the streamer head and analyze spatial distribution of the emission.

On the Figure 2.23 calculated emission and electric field distributions are shown. There is clear difference between spatial distribution of the emission and electric field. But the plasma region (electrodynamic radius) is the same for both cases and can be determined from emission distribution.

Calculated emission diameter is smaller than electrodynamic one (Fig. 2.24). If we compare the experimental data and results of numerical modeling we can see that the deviation increase for low pressure region. So, if we will determine the electrodynamic

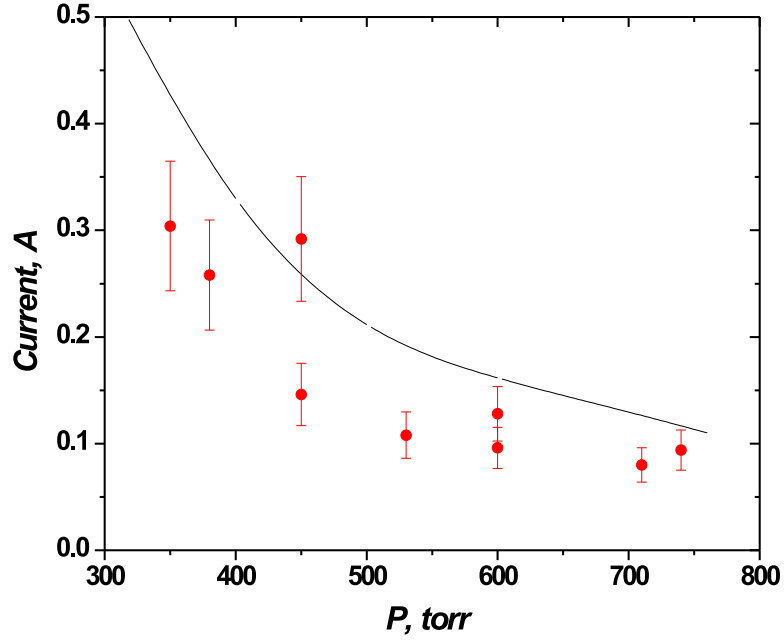


Figure 2.22: Current dependence on the Pressure. $U = 24$ kV. Discharge gap is 30 mm. Air. Cathode directed streamer. Dots are experimental results, curve is numerical modeling.

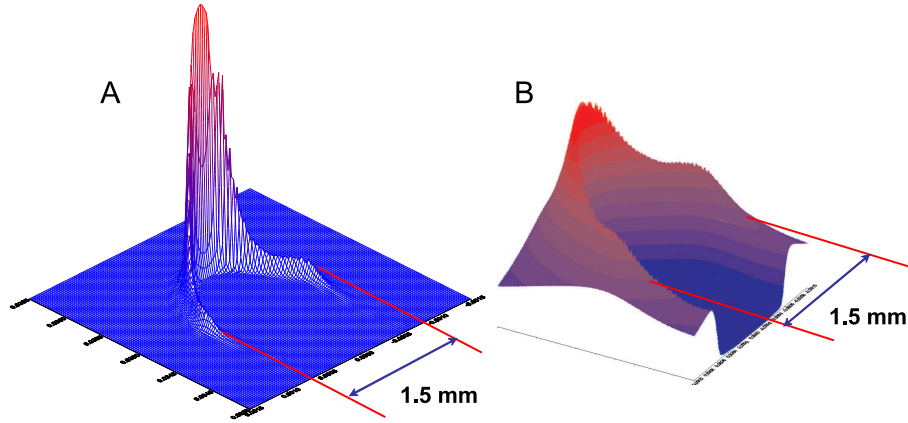


Figure 2.23: Calculated emission (A) and electric field (B) distributions. $U = 24$ kV. Discharge gap is 30 mm. Air. Cathode directed streamer.

radius from the experiment, we will obtain important additional parameter to compare with numerical model.

This technique is based on the suggestion that maximum of emission corresponds with field maximum. In fact, emission intensity of 2+ system is proportional to concentration of excited nitrogen molecules. And this concentration, as it follows from the given equation, has direct relation with constant of electron impact excitation rate and electron

concentration. This constant depends exponentially on the electrons temperature and, as a result, on the electric field value. So, when measuring emission distribution along the head section, we can determine the electrodynamic radius.

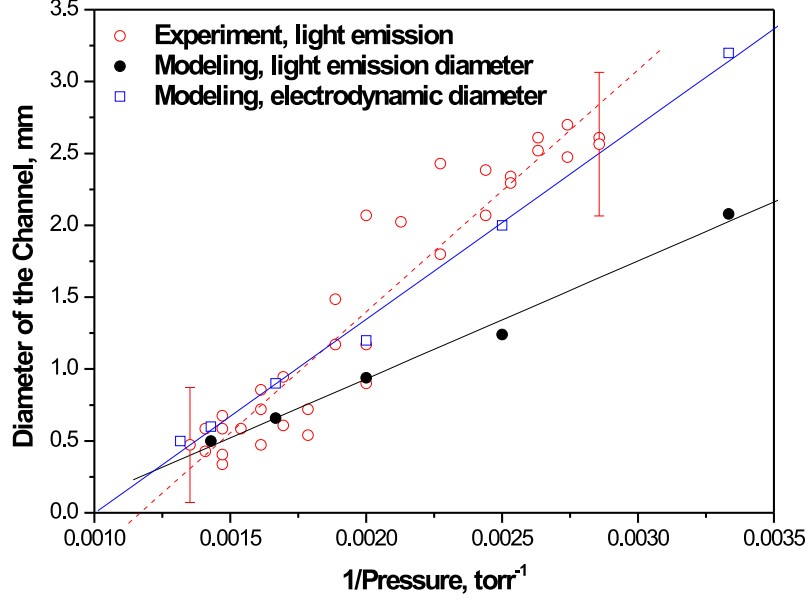


Figure 2.24: Comparison of the measured and calculated streamer channel diameter. $U = 24$ kV. Discharge gap is 30 mm. Air. Cathode directed streamer.

We have investigated the streamer head structure and velocity in stroboscopic mode of ICCD camera. We apply on the camera amplifier triggering sinusoidal signal with the frequency of 300 MHz. The form of the signal is presented in the Figure 2.25. In this operation mode emission intensity, which reach CCD-matrix, depends exponentially on the applied voltage. We suggest that gate corresponds to the lower part of synchrosignal and is equal to 200-400 ps. Image of anode-directed streamer in the stroboscopic mode If we know the time between intensity peaks on the streamer image, we can determine the mean velocity and the velocity along the gap section.

To restore the emission distribution in the streamer head we use the image, obtained with 300 picosecond gate. From the image we take emission profiles. The intensity dependence along the radius, perpendicular to the axis of development, was analyzed. The number of profiles was up to 10 per streamer head image (Figure 2.26).

The profile is obtained by summing of the intensity of two-dimensional cylindrical axis-symmetrical object. To restore emission pattern along streamer head radius we used inverse Abel transformation. If we know distance between this profiles, we can restore emission distribution in the streamer head. The distance between emission maximums is the streamer diameter. Streamer head diameter, which is obtained by picoseconds images and calculated by emission maximums, is 1.4 mm (Figure 2.27). We add results of numerical simulation to the experimental emission pattern. In the Figure emission distribution for N2 second positive system is shown, which were calculated for the conditions

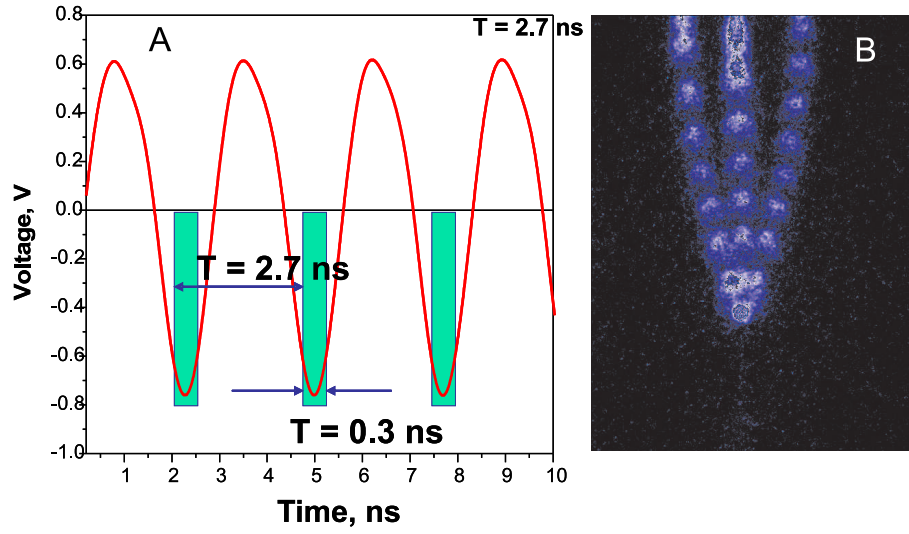


Figure 2.25: Voltage applied and image of the streamer in the stroboscopic mode.

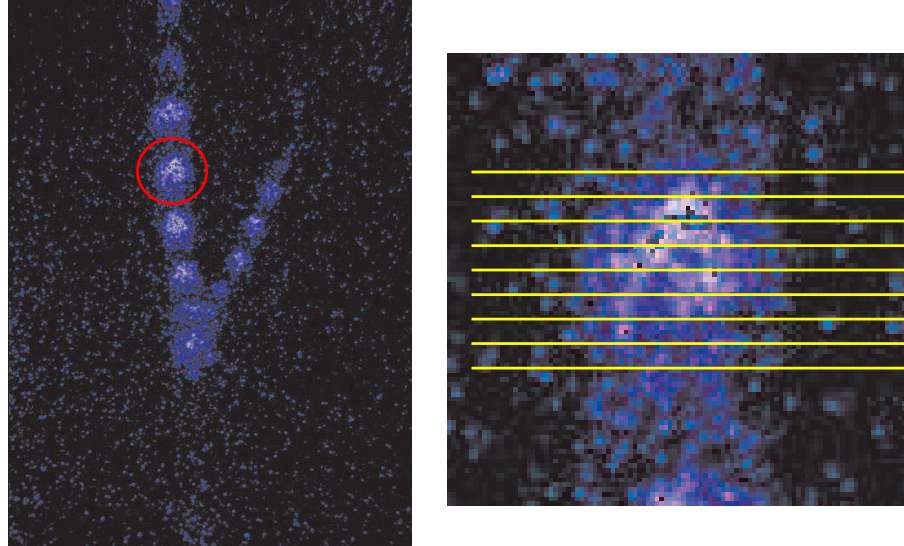


Figure 2.26: Emission distribution in the streamer head. Camera gate is 300 ps.

of experiment. Electrodynamic diameter obtained by numerical model is 1.5 mm. It is seen that in the case of experimental distribution the length of the emission zone along the streamer propagation is greater than calculated one and corresponds to 0.3 mm. This can be explained by the fact that streamer head is moving while the camera amplifier is switched on, and spatial resolution of the intensifier.

For interelectrode gap of 30 mm in a pressure range of 380—350 Torr the streamer channel bridges the discharge gap, and at further pressure decrease transforms to the spark.

Simultaneous synchronized measurements of electric parameters of the discharge demonstrate that at pressure decrease the current of a streamer, charge and energy input increase monotonically up to the transition to the spark.

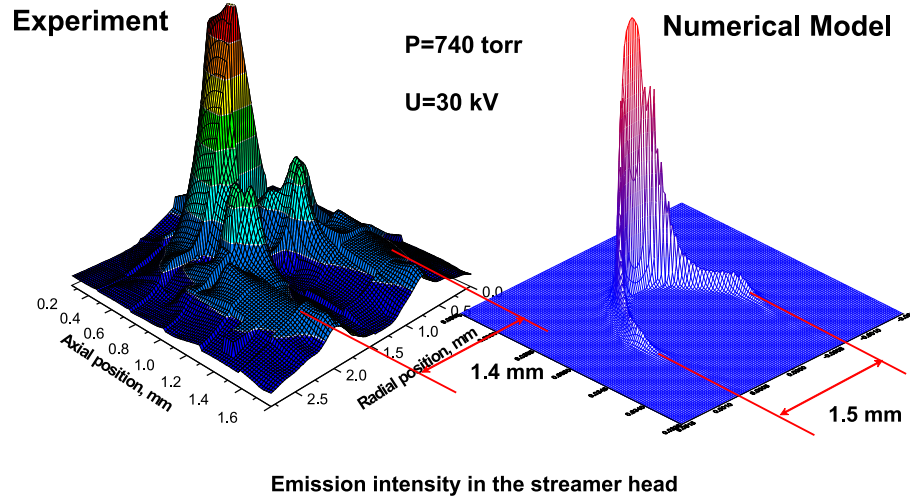


Figure 2.27: Streamer channel electrodynamic diameter. $U = 30$ kV, Air.

2.2.3 Streamer branching

In the pressure range of 680-1300 Torr we observe branched streamer flash only for all voltages applied. At diminishing the pressure the number of branches decrease, for example, at a pressure range of 620-650 Torr we observed three or less channels. Integral images of cathode-directed streamer show that number of branches growth with pressure increase, and growth with voltage increase at fixed pressure. The streamer branching depends strongly on the gas pressure and voltage applied. It was experimentally found that the number of branches is proportional to the pressure.

Figure 2.28 demonstrates typical dependance of the streamer flash structure on the pressure and voltage. The graph also shows the dependance of the branching length on the voltage for pressures 600, 740, 1000 Torr for cathode-directed streamer. It is clearly seen that the branching length exponentially increases with the voltage growth.

2.2.4 Numerical model of streamer discharge

The objective of this section is to describe a self-consistent description in the two-dimensional formulation of the problem studied in^{27,101} and to model the dynamics of streamer discharges in long gaps.

Main equations

Streamer discharge modelling was performed in the hydrodynamic approximation for the 2-dimensional geometry. The numerical model includes the following balance equations for charged particles:

$$\frac{\partial n_e}{\partial t} + \text{div}(\vec{v}_e \cdot n_e) = S_{ion} + S_{photo} - S_{att} - S_{rec}^{ei} \quad (2.1)$$

$$\frac{\partial n_p}{\partial t} = S_{ion} + S_{photo} - S_{rec}^{ei} - S_{rec}^{ii} \quad (2.2)$$

$$\frac{\partial n_n}{\partial t} = S_{att} - S_{rec}^{ii} \quad (2.3)$$

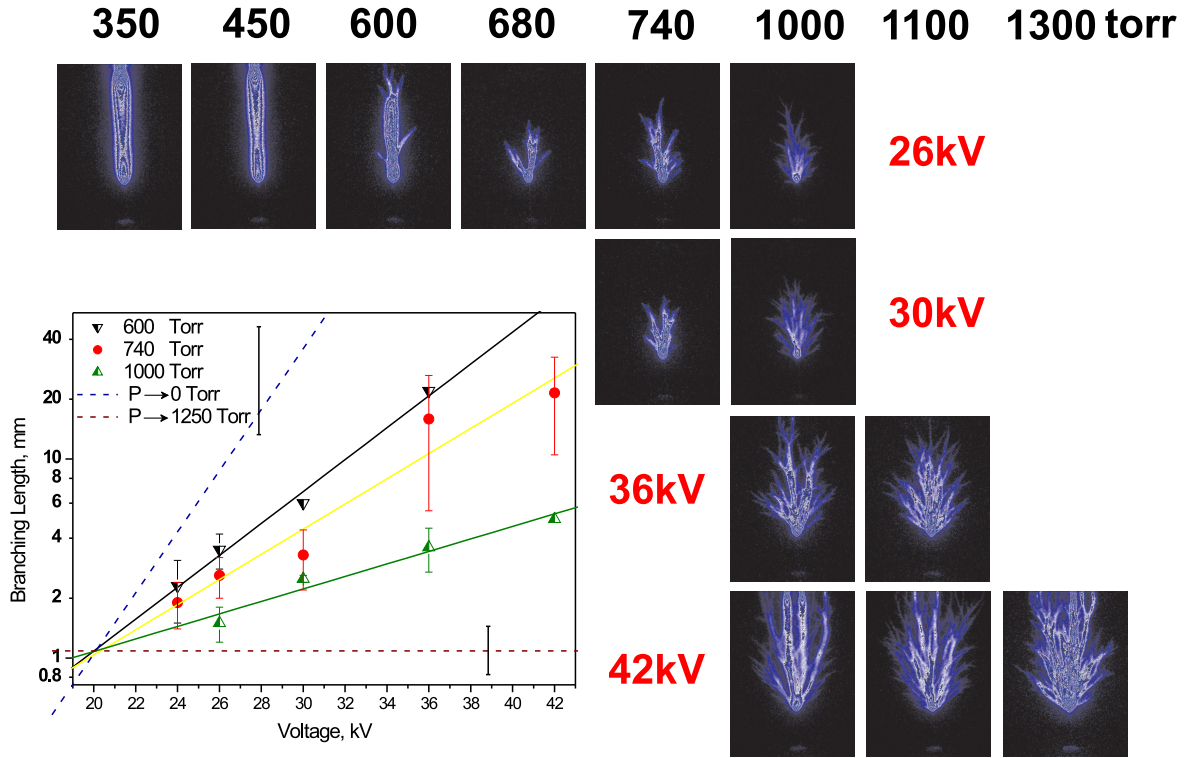


Figure 2.28: ICCD image of multi-channel flash for different pressures and voltages. Discharge gap is 30 mm. Air.

Here, n_e is the electron density; n_p and n_n are the concentrations of positively and negatively charged ions; \vec{v}_e is the drift velocity in a local electric field \vec{E} ; and S_{ion} , S_{photo} , S_{rec} , and S_{att} are, respectively, the rates of ionization, photoionization, electron-ion (ei) and ion-ion (ii) recombination, and electron attachment.

The electric field \vec{E} in the discharge gap is described in terms of the potential φ , whose distribution over the gap was determined by solving Poisson's equation with prescribed boundary conditions and distribution of charged particles of different species:

$$\vec{E} = -\nabla\varphi \quad (2.4)$$

$$\Delta\varphi = -\frac{e}{\varepsilon_0} (n_p - n_e - n_n) \quad (2.5)$$

Here, e is the elementary charge and ε_0 is the dielectric constant.

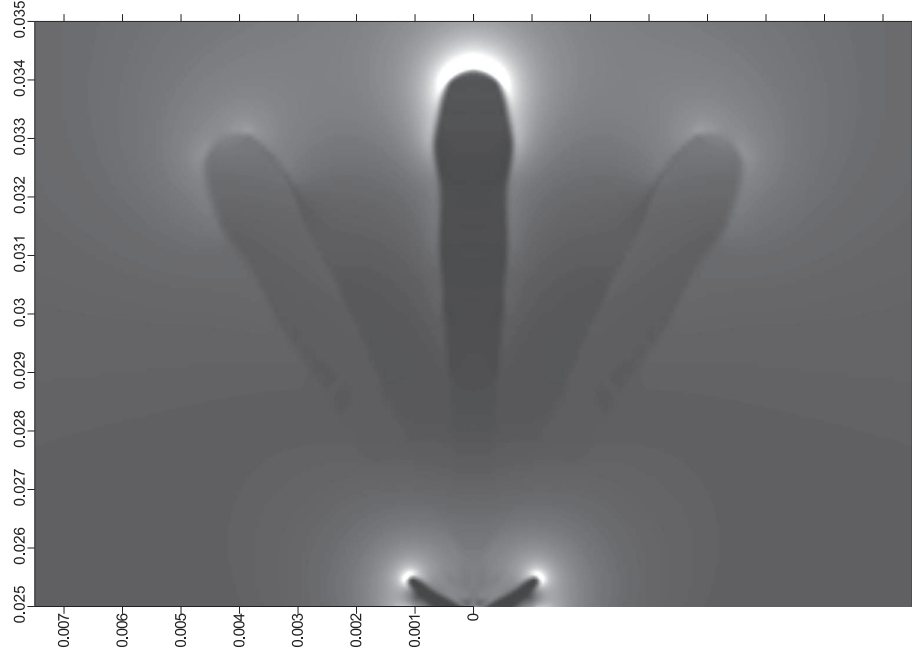


Figure 2.29: Electric field distribution in the gap ($\lg(E/n)$). Four additional "conical branches" are added.

Photoionization processes

The rate of gas photoionization, S_{photo} , is described in the same manner as in¹⁰¹ and based on the model:¹⁰²

$$S_{photo} = \frac{1}{4\pi} \cdot \frac{p_q}{p + p_q} \int_V d^3\vec{r}_1 \frac{S_{ion}(\vec{r}_1)}{|\vec{r} - \vec{r}_1|^2} \Psi(|\vec{r} - \vec{r}_1| \cdot p) \quad (2.6)$$

where $1/4\pi$ is the normalizing constant, p is the gas pressure, and $\Psi(|\vec{r} - \vec{r}_1| \cdot p)$ is the coefficient of absorption of the ionizing radiation in the medium. The quenching pressure of the emitting states p_q was set to be 60 Torr for pure nitrogen and 30 Torr for air¹⁰² and was recalculated for any percentage of oxygen in nitrogen gas.

To clear up a question of streamer branches' influence we designed a rough model allowing to estimate qualitatively influence of streamer's branches on its distribution. Branching of streamer was set in axial-symmetric model, as the cone ($\alpha = 0.5$ Rad) of charge surrounding basic streamer, and charge was considered to be equally distributed on volume of cone and its quantity was changed depending on the number of branches we wanted to estimate (Fig. 2.29). We supposed that after branching each branch of streamer is equal each other and carries identical charge. Therefore, using the model described earlier, we have roughly estimated which parameters branching of streamer influences on.

For initial configuration we have observed streamer channel with radius $R_{streamer} = 0.282$ mm, current $I = 14$ mA, total charge in the discharge gap $Q = 7.4 \times 10^{-10}$ Cl, streamer velocity $V = 5.06 \times 10^5$ m/s. For simultaneous propagation of two streamer branches we have $I = 10$ mA, $Q = 5.5 \times 10^{-10}$ Cl, $V = 4.85 \times 10^5$ m/s. So, strong influence of the streamer branching on the current is shown. It follows from the received

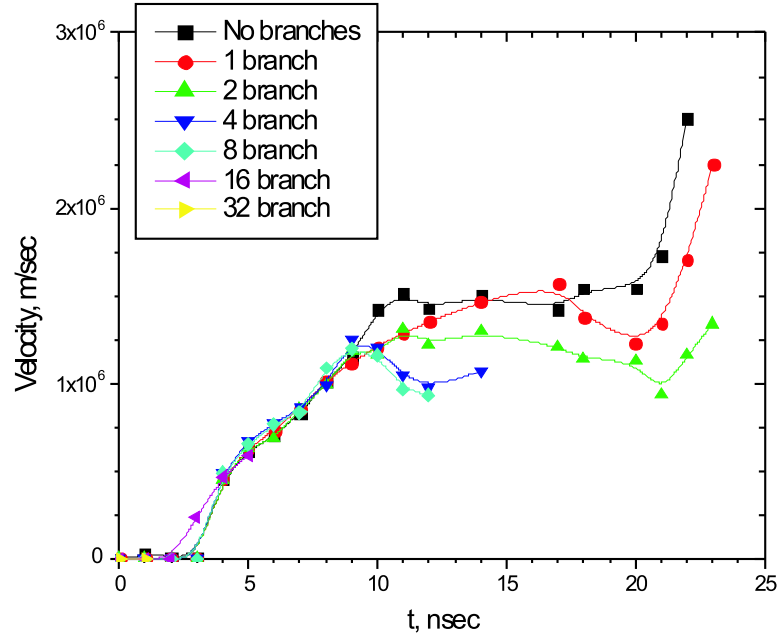


Figure 2.30: Dependence of the streamer velocity from number of branches. 30 mm. Air.

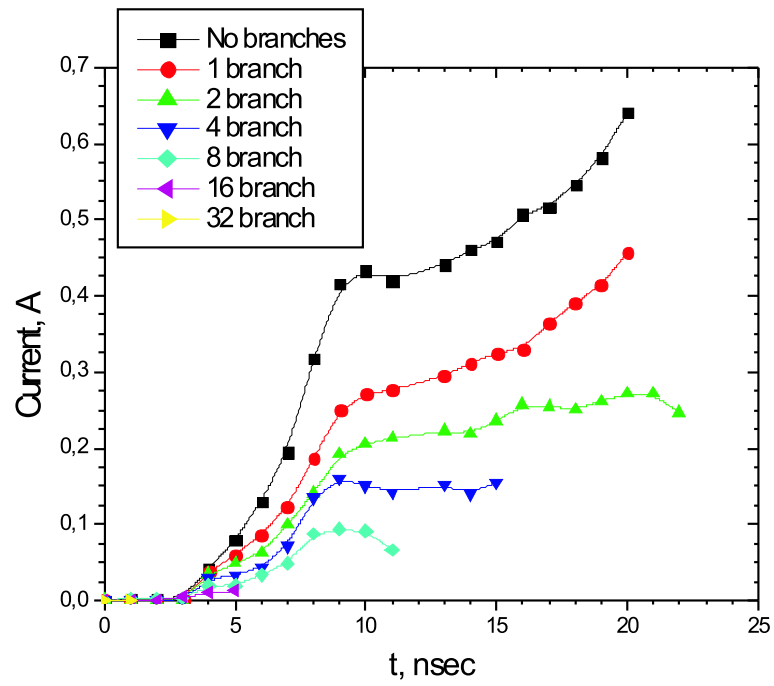


Figure 2.31: Dependence of the streamer current from number of branches. 30 mm. Air.

numerical data, first, that at the given pressures and voltages velocity of a streamer hardly depends on presence or lack of branching, second, that the branching influences mostly on a current of a streamer. We got, that velocity of propagation of single streamer in plane-plane gap and velocity of propagation of streamers in bunch, are in a good agreement with each other. This result confirms indirectly conclusion made above on the basis of rough model that branching of streamers hardly influences the velocity of branches propagation, and the branches of streamers hardly influence on velocities of each other.

For multichannel flash numerical model predicts some increase the flash current with increase of number of channels and very small decrease of the velocity. Dependencies of streamer velocity and current on the number of branches are presented at Fig.2.30, 2.31.

2.3 The study of fast ionization wave development at different pressures and plasma production by nanosecond discharge

Plasma-chemical investigations cover a wide range of problems from the development of chemical lasers and ozonizers to the processing of liquid and solid waste. Two major groups of applications may be identified, namely, applications in which plasma is used to heat reacting mixtures^{103,104} and applications in which excited and charged particles play an important part.^{103,105,106} Rather an obvious parameter, which defines the effectiveness of plasma sources in the applications of the second group, is the degree of state of disequilibrium of plasma: it may be defined as the ratio between the energy input to all internal degrees of freedom (excluding rotational) of gas and the total energy input. The reactivity of a gas mixture with a high degree of state of disequilibrium is many orders of magnitude higher than that for the equilibrium case subject to the condition of equal inputs of total energy. Most advantageous from the standpoint of chemical activity of a gas mixture are discharges in which the maximum of energy input to gas is shifted most appreciably towards higher-energy degrees of freedom. For numerous plasma-chemical applications, an important requirement is that of plasma homogeneity, for example, for homogeneous initiation of combustion.

As a result, considerable interest must be attracted by the development of generators of highly nonequilibrium homogeneous plasma exhibiting a high efficiency. A number of results have been obtained over the last decades, which point to the efficiency of nanosecond pulsed supply; this efficiency is due to the high reduced electric fields in the discharge, spatial homogeneity, and low gas temperature of plasma being generated. An effective source of highly nonequilibrium plasma may be provided by a discharge in the form of a fast ionization wave (FIW)^{14,86,94}). This part deals with the experimental investigation of the kinetics of electron density decay and spatial uniformity of a nanosecond pulsed discharge.

2.3.1 Ionization wave velocity and energy contributed into gas.

Ionization wave velocity along the tube was determined as the electric signal velocity recorded by traveling capacitance dividers. It is well known that there is a pressure range optimal for development of the uniform nanosecond breakdown; the ionization wave

velocity within this range is like a smooth curve with a maximum. Hence, monitoring of the wave front velocity in every series of experiments allowed to make a certain correlation with the pressure. As an example, Fig.2.32 represents propagation velocities of ionization wave of negative polarity which were determined with reference to a level of 0.5 of the signal amplitude at every cross-section for air, nitrogen and hydrogen.⁹⁴

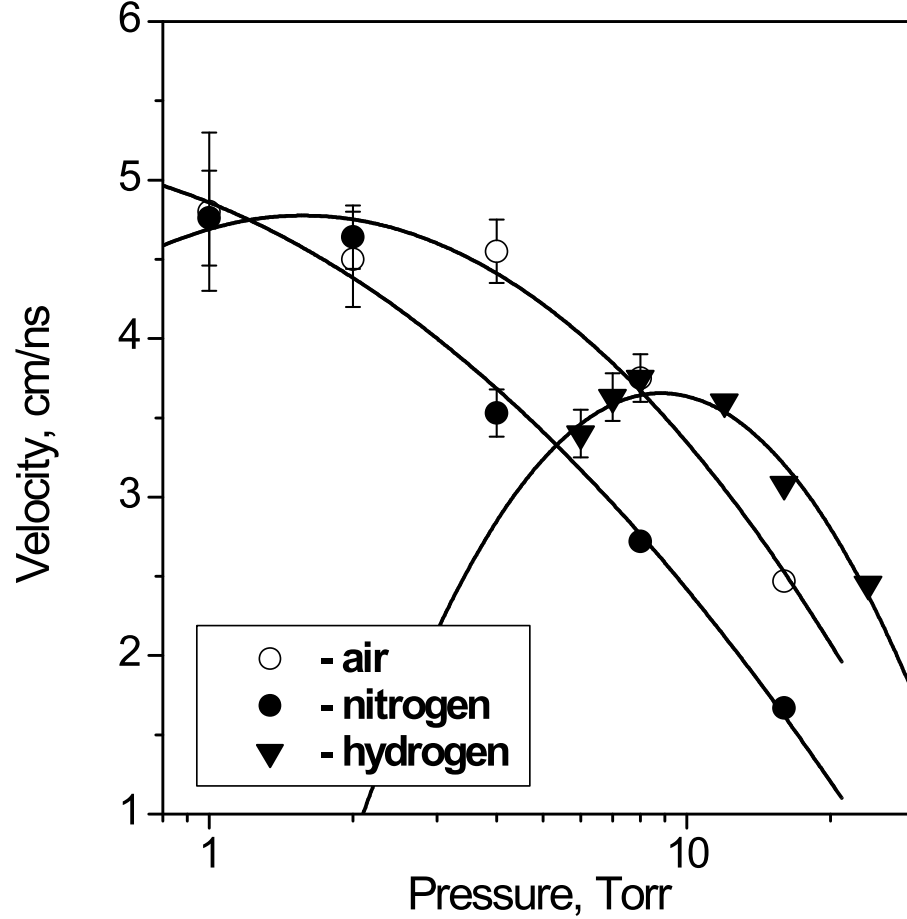


Figure 2.32: FIW front velocity upon pressure at a point $x=20$ cm from the high-voltage electrode for different gases. $U = -13.5$ kV, pulse duration is 25 ns, pulse front duration is 3 ns, $f = 40$ Hz, discharge tube diameter is 1.8 cm, tube length is 60 cm.

We investigated propagation of ionization wave of negative polarity with various types of the high-voltage electrodes and arrived at a conclusion that, beginning from a certain distance from the high-voltage electrode, breakdown development does not depend on the electrode shape. At the same time the use of an electrode with a point stood out, for instance, tapered one, stabilizes the ionization wave start at low pressures.

The energy contribution into gas was measured with the use of standard technique that analyzes current pulses incident on the discharge gap, reflected from it and passing through. In our experimental scheme the current pulse reflected from the discharge gap after arrival at the generator is reflected from it once more and goes back to the discharge tube. In the pressure range optimal for ionization wave propagation (10 - 20 Torr in oxygen and its mixtures with nitrogen at our experimental conditions) the electric pulse energy, as a rule, is absorbed by the plasma for the time of two arrivals of the pulse at

the tube. In a range of lower and higher pressures the energy is absorbed by the plasma for a greater number of rereflections.

It was shown that there are regimes on which, at least, 80 % of the energy supplied to the cable is contributed in the discharge gap. On the basis of numerous measurements in N_2 - O_2 mixtures the following fact was substantiated: the pressure dependence of the energy contribution is characterized by the shape similar to one of the pressure dependence of the velocity with the difference that position of the maximum is noticeably shifted to the left. As an example Fig.2.33 represents dependencies of the energy contributed into gas in the first pair of pulses W_I and the energy, taking into consideration one reflection W_{II} in oxygen of technical purity in a discharge tube of 20 cm length and 5 cm diameter.

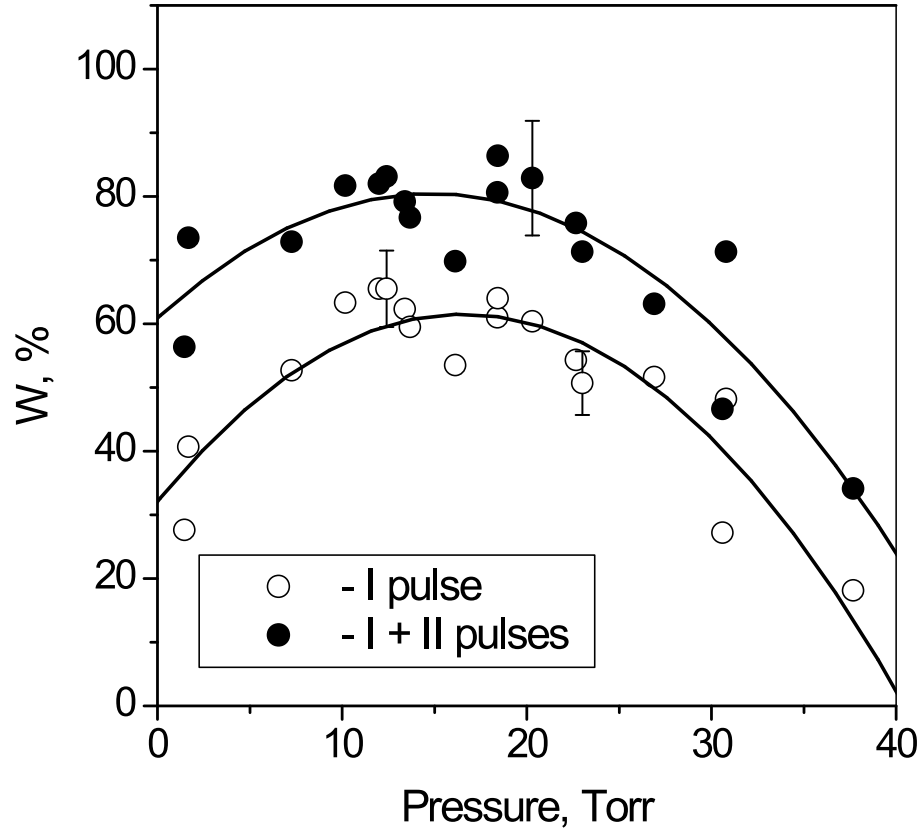


Figure 2.33: Energy contributed into gas in the first pair of pulses W_I and the energy, taking into consideration one reflection W_{II} in oxygen. $U = -15$ kV, pulse duration is 20 ns, pulse front duration is 8 ns, $f = 82$ Hz, discharge tube diameter is 4.7 cm, tube length is 20 cm.

2.3.2 Spatial uniformity of ionization wave. FIW in a large discharge volume.

So, there is certain range of gas densities where the fast ionization wave develops with high velocity. To study the spatial structure of the discharge and the uniformity of combustion, we carried out a series of experiments, in which the emission intensity (integrated over the wavelength range 300–800 nm) was registered with a PicoStar HR12 (La Vision) ICCD

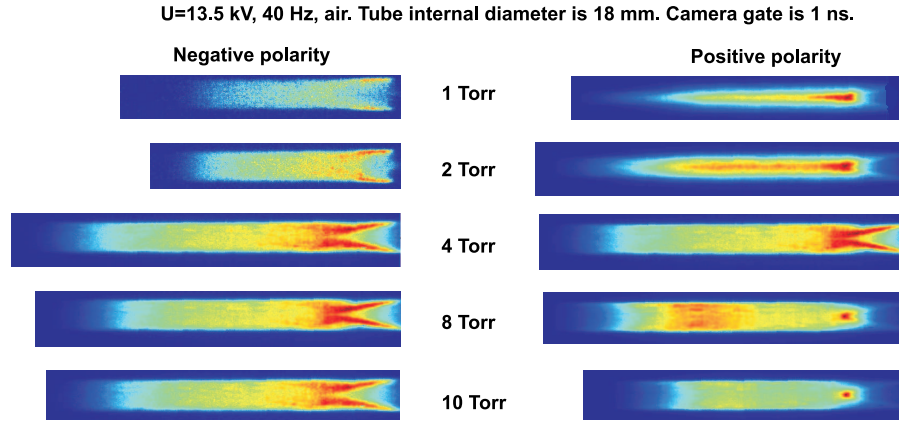


Figure 2.34: The imaging of nanosecond discharge propagation in long tube for different polarities of a high-voltage pulse. $U = \pm 13.5$ kV, pulse duration is 25 ns, pulse front duration is 3 ns, $f = 40$ Hz. Discharge tube diameter is 18 mm; interelectrode distance is 60 cm.

camera. Camera gate was equal to 1 ns, and we controlled discharge propagation from high voltage to low voltage electrode with time interval 1 ns between frames in periodical regime of the discharge operation. These results are represented in Fig. 2.34 for different polarities of a high-voltage pulse.

The sensitivity of ICCD system is the same for all the images. In controlled spectra range (300–800 nm) the main emission goes from the second positive system of molecular nitrogen (N_2 , $C^3\Pi_u - B^3\Pi_g$). The radiative life time of this system is 40 ns, this means that the second positive system gives quite a good imagination about plasma uniformity. The gate duration for any image comprises 1 ns, and a time from a moment of the discharge start from a high-voltage electrode is equal 10 ns everywhere. For negative polarity, we observe intensive emission around a conical electrode (cathode). The velocity of a discharge is slow for low pressures (1-2 Torr), the attenuation along a tube is high, but the emission is quite uniform. For positive polarity for the same pressures we observe higher velocities of propagation, but the discharge develops preferably along the discharge tube axis. The strongest emission for positive polarity images is observed at a region of electrode tip. At higher pressures (4-10 Torr) the discharge is relatively uniform for both polarities, but a character of its development is quite different. In part, for positive polarity we observe change of the shape of emission front from convex to concave with pressure increase.

It is clearly seen that the region which corresponds to maximal velocity of the fast ionization wave (that is 4–8 Torr at our experimental conditions) is a region of spatially uniform development of a discharge. Pressure range 4-8 Torr at ambient temperature corresponds to gas densities in a range of $(1.3 - 2.6) \cdot 10^{17} \text{ cm}^{-3}$. Increasing the amplitude of high voltage pulse, it is possible to shift the region of uniformity to higher gas densities.

It is interesting to compare dynamics of the nanosecond discharge development for different diameters of a discharge tube. The electrode and tube walls are marked with white lines in Fig. 2.35 which gives this comparison for positive pulse polarity. It is clearly seen that the pictures of a discharge development in a tube of 2 cm in diameter and in a tube of 5 cm in diameter at the same parameters of the electrical pulse are different.

P=2 Torr, d=5 cm

P=2 Torr, d=1.8 cm

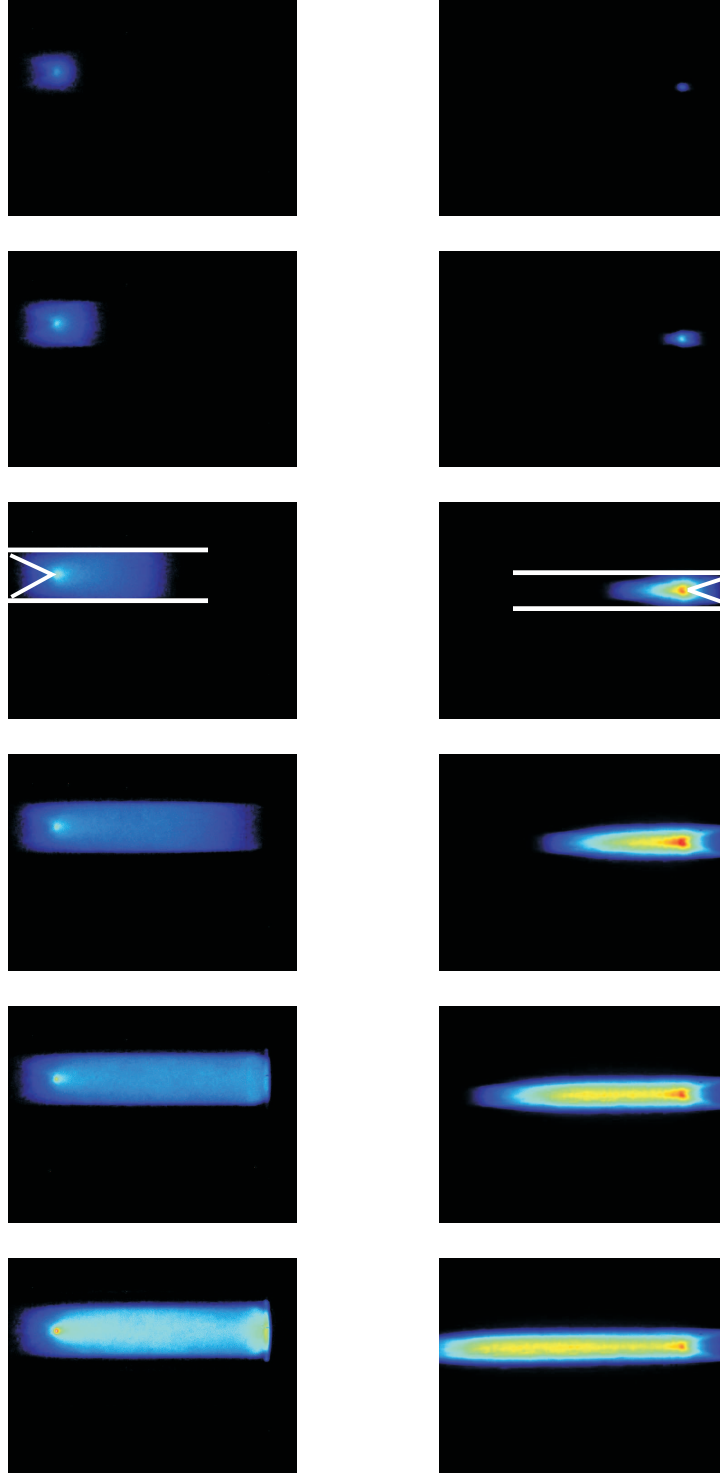


Figure 2.35: The imaging of nanosecond discharge propagation in tubes of different diameters. Positive polarity, $U = +13.5$ kV, pulse duration is 25 ns, pulse front duration is 3 ns, $f = 40$ Hz. Discharge tube diameter is 18 mm; interelectrode distance is 60 cm.

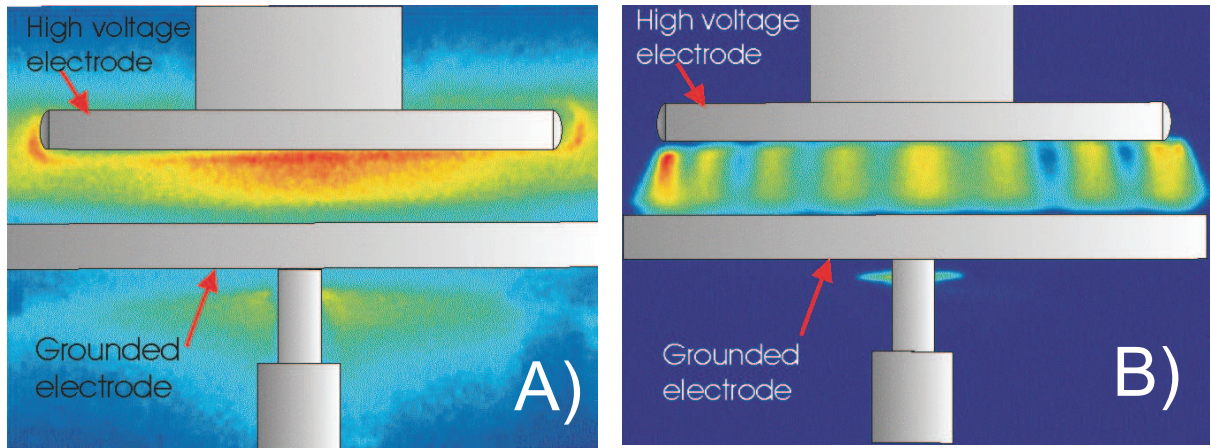


Figure 2.36: Emission image from a nanosecond discharge taken by LaVision ICCD camera. Camera gate is equal to 1 ns. Air, +5 kV pulse amplitude and 12 ns pulse duration. a) – 0.6 Torr; b) – 20 Torr.

For discharge tube of smaller diameter, we observe the formation of relatively narrow beam-like structure which propagates from high-voltage conical electrode (anode). For discharge tube 5 cm in diameter the emission is more uniform, and bright zone at the electrode tip is less-pronounced.

In our early papers the development of a nanosecond discharge in large volume was studied. It was shown that nanosecond discharge develops quasi-spherically from the high-voltage electrode, at least, while the field strength in the breakdown front is of the order of KV/cm Torr. If the pulse amplitude and duration are sufficiently high the discharge gap closure takes place, in this case the plasma region nearby the low voltage electrode is uniform. As pressure increases, the wave front comes to stop closer to the high-voltage electrode. In this case the second wave of the positive polarity starts from the low-voltage electrode surface towards FIW. The opposing wave arises due to effective preionization ahead of the FIW front and high potential difference between the low-voltage electrode and the FIW front. As pressure further increases, the diameter of a region on the surface of the low-voltage electrode from which the opposing FIW starts begins to decrease. At a certain pressure the opposing wave loses its uniformity and is transformed into a bunch of streamers that closes the discharge. Further increase of the pressure results in a decrease of the number of opposing streamers and, as a result, we can observe a spherical ionization wave that came to stop. And, finally, at high pressures FIW transforms into the pulsed corona from the high-voltage electrode. A similar pattern was observed if the amplitude of high-voltage pulses decreased at fixed pressure.

Additionally we studied the development of nanosecond discharge in a geometry of two parallel electrodes in air with relatively small distance between electrodes for a pressure range of 0.6-20 Torr for different repetitive frequencies of the discharge: starting from 3 Hz up to 30 kHz. Positive polarity of a high-voltage pulses was used; the amplitude of a pulses was equal to 5 kV. We controlled the emission of second positive system of molecular nitrogen with camera gate 1 ns and time intervals between frames of 1.3 ns. The distance between plane electrodes is equal 3 cm and diameter of upper electrode is equal to 12 cm. Fig. 2.36, a gives an image of emission 14.1 ns after high-voltage pulse is

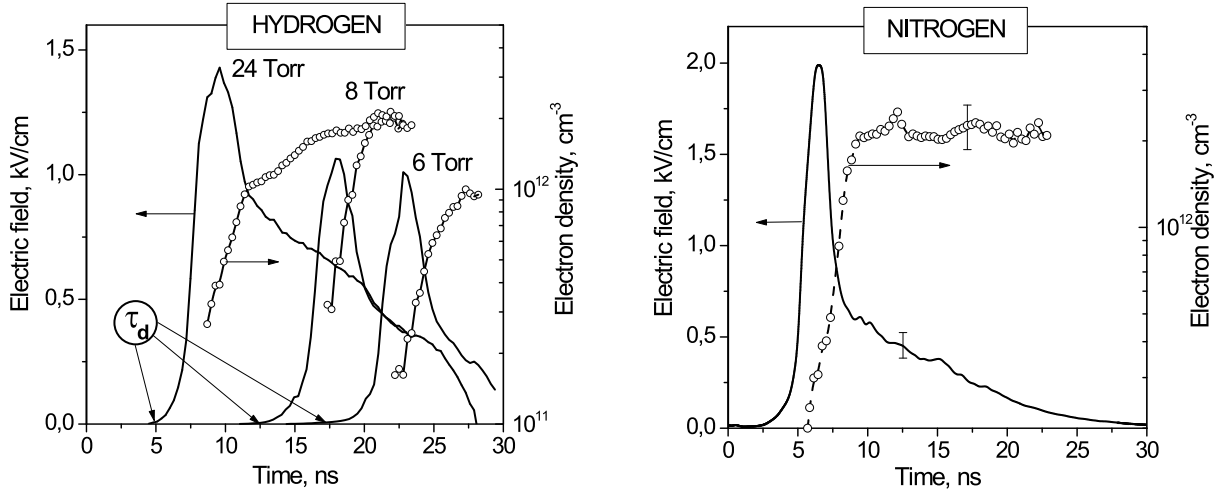


Figure 2.37: Electric field and electron density: typical temporal behavior. $U = -13.5$ kV, $x = 20$ cm from the cathode. Hydrogen pressure is pointed in the figure. Nitrogen pressure is equal 4 Torr.

applied to the electrodes at a pressure of 0.6 Torr and repetitive frequency of 30 kHz. At pressure increase, we obtain a chain of separate channels, which start on the boundary of electrode and close the discharge gap. These "streamers" are not fixed on the electrode, they travel along the boundary (see Fig. 2.36). Thus, we observe a phenomenon which has to be taken into account at organization of pulsed nanosecond discharge at different applications: the degree of uniformity of the discharge in a "free space" may be increased using special electrode systems which will not lead to destabilization of a discharge on boundary effects; increase of frequency influence on the discharge uniformity, but not too much: change of a frequency in a range of 3 Hz–3 kHz gives only a few Torr shift for the boundary between uniform and non-uniform discharge. It has to be noted that much stronger dependence is observed for change in pulse amplitude. Acting on a gas by high-voltage pulse approximately 100 kV in amplitude, we were able to obtain uniform discharge up to gas densities $\approx 5 \cdot 10^{18} \text{ cm}^{-3}$, which corresponds to pressure about of 150 Torr at ambient temperature.

2.3.3 Electric field and electron density

To perform the detailed kinetic analysis of FIW it was necessary to know the electric field and electron concentration behavior in time and space. Both the values may be obtained from the temporal spatial dynamics of excessive charge per unit length which is possible to measure by a capacitance sensor moving along the discharge tube. The technique, proposed at our laboratory for reconstruction of the excessive charge density per unit length was based on registration of signals from the capacitance sensors and subsequent solution of the reverse problem with consideration of the spatial sensitivity function of the sensor. The sensor that is actually a charge detector responds to excessive charge not only in a measuring cross-section but in a certain spatial region nearby it. The sensor signal is a convolution of actual distribution of the charge with the spatial function of the sensitivity. In case of random axially symmetric distribution of charge the potential at

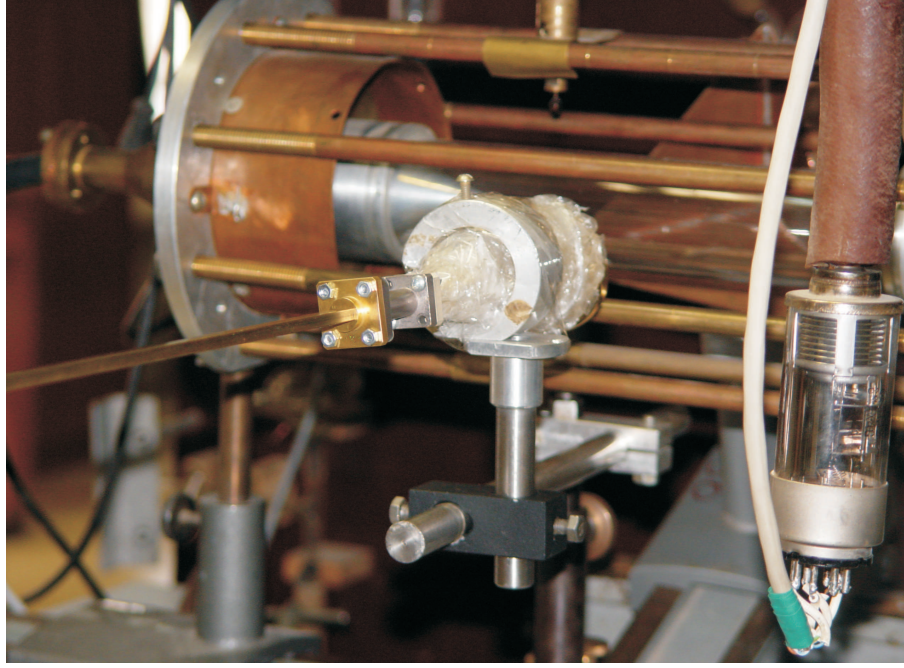


Figure 2.38: Photo of a microwave interferometer installed near the discharge tube. Microwave lens and a part of waveguide are clearly seen.

a point of sensor location is determined by only the tube charge density per unit length, which makes it possible to use the one-dimensional treatment.

The sensor sensitivity function $f(x)$ was obtained from special calibrating experiments described in.⁹¹ In this case a solution of the reverse problem to find the actual charge distribution is reduced to the search for the minimum of a functional of the following type:

$$F(q) | _t = \|V_{\text{exp}}(x_0) - \int_{-\infty}^{+\infty} f(x - x_0)q(x) dx\|, \quad (2.7)$$

where x_0 is a point of the sensor location, $V_{\text{exp}}(x_0)$ is a measured signal, $q(x)$ is a real charge distribution.

The dynamics of the longitudinal component of electric field and electron concentration were calculated with the use of the known charge distribution along the discharge device length. Assumptions that the charge distribution is quasi-stationary (considered that the capacitance signal is determined by the available charge distribution) and the excessive charge is located nearby the glass surface were used in data processing. The latter assumption automatically means that the minimum possible value of the longitudinal electric field component was determined in the wave front. Electron concentration was determined in the drift approximation on the basis of data on the charge and field dynamics. The methods of field and electron concentration from the electric signals determination were treated in more detail in,^{91, 92}

Examples of reconstructed electric field for nitrogen and hydrogen are given in Fig.2.37. It is seen that in all the cases the longitudinal electric field profile has a distinct narrow - only 2-4 ns - maximum. In the field maximum the fields are very high - up to \sim

$kV/(cmTorr)$. Then, the field decreases very rapidly, and for the pulse duration, i.e. up to 20-25 ns, its value is not over tens- hundreds of $V/(cm Torr)$. Electron concentration increases in time and in 5-10 ns after the field pulse start comes to the stationary value. The decrease of the total field peak duration in hydrogen, as pressure decreases, is caused by the growth of the breakdown start delay time that reaches 17 ns at hydrogen pressure of 6 Torr.

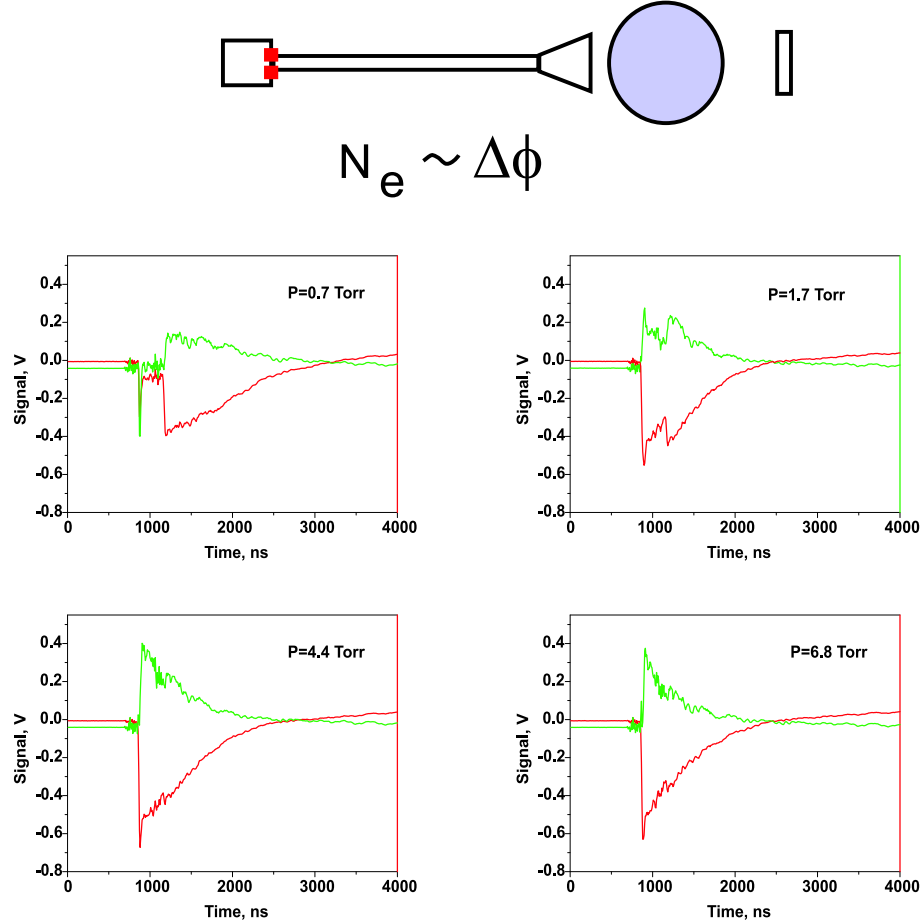


Figure 2.39: Scheme of the interferometer and examples of preliminary experimental data.

It should be noted that under the same conditions in nitrogen with the high-voltage pulse of positive polarity the field in the same way depends on time, but its absolute value is several times higher; behind the front, on the contrary, electric field is lower in several times than in FIW of negative polarity.⁹³ Within the limits of the dome-type pressure dependence of the wave velocity the absolute field value weakly increases no more than in 1.5-2 times, the reduced electric field strength value decreases by about the order of magnitude. This should result in the essential redistribution of the energy over internal degrees of gas freedom.

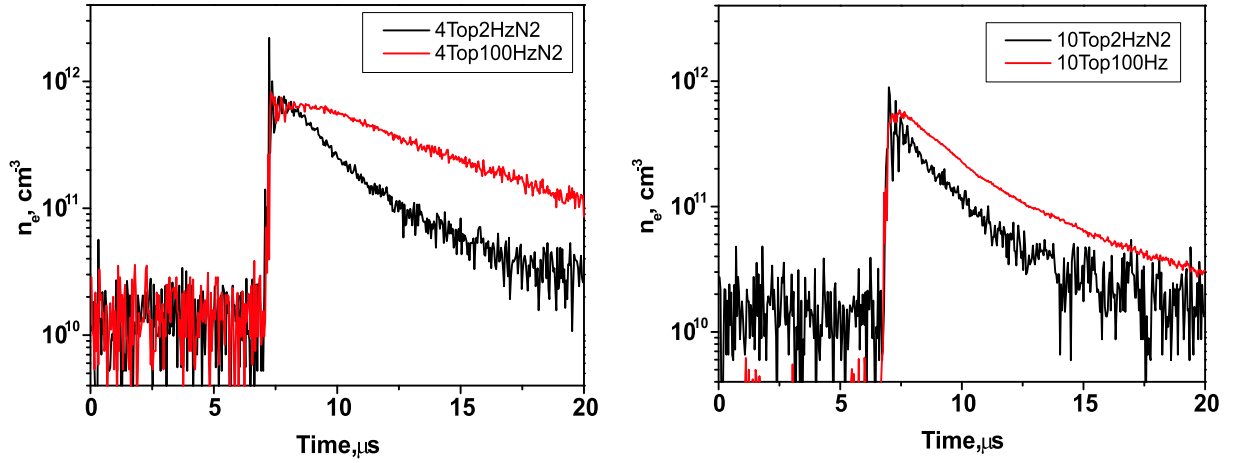


Figure 2.40: Electron density at different pressures. Pulse amplitude is equal to 13.5 kV, pulse duration is 12 ns.

2.4 Experimental investigation of electron density at low gas temperatures

Magnetohydrodynamic (MHD) effects have numerous applications, such as MHD flow control and MHD power generation. The MHD power generation has some advantages: the absence of moving parts and the possibility for exhaust flow use for power generation. But the exhaust flow has an insufficient level of ionization, so it is necessary to use an additional source of plasma production. The critical point for MHD applications are plasma density and the cost of plasma production. The report focuses on the problem of plasma production in hot exhaust gases.

There are numerous types of plasma sources: different types of electric discharges and electron beams. Among the sources of plasma the non-equilibrium discharges, like nanosecond discharges and e-beam, are more effective per one electron in plasma.

The goal of this work is a study of temperature influence on plasma decay process. For a successful application of MHD effects it is necessary to maintain electron concentration in the flow at a sufficient level. Thus, when nanosecond discharge is used as the plasma source, the "efficiency" of the discharge and minimum high-voltage pulse frequency are determined by a plasma decay time. that is, a plasma decay time determines electron energy cost.

The kinetics of excited states in a plasma has not yet been studied thoroughly. Most of the works on plasma kinetics study are performed in "cold" gas (300 – 400 K). A lack of verified data on plasma relaxation in "hot" gas (800 – 1500 K) restricts the development of MHD technologies (applications).

2.4.1 Experimental setup

Figure 2.41 shows a block diagram of the experimental setup. A discharge was excited in a discharge tube by negative-polarity pulses with an amplitude of 11 kV, duration at half-height of 25 ns, and rise time of 5 ns. A pulse from a high-voltage generator was delivered to a discharge device via RK-50-11-11 cable 30 m long. The discharge device

was a quartz tube with an inside diameter of 47 mm and outside diameter of 50 mm. The screen of the discharge device consisted of eight brass rods 12 mm in diameter spaced at equal distances in parallel with the discharge tube on a circle with a diameter of 140 mm. The high-voltage electrode was a duralumin cone with an angle of 60°. The low-voltage electrode was shorted against the screen. The distance between the tip of the high-voltage conical electrode and the low-voltage ring electrode was 200 mm. The mixture pressure was monitored by an MDx4S mechanotron.

The system of electrical diagnostics of the discharge consisted of an inverse current shunt built in a break in a shield of the high-voltage cable and a capacitive sensor movable along the discharge device. The current shunt was placed at such a distance from the discharge tube that the current pulse incident on the discharge device and that reflected from it were time separated.

To study the spatial structure of the discharge we carried out an additional series of experiments, in which the emission intensity (integrated over the wavelength range 300–800 nm) was registered with a PicoStar HR12 (La Vision) ICCD camera. After the initiation of the discharge, we observed an intense short-duration emission pulse from the discharge with a characteristic decay time of a few tens of nanoseconds. When obtaining images of a nanosecond discharge, the gate time of the ICCD camera was set to 1 ns. The triggering of the CCD camera was synchronized with the triggering of a high voltage generator. The main emission in a high-current nanosecond discharge in the wavelength range 300–800 nm air comes from the second positive system of molecular nitrogen ($\lambda = 337.1$ nm, $C^3\Pi_u(v' = 0) \rightarrow B^3\Pi_g(v'' = 0)$ transition). The life time of the upper level of the system is about 40 ns, so, it reflects adequately the spatial structure of the discharge.

The main block of the microwave diagnostics contains a microwave generator, a diode assembly and a calibrating unit. Microwave radiation (94 GHz) is transmitted from the main block to plasma and returned to the main block by the system of waveguides. To input the microwave radiation to plasma quartz windows are used. The microwave diagnostics is based on interferometrical measurement method.¹⁰⁷ Incursion, when the microwave radiation passes through plasma, equals to

$$\Delta\varphi[Rad] = \frac{l[cm] \cdot n_e[cm^{-3}]}{118.4 \cdot \nu[Hz]}, \quad (2.8)$$

where n_e is electron concentration. The diode assembly consists of two detectors spaced at quarter-wavelength, which detect sum of direct signal from the microwave generator and signal passed through plasma. Hereby signals of the detectors equal to

$$\begin{aligned} I &= A \cdot \cos\{(\Phi(t) + \Phi_0)\} - A \cdot \cos\{\Phi_0\}, \\ Q &= B \cdot \sin\{(\Phi(t) + \Phi_0)\} - B \cdot \sin\{\Phi_0\}, \end{aligned} \quad (2.9)$$

where Φ_0 is incursion, which is independent of time. Unfortunately, our diagnostics is a semiconductor device, which is very sensitive to pickups from a high-voltage discharge. Thus, the diagnostics during high-temperature experiments has a dead time of approximately 1 μ s, while the amplifier of the detector signal is overdriven due to electric noise from a high-voltage Marx generator.

Fig. 2.16 gives an example of a picture of fast ionization wave development in air obtained by the ICCD camera. The discharge was initiated by high voltage positive

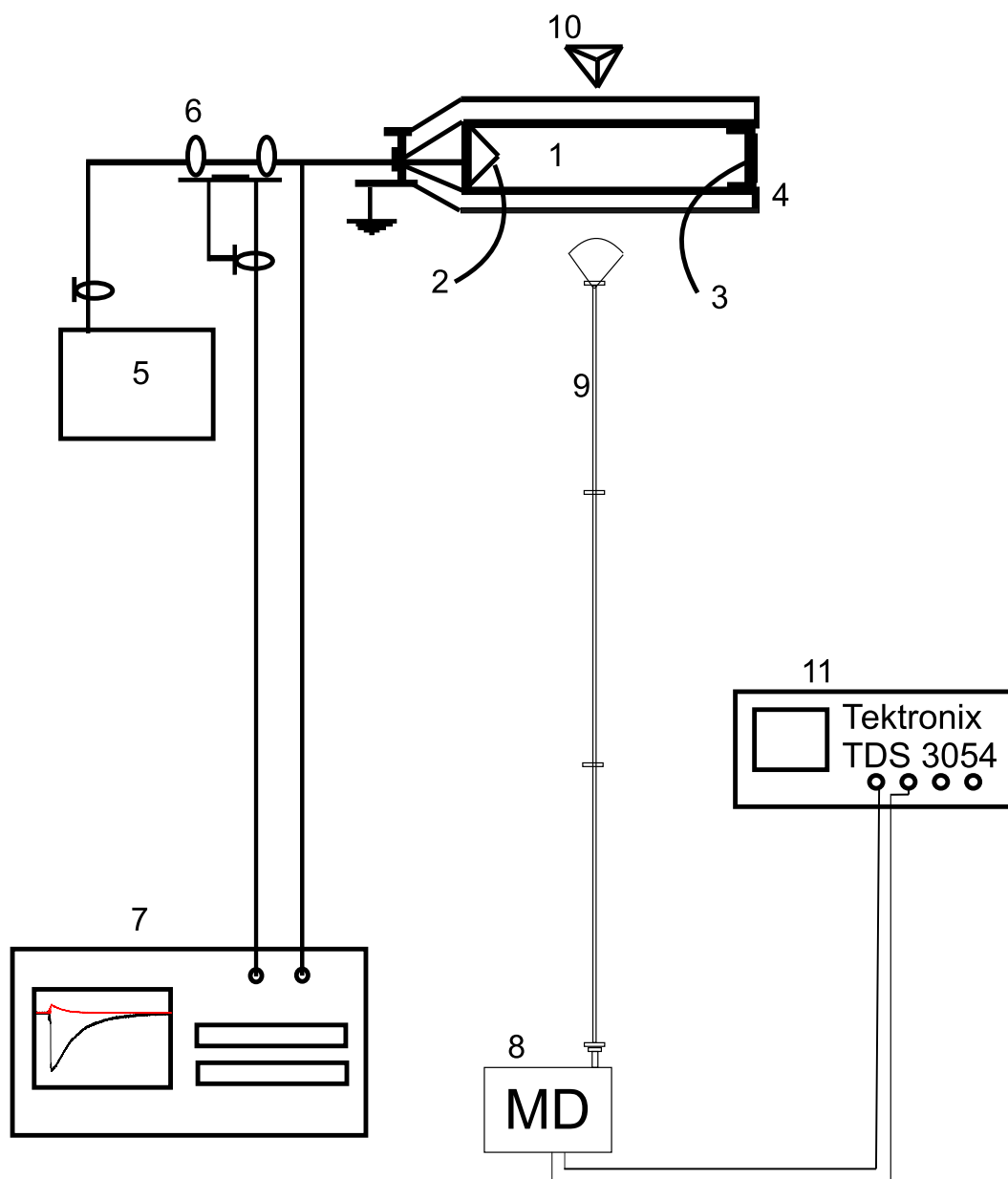


Figure 2.41: Experimental setup: 1 — discharge cell, 2,3 — electrodes, 4 — optical window (CaF_2), 5 — high voltage generator, 6 — back current shunt, 7 — oscilloscope Tektronix TDS-380, 8 — microwave interferometer, 9 — waveguide, 10 — angled reflector, 11 — oscilloscope Tektronix TDS-3054.

polarity pulses, where pulse amplitude in cable was 11 kV, duration at half-height was 25 ns, rise time was 5 ns, and repetitive frequency was 40 Hz. Some maxima are manifested near the electrodes, while on the whole, the discharge is developing uniformly. The velocity of front propagation may be estimated as 2.5 cm/ns that is clearly seen from a succession of images.

Electron density determined in previous papers of our team in the drift approximation⁹¹ on the basis of data on charge and field dynamics gave the values of $\sim 10^{12} \text{ cm}^{-3}$. Fig. 2.17 (¹⁴ according to the data taken from^{91,92}), displays typical temporal behaviour of the electric field, electron density and concentration of the electronically excited states.

The experiments has been carried out for N_2 , O_2 , CO_2 , $\text{N}_2\text{-O}_2$, and for a water vapor at different parameters of the experiments. The dependencies of electron density upon time at different repetitive frequency, gas polarity and gas pressure were obtained.

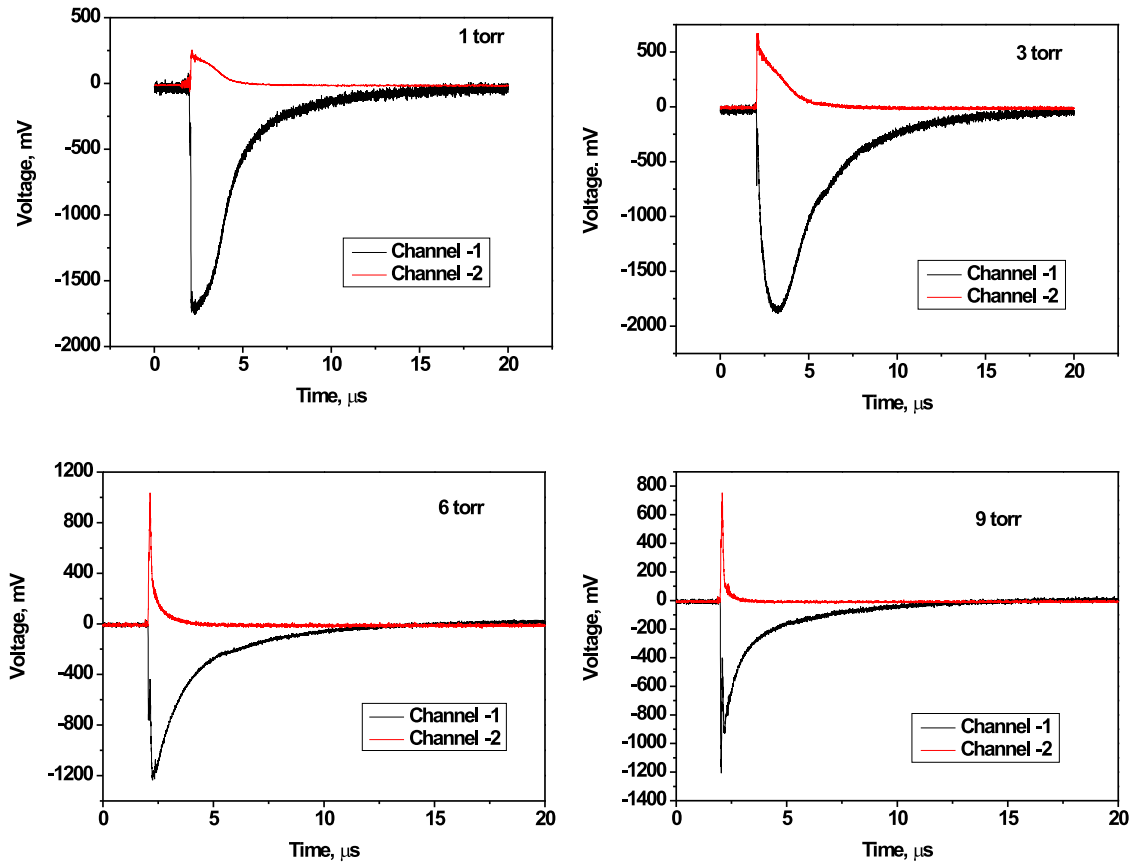


Figure 2.42: Oscillogrammes obtained by microwave technique in N_2 , $p= 1, 3, 6, 9$ Torr, $T= 295$ K, $U= 11$ kV in cable, positive polarity.

We observed longer decay time in experiments at high repetitive frequencies in a range of frequencies between 2 and 100 Hz (2, 40, 60, 80 and 100 Hz). The most reliable explanation lies in the fact that we have seed density of charged particles from pulse to pulse, and this background density influences the discharge development at high frequencies.

So, the major part of the experiments was performed at low repetitive frequency, equal to 2 Hz. We observed difference in absolute electron density between positive and negative polarity of a high-voltage pulse, and this may be connected with difference in electric fields at different polarities. This effect is discussed in details in.⁹³

2.4.2 Electron density decay in molecular nitrogen

Typical oscillogrammes obtained by a microwave technique are given in Fig. 2.42 for gas pressures 1, 3, 6, and 9 Torr. "Channel-1" means the first diagnostic channel, "Channel-2" – the second one, which is shifted by $\pi/2$ relatively to the first one. Calibration constants for the channels are $A=1960$ and $B=283$ respectively. Preliminary conclusions concerning the electron density behaviour can be made directly from the oscillogrammes. If there is an inflection of the kinetic curve, as it is clearly seen at a pressure 3 Torr ("Channel-1"), then the electron density is definitely not less than $\pi/2 \cdot 10^{12} \text{ cm}^{-3}$. Indeed, the phase shift in a peak is equal to $\pi/2$, and the expression for electron density calculation at plasma length equal to $L=5 \text{ cm}$ and microwave frequency equal to $\nu=94 \text{ Hhz}$ gives $n_e(t)=\phi(t) \cdot 10^{12} \text{ cm}^{-3}$. Further, the longer decay time at the oscillogramms, the longer recombination time for electrons in plasma.

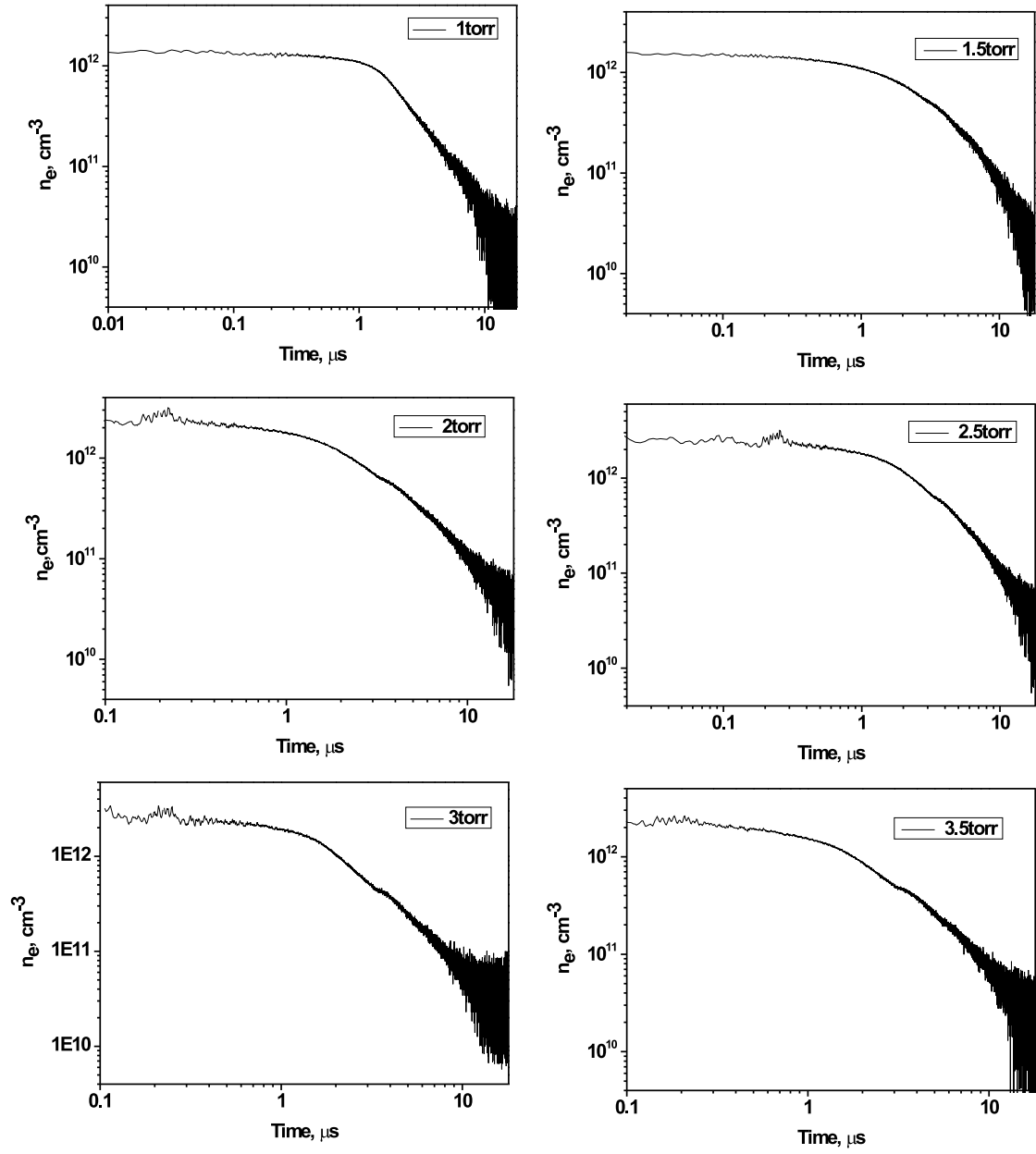


Figure 2.43: Electron density profiles in N_2 , $p=1-3.5$ Torr, $T=295$ K, $U=11$ kV, positive polarity.

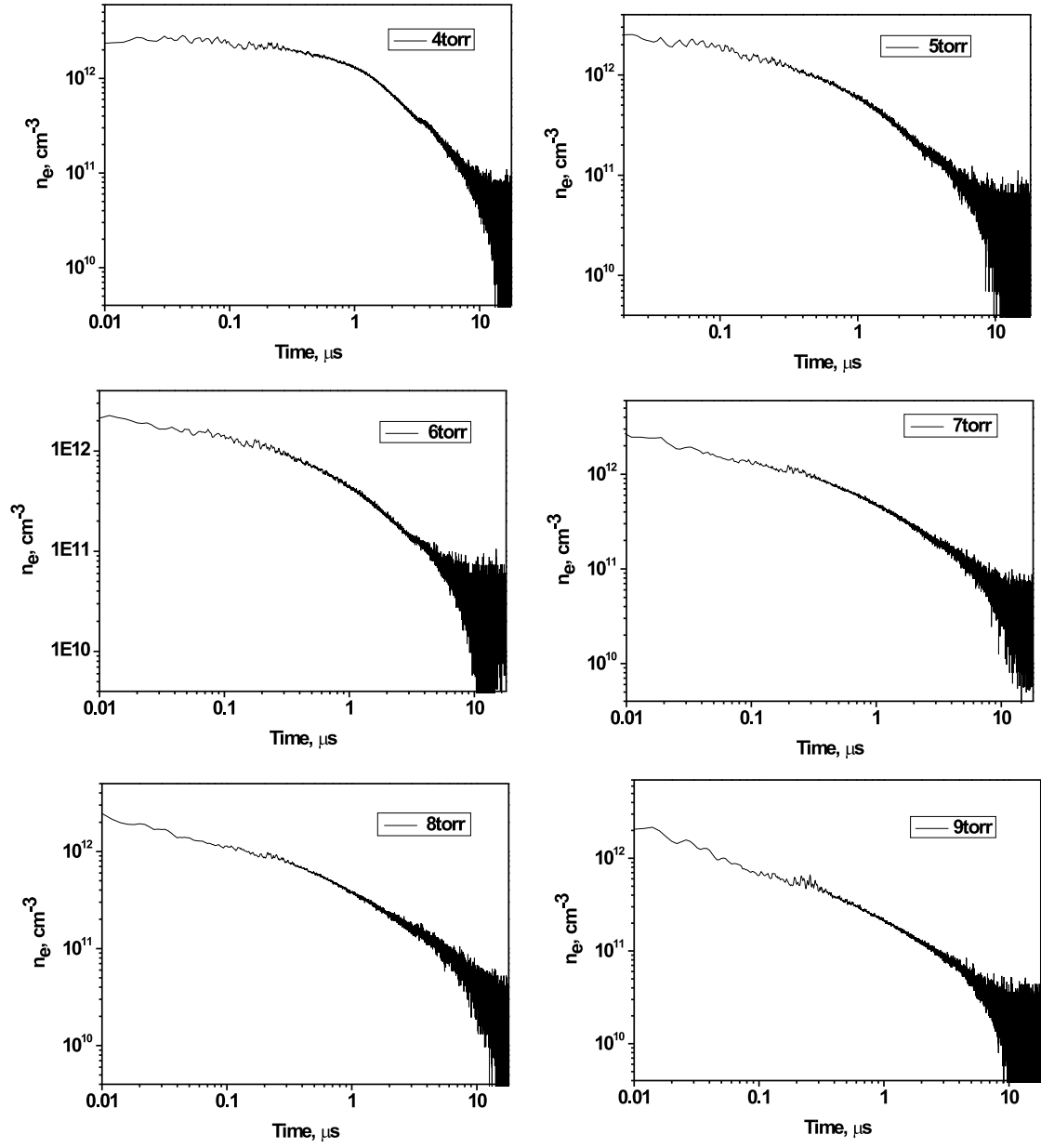


Figure 2.44: Electron density profiles in N_2 , $p=4\text{-}9$ Torr, $T=295$ K, $U=11$ kV, positive polarity.

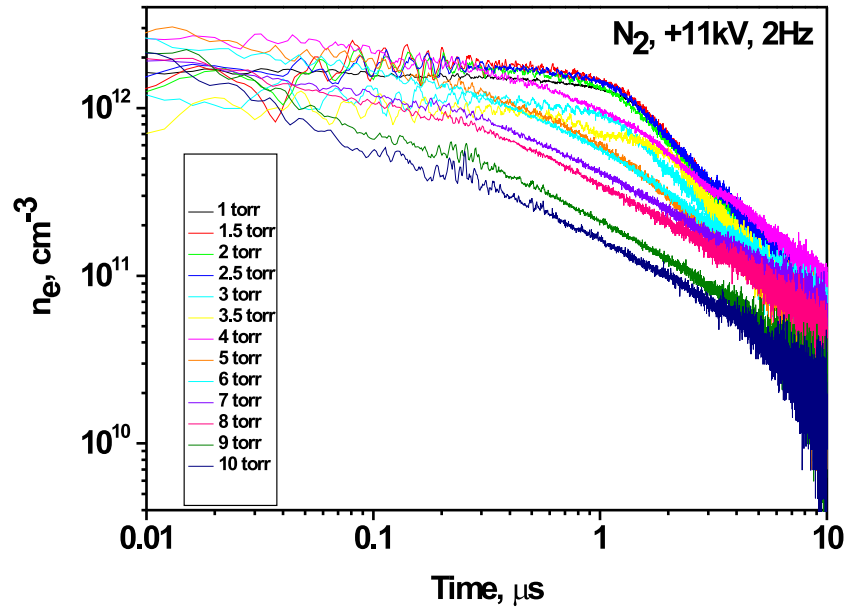


Figure 2.45: Electron density profiles in N_2 , $p = 1\text{-}10$ Torr, $T = 295$ K, $U = 11$ kV, positive polarity.

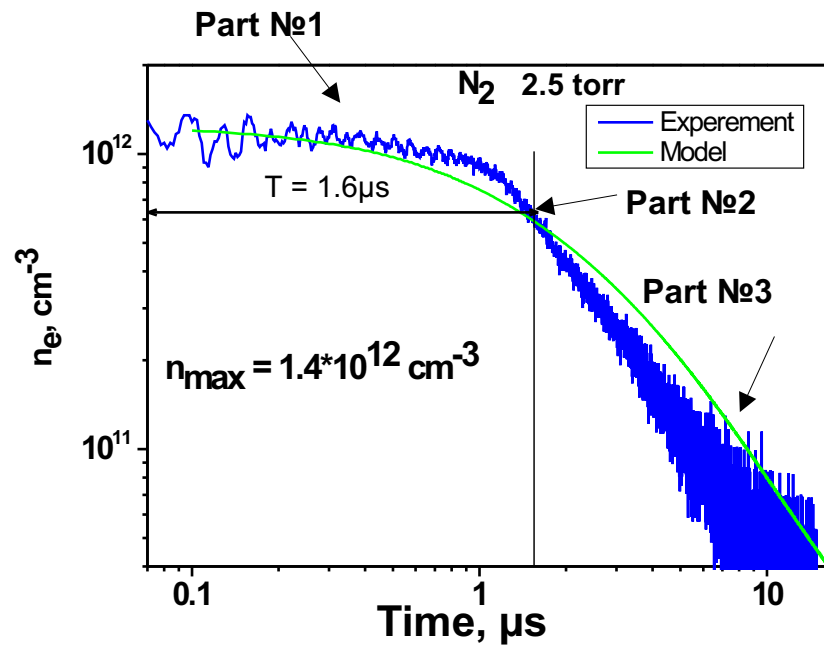


Figure 2.46: Electron density profile in N_2 , $p = 2.5$ Torr, $T = 295$ K, $U = 11$ kV, positive polarity.

Figs. 2.43, 2.44) give the electron density in N_2 for a pressure range from 1 to 9 Torr. It is obvious that the initial density slightly depends upon pressure, while decay time decreases with pressure. The initial electron density can be estimated as $n_{max} \approx 1 - 3 \cdot 10^{12} \text{ cm}^{-3}$ at $p=1-10$ Torr, $T=295$ K, $U=11$ kV in electric cable (22 kV at the high-voltage electrode), and positive polarity of the electric pulse. This is in reasonably good correlation with the paper,⁹³ where it was demonstrated on the basis of electric current measurements that the initial electron density depends slightly upon gas pressure, being equal to $(2 - 3) \cdot 10^{12} \text{ cm}^{-3}$.

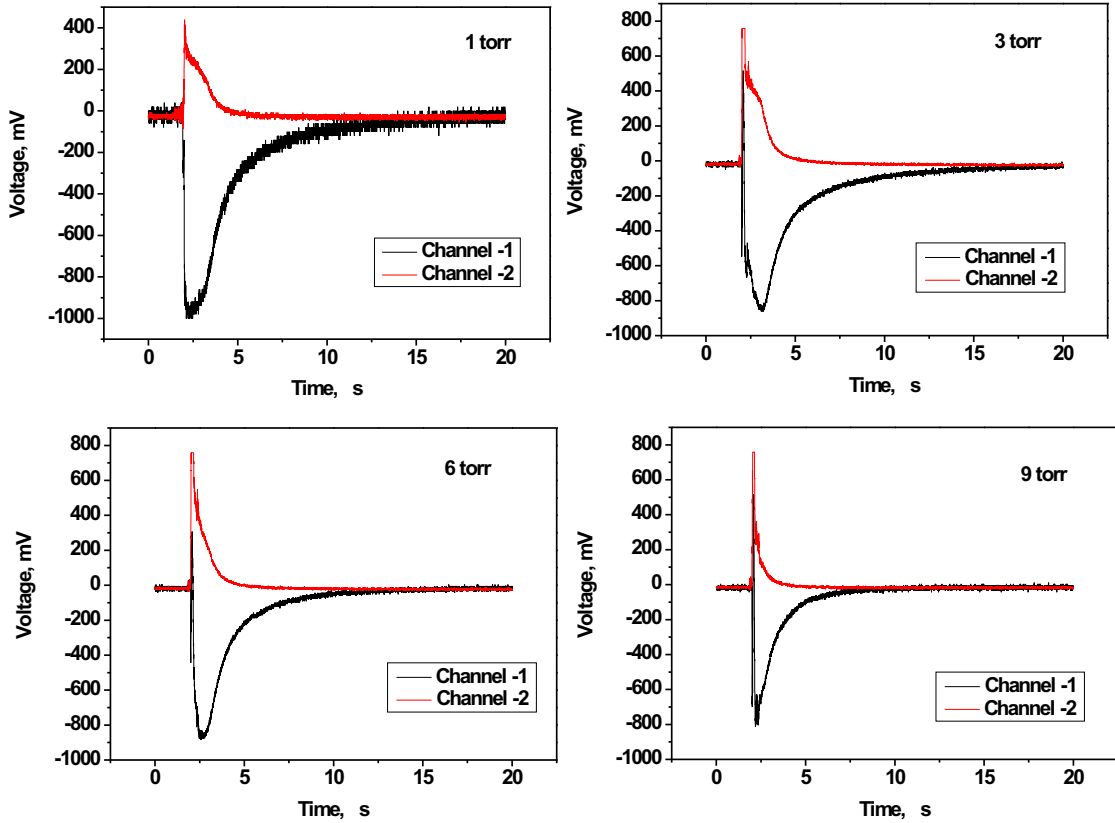


Figure 2.47: Oscillogrammes obtained by microwave technique in O_2 , $p=1, 3, 6, 9$ Torr, $T=295$ K, $U=11$ kV, positive polarity.

Fig. 2.46) gives electron density profile in N_2 at $p=2.5$ Torr. Plasma decay time has been determined as a time of the electron density decay by e times from its initial value. The decay time for nitrogen plasma is ($\tau \approx 1.6 \mu s$, $p=2.5$ Torr, $T=295$ K), and initial electron density here is equal to ($n_0 \approx 1.4 \cdot 10^{12} \text{ cm}^{-3}$).

Let us consider behavior of the electron density in detail (Fig. 2.46). It is clearly seen that we have slow decay during the first microsecond (region N 1), then we have the inflection of kinetic curve (region N 2) and the decay (region N 3). The first part of decay is determined by electron-ion recombination on N_2^+ ions, which is realized as $e+N_2^+ \Rightarrow 2N$ or $2e+N_2^+ \Rightarrow e+N_2$. The main process at the third stage (region N 3) is an electron-ion

recombination with the participation of N_4^+ ion. Thus, the region N 2 corresponds to ion conversion: $N_2^+ + 2N_2 \Rightarrow N_4^+ + N_2$. Preliminary results of the numerical calculations are given in Fig. 2.46) simultaneously with the experimentally obtained profile.

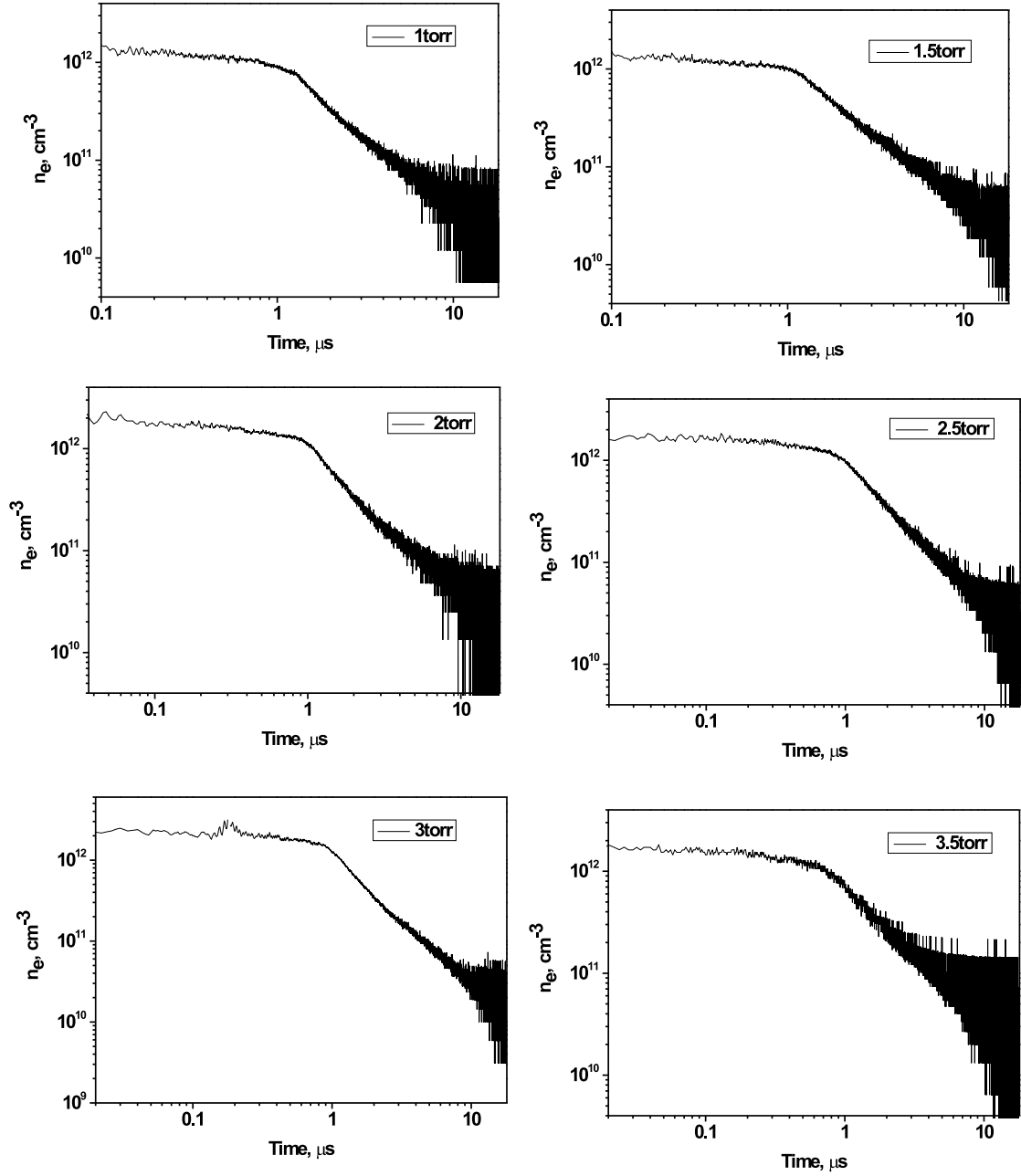


Figure 2.48: Electron density profiles in O_2 , $p = 1\text{--}3.5$ Torr, $T = 295$ K, $U = 11$ kV, positive polarity.

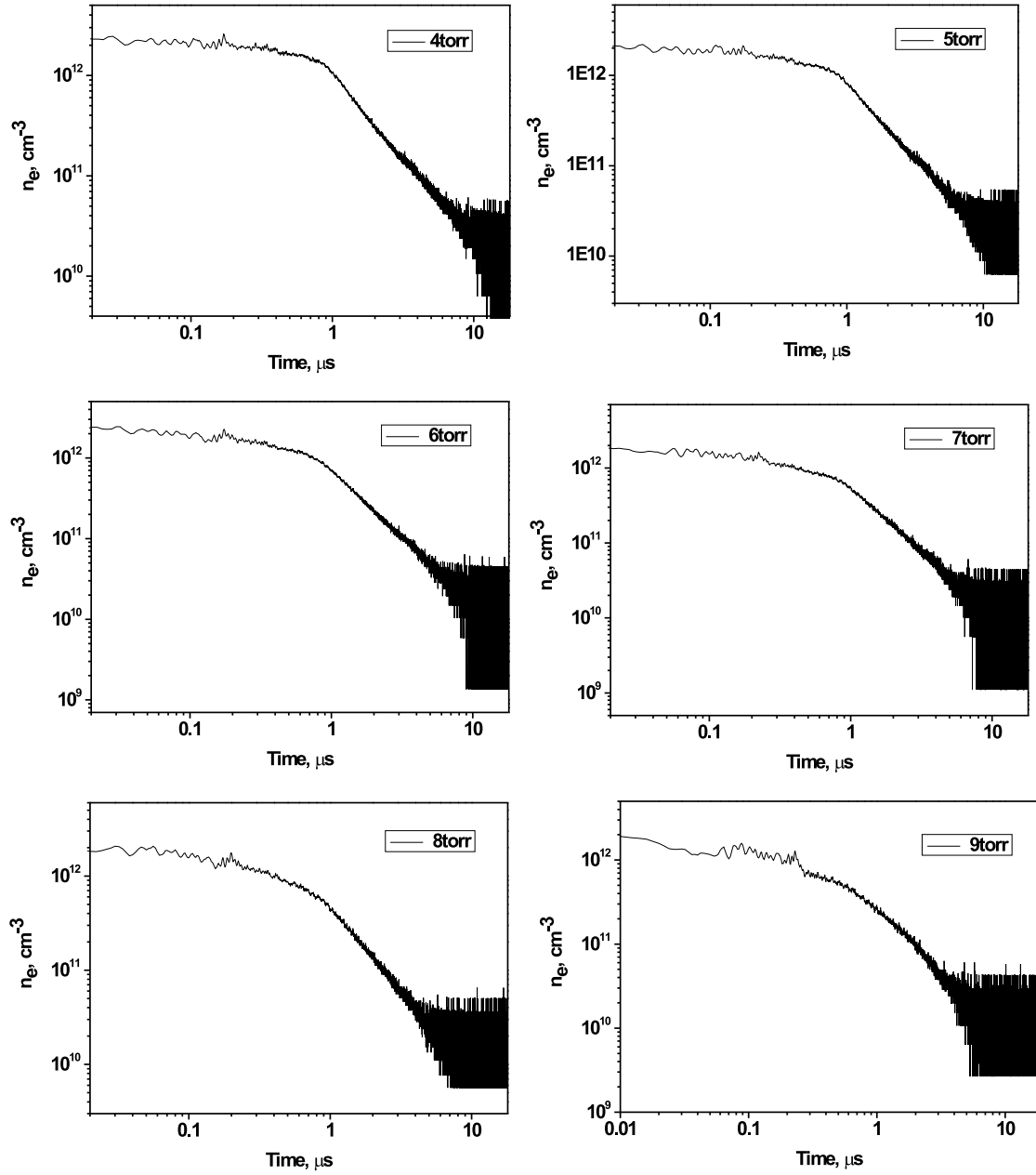


Figure 2.49: Electron density profiles in O_2 , $p = 4\text{-}9$ Torr, $T = 295$ K, $U = 11$ kV, positive polarity.

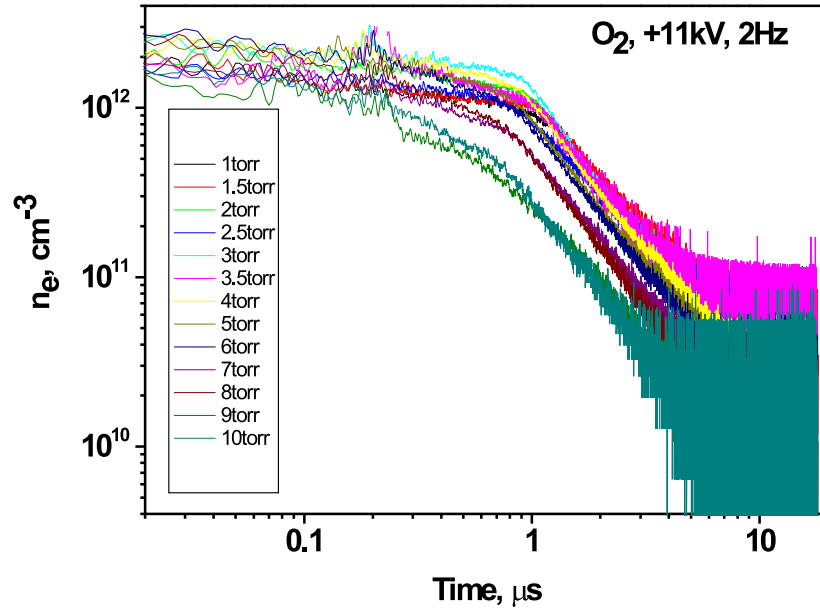


Figure 2.50: Electron density profiles in O₂, $p = 1-10$ Torr, $T = 295$ K, $U = 11$ kV, positive polarity.

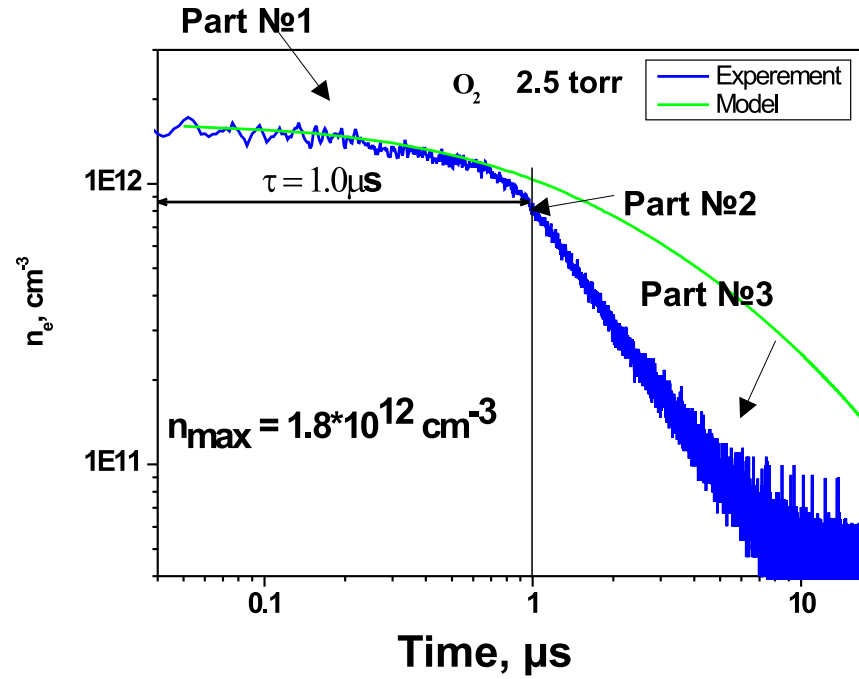


Figure 2.51: Electron density profile in O₂, $p = 2.5$ Torr, $T = 295$ K, $U = 11$ kV, positive polarity.

2.4.3 Electron density decay in molecular oxygen

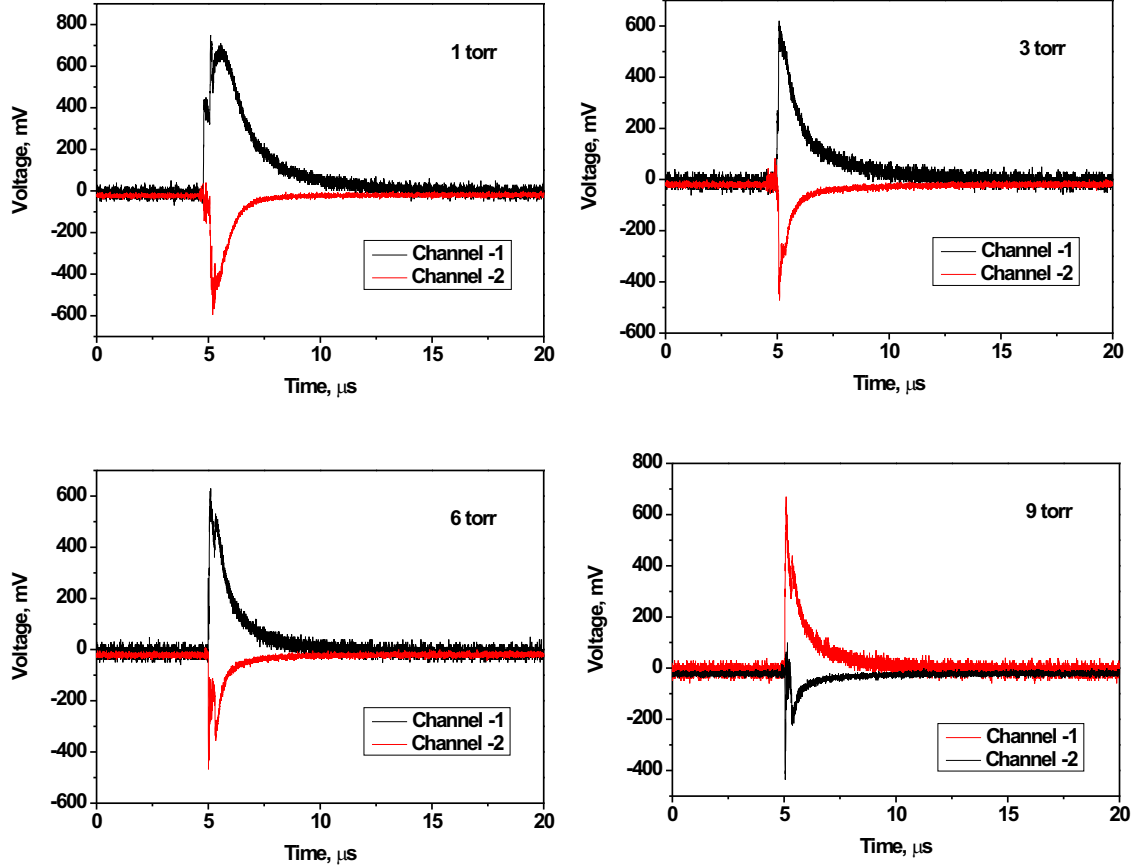


Figure 2.52: Oscillogrammes obtained by microwave technique in CO₂, $p = 1, 3, 6, 9$ Torr, $T = 295$ K, $U = 11$ kV, positive polarity.

Fig. 2.47 gives typical oscillogrammes obtained by microwave interferometry in molecular oxygen for gas pressures 1, 3, 6, and 9 Torr. Like in nitrogen, we observed slightly pronounced dependence of initial electron density upon gas pressure, and decrease of the electron density decay with pressure. Figs. 2.48, 2.49 illustrate electron density behavior in O₂ for a pressure range from 1 to 9 Torr. The same conclusion concerning initial electron density and the decrease of the density decay with pressure can be made from Fig. 2.50. Maximal electron density in molecular oxygen is estimated as $n_{max} \approx 1.5 - 3 \cdot 10^{12} \text{ cm}^{-3}$, at $p = 1-10$ Torr, $T = 295$ K, $U = 11$ kV, and positive polarity of the electric pulse).

The decay time for oxygen plasma is about $\tau \approx 1.1 \text{ μs}$, $p = 2.5$ Torr, $T = 295$ K), as it is seen from the profile in Fig. 2.51).

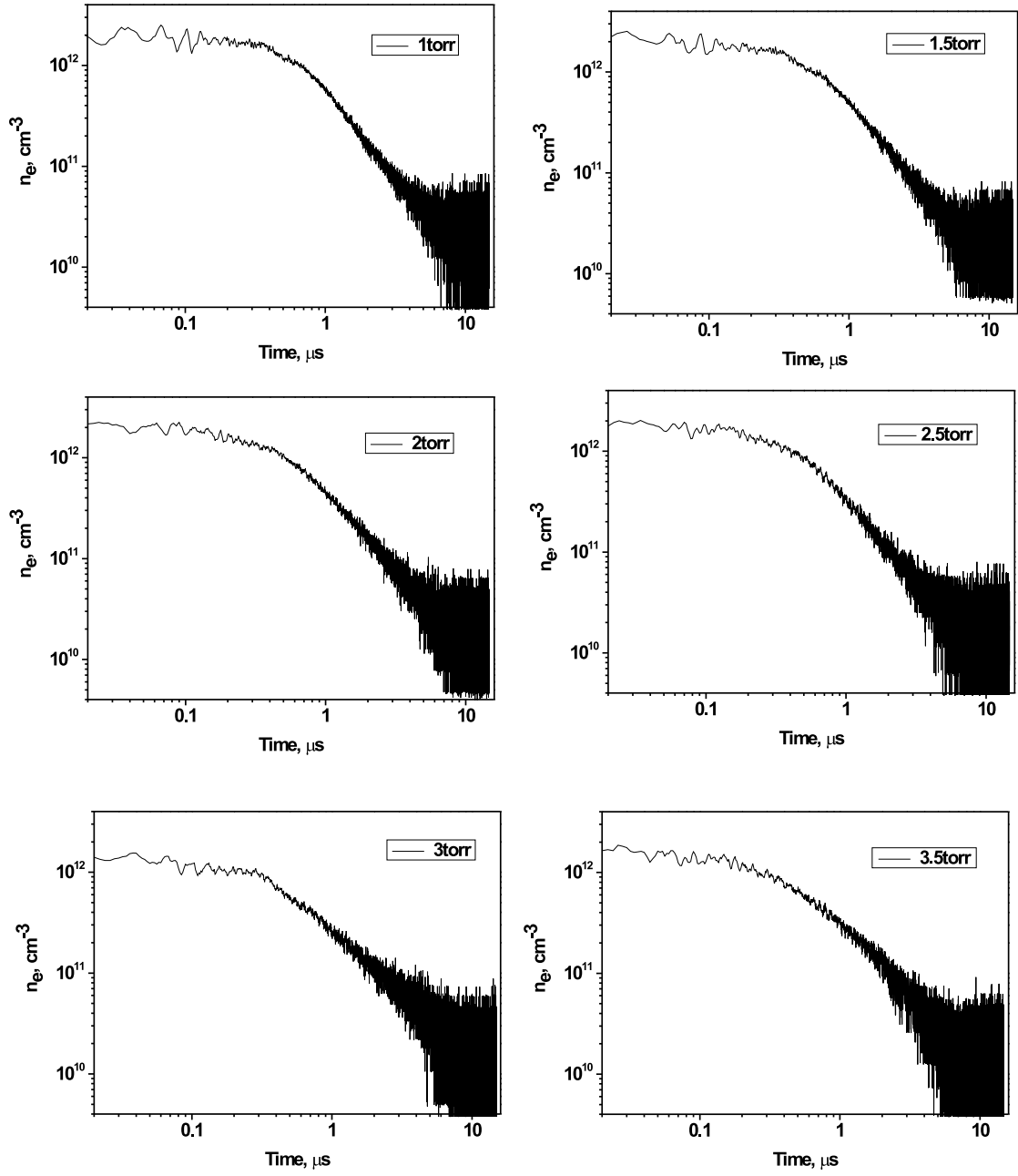


Figure 2.53: Electron density profiles in CO_2 , $p= 1\text{-}3.5$ Torr, $T= 295$ K, $U= 11$ kV, positive polarity.

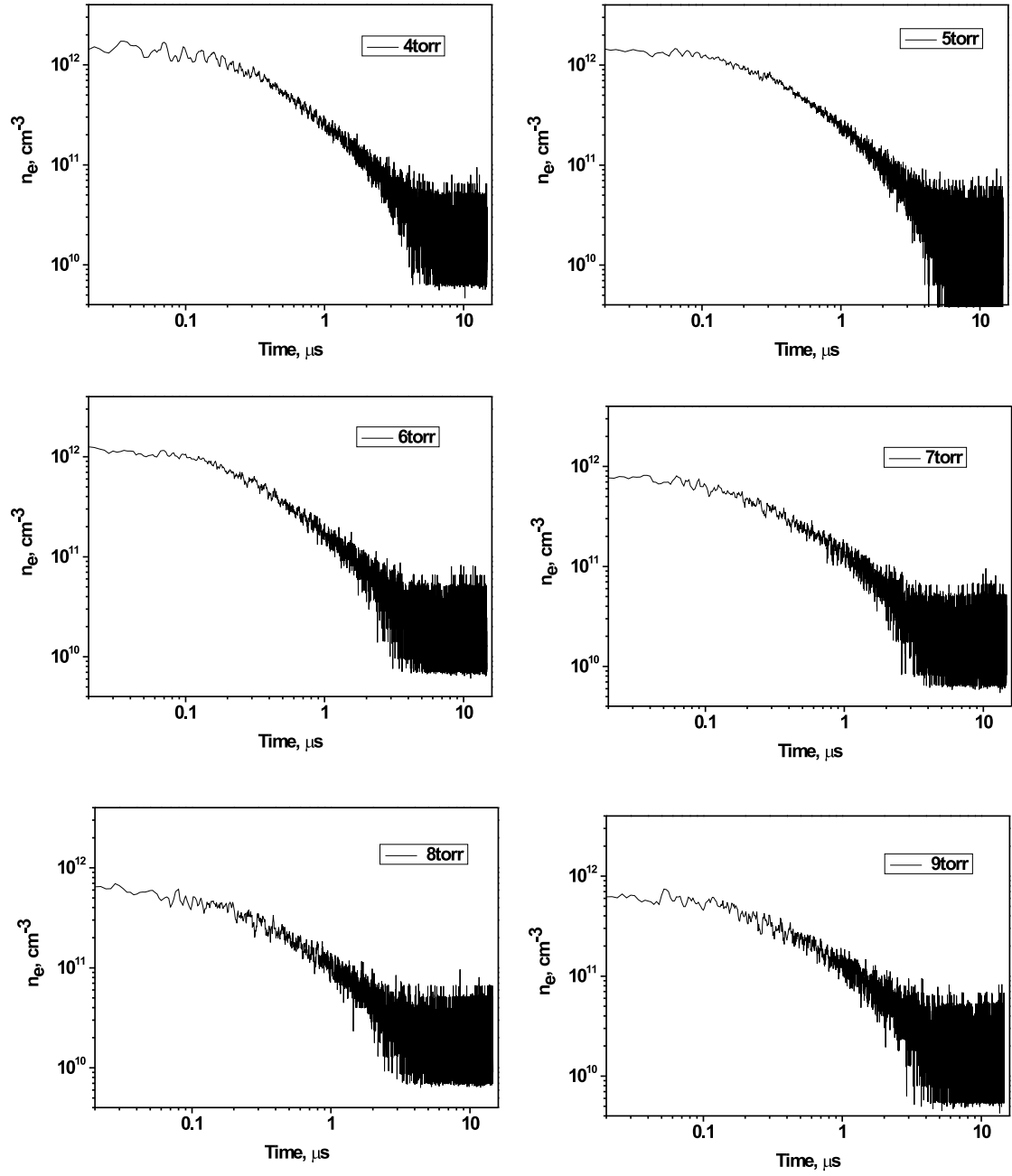


Figure 2.54: Electron density profiles in CO₂, $p=4-9$ Torr, $T=295$ K, $U=11$ kV, positive polarity.

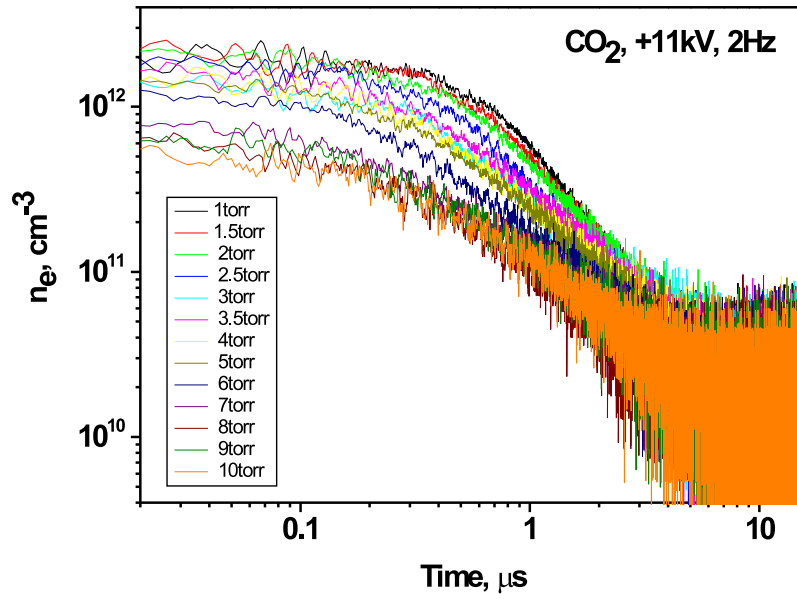


Figure 2.55: Electron density profiles in CO_2 , $p=1\text{-}10$ Torr, $T=295$ K, $U=11$ kV, positive polarity.

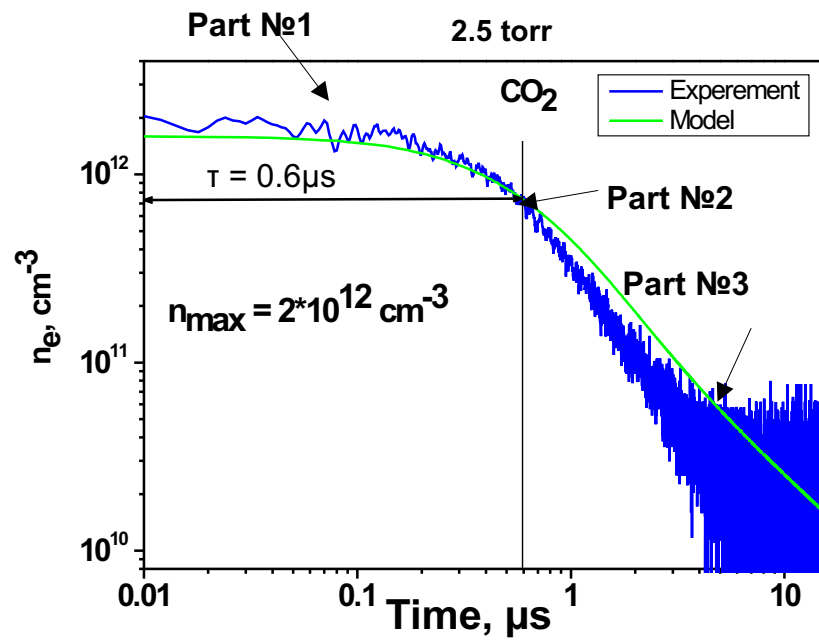


Figure 2.56: Electron density profile in CO_2 , $p=2.5$ Torr, $T=295$ K, $U=11$ kV, positive polarity.

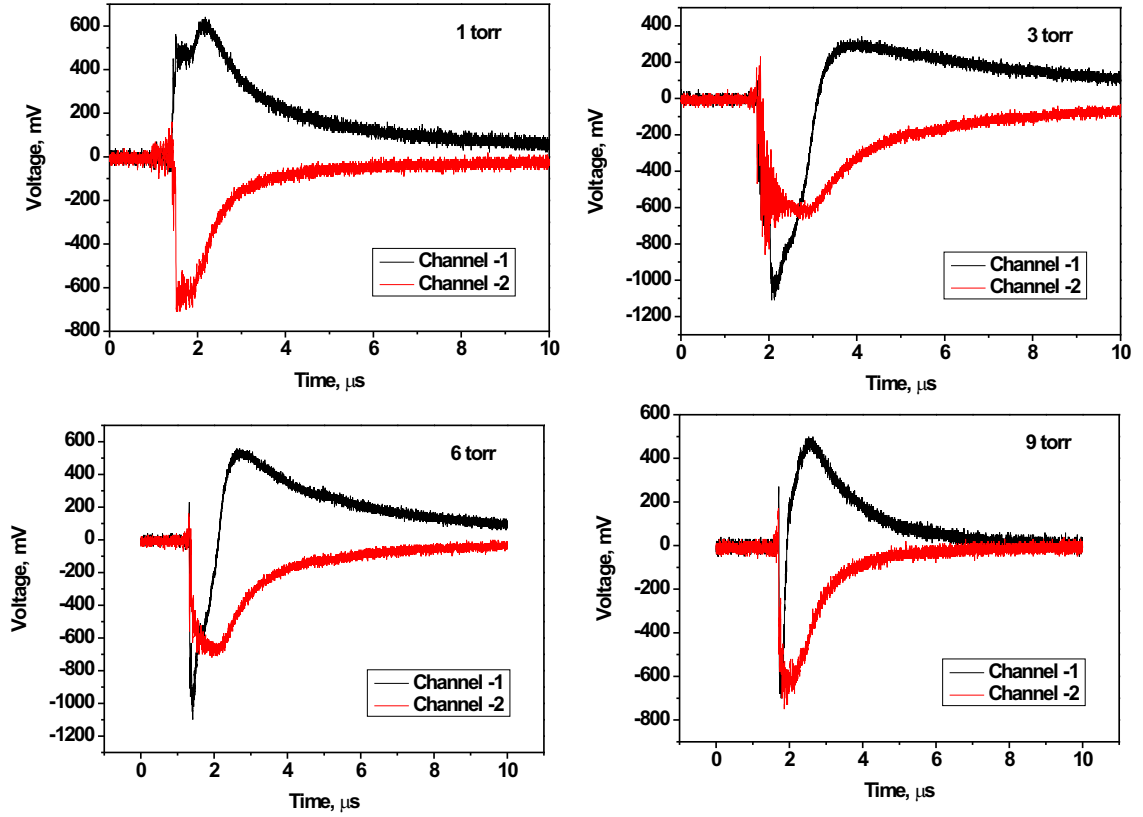


Figure 2.57: Oscillogrammes obtained by microwave technique in $N_2 : O_2 = 4 : 1$, $p = 1, 3, 6, 9$ Torr, $T = 295$ K, $U = 11$ kV, positive polarity.

The main ions considered in the oxygen plasma kinetics, were O_2^+ and O_4^+ . Reactions of ion conversion (O_2^+ , O_4^+) attachment–detachment with a production of O_2^- ion, electron–ion and ion–ion recombination were taken into account in the kinetic scheme. The three–body recombination with the participation of electrons as the third body may be important at our experimental parameters: $e + O_2^+ + e \Rightarrow O_2 + e$. The higher reaction rate for the three–body recombination, the sharper a slope of the kinetic curve at the initial part (region N 1). Attachment and detachment are not important in a pressure range between 1 and 10 Torr, and the role of the ion–ion recombination is negligible. The production of negative ions increases with pressure. Similar to molecular nitrogen, the last part of the kinetic curve is explained by recombination of O_4^+ ions in their reactions with the electrons.

2.4.4 Electron density decay in CO_2

Fig. 2.52 gives typical oscillogrammes obtained by microwave interferometry in CO_2 for gas pressures 1, 3, 6, and 9 Torr. Figs. 2.53, 2.54 illustrate electron density behavior in O_2 for a pressure range from 1 to 9 Torr. Maximal electron density in molecular oxygen is estimated as $n_{max} \approx 0.6 - 2.1 \cdot 10^{12} \text{ cm}^{-3}$, at $p = 1-10$ Torr, $T = 295$ K, $U = 11$ kV.

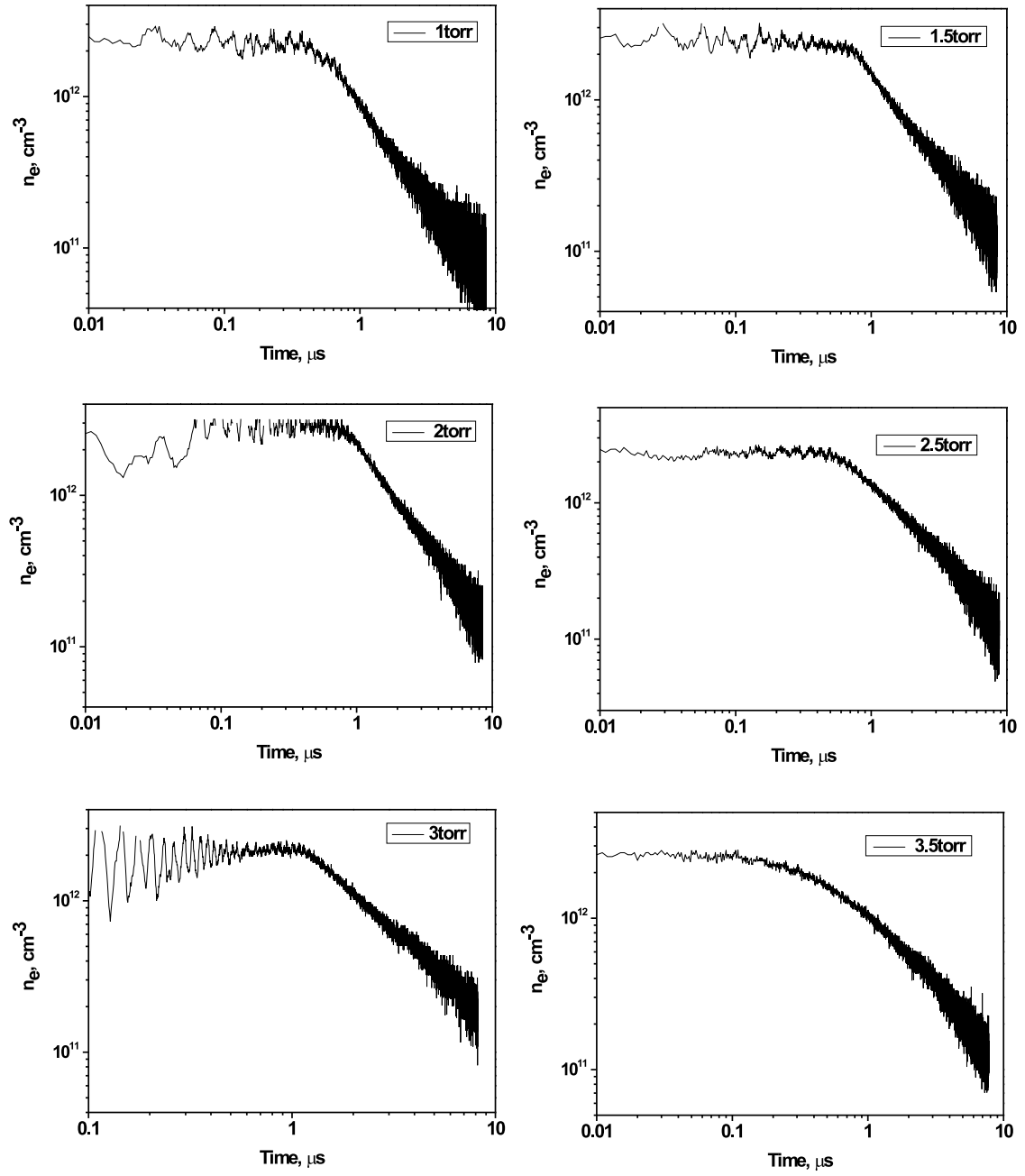


Figure 2.58: Electron density profiles in $\text{N}_2 : \text{O}_2 = 4 : 1$, $p = 1\text{-}3.5$ Torr, $T = 295$ K, $U = 11$ kV, positive polarity.

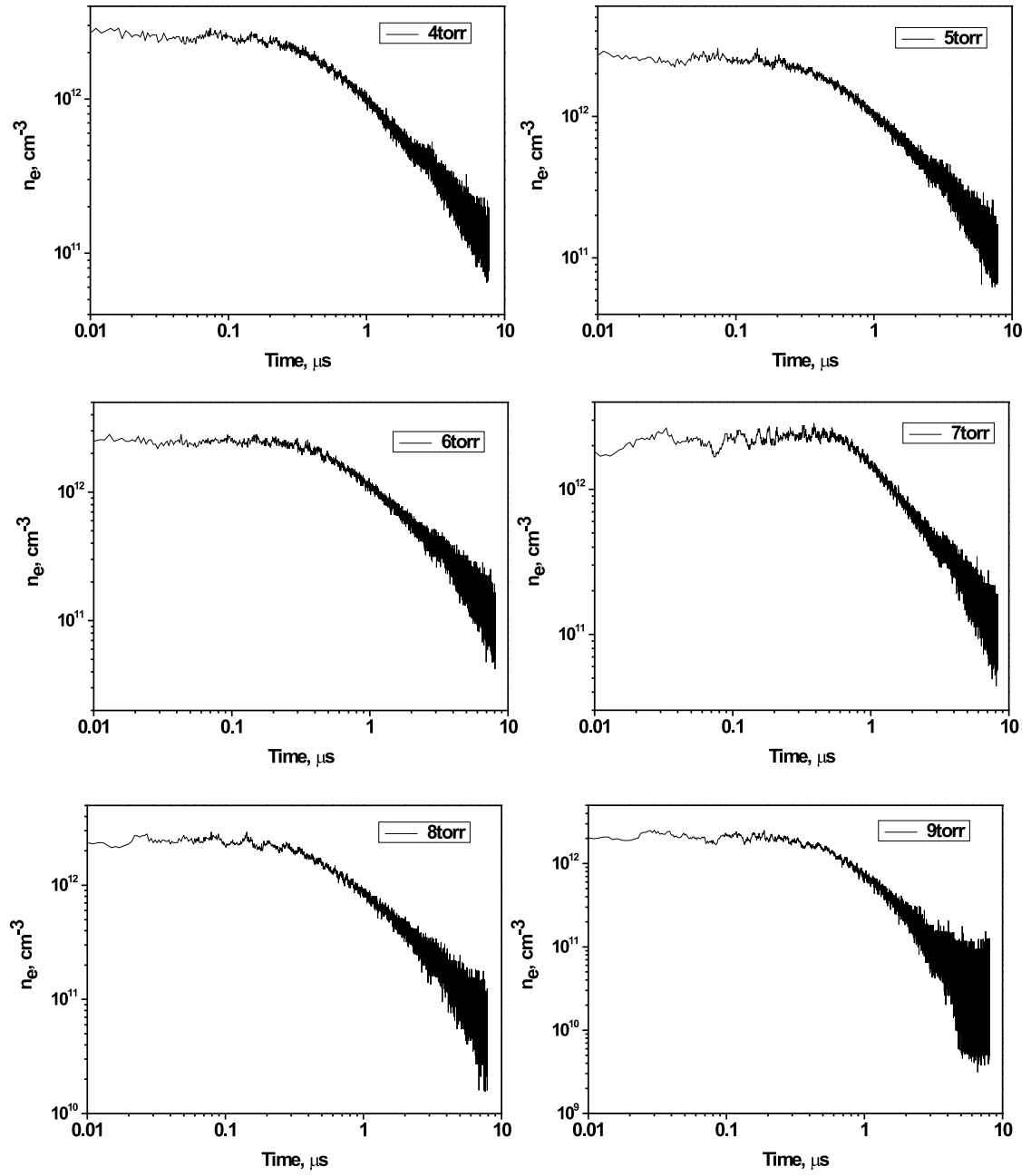


Figure 2.59: Electron density profiles in $\text{N}_2 : \text{O}_2 = 4 : 1$, $p = 4\text{--}9$ Torr, $T = 295$ K, $U = 11$ kV, positive polarity.

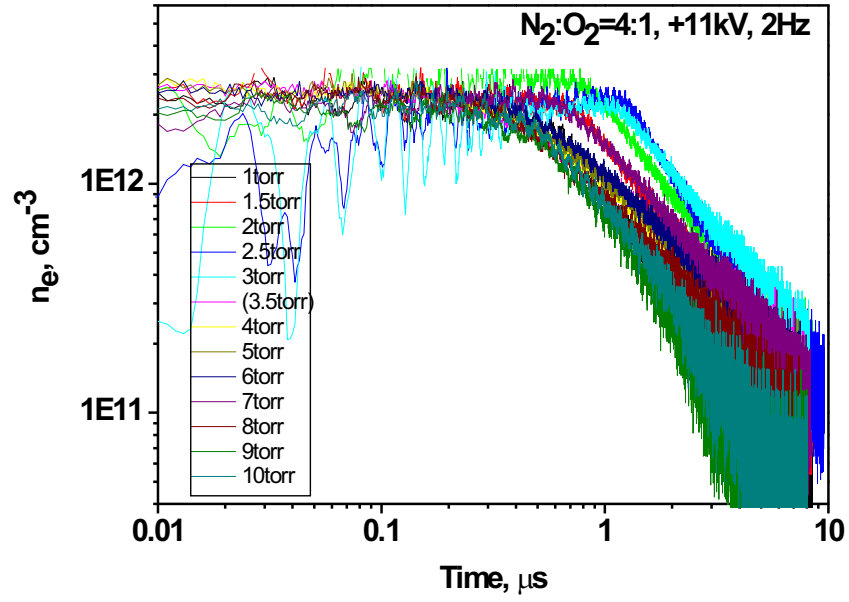


Figure 2.60: Electron density profiles in $\text{N}_2 : \text{O}_2 = 4 : 1$, $p = 1\text{--}10$ Torr, $T = 295$ K, $U = 11$ kV, positive polarity.

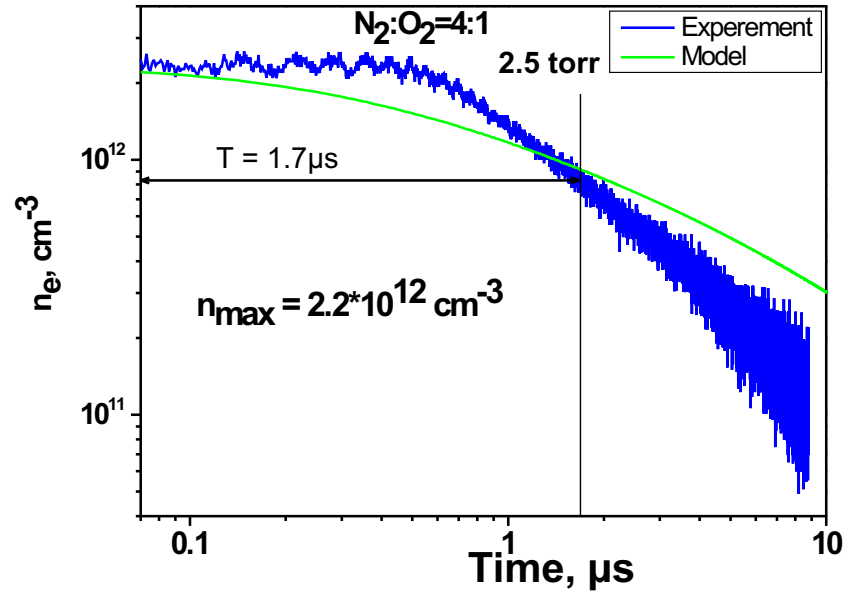


Figure 2.61: Electron density profile in $\text{N}_2 : \text{O}_2 = 4 : 1$, $p = 2.5$ Torr, $T = 295$ K, $U = 11$ kV, positive polarity.

Electron profiles for all investigated pressures are summarized in Fig. 2.55. Decay time for CO_2 is equal to $\tau \approx 0.6 \mu\text{s}$, $p=2.5$ Torr, $T=295$ K. It is determined from Fig. 2.56. It is necessary to take into account CO_2^+ C_2O_4^+ ions to describe kinetics in CO_2 . Reaction constant rates were taken mainly from.^{71,108,109} Reaction of ion conversion (CO_2^+ to C_2O_4^+) and three-body recombination are important here.

2.4.5 Electron density decay in $\text{N}_2 : \text{O}_2 = 4 : 1$

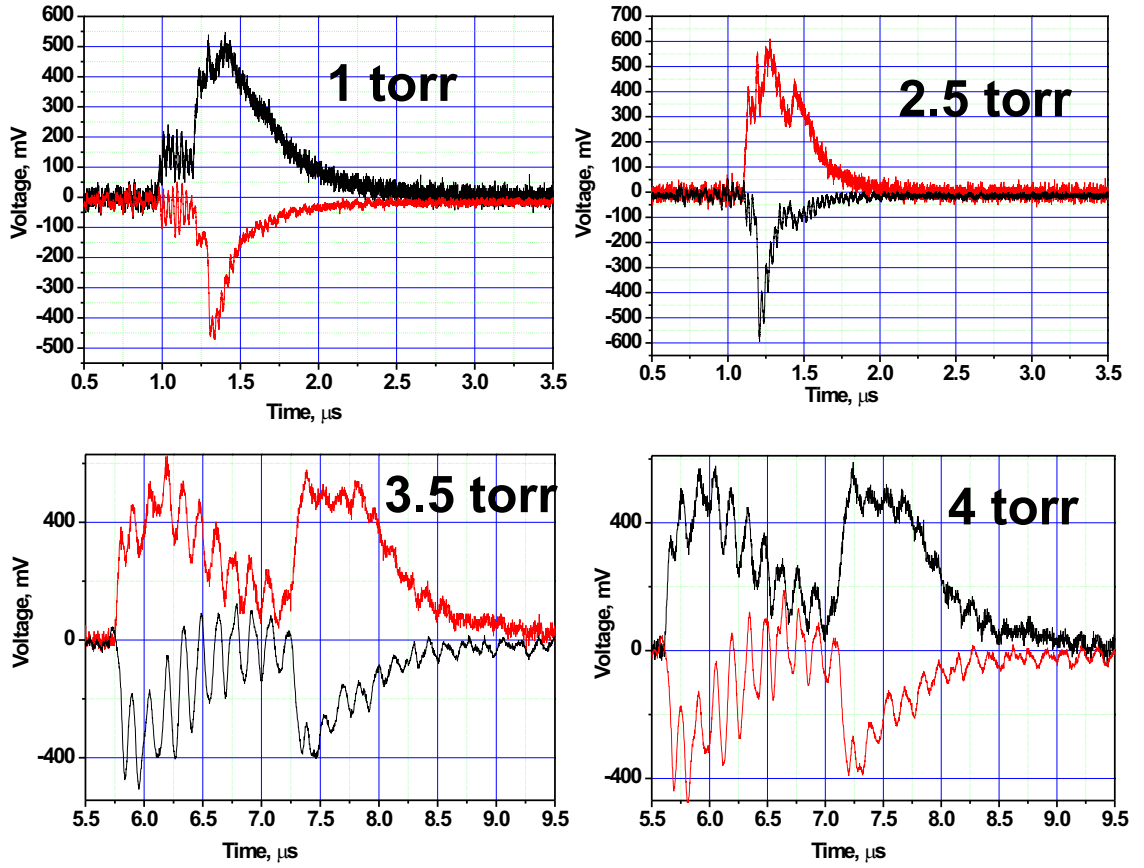


Figure 2.62: Oscillogrammes obtained by microwave technique in H_2O , $p=1, 2.5, 3.5, 4$ Torr, $T=295$ K, $U=11$ kV, positive polarity.

It is worth mentioning the high initial density of electrons in the synthetic air in comparing with the other investigated gases. Indeed, it is obvious from the oscillogrammes (Fig. 2.57) that for all tested pressures we obtain well-pronounced peak. this peak means that the electron density in the experiment is not lower than $\pi/2 \cdot 10^{12} \text{ cm}^{-3}$, while for the other gases the peak has been detected only within a pressure range 3–5 Torr. Figs. 2.58, 2.59 illustrate electron density behavior in $\text{N}_2 : \text{O}_2 = 4 : 1$ for a pressure range from 1 to 9 Torr. Fig. 2.60 gives electron density profiles for all the pressure range.

Maximal electron density in synthetic air is estimated as $n_{\text{max}} \approx 1.8 - 2 \cdot 10^{12} \text{ cm}^{-3}$,

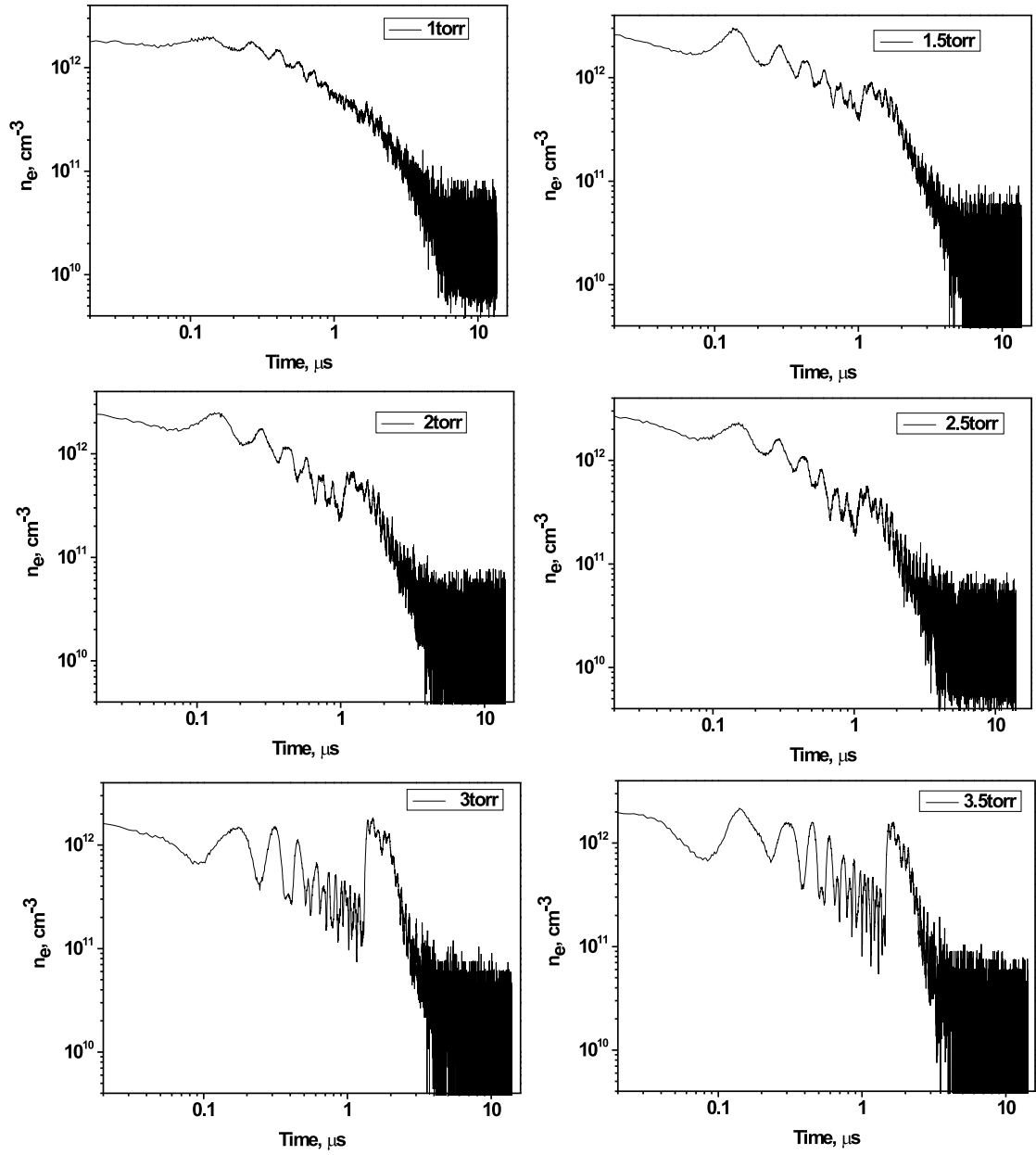


Figure 2.63: Electron density profiles in H_2O , $p = 1\text{-}3.5$ Torr, $T = 295$ K, $U = 11$ kV, positive polarity.

at $p=1\text{-}10$ Torr, $T = 295$ K, $U=11$ kV and positive polarity of the electric pulse. Plasma decay time in $\text{N}_2 : \text{O}_2 = 4 : 1$ mixture is equal to $\tau \approx 1.7 \mu\text{s}$, $p=2.5$ Torr, $T=295$ K), as it is clearly seen from Fig. 2.61.

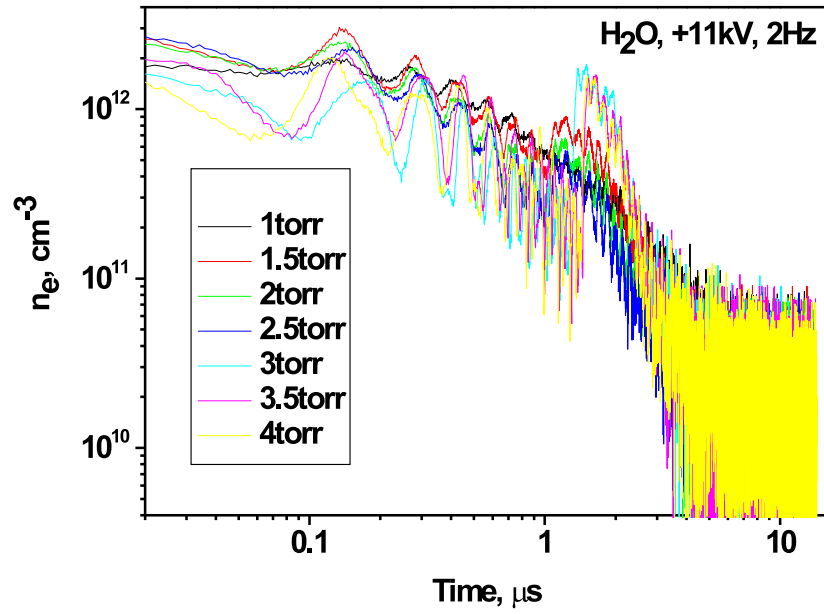


Figure 2.64: Electron density profiles in H_2O , $p=1\text{-}4$ Torr, $T=295$ K, $U=11$ kV, positive polarity.

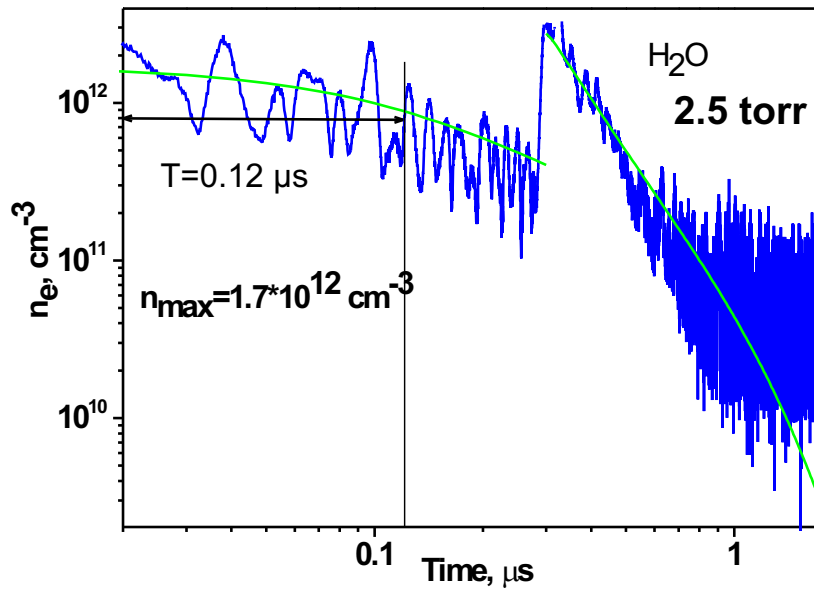


Figure 2.65: Electron density profile in H_2O , $p=2.5$ Torr, $T=295$ K, $U=11$ kV, positive polarity.

2.4.6 Electron density decay in water vapor

Under our experimental conditions, the experiments with water vapor was restricted by 8 Torr, such as the signal amplitude was not enough at higher pressure. The most reliable signal-to-noise ratio has been obtained within a pressure range 1–4 Torr. Fig. 2.63 gives electron density profiles in this pressure range, and Fig. 2.64 represents the same curves in double logarithmic scale.

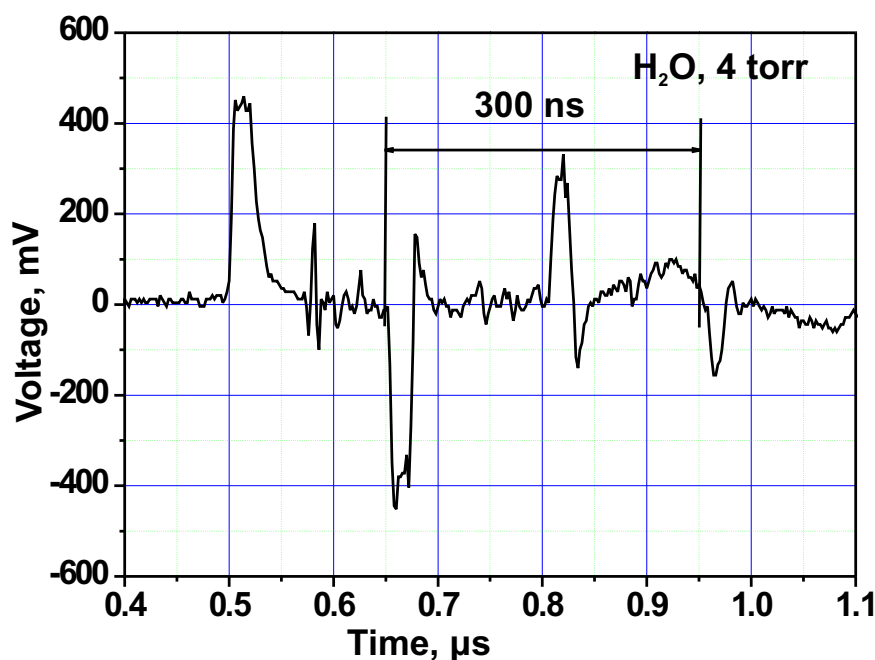


Figure 2.66: Pulse electrodynamics in the Water vapor. $p = 4$ Torr, $T = 295$ K, $U = 11$ kV, positive polarity.

The initial electron density in water vapor ($(1-3) \cdot 10^{12} \text{ cm}^{-3}$) is similar to the initial electron density in other gases, but the decay differs dramatically ($\tau \approx 0.12 \mu\text{s}$), and this is clearly seen from Fig. 2.65. Calculated kinetic curve for the electron density is given in the same figure.

Describing the kinetics in the water vapor, it is necessary to take clustered ions into account. The main ions in this system are H_2O^+ , H_3O^+ , H_5O_2^+ , H_9O_4^+ . Reactions of ions conversion, electron-ion recombination and three-body recombination have been considered. reaction rates were taken from.^{108–110}

Let us note a specific detail of the experiments: within a pressure range 2–4 Torr we observed two peaks of the electron density. It is clearly seen (Fig. 2.62) that the amplitude of the second peak increases with pressure, reaches its maximum at 4 Torr, and then decreases sharply. At 8 Torr the second peak is undetectable. The second peak, 300 ns after the first one, is easily explained by the second (reflected from the high voltage generator) high-voltage pulse, and this peak exists, but it is not observed in the other gases because of relatively long plasma decay (it is merged with the first

peak). This explanation is confirmed by electrodynamic data obtained by means of the reverse current shunt (Fig. 2.66). This correlates reasonably with the difference between the peaks at the oscillogramms from the microwave interferometer (Fig. 2.62) and with the simplest estimates: the velocity of the electric signal in a cable with a polyethylene feeling is 0.2 m/s, and in a 30 m cable the time for the signal to go from the discharge cell to the high-voltage generator and to come back to the discharge cell is equal to $t = 2L_{cable}/v_{signal} = 60/0.2 = 300$ ns.

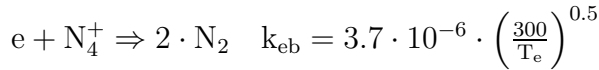
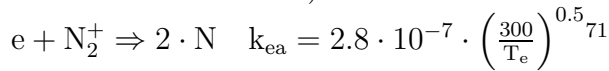
2.5 Modelling of the electron density decay at low gas pressure

Under our conditions, the ionization degree is equal to $10^{-5} - 10^{-3}$. Electron density in the experiments is equal to $10^{12} - 10^{13} \text{ cm}^{-3}$, while the density of neutral species is about $10^{16} - 10^{18} \text{ cm}^{-3}$. It follows from the low temperature experiments that the typical time of electron density decay is about a few microseconds. Typical time of reactions between neutrals is significantly longer. Thus, the reaction with participation of neutrals were not taken into account in the present kinetic scheme.

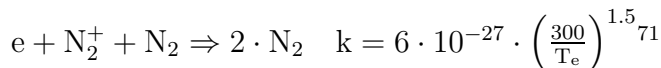
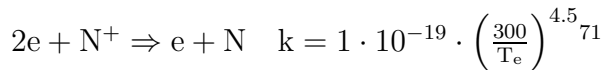
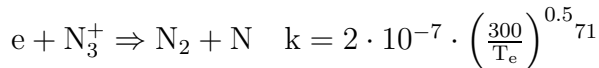
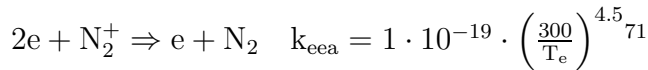
Electron density can be varied due to the attachment/detachment and recombination. Recombination itself may be subdivided into two main classes: three-body recombination and dissociative recombination. Dissociative recombination is important at low pressures, while the three-body recombination plays a dominant role at high pressures. We have to consider also ion-electron and ion-ion recombination. Under high electron densities, three-body recombination with participation of electrons becomes important.

2.5.1 Modelling of the decay of electron density in molecular nitrogen

We consider here⁷¹ positive ions, such as N^+ , N_2^+ , N_3^+ , N_4^+ and neutrals (N , N_2). The kinetic scheme is the following (here dimensions are cm^3/s for bimolecular and cm^6/s for three-molecular reactions):



This reaction rate constant is multiplied by a factor of 1.7 comparing to.⁷¹



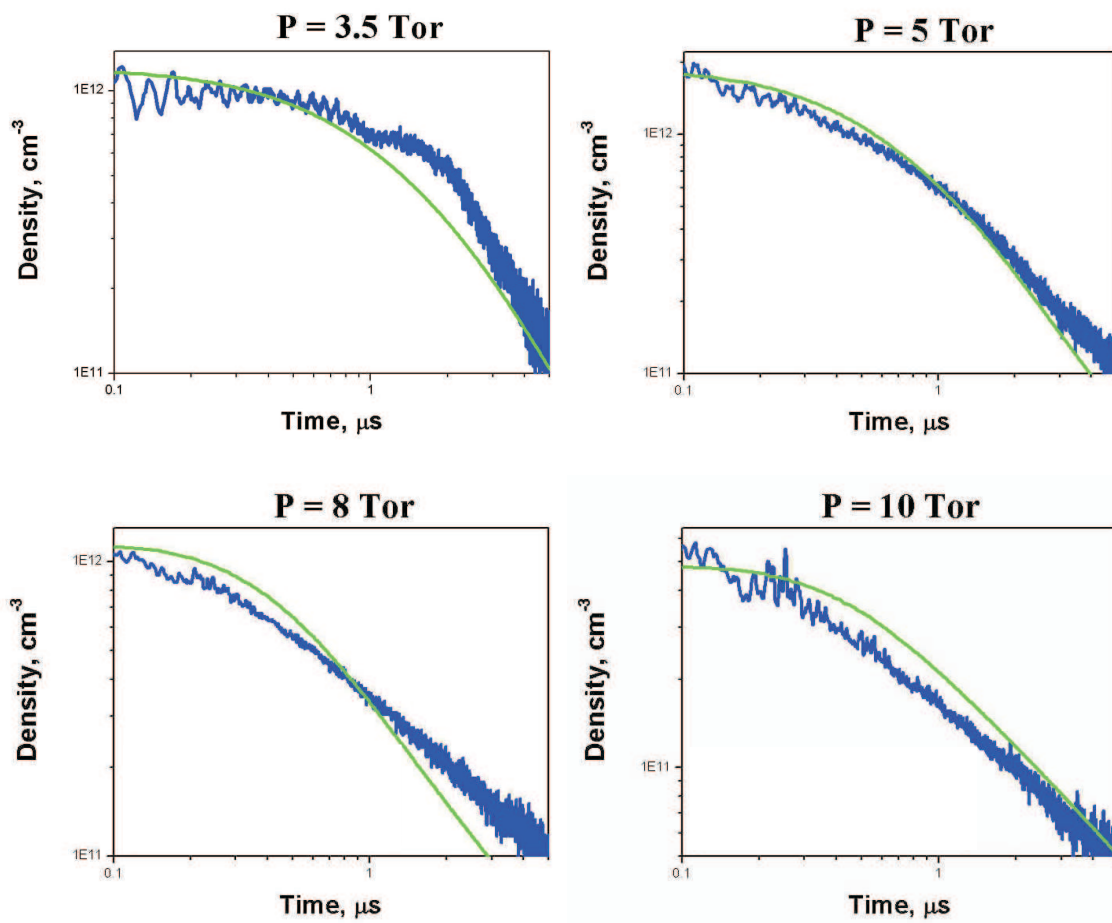
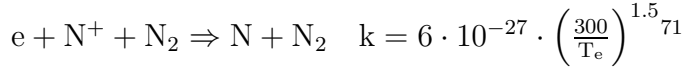
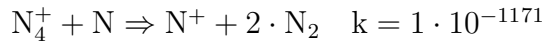
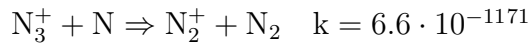
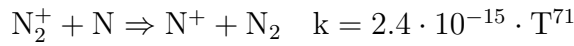
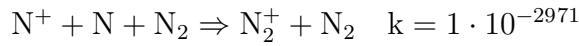
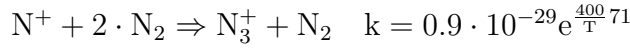
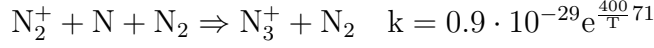
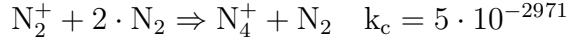


Figure 2.67: Electron density kinetic curve. Comparison of experiments (blue curves) and calculations (green curves). $T = 300 \text{ K}$, N_2 .



Conversion reactions:



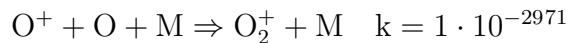
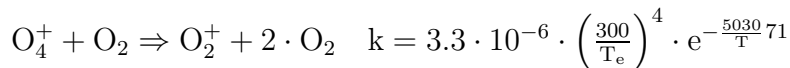
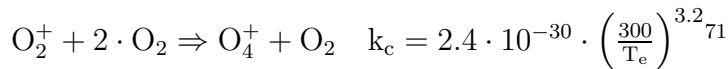
Comparison of experimental data with the calculations is given by Fig. 2.67. Numerical modelling performed at gas temperature $T = 300$ K within a pressure range $p = 1 - 10$ Torr.

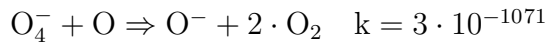
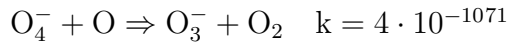
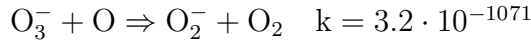
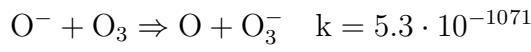
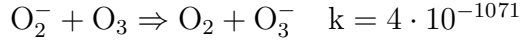
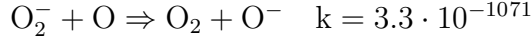
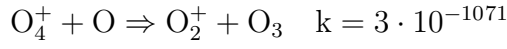
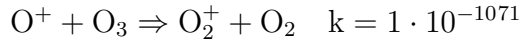
At low pressures (1 – 2 Torr) experimental values for electron density are lower than numerical ones. Probably, it may be explained by non-uniform filling of the tube cross-section by the discharge at these pressures. At moderate and high pressures (2.5 – 10 Torr) we obtain a reasonable agreement between the experiment and the calculations. Let us, consider, for example, the results for the pressure $p = 5$ Torr. Comparing numerical results with the calculations we conclude that the initial part (region N 1) is described mainly by electron-ion recombination with N_2^+ ion, sharp decrease is described by an electron-ion recombination with N_4^+ ion, and the inflection of curve is described by ion-ion conversion: N_2^+ to N_4^+ .

2.5.2 Modelling of the decay of electron density in molecular oxygen

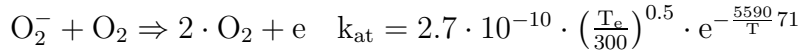
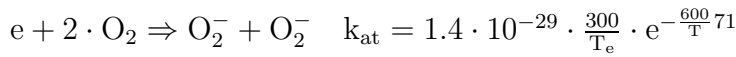
We consider positive ions (O^+ , O_2^+ , O_3^+ , O_4^+), negative ions (O^- , O_2^- , O_3^- , O_4^-) and neutrals (O , O_2 , O_3). The kinetic scheme is the following:

Ion conversion:

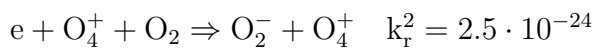
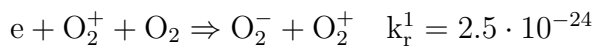




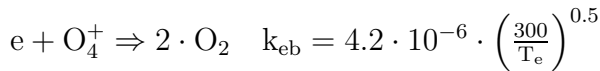
Detachment/attachment:



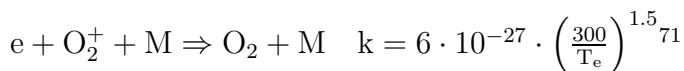
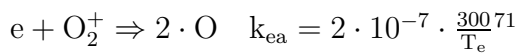
The following reaction rate constants were proposed in the present work:



Electron-ion recombination:



This reaction rate constant is multiplied by a factor of 1.7 comparing to.⁷¹



$$2 \cdot e + O^+ \Rightarrow e + O \quad k = 1 \cdot 10^{-19} \cdot \left(\frac{300}{T_e} \right)^{4.5}_{71}$$

$$e + O^+ + M \Rightarrow O + M \quad k = 6 \cdot 10^{-27} \cdot \left(\frac{300}{T_e} \right)^{1.5}_{71}$$

Ion-ion recombination:

$$O_2^- + O_4^+ + M \Rightarrow 3 \cdot O_2 + M \quad k = 2 \cdot 10^{-25}_{71}$$

$$O_2^- + O_2^+ + M \Rightarrow 2 \cdot O_2 + M \quad k = 2 \cdot 10^{-25}_{71}$$

$$O_2^- + O_4^+ \Rightarrow 3 \cdot O_2 \quad k = 1 \cdot 10^{-7}_{71}$$

$$O_2^- + O_2^+ \Rightarrow 2 \cdot O_2 \quad k = 2 \cdot 10^{-7} \cdot \left(\frac{300}{T_e} \right)^{0.5}_{71}$$

$$O_2^- + O_2^+ \Rightarrow O_2 + 2 \cdot O \quad k = 1 \cdot 10^{-7}_{71}$$

$$O_2^- + O + M \Rightarrow O_3 + M \quad k = 2 \cdot 10^{-25} \cdot \left(\frac{300}{T_e} \right)^{2.5}_{71}$$

$$O_3^- + O_2^+ \Rightarrow O_3 + O_2 \quad k = 2 \cdot 10^{-7} \cdot \left(\frac{300}{T_e} \right)^{0.5}_{71}$$

$$O_2^- + O^+ \Rightarrow O_2 + O \quad k = 2 \cdot 10^{-7} \cdot \left(\frac{300}{T_e} \right)^{0.5}_{71}$$

$$O^- + O^+ \Rightarrow \cdot O \quad k = 2 \cdot 10^{-7} \cdot \left(\frac{300}{T_e} \right)^{0.5}_{71}$$

$$O_3^- + O^+ \Rightarrow O_3 + O \quad k = 2 \cdot 10^{-7} \cdot \left(\frac{300}{T_e} \right)^{0.5}_{71}$$

$$O^- + O_2^+ \Rightarrow O + O_2 \quad k = 2 \cdot 10^{-7} \cdot \left(\frac{300}{T_e} \right)^{0.5}_{71}$$

$$O^- + O_2^+ \Rightarrow O + 2 \cdot O \quad k = 1 \cdot 10^{-7}_{71}$$

$$O_3^- + O_2^+ \Rightarrow O_3 + 2 \cdot O \quad k = 1 \cdot 10^{-7}_{71}$$

$$O^- + O_4^+ \Rightarrow O + 2 \cdot O_2 \quad k = 1 \cdot 10^{-7}_{71}$$

$$O_3^- + O_4^+ \Rightarrow O_3 + 2 \cdot O_2 \quad k = 1 \cdot 10^{-7}_{71}$$

$$O_4^- + O^+ \Rightarrow 2 \cdot O_2 + O \quad k = 1 \cdot 10^{-7}_{71}$$

$$O_4^- + O_4^+ \Rightarrow 4 \cdot O_2 \quad k = 1 \cdot 10^{-7}_{71}$$

$$O_2^- + O^+ + M \Rightarrow O_2 + O + M \quad k = 2 \cdot 10^{-25} \cdot \left(\frac{300}{T_e} \right)^{2.5}_{71}$$

$$O^- + O_2^+ + M \Rightarrow O + O_2 + M \quad k = 2 \cdot 10^{-25} \cdot \left(\frac{300}{T_e} \right)^{2.5}_{71}$$

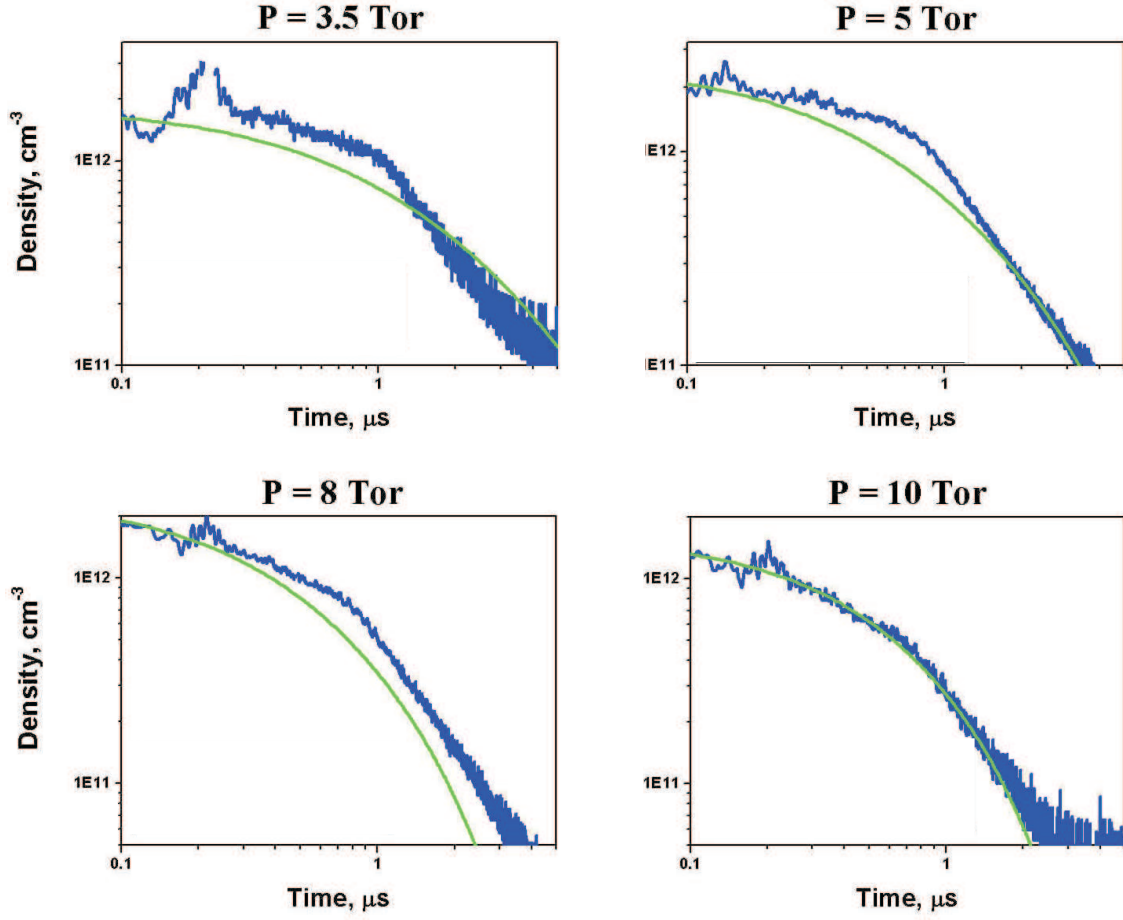
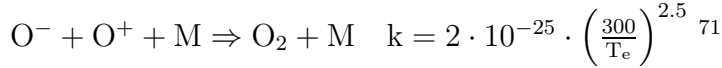
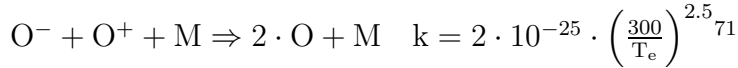
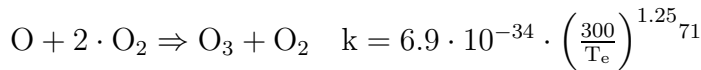
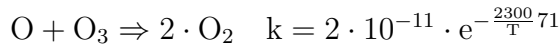


Figure 2.68: Electron density kinetic curve. Comparison of experiments (blue curves) and calculations (green curves). $T = 300$ K, O_2 .



Chemical reactions with O-atom:



Comparison of experimental data with the calculations is given by Fig. 2.68. Numerical modelling performed at gas temperature $T = 300$ K within a pressure range $p = 1 - 10$ Torr.

At low pressures (1 – 3 Torr) experimental values for electron density are lower than numerical ones. Probably, it may be explained by non-uniform filling of the tube cross-

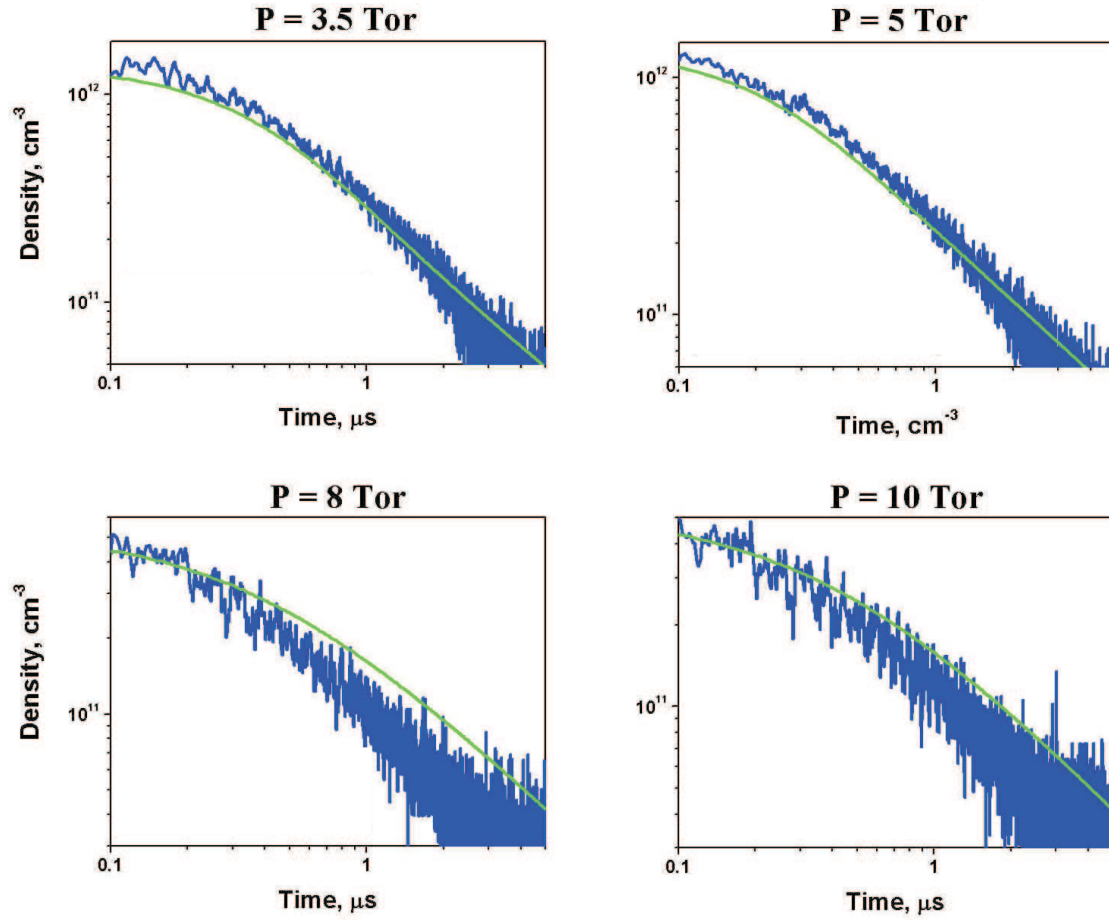


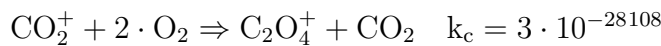
Figure 2.69: Electron density kinetic curve. Comparison of experiments (blue curves) and calculations (green curves). $T = 300$ K, CO_2 .

section by the discharge at these pressures. At moderate and high pressures (3.5 – 10 Torr) we obtain a reasonable agreement between the experiment and the calculations. Comparing numerical results with the calculations we conclude that the initial part (region N 1) is described mainly by electron–ion recombination with O_2^+ ion, sharp decrease is described by an electron–ion recombination with O_4^+ ion, and the inflection of curve is described by ion–ion conversion: O_2^+ to O_4^+ .

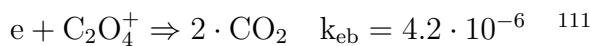
2.5.3 Modelling of the decay of electron density in CO_2

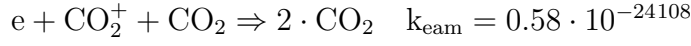
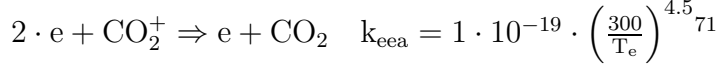
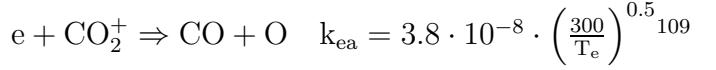
We consider positive ions (CO_2^+ , C_2O_4^+) and neutrals(O , CO , CO_2). The kinetic scheme is the following:

Conversion reaction:



Recombination:





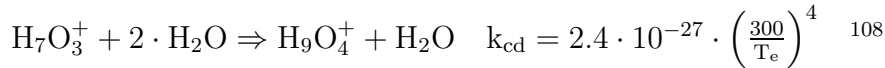
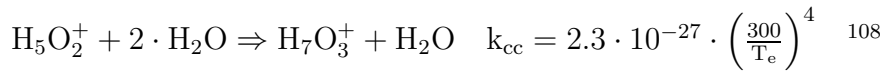
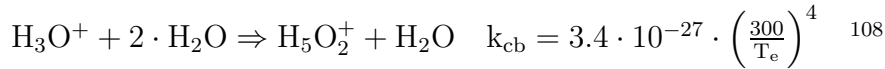
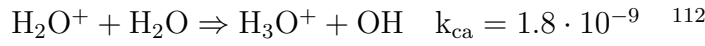
Comparison of experimental data with the calculations is given by Fig. 2.69. Numerical modelling performed at gas temperature $T = 300$ K within a pressure range $p = 1 - 8$ Torr. For all plots, green curves represent the results of calculations, while blue ones – experimental data.

Similar to N_2 and O_2 , the initial part is described mainly by electron–ion recombination with CO_2^+ ion, sharp decrease is described by an electron–ion recombination with CO_4^+ ion, and the inflection of curve is described by ion–ion conversion: CO_2^+ to CO_4^+ .

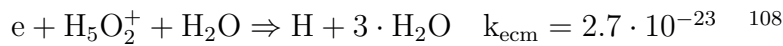
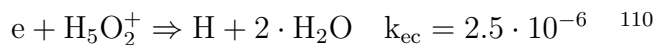
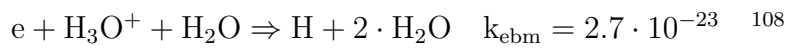
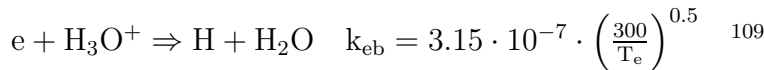
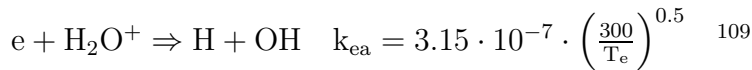
2.5.4 Modelling of the decay of electron density in water vapor

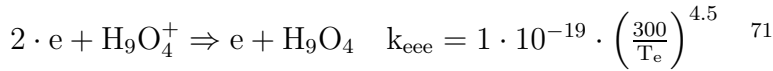
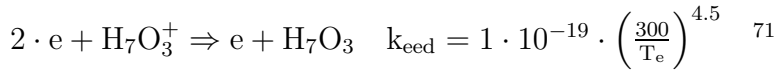
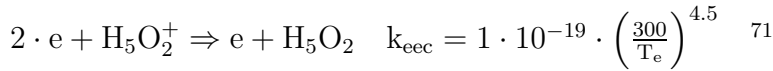
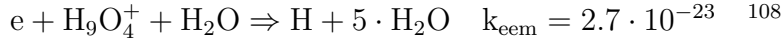
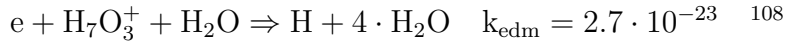
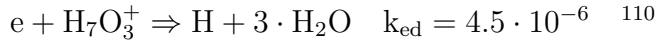
The kinetic scheme, based on papers ^{112, 108, 109, 110, 71} includes positive ions (H_2O^+ , H_3O^+ , H_5O_2^+ , H_7O_3^+ , H_9O_4^+) and neutrals (H , OH , H_2O , H_3O , H_5O_2 , H_7O_3 , H_9O_4). The kinetic scheme is the following:

Ion conversion:



Electron–ion recombination:





Comparison of experimental data with the calculations is given by Fig. 2.70. Numerical modelling performed at gas temperature $T = 300$ K within a pressure range $p = 1 - 8$ Torr. For all plots, green curves represent the results of calculations, while blue ones – experimental data. Red line gives the time moment of the reflected signal coming back to the discharge cell.

We can conclude that the agreement of the calculation and the second experimental peak is reasonable. The first peak is difficult to compare because of low signal-to-noise ratio under our experimental conditions.

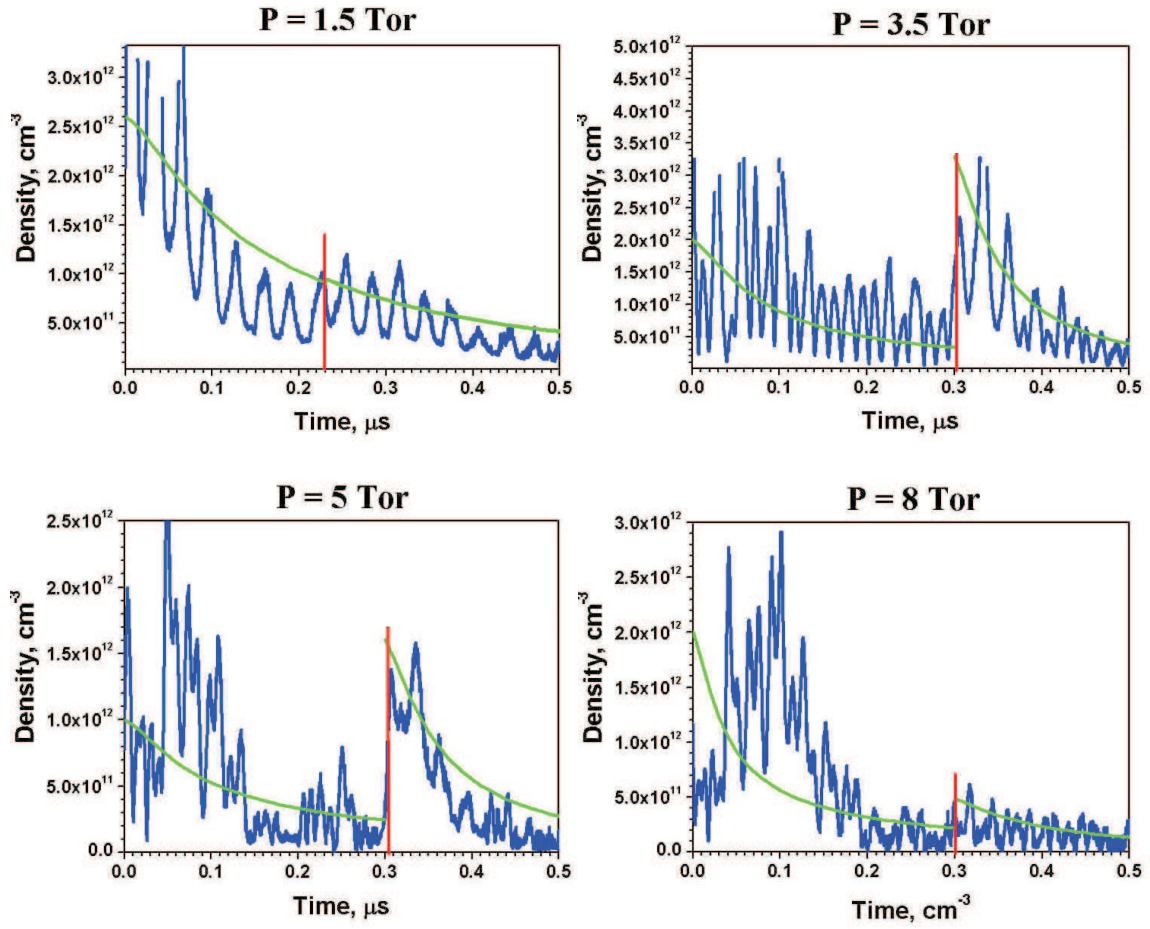


Figure 2.70: Electron density kinetic curve. Comparison of experiments (blue curves) and calculations (green curves). $T = 300 \text{ K}$, H_2O .

2.5.5 Experiments and modelling for the high gas temperature

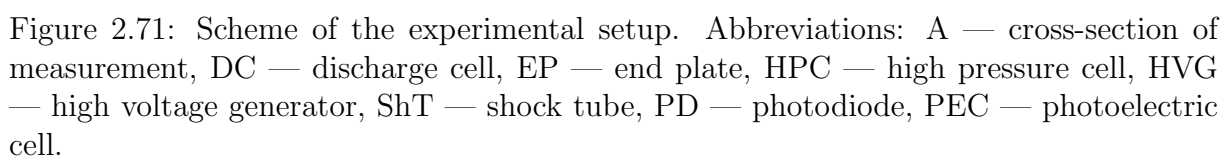
The main part of the experimental data was obtained in a shock tube with a discharge cell. The experiments were carried out behind incident and reflected shock waves. The experimental setup (see Fig. 4.6) consisted of the shock tube (ShT) with the discharge cell (DC), a gas evacuation and supply system, a system for initiation of discharge, and a diagnostic system. The shock tube (25×25 -mm square cross section) had a 1.6 m long working channel. The length of the high-pressure cell (HPC) was 60 cm. There were two pairs of windows for optical diagnostics along the stainless-steel working channel. The last section of the shock tube with a 25×25 -mm square cross section was made from 40 mm thick plexiglas and had eight optical windows (quartz and MgF_2). The metal end plate (EP) of the tube served as a high-voltage electrode. Another (grounded) electrode was the grounded steel section of the shock tube.

The nanosecond discharge was initiated at the moment when the incident (or reflected) shock wave arrived at the observation point (point *A* in Fig. 2.71). The time of initiation was determined by an adjusted delay from the signal of the first schlieren sensor. High-voltage pulses were produced by a Marx type high-voltage generator (HVG). At the output of the forming line, the voltage growth rate was about 8 kV/ns, which enabled the operation of the gas discharge in the form of a fast ionization wave (FIW) in the dielectric section of the shock tube. The velocity of the ionization wave front was 10^9 – 10^{10} cm/s, depending on the experimental parameters.

The diagnostic system consisted of a system for monitoring the shock wave parameters, a system for monitoring the electric parameters of the nanosecond discharge, and a microwave interference diagnostics. Velocity of the shock wave was measured by the schlieren system consisting of three He-Ne lasers and a set of quadrant photodiodes (PD). The gas density (ρ_5), pressure (P_5), and temperature (T_5) behind the reflected shock wave were defined by an ideal theory from the gas mixture composition, the initial pressure, and the velocity of the incident shock wave.

Simultaneously we controlled current through the discharge cell and voltage drop along the discharge section. Three capacitive and one current gauge are used for the measurements. These auxiliary measurements allow to estimate correctly the energy deposition in the discharge and other properties of the FIW. The measurement technique was described in work.¹¹³

The microwave diagnostics includes the main block, a system of waveguides with a horn antenna and an angle reflector. In contrast to Fig. 4.6, the microwave diagnostics is actually arranged in the measurement cross-section and horizontally, while the schlieren system is arranged vertically.



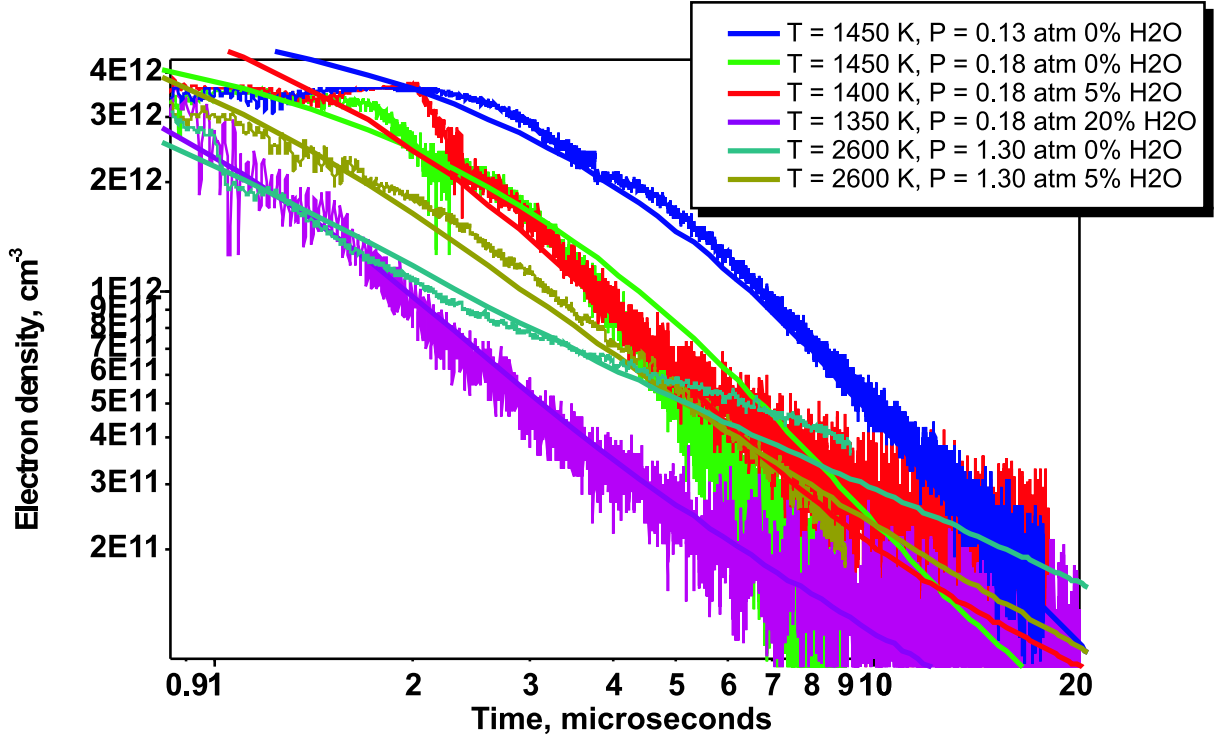
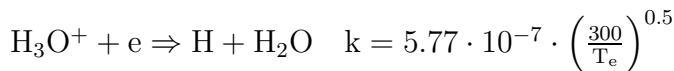
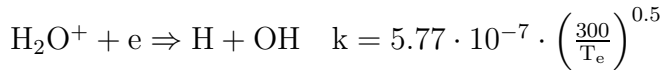
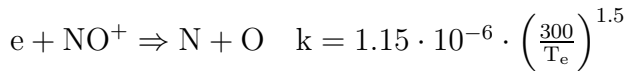
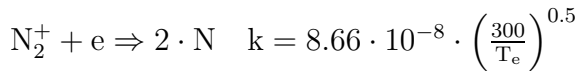
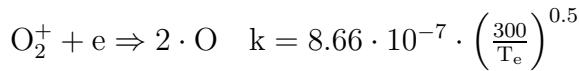


Figure 2.72: Results of high-temperature experiments (curves with the experimental noise) and their comparison with preliminary calculations (smooth curves). Gas mixture $\text{CO}_2:\text{O}_2:\text{N}_2=9:5:86$ with different admixtures of water.

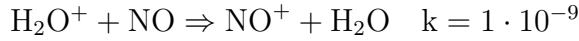
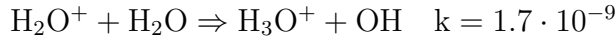
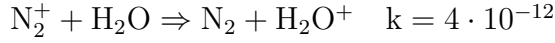
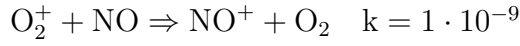
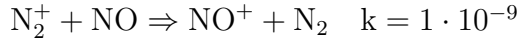
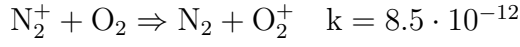
The results of high temperature experiments are given in Fig. 2.72 together with the results of numerical modelling. To model the decay of air plasma of a nanosecond discharge we used a set of assumptions and simplifications. The plasma of the discharge and of the discharge afterglow was considered spatially uniform. The kinetic model involves processes which are important at microsecond time scale. The kinetic model does not include the kinetics of neutral particles and does not take into account processes related with discharge cell walls.

For the high temperature experiments description of the model includes the following reactions:

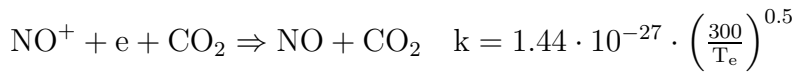
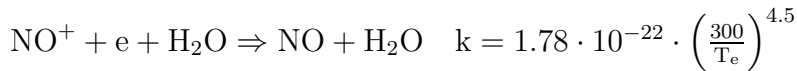
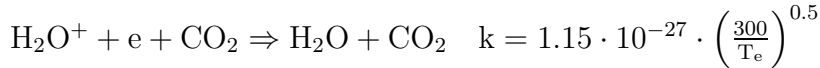
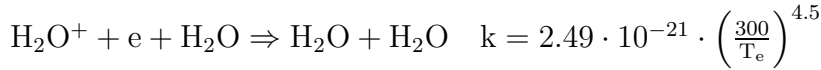
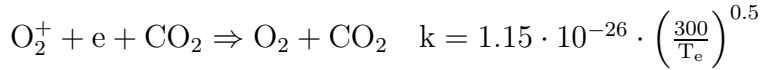
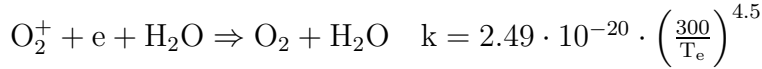
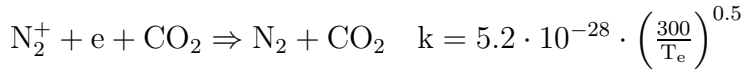
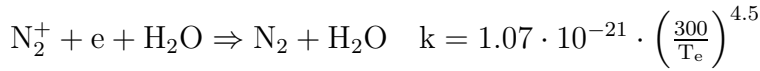
Dissociative recombination



Charge transfer



Three-body recombination



This model describes the experimental data obtained in the framework of the present project but the lack of the data for rate constants for high-temperature regimes pushes us to further kinetic model verification. Nevertheless the model proposed gives us at least good interpolation of the data obtained.

Chapter 3

Experimental and Numerical Investigation of Slow Hydrocarbon Oxidation in Nanosecond Discharge

The comprehensive experimental investigation of processes of alkanes slow oxidation in mixtures with oxygen and air under nanosecond uniform discharge has been performed. We have investigated kinetics of alkanes oxidation from methane to decane in stoichiometric and some lean mixtures with oxygen and air at room temperature under the action of high-voltage nanosecond uniform discharge. The discharge was initiated with repetition rate 40 Hz by the electric negative polarity pulses with 10 kV amplitude and 25 ns duration in the discharge screened tube with 5 cm diameter and 20 cm length. Mixtures initial pressures were varied in 0.76-10.6 torr range with 0.76 torr step. The discharge current, electric field and input energy have been measured with nanosecond time resolution. Emission intensities of following molecular bands $\text{NO}(A^2\Sigma \rightarrow X^2\Pi, \delta v = 3)$, $\text{N}_2(C^3\Pi, v' = 1 \rightarrow B^3\Pi, v'' = 7)$, $\text{N}_2(B^3\Pi, v' = 6 \rightarrow A^3\Sigma, v'' = 3)$, $\text{N}_2^+(B^2\Sigma, v' = 0 \rightarrow X^2\Sigma, v'' = 2)$, $\text{CO}_2^+(B^2\Sigma \rightarrow X^2\Pi, \delta v = 0)$, $\text{CH}(A^2\Delta, v' = 0 \rightarrow X^2\Pi, v'' = 0)$, $\text{OH}(A^2\Sigma, v' = 0 \rightarrow X^2\Pi, v'' = 0)$, $\text{CO}(B^1\Sigma, v' = 0 \rightarrow A^1\Pi, v'' = 2)$ have been measured in integral regime (integration time was 2.2 s) and with nanosecond resolution. Methane concentration was measured by absorption of He-Ne laser emission in integral regime. On the base of optical measurements time of full oxidation of alkanes was determined. Percentage of alkanes in all investigated mixtures is represented in the Table 3.1.

The investigation of processes of slow oxidation of different hydrocarbon-containing molecules in mixtures with oxygen and air under nanosecond uniform discharge has been performed additionally. We have investigated experimentally kinetics of $\text{C}_2\text{H}_5\text{OH}$, CH_3COCH_3 , C_2H_2 in their mixtures with oxygen and $\text{CO}:\text{O}_2$ mixtures with small controlled additives of water vapour.

Table 3.1: Investigated mixture.

Alkane	CH_4	C_2H_6	C_3H_8	C_4H_{10}	C_5H_{12}	C_6H_{14}
in mixture with O_2	33.3%	22.2%	16.6%	13.3%	11.1%	9.5%
n mixture with air	11.11%	—	—	—	3.03%	2.56%

3.1 Experimental setup

The scheme of experimental setup is represented in Figure 3.1. The electric pulses yielded to the discharge cell through 50-Ohm RF cable with 20 m length. The discharge cell consisted of thin-wall quartz discharge tube with 5 cm inner and 4.7 cm outer diameters, metallic screen, high and low-voltage electrodes. The screen was made of eight brass rods with 12 mm diameters uniformly installed on the 7 cm distance from the cell axis. The high voltage electrode had conical form with 60° opening angle. The low voltage one was a ring connected to the screen directly. The distance between the edges of the electrodes was 20 cm. The pressure of mixture during the oxidation process was controlled by mechanotron pressure gauge MDx4C.

Electrical characteristics of the discharge were measured by capacitive gauge movable along discharge cell axis and back current shunt mounted into the break of the supplying cable screen. The back current shunt was installed on the distance from the discharge cell at which incident to the cell and reflected from it current pulses are separated in time.

In all mixtures the emission intensity of the discharge was measured both in time resolved (band pass of signal route was 150 MHz) and in integral regimes. Emission intensities were measured through the optical CaF_2 window with 3 cm diameter mounted in the low-voltage ring electrode with using monochromator MDR-23 (its linear dispersion was 1.2 nm/mm with 1200 groves per mm grating) and photomultiplier FEU-100 (rise-time of signal was not longer than 3 ns, spectral sensitivity bandwidth was 200-800 nm). Distance between the window and entry slit of monochromator was 12 cm, at that emission from the practically whole discharge volume passed through monochromator.

Excluding potential distribution along the discharge tube all time resolved measurements were fulfilled in time when discharge switch on and after finishing of oxidation process in regime of averaging over 128 pulses (in our case time of averaging was 3.2 s). Measurements of temporal-space dynamics of the potential distribution were fulfilled in processed mixtures only.

In mixtures with methane absorption of He-Ne laser emission on $3.33922\ \mu\text{m}$ was measured in addition to general set of parameters.

Time resolved signals were registered by oscilloscope Tektronix TDS 380 (band pass was 400 MHz). The integral measurements was fulfilled by oscilloscope S9-8 with 100, 200 and 400 s per scale.

Mixtures of heavy hydrocarbons were prepared under condition when partial pressure of an alkane lower than saturated vapor pressure at room temperature. A portion of an alkane was injected into the 10-liter vacuum-processed. The mass of the portion was smaller on 20% than mass of saturated vapor pressure of this alkane in this volume at room temperature. The control of pressure of gas in the volume (the pressure increased and reached steady-state value in the process of alkane evaporation and heating up to the room temperature) allowed to measure the alkane concentration in the volume. Later we filled the volume by the oxygen up to the required pressure. Gases mixed during the two days. After the experiments with the alkane-oxygen mixture, nitrogen was added in the residuary mixture to obtain the alkane-air mixture.

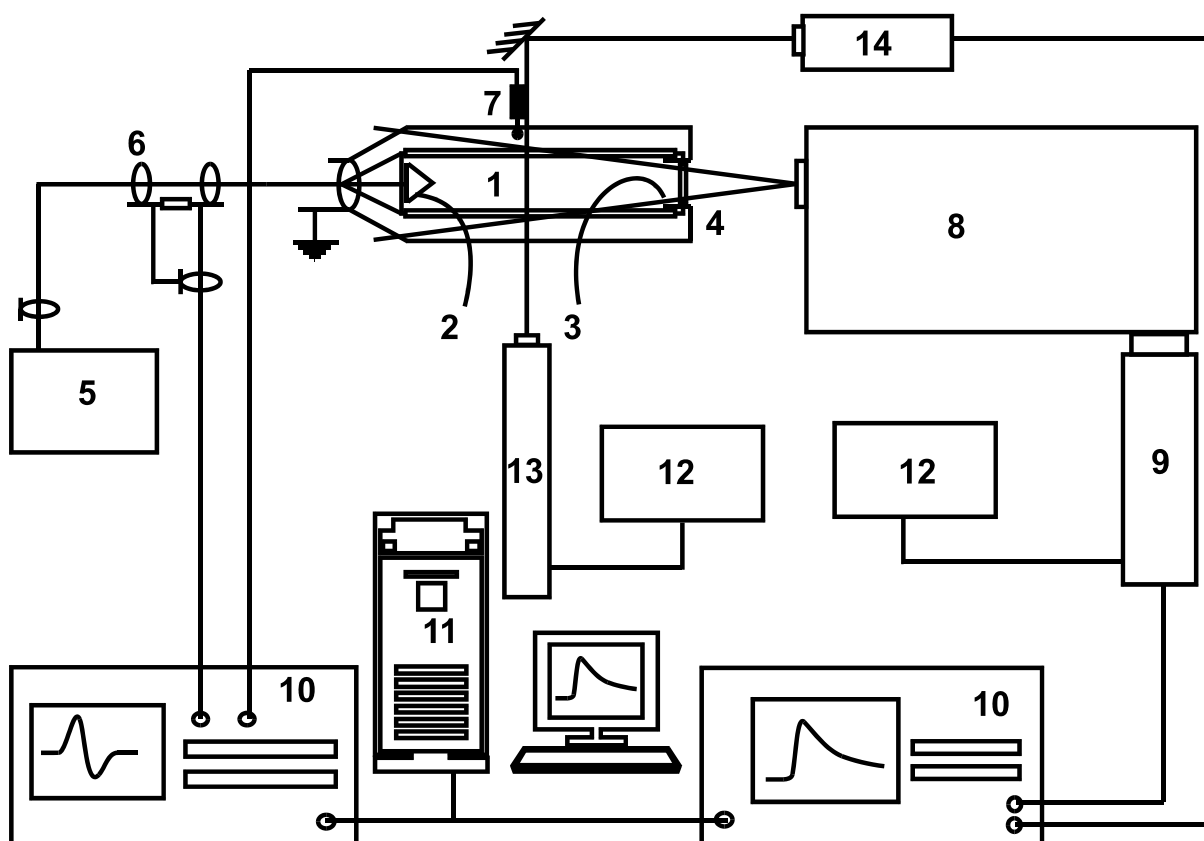


Figure 3.1: Experimental setup: 1 - discharge cell, 2,3 - electrodes, 4 - optical window (CaF_2), 5 - high-voltage generator, 6 - back current shunt, 7 - capacitive gauge, 8 - monochromator, 9 - photomultiplier FEU-100, 10 - oscilloscopes S9-8 and TDS-380, 11 - computer, 12 - power supplies, 13 - He-Ne laser ($\lambda = 3.3922\mu\text{m}$), 14 - photodetector Pb-Se.

3.2 Experimental methods

3.2.1 Finding of electric current, electric field and energy input

The distribution of the potential along discharge cell $V_i(t)$ was measured by capacitive gauge mounted in sections $x_i = 0.0; 3.6; 7.2; 10.8; 14.4; 18.0$ cm sequentially. Section $x_0 = 0.0$ corresponded to the edge of conical electrode.

Measurements of the current through the high-voltage electrode $J_0(t)$ with the aid of standard technique described in.¹¹⁴ Typical oscillogram of the signal from the shunt is showed in the Figure 3.2a. The first pulse of the current ("incident") is a pulse which moves from the high-voltage generator to the discharge cell. This pulse reflects from the discharge cell and returns to the shunt installation section in 100 ns. This is second pulse ("reflected") showed in the Figure 3.2. Further the pulse returns to the generator and reflecting from it returns to the shunt and later to the discharge cell. That is the process of pulse propagation repeats. Thus, the current shunt registers pair of pulses ("incident" and "reflected"), which come through it with period of 200 ns. The energy, which contributes in the gas in the first pulse, is equal to the difference of energies of "incident" and "reflected" pulses. The current, which passes through the discharge cell was obtained from the continuity equation of charge at the section of the high voltage electrode (Figure 3.2). Taking into account directions of pulses propagation, which determine polarities of signals on the back current shunt:

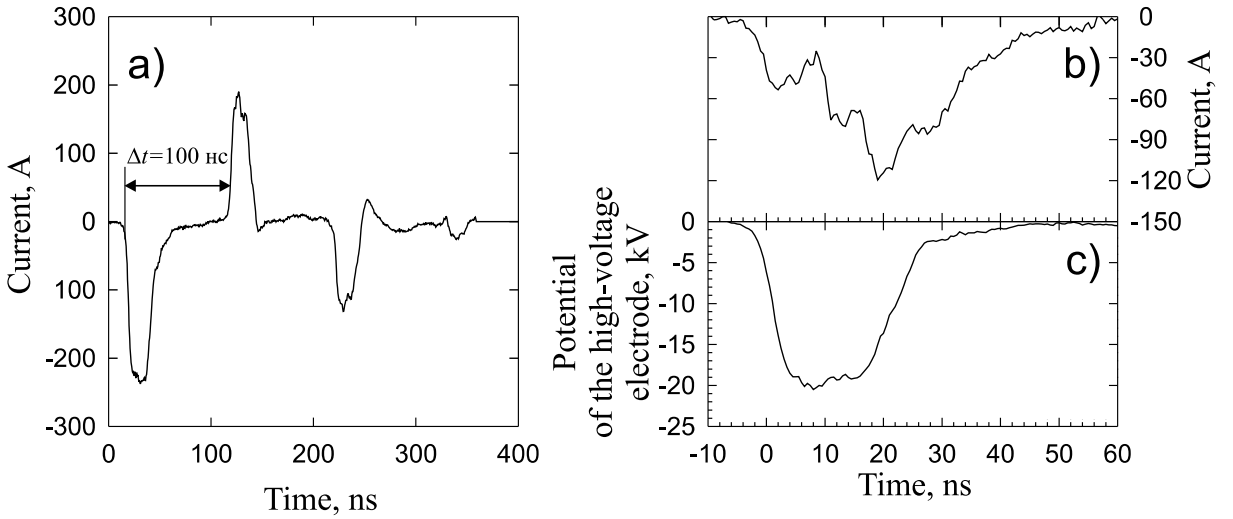


Figure 3.2: Characteristics measured by the current shunt: a) - the oscillogram of the current in the cable, b) - the current through the high voltage electrode, c) - the high-voltage electrode potential. The initial pressure of the mixture $\text{CH}_4 + \text{air}$ is 1.5 torr.

$$J_0(t) = J_{\text{sh}}(t) + J_{\text{sh}}(t + 2\Delta t) \quad (3.1)$$

where $J_{\text{inc}} = J_{\text{sh}}(t)$ was the current in the incident pulse, $J_{\text{ref}} = J_{\text{sh}}(t + 2\Delta t)$ is the current in the reflected pulse (Figure 3.2), Δt is the time of the pulse propagation from the current shunt to the high-voltage electrode. Besides, the current shunt measurements allow to obtain as the current through the high electrode so the potential on the electrode U_0

(Fig. 3.2). The potential on the high-voltage electrode is proportional to the difference of currents in the first and second pulse of the pair:

$$U_0(t) = R[J_{\text{sh}}(t) - J_{\text{sh}}(t + 2\Delta t)], \quad (3.2)$$

where $R = 50 \text{ Ohm}$ is the impedance of the RF cable.

To obtain electric field and current in different sections along the discharge cell we used telegraph equations, at that the capacity and the inductance of discharge setup per unit length expected to be constant. We calculated the capacity per unit length ($C = 5.2 \text{ pF/cm}$) in the approximation that the excess charge accumulates near the cell wall. The inductance per unit length ($L = 2.8 \text{ nH/cm}$) was calculated in the approximation that current density is uniform in all cross-sections of the discharge cell. The resistance per unit length of the cell was assumed to be variable in space and time. Let us write telegraph equation:

$$\begin{cases} \frac{\partial V}{\partial x} + RJ &= -L \frac{\partial J}{\partial t} \\ \frac{\partial J}{\partial x} &= -C \frac{\partial V}{\partial t} \end{cases} \quad (3.3)$$

We assume that $E_l(x, t) = J(x, t)R(x, t)$, where $E_l(x, t)$ is a longitudinal component of the electric field, which we denotes below as E ,

$$\begin{cases} \frac{\partial V}{\partial x} + E &= -L \frac{\partial J}{\partial t} \\ \frac{\partial J}{\partial x} &= -C \frac{\partial V}{\partial t} \end{cases} \quad (3.4)$$

where $J(x, t)$ is a current, $V(x, t)$ is a potential and $R(x, t)$ is a resistance per unit length in the section x at instant of time t .

Inasmuch as measurement were fulfilled in discrete set of point, to solve the problem we approximate potential $V_i(t)$ and current $J_i(t)$ in sections linearly between these sections. Then on the interval $i = (x_i, x_{i+1})$:

$$\begin{cases} V &= V_i(t) + \frac{x-x_i}{x_{i+1}-x_i}(V_{i+1}(t) - V_i(t)) \\ J &= J_i(t) + \frac{x-x_i}{x_{i+1}-x_i}(J_{i+1}(t) - J_i(t)) \end{cases} \quad (3.5)$$

In the discrete approximation the second equation of the system (5.2) can be represented as

$$\frac{J_{i+1}(t) - J_i(t)}{x_{i+1} - x_i} = -C \frac{\partial V}{\partial t} \quad (3.6)$$

The right side of the equation depends on x , but the left one does not depend on x , and so to solve the equation we average the right side of the equation over the interval $[x_i, x_{i+1}]$.

$$J_{i+1} = J_i - \frac{C(x_{i+1} - x_i)}{2} \frac{\partial}{\partial t} [V_i + V_{i+1}] \quad (3.7)$$

As result current in any given cross-section corresponded to the x_{i+1} coordinate is expressed by the relationship:

$$J_{i+1} = J_0 - \sum_{k=0}^i \frac{C(x_{k+1} - x_k)}{2} \frac{\partial}{\partial t} [V_k + V_{k+1}] \quad (3.8)$$

To obtain the electric field E we average the equation (3.4) over interval $i = (x_i, x_{i+1})$:

$$\frac{E_{i+1}(t) + E_i(t)}{2} = -\frac{V_{i+1}(t) - V_i(t)}{x_{i+1} - x_i} - \frac{L}{2} \frac{\partial}{\partial t} [J_i(t) + J_{i+1}] \quad (3.9)$$

Thus, taking into account the inductance and the capacity of the discharge cell the current through the high-voltage electrode and the potential distribution along the discharge cell measured experimentally were transformed to the current and the electric field distributions along the discharge cell.

Obtained values $E(x, t)$ and $J(x, t)$ were used for calculating dynamics of contributed power per unit volume $P(x, t) = E(x, t)J(x, t)/S$ (S is a square of discharge tube cross-section).

It is important to note that the used approximations do not allow describing the electric field dynamics in the fast ionization wave front,⁹⁴ as for the reason of using the delta-function as the space sensitivity function of the capacitive gauge so for the reason of neglect of radial components of the current and the electric field. However, beyond the front and later, on the closing of the discharge to the low-voltage electrode stage these approximations are quite justified.⁹⁴ Using of the delta-function as the sensitivity function did not allow to reconstruct the electric field near the cathode. It is necessary to note that for the pressure $p > 3$ torr (range of the maximal energy contribution) in our experimental condition the main part of the energy contributed in gas at later stage of discharge, and so the cathode drop is negligible. Thus, the used method of the reconstruction allowed to obtain the distribution of the electric field at the time range which was important for the gas excitation.

3.2.2 Emission spectroscopy. Experimental investigation of optical characteristics of the discharge.

Full oxidation of alkanes in our conditions takes place under the action of a few thousands pulses (for tens and hundreds second), therefore integral over the time signal from the photomultiplier tube contains information about the hydrocarbons oxidation process. As the integrator the capacitor shunted the input of the oscilloscope was used. The integration time ($\tau_0 = CR_0 = 0.25$ s) was ruled by capacity of the integrator $C = 2.5$ pF and input resistance of oscilloscope $R_0 = 1$ MOhm. Inasmuch as a photomultiplier tube is the source of current, then the Ohm law for the measuring circuite can be written as

$$\frac{U}{R_0} + \frac{dq}{dt} = J, \quad (3.10)$$

hence

$$U + \tau \frac{dU}{dt} = R_0 J, \quad (3.11)$$

where U is a voltage on a oscilloscope, q is a discharge of the capacitor, J is the current from the multiplier.

Since as characteristic time of the discharge emission is much smaller than the integration time, then we can suppose that for the time of the emission the capacitor accumulates charge only, at that the capacitor discharges through the oscilloscope for the time between

pulses. Lifetimes of investigated states ($< 10 \text{ } \mu\text{s}$) is much smaller than time between pulses $1/f \approx 25 \text{ ms}$. Hence, we can neglect by current of preceding pulses. Then we can write current in the pulse came from the multiplier as

$$J(\delta t) = \frac{IAk_{\text{exc}}N'_0}{\tau_l} \exp \left[-\frac{\delta t}{\tau_l^{\text{eff}}} \right], \quad (3.12)$$

where I is an emission intensity on a separated wavelength λ , $A = A(\lambda)$ is the spectral sensitivity of the optical system monochromator-photomultiplier, N'_0 is a concentration of non-excited molecules, from which an emitted states produced, k_{exc} is the excitation of the higher state of the transition constant, which integrated over the time of the excitation in the one high-voltage pulse, τ_l is the radiative lifetime of the higher sates, τ_l^{eff} is an effective lifetime of the higher state, δt is variable, which is the time from the arrival of the last preceding pulse. The effective lifetime takes into account the radiative and collisional deactivation of the state.

$$\tau_l^{\text{eff}} = \frac{1}{1/\tau_l + N_0 \sum_i^M \alpha_i k_i^q}, \quad (3.13)$$

where M is a number of a stable components in a mixture, α_i is a part of a component i , k_i^q is a constant of quenching by i -component, N_0 is a full concentration of stable component.

In a case of slow reacted mixture (mixture, which characteristic time of a composition change is much more than an integration time) the excitation rate of the state k_{exc} and the effective lifetime τ_l^{eff} weakly changes from pulse to pulse.

The initial voltage on the capacitor is equal to the residuary voltage of the preceding pulse, and so we solve the equation (3.11) on the $n + 1$ interval of time with starting condition $U_{n+1}(0) = U_n(n/f)$:

$$U_{n+1} + \tau_0 \frac{dU_{n+1}}{dt} = \frac{AR_0 k_{\text{exc}} N'_0}{\tau_l} \exp \left[-\frac{t}{\tau_l^{\text{eff}}} \right] \quad (3.14)$$

The characteristic transient period of the signal from the photomultiplier has the order of magnitude τ_0 , and if the characteristic time of the composition change of the mixture is much more than τ_0 then the solution of equation (3.14) is the superposition of the slowly changed function $\langle U \rangle(t)$ and periodic function with the period $1/f$ and the amplitude $\delta U(t)$:

$$\langle U \rangle \approx \frac{AR_0 k_{\text{exc}}(t) N'_0(t) f}{1 + \tau_l N_0 \sum_i^M \alpha_i(t) k_i^q} \quad (3.15)$$

$$\delta U \approx \frac{\langle U \rangle}{2\tau_0 f} \quad (3.16)$$

As the result of the every pulse of the discharge the peak of the emission decayed for the time τ_0 was observed, at the same time signals from consequently following pulses were accumulated and formed the integral signal.

Thus, measured integral characteristics of emission give the information about current composition of reactive mixture. In our case $f\tau_0 \approx 100$, therefore the amplitude of oscillations was not more than 3% from the average signal $\langle U \rangle(t)$. In data processing,

signals from the oscilloscope were averaged over the period of discharge repeating, that allowed to diminish the oscillations.

The control of emission intensity has been carried out for set of spectral transitions, at that some bands have been overlapped. In the Table 3.2 transitions, which were controlled in all mixtures are represented. Table 3.3 contains transitions, which have been investigated in mixtures with air, in addition to those represented in the Table 3.2. It is necessary to note that intensities of the transitions mentioned in the Table 3.3 were so large that the emission of the overlapped bands was negligible.

Table 3.2: Transitions, controlled in all mixtures.

λ, nm	$\delta\lambda, \text{nm}$	measured band	overlapped system of bands
518.6 nm	2.8 nm	CO Angstrom, $\text{CO}(B^1\Sigma, v' = 0 \rightarrow A^1\Pi, v'' = 2)$	—
430 nm	3 nm	$\text{CH}(A^2\Delta, v' = 0 \rightarrow X^2\Pi, v'' = 0)$	$\text{CO}_2^+(A^2\Pi \rightarrow X^2\Pi)$, first negative and second positive systems of nitrogen
307.8 nm	3.4 nm	$\text{OH}(A^2\Sigma, v' = 0 \rightarrow X^2\Pi, v'' = 0)$	$\text{CO}_2^+(A^2\Pi \rightarrow X^2\Pi)$ second positive systems of nitrogen,
290 nm	2.8 nm	$\text{CO}_2^+(B^2\Sigma \rightarrow X^2\Pi, \delta v = 0)$	$\text{OH}(A^2\Sigma \rightarrow X^2\Pi)$

Table 3.3: Transitions, controlled in air mixtures.

λ, nm	$\delta\lambda, \text{nm}$	measured band	overlapped system of bands
258.2 nm	3.7 nm	γ -system NO, $\text{NO}(A^2\Sigma \rightarrow X^2\Pi, \delta v = 3)$	—
490 nm	3.7 nm	$\text{N}_2(C^3\Pi, v' = 1 \rightarrow B^3\Pi, v'' = 7)$	$\text{CO}_2^+(A^2\Pi \rightarrow X^2\Pi)$
669.6 nm	3.7 nm	$\text{N}_2(B^3\Pi, v' = 6 \rightarrow A^3\Sigma, v'' = 3)$	$\text{CO}_2^+(A^2\Pi \rightarrow X^2\Pi)$
469.2 nm	3.3 nm	$\text{N}_2^+(B^2\Sigma, v' = 0 \rightarrow X^2\Sigma, v'' = 2)$	$\text{CO}_2^+(A^2\Pi \rightarrow X^2\Pi)$

In the case of essential overlap of the emitted bands to identify the band the emission intensities were measured in time-resolved regime for instants at the time when discharge switched on and when oxidation process was finished (when signal from the photomultiplier reached steady-state value). Also, measurements of emission intensities in time resolved regime were used for obtaining quenching constant rates in initial and final mixtures. Taking into account the constant rates of the quenching the excitation rates of higher states have been obtained.

3.2.3 Absorption spectroscopy. Methane concentration measurements.

The methane concentration was measured by absorption of the emission of the He-Ne laser LGN-118 ($\lambda = 3.3922 \mu\text{m}$). The laser emission, which wavelength is practically the same as wavelength of the vibrational transition of the asymmetric mode of the CH_3 -group vibration, propagated through the discharge cell by the mixture perpendicularly to its axis and came to the Pb-Se (band of the spectral sensitivity is $2\text{--}4 \mu\text{m}$). Filling the discharge cell by the mixture we registered signals from mechanotron and photodetector by oscilloscope S9-8 simultaneously. By the known composition of mixture and obtained dependence of signal from photodetector on the mixture pressure $I(p)$ the calibration curve $I([\text{CH}_4])$ was obtained for every experiment. Concentrations of other alkanes did not measured by technique owing to small coefficients of absorption on the wavelength $3.3922 \mu\text{m}$ for other alkanes and those lower concentrations in stoichiometric and lean mixtures.

3.3 Results and discussion

3.3.1 Electrodynamic situation of the discharge.

Distributions of potential, current, reduced electric field and power per unit volume along discharge gap obtained from capacitive gauge and shunt measurements in methane-air stoichiometric mixture are represented in the Figure 3.3. With the aim to investigate the behavior of the electrodynamic characteristics in the high pressure region these characteristics have been measured at pressure 18 torr in addition to the standard set of parameters.

Let us consider importance of taking into account of the capacity and the inductance of the discharge cell. From the equation (3.4) it is followed that

$$E = -\frac{\partial V}{\partial x} - L \frac{\partial J}{\partial t}$$

Thus, it is important to take into account the inductance in the case of low electric field and fast change of the current. From the Figure 3.3 it is seen, that the low electric field with fast change of current was realized on the back front of the high-voltage pulse. For pressure 6.05 torr this is the time interval $t > 25 \text{ ns}$, as it is clearly seen from the Figure 3.3. So, for $t = 25 \text{ ns}$ the rate of rise of the current amounted to the 20 A/ns and inductive addition to the electric field amounted to 60 V/cm or 10 V/(cm torr) , that comparable to the electric field value itself. The fast ionization wave development is caused by charging of capacity of the discharge cell, therefore the current on the wave stage decreased with the increasing distance from the high-voltage electrode. On the later stages of the discharge the influence of the capacity is negligible.

As a whole, electrodynamic situation of the discharge in the relatively short discharge gap is comprehensive and essentially differs from the situation in the long gap.⁹⁴ Typical values of the fast ionization wave velocity amounted to $2\text{--}3 \text{ cm/ns}$, and the time of the wave propagation along the discharge cell was $7\text{--}15 \text{ ns}$, that was shorter than pulse duration. Because of this feature the regime of short circuit, which did not observed in,⁹⁴ was realized in our conditions. In this regime the electric field density and current do not vary

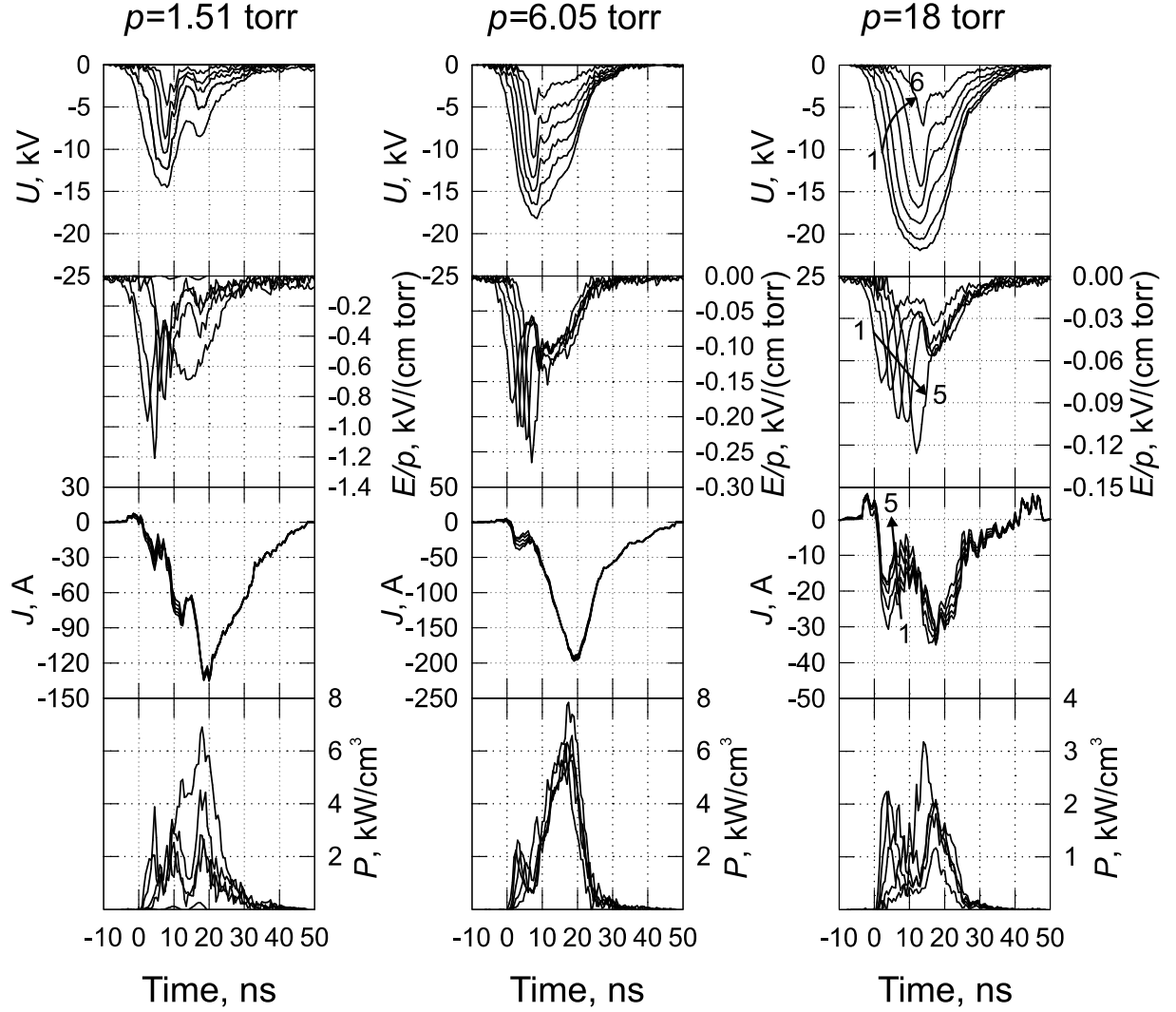


Figure 3.3: Electrodynamics characteristics in the first high voltage pulse represented for three different pressures — 1.51, 6.05 and 18 torr. Potential distributions $U(t)$ are represented in sections $x = 0.0, 3.6, 7.2, 10.8, 14.4, 18.0$ cm. Distributions of reduced electric fields $E(t)/p$, currents $J(t)$, volumetric power densities $W(t)$ averaged over the intervals are represented for the intervals 0.0–3.6, 3.6–7.2, 7.2–10.8, 10.8–14.4 and 14.4–18.0 cm. Curves are enumerated from 1 to 6 for the potential and from 1 to 6 for other values consequently. Arrows in figures show directions of curves shifts with the consequent change from the 1-st to the 6-th section for voltage and from the 1-st to 5-th interval for other values. The mixture is the products of the oxidation of CH_4 in the methane–air stoichiometric mixture.

along the discharge cell, and relatively slow change in time. For example, at the pressure $p = 6.05$ torr this stage began with $t = 10$ ns.

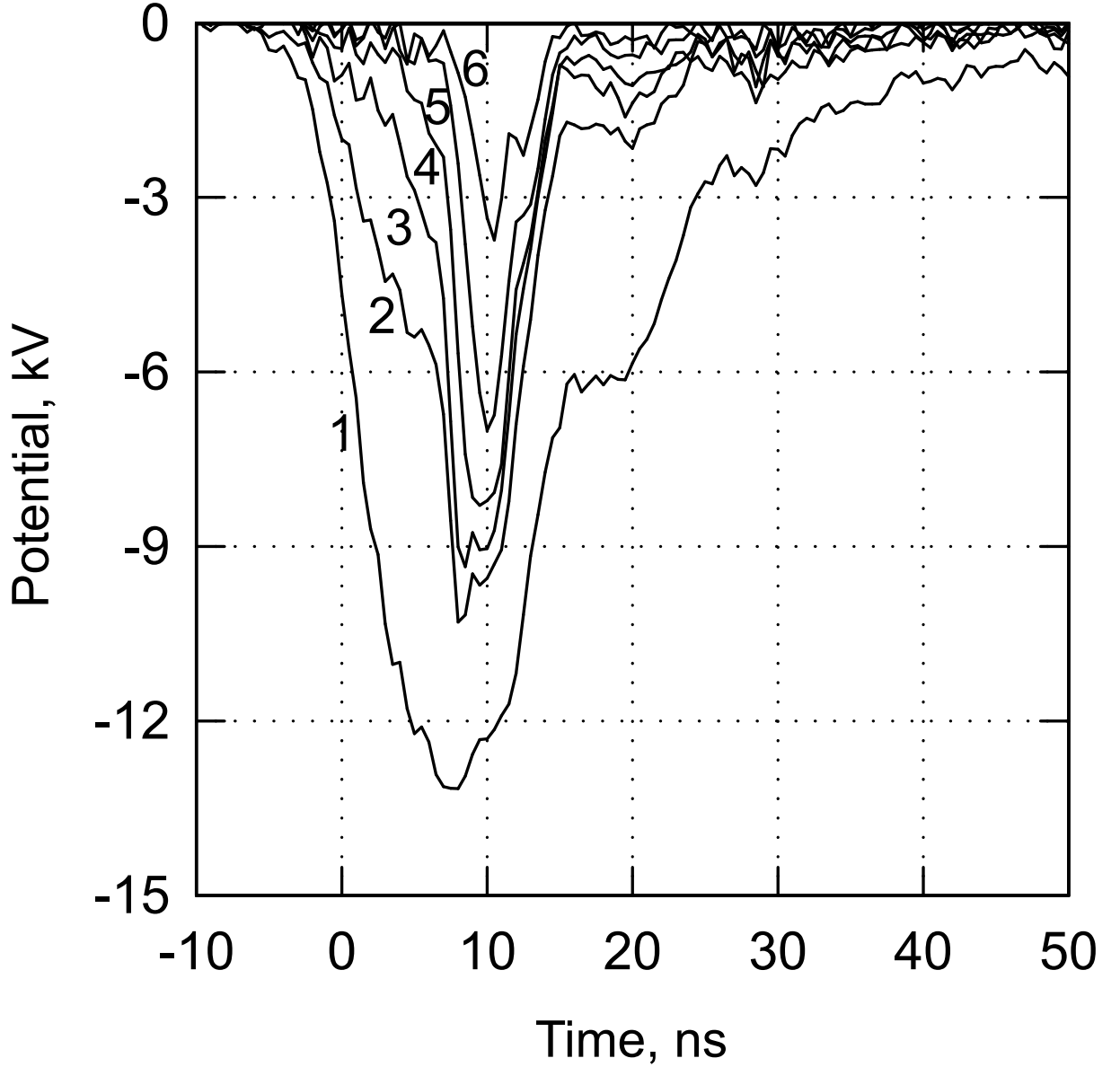


Figure 3.4: Distributions of the potential in the first high-voltage pulse for the pressure 0.76 torr in sections $x = 0.0, 3.6, 7.2, 10.8, 14.4, 18.0$ cm, which are enumerated from 1 to 6 consequently. The mixture is products of oxidation of CH_4 in the stoichiometric mixture with air.

At the pressure 0.76 torr precursor, which is the fast ionization wave developed on the background of the high value of cathode drop and characterizes by weak current through the cathode (in the Figure 3.4 $t < 8$ ns), stand out. The development of the precursor and main ionization wave in the long tube has been investigated in detail in.^{94,115} The start of the main wave leads to the compensation of the positive charge in vicinity of the cathode and to sharp reduction of the cathode drop.

It has been shown that, the precursor appeared on the initial stage of the discharge,

and its development was ruled by polarization current near the cathode, at the same time the emission current was the relatively weak. The polarization near the cathode led to the growth of electric field near the cathode and to the sharp growth of the emission current, which resulted to the main wave start. The main wave propagates through the pre-ionized gas with the velocity, which is much more higher than velocity of the precursor, and caught up it. After the main wave merging with the precursor the only one ionization wave propagates forward. The velocity of this wave is higher than the velocity of the precursor and lower the velocity of the main wave before merging. The main wave start leads to the compensation of the exceed positive charge near the cathode and to sharp reduction of the cathode drop, so in⁹⁴ after the main wave start the cathode drop was lower than the level of the experimental inaccuracy.

In our case, at a pressure of 0.76 torr two characteristic features can be noted: before main wave start the precursor reaches anode; during all time of the discharge the essential cathode drop is observed. The first feature can be explained by the fact, that the length of the discharge tube in this work (20 cm) is shorter by three times then one in the work⁹⁴ (60 cm), and so with approximately the same values of the delay time of the main wave start and the precursor velocity the precursor has time to reach anode before start of the main wave. This feature leads to the main wave propagation through the pre-ionized gas and so it passes the discharge cell for 2 ns approximately (main wave velocity is about 10^{10} cm/c). The second feature is also explained by the difference of the discharge cell sizes, as lower length, so that the diameter is large by 2.5 times, in our case than in.⁹⁴ For the comparable electron density the resistance of the discharge cell, excluding cathode layer, was smaller by 20 times in our case than in.⁹⁴ As the consequence, the essential higher voltage dropped on the cathode layer in our case.

At low pressures ($p < 4$ torr) both ionization wave development and short circuit stage take place on the background of high cathode drop. It is important to note, that the electric field in the cathode layer at $p < 4$ torr essentially higher (by orders of magnitude) than it showed in the figure, owing to the essential value (about screen diameter) of the halfwidth of the capacitive gauge sensitivity function.⁹⁴ The thickness of the cathode layer can be estimated using the theory of glow discharge. In our experimental condition the cathode layer corresponded to the case of the anomalous glow discharge, since typical current density amounted to some or dozens of A/cm², that is more by 3–4 of the order of the magnitude than the normal current density. From this directly follows, that the parameter (pd) was approximately equal to value $(pd)_{norm}/e$ [torr·cm],¹⁵ where d is the cathode layer width, $(pd)_{norm}$ is the normal reduced cathode layer width. For aluminum cathode in air $(pd)_{norm} \approx 0.25$ [torr·cm],¹⁵ from which follows $pd \approx 0.09$ [torr·cm]. For the pressure $p = 0.76$ tor — $d = 1.2$ mm, and for the pressure $p = 9.83$ torr — $d \approx 100\mu\text{m}$.

Lets consider data at the pressure $p = 1.51$ torr in more detail. The cathode layer thickness was equal to $d = 0.6$ mm. In the Figure 3.3 it is clearly seen, that in the discharge cell quasisteady-state distribution of the electric field was formed beginning at $t = 10$ ns. Voltage on the discharge cell in this moment amounted to 20 kV approximately (Figure 3.2), at the same time on the discharge cell, excluding cathode, drops 10 kV approximately (from Figure 3.3 it is clearly seen that at the point $x = 3.6$ cm voltage amounted to 8 kV and electric field in the main part of discharge cell amounted to ~ 600 V/cm). Thus, the electric field in the cathode layer amounted to $(20000 - 10000)/0.06 = 1.7 \cdot 10^5$ V/cm approximately. This value is enough to vacuum breakdown in a discharge gap with an

aluminum cathode trained by a pulsed discharge.¹¹⁶ In the next 3 ns potential drop on the main part of the discharge column decreased to ~ 2 kV. For the same time potential on the high voltage electrode practically remained unchanged (decreased to 19 kV), that led to the growth of the electric field in the cathode layer up to $2.8 \cdot 10^5$ V/cm and to the multiply growth of the field-emission current from the cathode. The growth of the emission current led to the field-emission breakdown of the cathode layer and formation of the wave of the repeated breakdown, which redistributed potential between the cathode layer and the main part of the discharge column. It is seen from the Figure 3.4 that for pressure 0.76 torr two waves of the repeated breakdown ($t = 20$ ns and $t = 27$ ns) were observed; for the pressure range $p = 1.51 - 3.02$ torr cathode layer was unloaded only ones, for higher pressures it was not unloaded for all time of the pulse (Figure 3.3).

Fulfilled analysis allowed to predicate that for pressures lower than 3–4 torr the considerable part of energy contributes to the thin cathode layer. Besides, the considerable part of the energy contributes on the stage of the ionization wave propagation. At the same time it is clearly seen from the figure that already for pressure 3.02 torr the main part energy contributed in gas on the short circuit stage at that part of energy contributed in the cathode layer for all time of the discharge and in the main part of the discharge column in the wave propagation stage was negligible. For pressures higher then 10 torr the energy contribution on the short circuit stage decreased when the pressure increased, but even for the 18 torr pressure its value was higher that one in the wave stage by 3 times.

As it has been shown previously, a part of the pulse reflected from the discharge cell and returned to the generator, reflected from it and came to the discharge cell again. The discharge initiated by these secondary pulses formed on the stage of short circuit immediately. Cathode drop in these pulses was not observed for pressure more than 0.76 torr and so the energy contribution in these pulses was uniform.

Dependence of the energy contribution on pressure is showed in the Figure 3.5. It is clearly seen that for the pressure of 0.76 torr the energy contribution in the second pulse is higher than it in the first pulse. With the growth of pressure the energy contribution increases and reaches the maximum value with pressure 3.5 torr approximately, while the energy contribution in the second pulse decreases and beginning with pressure 3.5 torr become the constant. The energy contribution in the third and others pulses are lower than 2%. It is important to note that high value of energy contribution in the second pulse partially compensates nonuniformity of the contribution at low pressures.

Thus, the main part of energy in the pressure range (0.76–10.6 torr), in which investigations were fulfilled, contributes in gas on the stage of short circuit in the first or the second pulse. At the same time nonuniformity of the discharge caused by cathode layer can be neglected. The noted feature allows measuring local electric field and current during the time of maximal energy contribution using only a back current shunt, that is especially important for investigation of chemical reactive mixtures, in which changes of a composition lead to the changes of electrodynamic characteristics. The electrical measurements, which were fulfilled in the processed stoichiometric mixtures (from ethane to hexane) with oxygen or air, gave results, which are the same as the above-mentioned.

In the Figure 3.6 the energy contribution is represented for all investigated mixture in the beginning of the discharge and after oxidation process. The total energy of the pulse reaches to 60 mJ. It is seen from the figure that in the beginning of the process

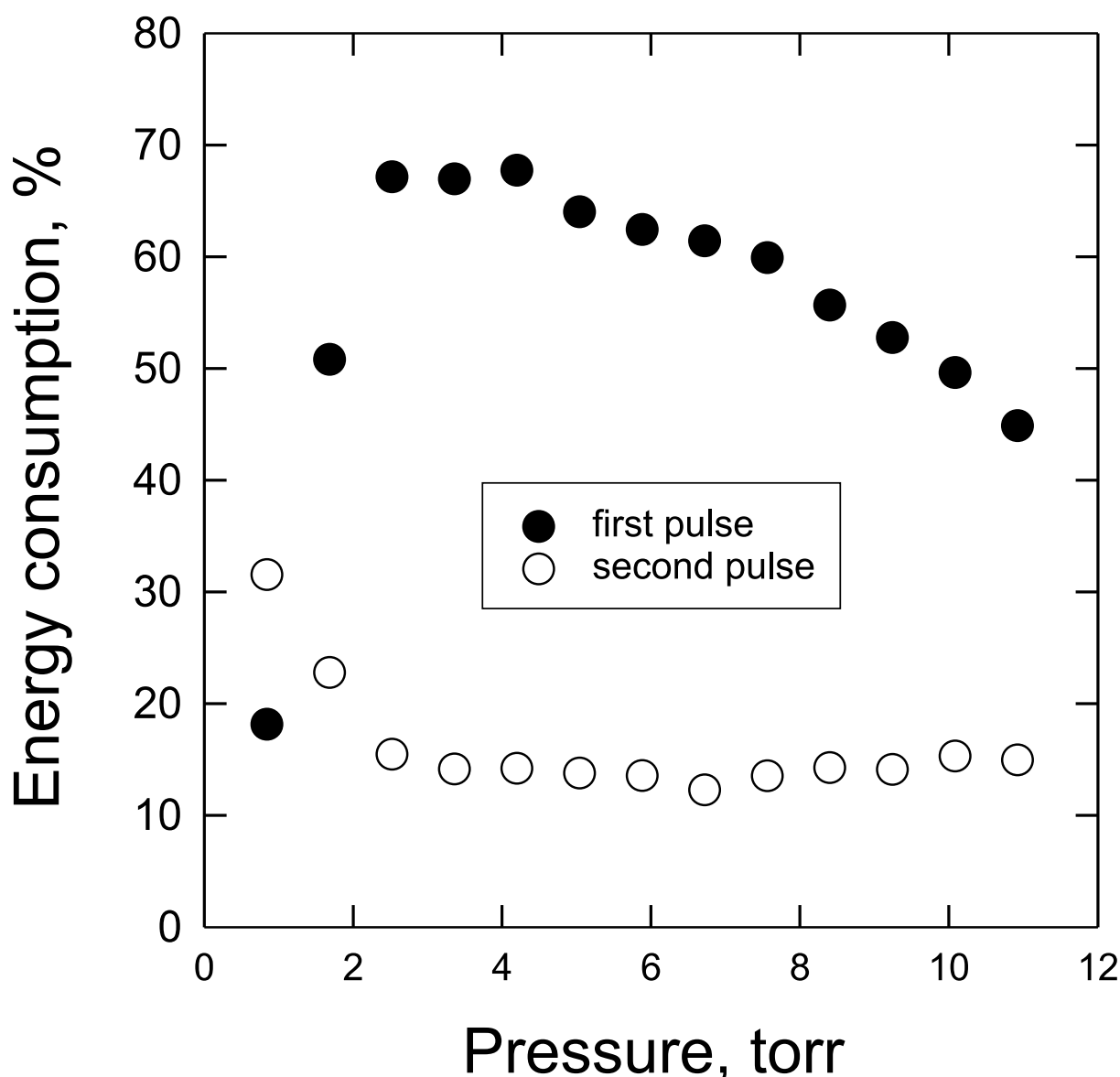


Figure 3.5: The energy input in the discharge for the first and the second pulses in the processed methane-air mixture in dependence on the initial pressure of the mixture.

of oxidation the energy contribution in any mixture with oxygen for pressures higher than 3 torr is systematically higher than for a mixture with air. With the growth of the pressure the difference increases and reaches 12% for the $p = 10.6$ torr. In processed mixtures variations of the energy contribution from a mixture to a mixture are negligible and even presence of nitrogen does not effect essentially. The energy contribution in the methane–oxygen processed mixture only is rather higher than one in other mixtures.

3.3.2 Kinetics of alkanes oxidation in the discharge.

Emission spectra of the discharge in the pure methane and in the processed methane-oxygen stoichiometric mixture are represented in the figure 3.7. The spectrum in the pure methane consist of the repulsive continuum of hydrogen (the transition $H_2(a^3\Pi - b^3\Sigma)$).

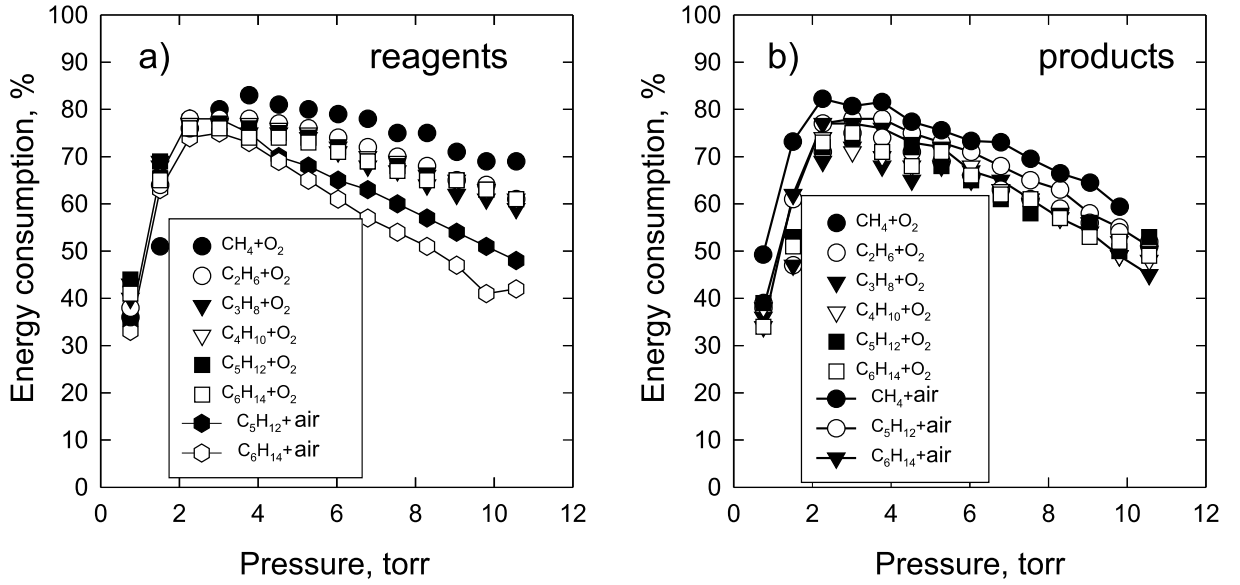


Figure 3.6: The sum of the energy input in the first and the second high-voltage pulses: a) in the initial mixture, b) in the mixture transformed by the discharge.

The emission band of $\text{CH}(A^2\Delta \rightarrow X^2\Pi)$ which corresponds to the transition $v' = 0 \rightarrow v'' = 0$ is good identified. The main part of molecular bands of visible and near ultraviolet ranges, which appears in the processed methane-oxygen mixture, belongs to the molecule $\text{CO}_2^+(A^2\Pi)$. Bands of the radical $\text{OH}(A^2\Sigma \rightarrow X^2\Pi)$ are also clearly stands out. We are able to identify and control some weak bands of CO Angstrom system ($\text{CO}(B^1\Sigma \rightarrow A^1\Pi)$).

From the figure it is clearly seen that the $\text{CH}(A^2\Delta \rightarrow X^2\Pi)$ band emission in the methane strongly overlaps by the $\text{CO}_2^+(A^2\Pi \rightarrow X^2\Pi)$ in the mixture. Hence, on the early stage of methane-oxygen mixture processing it is important to take necessary steps to separate these bands. The $\text{OH}(A^2\Sigma \rightarrow X^2\Pi)$ spectrum also overlaps by the CO_2^+ emission spectrum. In mixtures of alkanes with air multiple and strong bands of 1-st negative and 1-st and 2-nd positive systems of nitrogen appear in the spectrum. They partially overlap the emission spectrum of CH, CO_2^+ and OH bands. In the system of Angstrom the band on the 518.6 nm is not overlapped by another bands. In all experiments weak lines of Balmer series of hydrogen were observed.

As it has been indicated above, the identification of bands in the case, when they overlap in a narrow spectral band, was realized on the basis of the time-resolved experiments with nanosecond resolution. In the Figure 3.8 the example of time resolved signals of emission on 430 nm wavelength at the beginning of the oxidation process and after finishing are represented. Two peaks of the emission corresponded to two pulses of high-voltage are clearly seen. The decay of emission can be approximated with the good accuracy by the sum of two exponential functions with the essentially different characteristic time. It is well known that lifetime of $\text{CO}_2^+(A^2\Pi)$ state ($\tau = 124 \text{ ns}$,¹¹⁷) is larger by the several times than the lifetime of $\text{CH}(A^2\Delta)$ ($\tau = 600 \text{ ns}$,¹¹⁸). Then the exponent with larger characteristic time was corresponded to the emission of the $\text{CH}(A^2\Delta)$ state, and with the smaller one was corresponded to the emission $\text{CO}_2^+(B^2\Sigma)$ state. From this figure, it clearly seen that the emission intensity, which is corresponded to $\text{CH}(A^2\Delta \rightarrow X^2\Pi)$ transition decreases by several times in oxidation process and the emission intensity corresponded to

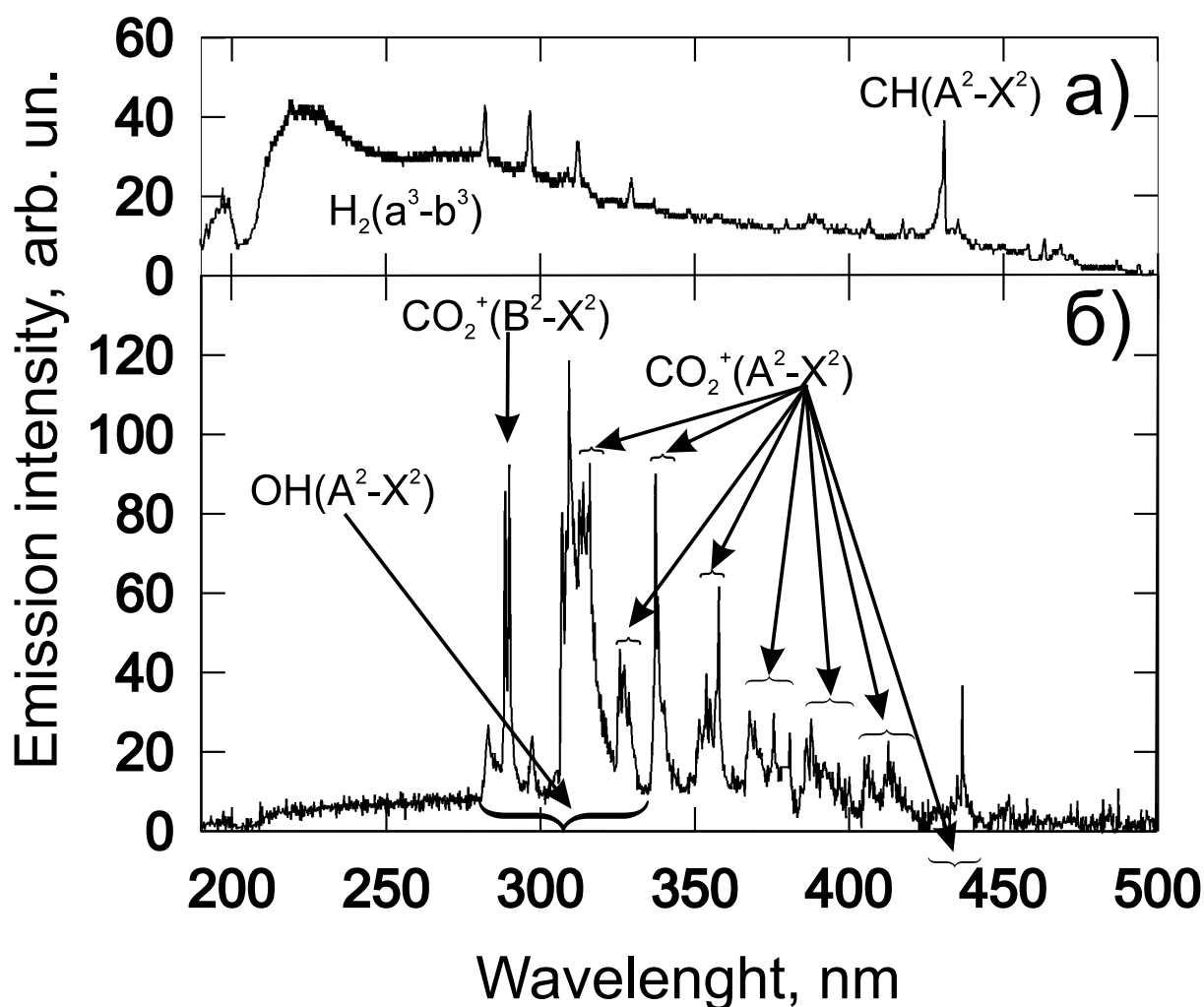


Figure 3.7: Spectrum of the discharge emission a) — in pure methane and b) — in the processed methane-oxygen mixture. The pressure is 4 torr.

$CO_2^+(A^2\Pi \rightarrow X^2\Pi)$ transition, increases by several times on the contrary. The lifetime and quenching constants obtained for the “fast” emission were practically the same as for the emission CO_2^+ on the 290 nm wavelength, and so the integral dependence on time of the emission intensity of $CH(A^2\Delta \rightarrow X^2\Pi)$ can be obtained by the subtraction of the standardized curve of the emission on 290 nm wavelength from the curve of the emission measured on the wavelength 430 nm. The normalization factor was selected so that the time-resolved signal of the emission on the 290 nm was in close agreement with the “fast” signal on the 430 nm wavelength.

The time-resolved measurements allowed to select interval of wavelength capable to measuring the emission of $OH(A^2\Sigma)$. In this interval the overlap by both nitrogen second negative system of bands and carbon dioxide band is negligible. The $CO_2^+(B^2\Sigma \rightarrow X^2\Pi)$ overlap by $OH(A^2\Sigma \rightarrow X^2\Pi)$ bands, corresponded to the transition from $(v' = 1 - 3)$ vibrational states was negligible for 290 nm wavelength.

The listed bands of the molecules were registered in all investigated stoichiometric mixtures, both in mixtures with oxygen and with air, and these bands were used as indicators of hydrocarbons oxidation process in the discharge.

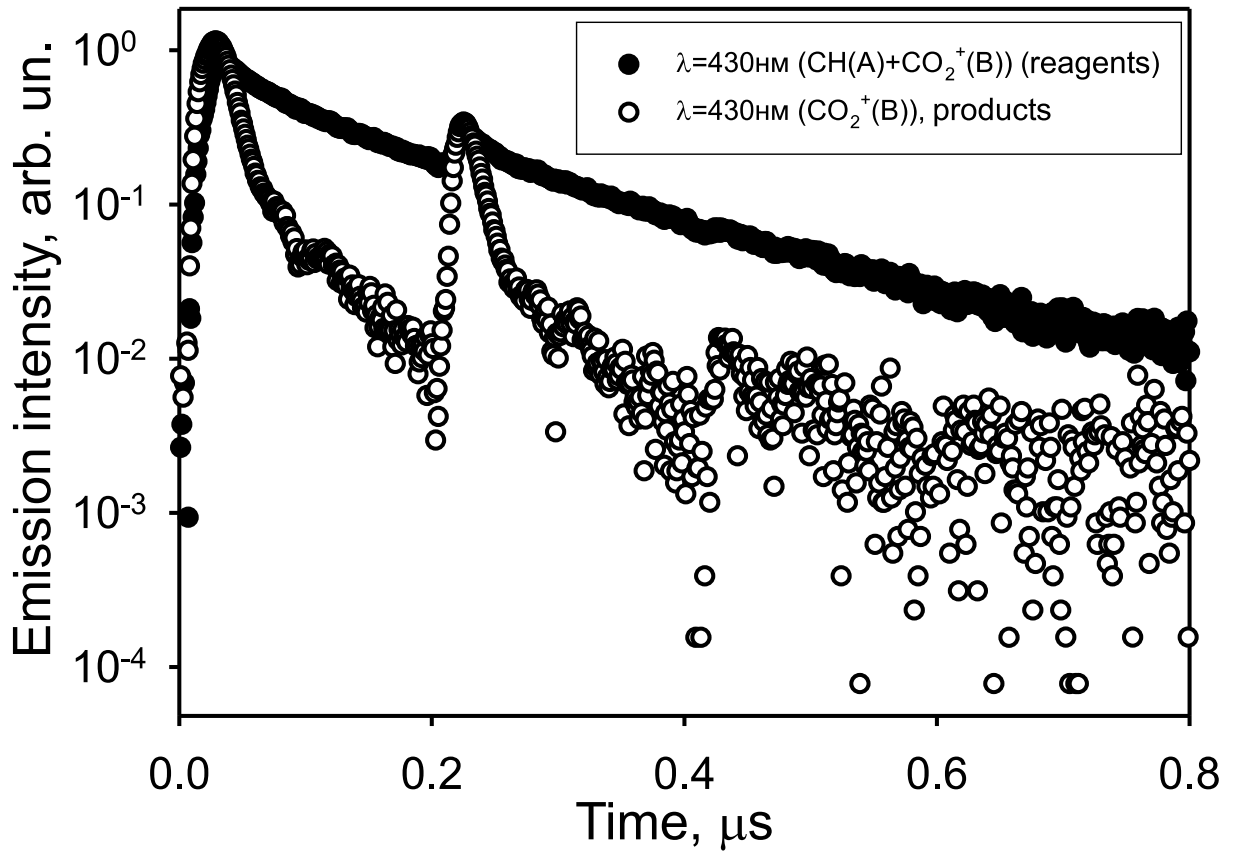


Figure 3.8: Timeresolved intensities of the emission on the wavelength $\lambda = 430$ nm in the initial ($\text{CH}_4 + \text{O}_2$) and the corresponded processed mixtures. The initial pressure is 3.78 torr.

Taking into account quenching constants and life-time of these states, measured in time-resolved experiments (the method is described in detail in⁹²), excitation rates of emitting states integrated over the discharge action time were reconstructed. It is necessary to note that quenching constants of ions $\text{CO}_2^+(B^2\Sigma)$, $\text{CO}_2^+(A^2\Pi)$ and $\text{N}_2^+(B^2\Sigma)$ by reagents and products are not differ practically. On the contrary, quenching constants of $\text{CO}(B^1\Sigma)$, $\text{CH}(A^2\Delta)$ and $\text{OH}(A^2\Sigma)$ states are approximately 30-50% higher in products than these in reagents. This fact can be explained by appearance of water in the products.

In stoichiometric mixtures of alkanes with air excitation rates of $\text{N}_2(C^3\Pi, v' = 1)$, $\text{N}_2(B^3\Pi, v' = 6)$ and $\text{N}_2^+(B^2\Sigma, v' = 0)$ have been obtained on the basis of the time-resolved emission of transitions $\text{N}_2(C^3\Pi, v' = 1 \rightarrow B^3\Pi, v'' = 7)$, $\text{N}_2(B^3\Pi, v' = 6 \rightarrow A^3\Sigma, v'' = 3)$ and $\text{N}_2^+(B^2\Sigma, v' = 0 \rightarrow X^2\Sigma, v'' = 2)$. These rates were reconstructed at the instant of time when discharge switched on and after the oxidation is fulfilled. We integrated these rates over the time of the discharge. It has been shown that the integral rates in the instant of time corresponded to the discharge beginning are not changed to the instant, when oxidation was fulfilled, on 10% for $\text{N}_2(C^3\Pi)$ and $\text{N}_2^+(B^2\Sigma)$ states. At that, in the process of oxidation the rate of $\text{N}_2^+(B^2\Sigma, v' = 0)$ state excitation diminished on 25% approximately. In the work⁹² under analogous condition it has been shown that $\text{N}_2(C^3\Pi, v' = 1)$ and $\text{N}_2^+(B^2\Sigma, v' = 0)$ states are excited by the direct electron impact from the ground state of molecular nitrogen. Inasmuch as in the

discharge the nitrogen concentration is practically constant that the integral rates constants of $N_2(C^3\Pi, v' = 1)$ and $N_2^+(B^2\Sigma, v' = 0)$ states excitation are changed in the process of oxidation on 10% and 25% correspondingly. We noted that the excitation of $N_2(C^3\Pi, v' = 1)$ and $N_2^+(B^2\Sigma, v' = 0)$ takes place during the pulses of the high-voltage, at that time $N_2(B^3\Pi, v' = 6)$ excites in the discharge afterglow in generally and its excitation rate was correlated with the emission of $N_2(C^3\Pi, v' = 1 \rightarrow B^3\Pi, v'' = 7)$ transition. From this fact followed that the $N_2(B^3\Pi, v' = 6)$ state excited in processes of deactivation of $N_2(C^3\Pi)$ state. Thresholds of excitation of $N_2(C^3\Pi, v' = 1)$ and $N_2^+(B^2\Sigma, v' = 0)$ states by electron impact are equal to ~ 12 and 19 eV correspondingly. Inasmuch as thresholds of all investigated states are lower than 19 eV, it can be assumed that constant rates of excitation of these electronic states integrated over the discharge emission time were not changed more than on 25% during the oxidation process. At the same time the threshold is lower the change of rate constant in oxidation process is smaller.

Thus, composition mixture changes in the oxidation process is caused by changes of quenching and excitation rates change an integral intensity of any controlled band no more than 50 %. Hence, on the basis of the integral emission intensity we can obtain qualitative dependencies of concentrations, from which produced excited states. At the same time this fact weakly influences on the characteristic time obtained from the integral emission of transitions $CO(B^1\Sigma \rightarrow A^1\Pi)$, $CO_2^+(B^2\Sigma \rightarrow X^2\Pi)$, $OH(A^2\Sigma \rightarrow X^2\Pi)$ and $CH(A^2\Delta \rightarrow X^2\Pi)$.

The dependencies of the integral intensity of the emission on time in the methane mixtures were approximated by the function $\exp(-t/\tau(p))$ or the function $1 - \exp(-t/\tau(p))$ with the good accuracy (see Figure 3.9). It is necessary to note that in the experiment the full oxidation of methane was registered that clearly seen by the $[CH_4](t)$ curve obtained from laser absorption measurements in the Figure 3.9. Here you can see the integral emission of $CH(A^2\Delta \rightarrow X^2\Pi)$ radical. It is clearly seen, that beginning with the discharge practically the curve of the emission intensity of $CH(A^2\Delta \rightarrow X^2\Pi)$ is not differ from the methane concentration curve. This fact allows to assume that the $CH(A^2\Delta \rightarrow X^2\Pi)$ emission is the good indicator of hydrocarbons in the discharge.

In mixtures of alkanes, which is more heavy than methane, dependencies of emission have more comprehensive form that can be explained by accumulation of intermediates (probably CO and unsaturated hydrocarbons) in the alkane oxidation process and consequent those afteroxidation. The example of integral oxidation of the ethane for 7.54 torr pressure is represented in the Figure 3.10. It is clearly seen that curves are not described by simple functions and essentially differ from each other.

In the Figure 3.11 times of the full oxidation obtained from emissions of different bands are showed for mixtures of alkanes from ethane to hexane with oxygen. Time of full oxidation is defined as time at which the signal from photomultiplier reaches level of $0.95I_\infty$ for wavelengths (290 and 307,8 nm) corresponded to $OH(A^2\Sigma \rightarrow X^2\Pi)$ and $CO(B^1\Sigma \rightarrow A^1\Pi)$ transition and level $1.05I_\infty$ for wavelengths (430 and 518.6 nm) corresponded to $CO_2^+(B^2\Sigma \rightarrow X^2\Pi)$ and $CH(A^2\Delta \rightarrow X^2\Pi)$ transitions.

It is important to note that times of oxidation obtained from emission of different bands in the same experimental condition are rather different, owing to different influence of processes of excitation and quenching on different states during the mixture transformation, but times obtained from emission of the same band in different mixtures are practically the same within the experimental accuracy. Because of the fact that the

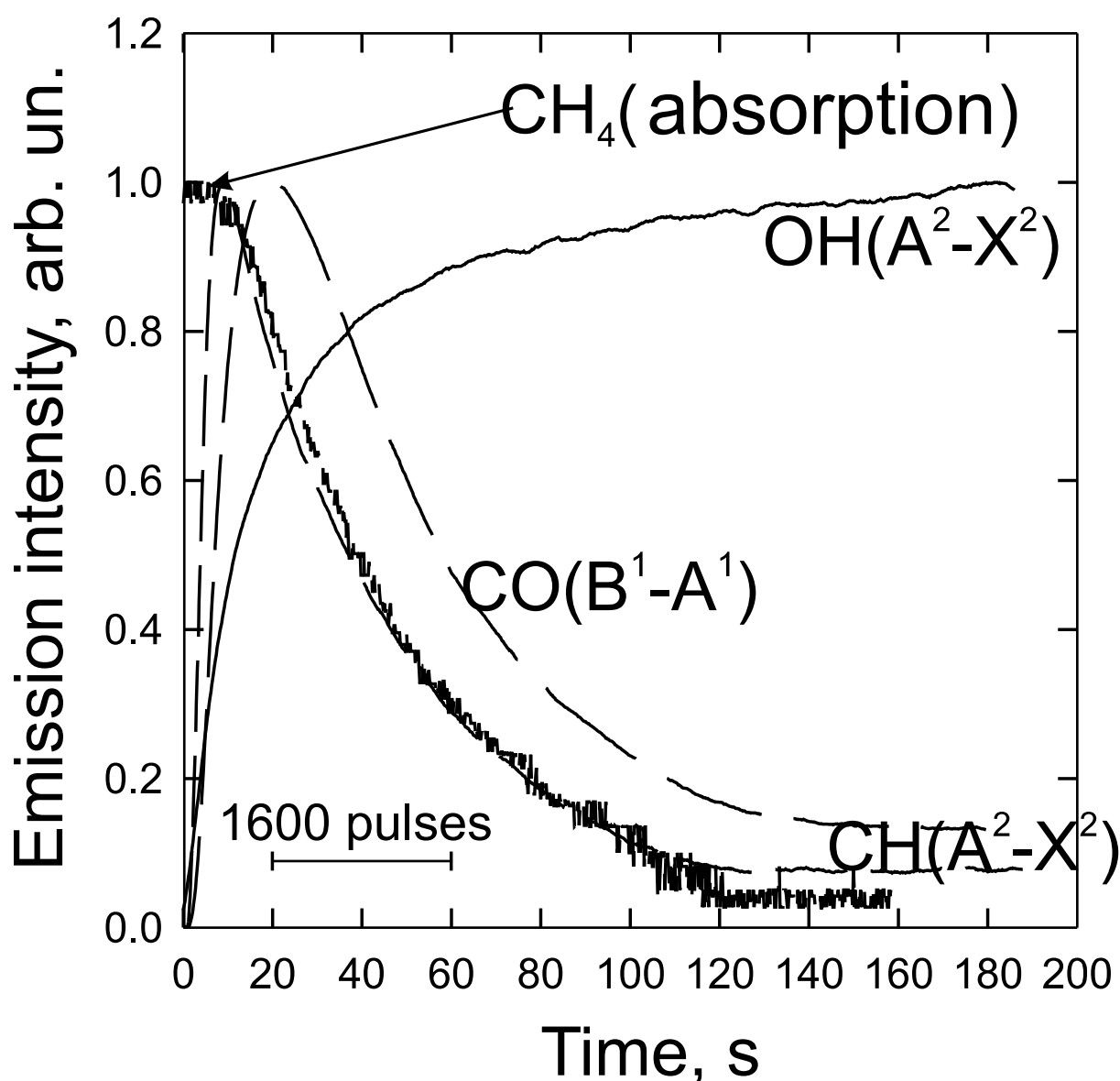


Figure 3.9: Integral over time emission intensities of transitions $\text{CH}(A^2\Delta \rightarrow X^2\Pi)$, $\text{CO}(B^1\Sigma \rightarrow A^1\Pi)$, $\text{OH}(A^2\Sigma \rightarrow X^2\Pi)$ and methane concentration, measured by the absorption of the He-Ne laser emission on the wavelength $\lambda = 3.3922\mu\text{ m}$, in the discharge. The initial pressure of the mixture $\text{CH}_4 + \text{O}_2$ is 7.56 torr.

experimental dispersion is minimal for the time obtained from $\text{CO}(B^1\Sigma \rightarrow A^1\Pi)$ band emission, we designate time obtained from the emission of this band as the time of alkane full oxidation.

In the Figure 3.12 and in the table 3.4 times of full oxidation for different alkanes are represented. It is clearly seen, that time of methane full oxidation is nearly twice as large as times of full oxidation for other alkanes as in mixtures with oxygen so in mixtures with air. For other alkanes times of full oxidation are not differ with the experimental dispersion. In mixture with air times of full oxidation are twice or more as small as times in the same mixtures with oxygen. Taking into account that total quantity of alkanes smaller in stoichiometric mixtures with air than one in mixtures with oxygen, rates of

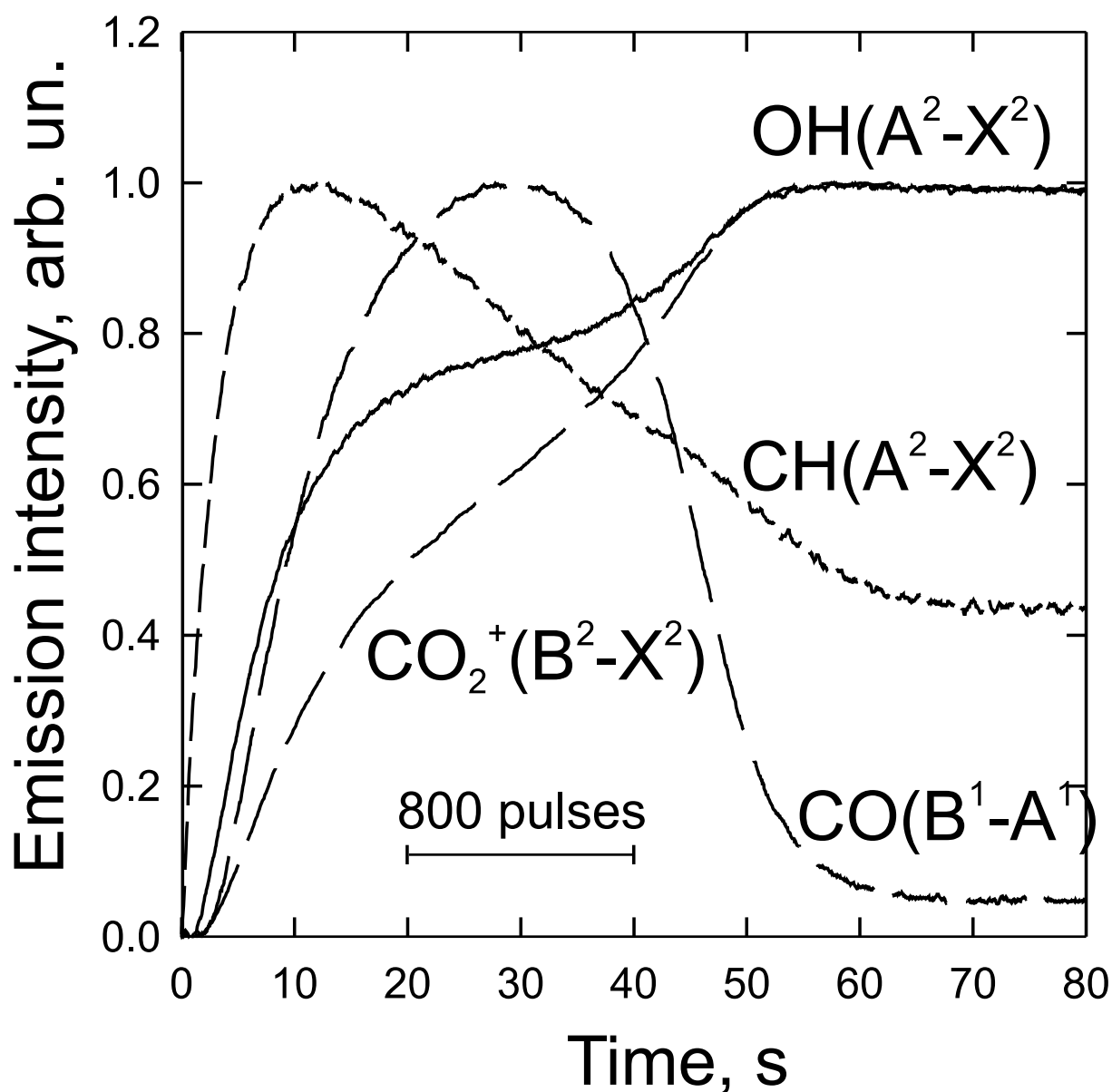


Figure 3.10: Integral over time emission intensities of transitions $\text{CH}(A^2\Delta \rightarrow X^2\Pi)$, $\text{CO}(B^1\Sigma \rightarrow A^1\Pi)$, $\text{CO}_2^+(B^2\Sigma \rightarrow X^2\Pi)$ and $\text{OH}(A^2\Sigma \rightarrow X^2\Pi)$ in the discharge. The initial pressure of the mixture $\text{C}_2\text{H}_6 + \text{O}_2$ is 7.56 torr.

alkanes in mixtures with oxygen oxidation are twice as small as one in mixtures with oxygen.

Thus, stoichiometric mixtures of alkanes with air and oxygen under nanosecond uniform discharge action at ambient temperature have been oxidized entirely. Oxidation of all alkanes beginning with ethane takes place for the same time in stoichiometric mixtures. The methane oxidizes in two times more slowly than other investigated alkanes.

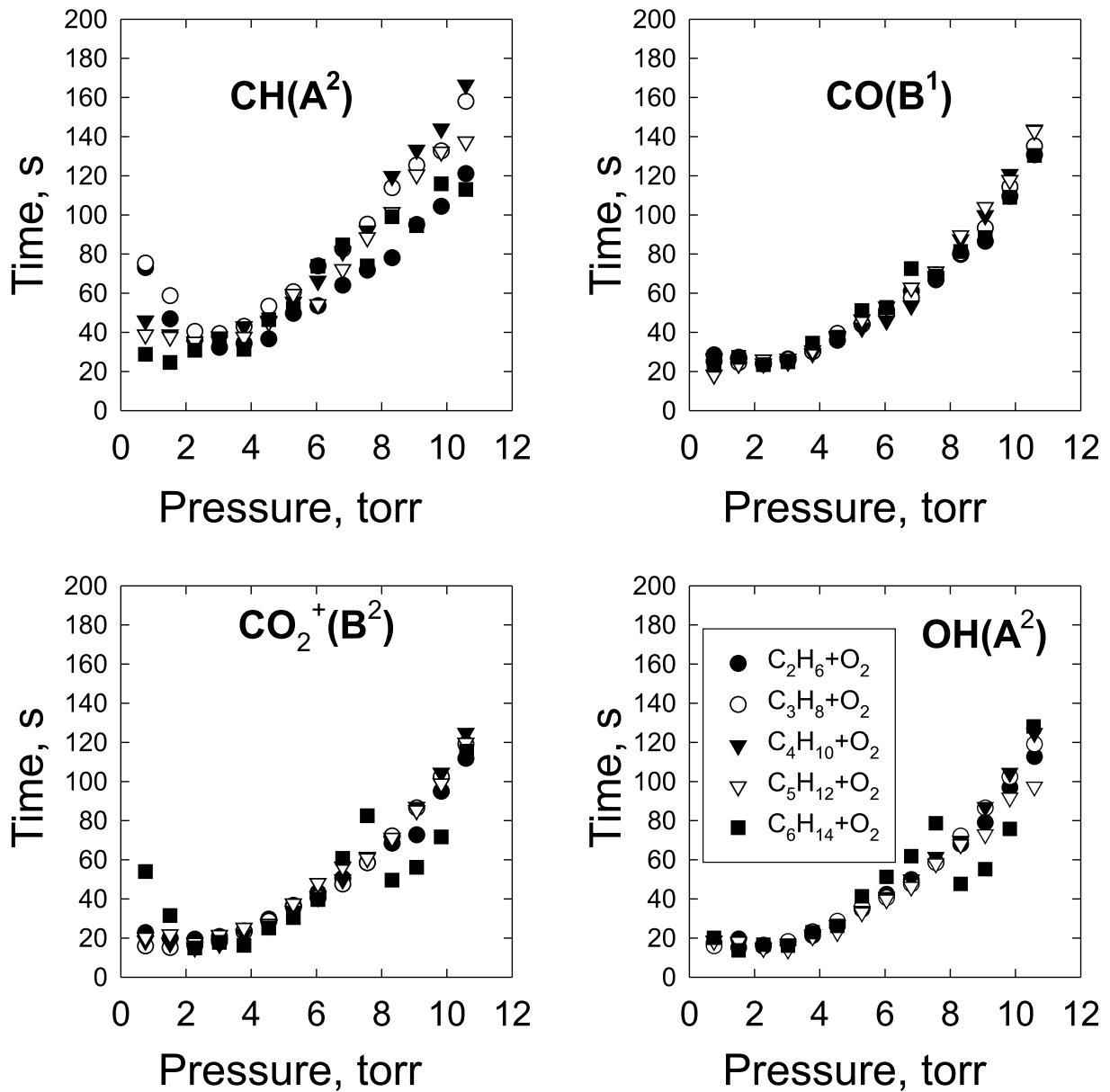


Figure 3.11: Dependencies of alkanes full oxidation times on initial pressures of stoichiometric mixtures, obtained from CH($A^2\Delta \rightarrow X^2\Pi$), CO($B^1\Sigma \rightarrow A^1\Pi$), CO $_2^+$ ($B^2\Sigma \rightarrow X^2\Pi$), OH($A^2\Sigma \rightarrow X^2\Pi$) bands emissions.

3.3.3 C $_4$ H $_{10}$ oxidation in lean mixtures with oxygen under nanosecond discharge

As indicated above, oxidation of alkanes beginning with ethane under nanosecond discharge action proceeds for the same time under the same experimental conditions (initial pressure, energy input). One can explain this fact most logically in approximation of weak influence of excited and charged particles producing by electron impact to molecules of fuel in compare with influence of the impact to molecules of oxygen, intermediates and products, at first time water. It is known that electron impact thresholds of alkanes (in set methane–propane) dissociation reduce on 1 eV approximately with a increasing on a car-

Table 3.4: Times of full oxidation of alkanes τ_{ox} in s, obtained from emission intensity of the emission $\text{CO}(B^1\Sigma \rightarrow A^1\Pi)$ transition, represented in dependence of initial pressure mixture.

Pressure, Torr	0.76	1.51	2.27	3.02	3.78	4.54	5.29
$\text{CH}_4 + \text{O}_2$	17	43	63	69	74	84	97
$\text{C}_2\text{H}_6 + \text{O}_2$	28	27	24	26	30	36	44
$\text{C}_3\text{H}_8 + \text{O}_2$	25	25	24	26	30	39	44
$\text{C}_4\text{H}_{10} + \text{O}_2$	26	25	24	26	29	38	42
$\text{C}_5\text{H}_{12} + \text{O}_2$	18	24	26	25	31	38	47
$\text{C}_6\text{H}_{14} + \text{O}_2$	23	27	24	25	34	38	51
$\text{CH}_4 + \text{air}$	26	18	19	24	22	29	33
$\text{C}_5\text{H}_{12} + \text{air}$	34	16	14	14	16	18	19
$\text{C}_6\text{H}_{14} + \text{air}$	45	13	17	17	17	14	20
Pressure, Torr	6.05	6.80	7.56	8.32	9.07	9.83	10.06
$\text{CH}_4 + \text{O}_2$	125	149	131	172	175	320	294
$\text{C}_2\text{H}_6 + \text{O}_2$	51	61	67	80	87	110	131
$\text{C}_3\text{H}_8 + \text{O}_2$	50	58	69	81	93	114	135
$\text{C}_4\text{H}_{10} + \text{O}_2$	46	54	69	87	100	121	144
$\text{C}_5\text{H}_{12} + \text{O}_2$	53	63	71	90	104	118	143
$\text{C}_6\text{H}_{14} + \text{O}_2$	53	73	69	81	88	109	130
$\text{CH}_4 + \text{air}$	34	44	46	47	56	73	—
$\text{C}_5\text{H}_{12} + \text{air}$	20	20	25	33	34	37	45
$\text{C}_6\text{H}_{14} + \text{air}$	22	22	22	28	27	33	35

bon's atom. Steric factor increases proportionally to a quantity of C atom in molecules of alkanes, at the same time a concentration of an alkan in stoichiometric mixture decreases inversely proportional to the quantity of C atom. Thus, it should be expected, that with change of stoichiometric mixtures from light to heavy alkanes the variation of an alkane concentration be compensated by variation of steric factor. However, with a quantity of carbon's atom in an alkane molecule increasing a dissociation threshold by electron impact is decreased. It should be expected, of course, faster oxidation of more heavy alkanes in compare with more lightly, which did not obtain in experiments. Let us consider possible explanations of this fact.

1. Heavy alkanes are destroyed quickly under electron impact action and transformed to an intermediate, which is the same for all alkanes beginning ethane and slow oxidized in the discharge. At this case the rate of alkane oxidation is ruled by the oxidation rate of this intermediate. Ethane is unique from hydrocarbons, which can pretended on the role of this intermediate, because of C_2H_2 and C_2H_4 , and so alcohols and aldehydes have essentially lower thresholds of electron impact dissociation and its decay in discharge can not limit the rate of oxidation. It is evidently, that in the results of the dissociation of heavy alkanes, ethane cannot be generated only. In this process hydrocarbon radicals are generated too. Moreover, most probably products of dissociation are multiple alkyl radicals. Recombination of these radical can give ethane, but cannot be essential process in the oxygen presence. These

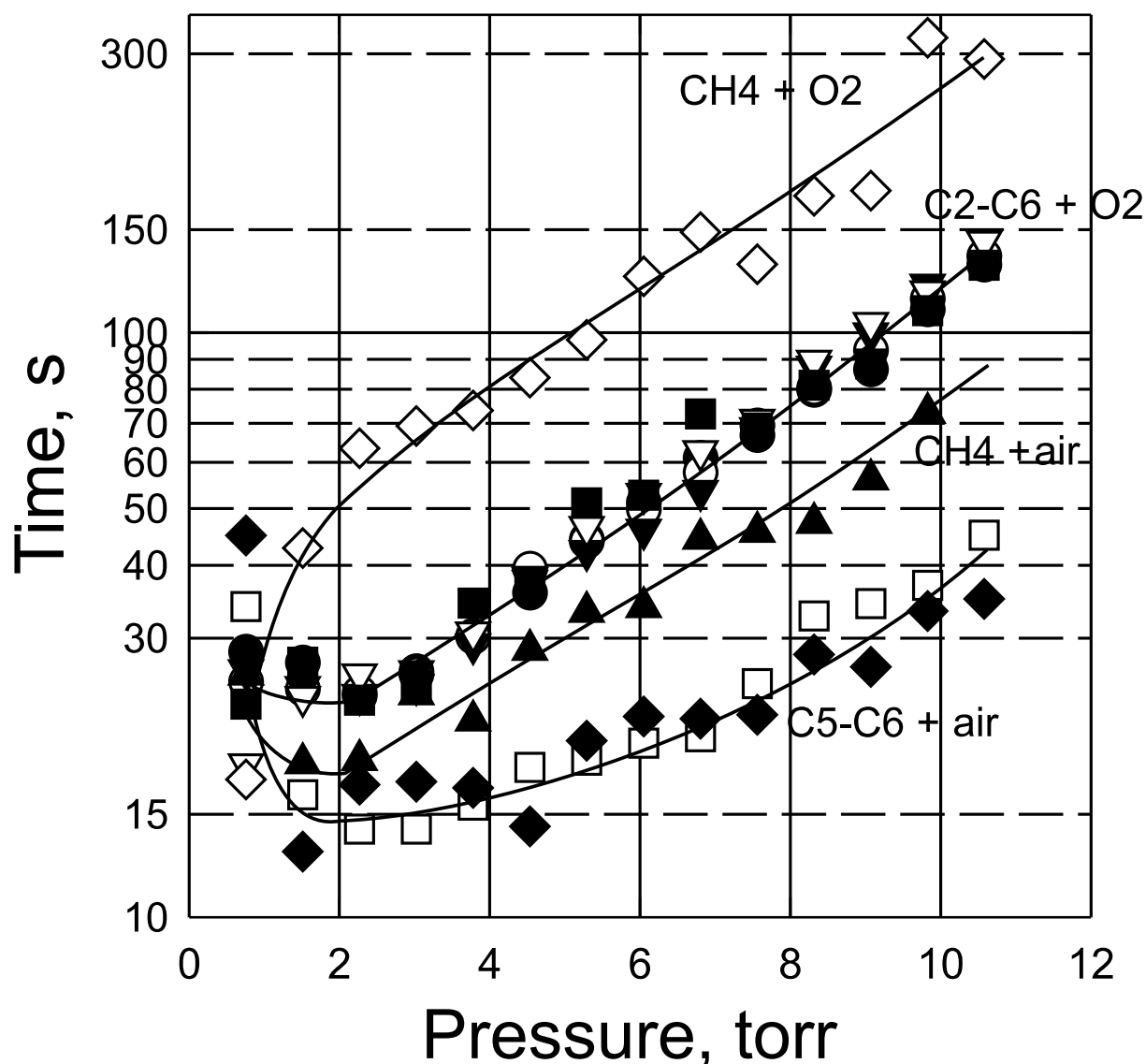


Figure 3.12: Dependencies of alkanes full oxidation times on initial pressures of stoichiometric mixtures, obtained from $\text{CO}(B^1\Sigma \rightarrow A^1\Pi)$ band emission. The data for the stoichiometric mixtures of oxygen with alkanes from ethane to hexane are denoted as “C2–C6+O2”, and data for the stoichiometric mixtures of oxygen with alkanes from ethane to hexane are denoted as “C5–C6+air” (see table 1 and 4).

radicals have not time to recombine and are converted to alkylperoxyradicals very quickly.

- Thus, it does not exist a hydrocarbon, which can pretend to the role of the stable unique intermediate. It is evidently, that this role can be ascribed to CO. However, emission of $\text{CH}(A^2\Delta \rightarrow X^2\Pi)$ radical sharply increases when discharge switch on and later decreased relatively slow during all time of oxidation process, at that intensity of this band emission weakly changes for different alkane beginning with ethane stoichiometric mixtures. Thus, assumption about that heavy alkanes are oxidized to CO rapidly and later CO is oxidized to CO_2 slowly is wrong. Nevertheless, CO

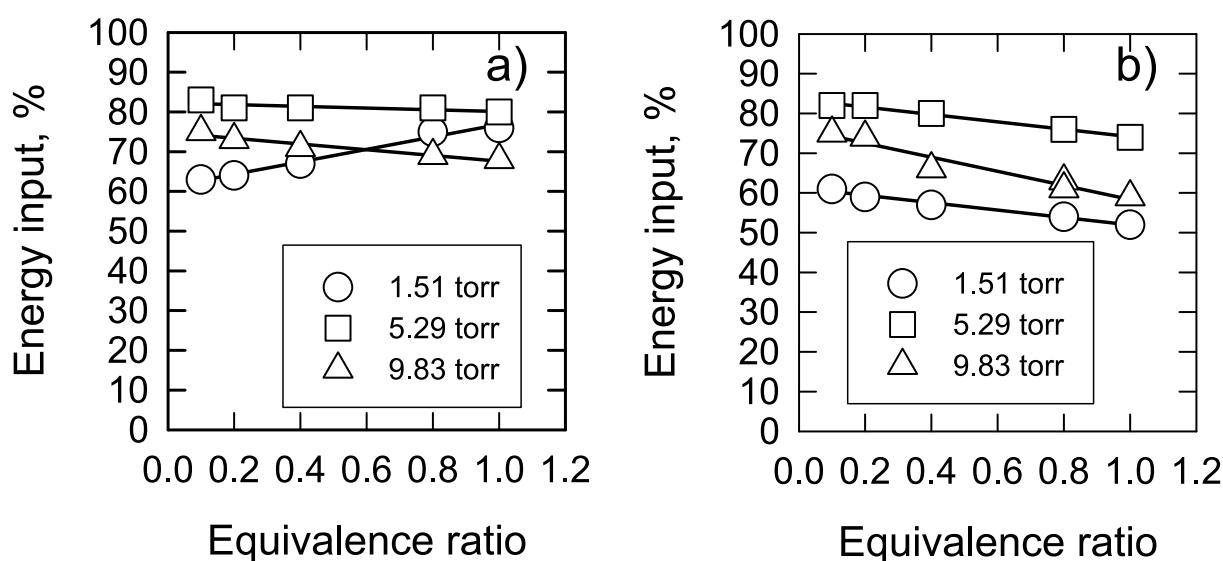


Figure 3.13: The sum of the energy input in the first and the second high-voltage pulses: a) in the initial mixture, b) in the mixture transformed by the discharge.

is the main intermediate in alkanes oxidation process. Let us suppose now, that the dissociation of alkanes occur under very high-reduced electric field conditions, when average electron energy high then electron impact thresholds of any alkanes beginning with ethane. Then rate of dissociation weakly depends on the values of thresholds and depends on steric factor of molecule and alkane concentration. At that it is assumed that molecule of any heavy alkane dissociate to radicals, which are oxidized to water and carbon dioxide.

3. Excitation of molecular oxygen, its dissociation and ionization and so may be excitation and dissociation of products (at first time water) and intermediates entirely govern the alkanes oxidation. It is need to note, that in stoichiometric mixtures the quantity of oxygen is weakly varied from an alkane to another alkane and after processing in all mixtures the same quantity of water is produced. Difference in quantity of the carbon dioxide produced in oxidation process in all mixtures is negligible. So, the quantity of oxygen in stoichiometric mixture with ethane is 20% lower than it in mixture with hexane, on the same percents quantity of carbon dioxide produced in oxidation process is lower. It is necessary to note that water dissociates by electron impact more easily in comparison with carbon dioxide — water has larger absolute values of cross-sections of electron impact processes and essentially lowers thresholds; radicals generated from water are more active.

Thus, produced active particles of oxidant react with non-excited hydrocarbon's molecules, at that excitation, dissociation and ionization of hydrocarbons itself do not influence on oxidation rate. At that charge and energy transfers from atoms, molecules and ions of oxygen, products and intermediates to the hydrocarbon weakly influence on the oxidation process, otherwise we should be return to hypothesis of universal slowly oxidized intermediate. That is, only chemical reactions with non-excited hydrocarbons and excited oxidants can influence on the oxidation rate. Thus, the first choice of explanation is improbable. The second choice needs the electron energy should be higher 7 eV, and it is

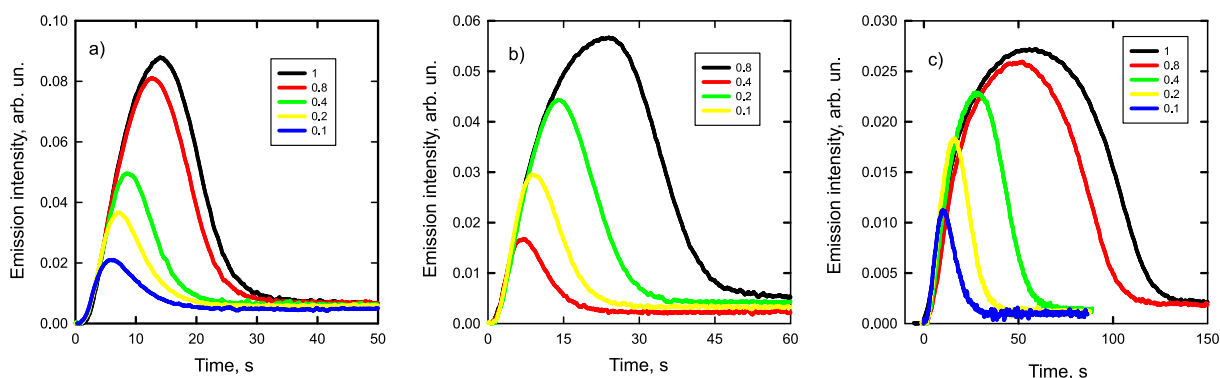


Figure 3.14: Integral over time emission intensities of transition $\text{CO}(B^1\Sigma \rightarrow A^1\Pi)$ in the discharge. The initial pressures of the mixtures are 1.51 torr for a), 5.29 torr for b) and 9.83 Torr for c).

improbable too, however to make a correct choice we have to perform a set of additional experiments. Using the methods described above, we have investigated oxidation of lean mixture of butane with oxygen. In the Figure 3.13 the energy input for stoichiometric and some lean mixtures in dependence on the mixture pressure is represented. It is clearly seen that changes of energy input with equivalence ratio are not higher than 13% of pulse energy and specifically small for the range of maximum energy input in the initial mixture. And so we can assume that the discharge condition, which control excitation processes are not differ essentially for mixtures with different equivalence ratio from 0 to 1. In the Figure 3.14 dynamics of the $\text{CO}(B^1\Sigma \rightarrow A^1\Pi)$ integral emission in the investigated mixtures is represented. It has clearly seen that with decreasing of the equivalence ratio the time of full oxidation decreases. Based on this, we discard the second hypothesis. Really, if the oxidation time is controlled by rates of excitation, dissociation and ionization of butane, then the time of full oxidation should not depend on the equivalence ratio, because with decreasing of the equivalence ratio the initial concentration of butane and the rate of oxidation decrease proportionally. Also it is necessary to note that there are growing parts of emission curves which practically coincides to each over.

Time of full oxidation obtained from $\text{CO}(B^1\Sigma \rightarrow A^1\Pi)$ integral emission and time of of maximum of $\text{CO}(B^1\Sigma \rightarrow A^1\Pi)$ emission are represented in the Figure 3.15. It is clearly seen that the time decreases linearly with decreasing the equivalence ratio that should be expected in the case of weak influence of excitation, dissociation and ionization of alkanes by the discharge. Really, the quantity of oxygen in stoichiometric mixture differs from it in mixture with equivalence ratio 0.1 on 11%, hence variations of concentrations of excited molecules, ions and atoms of oxygen no more than 11%. At the same time the concentration of butane changes in one order of magnitude, therefore dependence of time of full oxidation on equivalence ratio have to be linear with the good accuracy. Thus, under our experimental condition, excitation, ionization and dissociation of an alkane by electron impact did not influence on the rate of the alkane oxidation. The oxidation process is controlled by processes of producing of ions, excited molecules and atoms from oxygen, water, and carbon dioxide and probably from intermediates, which produce on the early stage of hydrocarbons oxidation process.

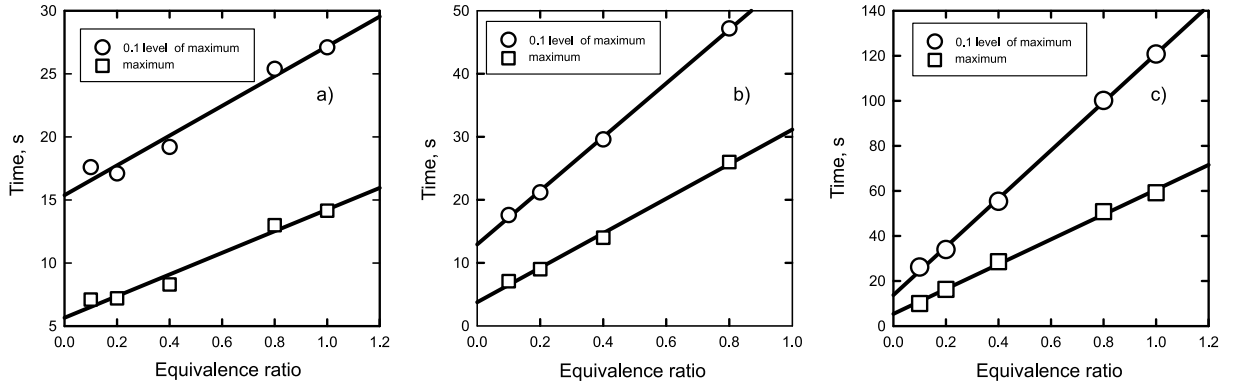
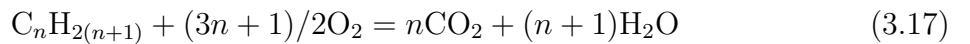


Figure 3.15: Time of full oxidation obtained from $\text{CO}(B^1\Sigma \rightarrow A^1\Pi)$ band emission - a) and time of $\text{CO}(B^1\Sigma \rightarrow A^1\Pi)$ band emission maximum versus initial pressure of butane with oxygen lean mixtures.

3.3.4 $\text{C}_{10}\text{H}_{22}$ oxidation in lean mixture with oxygen under nanosecond discharge action

Real fuels used in internal-combustion engines consist of hydrocarbons $\text{C}_8\text{-C}_{16}$, therefore it should be examine universality of above drawn conclusions on the example of alkane higher than C_6 . For this work we choose n-decane $\text{C}_{10}\text{H}_{22}$. At 25°C saturated vapor pressure of n-decane is equal 0.9 torr, and so the maximal pressure of stoichiometric mixture with oxygen is equal 18 torr. The preparation of the mixture was analogous as for hexane and pentane mixtures. A portion of decane was injected into the 10-liter vacuum-processed volume. The portion of decane was smaller than value of saturated vapor pressure of n-decane at 25°C in 10-liter volume. Later we added oxygen into the volume. The mixture was mixed by ventilator. In spite of the forced mixing, concentration of decane increases very slowly (Figure 3.16), that we explained by very slow evaporation of decane under ambient temperature condition.

As unit was used the emission intensity of $\text{OH}(A^2\Sigma \rightarrow X^2\Pi)$ in the processed stoichiometric mixture of butane with oxygen. We controlled the concentration of decane by following method. The current mixture was oxidized in nanosecond discharge. The spectrum of emission of the mixture compared with spectra obtained in processed mixtures of butane and oxygen with different equivalence ratios. Let us consider the method of equivalence ratio determination in detail. Oxidation of alkanes in stoichiometric mixture with oxygen is described by total reaction:



Let us suppose that N is total a quantity of molecules in discharge volume, then a quantity of alkane molecules is:

$$[\text{C}_n\text{H}_{2(n+1)}] = 2/3N/(n + 1), \quad (3.18)$$

and quantity of oxygen molecules amounts to

$$[\text{O}_2] = N(n + 1/3)/(n + 1). \quad (3.19)$$

Further, quantity of hydrogen atoms is

$$[\text{H}] = [\text{C}_n\text{H}_{2(n+1)}]/2/(n + 1) = 4/3N, \quad (3.20)$$

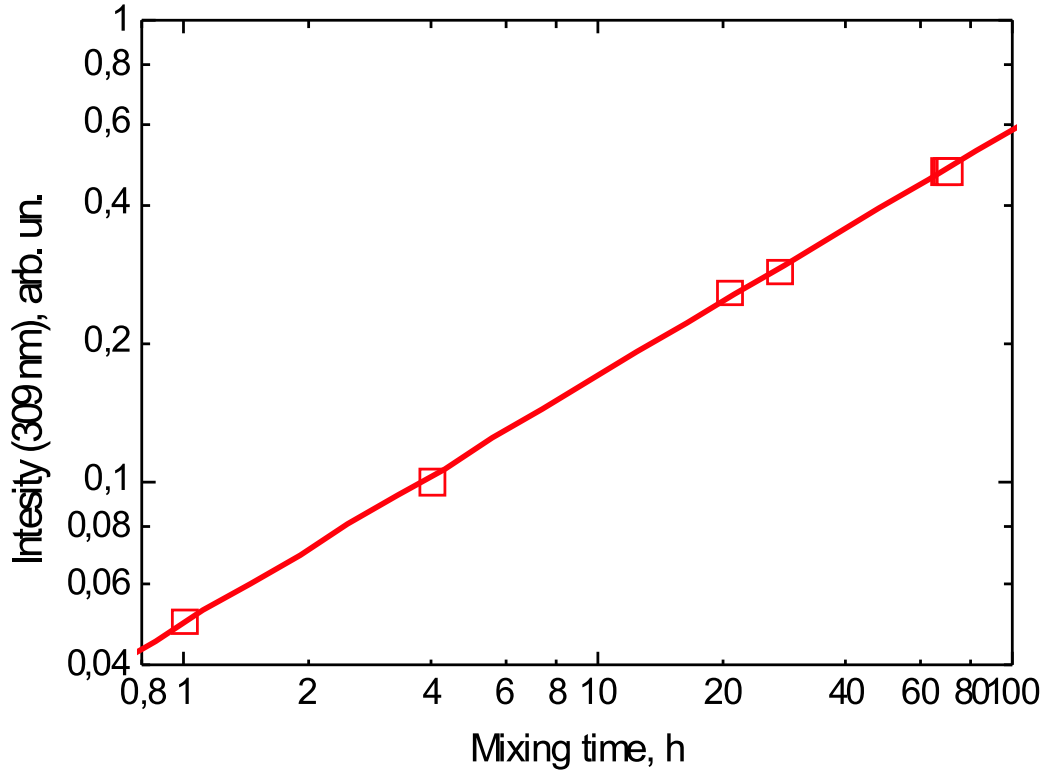


Figure 3.16: Intensity of $\text{OH}(A^2\Sigma \rightarrow X^2\Pi)$ band emission in the processed mixture of decane with oxygen versus time of mixing. The unit emission intensity level coincides to the emission intensity of $\text{OH}(A^2\Sigma \rightarrow X^2\Pi)$ in butane-oxygen stoichiometric mixture. The initial pressure of the mixture $\text{C}_{10}\text{H}_{22} + \text{O}_2$ is 4 torr.

and quantity of carbon atoms is

$$[\text{C}] = [\text{C}_n\text{H}_{2(n+1)}]n = 2/3N/(n+1)n = 2/3N/(1 + 1/n). \quad (3.21)$$

Then quantity of carbon dioxide molecules in the processed mixture is

$$[\text{CO}_2] = 2/3N/(1 + 1/n), \quad (3.22)$$

and quantity of water molecules is

$$[\text{H}_2\text{O}] = [\text{H}]/2 = 2/3N. \quad (3.23)$$

Let us consider the difference in the quantity of carbon dioxide molecules in stoichiometric mixtures of butane and decane with oxygen.

$$[\text{CO}_2]_{\text{C}_4} = 2/3N \times 0.8 \quad (3.24)$$

$$[\text{CO}_2]_{\text{C}_{10}} = 2/3N \times 0.91 \quad (3.25)$$

Here and later indexes C4 and C10 denote that a value amount to butane and decane mixtures with oxygen correspondingly.

$$[\text{CO}_2]_{C10}/[\text{CO}_2]_{C4} = 1.14 \quad (3.26)$$

Then total pressure in processed mixtures are

$$p_{C4} = 2/3N \times 1.8 = 1.2p_{in} \quad (3.27)$$

$$p_{C10} = 2/3N \times 1.91 = 1.27 \times p_{in} \quad (3.28)$$

$$P_{C10}/p_{C4} = 1.06 \quad (3.29)$$

where p_{in} is the pressure of the initial mixture.

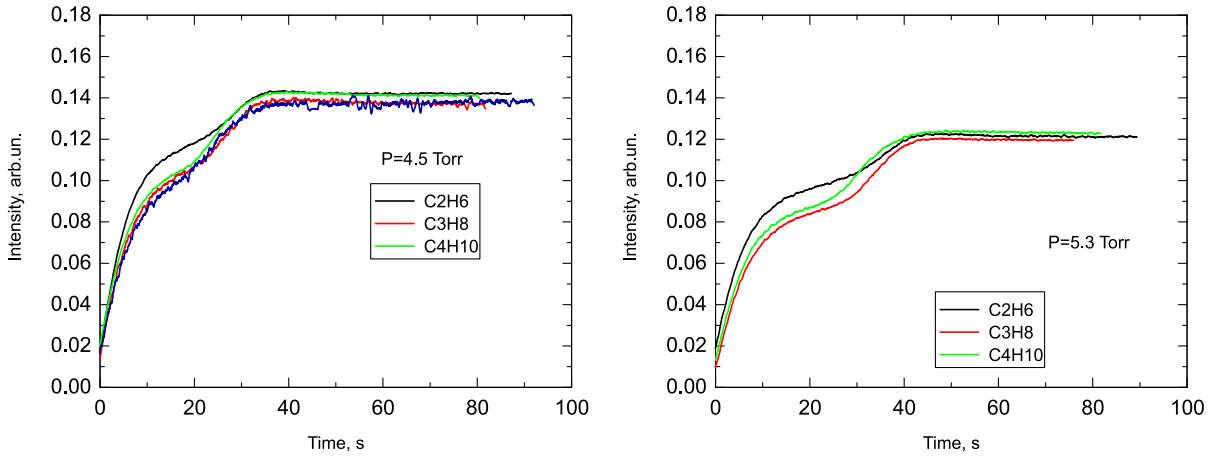


Figure 3.17: Intensities of $\text{OH}(A^2\Sigma \rightarrow X^2\Pi)$ band emission in mixtures of oxygen with different alkanes.

From the above-described experiments it is known, that quenching rates of CO_2^+ weakly depend on kind of quencher. From this reason the rate of quenching changes proportionally to the pressure changes, and the emission intensities of CO_2^+ bands is lower no more than on 6% in the decane processed mixture in comparison with the butane one. Energy input changes weakly from mixture to mixture, and so we can assume that excitation rates of CO_2^+ bands changes proportionally to the CO_2 concentration, that is these rates increases on 14% in the decane processed mixture in comparison with the butane one. Thus, emission intensity of a CO_2^+ band in the processed mixture of decane have exceed one in the butane mixture on 8-14% in dependence on the initial mixture pressure. It is well known, that the water is better quencher than carbon dioxide. It is well known too, that energy loss of electron essentially higher in electron collisions with water than in collisions with carbon dioxide. In the experiments with stoichiometric alkane-oxygen mixtures it was shown that quenching rates of $\text{OH}(A^2\Sigma \rightarrow X^2\Pi)$ essentially (on 50%) increase in the process of the mixture transformation under nanosecond discharge action and slightly depend on kind of an alkane. Change of the emission intensity with switch from butane-oxygen mixtures to the decane-oxygen mixtures has to be minimal, owing to the same quantity of water in processed mixtures, which influence is determinative as on quenching processes and on formation of electron energy distribution function. Emission

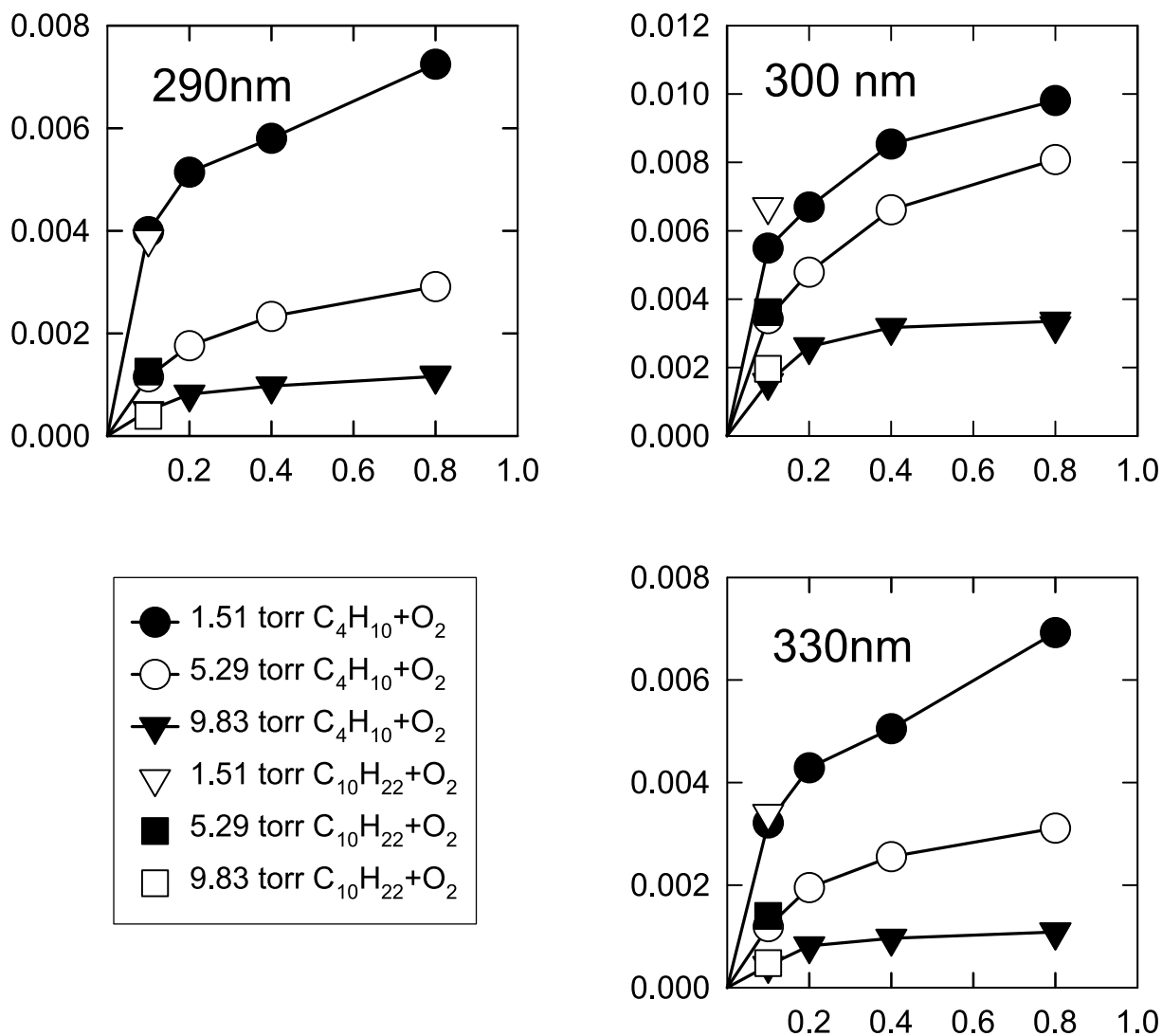


Figure 3.18: Integral over time emission intensities of transitions $CO_2^+(B^2\Sigma \rightarrow X^2\Pi)$ (290 nm), $OH(A^2\Sigma \rightarrow X^2\Pi)$ (306 nm), $CO_2^+(A^2\Pi \rightarrow X^2\Pi)$ (330 nm) in the discharge versus the equivalence ratio of the mixture. All points corresponded to the decane mixture are demonstrated at 0.1 equivalence ratio point.

intensity of OH in process of transformation of stoichiometric mixtures of oxygen with ethane, propane and butane is shown in the Figure 3.17. It is clearly seen that steady-state values of emission intensity (when process of oxidation has been finished) are practically the same for all mixtures.

Dependencies of emission intensity of OH and CO_2^+ bands in processed butane-oxygen mixtures upon equivalence ratio, which used to obtain decane concentration has been shown in the Figure 3.18. It is clearly seen that the emission intensities corresponded to all measured bands depend on equivalence ratio essentially non-linearly. We explained this fact by the influence of concentration of water on electron energy distribution function that is by changes of constants of excitation of these states by electron impact with water concentration changes. In this figure also emission intensities of processed decane oxygen mixture on the same wavelengths are represented. The emission intensities of different bands were interpolated between measured points and extrapolated to the zero point linearly. These dependencies allowed to obtain the equivalence ratio of the decane mixture. Values of the equivalence ratio determined from measurements fulfilled on different wavelengths and in different pressures are represented in the table 3.5. The concentration of n-decane obtained by this method amounted to 0.12 during 3 days of mixing. That is necessary 30 days to obtain the stoichiometric mixture of n-decane with oxygen. Thus, there is no sense to prepare stoichiometric mixture of n-decane with oxygen in room temperature owing to very long preparation time, and so we investigated oxidation process in the mixture with 0.12 ± 0.01 stoichiometric ratio. In the mixture was registered energy contribution and $\text{CO}(B^1\Sigma \rightarrow A^1\Pi)$ emission intensity. The energy contribution in dependence on the pressure is represented in the Figure 3.19 both for decane mixture and for butane mixtures. It is necessary to note that difference between energy inputs in initial and in processed mixtures is negligibly small owing to the oxygen is the main constituent of these mixtures. It is clearly seen that energy contribution in different mixture does not differ within the range of experimental data scattering. Thus, excitation of a gas occurred with the same intensity for all mixtures.

In the Figure 3.20 times of full oxidation obtained by emission intensities of $\text{CO}(B^1\Sigma \rightarrow A^1\Pi)$ bands for butane-oxygen mixtures and for the decane-oxygen mixture are represented. It is clearly seen that time of full oxidation of n-decane is approximately equal to the time of full oxidation of butane in mixture with 0.1 equivalence ratio. Thus, the conclusions, which we have made for mixtures of alkanes C2-C6 early, can be extended on alkanes that are more heavy.

Table 3.5: Equivalence ratio.

Pressure, torr	1.51	5.29	9.83
$\lambda = 290 \text{ nm}$	0.096	0.116	0.08
$\lambda = 306 \text{ nm}$	0.205	0.114	0.135
$\lambda = 330 \text{ nm}$	0.12	0.129	0.113

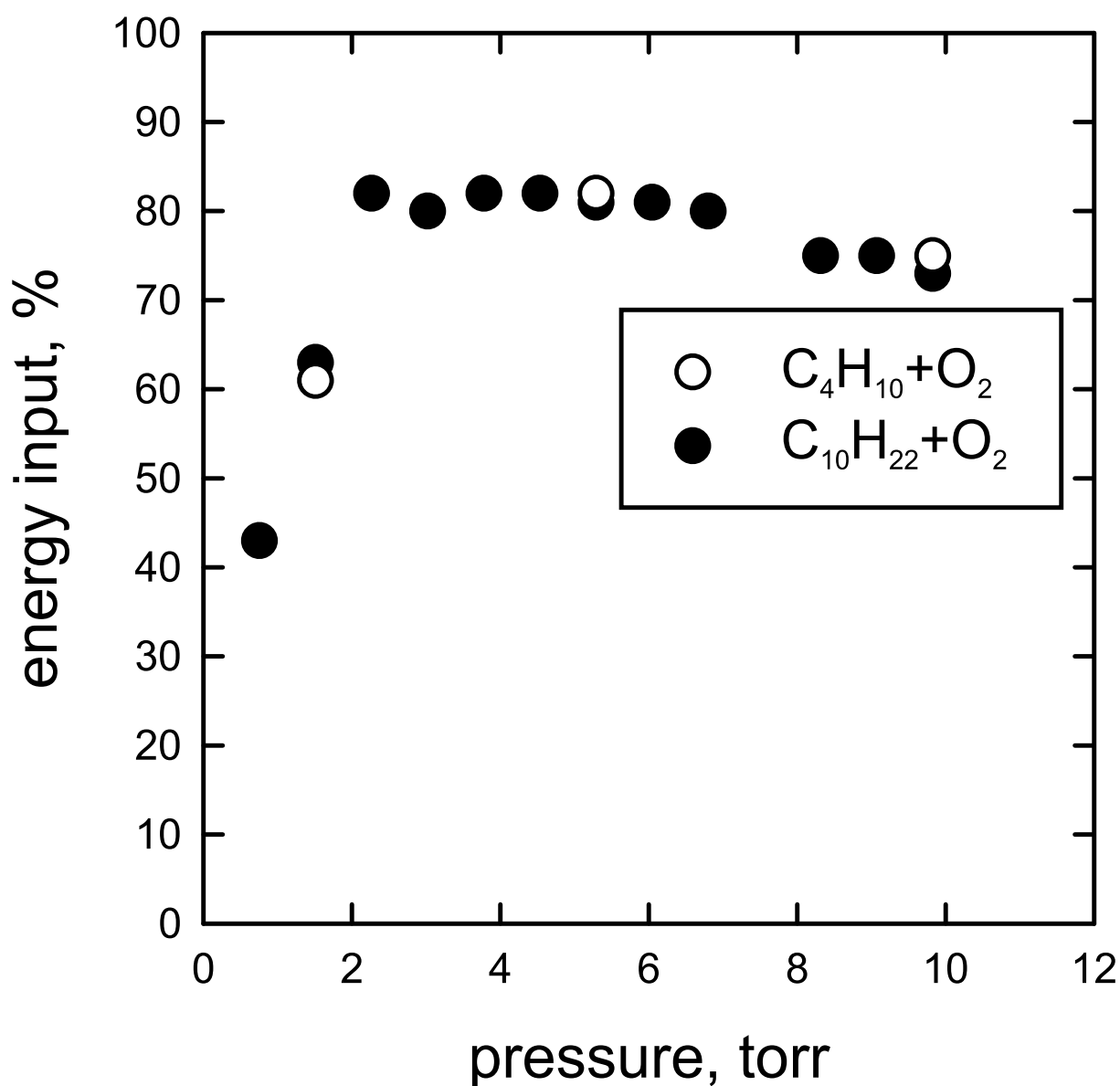


Figure 3.19: Energy input for butane and decane mixtures with oxygen. Equivalence ratio of the butane mixture is 0.1 and one of the decane mixture is 0.12 ± 0.01 .

3.4 Numerical calculation of C_2H_6 , CH_4 , H_2 , C_2H_5OH oxidation by nanosecond discharge

To investigate a kinetics of hydrocarbons oxidation we chose the relatively small molecules. The choice have allowed to construct the compact kinetic scheme, which explains the main experimental results. We assume that the initial density of radicals is produced by electron impact. In further consideration we will call primary radicals, the radicals, which are produced by electron impact from stable species. The most important are radicals produced from reagents and products. The less important are radicals produced from stable intermediates.

It is well known that radicals are produced by excitation of repulsive or pre-dissociated

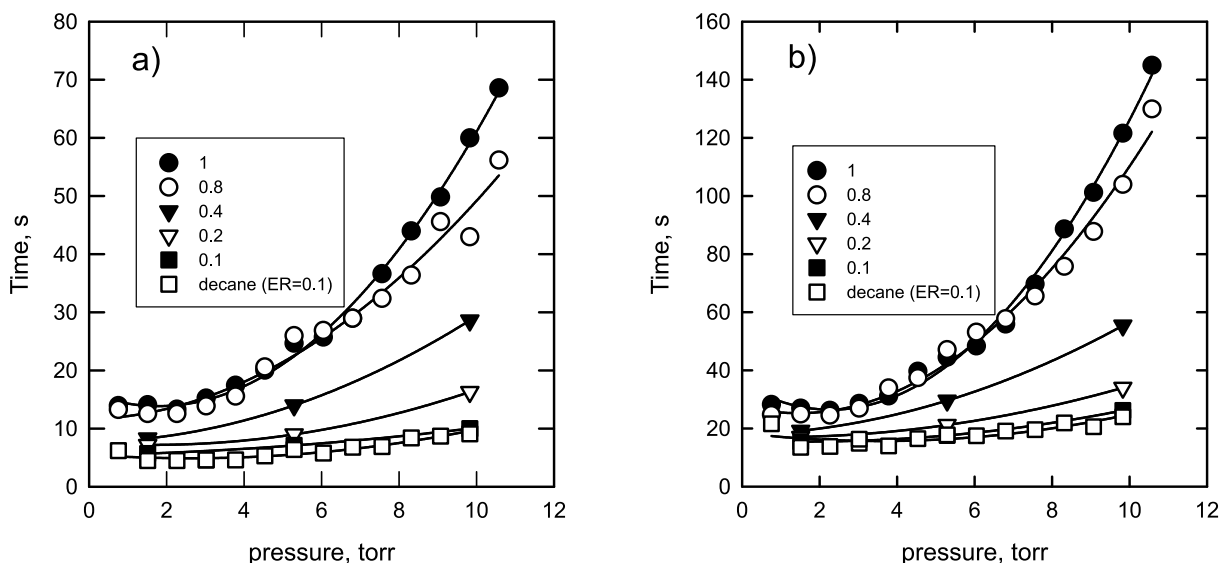


Figure 3.20: Time intervals between instants of discharge beginning and $\text{CO}(B^1\Sigma \rightarrow A^1\Pi)$ emission maximum — a) and instants of full oxidation — b).

electronic terms. Also, it is well known that practically all polyatomic molecules, excluding some positive triatomic ions, don't irradiate in visible and UV range hence they have only metastable, repulsive or highly pre-dissociated electronic terms. It is necessary to note that metastable states of practically all polyatomic molecules are strongly pre-dissociated or repulsive, if the energies of these states are higher, than first dissociative limit of the molecule.¹¹⁹

It is necessary to note that the electron impact produces not only radicals. Positive and negative ions, electronically and vibration excited particles are produced, too. Inasmuch as the discharge operates in pulsed-periodic regime, the short periods (~ 30 ns) of the ions production in the discharge alternate with long periods (~ 30 ms) of the ions transformation and loss in the afterglow. Positive ions are produced in the discharge can be different, but the major amount of ions is produced from stable molecules.

3.4.1 Electron impact processes in the discharge

In the previous report we investigated alkanes oxidation experimentally. We measured electrical power of the discharge and reduced electric fields in the discharge. As we showed previously, main part of energy contributed to gas uniformly in space in the stage of short circuite of the discharge gap. To analyze efficiency of radicals and ions production we have calculated energy branching in the discharge phase using "BOLSIG" numerical code.¹²⁰ The results of these calculations are showed in the Figures 3.21,3.22. In these figures reduced electric measured in the experiments field are showed. The values of the field are corresponded to the maximal in time value of contributed power. It is clearly seen that for our experimental conditions dissociative attachment, metastables of molecular oxygen excitation and vibrational excitation of molecules by electron impact can be neglected. The main excitation processes are dissociation and ionization of the molecules. More than 80% of energy in total range of experimental condition are directed to these process. It is necessary to say, that practically all our experiments have been performed at pressure less

than 11 torr, and for this reason we can neglect of vibrational excitation, which consumes $\sim 20\%$ of energy input at high pressure in the proceeded mixture.

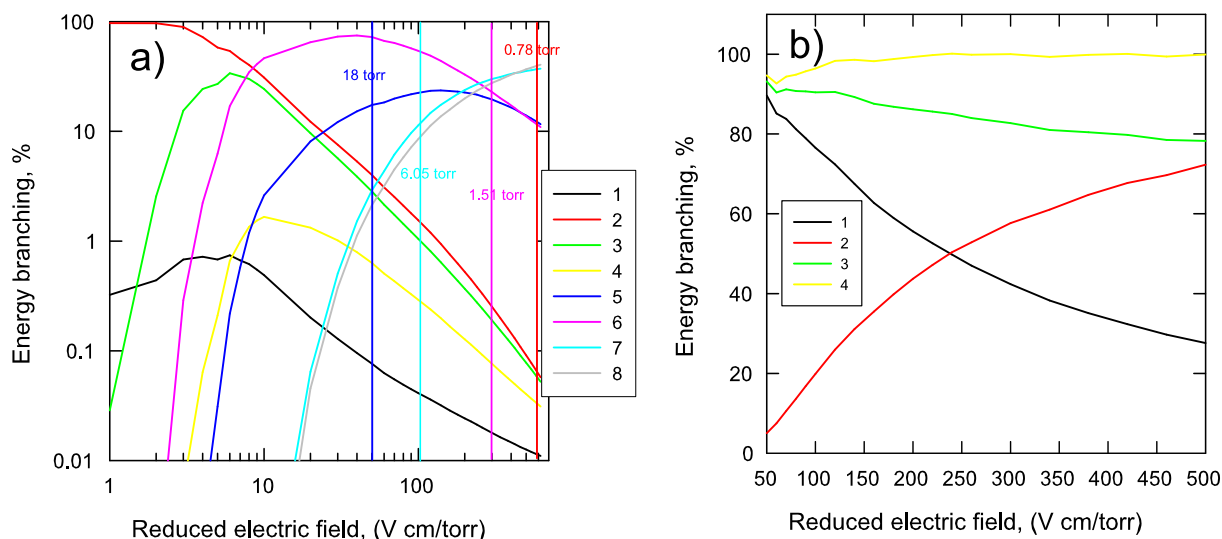


Figure 3.21: Energy branching in the discharge (stoichiometric mixture $C_2H_6-O_2$). In the figure a) detailed energy branching is shown. Curves are designate percentage of energy directed on: 1) elastic collisions, 2) vibrational collisions (both C_2H_5OH and O_2), 3) singlet molecular oxygen (both states), 4) dissociative attachment (C_2H_6 and O_2), 5) C_2H_6 dissociation, 6) O_2 dissociation, 7) C_2H_6 ionization, 8) O_2 ionization. Vertical lines show measured experimentally reduced electric field values, which are corresponded to maximum power in the discharge. In the figure b) summary energy branching is shown. Curves are designate percentage of energy directed on: 1) total (C_2H_6 and O_2) dissociation, 2) total (C_2H_6 and O_2) ionization, 3) total dissociation + 0.7 total ionization, 4) total dissociation + total ionization.

In a partially proceeded mixture, essential part of energy input can be directed to an excitation of different degrees of freedom of stable intermediates, but for preliminary analysis we will neglect of any excitation process of an manifold intermediates. Bellow we represent the kinetics model which is allowed us to mark out main intermediates.

Thus, we have showed that the main active particles produced in the discharge are positive ions and radicals produced by electron impact from the stable molecules.

3.4.2 Positive ions kinetics

Let us consider initial stage of oxidation process. At these stage, when near only reagents exist, two main types of positive ions are produced in the discharge: O_2^+ and the initial hydrocarbon's ion. The proton affinity of molecular oxygen is less then dissociation limit of any mentioned hydrogen-containing molecules and for this reason under room temperature conditions the ion can be lost in reactions of electron transfer only.

In the case of methane or hydrogen this reaction is essentially endothermic and so the reaction has the negligible small constant rate. Thus, in hydrogen or methane-oxygen mixtures O_2^+ may be converted to O_4^+ . The rate of conversion is about of $1.6 \cdot 10^{-13} \text{ cm}^3 \text{ s}^{-1}$. At oxygen pressure 3 torr this value corresponds to $\sim 6 \text{ ms}$. On the other hand, the rate

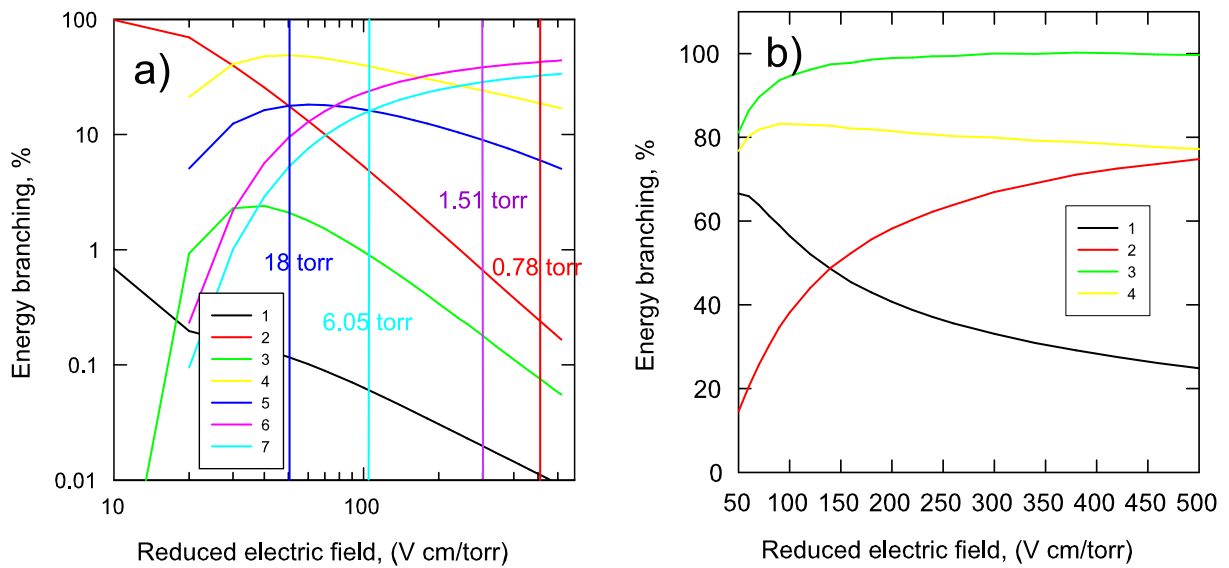


Figure 3.22: Energy branching in the discharge (mixture CO₂:H₂O=2:3). In the figure a) detailed energy branching is shown. Curves are designate percentage of energy directed on: 1) elastic collisions, 2) vibrational collisions (both CO₂ and H₂O), 3) singlet molecular oxygen (both states), 4) dissociative attachment (CO₂ and H₂O), 5) CO₂ dissociation, 6) H₂O dissociation, 7) H₂O ionization, 8) CO₂ ionization. Vertical lines show measured experimentally reduced electric field values, which are corresponded to maximum power in the discharge. In the figure b) summary energy branching is shown. Curves are designate percentage of energy directed on: 1) total (CO₂ and H₂O) dissociation, 2) total (CO₂ and H₂O) ionization, 3) total dissociation + 0.7 total ionization, 4) total dissociation + total ionization.

of dissociative recombination is $2 \cdot 10^{-7} \text{ cm}^3 \text{ s}^{-1}$ and at typical for this discharge electron density ($\sim 10^{12} \text{ cm}^{-3}$)⁹⁴ the characteristic time of the recombination is $5 \mu\text{s}$. It is evidently that O₂⁺ in mixtures with hydrogen or methane recombines without conversion. In the results of the process oxygen O and O(¹D) atoms are produced.

A CH₄⁺ ion have the proton affinity, which is enough to dissociate a methane molecule. For this reason the proton reaction transfer proceeds with significantly higher rate $1.5 \cdot 10^{-9} \text{ cm}^3 \text{ s}^{-1}$. The electron transfer reaction from O₂ to the CH₄⁺ is also exothermic and has the essential value of the reaction rate ($\sim 10^{-9} \text{ cm}^3 \text{ s}^{-1}$). Thus, CH₄⁺ converts to O₂⁺ and CH₅⁺ rapidly (during tens ns). The main dissociative recombination channel of CH₅⁺ is CH₃+2H (70%). In the case of hydrogen-oxygen mixture the main channel of H₂⁺ loss is recharging on the molecular oxygen, because the proton affinity energy of hydrogen is rather higher than the energy dissociation.

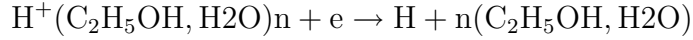
In the case of ethane-oxygen mixture the main positive ions produced in the discharge are O₂⁺ and C₂H₆⁺. In this mixtures main part of O₂⁺ would be lost in the process of electron transfer from C₂H₆, because the ionization potential of ethane essentially lower than one of oxygen. The proton transfer process is exothermic for C₂H₆⁺-C₂H₆ collision and so, very fast. The product of the process, C₂H₇⁺, has essentially higher dissociative recombination constant rate ($\sim 10^{-6} \text{ cm}^3 \text{ s}^{-1}$) than any of the initial ions. The ions loss time corresponded to the process is $1 \mu\text{s}$ approximately. The recombination products can be C₂H₅+2H. Thus one ionization act produces in this mixtures up to 4 radicals (2C₂H₅

Table 3.6: Stable molecules ionization potential, affinity to proton and R-H bond strength.

molecule	H ₂	CO	CO ₂	CH ₄	H ₂ O	O ₂	C ₂ H ₆	C ₂ H ₂	CH ₃ OH	C ₂ H ₄	C ₂ H ₅ OH	H ₂
I, eV	15.43	14.01	13.79	12.98	12.61	12.08	11.50	11.41	10.85	10.51	10.47	10.47
P_a, eV	4.4	6.15	5.5	5.4	7.23	4.1	6.9	6.71	7.89	7.12	8.1	7.12
E_H, eV	4.478	—	—	4.51	5.12	—	4.3	4.9	4.47	4.6	4.4	3.4

and 2H).

In the case of ethyl alcohol-oxygen mixture the main positive ions produced in the discharge are O_2^+ and $\text{C}_2\text{H}_5\text{OH}^+$. As for ethane mixture, main part of O_2^+ losses is the process of electron transfer from $\text{C}_2\text{H}_5\text{OH}$. $\text{C}_2\text{H}_5\text{OH}$ has the maximal value of proton affinity (it is clear from the table 3.6). This denotes that not only $\text{C}_2\text{H}_5\text{OH}^+$ but any molecular ion containing hydrogen in collision with $\text{C}_2\text{H}_5\text{OH}^+$ needs to convert to $\text{H}^+\text{C}_2\text{H}_5\text{OH}$ with rate constant $\sim 10^{-9} \text{ cm}^3\text{s}^{-1}$ (time approximately equals to tens nanosecond). Thus, until concentration of the alcohol is sufficiently high, the main positive ion is $\text{H}^+\text{C}_2\text{H}_5\text{OH}$. This ion can add molecules of the alcohol or water, but can not take part in proton or electron transfer in a collision with stable molecules. Beginning with some number of added molecules, growth of a cluster ion does not change products of it's dissociative recombination the recombination constant increases. The single exothermic channel of these ions recombination is



Thus, in this case, per one ionization act two radicals are produced after $1 \mu\text{s}$ approximately — $\text{C}_2\text{H}_5\text{O}$ is produced in the process of proton transfer from $\text{C}_2\text{H}_5\text{OH}$ to the $\text{C}_2\text{H}_5\text{OH}^+$ (or other radicals which are produced in the proton transfer from another stable hydrogen containing molecule) and H is produced in the dissociative recombination of ions. In the case, when a relatively small ion recombines, the recombination leads to production of more than two radicals per one ionization act. Nevertheless, dissociative recombination is the most important process which provides some initial concentration of radicals in our case. In this process two or more radicals produces that depends on relation of the recombination and clusterization rates. We don't know ions kinetics in $\text{C}_2\text{H}_5\text{OH}$ sufficiently good but it is reasonably to assume that it is like water-ions kinetics (see bellow).

Table 3.7: Main loss processes of $\text{H}^+(\text{H}_2\text{O})_n$ ions.

index	process	reaction
c	Clusterization	$\text{H}^+(\text{H}_2\text{O})_n + \text{H}_2\text{O} \rightarrow \text{H}^+(\text{H}_2\text{O})_{n+1}$
d	Decay	$\text{H}^+(\text{H}_2\text{O})_n \rightarrow \text{H}^+(\text{H}_2\text{O})_{n-1} + \text{H}_2\text{O}$
r	Recombination	$\text{H}^+(\text{H}_2\text{O})_n + \text{e} \rightarrow \text{H} + n\text{H}_2\text{O}$

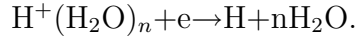
Further, we consider ions production in proceeded mixtures. These mixtures consist of carbon dioxide and water vapor near only. The main ions produced in the discharge are H_2O^+ and CO_2^+ .

Table 3.8: Kinetics of $H^+(H_2O)_n$ ions. Temperature is 300 K. Electron density is $2 \cdot 10^{12} \text{ cm}^{-3}$.

Ion	k^c	T_c	k^d	T_d	k^r	T_r
Pressure is 1 torr.						
$H^+(H_2O)_2$	$2.0 \cdot 10^{-10}$	$1.6 \cdot 10^{-7}$	1.7	0.6	$2.2 \cdot 10^{-6}$	$4.5 \cdot 10^{-7}$
$H^+(H_2O)_3$	$7.3 \cdot 10^{-11}$	$4.6 \cdot 10^{-7}$	440	$2.3 \cdot 10^{-3}$	$3.8 \cdot 10^{-6}$	$2.6 \cdot 10^{-7}$
$H^+(H_2O)_4$	$1.0 \cdot 10^{-11}$	$3.4 \cdot 10^{-6}$	$1.8 \cdot 10^5$	$5.5 \cdot 10^{-6}$	$4.9 \cdot 10^{-6}$	$2.0 \cdot 10^{-7}$
$H^+(H_2O)_5$	$1.2 \cdot 10^{-12}$	$2.8 \cdot 10^{-5}$	$5.8 \cdot 10^4$	$1.7 \cdot 10^{-5}$	$6.0 \cdot 10^{-6}$	$1.7 \cdot 10^{-7}$
$H^+(H_2O)_6$	$1.3 \cdot 10^{-13}$	$2.5 \cdot 10^{-4}$	$7.9 \cdot 10^5$	$1.3 \cdot 10^{-6}$	$> 6.0 \cdot 10^{-6}$	$< 1.7 \cdot 10^{-7}$
Pressure is 10 torr.						
$H^+(H_2O)_2$	$1.2 \cdot 10^{-9}$	$2.8 \cdot 10^{-9}$	10	0.1	$2.2 \cdot 10^{-6}$	$4.5 \cdot 10^{-7}$
$H^+(H_2O)_3$	$5.7 \cdot 10^{-10}$	$4.6 \cdot 10^{-9}$	3450	$2.3 \cdot 10^{-3}$	$3.8 \cdot 10^{-6}$	$2.6 \cdot 10^{-7}$
$H^+(H_2O)_4$	$9.5 \cdot 10^{-11}$	$3.4 \cdot 10^{-8}$	$1.3 \cdot 10^6$	$5.6 \cdot 10^{-7}$	$4.9 \cdot 10^{-6}$	$2.0 \cdot 10^{-7}$
$H^+(H_2O)_5$	$1.2 \cdot 10^{-11}$	$2.8 \cdot 10^{-7}$	$5.7 \cdot 10^5$	$1.7 \cdot 10^{-6}$	$6.0 \cdot 10^{-6}$	$1.7 \cdot 10^{-7}$
$H^+(H_2O)_6$	$1.3 \cdot 10^{-12}$	$2.5 \cdot 10^{-6}$	$7.5 \cdot 10^6$	$1.3 \cdot 10^{-7}$	$> 6.0 \cdot 10^{-6}$	$< 1.7 \cdot 10^{-7}$

From the table 3.6 it is clearly seen that CO_2^+ can convert into CO_2H^+ and H_3O^+ in reactions of electron and proton transfers. This conversion needs to be very fast (total constant rate is $2 \cdot 10^{-9} \text{ cm}^3\text{s}^{-1}$ approximately), because both channels are exothermic. A CO_2 has essentially lower energy of proton affinity and, so, CO_2H^+ for 1-2 collisions with H_2O needs to convert to H_3O^+ . Thus, tens nanosecond after discharge is switched off, the main positive ion is H_3O^+ . At room temperature and few or higher torrs pressure this ion converts to $H^+(H_2O)_2$ with $1 \cdot 10^{-10} \text{ cm}^3\text{s}^{-1}$ constant rate (typical time is 100 ns). With the practically same constant this ions convert to the $H^+(H_2O)_3$. The recombination constant rate of $H^+(H_2O)_2$ and $H^+(H_2O)_3$ are by the order of the magnitude higher than one for H_3O^+ ($3 \cdot 10^{-7} \text{ cm}^3\text{s}^{-1}$, ¹²¹).

In the table 3.8 constants rate and characteristic times of different process of $H^+(H_2O)_n$ ions are shown for pressures corresponded to the low and high limits of the pressure range of the investigations. These values has been calculated for room temperature and mentioned pressures. The indexes of times and constant rates corresponds to the following processes (3.7). It is clearly seen that for our range H_3O^+ ions successfully transforms to different cluster ions before the recombination. Main ions, which life-time is enough to recombine at these conditions, are $H^+(H_2O)_4$ and $H^+(H_2O)_5$, $H^+(H_2O)_6$ for pressures 1 and 10 torr correspondingly. These ions have only one endothermic channel:



Thus, the ionization in proceeded mixtures leads to production only 2 products — H and OH. OH is produced in the proton transfer reactions and H is produced in dissociative recombination process. At typical electron density $2 \cdot 10^{12} \text{ cm}^{-3}$ the recombination time is 200 ns approximately.

These conversion processes are very fast because water has essential value of permanent dipole moment and high value of polarization. These features guarantee high rates of ion-molecular reaction. It is necessary to say that radicals have essential polarization and dipole moment, too. Let us consider ion-radical reaction in our mixtures at our conditions. A concentration of radicals can not be higher than $1.5 \cdot 10^{14} \text{ cm}^{-3}$ for our conditions. To make this estimation we assume that the all energy of the electric pulse

is spent to dissociation of molecules with 8 eV per a molecule average energy. Constants rates of ion–radical reactions are less than $3 \cdot 10^{-9} \text{cm}^3 \text{s}^{-1}$. Thus, a characteristic time of ion–radical reactions are not shorter than $2\mu\text{s}$ after the discharge is switched off. On the other hand, typical constants rate of ion–water reactions have the same value, and for this reason we can neglect of ion–radical reaction entirely — the water concentration produced for the initial ten discharge pulses is enough to this assumption.

Table 3.9: Stable molecules dissociation channels.

Reaction	Importance of channel	Reference	Degree of dissociation
$\text{H}_2 + e \rightarrow 2\text{H} + e$	main channel	our estimation	α
$\text{CO}_2 + e \rightarrow \text{CO} + \text{O}(^1\text{D}) + e$	main channel	our estimation	α
$\text{CH}_4 + e \rightarrow \text{CH}_3 + \text{H} + e$	70% main channel	our estimation	α
$\text{CH}_4 + e \rightarrow \text{CH}_2 + 2\text{H} + e$	30%	our estimation	0
$\text{H}_2\text{O} + e \rightarrow \text{H} + \text{OH} + e$	main channel	122	α
$\text{O}_2 + e \rightarrow \text{O} + \text{O}(^1\text{D}) + e$	main channel	103	α
$\text{O}_2 + e \rightarrow \text{O} + \text{O} + e$	minor channel	103	0
$\text{O}_2 + e \rightarrow \text{O} + \text{O}(^1\text{S}) + e$	minor channel	103	0
$\text{C}_2\text{H}_6 + e \rightarrow 2\text{CH}_3 + e$	50%	our estimation	$\alpha/2$
$\text{C}_2\text{H}_6 + e \rightarrow \text{C}_2\text{H}_5 + \text{H} + e$	50%	our estimation	$\alpha/2$
$\text{C}_2\text{H}_5\text{OH} \rightarrow \text{C}_2\text{H}_5\text{O} + \text{H} + e$	main channel	our estimation	α

Let us consider intermediate mixtures. In this mixtures essential concentrations of CO and H_2O_2 or some hydrocarbons could be accumulated. Ions produced from these molecules need to convert in electron or proton transfer reactions to the ions which have been described early. Following kinetics is combination of these two cases. In addition we need to note that water–ions kinetics is more important than kinetics of initial substances–ions because water has higher proton affinity energy than reagents (excluding $\text{C}_2\text{H}_5\text{OH}$). In the case of $\text{C}_2\text{H}_5\text{OH}$ the most important reaction is water replacement reaction of $\text{C}_2\text{H}_5\text{OH}$ in a $\text{H}^+(\text{C}_2\text{H}_5\text{OH}, \text{H}_2\text{O})$ ion. This reaction is exothermic and has $3 \cdot 10^{-9} \text{cm}^3 \text{s}^{-1}$ rate constant. Quantity of H atoms in $\text{C}_2\text{H}_5\text{OH}$ is 3 times higher than one in water, and concentrations of water and the alcohol in intermediate mixtures are the same if only 1/4 of $\text{C}_2\text{H}_5\text{OH}$ is converted. Thus, water–ions kinetics becomes more important than kinetics of initial substances–ions at relatively early stage of ethyl alcohol oxidation too.

3.4.3 Production of radicals by electron impact

As we mentioned previously, one of two main processes taken place in the discharge is a dissociation by electron impact. The dissociation occurs from excitation of repulsive and pre–dissociated electronic terms or pre–dissociated regions of the terms. In the table 3.9 we have shown dissociation channels of the main stable molecules.

Dissociation of hydrogen occurs through excitation of group of triplet states which connected to repulsive $\text{H}_2(b^3\Sigma)$ state by radiative and collision transition. This repulsive state converges to 4.5 eV limit. Next dissociation limit is 13 eV approximately, and for this reason we can neglect of dissociation from the dissociation channels, which produces electronically excited H atoms. With 90% probability H_2O dissociates in VUV absorption process on H and OH.¹²² We have not a reason to assume that the electron impact changes the dissociation channels essentially. As we have shown previously, dissociation of a heavy alkane (C_2H_6 – C_6H_{14}) by electron impact can not effect essentially on the oxidation process. Thus, to obtain good results the dissociation channels of alkanes can be estimated roughly only or can be neglected.

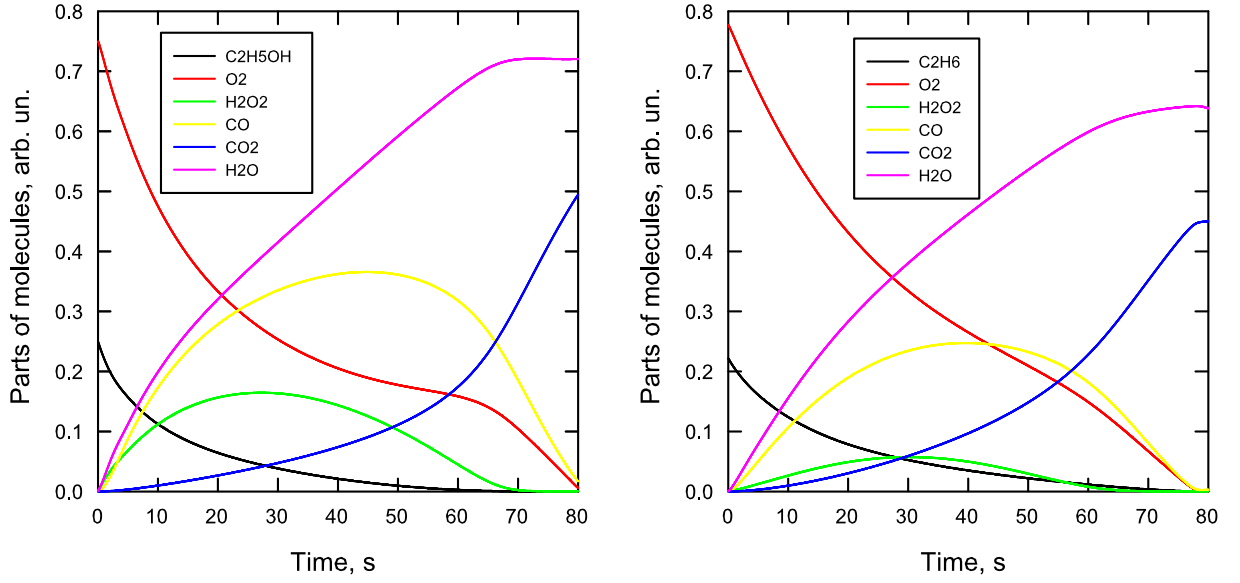


Figure 3.23: The calculated parts of the molecules during oxidation process of C_2H_5OH and C_2H_6 in stoichiometric mixtures with oxygen. The initial pressure of the mixture is 6.8 torr. Dissociation degrees are corresponded to the 70% of the measured experimentally energy input in the discharge.

3.4.4 Numerical model

Thus, we conclude that the discharge produces set of radicals, which initialize the oxidation process. To analyze the hydrocarbons oxidation we have constructed the simple kinetic scheme. To reduce kinetics we assume that the discharge produce radicals represented in the table 3.9 and marked as "main channel". For the C_2H_6 we used both channels.

We constructed kinetics scheme in following way. These radicals react with main substances and produce another radicals and stable molecules. We add to the scheme these secondary radicals and stable molecules. The secondary radicals react with main substances and produced another radicals and stable molecules. We add new molecules to the scheme. We repeated the procedure until new molecules are appeared. We entirely discard reactions and species produced in the reactions, which constant rates were smaller than $1 \cdot 10^{-19} \text{ cm}^3 \text{ s}^{-1}$ at room temperature. To construct the scheme we used the constant rates from online NIST database and from.¹²²

To find the initial concentration of the primary radicals we used experimentally measured energy input E_{exp} . Inasmuch as, we have measured energy input in 2 points (at the beginning and at the finish of the process) of oxidation process, the E_{exp} value were calculated as average of these values. We assumed that the average energy is spent to single dissociation act at $E_{thr} = 8 \text{ eV}$. Also in main calculations we assume, that 70 % of experimentally measured energy input is directed to the dissociation. In this assumptions we defined average degree of dissociation:

$$\alpha = 0.7 \frac{E_{exp}}{E_{thr}NV},$$

where N is the total concentration of stable molecules, and V is the discharge volume.

The radicals produced with 40 Hz frequency from the stable molecules in accordance with the channels form the table 3.9. Between the pulses the "excited" mixture proceeds without an external disturbance in accordance with the scheme (see table 3.15).

It is necessary to note, that ionization leads to dissociation of molecules with typical average energy of about 12 eV. For this reason we assumed that only 70 % percents of the energy is directed to the dissociation (see Figures 3.21 and 3.22). So, the ionization can lead to the two dissociation acts per one ionization, but as we shown above, this situation is realized at only early stage of the oxidation. Later water complex ions recombine with only 2 radical production.

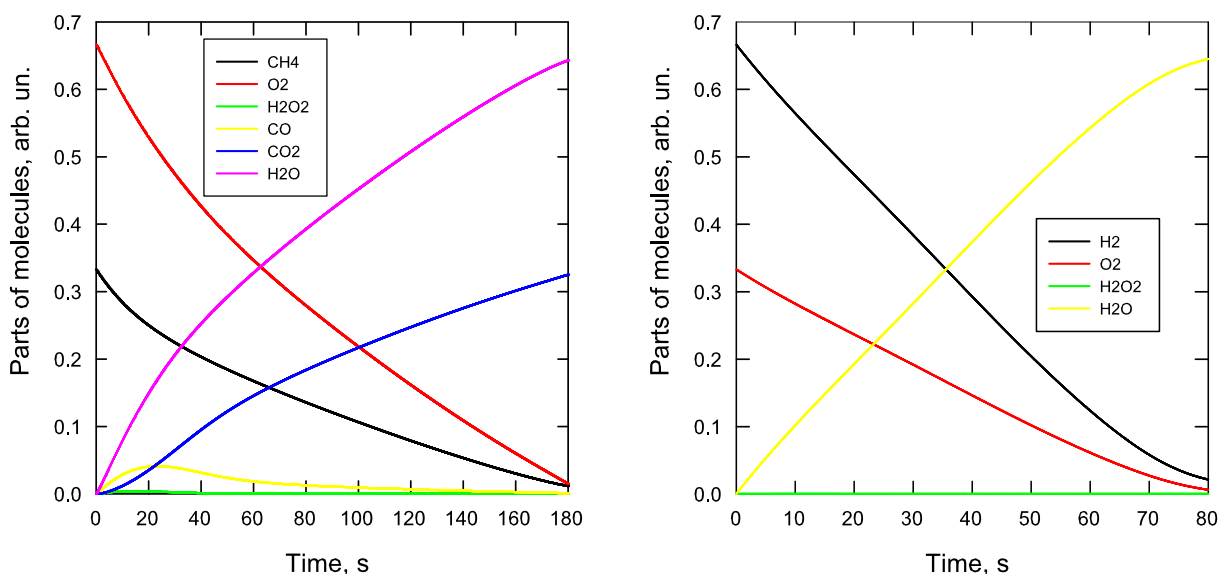


Figure 3.24: The calculated parts of the molecules during oxidation process of CH₄ in stoichiometric mixture with oxygen. The initial pressure of the mixture is 6.8 torr. Dissociation degrees are corresponded to the 70% of the measured experimentally energy input in the discharge.

So we discard reactions N 45, 172, 182, 185, 190 and 207 (see table 3.15), in which molecules with more than 2 C atoms create. It is a reasonable assumption, because large concentration of molecular oxygen are presented in the mixtures. Reactions in this table are expressed in $\text{cm}^{-3}\text{s}^{-1}$ (for bimolecular reactions) and $\text{cm}^{-6}\text{s}^{-1}$ (for trimolecular reactions) units. All constant rates are represented for 300 K temperature.

3.4.5 The results of calculations

The typical kinetic curves calculated by our scheme are represented in the Figures 3.23 (for C₂H₆ and C₂H₅OH) and 3.24 (for H₂ and CH₄). The main difference in these figures is a twice longer oxidation time of CH₄ and another substances, and essential concentrations of CO and H₂O₂ accumulated in the process of C₂H₆ and C₂H₅OH oxidation. So it is necessary to say that C₂H₆ and C₂H₅OH oxidize for the same time practically. As we showed previously in the experiment, the alkanes that are heavier than methane, oxidize for the same time, and accumulation of stable intermediates plays essential role in the oxidation processes. Thus, the calculation reproduces these characteristic features.

The difference of methane or hydrogen kinetics from ethane or methyl alcohol can be explained by different role of OH radicals in these oxidation processes. The OH radical actively reacts with C_2H_6 and C_2H_5OH , but can not react with H_2 and CH_4 under room temperature (see table 3.15, reactions N 3, 17, 24, 59). Constants rate of reactions of OH with C_2H_6 or C_2H_5OH is higher 2-3 order of magnitude higher than ones for H_2 or CH_4 . For this reason in the mixtures H_2 or CH_4 OH is lost in the reaction with H_2O_2 , CO and radicals only. In the case of C_2H_6 or C_2H_5OH mixtures the one of important channel of OH losses is reaction with the initial substance.

To estimate adequacy of concerning energy branching in the discharge we have calculated time of full oxidation for C_2H_6 , C_2H_5OH , H_2 and CH_4 with stoichiometric mixtures with O_2 . In the Figures 3.25 experimental and calculated times of full oxidation are represented. The experimental times were calculated as the time, when $CO(B^1\Sigma \rightarrow A^1\Pi)$ emission intensity fallen to the 10 % of it's maximum. The calculated times of all hydrocarbons were determined as the time, when CO concentration fallen to the 10 % of it's maximum. In the case of H_2 oxidation time was calculated as time then H_2 concentration fallen to the 10 % of it's maximum.

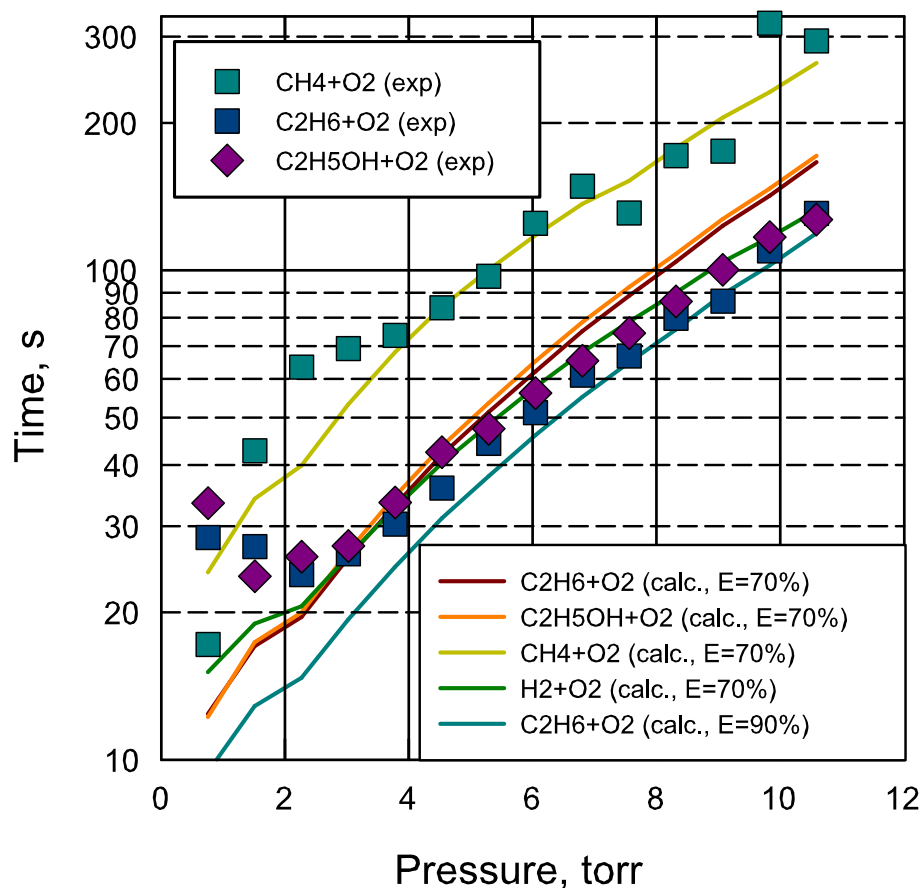


Figure 3.25: The calculated and measured oxidation times of C_2H_6 , CH_4 , H_2 , C_2H_5OH molecules during oxidation process in stoichiometric mixtures with oxygen. Dissociation degrees are corresponded to the 70% (with single exception of turquoise curve which corresponded to the case when 90% of energy input is pointed to the dissociation) of the measured experimentally energy input in the discharge.

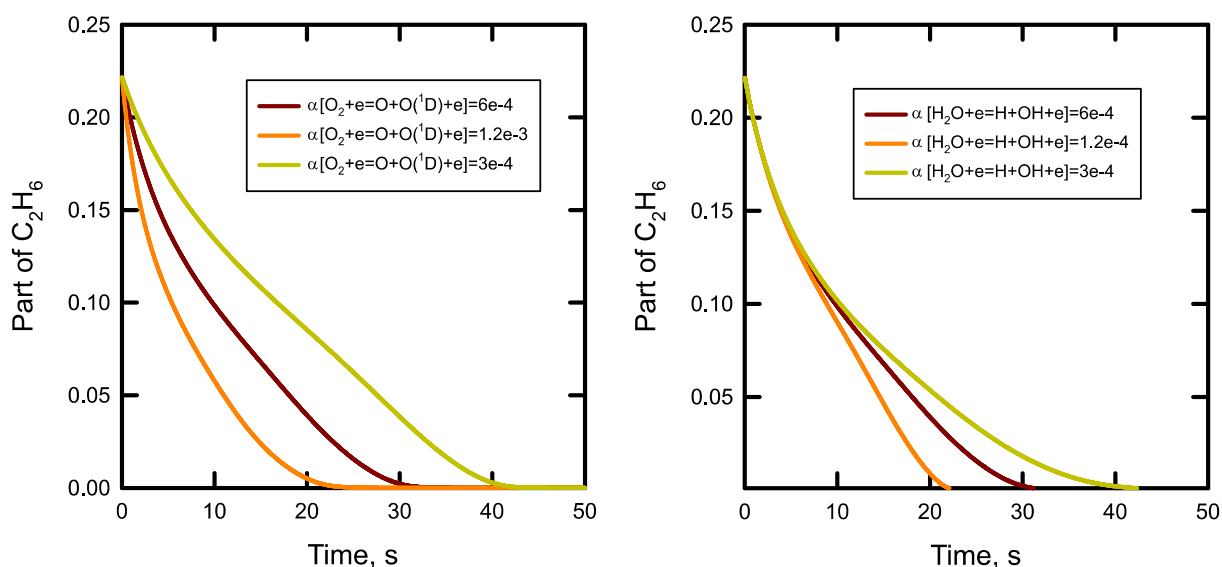


Figure 3.26: The calculated parts of C_2H_6 molecules during oxidation process in the stoichiometric mixture with oxygen. The initial pressure of the mixture is 3.78 torr. Dissociation degrees correspond to the 70% of the measured experimentally energy input in the discharge.

It is clearly seen that the oxidation times of C_2H_6 and C_2H_5OH are practically the same, but the C_2H_5OH oxidation time is slightly higher than the C_2H_6 time, as in experiments. So the CH_4 oxidation time is two times longer than the one for another substances, as in experiments.

At high limit of investigated pressure range the calculated oxidation time is higher than the experimental one and at the low limit of one the time is lower. For this reason we calculated the oxidation time of C_2H_6 in the assumption that 90 % of energy is directed to dissociation.

The calculated time is systematically lower than the experimental one. This feature can be explained by the fact that at high pressure main part of energy input directed to the dissociation directly. At low pressure main part of energy input directed to the ionization. After that in dissociative recombination another radicals produced than in the case of dissociation. The different radicals have different activities and for this reason ionization can be less effective for oxidation process than dissociation. Another possible explanation is the essential by different branching among dissociation channels and it's essential changes with pressure — we fulfilled the calculation with the same efficiency of the dissociation channels which didn't depend on the pressure. So we do not take into account the electron collisions the intermediates. However, this calculation reproduces main features (Figure 3.25) of experimental data and allow to determine the main intermediates (CO and H_2O_2).

Further we investigated the importance of different dissociation channels. In the Figures 3.27 and 3.26 the calculated kinetic curves for varied dissociation degrees via chosen channel are plotted. It's clearly seen, that dissociation of CO_2 and a hydrocarbons provides a weak influence. The most important dissociation channels are dissociation of water and oxygen (Figure 3.26).

The next figures demonstrate the same features, but leads to conclusion that the right

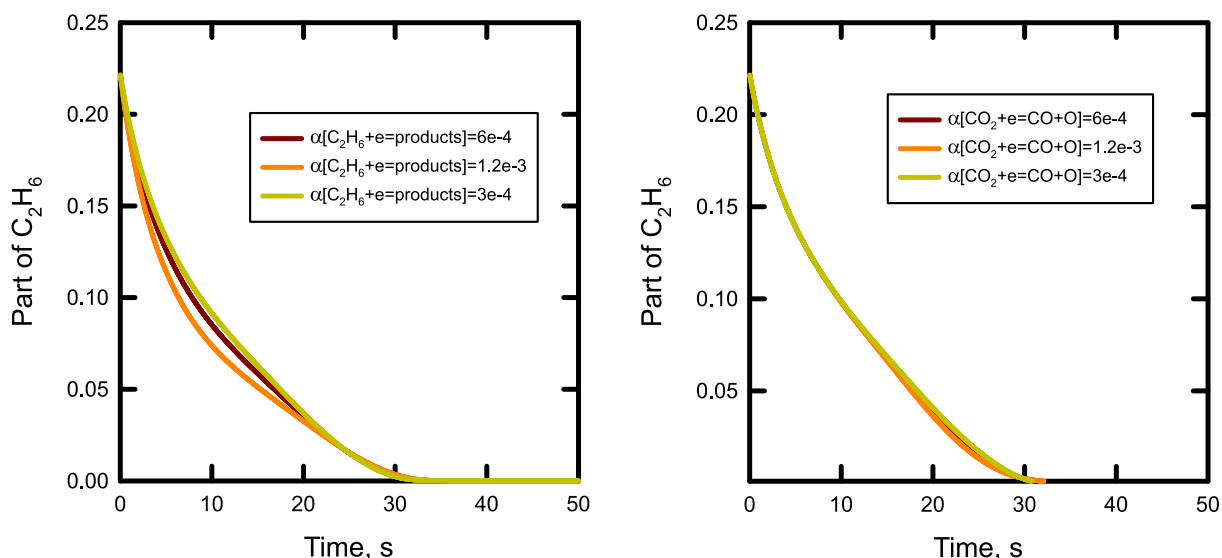


Figure 3.27: The calculated parts of C_2H_6 molecules during oxidation process in the stoichiometric mixture with oxygen. The initial pressure of the mixture is 3.78 torr. Dissociation degrees correspond to the 70% of the measured experimentally energy input in the discharge. Dissociation degrees of C_2H_6 and O_2 are varied.

choice of the dissociation channel of O_2 is most important at early stage of the oxidation process only. Later, the choice of channels does not play essential role. The switching-off O_2 or H_2O dissociation channels leads to disastrous deceleration of the oxidation.

Thus, OH radical is the most important radical in the oxidation processes of the investigated heavy hydrocarbons. O and $O(^1D)$ play the important role also.

It is necessary to note that the constant rate of the reaction C_2H_6 with OH (N 24) approximately 5 times less than the one of the reaction C_2H_5OH with OH (N 59). This essential difference does not lead to the same scale difference in oxidation times. This feature can be explained by that the intermediates produced from a main hydrocarbon in the oxidation process are effective inhibitors. So the systems has effective negative feedback. On the other hand in the system of H_2 or CH_4 with oxygen the feedback does not create.

Thus, we have construct numerical model, which describes main experimental features of oxidation process of hydrocarbons by nanosecond discharge. We have shown the importance of dissociation of molecular oxygen and water by electron impact.

3.5 Acetone's, acetylene and ethyl alcohol's oxidation under discharge action. Experimental investigation and analysis

The experimental study of saturated hydrocarbons gives the data for the kinetic model development. At the same time, it's necessary to have additional experimental data with another types of hydrocarbons for detailed analysis of the kinetics. Thus, the experiments with acetone, acetylene and ethyl alcohol oxidation were performed using the setup de-

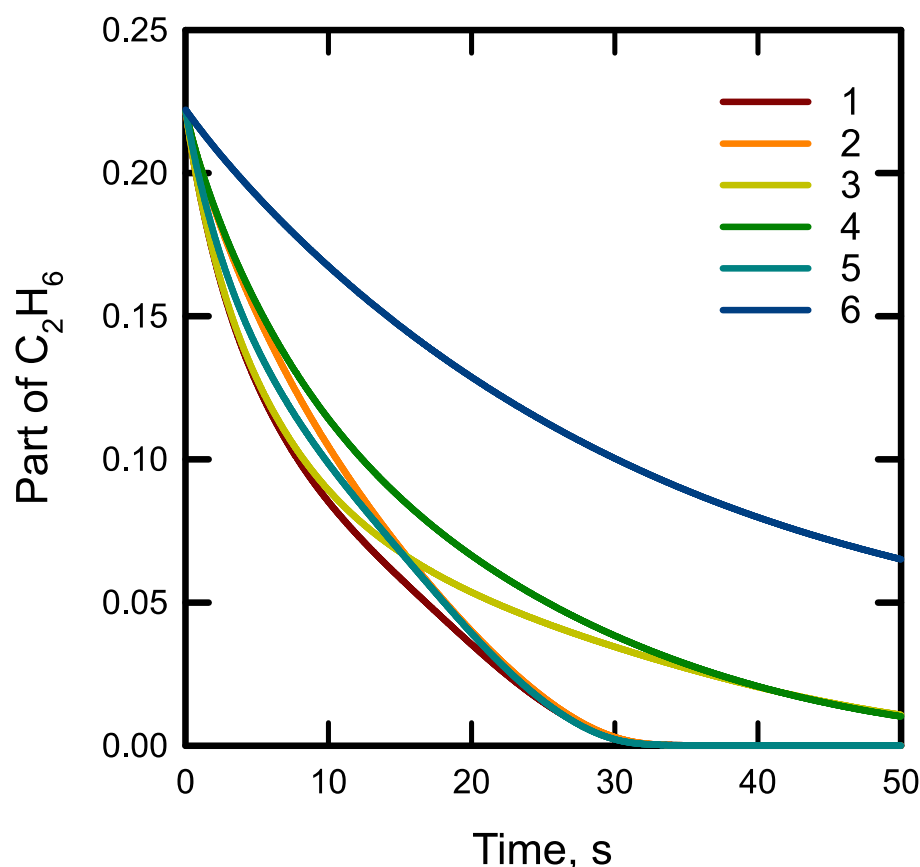


Figure 3.28: The calculated parts of C_2H_6 molecules during oxidation process in the stoichiometric mixture with oxygen. The initial pressure of the mixture is 3.78 torr. Dissociation degrees correspond to the 70% of the measured experimentally energy input. Dissociation channels are changed or switched off in a following ways: 1) all dissociation channels are in accordance with table 3.9, 2) O_2 dissociates to ground state O-atoms only, 3) dissociation of water is switched off, 4) O_2 dissociates to ground state O-atoms only and dissociation of water is switched off, 5) dissociation of ethane is switched off, 6) dissociation of oxygen is switched off.

scribed above.

3.5.1 Results and discussion

It has been shown that acetone and ethyl alcohol oxidize at the same time as the heavy alkanes under the same experimental conditions. Thus, all conclusions about the alkane's kinetics are right for these hydrocarbons too. Moreover, we have not a reason to expect that other cetones and saturated alcohols oxidation kinetics are essentially different. The results of the investigations are shown in the Figure 3.29.

The oxidation of acetylene

The oxidation of acetylene is completed for half of other investigated hydrocarbons oxidation time under the same condition (see Figure 3.29). Let us consider the oxidation

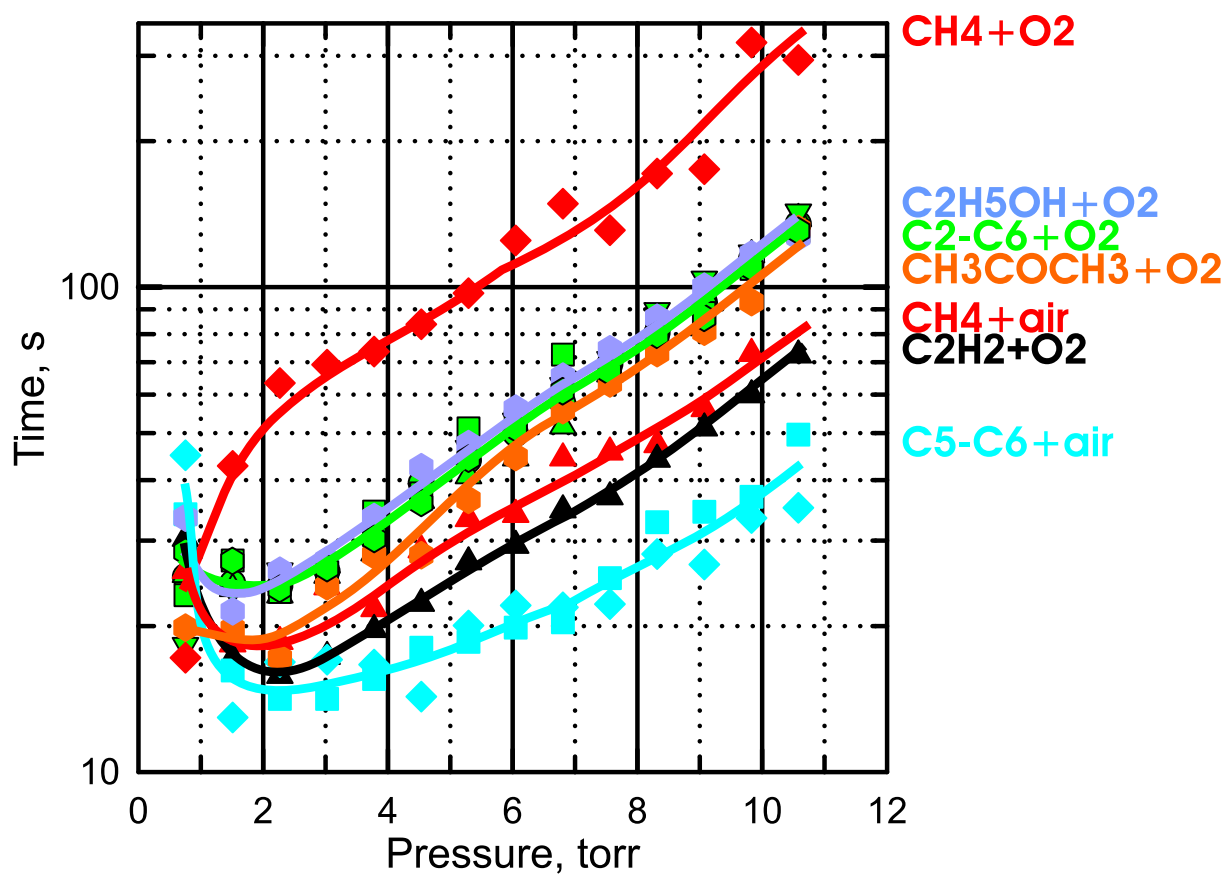


Figure 3.29: Oxidation time determined by $\text{CO}(B^1\Sigma \rightarrow A^1\Pi)$ transition intensity. C2–C6 and C5–C6 denote $\text{C}_2\text{H}_6\text{--C}_6\text{H}_{14}$ and $\text{C}_5\text{H}_{12}\text{--C}_6\text{H}_{14}$ correspondingly. These series of alkanes have practically the same oxidation times.

Table 3.10: Investigated mixture.

Equivalence ratio	C ₂ H ₅ OH	CH ₃ COCH ₃	C ₂ H ₂
1.0	25%	20%	16.7%
0.8	—	—	13.8%
0.4	—	—	7.4%
0.2	—	—	3.8%

kinetics in the acetylene–oxygen mixture.

It is known for certain that the unsaturated hydrocarbons react with molecular singlet oxygen directly in contrast to saturated hydrocarbons which are quenchers. Singlet molecular oxygen is produced effectively under reduced electric field of 10-15 V/(cm torr). Thus, the role which play singlet molecular oxygen in nanosecond discharge is negligible because, as we showed previously, the main part of the energy puts into the discharge at essentially higher electric fields.

To understand an influence of collisions with the fuel and oxygen on the acetylene oxidation kinetics we investigated the oxidation of acetylene in lean mixtures with oxygen experimentally, as well as butane kinetics has been investigated previously. It has been shown that independency of oxidation time can be explained by governing influence of excitation (dissociation, ionization and others) of fuel by electron impact.

It was found, that for pressure lower than 4 torr the electron collisions with acetylene molecules control the oxidation process entirely (see Figure 3.30). The change of the time of acetylene oxidation with change of equivalence ratio of mixture at pressures higher than 4 torr can not be explained in the assumption of essential acetylene dissociation by an electron impact. So the decrease of acetylene part in mixture results in proportional decrease of rate of the acetylene dissociation by electron impact inasmuch as the electron concentration produced in the discharge depends on the full concentration of molecules in our case. Hence the oxidation time does not change essentially with the part of acetylene under constant pressure condition. This situation we observe at low pressure; the time of oxidation does not depend on the acetylene part in the mixtures. Thus, it can be concluded that dissociation of acetylene by electron impact determines the oxidation process at low pressure. At the pressures higher than 4 torr influence of electron impact on the acetylene decreases with pressure and at the pressure about of 10 torr another processes become the governing factors of oxidation.

It is known, that under room temperature condition a thresholds of an electron impact excitation of alkanes electronic terms are higher (essentially higher for small alkanes) than a first dissociation limit of an alkane. Also it is known, that alkanes have repulsive or highly-predissociated terms, therefore an electron impact excitation of an electronic terms of alkane leads to fast dissociation of the alkane. The dissociation proceeds through the different main ways inasmuch as the energy of the dissociation threshold is more than enough for that and electronic terms of alkanes are strongly coupled to each other by non-radiative transitions. Fragments of dissociated molecules originate with high external or (and) internal energy.

Let us consider the acetylene excitation by electron impact. Noticeable intense emission of acetylene has not been observed.¹¹⁹ The first dissociation limit of acetylene

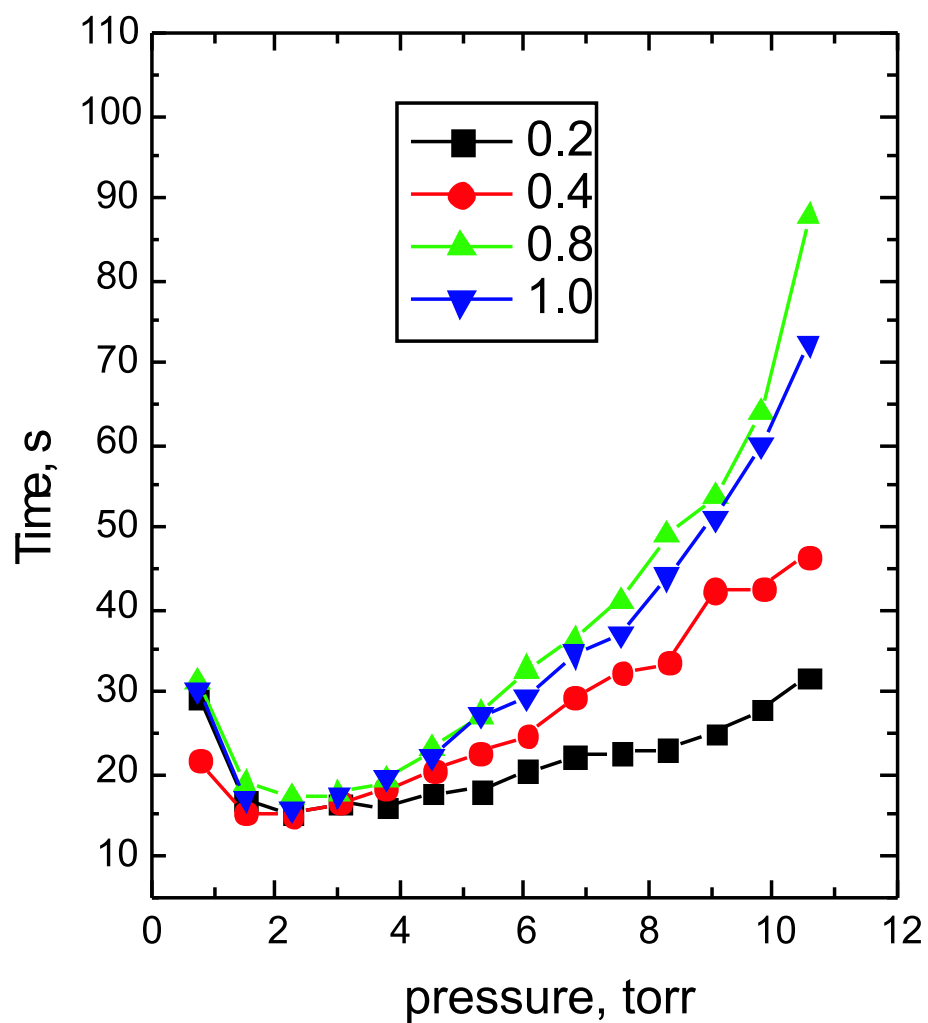
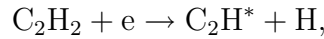


Figure 3.30: Oxidation times of acetylene determined from $\text{CO}(B^1\Sigma \rightarrow A^1\Pi)$ emission intensity in the different equivalence ratio mixtures. The equivalence ratio of the mixture changes from 1 to 0.2.

Table 3.11: Kinetics of C₂H radical in acetylene-oxygen mixtures.

N	Reaction	Constant rate cm ³ s ⁻¹	Reaction characteristic time
1.	C ₂ H+O ₂ = O+HCCO	1 · 10 ⁻¹² cm ³ s ⁻¹	~ 10μs
2.	C ₂ H+O ₂ = CO+HCO	4 · 10 ⁻¹² cm ³ s ⁻¹	~ 3μs
3.	HCO+O ₂ = CO+HO ₂	5.5 · 10 ⁻¹² cm ³ s ⁻¹	~ 2μs
4.	HCCO+O ₂ = CO ₂ +CO+H	6 · 10 ⁻¹³ cm ³ s ⁻¹	~ 20μs
5.	HCCO+O ₂ = CO+CO+OH	6 · 10 ⁻¹⁴ cm ³ s ⁻¹	~ 200μs

amounts to 4.9 eV,¹¹⁹ but thresholds of two lowest terms of acetylene are 1.9 and 5.1 eV.¹²³ It is evident that the lowest state is metastable triplet one and i.e. biradical. It is more difficult to say about the second state particularly. It has been detected very weak absorption bands of acetylene in 200-240nm (6.25-5.2eV).¹¹⁹ These bands have very well resolved vibrational and rotational structure that denotes the high states of the transitions are stable. Thus, we can assume that the 5.1 eV state is metastable also, because it does not irradiate. It is necessary to note, that the efficiency of electron impact excitation of states with so low thresholds is by several times higher at a pressure of 8 torr than at 4 torr pressure. Thus, we can assume that the excitation of this states effects on the rate of the acetylene oxidation process insignificantly in comparison with excitation of states with higher energy. The next electronic state of acetylene has excitation threshold 7.9 eV and four times higher peak of the excitation cross-section.¹²³ This electronic term can be related to the dissociation by the channel:



where C₂H* hold a portion, it can be essential portion, of internal (vibration or electronic) energy. Another dissociation channels need more energy. Inasmuch as absorption spectrum in wavelength range lower than 200 nm (energy higher than 6.25 eV) is diffuse then states with thresholds higher than 6.25 eV are predissociated.¹¹⁹ A system of very strong diffuse bands is located near 152 nm (8.2 eV).¹¹⁹ As long as the system of bands is very intensive, diffuse and does not registered in emission then evidently that these bands correspond to the dipole-allowed transition which higher state strongly predissociated. Thus, the state with the 7.9 eV threshold¹²³ necessarily corresponds to the dissociation by the mentioned channel. Let us consider the C₂H-radical kinetics:

In the right column of the table 3.11 time of a radical life is mentioned in the acetylene-oxygen stoichiometric mixture at pressure 10 torr. Thus, C₂H radicals in the presence of oxygen under our experimental conditions are oxidized to the CO and CO₂ for the time interval shorter than 1 ms. At that time a set of hydrogen containing radicals originates. It is necessary to note that at the low pressure (lower than 4 Torr) the degree of the dissociation of molecular oxygen and water for one pulse are essentially lower than one of acetylene. Acetylene has cross-section which maximum is few times higher than one for water and O₂. With pressure increase the degree of acetylene (threshold is 7.9 eV) dissociation decreases more sharply than one of water(threshold is 7 eV). The oxygen dissociation degree decreases with pressure the most quickly (threshold of main dissociation channel is 8.4 eV). Apparently, the experimental dependency of oxidation time on equivalence ratio can be explained by defining influence of electron impact dissociation of acetylene at low pressure range. At higher pressure efficiency of C₂H₂ dissociation

Table 3.12: Kinetics of OH radical in acetylene-oxygen mixtures.

1.	$\text{C}_2\text{H}_2 + \text{OH} + \text{M} \rightarrow \text{CH}=\text{CHOH} + \text{M}$	$k_1 = 4 \cdot 10^{-29} \text{cm}^6 \text{s}^{-1}$
2.	$\text{CH}=\text{CHOH} + \text{O}_2 \rightarrow \text{OH} + (\text{CHO})_2$	$k_2 = 4.2 \cdot 10^{-12} \text{cm}^3 \text{s}^{-1}$
3.	$(\text{CHO})_2 + \text{OH} \rightarrow \text{H}_2\text{O} + \text{HC}(\text{O})\text{CO}$	$k_3 = 4.2 \cdot 10^{-11} \text{cm}^3 \text{s}^{-1}$
4.	$(\text{CHO})_2 + \text{HO}_2 \rightarrow \text{H}_2\text{O}_2 + \text{HC}(\text{O})\text{CO}$	$k_4 = 5 \cdot 10^{-16} \text{cm}^3 \text{s}^{-1}$
5.	$\text{HC}(\text{O})\text{CO} \rightarrow \text{CO} + \text{HCO}$	$k_5 = 3.7 \cdot 10^7 \text{s}^{-1}$
6.	$\text{HC}(\text{O})\text{CO} + \text{O}_2 \rightarrow 2\text{CO} + \text{HCO}$	$k_6 = 1 \cdot 10^{-11} \text{cm}^3 \text{s}^{-1}$
7.	$\text{HCO} + \text{O}_2 = \text{CO} + \text{HO}_2$	$k_7 = 5.5 \cdot 10^{-12} \text{cm}^3 \text{s}^{-1}$
8.	$\text{CO} + \text{OH} \rightarrow \text{products}$	$k_8 = 1.7 \cdot 10^{-13} \text{cm}^3 \text{s}^{-1}$

degree decreases and it is possible that the water dissociation process becomes more important, as for alkanes. It is necessary to note, that in the case of acetylene too, OH radical is the most active in oxidation process. However, in contrast to alkanes, the main channel of reaction is the addition of OH radicals to acetylene molecules in third order reaction (see table 3.12).

In the case of 5 torr initial pressure the constant rate in the count on the second order is $6 \cdot 10^{-12}$ that is essentially higher than other constants of OH loss processes. The originated radical $\text{OHCH}=\text{CH}$ reacts with O_2 very fast in the reaction (2) (table 3.12). It is evident, that reactions (1) and (2) organize the chain reaction. The main termination reaction for this chain is the next reaction (3). Rate of OH loss in the chain termination reaction becomes the same as the loss in the acetylene oxidation process in the case when the $(\text{CHO})_2$ (formyl) concentration is approximately equal to the acetylene one. It is necessary to note that formyl is more weak-bond molecule than CO and for this reason it can be oxidized by HO_2 radical more effectively. This denotes that the C_2H_2 oxidizes to CO in mentioned reactions (table 3.12) at first and after that CO oxidizes to CO_2 . As long as the reaction (1) is three-particle then with pressure growth the influence of OH would be increased. In the experiment in stoichiometric mixture of acetylene and oxygen this feature is very clear. With the pressure oxidation difference in times defined from $\text{CO}(B^1\Sigma \rightarrow A^1\Pi)$ and $\text{CH}(A^2\Delta \rightarrow X^2\Pi)$ emissions increases (Figure 3.31) i.e. CO oxidizes essentially later than acetylene.

Let us compare emission intensities of different molecular bands in acetylene–oxygen (Figure 3.33) and ethane–oxygen (Figure 3.32) stoichiometric mixtures. It is clearly seen that for ethane–oxygen mixture in the point of time when $\text{CO}(B^1\Sigma \rightarrow A^1\Pi)$ band emission is maximal the intensity of $\text{CH}(A^2\Delta \rightarrow X^2\Pi)$ band emission amounts to 0.6 of $\text{CH}(A^2\Delta \rightarrow X^2\Pi)$ emission maximum approximately. At the same time for the acetylene–oxygen mixture the point of $\text{CO}(B^1\Sigma \rightarrow A^1\Pi)$ band emission maximum corresponds to the point of 0.35 of $\text{CH}(A^2\Delta \rightarrow X^2\Pi)$ emission maximum. Also, it is necessary to note, that the emission intensity of $\text{OH}(A^2\Sigma \rightarrow X^2\Pi)$ band in the acetylene–oxygen mixture increase slowly relative to the emission in ethane–oxygen mixture, in which the emission rapidly increases to two thirds of the maximum value and after that stay on the level up to sharp decreasing of $\text{CO}(B^1\Sigma \rightarrow A^1\Pi)$ band emission point of time. This difference clearly points to different kinetics of OH radical in these mixtures.

In ethane–oxygen mixture OH-radical is the main radical which determines the ethane

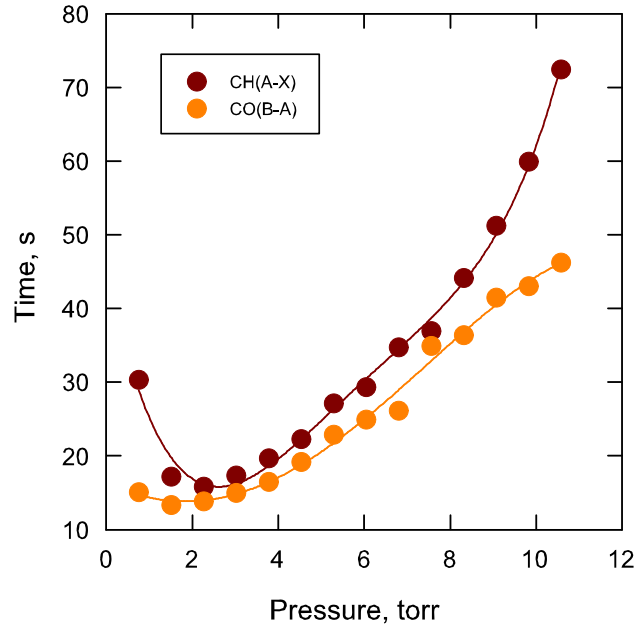


Figure 3.31: Oxidation times of acetylene determined from $\text{CO}(B^1\Sigma \rightarrow A^1\Pi)$ and $\text{CH}(A^2\Delta \rightarrow X^2\Pi)$ emission intensities.

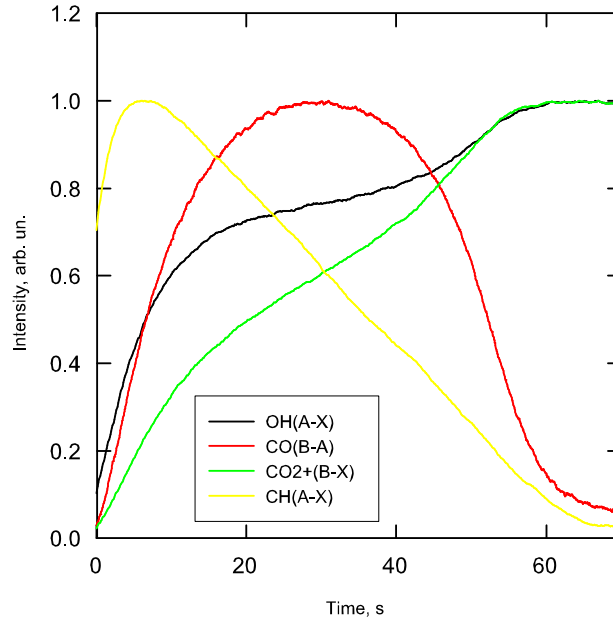


Figure 3.32: Emission intensities of $\text{OH}(A^2\Sigma \rightarrow X^2\Pi)$, $\text{CO}(B^1\Sigma \rightarrow A^1\Pi)$, $\text{CO}_2^+(B^2\Sigma \rightarrow X^2\Pi)$, $\text{CH}(A^2\Delta \rightarrow X^2\Pi)$ bands. Initial pressure of ethane-oxygen stoichiometric mixture is 6.8 torr.

oxidation. OH concentration is governed by four main processes (Table 3.13). In the processes (1)-(4) OH is produced. In the process (5) C_2H_6 is oxidized after that C_2H_5 is oxidized in series of processes in the results of which CO is produced. CO is oxidized in the process (6) most effectively. This process leads to diminish of OH radical. Thus the process oxidation under the discharge action is the process with negative feedback inasmuch as increase of OH concentration leads to increase of CO which consumes the radical and leads to diminishing of the oxidation rate. So after initial sharp growth the intensity of $OH(A^2\Sigma \rightarrow X^2\Pi)$ emission remains practically constant at the same time emission intensity of $CO(B^1\Sigma \rightarrow A^1\Pi)$ band has the flat maximum. After $CH(A^2\Delta \rightarrow X^2\Pi)$ emission comes to nearly constant level, which corresponds to full hydrocarbon oxidation, the emission intensity of the $CO(B^1\Sigma \rightarrow A^1\Pi)$ band decreases to low stationary level sharply; at the same time $OH(A^2\Sigma \rightarrow X^2\Pi)$ band emission intensity reaches up to the stationary level rapidly. After the ethane conversion, the source of CO disappears and it's residual oxidizes very fast, inasmuch as the negative feedback in the system disappears.

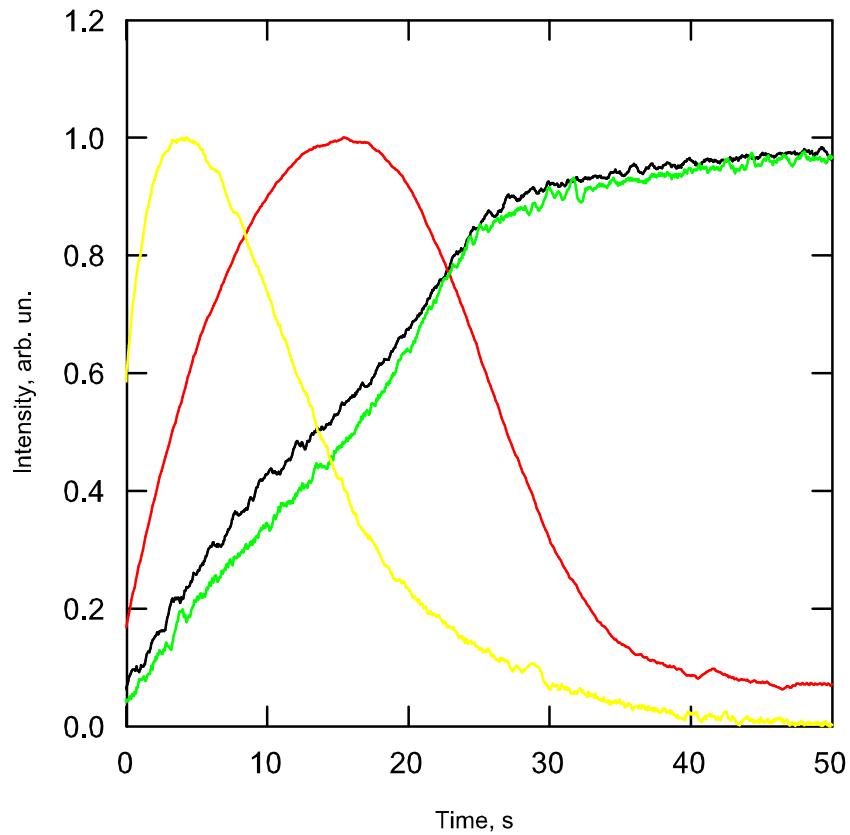


Figure 3.33: Emission intensities of $OH(A^2\Sigma \rightarrow X^2\Pi)$, $CO(B^1\Sigma \rightarrow A^1\Pi)$, $CO_2^+(B^2\Sigma \rightarrow X^2\Pi)$, $CH(A^2\Delta \rightarrow X^2\Pi)$ bands. Initial pressure of acetylene-oxygen stoichiometric mixture is 6.8 torr.

In the case of acetylene oxidation negative feedback is formed on the later stage when enough formyl radical is accumulated. Inasmuch as formyl oxidizes more intensively than CO, it accumulates on the later stage. At that, processes oxidation of acetylene and

Table 3.13: Kinetics of C₂H₆ oxidation.

1.	Electron impact to O ₂	$e + O_2 \rightarrow O(^1D) + O + e$
2.	Production in the process	$O(^1D) + H_2O \rightarrow 2OH$
3.	Production in the process	$O(^1D) + C_2H_6 \rightarrow C_2H_5 + OH$
4.	Electron impact to H ₂ O	$e + H_2O \rightarrow OH + H + e$
5.	Loss in the process of C ₂ H ₆ oxidation	$C_2H_6 + OH \rightarrow C_2H_5 + H_2O$
6.	Loss in the process of CO oxidation	$CO + OH \rightarrow \text{products}$

CO should be separated in time. The separation in time of these processes increases with pressure that is explained by determining influence of addition of OH to acetylene (reaction 1 is three particle reaction). It is necessary to note that the increase of the oxidation time with the increasing of acetylene part in mixture is well explained in assumption of determining influence of OH-radical. Decreasing of acetylene concentration in initial mixture, hence decreasing of water concentration in proceeded mixture leads to decreasing of OH production by electron impact during all oxidation process. However in lean mixtures exceed oxygen is a source of additional concentration of O(¹D) states which is produced by electron collisions with molecular oxygen. This state reacts with water producing two OH-radicals, in place of one in the case of hydrocarbon collision. Thus the rate of hydrocarbon oxidation changes weakly with a change of equivalence ratio of the mixture.

Thus, we conclude that the main processes, which control of acetylene oxidation are dissociation of acetylene by electron impact and addition of OH-radical to an acetylene molecule. OH-radicals produce from water by electron impact and in collisions with O(¹D).

3.6 Carbon monoxide oxidation in mixtures with oxygen and water. Experimental investigation and analysis

3.6.1 Experiment

As we showed previously, carbon monoxide plays essential role in processes of hydrocarbons oxidation. To learn the kinetics of carbon monoxide in hydrocarbon-oxygen mixtures we have investigated oxidation of CO in stoichiometric mixtures with O₂ and small addition of water. Experimental setup and methods were used the same as early, but preparation of the installation and mixtures was essentially different. Mixture of CO(67%) and O₂(33%) was prepared in balloon preliminary. The vapor was prepared preliminary too. The water was injected into the pumped vessel. After evaporation the water vapor was prepared to injection into the discharge cell. After water vapor injection into the cell the CO-O₂ mixture was added to the vapor. The mixing of water and CO-O₂ mixture took place within 2 minutes. Inasmuch as, total pressure was lower than 11 torr and the length of the discharge cell was 25 cm then this time enough to mix water with the mixture (diffusion time is $t \sim L^2/D < 30$ s for all pressure range).

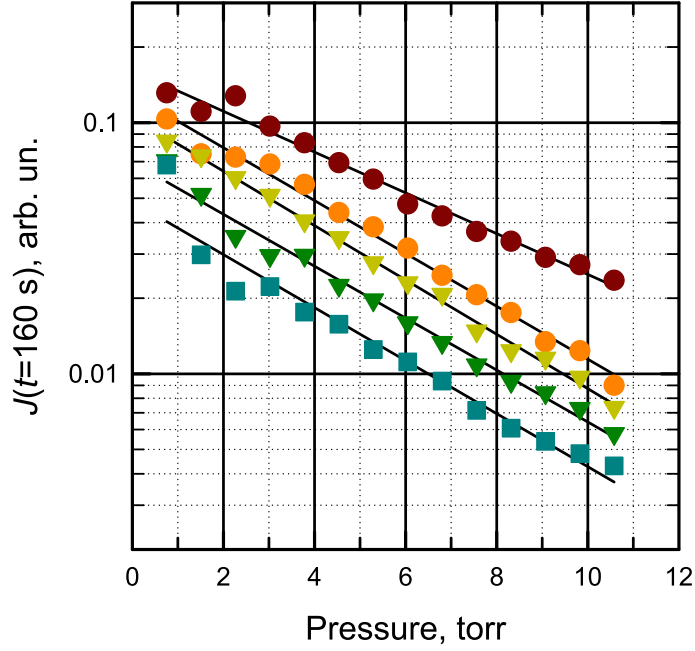


Figure 3.34: $\text{CO}(B^1\Sigma \rightarrow A^1\Pi)$ emission intensity after 160 s from instant, when the discharge is switched on, versus the mixture initial pressure. Mixtures are CO-O_2 stoichiometric with small addition of water vapor.

3.6.2 Discussion

The emission intensity of $\text{CO}(B^1\Sigma \rightarrow A^1\Pi)$ band, voltage on the discharge cell, the electric current through the discharge cell were measured with nanosecond resolution and in the integral regime. Pressure in the discharge was measured in the integral regime. The methods of the investigations are described in detail in the first part of the paper. Investigations were performed for mixtures which include 1, 2, 4 and 8% of water. The emission intensities of $\text{CO}(B^1\Sigma \rightarrow A^1\Pi)$ band and their time derivatives versus time at pressure 3.78 torr are shown in the Figure 3.34 for different concentrations of water.

It is necessary to note, that the intensities of $\text{CO}(B^1\Sigma \rightarrow A^1\Pi)$ emission can be associated with carbon monoxide concentration directly because so small addition of water can not effect so significantly on integral emission. It is clearly seen that a small water addition accelerates the oxidation process and increases final CO processing dramatically. In the Figure 3.35 emission intensity of $\text{CO}(B^1\Sigma \rightarrow A^1\Pi)$ band at a time of $t = 160$ s (this value at fixed initial pressure can be associated with CO conversion level relative to this level without water) and minimum value of time derivatives of emission $\frac{dI^{\text{CO}}(t)}{dt}$ (this value at fixed initial pressure can be associated with maximal rate of CO oxidation relative to the rate without water) versus initial pressure are shown for different percentage of water vapor. It is needed to note that the minimums of the derivatives can be represented in the same form for all experimental data:

$$\frac{dI}{dt} = \left. \frac{dI}{dt} \right|_{[\text{H}_2\text{O}]=0} + F(p) \ln[\text{H}_2\text{O}],$$

where $F(p)$ is universal function, which has not dependency on H_2O concentration. Also,

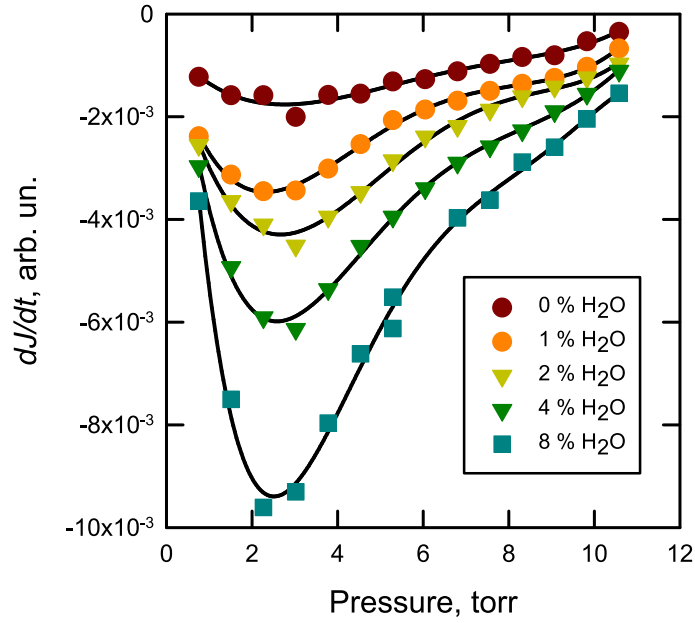


Figure 3.35: Minimum values of $\text{CO}(B^1\Sigma \rightarrow A^1\Pi)$ emission intensity time derivative, when the discharge is switched on, versus the mixture initial pressure. Mixtures are CO-O_2 stoichiometric with small addition of water vapor.

it is clearly seen that the emission intensities $I(t = 160, p)$ have the same pressure logarithmic derivatives when water is added:

$$(I(t = 160, p) = I_0(1 - \ln[\text{H}_2\text{O}]^{0.307}) \exp(-0.243p),$$

and essentially different without water addition:

$$I(t = 160, p) \sim \exp(-0.187p).$$

Here $[\text{H}_2\text{O}]$ is a percentage of water, p is the initial pressure expressed in torr.

This feature denotes that the residual concentration of water or hydrocarbons (actuating fluid of pump) is practically constant and does not depend on the mixture's pressure. It is clearly seen that the water influence on the rate of CO oxidation is very strong. For this reason we were forced to prepare the discharge cell before the water filling with especial carefulness. After each experiment we pumped and cleaned out by air blowing the discharge cell three and more times. All experiments without water addition were carried out more than two times (up to 5). In the figures we have shown only one of points for each pressure. These points were corresponded to lowest value of the emission intensity derivative and, as we assume, minimal hydrogen containing admixture. To prepare discharge cell to hydrocarbons-oxygen (excluding lean acetylene-oxygen mixtures) experiments these precautions were not needed because these mixtures already contain essential concentration of hydrogen containing molecules.

In assumption that background admixture of hydrogen containing molecules does not change with pressure and composition of mixture we approximate with the good accuracy all measured data $I(t = 160)$ by following function:

$$(I(t = 160, p, [\text{H}_2\text{O}]) = I_0[1 - 0.308 \ln([\text{H}_2\text{O}] + 100a/p)] \exp(-0.243p),$$

Table 3.14: Kinetics of CO oxidation in the discharge.

1.	Electron impact to CO	$e + \text{CO} \rightarrow \text{C} + \text{O}$	$F(E/N), \delta\varepsilon \approx 12\text{eV}$
2.	C atoms losses	$\text{C} + \text{O}_2 \rightarrow \text{CO} + \text{O}(^1D)$	$5 \cdot 10^{-11}$
		$\text{C} + \text{H}_2\text{O} \rightarrow \text{CH} + \text{OH}$	$< 1 \cdot 10^{-12}$
		$\text{C} + \text{CO}_2 \rightarrow 2\text{CO}$	$< 1 \cdot 10^{-15}$
3.	Electron impact to H ₂ O	$e + \text{H}_2\text{O} \rightarrow \text{OH} + \text{H} + e$	$F(E/N), \delta\varepsilon \approx 7\text{eV}$
5.	OH production in the process	$\text{O}(^1D) + \text{H}_2\text{O} \rightarrow 2\text{OH}$	$1.1 \cdot 10^{-10}$
6.	Loss in the processes of CO oxidation	$\text{CO} + \text{OH} \rightarrow \text{CO}_2 + \text{H}$	$1.7 \cdot 10^{-13}$

where $a=4.5 \cdot 10^{-3}$ torr is a pressure of hydrogen containing molecules converting to the water molecules. Pumping of the discharge cell was produced by roughing-down pump and this value seems to be adequate taking into account multiple cleaning by air.

It is not possible to extrapolate this dependency to the $[\text{H}_2\text{O}]=0$ limit, but we can estimate $I(t, p, 8\%)/I(t, p, 1\%) = 2.8$. As we mentioned previously, this relation directly connected to the level of CO conversion - at the 8% water presence the conversion level is 2.8 times higher than the level at the 1 % water presence. The maximal oxidation rate at that changes to 3 times too approximately.

So strong coupling of the rate oxidation and the conversion level of CO with water concentration can be explained by the fact that the main part of CO oxidizes under nanosecond discharge action at low temperature in the processes showed in the table 3.14. At that time any channel without OH radical is very weak.

It is necessary to note that a CO molecule is very stable. It's ionization potential and the first dissociation limit are 14.01 and 11.09 eV correspondingly. Thus, dissociation or ionization of CO in the discharge are not main channel of energy branching, but one act of CO dissociation leads to produce one O atom, one CO molecule and 2 OH radicals in the series of fast reactions (table 3.14). These two OH radicals are consumed to production of two CO₂ molecules. Thus, in the presence of water dissociation of CO leads to fast and effective conversion of CO molecules.

3.7 Kinetics of neutrals in hydrocarbons (C₂H₆, CH₄, H₂, C₂H₅OH)–oxygen mixtures

Kinetics of neutrals in hydrocarbons(C₂H₆, CH₄, H₂, C₂H₅OH)–oxygen mixtures.

N	Reaction	Rate constants, cm ³ /s
1.	$\text{H}_2 + \text{O}(^1D) = \text{H} + \text{OH}$	$1.1 \cdot 10^{-10}$
2.	$\text{H}_2 + \text{O} = \text{H} + \text{OH}$	$1 \cdot 10^{-17}$
3.	$\text{H}_2 + \text{OH} = \text{H}_2\text{O} + \text{H}$	$7 \cdot 10^{-15}$
4.	$\text{H}_2 + \text{CHO} = \text{H} + \text{CH}_2\text{O}$	$2.8 \cdot 10^{-26}$
5.	$\text{H}_2 + \text{CH}_3\text{O} = \text{H} + \text{CH}_3\text{OH}$	$3.7 \cdot 10^{-9}$
6.	$\text{O}_2 + \text{O}(^1D) = \text{O}_2 + \text{O}$	$4 \cdot 10^{-11}$
7.	$\text{O}_2 + \text{O} + \text{M} = \text{O}_3 + \text{M}$	$6 \cdot 10^{-34}$
8.	$\text{O}_2 + \text{H} + \text{M} = \text{HO}_2 + \text{M}$	$5.7 \cdot 10^{-32}$
9.	$\text{O}_2 + \text{CH}_3 + \text{M} = \text{CH}_3\text{O}_2 + \text{M}$	$4.5 \cdot 10^{-31}$

N	Reaction	Rate constant, cm ³ /s
10.	$\text{O}_2 + \text{C}_2\text{H}_5 + \text{M} = \text{C}_2\text{H}_5\text{O}_2 + \text{M}$	$1.5 \cdot 10^{-28}$
11.	$\text{O}_2 + \text{CHO} = \text{CO} + \text{HO}_2$	$5.5 \cdot 10^{-12}$
12.	$\text{O}_2 + \text{CHO} = \text{CO}_2 + \text{OH}$	$1.1 \cdot 10^{-13}$
13.	$\text{O}_2 + \text{CH}_3\text{O} = \text{CH}_2\text{O} + \text{HO}_2$	$2 \cdot 10^{-15}$
14.	$\text{O}_2 + \text{CH}_3\text{CO} = \text{CH}_2\text{O} + \text{CO} + \text{OH}$	$3 \cdot 10^{-12}$
15.	$\text{CH}_4 + \text{O}(^1\text{D}) = \text{CH}_3 + \text{OH}$	$2.2 \cdot 10^{-10}$
16.	$\text{CH}_4 + \text{O} = \text{CH}_3 + \text{OH}$	$1 \cdot 10^{-17}$
17.	$\text{CH}_4 + \text{OH} = \text{CH}_3 + \text{H}_2\text{O}$	$6.3 \cdot 10^{-15}$
18.	$\text{CH}_4 + \text{H} = \text{CH}_3 + \text{H}_2$	$1 \cdot 10^{-17}$
19.	$\text{C}_2\text{H}_4 + \text{O} = \text{H} + \text{CH}_2\text{CHO}$	$6.24 \cdot 10^{-13}$
20.	$\text{C}_2\text{H}_4 + \text{OH} + \text{M} = \text{HOCH}_2\text{CH}_2 + \text{M}$	$1 \cdot 10^{-28}$
21.	$\text{C}_2\text{H}_4 + \text{H} + \text{M} = \text{C}_2\text{H}_5 + \text{M}$	$2 \cdot 10^{-30}$
22.	$\text{C}_2\text{H}_6 + \text{O}(^1\text{D}) = \text{C}_2\text{H}_5 + \text{OH}$	$6.3 \cdot 10^{-10}$
23.	$\text{C}_2\text{H}_6 + \text{O} = \text{C}_2\text{H}_5 + \text{OH}$	$5 \cdot 10^{-16}$
24.	$\text{C}_2\text{H}_6 + \text{OH} = \text{C}_2\text{H}_5 + \text{H}_2\text{O}$	$2.5 \cdot 10^{-13}$
25.	$\text{CO} + \text{O}(^1\text{D}) = \text{CO}_2$	$7.3 \cdot 10^{-11}$
26.	$\text{CO} + \text{O}(^1\text{D}) = \text{CO} + \text{O}$	$2.1 \cdot 10^{-10}$
27.	$\text{CO} + \text{O} + \text{O}_2 = \text{CO}_2 + \text{O}_2$	$6 \cdot 10^{-35}$
28.	$\text{CO} + \text{O} + \text{H}_2\text{O} = \text{CO}_2 + \text{H}_2\text{O}$	$6 \cdot 10^{-35}$
29.	$\text{CO} + \text{O} + \text{CO}_2 = 2\text{CO}_2$	$3.5 \cdot 10^{-35}$
30.	$\text{CO} + \text{OH} = \text{HOCO}$	$1.5 \cdot 10^{-13}$
31.	$\text{HOCO} + \text{O}_2 = \text{CO}_2 + \text{HO}_2$	$1.5 \cdot 10^{-12}$
32.	$\text{CO} + \text{OH} = \text{CO}_2 + \text{H}$	$1.7 \cdot 10^{-13}$
33.	$\text{CO} + \text{H} + \text{M} = \text{CHO} + \text{M}$	$1.5 \cdot 10^{-34}$
34.	$\text{CO} + \text{CH}_3 + \text{M} = \text{CH}_3\text{CO} + \text{M}$	$4.2 \cdot 10^{-36}$
35.	$\text{CO} + \text{C}_2\text{H}_5 = \text{C}_2\text{H}_5\text{CO}$	$8.1 \cdot 10^{-17}$
36.	$\text{CO}_2 + \text{O}(^1\text{D}) = \text{CO}_2 + \text{O}$	$1.1 \cdot 10^{-10}$
37.	$\text{CH}_3\text{CHO} + \text{O}(^1\text{D}) = \text{OH} + \text{CH}_3\text{CO}$	$3 \cdot 10^{-10}$
38.	$\text{CH}_3\text{CHO} + \text{O} = \text{CH}_3\text{CO} + \text{OH}$	$4.3 \cdot 10^{-13}$
39.	$\text{CH}_3\text{CHO} + \text{OH} = \text{CH}_3\text{CO} + \text{H}_2\text{O}$	$1.45 \cdot 10^{-11}$
40.	$\text{CH}_3\text{CHO} + \text{H} = \text{CH}_3\text{CO} + \text{H}_2$	$1 \cdot 10^{-13}$
41.	$\text{CH}_3\text{CHO} + \text{CH}_3 = \text{CH}_3\text{CO} + \text{CH}_4$	$5 \cdot 10^{-18}$
42.	$\text{CH}_3\text{CHO} + \text{C}_2\text{H}_5 = \text{CH}_3\text{CO} + \text{C}_2\text{H}_6$	$1 \cdot 10^{-17}$
43.	$\text{CH}_3\text{CHO} + \text{CHO} = \text{CHO} + \text{CO} + \text{CH}_4$	$2 \cdot 10^{-17}$
44.	$\text{CH}_3\text{CHO} + \text{CH}_3\text{O} = \text{CH}_3\text{CO} + \text{CH}_3\text{OH}$	$1 \cdot 10^{-14}$
45.	$\text{CH}_3\text{CHO} + \text{CH}_3\text{CO} = \text{CHO} + \text{C}_2\text{H}_6\text{CO}$	$2.8 \cdot 10^{-13}$
46.	$\text{CH}_2\text{O} + \text{O}(^1\text{D}) = \text{OH} + \text{CHO}$	$3 \cdot 10^{-10}$
47.	$\text{CH}_2\text{O} + \text{O} = \text{OH} + \text{CHO}$	$1.7 \cdot 10^{-13}$
48.	$\text{CH}_2\text{O} + \text{OH} = \text{H}_2\text{O} + \text{CHO}$	$9.4 \cdot 10^{-12}$
49.	$\text{CH}_2\text{O} + \text{H} = \text{H}_2 + \text{CHO}$	$5.7 \cdot 10^{-14}$
50.	$\text{CH}_2\text{O} + \text{CH}_3\text{O} = \text{CH}_3\text{OH} + \text{CHO}$	$1.1 \cdot 10^{-15}$
51.	$\text{CH}_3\text{OH} + \text{O}(^1\text{D}) = \text{CH}_3\text{O} + \text{OH}$	$5.1 \cdot 10^{-10}$
52.	$\text{CH}_3\text{OH} + \text{O} = \text{CH}_3\text{O} + \text{OH}$	$7 \cdot 10^{-15}$
53.	$\text{CH}_3\text{OH} + \text{OH} = \text{CH}_2\text{OH} + \text{H}_2\text{O}$	$9.3 \cdot 10^{-13}$
54.	$\text{CH}_3\text{OH} + \text{OH} = \text{CH}_3\text{O} + \text{H}_2\text{O}$	$1.4 \cdot 10^{-13}$

N	Reaction	Rate constant, cm ³ /s
55.	CH ₃ OH+H = CH ₂ OH+H ₂	1.3·10 ⁻¹⁵
56.	CH ₃ OH+CH ₃ O = CH ₂ OH+CH ₃ OH	5.4·10 ⁻¹⁶
57.	C ₂ H ₅ OH+O(¹ D) = C ₂ H ₅ O+OH	5·10 ⁻¹⁰
58.	C ₂ H ₅ OH+O = CH ₃ CHOH+OH	1·10 ⁻¹³
59.	C ₂ H ₅ OH+OH = CH ₃ CHOH+H ₂ O	1.3·10 ⁻¹²
60.	C ₂ H ₅ OH+H = CH ₃ CHOH+H ₂	3·10 ⁻¹⁵
61.	CH ₃ OOH+O(¹ D) = CH ₃ O ₂ +OH	5·10 ⁻¹⁰
62.	CH ₃ OOH+O = CH ₃ O ₂ +OH	1·10 ⁻¹⁴
63.	CH ₃ OOH+OH = CH ₃ O ₂ +H ₂ O	3.6·10 ⁻¹²
64.	CH ₃ OOH+OH = CH ₂ OOH+H ₂ O	1.9·10 ⁻¹²
65.	CH ₃ OOH+H = CH ₂ OOH+H ₂	1·10 ⁻¹⁵
66.	CH ₃ OOH+H = CH ₃ O+H ₂ O	4·10 ⁻¹⁶
67.	CH ₃ OOH+H = CH ₃ O ₂ +H ₂	5·10 ⁻¹⁶
68.	C ₂ H ₅ OOH+O(¹ D) = C ₂ H ₅ O ₂ +OH	5·10 ⁻¹⁰
69.	C ₂ H ₅ OOH+O = C ₂ H ₅ O ₂ +OH	1.2·10 ⁻¹⁴
70.	C ₂ H ₅ OOH+OH = C ₂ H ₅ O ₂ +H ₂ O	3.7·10 ⁻¹²
71.	C ₂ H ₅ OOH+OH = CH ₃ CHO+H ₂ O+OH	2·10 ⁻¹²
72.	C ₂ H ₅ OOH+H = CH ₃ CHO+H ₂ +OH	1·10 ⁻¹⁵
73.	C ₂ H ₅ OOH+H = C ₂ H ₅ O+H ₂ O	4·10 ⁻¹⁶
74.	C ₂ H ₅ OOH+H = C ₂ H ₅ O ₂ +H ₂	5·10 ⁻¹⁶
75.	H ₂ O ₂ +O(¹ D) = OH+HO ₂	5.2·10 ⁻¹⁰
76.	H ₂ O ₂ +O = OH+HO ₂	1.8·10 ⁻¹⁵
77.	H ₂ O ₂ +OH = H ₂ O+HO ₂	1.7·10 ⁻¹²
78.	H ₂ O ₂ +H = H ₂ O+OH	4.2·10 ⁻¹⁴
79.	H ₂ O ₂ +CH ₃ = CH ₄ +HO ₂	5.5·10 ⁻¹⁴
80.	H ₂ O ₂ +C ₂ H ₅ = C ₂ H ₆ +HO ₂	2.8·10 ⁻¹⁵
81.	H ₂ O ₂ +CH ₃ O = CH ₃ OH+HO ₂	1·10 ⁻¹⁴
82.	H ₂ O+O(¹ D) = OH+OH	2.2·10 ⁻¹⁰
84.	O(¹ D)+O ₃ = 2O ₂	1.2·10 ⁻¹⁰
85.	O(¹ D)+O ₃ = 2O+O ₂	1.2·10 ⁻¹⁰
86.	O+O+O ₂ = O ₂ +O ₂	1·10 ⁻³²
87.	O+O+H ₂ = O ₂ +H ₂	2.6·10 ⁻³³
88.	O+O+H ₂ O = H ₂ O+O ₂	1.7·10 ⁻³²
89.	O+O+CH ₄ = CH ₄ +O ₂	2.2·10 ⁻³³
90.	O+O+CO = CO+O ₂	1.9·10 ⁻³³
91.	O+O+CO ₂ = CO ₂ +O ₂	4·10 ⁻³³
92.	O+O+C ₂ H ₆ = C ₂ H ₆ +O ₂	3.3·10 ⁻³³
93.	O+O ₃ = 2O ₂	8.3·10 ⁻¹⁵
94.	O+OH = H+O ₂	3.5·10 ⁻¹¹
95.	O+H+H ₂ = OH+H ₂	9.2·10 ⁻³³
96.	O+H+CH ₄ = OH+CH ₄	9.2·10 ⁻³³
97.	O+H+CO ₂ = OH+CO ₂	9.2·10 ⁻³³
98.	O+H+CO = OH+CO	6.9·10 ⁻³³
99.	O+H+H ₂ O = OH+H ₂ O	2.8·10 ⁻³²
100.	O+H+C ₂ H ₆ = OH+C ₂ H ₆	1.4·10 ⁻³²

N	Reaction	Rate constant, cm ³ /s
101.	O+HO ₂ = OH+O ₂	5.7·10 ⁻¹¹
102.	O+CH ₃ = H+H ₂ +CO	3·10 ⁻¹¹
103.	O+CH ₃ = H+CH ₂ O	1·10 ⁻¹⁰
104.	O+C ₂ H ₅ = CH ₃ CHO+H	1.3·10 ⁻¹⁰
105.	O+C ₂ H ₅ = CH ₂ O+CH ₃	2.7·10 ⁻¹¹
106.	O+CHO = H+CO ₂	5·10 ⁻¹¹
107.	O+CHO = OH+CO	5·10 ⁻¹¹
108.	O+CH ₃ O = CH ₃ +O ₂	2.5·10 ⁻¹²
109.	O+CH ₃ O = CH ₂ O+OH	2.4·10 ⁻¹¹
110.	O+CH ₃ CO = CO ₂ +CH ₃	3.3·10 ⁻¹¹
111.	O+CH ₃ O ₂ = CH ₃ O+O ₂	5·10 ⁻¹¹
112.	O+C ₂ H ₅ O ₂ = C ₂ H ₅ O+O ₂	7·10 ⁻¹¹
113.	O ₃ +OH = O ₂ +HO ₂	7.4·10 ⁻¹⁴
114.	O ₃ +H = OH+O ₂	3·10 ⁻¹¹
115.	O ₃ +HO ₂ = 2O ₂ +OH	2.1·10 ⁻¹⁵
116.	O ₃ +CH ₃ = CH ₃ O+O ₂	2.6·10 ⁻¹²
117.	O ₃ +C ₂ H ₅ = C ₂ H ₅ O+O ₂	2.5·10 ⁻¹¹
118.	O ₃ +CHO = H+O ₂ +CO ₂	1·10 ⁻¹²
119.	O ₃ +CH ₃ O ₂ = 2O ₂ +CH ₃ O	1·10 ⁻¹⁷
120.	O ₃ +C ₂ H ₅ O ₂ = 2O ₂ +C ₂ H ₅ O	1·10 ⁻¹⁷
121.	OH+OH = O+H ₂ O	1.4·10 ⁻¹²
122.	OH+H+H ₂ O = H ₂ O+H ₂ O	4.3·10 ⁻³⁰
123.	OH+H+H ₂ = H ₂ O+H ₂	8.6·10 ⁻³¹
124.	OH+H+C ₂ H ₆ = C ₂ H ₆ +H ₂ O	3.5·10 ⁻³⁰
125.	OH+H+O ₂ = H ₂ O+O ₂	6.8·10 ⁻³¹
126.	OH+H+CO ₂ = H ₂ O+CO ₂	9·10 ⁻³¹
127.	OH+H+CO = H ₂ O+CO	4.5·10 ⁻³¹
128.	OH+HO ₂ = H ₂ O+O ₂	1.1·10 ⁻¹⁰
129.	OH+CH ₃ = CH ₂ OH+H	1.3·10 ⁻¹¹
130.	OH+CH ₃ = CH ₃ O+H	1.6·10 ⁻¹⁰
131.	OH+CH ₃ = CH ₃ OH	1·10 ⁻¹⁰
132.	OH+C ₂ H ₅ = C ₂ H ₄ +H ₂ O	4·10 ⁻¹¹
133.	OH+C ₂ H ₅ = C ₂ H ₅ OH	1.2·10 ⁻¹⁰
134.	OH+CHO = H ₂ O+CO	1.7·10 ⁻¹⁰
135.	OH+CH ₃ O = H ₂ O+CH ₂ O	3·10 ⁻¹¹
136.	OH+CH ₃ CO = CH ₂ CO+H ₂ O	2·10 ⁻¹¹
137.	OH+CH ₃ O ₂ = O ₂ +CH ₃ OH	1·10 ⁻¹⁰
138.	OH+C ₂ H ₅ O ₂ = O ₂ +C ₂ H ₅ OH	1·10 ⁻¹⁰
139.	H+H+H ₂ = H ₂ +H ₂	8.9·10 ⁻³³
140.	H+H+CH ₄ = H ₂ +CH ₄	1.8·10 ⁻³²
141.	H+H+CO ₂ = H ₂ +CO ₂	1.7·10 ⁻³²
142.	H+H+C ₂ H ₆ = H ₂ +C ₂ H ₆	2.8·10 ⁻³²
143.	H+H+H ₂ O = H ₂ +H ₂ O	9.2·10 ⁻³²
144.	H+HO ₂ = H ₂ O+O	2.4·10 ⁻¹²
145.	H+HO ₂ = H ₂ +O ₂	5.6·10 ⁻¹²

N	Reaction	Rate constant, cm ³ /s
146.	H+HO ₂ = 2OH	7.2·10 ⁻¹¹
147.	H+CH ₃ +C ₂ H ₆ = CH ₄ +C ₂ H ₆	3·10 ⁻²⁸
148.	H+CH ₃ +H ₂ O = CH ₄ +H ₂ O	6·10 ⁻²⁸
149.	H+CH ₃ +H ₂ = CH ₄ +H ₂	2·10 ⁻²⁸
150.	H+CH ₃ +CH ₄ = 2CH ₄	2·10 ⁻²⁸
151.	H+CH ₃ +CO = CH ₄ +CO	1.5·10 ⁻²⁸
152.	H+CH ₃ +CO ₂ = CH ₄ +CO ₂	2·10 ⁻²⁸
153.	H+C ₂ H ₅ = 2CH ₃	1.25·10 ⁻¹⁰
154.	H+CHO = H ₂ +CO	1.13·10 ⁻¹⁰
155.	H+CH ₃ O = H ₂ +CH ₂ O	3·10 ⁻¹¹
156.	H+CH ₃ CO = CHO+CH ₃	3.6·10 ⁻¹¹
157.	H+CH ₃ CO = CH ₂ CO+H ₂	1.9·10 ⁻¹¹
158.	H+CH ₃ O ₂ = CH ₃ O+OH	1.6·10 ⁻¹⁰
159.	H+C ₂ H ₅ O ₂ = C ₂ H ₅ O+OH	1.6·10 ⁻¹⁰
160.	HO ₂ +HO ₂ +M = O ₂ +H ₂ O ₂ +M	4.5·10 ⁻³²
161.	HO ₂ +HO ₂ = O ₂ +H ₂ O ₂	1.7·10 ⁻¹²
162.	HO ₂ +CH ₃ = CH ₃ O+OH	3·10 ⁻¹¹
163.	HO ₂ +CH ₃ = CH ₄ +O ₂	6·10 ⁻¹²
164.	HO ₂ +C ₂ H ₅ = O ₂ +C ₂ H ₆	5·10 ⁻¹³
165.	HO ₂ +C ₂ H ₅ = H ₂ O ₂ +C ₂ H ₄	3·10 ⁻¹²
166.	HO ₂ +C ₂ H ₅ = OH+C ₂ H ₅ O	5·10 ⁻¹¹
167.	HO ₂ +CHO = CH ₂ O+O ₂	5·10 ⁻¹¹
168.	HO ₂ +CH ₃ O = CH ₂ O+H ₂ O ₂	5·10 ⁻¹³
169.	HO ₂ +CH ₃ CO = CH ₃ +CO ₂ +OH	5·10 ⁻¹¹
170.	HO ₂ +CH ₃ O ₂ = O ₂ +CH ₃ OOH	5.8·10 ⁻¹²
171.	HO ₂ +C ₂ H ₅ O ₂ = O ₂ +C ₂ H ₅ OOH	7.63·10 ⁻¹²
172.	CH ₃ +CH ₃ = C ₂ H ₆	4.6·10 ⁻¹¹
173.	CH ₃ +C ₂ H ₅ = C ₃ H ₈	5.6·10 ⁻¹¹
174.	CH ₃ +C ₂ H ₅ = C ₂ H ₄ +CH ₄	1.9·10 ⁻¹²
175.	CH ₃ +CHO = CH ₄ +CO	4.4·10 ⁻¹¹
176.	CH ₃ +CHO = CH ₃ CHO	6.3·10 ⁻¹²
177.	CH ₃ +CH ₃ O = CH ₄ +CH ₂ O	4·10 ⁻¹¹
178.	CH ₃ +CH ₃ CO = CO+C ₂ H ₆	5.3·10 ⁻¹¹
179.	CH ₃ +CH ₃ CO = CH ₂ CO+CH ₄	1·10 ⁻¹¹
180.	CH ₃ +CH ₃ O ₂ = 2CH ₃ O	4·10 ⁻¹¹
181.	CH ₃ +C ₂ H ₅ O ₂ = CH ₃ O+C ₂ H ₅ O	4·10 ⁻¹¹
182.	C ₂ H ₅ +C ₂ H ₅ = C ₂ H ₄ +C ₂ H ₆	2.4·10 ⁻¹²
183.	C ₂ H ₅ +C ₂ H ₅ = C ₄ H ₁₀	1.9·10 ⁻¹¹
184.	C ₂ H ₅ +CHO = CO+C ₂ H ₆	2·10 ⁻¹⁰
185.	C ₂ H ₅ +CH ₃ O = CH ₂ O+C ₂ H ₆	4·10 ⁻¹¹
186.	C ₂ H ₅ +CH ₃ CO = C ₂ H ₅ COCH ₃	3·10 ⁻¹¹
187.	C ₂ H ₅ +CH ₃ O ₂ = C ₂ H ₅ O+CH ₃ O	4·10 ⁻¹¹
188.	C ₂ H ₅ +C ₂ H ₅ O ₂ = 2C ₂ H ₅ O	4·10 ⁻¹¹
189.	CHO+CHO = CO+CH ₂ O	5·10 ⁻¹¹
190.	CHO+CH ₃ O = CO+CH ₃ OH	1.5·10 ⁻¹⁰

N	Reaction	Rate constant, cm ³ /s
191.	CHO+CH ₃ CO = CH ₃ COCHO	3·10 ⁻¹¹
192.	CHO+CH ₃ CO = CH ₃ CHO+CO	1.5·10 ⁻¹¹
193.	CHO+CH ₃ O ₂ = CH ₃ OOH+CO	5·10 ⁻¹¹
194.	CHO+C ₂ H ₅ O ₂ = C ₂ H ₅ OOH+CO	5·10 ⁻¹¹
195.	CH ₃ O+CH ₃ O = CH ₃ OH+CH ₂ O	1·10 ⁻¹⁰
196.	CH ₃ O+CH ₃ CO = CH ₃ OH+CH ₂ CO	1·10 ⁻¹¹
197.	CH ₃ O+CH ₃ CO = CH ₃ CHO+CH ₂ O	1·10 ⁻¹¹
198.	CH ₃ O+CH ₃ O ₂ = CH ₃ OOH+CH ₂ O	5·10 ⁻¹³
199.	CH ₃ O+C ₂ H ₅ O ₂ = C ₂ H ₅ OOH+CH ₂ O	5·10 ⁻¹³
200.	CH ₃ CO+CH ₃ CO = CH ₂ CO+CH ₃ CHO	1.5·10 ⁻¹¹
201.	CH ₃ CO+CH ₃ O ₂ = CH ₃ +CO ₂ +CH ₃ O	4·10 ⁻¹¹
202.	CH ₃ CO+C ₂ H ₅ O ₂ = C ₂ H ₅ +CO ₂ +CH ₃ O	4·10 ⁻¹¹
203.	CH ₃ O ₂ +CH ₃ O ₂ = 2CH ₃ O+O ₂	1.3·10 ⁻¹³
204.	CH ₃ O ₂ +C ₂ H ₅ O ₂ = CH ₃ O+C ₂ H ₅ O+O ₂	2·10 ⁻¹³
205.	C ₂ H ₅ O ₂ +C ₂ H ₅ O ₂ = 2C ₂ H ₅ O+O ₂	4·10 ⁻¹⁴
206.	CH ₂ OOH = CH ₂ O+OH	5·10 ⁴
207.	O ₂ +C ₂ H ₅ CO = CH ₃ CHO+CO+OH	3·10 ⁻¹²
208.	CH ₃ CHO+C ₂ H ₅ CO = C ₃ H ₈ CO+CHO	2.8·10 ⁻¹³
209.	O ₂ +CH ₃ CHOH = CH ₃ CHO+HO ₂	1.9·10 ⁻¹¹
210.	CH ₃ CHOH+O = CH ₃ CHO+OH	3.2·10 ⁻¹⁰
211.	CH ₃ CHOH+H = CH ₃ CHO+H ₂	8·10 ⁻¹¹
212.	CH ₂ CO+O = 2CHO	7·10 ⁻¹³
213.	CH ₂ CO+OH = CH ₂ OH+CO	1.2·10 ⁻¹¹
214.	C ₂ H ₅ O+O ₂ = CH ₃ CHO+HO ₂	1·10 ⁻¹⁴
215.	HOCH ₂ CH ₂ +H = CH ₃ CHO+H ₂	8.3·10 ⁻¹¹
216.	HOCH ₂ CH ₂ +O ₂ = CH ₃ CHO+HO ₂	3·10 ⁻¹²
217.	CH ₂ OH+O = OH+CH ₂ O	1.5·10 ⁻¹⁰
218.	CH ₂ OH+H = H ₂ +CH ₂ O	5·10 ⁻¹¹
219.	CH ₂ OH+O ₂ = HO ₂ +CH ₂ O	9.6·10 ⁻¹²
220.	CH ₂ OH+OH = H ₂ O+CH ₂ O	9.6·10 ⁻¹²
221.	CH ₂ OH+HO ₂ = H ₂ O ₂ +CH ₂ O	2·10 ⁻¹¹
222.	CH ₂ OH+CHO = CO+CH ₃ OH	2·10 ⁻¹¹
223.	CH ₂ OH+CHO = 2CH ₂ O	3·10 ⁻¹¹
224.	CH ₂ OH+CH ₃ O = CH ₃ OH+CH ₂ O	4·10 ⁻¹¹
225.	CH ₂ OH+C ₂ H ₅ O = C ₂ H ₅ OH+CH ₂ O	4·10 ⁻¹¹
226.	CH ₂ OH+CH ₃ = CH ₄ +CH ₂ O	1.4·10 ⁻¹⁰
227.	CH ₂ OH+C ₂ H ₅ = C ₂ H ₆ +CH ₂ O	4·10 ⁻¹²
228.	CH ₂ OH+C ₂ H ₅ = C ₂ H ₄ +CH ₃ OH	4·10 ⁻¹²
229.	CH ₂ OH+H ₂ = CH ₃ OH+H	1·10 ⁻¹³
230.	CH ₂ CHO+O ₂ = CH ₂ O+OH+CO	3·10 ⁻¹⁴
231.	H+CO ₂ = CO+OH	1·10 ⁻²⁹

Thus, slow oxidation of C₂H₂, CH₃COCH₃ and C₂H₅OH in stoichiometric and some lean mixtures with oxygen under the action of the nanosecond pulsed-periodic discharge has

been investigated experimentally. CO oxidation under the action of the discharge in the stoichiometric mixture with O_2 in the presence of small additions of H_2 has been investigated experimentally. The kinetics of slow oxidation of H_2 , CH_4 , C_2H_6 , C_2H_5OH , C_2H_2 , CH_3COCH_3 under the action of the nanosecond pulsed-periodic discharge in mixtures with oxygen at room temperature under nanosecond uniform discharge have been considered. The main role of $O(^1D)$ and OH-radical has been determined in the kinetics. Main paths of radicals and atoms creation in the discharge has been shown. The kinetic scheme for the H_2 , CH_4 , C_2H_6 and C_2H_5OH oxidation at room temperature under the nanosecond discharge action has been developed. The results of calculation using this scheme are in the good agreement with experimental results.

Chapter 4

The Experimental and Numerical Study of High-Temperature Kinetic of H_2 and $\text{C}_1\text{-C}_5$ PAI

4.1 Nanosecond gas discharge ignition of $\text{H}_2\text{-O}_2\text{-Ar}$ mixtures.

4.1.1 Theoretical analysis of ignition efficiency

To determine the region of parameters for the experiment, a detailed numerical analysis of the ignition efficiency under the action of a nanosecond discharge has been performed. Let us consider gas mixture at specified parameters (pressure, temperature, density). The discharge propagating through the mixture produces active particles. To estimate the influence of the fast ionization wave on combustion we have to calculate the density of active particles in the discharge. Taking into account that the discharge duration (40 ns in our case) is significantly smaller than the typical combustion time (microseconds), we consider the discharge as an initial step and calculate the processes in the discharge and the chemistry in the afterglow as two separate parts. Data on the concentrations of atoms and radicals produced in the discharge are taken as the initial data for high-temperature calculations in the afterglow.

Detailed experimental investigations of nanosecond discharge have proved⁹¹ that for the first several nanoseconds the electric field burst is observed in the ionization wave front, its maximum value being close to the electron runaway threshold or over it. For the following several tens of nanoseconds the field decreases from values corresponding to active excitation of the inner gas degrees of freedom to zero. It was shown⁹² that the intensive production of electrons, as well as the population of electron states take place behind the ionization wave front in “residual” fields (hundreds of V/(cm·Torr)). In the case of a relatively short discharge gap we can neglect the production of active particles in the discharge front and consider the formation of atoms and radicals only after the overlap of the electric gap.¹²⁴ The typical velocity of nanosecond discharge propagation is 5 – 10 cm/ns. For a 20 cm discharge gap, the time of the discharge propagation from the high-voltage electrode to the low-voltage one can be estimated as 2 – 4 ns, which is significantly smaller than the pulse duration.

To calculate the densities of active particles, one has to determine electron energy distribution function (EEDF) by solving Boltzmann equation for electrons. In the case of high electric fields, the exact solution of this equation requires statistical modelling.¹⁴ If we do not consider the FIW front, as it was mentioned above, we can use two-term approximation of Boltzmann equation.¹²⁵ For discharge calculations, we used standard BOLSIG software¹²⁰ or Gordeev solver.¹²⁶ Both codes calculate a stationary electron energy distribution function and a fractional energy deposited in different collisional processes. The input is a list of reduced electric fields E/N (here E is an electric field and N is a gas density) to be treated and the gas composition. The output is the densities of vibrationally and electronically excited particles, atoms and radicals dissociated via electronically excited states. The list of the processes used for EEDF computation for hydrogen-oxygen mixture is given in the Tables 4.1, 4.2. The excitation cross-sections were taken from^{127–129} for hydrogen, and from^{130–135} for oxygen, dissociation was treated in accordance with.¹⁰³ For the hydrogen molecule, the dissociation takes place via $b^3\Sigma_u^+$ and $a^3\Sigma_g^+$ electronically excited states, while for oxygen via $A^3\Sigma_u^+$ and $B^3\Sigma_u^-$ states. The concentrations of atoms and radicals created in the discharge were taken as the initial data for the high-temperature calculations. All other mixtures were considered in a similar way.

Table 4.1: Excitation of H_2 by electron impact. ΔE is a threshold of the process.

Process	ΔE , eV	Reference
$e + H_2 \rightarrow e + H_2(v = 1)$	0.516	¹²⁹
$e + H_2 \rightarrow e + H_2(v = 2)$	1.000	¹²⁹
$e + H_2 \rightarrow e + H_2(v = 3)$	1.500	¹²⁹
$e + H_2 \rightarrow e + H_2(rot)$	0.044	¹²⁹
$e + H_2 \rightarrow e + H_2(d^3\Pi_u)$	14.00	¹²⁸
$e + H_2 \rightarrow e + H_2(a^3\Sigma_g^+)$	11.80	¹²⁸
$e + H_2 \rightarrow e + H_2(b^3\Sigma_g^-)$	8.900	¹²⁸
$e + H_2 \rightarrow e + H_2(c^3\Pi_u)$	11.75	¹²⁸
$e + H_2 \rightarrow e + H_2(B^{1'}\Sigma_u^+)$	12.62	¹²⁸
$e + H_2 \rightarrow e + H_2(B^1\Sigma_u^+)$	11.30	¹²⁸
$e + H_2 \rightarrow e + H_2(E^1\Sigma_g^+)$	11.99	¹²⁸
$e + H_2 \rightarrow e + H_2(C^1\Pi_u)$	12.40	¹²⁸
$e + H_2 \rightarrow e + H_2(e^3\Sigma_u^+)$	12.83	¹²⁸
$e + H_2 \rightarrow e + e + H_2^+$	15.40	¹²⁹

The numerical code for the description of high-temperature ignition kinetics under the action of a high-voltage nanosecond discharge has been developed on the basis of a kinetic scheme¹³⁶ and the GRI-Mech 3.0 mechanism. CHEMKIN2 solver was used for calculations. Both kinetic schemes gave the same results for investigated mixtures. It should be noted that kinetics of the electronically excited particles is important in an afterglow of the pulsed nonequilibrium gas discharge, and the problem of influence of the excited particles on the ignition processes is under discussion now. But we included only ground state particles in our model. More explanation about this fact is given in the section “Results”.

In summary, the initial parameters of task were gas composition, initial temperature, and pressure. The discharge was assumed as a square pulse of the electric field at a given

Table 4.2: Excitation of O₂ by electron impact. ΔE is a threshold of the process.

Process	ΔE , eV	Reference
$e + O_2(j_1) \rightarrow e + O_2(j_2)$	0.005	¹³¹
$e + O_2 \rightarrow e + O_2(v = 1)$	0.193	¹²⁶
$e + O_2 \rightarrow e + O_2(v = 2)$	0.382	¹²⁶
$e + O_2 \rightarrow e + O_2(v = 3)$	0.569	¹²⁶
$e + O_2 \rightarrow e + O_2(v = 4)$	0.752	¹²⁶
$e + O_2 \rightarrow e + O_2(a^1\Delta_g)$	0.983	¹³¹
$e + O_2 \rightarrow e + O_2(b^1\Sigma_g^+)$	1.64	¹³¹
$e + O_2 \rightarrow e + O_2(B^3\Sigma_u^-)$	8.40	¹³¹
$e + O_2 \rightarrow e + O_2(A^3\Sigma_u^+)$	4.50	¹³¹
$e + O_2 \rightarrow e + O_2(C^3\Delta_u)$	6.87	¹³²
$e + O_2 \rightarrow e + O_2(9.9eV)$	9.90	¹³¹
$e + O_2 \rightarrow e + O_2(Rydberg)$	13.5	¹³¹
$e + O_2 \rightarrow O_2^-(X^2\Pi_g) \rightarrow O^-(^2P^0) + O(^3P)$	4.25	¹³³
$e + O_2 \rightarrow e + O^+ + O^-$	15.0	¹³³
$e + O_2 \rightarrow e + e + O(^3P) + O^+(^4S)$	18.0	¹³⁵

amplitude and with a duration of 40 ns. For test calculations, we have chosen the electric field value $E/N = 300$ Td ('Td', or Townsend, is used in the gas discharge physics, and $1 \text{ Td} = 0.33 \text{ V}/(\text{cm Torr}) = 10^{-17} \text{ V}\cdot\text{cm}^2$ at 20°C), which is typical for a nanosecond discharge after the breakdown front. For the first stage, we calculated EEDF, energy branching, and densities of atoms and radicals in the discharge. The mixture composition, including atom/radical density after the discharge action, and the gas temperature were taken as initial parameters for the calculations of the ignition problem. As a first approximation, we neglected the kinetics of electronically excited states in the afterglow. The final results were the kinetic curves of combustion species. Ignition delay in the calculations was defined by an temperature increase of 200 K.

As a result of the numerical modelling, the range of parameters where the system is most sensitive to the discharge action has been found. Figure 4.1 shows the results of the numerical calculations of the ignition delay time in a H₂-air stoichiometric mixture at a total pressure of $P = 1$ atm. These calculations were performed both for autoignition and for nanosecond discharge conditions. The case with zero excitation energy corresponds to the autoignition at the given temperature. The ignition delay time in the system is very sensitive to additional nonequilibrium gas excitation. Even an excitation with the energy $W = 4 \times 10^{-4} \text{ J}/\text{cm}^3$ causes a considerable decrease of the ignition delay time and the ignition temperature threshold. For the energy level of $W = 4 \times 10^{-1} \text{ J}/\text{cm}^3$ the ignition threshold shift reaches the value of 400 K. Thus, a discharge energy variation allows the ignition threshold value and ignition delay time in H₂-air mixture to be changed in a wide range.

For the CH₄-air mixture, the excitation under the action of the pulse discharge is substantially weaker than for the H₂-air mixture. The methane molecule has a relatively small cross-section for dissociation by electron impact. Besides, the methane density in the stoichiometric mixture with air is considerably lower, than the H₂ density. Therefore, the ignition threshold shift for CH₄-air mixtures is small at low values of discharge energies.

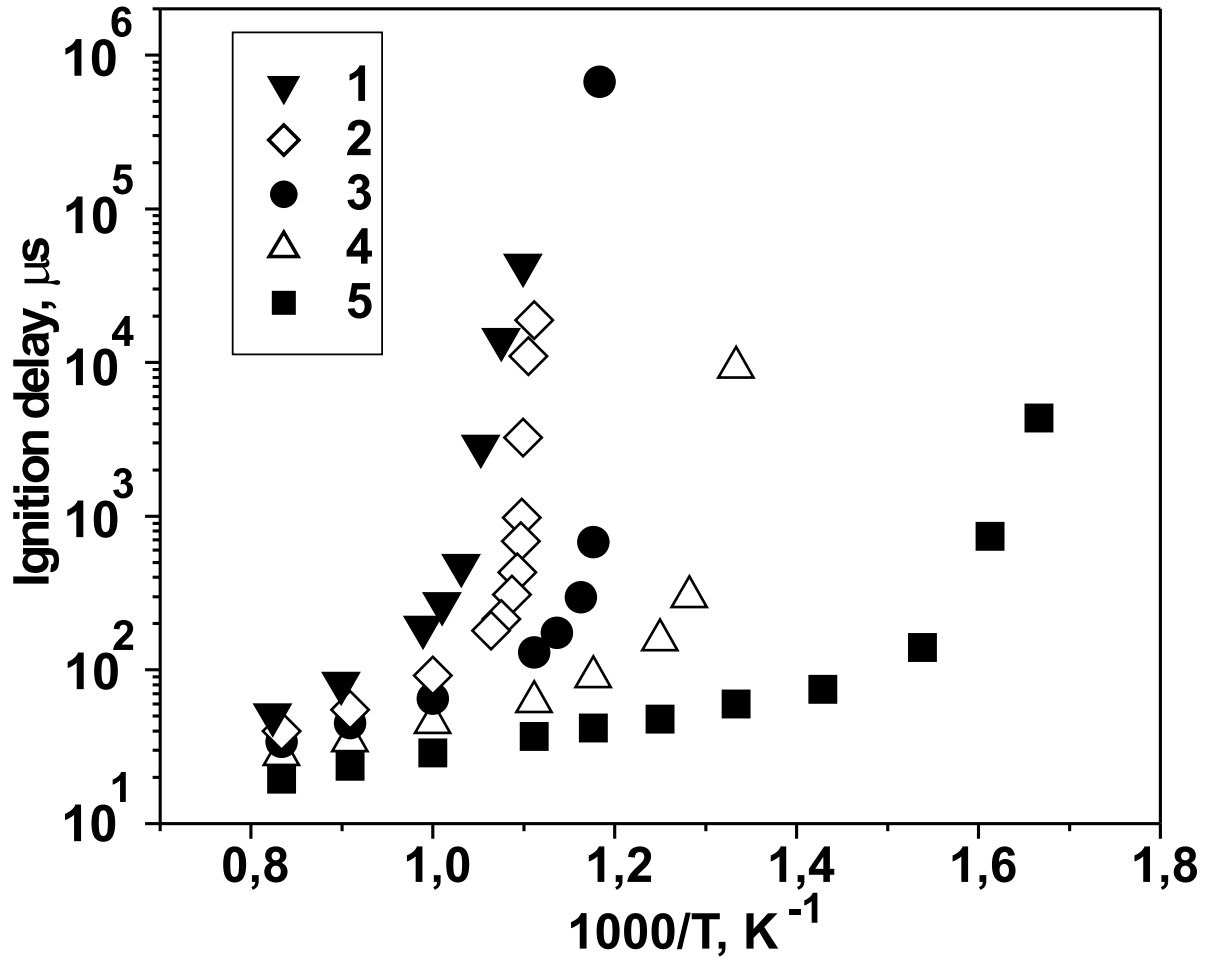


Figure 4.1: Calculated ignition delay time *vs* initial gas temperature. H_2 : O_2 : $\text{N}_2 = 29.6$: 14.8 : 55.6 mixture. $P = 1$ atm. Non-equilibrium excitation. $E/N=300$ Td. Different curves correspond to different energy consumption: 1 – 0 J/cm^3 (autoignition); 2 – $4 \cdot 10^{-4} \text{ J/cm}^3$; 3 – $4 \cdot 10^{-3} \text{ J/cm}^3$; 4 – $4 \cdot 10^{-2} \text{ J/cm}^3$; 5 – $4 \cdot 10^{-1} \text{ J/cm}^3$.

On the other hand, at a high discharge energy ($W = 0.4 \text{ J/cm}^3$), the ignition threshold shift exceeds 400 K in the temperature range investigated (Figure 4.2, the energy release is indicated in the figure).

It is interesting to compare these results with results obtained in the case of the equilibrium excitation, that is thermal heating. Figure 4.3 gives this analysis for the H_2 -air mixture. The ignition delay time changes even in the case of equilibrium excitation, where all degrees of freedom are heated simultaneously. However, at the same energy release, $W = 4 \times 10^{-3} \text{ J/cm}^3$, the gas excitation by a nonequilibrium discharge at reduced electric field $E/N=300$ Td leads to more pronounced decrease of the ignition threshold. This difference in efficiency of ignition by the FIW and by the heating depends upon a value of contributed energy (Figure 4.4). The nonequilibrium excitation is much more efficient at a low energy input. Physically this is clear: production of atoms and radicals without the additional heating of the system increases the reaction rate and significantly shifts the ignition delay. The influence of nonequilibrium energy input becomes the same

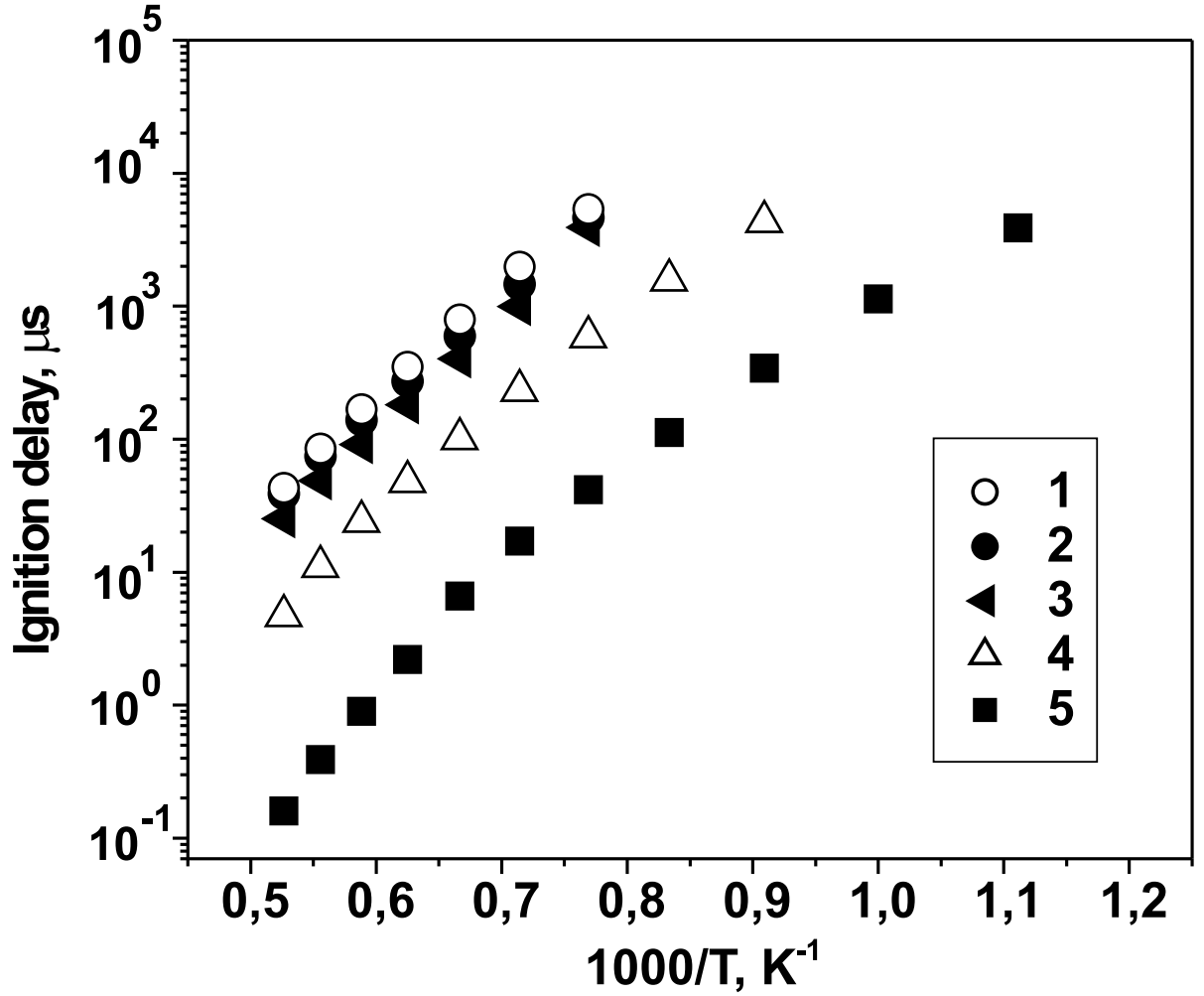


Figure 4.2: Calculated ignition delay time *vs* initial gas temperature. CH_4 : O_2 : N_2 = 9.4: 18.8: 71.8 mixture. $P = 1$ atm. Non-equilibrium excitation. $E/N=300$ Td. Different curves correspond to different energy consumption: 1 – 0 J/cm^3 (autoignition); 2 – 10^{-3} J/cm^3 ; 3 – 10^{-2} J/cm^3 ; 4 – 10^{-1} J/cm^3 ; 5 – $4 \cdot 10^{-1}$ J/cm^3 .

as the influence of heating at an energy input of 0.1 J/cm^3 . The typical energy input by the nanosecond discharge in our experiments was $10^{-3} - 5 \cdot 10^{-2}$ J/cm^3 ; it was in the region, where thermal ignition due to additional heating is less efficient than the effect of the gas discharge.

In addition, we analyzed the influence of the electric field value in the discharge on the ignition delay time (Figure 4.5). We have concluded that the region of reduced electric fields, where gas excitation is the most efficient, from the point of view of ignition initiation, is from 250 to 350 Td. This value coincides with the reduced electric field values in the region of the maximum energy release in the fast ionization wave.⁹⁴

So, the preliminary numerical modelling has predicted the range of temperatures and electric fields, which are suitable for an experimental check of the ignition delay decrease. The most interesting region of temperatures for experiments is 800-1000 K for a hydrogen-containing mixture and 1200-1800 K for one containing methane. This region can easily

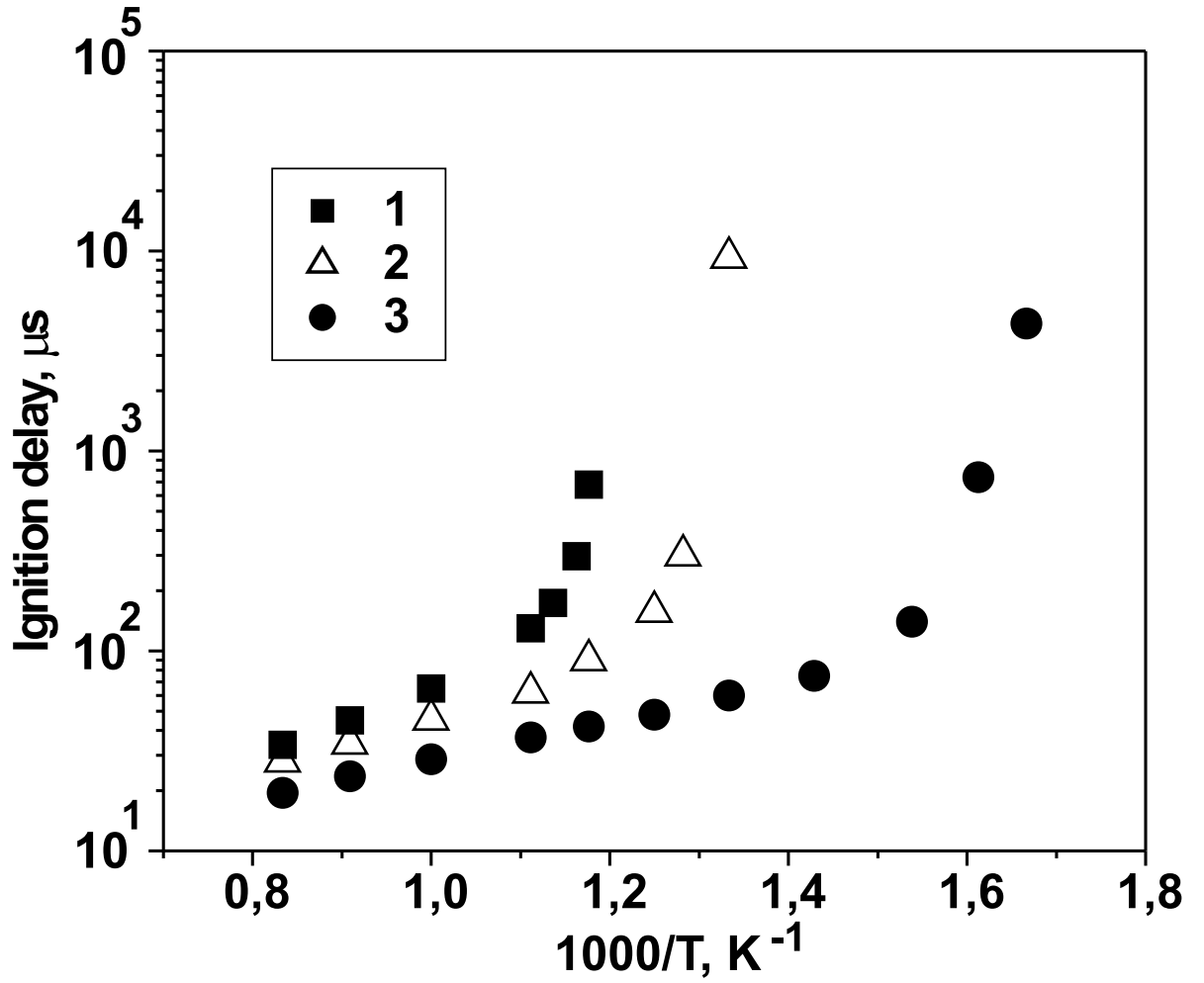


Figure 4.3: Calculated ignition delay time *vs* initial gas temperature for thermal and nonequilibrium plasma excitation. H_2 : O_2 : $\text{N}_2 = 29.6$: 14.8 : 55.6 mixture. $P = 1$ atm. Total energy release $W = 4 \times 10^{-3}$ J/cm³. Reduced electric field is $E/N = 300$ Td. 1 – autoignition; 2 – equilibrium excitation; 3 – nonequilibrium excitation.

be reached by using shock tube technique.¹³⁷

4.1.2 Description of experiment

Shock tube

The apparatus used to investigate the fast homogeneous ignition of combustible mixtures (Figure 4.6) consists of a shock tube (ShT), discharge cell (DC) connected to the shock tube, the gas evacuation and supply system, the system of discharge initiation, and the diagnostic system.

The shock tube is made of stainless steel and has a square cross section of 25x25 mm with a 1.6 m working channel length. The high pressure cell (HPC) length is 60 cm. There are 2 pairs of diagnostic optical windows along the stainless steel working channel. The windows were aligned with respect to inner shock tube walls and walls were polished

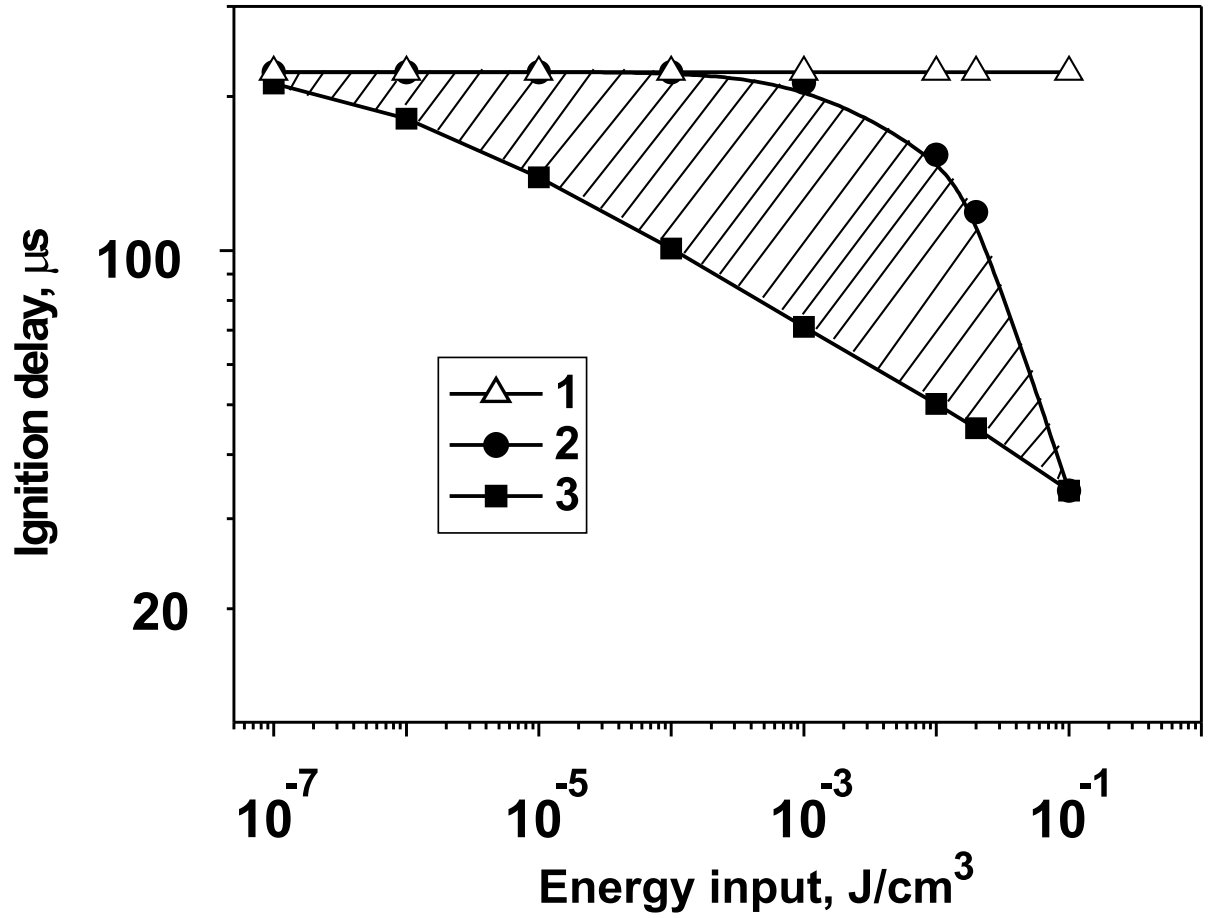


Figure 4.4: Calculated ignition delay time *vs* energy input for thermal and nonequilibrium plasma excitation. H_2 : O_2 : $\text{N}_2 = 29.6$: 14.8 : 55.6 mixture. $P = 1$ atm; $T_0 = 1000$ K; $E/N = 300$ Td. 1 – autoignition (corresponds to zero energy input); 2 – equilibrium excitation; 3 – nonequilibrium excitation ($E/N = 300$ Td, $t = 40$ ns).

to decrease disturbances of flow. The last section of the shock tube is made from a transparent dielectric material. We used two different sections in our experiments. The first one is made from a 10 mm thick quartz plates surrounded by an organic glass 20 mm in thickness and has twelve quartz optical windows for an emission output. The second one is made from an organic glass and has eight optical windows (6 of them are made from quartz and 2 are made from MgF_2). Both sections have 25x25 mm the inner square cross-section and are 20 cm in length. The results were the same for both sections, therefore we shall not specify which of sections was used. The uniform nanosecond discharge in the form of the fast ionization wave was organized in the dielectric section; the end plate (EP) of the shock tube is a high-voltage electrode of the discharge system; the electric circuit is closed via grounded stainless steel driven section of the shock tube.

Discharge initiation

The nanosecond discharge initiation was synchronized with the reflected shock wave coming to the observation point (point A in the figure) by means of a microsecond pulse

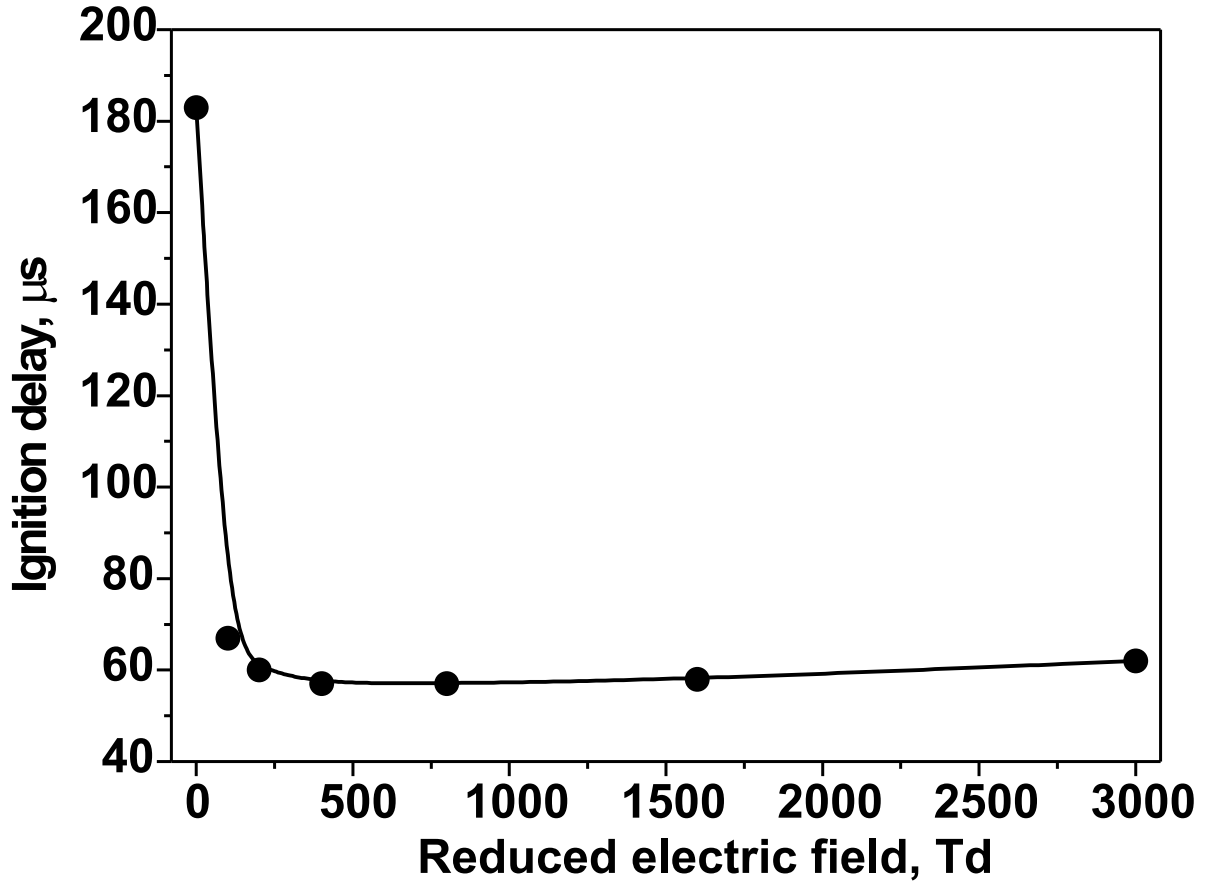


Figure 4.5: Calculated ignition delay time *vs* reduced electric field. H_2 : O_2 : $\text{N}_2 = 29.6$: 14.8 : 55.6 mixture. $P = 1$ atm; $T_0 = 1000$ K. Energy release is $W = 4 \times 10^{-3}$ J/cm³; $t = 40$ ns.

generator (PG). To obtain high-voltage pulse we used Marks-type generator. The GIN-9 high voltage Marks generator (HVG) consists of 10 stages. To provide the spark gap operation, the pulsed voltage generator is filled with nitrogen at a pressure of 3 atm, which provides a starting voltage range from 100 to 160 kV. To sharpen the voltage impulse coming from the generator to the discharge gap, a forming ferrite line of wave resistance $Z = 40$ Ohm is used. At the forming line output, the voltage rise rate is 8 kV/ns, which provides the formation of gas discharge in the form of a fast ionization wave in the dielectric section of the shock tube. The velocity of the ionization wave front propagation is $10^9 - 10^{10}$ cm/s with a dependence on parameters.

Vacuum system and mixtures used

To evacuate the system, rotary and diffusive pumps were used. Having been pumped the system was filled with investigated gas mixture. We used gas mixtures (for details see Table 4.3) of methane or hydrogen with oxygen diluted with Ar or He in order to reach the desired pressure and temperature behind the reflected shock wave. The initial pressure in the driven section was varied from 5 to 40 Torr. Dilution by Ar or He increased the

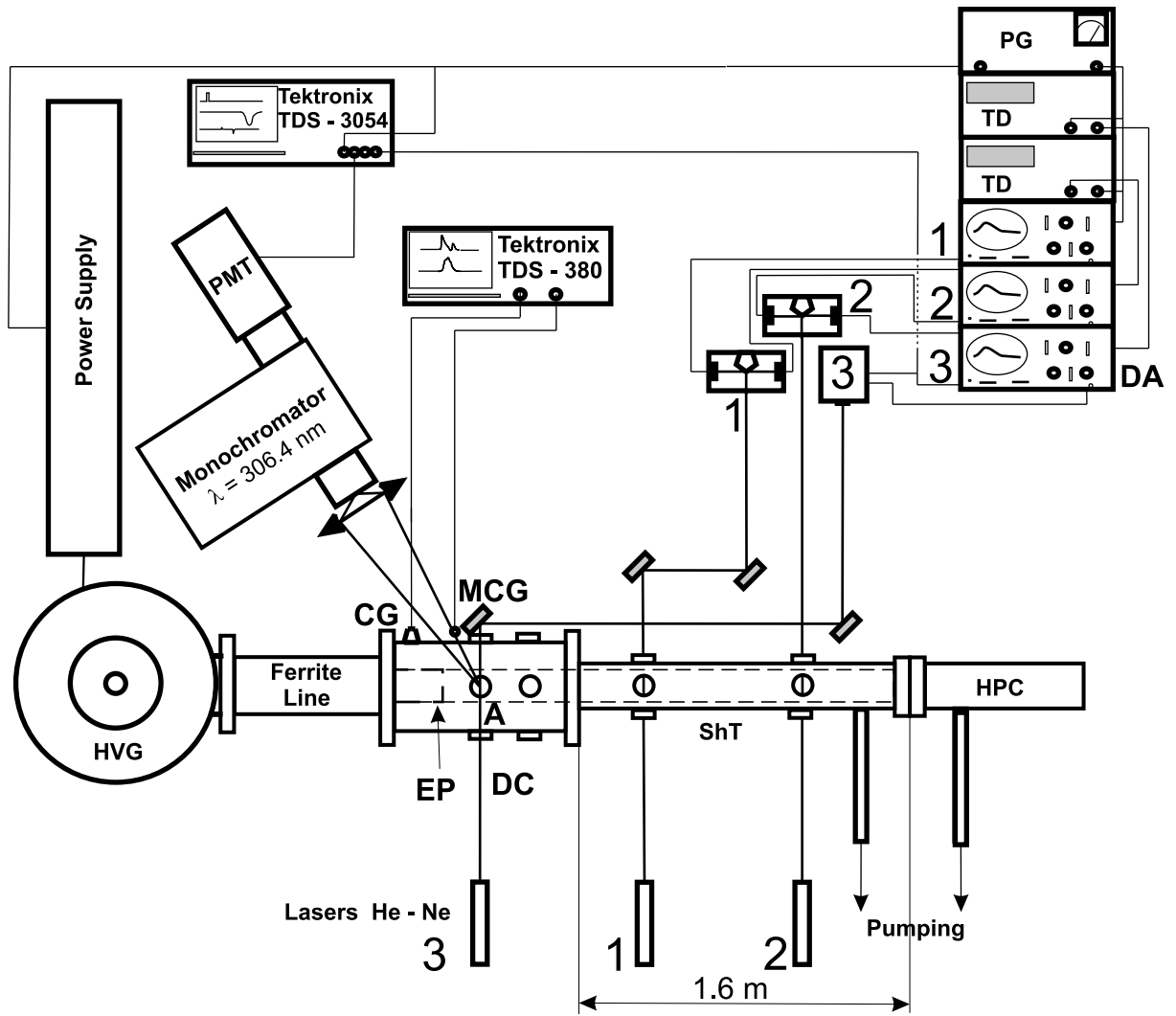


Figure 4.6: Scheme of the experimental setup.

specific heat ratio, and allowed higher temperatures to be reached behind the reflected shock wave. He, dry air, or CO_2 were used as driver gases. In some experiments special perforated flow plate was inserted between high pressure section and driven section before the diaphragm. This plate allowed us to decrease the shock wave velocity at the same initial conditions.

Table 4.3: Composition of the gas mixtures.

$\text{H}_2, \%$	$\text{O}_2, \%$	He, %	Ar, %
12	6	—	82
12	6	82	—

Diagnostic system

Diagnostic system consists of three parts. They are the system monitoring shock wave parameters, the system monitoring the nanosecond discharge electrical parameters and the system registering ignition.

The system monitoring the shock wave parameters includes the system measuring the incident and reflected shock wave velocity by the laser schlieren technique and the system controlling the initial pressure. The schlieren system consists of 3 He-Ne lasers mounted along the shock tube at different points and 3 pairs of photodiodes with differential analyzers (DA); the time delays between points 2-1 and 1-3 along the tube were registered by time-delay analyzers (TD) and monitored by the Tektronix TDS 3054 oscilloscope. From the initial gas mixture composition, the initial pressure and velocity of the incident shock wave, we determined the pressure, gas density and temperature behind the reflected shock wave by solving the conservation laws, assuming a full relaxation and no chemical reactions. Thermodynamic data were taken from.¹³⁸

The system monitoring the nanosecond discharge electrical parameters includes a calibrated magnetic current gauge (MCG) to control current pulse and a capacitance gauge (CG) over the high-voltage electrode to monitor the high-voltage pulse shape and amplitude. We placed an additional capacitive gauge near the observation point (12 cm apart from the CG) to measure the velocity of the discharge development. The signals from electrical gauges were monitored by using a Tektronix TDS 380 oscilloscope. All cables were additionally screened and oscilloscopes were placed into the shielded room to diminish high-frequency electrical noise. Figure 4.7 represents the typical behavior of voltage on the electrode, voltage and current near the observation point. Velocity of the fast ionization wave propagation can be determined from the signals from capacitance gauges. In this case, the velocity is about of 10 cm/ns. It is clearly seen that maximal energy consumption takes place during first 20–30 ns, when the current is high enough. Under these conditions, the formation of active particles in the discharge and ignition/combustion can be considered as successive processes from the point of view of both numerical modelling and the experiment.

The combustion process was investigated by using emission spectroscopy. Emission originating due to the combustion process was monitored in the direction perpendicular to the shock tube axis at a distance of 55 mm from the end plate (point A) with the use of a MDR-23 monochromator (1.2 nm mm^{-1} , 1.2 m focal length, 1200 mm^{-1} , LOMO), a FEU-100 photomultiplier (MELZ), and a Tektronix TDS 3054 oscilloscope. The observation point is rather far from the end plate. To decrease influence of boundary layers it is more usual for kinetic measurements to be made in the vicinity of end plate. However we had to choose position of the observation point in such way to avoid electric field disturbances caused by high voltage electrode. Accuracy of the temperature determination on the basis of the ideal shock tube theory will be discussed in the section “Results”. We measured the OH emission ($\lambda = 306.4 \text{ nm}$, $A^2\Sigma(v' = 0) \rightarrow X^2\Pi(v'' = 0)$ transition) in a wide range of experimental conditions: mixtures of various compositions, temperature variations from 750 to 2250 K, pressure variations from 0.3 to 2.3 atm. The same experiments were repeated under a discharge action, at high-voltage pulse amplitude variations from 100 to 160 kV on the electrode and a pulse duration of about 30-40 ns at a half-height of an amplitude (FWHM).

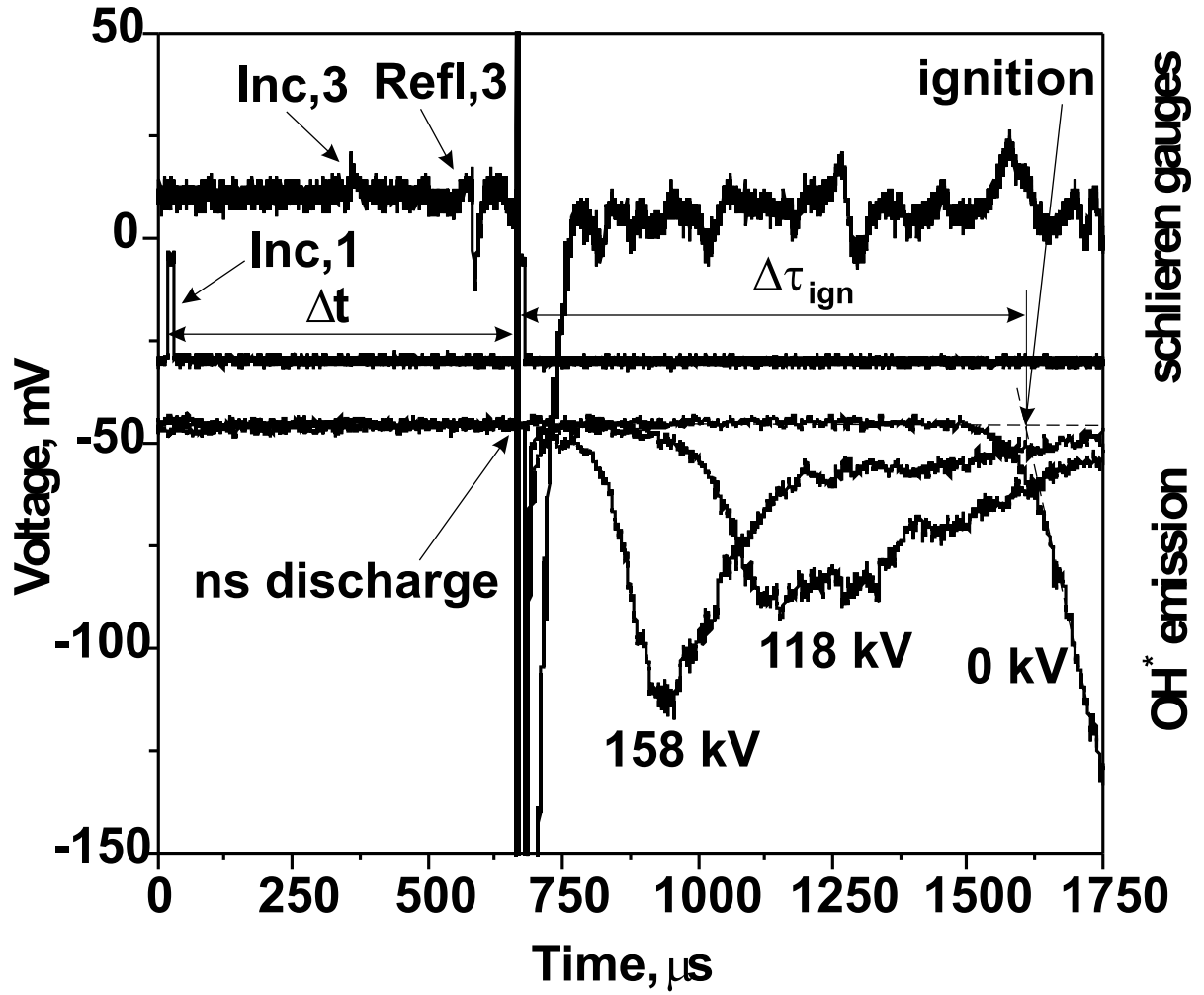


Figure 4.7: Typical behavior of synchronized signals from the N 3 schlieren gauge, synchrogenerator and photomultiplier at different amplitudes of high-voltage pulse. Mixture H_2 : O_2 : N_2 : Ar = 6: 3: 11: 80.

Synchronization

The typical behavior of the synchronized signals from the N 3 schlieren gauge, the synchrogenerator, and the photomultiplier at different amplitudes of high-voltage pulse from the generator is represented in Figure 4.8. Signals from different gauges are shifted along y -axis relative to each other for convenience. The upper curve represents a signal from the N 3 schlieren gauge, placed at the observation point. Peaks corresponding to incident (marked with “Inc,3”) and reflected (“Refl,3”) shock waves are well-pronounced. The second curve corresponds to synchrosignal which correlates with the incident wave coming to the N 1 schlieren gauge (the time moment is indicated as “Inc,1” in the figure). A variable delay Δt allows the adjustment of the discharge initiation so that discharge starts after the reflected shock wave coming to the point A. The time interval between the signal from the schlieren gauge and the initiation of discharge was significantly smaller than the ignition delay in the autoignition case for the same temperature. As a rule, this

time (between points “Refl.,3” and “ns discharge” in the figure) was 20–40 μs .

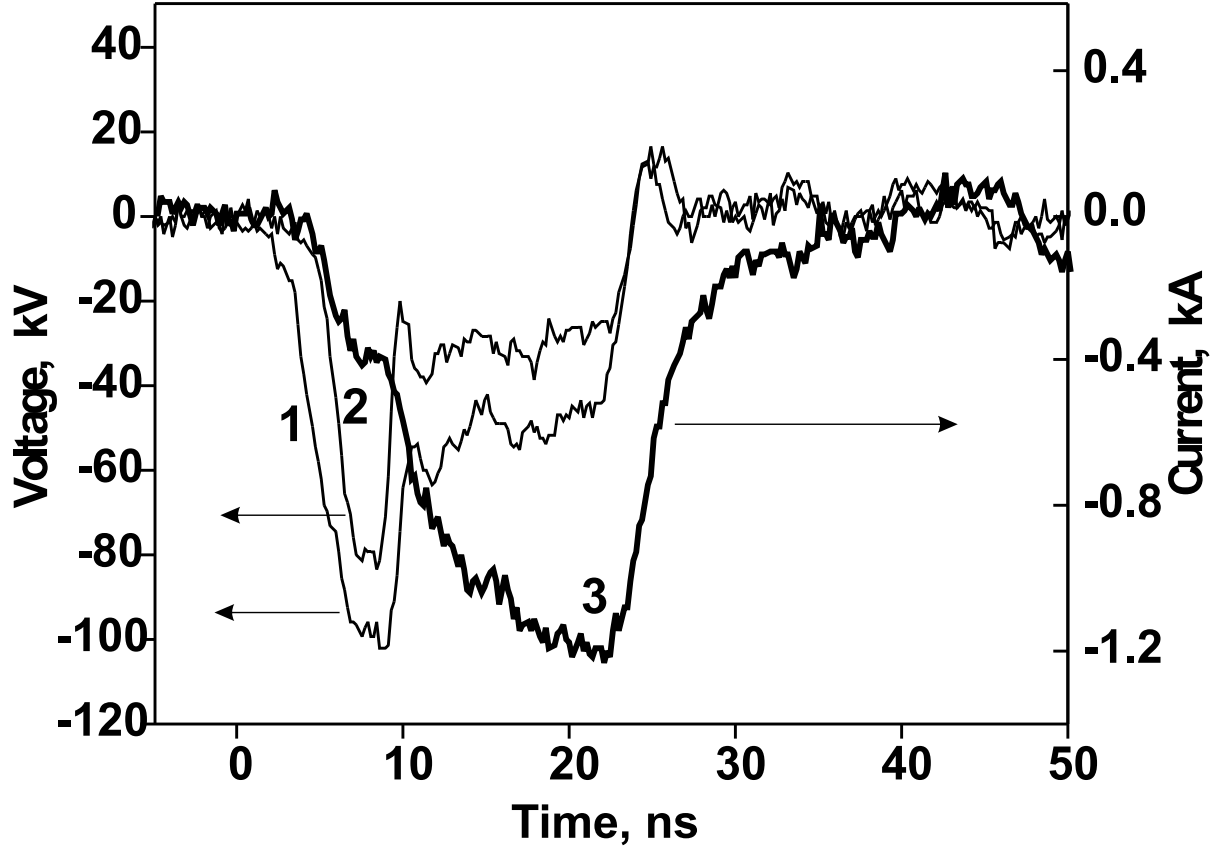


Figure 4.8: Typical voltage on the electrode (1), voltage (2) and current (3) at the observation point.

The sharp narrow peak at 660 μs is the electrical noise and OH emission from the discharge. After this peak we observe an OH radical emission due to the combustion processes. For all the cases, ignition delay time $\Delta\tau$ was determined as a time delay between the last physical action (that is, the reflected shock wave signal from the N 3 schlieren gauge in a case of autoignition or the discharge initiation when the nanosecond discharge being used) and the start of OH emission. The ignition delay decreases under the action of the FIW, the higher the voltage, the shorter the delay. It has to be indicated that in this example the ignition delay time for autoignition exceeds operating time for our system, and we represent this result to demonstrate the wide range of the discharge influence. The operating time was $t_{max} \approx 400 - 500 \mu\text{s}$. In the figures we have represented all obtained points, even those for which ignition delay time $\tau_{ign} > t_{max}$, to give reference points for the comparison with the ignition by the nanosecond discharge.

ICCD PicoStar HR12 camera system for spatial/temporal discharge dynamics measurements

ICCD camera PicoStar HR12 was used to obtain discharge image in a hot mixture with high temporal resolution. The wavelength sensitivity of the optical system was 300-

800 nm. We obtained integral in spectra images. The scheme of the camera system is represented in Fig. 4.9. The gate was 1 ns for nanosecond images of the discharge and 30 ms for microsecond images of the combustion.



Figure 4.9: LaVision ICCD camera PicoStar HR12 used in experiments for analysis of homogeneity of the discharge development and ignition initiation

The PicoStar HR12 is a state-of-the-art intensified gated/modulated CCD camera system. It incorporates a very high trigger rate gated intensifier intended for applications such as fluorescence lifetime imaging and time resolved spectroscopy. Its gate pulse driver has a bandwidth of 1 GHz and it has internal pulse forming circuitry to provide gate widths to less than 200 ps at trigger rates from single shot to greater than 110 MHz. It features an internal micro-controller with a front panel LCD display and keypad for all functions (except analogue input attenuation level). In addition it has an RS232 interface to allow

remote operation. It is able to provide RF modulation of the intensifier gain at frequencies up to 1 GHz. The intensifier and the CCD are provided in a remote housing with a flexible connection to the respective control units. The control units are self contained and include trigger input conditioning circuitry, intensifier high voltage supplies and protection, gain control, bias circuitry and remote computer control. All camera functions (gate width, timing, gain, CCD-exposure time, binning, skipping, windowing etc.), peripheral devices as well as image acquisition and processing are controlled via high performance DaVis software package.

General system specifications

- Gate width 200ps - 1ms
- Sensitivity 70 counts/photoelectron @ max. gain
- System dynamic > 2000 : 1
- Spatial resolution 8-12 lp/mm
- Spectral range 200-800nm (S20 photocathode types)

CCD Chip and control unit

- Sensor Interline Progressive Scan with "lens-on-chip"
- Active image array VGA 640 (H) x 480 (V)
- Pixel size 9.9 μm x 9.9 μm
- Scan area 6.3 mm x 4.8 mm
- Full well capacity 35,000 e-
- Average dark current < 0.1 e-/pixel \times sec
- Digitization 12 bit
- Pixel readout rate 12.5 MHz
- Readout noise > 2 counts (13...14 e)
- Frame rate > 25 frames/s
- Binning Horizontal (1...8), Vertical (1...32); ROI (min. 32x32 pixel)
- Cooling 2-stage Peltier with forced air cooling, -15 C
- Exposure control var. exposure time (1ms-1000s), start and timing via TTL
- Camera interface data transfer (FOL), control output, trigger input, gate disable

Image Intensifier Head and Control Unit

- Design 2nd gen. proximity focussed, single stage MCP
- Diameter 18 mm
- Coupling to CCD 2:1 Relay lens
- Photocathode S20
- Phosphor P43
- Operating modes:
 - Slave
Intensifier gate is slaved to a logic input (TTL or ECL). trigger input: TTL or ECL; duty cycle: 5%; gate voltage: 50 V gate width: < 0.2 ns - 1 ms; spatial resolution: 15 lp/mm (typ.)
 - Slave(high duty)
Intensifier gate is slaved to a logic input (TTL or ECL) but the gate voltage is reduced to allow a greater duty cycle.
trigger input: TTL or ECL; duty cycle: 50%; gate voltage: 20 V gate width: < 0.2 ns - 1ms; spatial resolution: 15 lp/mm (typ.)
 - Comb
The input trigger signal is converted to a comb of impulses internally and this is fed to the gate circuit. The trigger rate is up to 110 MHz. This mode is most suitable for use with mode locked laser sources and will produce a gate width less than 300ps at the laser frequency.
trigger input:
sinusoid, TTL or ECL; max duty cycle: 50%; gate voltage: 30 V gate width: < 0.3 ns - 1ns; spatial resolution: 15 lp/mm (typ.)
 - Gain Modulation
input sinusoid, TTL or ECL; 2V p-p into 50 ohm AC-coupled, input frequency 1MHz - 1GHz, max duty cycle 50%, switched voltage 20V, spatial resolution 10 lp/mm
 - DC
Active while the DC button is pressed.
- Jitter < 20 ps typical
- Intrinsic delay < 30 ns typical

DaVis software

single and continuous image grabbing, burst mode, powerful image and data processing tools, 3D onscreen graphics, process control via macro programs, binning, skipping and windowing functions, system integration features such as TTL synchronization with laser, and control of e.g. spectrograph, stepper motor, light chopper, filter wheel, shutter, oscilloscope and other devices. Communications: RS232 and GPIB.

4.1.3 Ignition delay time change in H₂-O₂ mixture by pulsed discharge

Typical data from capacitive detector and magnetic current detector are given in the Fig.4.8. The electric field was determined as U_2-U_1/l , where l is a distance between the capacitive detectors. The energy input was calculated integrating UI product by time.

The Table 4.4 gives the gas parameters (pressure, temperature and density) behind the reflected shock wave for different experimental regimes. In experiments where driver gas is marked with †, a flow plate was used. The discharge development, at given parameters of the generator, is most efficient at gas densities of about of 10^{18} cm^{-3} . At this gas number density, the energy consumption in the discharge is maximal. A decrease of the pressure P_5 , and, consequently, of the number density of the particles from $\sim 10^{19}$ to 10^{18} cm^{-3} , leads to higher energy consumption, and, as a result, to a significant decrease in the ignition delay.

Table 4.4: Parameters of the gas mixtures behind the reflected shock wave.

Mixture	Driver gas	T_5 , K	P_5 , atm	$^*\tau_0$, μs	τ_+ , μs	τ_- , μs
H ₂ -O ₂ -Ar	Air	1391	0.31	65.5	-	-
H ₂ -O ₂ -Ar	Air	1365	0.30	-	< 2	-
H ₂ -O ₂ -Ar	Air	1278	0.40	102.9	-	-
H ₂ -O ₂ -Ar	Air	1268	0.39	-	< 2	-
H ₂ -O ₂ -Ar	Air	1200	0.48	-	< 2	-
H ₂ -O ₂ -Ar	Air	1192	0.47	160.3	-	-
H ₂ -O ₂ -Ar	Air	1146	0.55	-	28.6	-
H ₂ -O ₂ -Ar	Air	1138	0.55	203.4	-	-
H ₂ -O ₂ -Ar	Air	1136	0.54	222.7	-	-
H ₂ -O ₂ -Ar	Air	1126	0.54	-	33.6	-
H ₂ -O ₂ -Ar	Air	1097	0.51	-	36.6	-
H ₂ -O ₂ -Ar	Air	1056	0.60	340.2	-	-
H ₂ -O ₂ -Ar	Air	1056	0.60	-	73.1	-
H ₂ -O ₂ -Ar	Air	1017	0.45	449.9	-	-
H ₂ -O ₂ -Ar	CO ₂	1170	0.23	339.9	-	-
H ₂ -O ₂ -Ar	CO ₂	1168	0.26	312.4	-	-
H ₂ -O ₂ -Ar	CO ₂	1155	0.25	347.5	-	-
H ₂ -O ₂ -Ar	CO ₂	1146	0.22	-	< 2	-
H ₂ -O ₂ -Ar	CO ₂	1129	0.24	-	< 2	-
H ₂ -O ₂ -Ar	CO ₂	1088	0.33	432.7	-	-
H ₂ -O ₂ -Ar	CO ₂	1086	0.33	-	< 2	-
H ₂ -O ₂ -Ar	CO ₂	1075	0.40	421.6	-	-
H ₂ -O ₂ -Ar	CO ₂	1061	0.34	505.2	-	-
H ₂ -O ₂ -Ar	CO ₂	1059	0.34	-	32.2	-
H ₂ -O ₂ -Ar	CO ₂	1019	0.36	-	69.7	-
H ₂ -O ₂ -Ar	CO ₂	1007	0.35	742.6	-	-
H ₂ -O ₂ -Ar	CO ₂	961	0.52	-	107.5	-

Table 4.4: Parameters of the gas mixtures behind the reflected shock wave.

Mixture	Driver gas	T_5 , K	P_5 , atm	$^*\tau_0$, μs	τ_+ , μs	τ_- , μs
H ₂ -O ₂ -Ar	CO ₂	956	0.44	820.1	-	-
H ₂ -O ₂ -Ar	CO ₂	945	0.45	-	126.8	-
H ₂ -O ₂ -Ar	CO ₂	945	0.57	-	152.5	-
H ₂ -O ₂ -Ar	CO ₂	938	0.50	881.3	-	-
H ₂ -O ₂ -Ar	CO ₂	901	0.59	-	212.6	-
H ₂ -O ₂ -Ar	CO ₂	883	0.62	1020.1	-	-
H ₂ -O ₂ -Ar	CO ₂	858	0.67	-	325.8	-
H ₂ -O ₂ -Ar	CO ₂	855	0.58	-	160.6	-
H ₂ -O ₂ -Ar	CO ₂	853	0.72	-	521.3	-
H ₂ -O ₂ -Ar	CO ₂	823	0.73	-	523.8	-
H ₂ -O ₂ -Ar	CO ₂ [†]	1068	0.32	-	< 2	-
H ₂ -O ₂ -Ar	CO ₂ [†]	1040	0.30	-	-	< 2
H ₂ -O ₂ -Ar	CO ₂ [†]	1023	0.39	-	-	< 2
H ₂ -O ₂ -Ar	CO ₂ [†]	1013	0.38	-	23.4	-
H ₂ -O ₂ -Ar	CO ₂ [†]	990	0.45	-	-	45.6
H ₂ -O ₂ -Ar	CO ₂ [†]	986	0.44	-	54.6	-
H ₂ -O ₂ -Ar	CO ₂ [†]	960	0.50	-	-	84.9
H ₂ -O ₂ -Ar	CO ₂ [†]	946	0.49	-	150.8	-
H ₂ -O ₂ -Ar	CO ₂ [†]	916	0.53	-	-	130.5
H ₂ -O ₂ -Ar	CO ₂ [†]	911	0.55	-	223.6	-
H ₂ -O ₂ -Ar	CO ₂ [†]	906	0.52	-	256.4	-
H ₂ -O ₂ -Ar	CO ₂ [†]	896	0.60	-	238.4	-
H ₂ -O ₂ -Ar	CO ₂ [†]	888	0.57	-	-	169.6
H ₂ -O ₂ -Ar	CO ₂ [†]	878	0.65	-	-	261.8
H ₂ -O ₂ -Ar	CO ₂ [†]	877	0.64	-	345	-
H ₂ -O ₂ -Ar	CO ₂ [†]	866	0.66	-	427.4	-
H ₂ -O ₂ -Ar	CO ₂ [†]	863	0.61	-	-	261
H ₂ -O ₂ -Ar	CO ₂ [†]	858	0.67	-	-	285.3
H ₂ -O ₂ -Ar	CO ₂ [†]	852	0.67	-	407.4	-
H ₂ -O ₂ -Ar	CO ₂ [†]	851	0.67	-	-	524.4
H ₂ -O ₂ -Ar	CO ₂ [†]	831	0.61	-	-	539.3
H ₂ -O ₂ -He	He [†]	920	0.48	-	36	-
H ₂ -O ₂ -He	He [†]	914	0.34	-	-	< 2
H ₂ -O ₂ -He	He [†]	902	0.67	-	-	76.9
H ₂ -O ₂ -He	He [†]	882	0.42	-	-	40.6
H ₂ -O ₂ -He	He [†]	873	0.54	-	59.3	-
H ₂ -O ₂ -He	He [†]	856	0.61	-	56.3	-
H ₂ -O ₂ -He	He [†]	849	0.48	-	-	69.7
H ₂ -O ₂ -He	He [†]	839	0.49	-	-	78.5

Table 4.4: Parameters of the gas mixtures behind the reflected shock wave.

Mixture	Driver gas	T_5 , K	P_5 , atm	$^*\tau_0$, μs	τ_+ , μs	τ_- , μs
H ₂ -O ₂ -He	He [†]	837	0.52	-	-	87.7
H ₂ -O ₂ -He	He [†]	835	0.62	-	124	-
H ₂ -O ₂ -He	He [†]	825	0.53	-	-	99.9
H ₂ -O ₂ -He	He [†]	820	0.53	-	100.6	-
H ₂ -O ₂ -He	He [†]	816	0.65	-	133	-
H ₂ -O ₂ -He	He [†]	805	0.61	-	-	230.3
H ₂ -O ₂ -He	He [†]	798	0.59	-	166	-
H ₂ -O ₂ -He	He [†]	797	0.63	-	-	171.1
H ₂ -O ₂ -He	He [†]	789	0.47	-	117.9	-
H ₂ -O ₂ -He	He [†]	788	0.54	-	-	188.2
H ₂ -O ₂ -He	He [†]	785	0.56	-	-	182.3
H ₂ -O ₂ -He	He [†]	781	0.65	-	274.4	-
H ₂ -O ₂ -He	He [†]	774	0.66	-	315	-
H ₂ -O ₂ -He	He [†]	761	0.62	-	-	359.1
H ₂ -O ₂ -He	He [†]	749	0.58	-	-	372.1

* In the Table, τ_0 is a delay time for autoignition, τ_+ is a delay time in the case of ignition by nanosecond pulse of positive polarity with the amplitude of 160 kV, τ_- is a delay time in the case of ignition by nanosecond pulse of negative polarity with the amplitude of 160 kV.

In the case where we have relatively low gas number densities, we can expect to shift the ignition curve (the dependence of ignition delay time τ upon temperature) to as low of temperatures as possible. We carried out experiments with different mixtures, high pressure chamber gases, and diaphragms trying to reach the particle number densities behind the reflected shock wave, which would be the most efficient for the discharge development. To give an idea about the gas number densities, Figure 4.10 represents the gas density behind the reflected shock wave for different mixtures. It is clearly seen that it is possible to vary the parameters of the system to handle the gas density. The arrow indicates the direction of the gas number density decrease. We can change the high pressure gas, add a flow plate, or change the gas for dilution. As a result, the curve $\rho_5(T)$ will shift to the left. The lowest temperature obtained in these experiments was about of 750 K, when the mixture H₂: O₂: He = 12: 6: 82 was ignited (Figure 4.11). In general, there are two ways to make ignition more efficient in this region of parameters: try to decrease the density to the values indicated by the hatched circle in the Figure 4.10 or to increase the high voltage amplitude. We considered both of them above.

We have also investigated the difference in the influence of the positive and negative polarity pulses on the ignition. It is well-known that for both polarities, discharge develops from the high-voltage electrode to the low-voltage one,⁸⁶ but the start conditions, the breakdown propagation velocity, the electric field which is realized in the discharge, and other parameters strongly depend upon the polarity.¹³⁹ Figure 4.11 gives an example of ignition delays obtained at different polarities of the electric pulse. For the H₂: O₂: Ar = 12: 6: 82 mixture, the difference in ignition threshold is 30-40 K, whereas for H₂: O₂: He

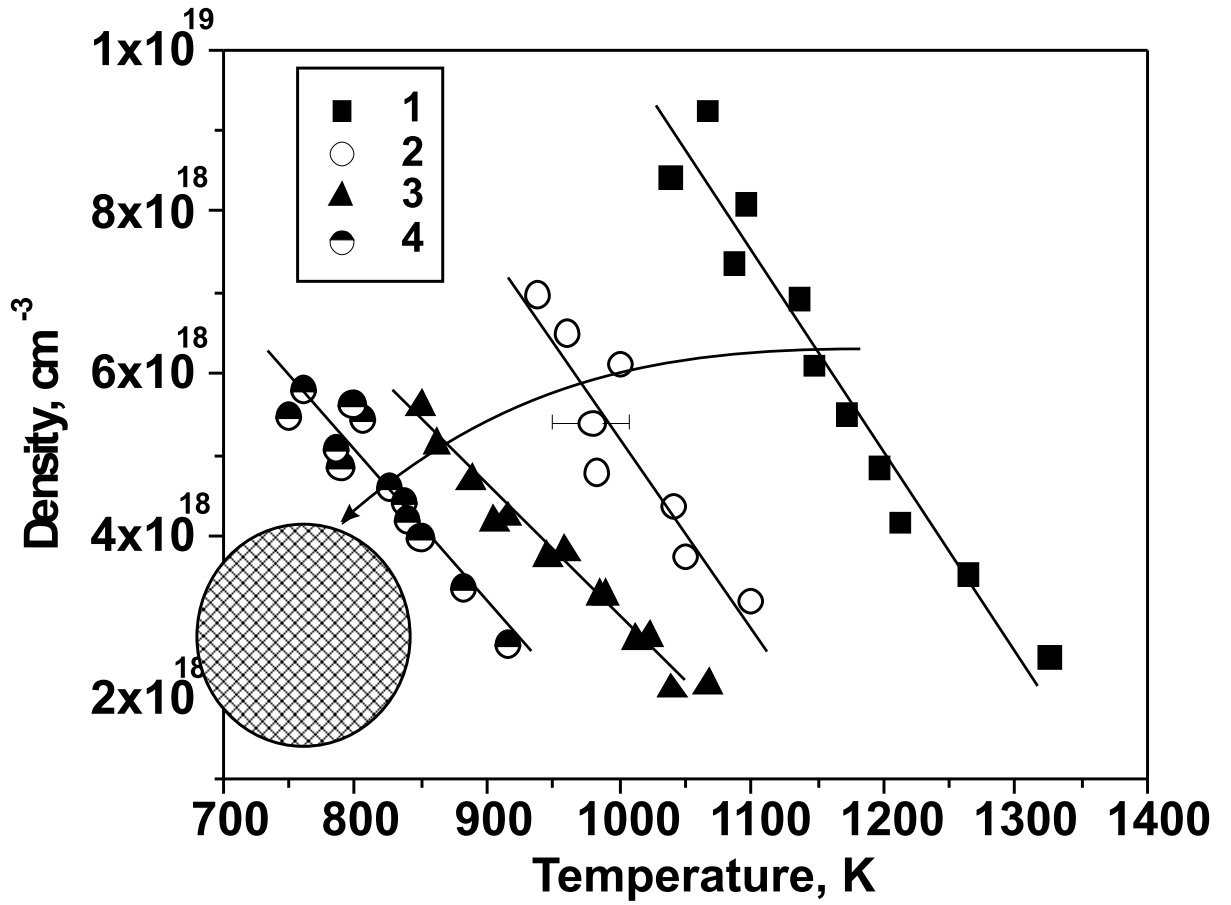


Figure 4.10: Densities behind the reflected shock wave, realized in different mixtures, *vs* temperature. 1 – mixture H_2 : O_2 : $\text{Ar} = 12: 6: 82$, high pressure gas is air; 2,3 – mixture H_2 : O_2 : $\text{Ar} = 12: 6: 82$, high pressure gas is CO_2 , in the case of curve 3 special flow plate was used to decrease shock wave velocity; 4 – mixture H_2 : O_2 : $\text{He} = 12: 6: 82$, high pressure gas is He, experiments with flow plate. Dashed circle corresponds to a region of densities where discharge development is optimal.

$= 12: 6: 82$, we have not seen any noticeable difference. To answer the question which polarity is more suitable for ignition, the problem has to be considered more thoroughly, with a detailed study of the discharge influence on kinetics in the system.

Having completed the experiments we simulated the ignition of the H_2 : O_2 : $\text{Ar} = 0.12: 0.06: 0.82$ mixture under experimental conditions by using method described above. Figure 4.12 represents the comparison between calculated and measured results. The voltage on high voltage electrode was 160 kV, and the pulse duration was 40 ns. To calculate the density of O and H atoms, we used experimental estimations of temporal electric field profile in the discharge $E(t)$ and a standard BOLSIG solver.¹²⁰ To simulate kinetics in the afterglow at high temperatures, a GRI-Mech 3.0 mechanism was used.⁴ The ignition delay time in these calculations was determined from a sharp increase of an OH mole fraction.

A GRI-Mech 3.0 mechanism is well-verified for conditions of our experiments, and a good coincidence between the measured ignition delays and the results of the calculations

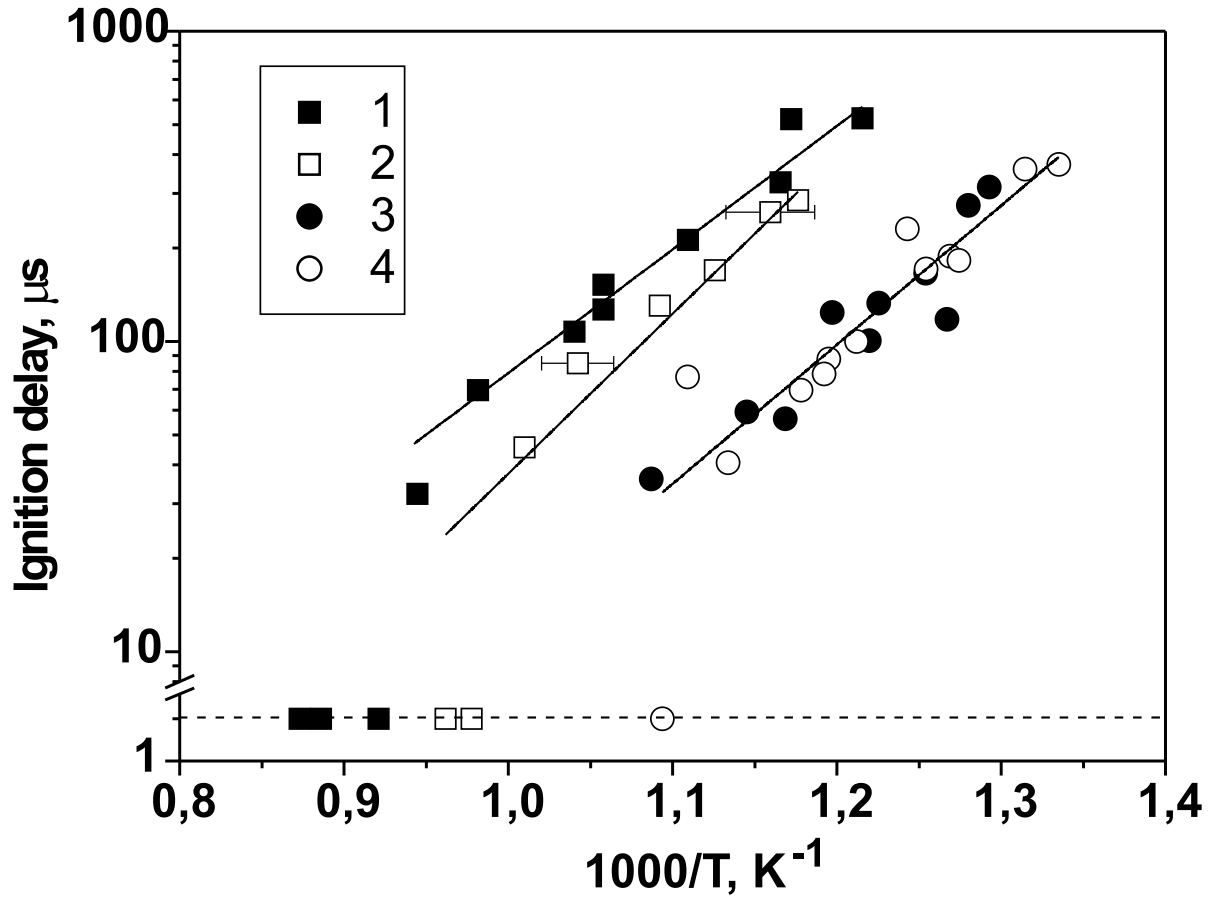


Figure 4.11: Measured ignition delay *vs* gas temperature for different voltage polarity. 1,2 – Mixture H₂: O₂: Ar = 12: 6: 82; 3,4 – Mixture H₂: O₂: He = 12: 6: 82. 1,3 – positive polarity of the electric pulse; 2,4 – negative polarity. $U = 160$ kV.

at the temperatures $T < 1200$ and $\tau_{ign} < 600 \mu s$ proves the validity of the experimental data. For the experiments where $T > 1200$ K, the initial pressure was lower than 10 Torr. Consequently, the discrepancy in this region can be explained by significant boundary layers influence on the flow parameters. It is obvious that the correlation between the measurements and the calculations is also good enough for the case of the discharge initiation of the ignition. It should be noted that we did not take into account the electronically excited particles created in the discharge, we considered only the density of the dissociated particles. The role of excited particles has to be revealed by detailed numerical modelling. Nevertheless, the good agreement between the experiments and the simulations allows this kinetic scheme to be used for the estimation of the nanosecond discharge efficiency for the ignition of combustible mixtures.

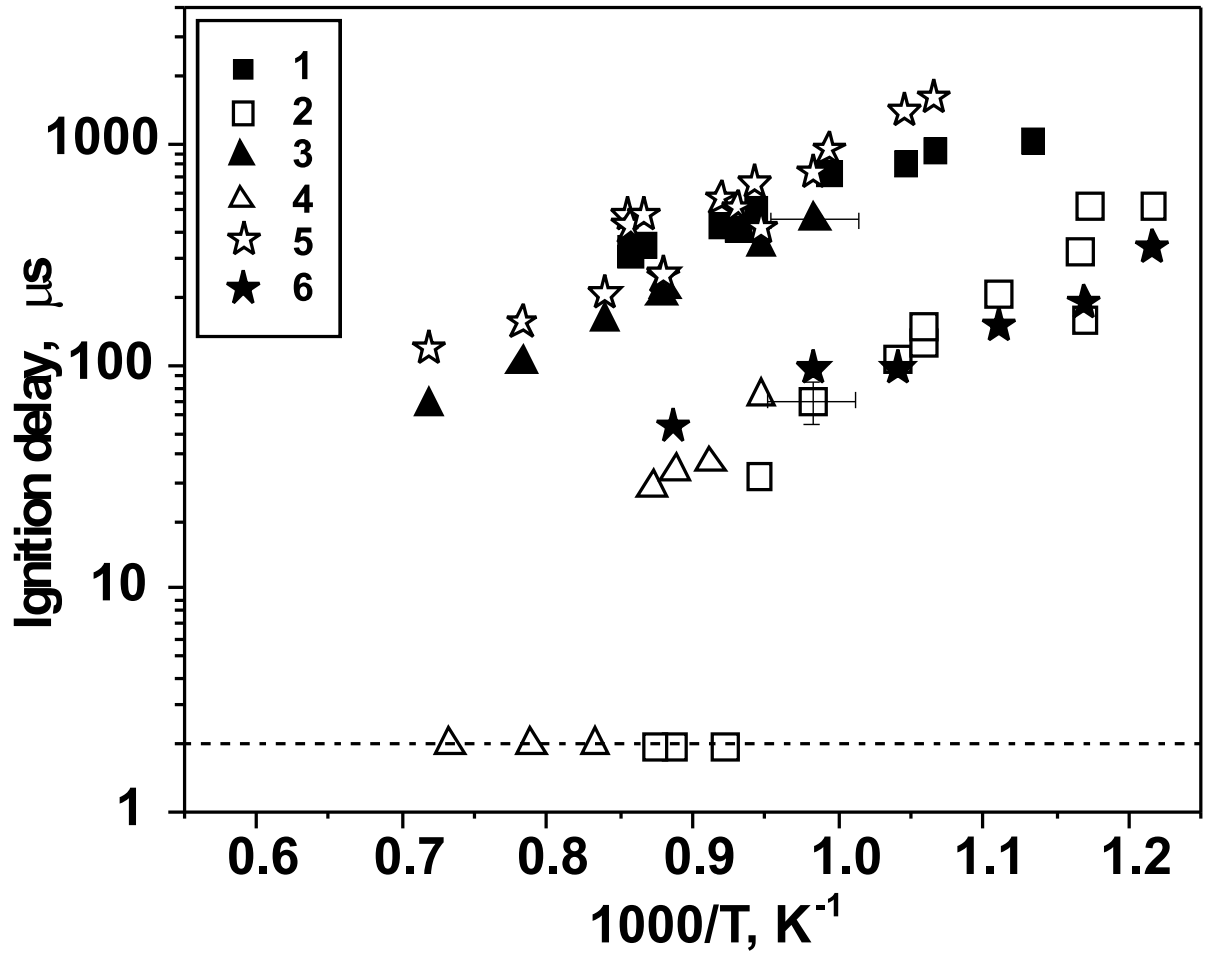


Figure 4.12: Comparison of the measured ignition delay time with calculated one. Mixture H_2 : O_2 : Ar = 12: 6: 82. 1 – autoignition, high pressure gas is CO_2 ; 2 – with discharge, high pressure gas is CO_2 ; 3 – autoignition, high pressure gas is air; 4 – with discharge, high pressure gas is air; 5 – numerical simulation for autoignition, GRI-Mech 3.0; 6 – numerical simulation for the shock wave and the discharge action, BOLSIG + GRI-Mech 3.0.

4.2 Ignition delay time change in H₂-air mixture by pulsed discharge

4.2.1 Experiments in H₂: O₂: N₂: Ar mixture

We determined the dependence of ignition delay upon the temperature at fixed voltage $U = 160$ kV (Table 4.5). The measured time delays of the ignition of the H₂-air-Ar mixture are shown in Figure 4.13. At $T = 1000$ K, the energy input in the discharge decreases the ignition delay time by a factor of 4.8, from 860 to 140 μ s. It should be noted that in this figure and in the next figures devoted to the experimentally measured ignition delay, the dashed line at 2 μ s means some conventional value, which actually gives the typical duration of the electrical noise from the discharge. If ignition delay is shorter, we can not resolve it in the present experiments; this is the lower limit of our measurements.

Table 4.5: Composition of the gas mixtures.

H ₂ ,%	O ₂ ,%	N ₂ ,%	Ar,%
6	3	11	80
16.7	16.7	66.6	—

The Table 4.6 gives the gas parameters (pressure, temperature and density) behind the reflected shock wave for different experimental regimes. The discharge development, at given parameters of the generator, is most efficient at gas densities of about of 10^{18} cm⁻³. At this gas number density, the energy consumption in the discharge is maximal. A decrease of the pressure P_5 , and, consequently, of the number density of the particles from $\sim 10^{19}$ to 10^{18} cm⁻³, leads to higher energy consumption, and, as a result, to a significant decrease in the ignition delay.

Table 4.6: Parameters of the gas behind the reflected shock wave for H₂-O₂-N₂-Ar= 6 : 3 : 11 : 80 mixture.

Mixture	Driver gas	T_5 , K	P_5 , atm	$^*\tau_0$, μ s	τ_+ , μ s
H ₂ -O ₂ -N ₂ -Ar	Air	1512	0.18	115	-
H ₂ -O ₂ -N ₂ -Ar	Air	1371	0.23	107	-
H ₂ -O ₂ -N ₂ -Ar	Air	1250	0.31	129	-
H ₂ -O ₂ -N ₂ -Ar	Air	1235	0.39	178	-
H ₂ -O ₂ -N ₂ -Ar	Air	1197	0.46	174	-
H ₂ -O ₂ -N ₂ -Ar	Air	1185	0.54	240	-
H ₂ -O ₂ -N ₂ -Ar	Air	1173	0.47	190	-
H ₂ -O ₂ -N ₂ -Ar	Air	1132	0.53	340	-
H ₂ -O ₂ -N ₂ -Ar	Air	1127	0.55	281	-
H ₂ -O ₂ -N ₂ -Ar	Air	1065	0.57	423	-
H ₂ -O ₂ -N ₂ -Ar	Air	1059	0.68	472	-
H ₂ -O ₂ -N ₂ -Ar	Air	1033	0.63	709	-
H ₂ -O ₂ -N ₂ -Ar	Air	987	0.78	795	-
H ₂ -O ₂ -N ₂ -Ar	Air	975	0.67	1003	-

Table 4.6: Parameters of the gas behind the reflected shock wave for $\text{H}_2\text{-O}_2\text{-N}_2\text{-Ar} = 6 : 3 : 11 : 80$ mixture.

Mixture	Driver gas	T_5 , K	P_5 , atm	$^*\tau_0$, μs	τ_+ , μs
$\text{H}_2\text{-O}_2\text{-N}_2\text{-Ar}$	Air	1404	0.24	-	< 2
$\text{H}_2\text{-O}_2\text{-N}_2\text{-Ar}$	Air	1269	0.35	-	< 2
$\text{H}_2\text{-O}_2\text{-N}_2\text{-Ar}$	Air	1194	0.36	-	< 2
$\text{H}_2\text{-O}_2\text{-N}_2\text{-Ar}$	Air	1190	0.55	-	< 2
$\text{H}_2\text{-O}_2\text{-N}_2\text{-Ar}$	Air	1176	0.45	-	< 2
$\text{H}_2\text{-O}_2\text{-N}_2\text{-Ar}$	Air	1144	0.54	-	< 2
$\text{H}_2\text{-O}_2\text{-N}_2\text{-Ar}$	Air	1070	0.59	-	46
$\text{H}_2\text{-O}_2\text{-N}_2\text{-Ar}$	Air	1054	0.68	-	122
$\text{H}_2\text{-O}_2\text{-N}_2\text{-Ar}$	Air	1053	0.53	-	63
$\text{H}_2\text{-O}_2\text{-N}_2\text{-Ar}$	Air	1038	0.63	-	110
$\text{H}_2\text{-O}_2\text{-N}_2\text{-Ar}$	Air	1006	0.71	-	151
$\text{H}_2\text{-O}_2\text{-N}_2\text{-Ar}$	Air	999	0.75	-	183
$\text{H}_2\text{-O}_2\text{-N}_2\text{-Ar}$	Air	980	0.68	-	142
$\text{H}_2\text{-O}_2\text{-N}_2\text{-Ar}$	Air	960	0.74	-	225
$\text{H}_2\text{-O}_2\text{-N}_2\text{-Ar}$	Air	957	0.81	-	283
$\text{H}_2\text{-O}_2\text{-N}_2\text{-Ar}$	Air	930	0.77	-	335
$\text{H}_2\text{-O}_2\text{-N}_2\text{-Ar}$	Air	925	0.69	-	253
$\text{H}_2\text{-O}_2\text{-N}_2\text{-Ar}$	Air	912	0.82	-	359
$\text{H}_2\text{-O}_2\text{-N}_2\text{-Ar}$	Air	881	0.84	-	589

* In the Table, τ_0 is a delay time for autoignition, τ_+ is a delay time in the case of ignition by nanosecond pulse of positive polarity with the amplitude of 160 kV, τ_- is a delay time in the case of ignition by nanosecond pulse of negative polarity with the amplitude of 160 kV.

In the case where we have relatively low gas number densities, we can expect to shift the ignition curve (the dependence of ignition delay time τ upon temperature) to as low of temperatures as possible. We carried out experiments with different mixtures, high pressure chamber gases, and diaphragms trying to reach the particle number densities behind the reflected shock wave, which would be the most efficient for the discharge development.

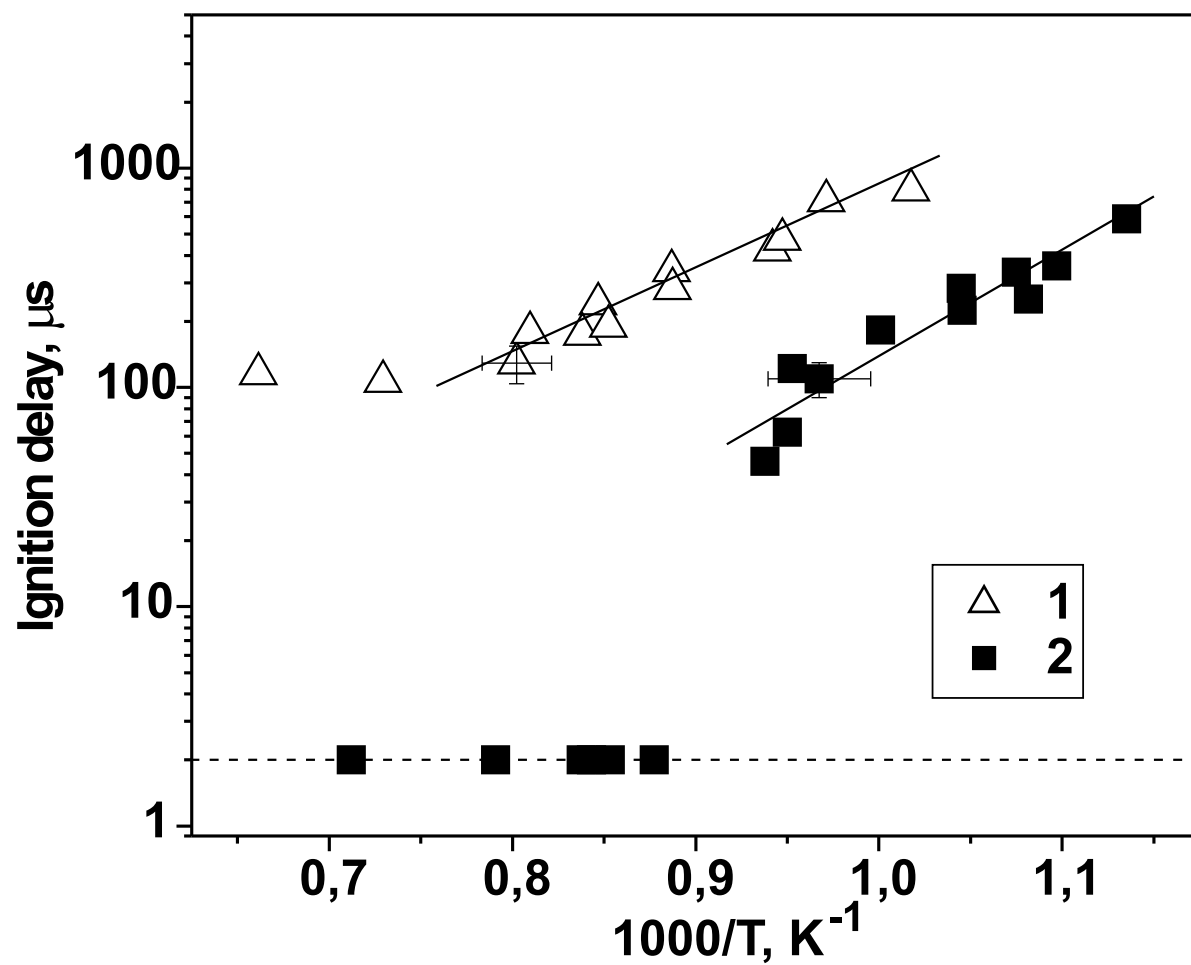


Figure 4.13: Measured ignition delay time *vs* gas temperature. Mixture H₂: O₂: N₂: Ar = 6: 3: 11: 80. 1 – autoignition, 2 – with nanosecond discharge. $U = 160$ kV.

4.2.2 Experiments in H₂: O₂: N₂ mixture

Mixture H₂: O₂: N₂ has different characteristics from the point of view of both discharge development and chemical reactions because of large amount of nitrogen. During the discharge stage it leads to the energy deposition into vibrational degrees of freedom of N₂, excitation of electronic levels of N₂ (for example, A^3 , B^3 , C^3). During the afterglow stage electronically-excited levels of N₂ are quenched by molecular oxygen with atomic oxygen production. Thus in the mixtures with N₂ we have to take into account additional processes both during the discharge stage and afterglow stage.

Table 4.7: Parameters of the gas behind the reflected shock wave for H₂-O₂-N₂ = 16.7 : 16.7 : 66.6 mixture.

Mixture	Driver gas	T_5 , K	P_5 , atm	$^*\tau_0$, μ s	τ_+ , μ s
H ₂ -O ₂ -N ₂	Air	884	0.39	-	102
H ₂ -O ₂ -N ₂	Air	850	0.43	-	152
H ₂ -O ₂ -N ₂	Air	843	0.47	-	167
H ₂ -O ₂ -N ₂	Air	806	0.46	-	419
H ₂ -O ₂ -N ₂	Air	806	0.51	-	556
H ₂ -O ₂ -N ₂	Air	784	0.52	-	1139
H ₂ -O ₂ -N ₂	Air	895	0.34	-	97
H ₂ -O ₂ -N ₂	Air	918	0.32	-	76
H ₂ -O ₂ -N ₂	Air	960	0.28	-	60
H ₂ -O ₂ -N ₂	Air	1005	0.23	-	42
H ₂ -O ₂ -N ₂	Air	1082	0.19	-	2
H ₂ -O ₂ -N ₂	Air	899	0.34	-	76
H ₂ -O ₂ -N ₂	Air	850	0.39	1152	-
H ₂ -O ₂ -N ₂	Air	869	0.29	890	-
H ₂ -O ₂ -N ₂	Air	970	0.22	420	-
H ₂ -O ₂ -N ₂	Air	1065	0.16	246	-
H ₂ -O ₂ -N ₂	Air	1109	0.13	256	-
H ₂ -O ₂ -N ₂	Air	821	0.36	1577	-
H ₂ -O ₂ -N ₂	Air	820	0.26	1564	-
H ₂ -O ₂ -N ₂	Air	877	0.20	769	-
H ₂ -O ₂ -N ₂	Air	886	0.37	656	-
H ₂ -O ₂ -N ₂	Air	889	0.32	718	-
H ₂ -O ₂ -N ₂	Air	931	0.28	519	-
H ₂ -O ₂ -N ₂	Air	971	0.24	412	-
H ₂ -O ₂ -N ₂	Air	1083	0.20	228	-
H ₂ -O ₂ -N ₂	Air	1107	0.15	221	-
H ₂ -O ₂ -N ₂	Air	1069	0.16	197	-
H ₂ -O ₂ -N ₂	Air	1021	0.19	332	-
H ₂ -O ₂ -N ₂	Air	1053	0.18	287	-

* In the Table, τ_0 is a delay time for autoignition, τ_+ is a delay time in the case of ignition by nanosecond pulse of positive polarity with the amplitude of 160 kV, τ_- is

a delay time in the case of ignition by nanosecond pulse of negative polarity with the amplitude of 160 kV.

The shock tube installation used in the experiments was carefully designed to obtain high repeatability of the experimental conditions. Figure 4.14 demonstrates the reproducibility of shock wave velocities from one experiment to another together with the shock wave attenuation in the channel because of viscous dissipation.

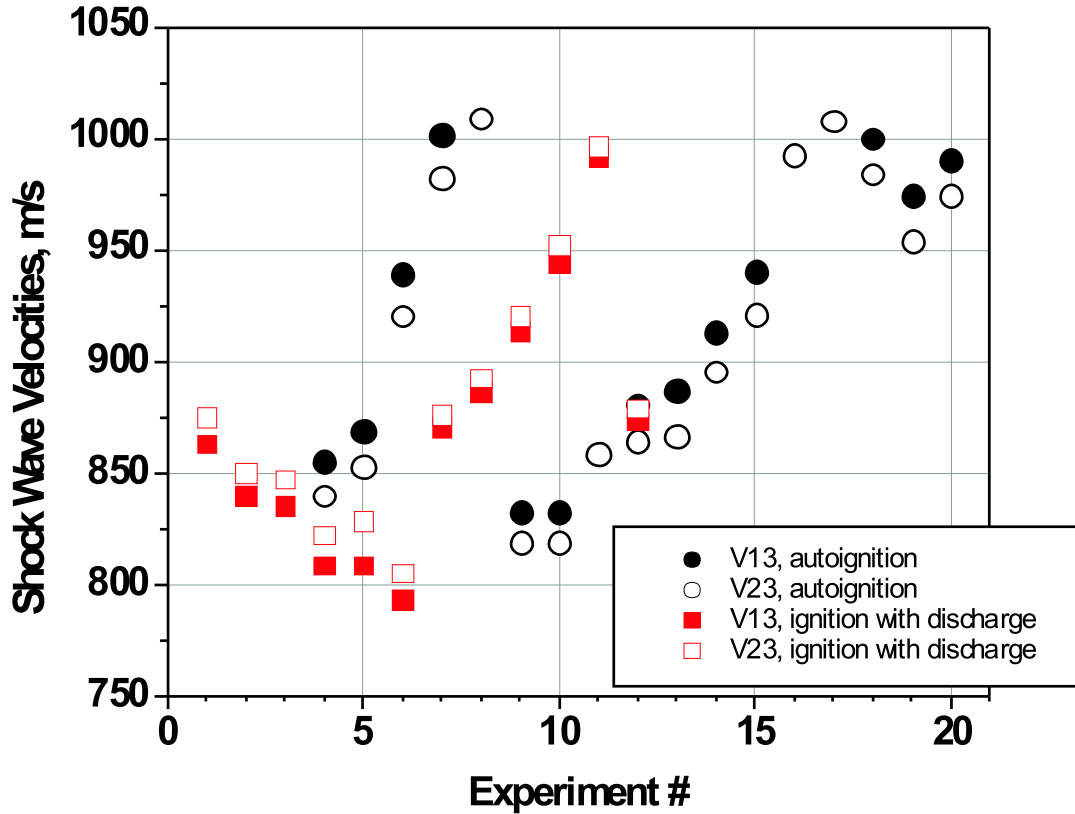


Figure 4.14: Velocity of the incident shock wave. $\text{H}_2\text{-O}_2\text{-N}_2 = 16.7 : 16.7 : 66.6$ mixture.

To give an idea about the gas number densities, Figure 4.15 represents the gas density behind the reflected shock wave for different experiments. It is clearly seen that it is possible to vary the parameters of the system to handle the gas density. We can change the high pressure gas, add a flow plate, or change the mixture composition. In general, there are two ways to make ignition more efficient in this region of parameters: try to adjust the gas density to the optimal values or to adjust the high voltage amplitude. In the present part of work we keep the voltage at the same level (100 kV) and the energy input variation (see Figure 4.16) are only due to gas density change.

The pressure range corresponded to the experimental conditions of this work is shown on the Figure 4.17. The pressure behind the reflected shock wave was in the range from 0.1 to 0.6 atmospheres. These conditions allow us to obtain the uniform discharge

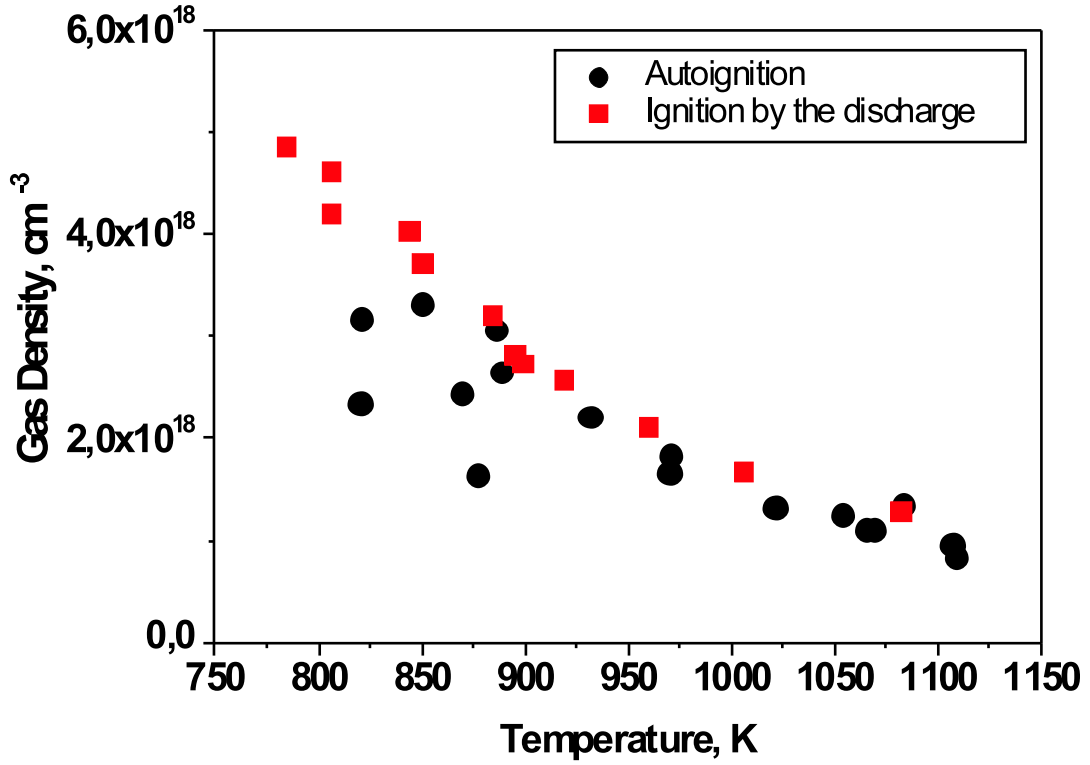


Figure 4.15: Gas density behind the reflected shock wave. $\text{H}_2\text{-O}_2\text{-N}_2 = 16.7 : 16.7 : 66.6$ mixture.

development in the discharge section.

We determined the dependence of ignition delay upon the temperature at fixed voltage $U = 100$ kV. The measured time delays of the ignition of the H_2 -air mixture are shown in Figure 4.18. The obvious difference of the undiluted H_2 -air mixture with compare to the mixture, diluted with Ar, is specific heat ratio. For H_2 -air mixture we have $\gamma = 1.4$, and for mixture H_2 -air-Ar we have $\gamma \simeq 1.6$. This difference leads in the case of H_2 -air mixture to the strong interaction between reflected shock wave and boundary layer. So-called λ -shaped configuration is formed and gas parameters behind the reflected shock wave are far from the 1D theory predictions. In particular, this leads to some discrepancy between measured and calculated ignition delay times for H_2 -air mixture (Figure 4.18). We will discuss this discrepancy in the next part of the report.

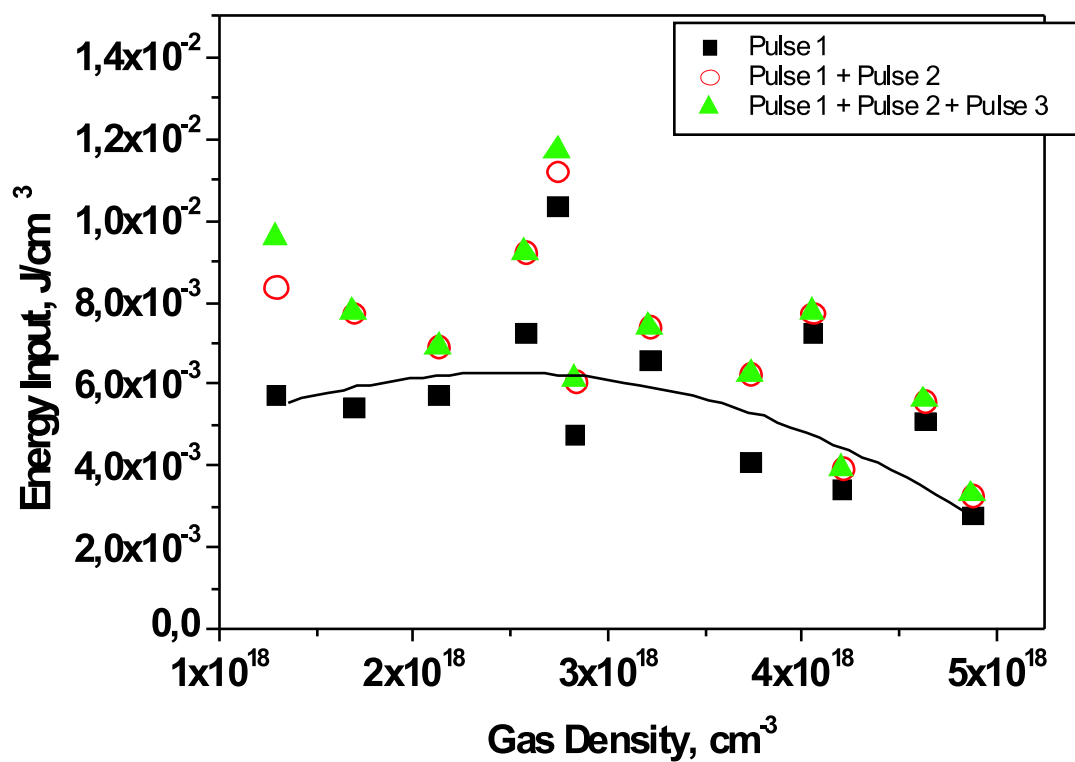


Figure 4.16: Energy of the discharge for different gas densities. H₂-O₂-N₂ = 16.7 : 16.7 : 66.6 mixture.

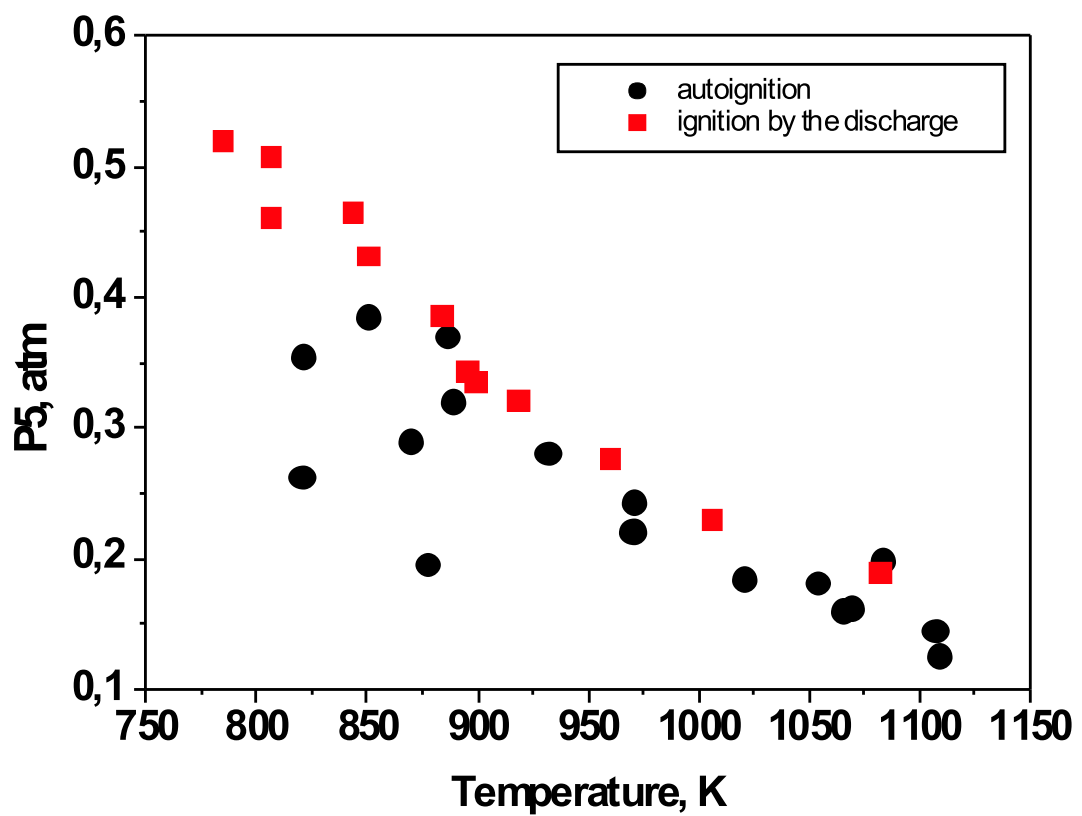


Figure 4.17: Pressure behind the reflected shock wave. $H_2-O_2-N_2 = 16.7 : 16.7 : 66.6$ mixture.

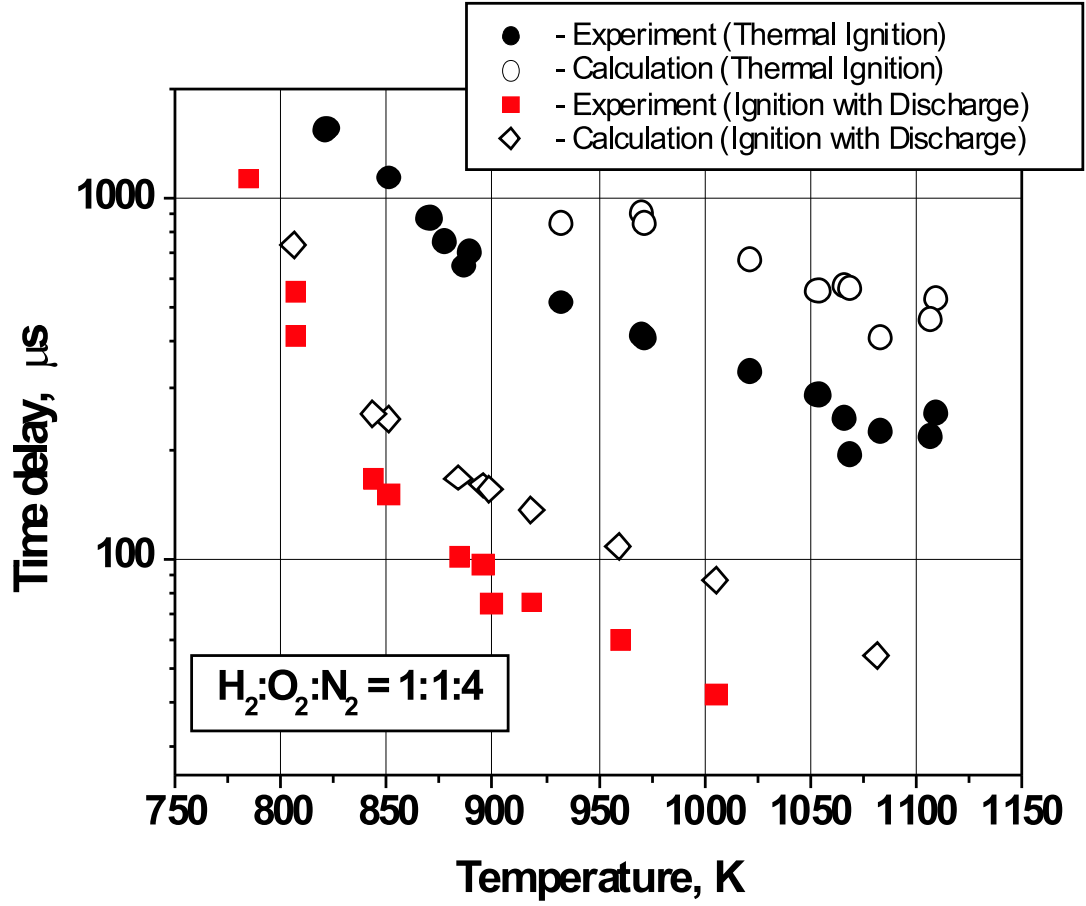


Figure 4.18: Comparison of the measured ignition delay time with calculated one. Mixture $\text{H}_2:\text{O}_2:\text{N}_2 = 0.167:0.167:0.666$. 1 – autoignition; 3 – with discharge; 2 – numerical simulation for autoignition, GRI-Mech 3.0, no gasdynamic correction; 4 – numerical simulation for the shock wave and the discharge action, BOLSIG + GRI-Mech 3.0, no gasdynamic correction. Log scale.

4.3 Comparison with the computational model

4.3.1 Flow model

The non-equilibrium flow behind the reflected shock wave was investigated numerically. 2D axially-symmetric calculations of the flow were performed. We analyzed regimes with independent variation of vibrational temperature in the hypersonic flow. MacCormack scheme with FCT correction was used for solving the components, mass, momentum and energy conserve equations:

$$\begin{aligned}\rho_t + (\rho u)_x + (\rho v)_y &= 0 \\ (\rho u)_t + (\rho u^2 + p)_x + (\rho uv)_y &= 0 \\ (\rho v)_t + (\rho v^2 + p)_y + (\rho uv)_x &= 0 \\ e_t + ((e + p)u)_x + ((e + p)v)_y &= S_i h_i^0 w_i \\ (c_i \rho)_t + (c_i \rho u)_x + (c_i \rho v)_y &= 0, \quad i = 1, n\end{aligned}$$

Vibrational excitation and energy exchange in $\text{N}_2\text{-O}_2\text{-H}_2$ plasma flow were taken into account (Figure 4.19).

Boundary layer was taken into account as initial and boundary conditions for the flow field. This allows us to analyze the flow structure in the shock tube with minimal computational resources.

Figure 4.19 clearly shows the strong interaction between reflected shock wave and boundary layer. So-called λ -shaped configuration is formed and gas parameters behind the reflected shock wave changes. Typical deviation from the 1D-theory predictions in this case is about 100-150 K during the ignition delay time. Calculations also shows the dependence of the deviation value from the boundary layer regime (laminar or turbulent). It is very difficult to reconstruct the real flow structure in the shock tube with good accuracy, so we consider the numerical results as semi-quantitative only. Real deviation can be analyzed on the basis of IR-emission measurements.

This time we will consider the flow parameters behind reflected shock wave and deviation of these parameters from 1D-model using results of our 2D-modelling and experimental results of autoignition. The autoignition delay time for $\text{H}_2\text{-O}_2\text{-N}_2$ mixture can be predicted numerically with very high accuracy. So, we have so-called "kinetic thermometer" for our experimental conditions. The typical value of temperature deviation due to gasdynamic effects, estimated using this "kinetic thermometer" is very close to the value predicted by numerical model — 120-160 K. This allows us to make the semi-quantitative correction for the temperatures both for experiments with autoignition and experiments with ignition by pulsed discharge.

4.3.2 Kinetic model

To calculate the densities of active particles, one has to determine electron energy distribution function (EEDF) by solving Boltzmann equation for electrons. In the case of high electric fields, the exact solution of this equation requires statistical modelling.¹⁴ If we do not consider the FIW front, as it was mentioned above, we can use two-term approximation of Boltzmann equation.¹²⁵ For discharge calculations, we used standard

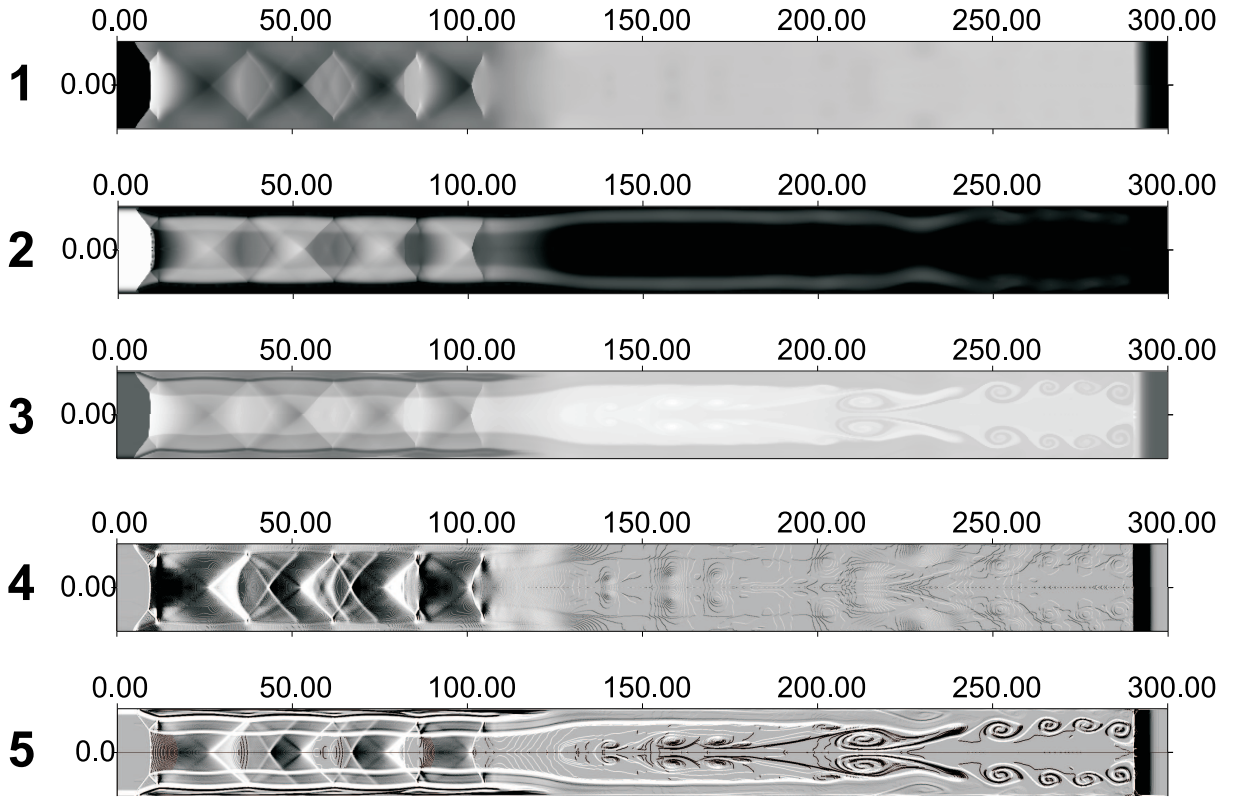


Figure 4.19: Gas Dynamic Fields. $\text{H}_2\text{-O}_2\text{-N}_2 = 16.7 : 16.7 : 66.6$ mixture. 1 – pressure field; 2 – v_x velocity field; 3 – temperature field; 4 – pressure gradients picture; 5 – temperature gradients picture. Incident shock wave velocity 900 m/s. $p_0 = 10$ Torr

BOLSIG software¹²⁰ or Gordeev solver.¹²⁶ Both codes calculate a stationary electron energy distribution function and a fractional energy deposited in different collisional processes. The input is a list of reduced electric fields E/N (here E is an electric field and N is a gas density) to be treated and the gas composition. The output is the densities of vibrationally and electronically excited particles, atoms and radicals dissociated via electronically excited states. The list of the processes used for EEDF computation for hydrogen-air mixture is given above and in the Table 4.8. The excitation cross-sections were taken from^{127–129} for hydrogen, and from^{130–135} for oxygen, dissociation was treated in accordance with.¹⁰³ For the hydrogen molecule, the dissociation takes place via $b^3\Sigma_u^+$ and $a^3\Sigma_g^+$ electronically excited states, while for oxygen via $A^3\Sigma_u^+$ and $B^3\Sigma_u^-$ states. The concentrations of atoms and radicals created in the discharge were taken as the initial data for the high-temperature calculations. All other mixtures were considered in a similar way.

The numerical code for the description of high-temperature ignition kinetics under the action of a high-voltage nanosecond discharge has been developed on the basis of a kinetic scheme¹³⁶ and the GRI-Mech 3.0 mechanism. CHEMKIN2 solver was used for calculations. Both kinetic schemes gave the same results for investigated mixtures. It should be noted that kinetics of the electronically excited particles is important in an afterglow of the pulsed nonequilibrium gas discharge, and the problem of influence of the excited particles on the ignition processes is under discussion now. But we included only ground state particles in our model.

Table 4.8: Excitation of N₂ by electron impact. ΔE is a threshold of the process.

Process	ΔE , eV	Reference
$e + N_2 \rightarrow e + N_2(v = 1)$	0.290	¹⁴⁰
$e + N_2 \rightarrow e + N_2(v = 2)$	0.585	¹⁴⁰
$e + N_2 \rightarrow e + N_2(v = 3)$	0.877	¹⁴⁰
$e + N_2 \rightarrow e + N_2(v = 4)$	1.170	¹⁴⁰
$e + N_2 \rightarrow e + N_2(v = 5)$	1.460	¹⁴⁰
$e + N_2 \rightarrow e + N_2(v = 6)$	1.750	¹⁴⁰
$e + N_2 \rightarrow e + N_2(v = 7)$	2.050	¹⁴⁰
$e + N_2 \rightarrow e + N_2(v = 8)$	2.340	¹⁴⁰
$e + N_2 \rightarrow e + N_2(v = 9)$	2.450	¹⁴¹
$e + N_2 \rightarrow e + N_2(v = 10)$	2.710	¹⁴¹
$e + N_2 \rightarrow e + N_2(A^3\Sigma_u^+)$	6.224	¹⁴²
$e + N_2 \rightarrow e + N_2(B^3\Pi_g)$	7.392	¹⁴²
$e + N_2 \rightarrow e + N_2(C^3\Pi_u)$	11.05	¹⁴²
$e + N_2 \rightarrow e + N_2(W^1\Delta_u)$	8.939	¹⁴²
$e + N_2 \rightarrow e + N_2(W^3\Delta_u)$	7.415	¹⁴²
$e + N_2 \rightarrow e + N_2(a^{1'}\Sigma_u^-)$	8.450	¹⁴²
$e + N_2 \rightarrow e + N_2(a^1\Pi_g)$	8.590	¹⁴²
$e + N_2 \rightarrow e + N_2(a^{1''}\Sigma_g)$	12.40	¹⁴²
$e + N_2 \rightarrow e + N_2(B'^3\Sigma_u^-)$	8.217	¹⁴²
$e + N_2 \rightarrow e + N_2(B^1\Pi_u)$	12.50	¹⁴³
$e + N_2 \rightarrow e + N_2(E^3\Sigma_g^+)$	11.88	¹⁴²
$e + N_2 \rightarrow e + N_2(Rydber)$	13.75	¹⁴²
$e + N_2 \rightarrow N_2^- \rightarrow e + N(^4S^0) + N(^4S^0)$	9.551	¹⁴⁴
$e + N_2 \rightarrow N + N$	10.00	^{145, 146}
$e + N_2 \rightarrow e + e + N_2^+$	15.58	¹³⁴
$e + N_2 \rightarrow N(^4S^0) + N^+(^3P) + e + e$	25.00	¹³⁵
$e + N_2(j = 0) \rightarrow e + N_2(j = 2, 4, 6, 8)$	0.025	¹⁴⁷

In summary, the initial parameters of task were gas composition, initial temperature, and pressure. The discharge was assumed as a square pulse of the electric field at a given amplitude and with a duration of 40 ns. For test calculations, we have chosen the electric field value $E/N = 300$ Td ('Td', or Townsend, is used in the gas discharge physics, and $1 \text{ Td} = 0.33 \text{ V}/(\text{cm Torr}) = 10^{-17} \text{ V}\cdot\text{cm}^2$ at 20^0 C), which is typical for a nanosecond discharge after the breakdown front. For the first stage, we calculated EEDF, energy branching, and densities of atoms and radicals in the discharge. The mixture composition, including atom/radical density after the discharge action, and the gas temperature were taken as initial parameters for the calculations of the ignition problem. As a first approximation, we neglected the kinetics of electronically excited states in the afterglow. The final results were the kinetic curves of combustion species. Ignition delay in the calculations was defined by an temperature increase of 200 K.

Having completed the experiments we simulated the ignition of the H₂: O₂: N₂ = 0.167: 0.167: 0.666 mixture under experimental conditions by using method described above. Figure 4.20 represents the comparison between calculated and measured results.

The voltage on high voltage electrode was 160 kV, and the pulse duration was 40 ns. To calculate the density of O and H atoms, we used experimental estimations of temporal electric field profile in the discharge $E(t)$ and a standard BOLSIG solver.¹²⁰ To simulate kinetics in the afterglow at high temperatures, a GRI-Mech 3.0 mechanism was used.⁴ The ignition delay time in these calculations was determined from a sharp increase of an OH mole fraction.

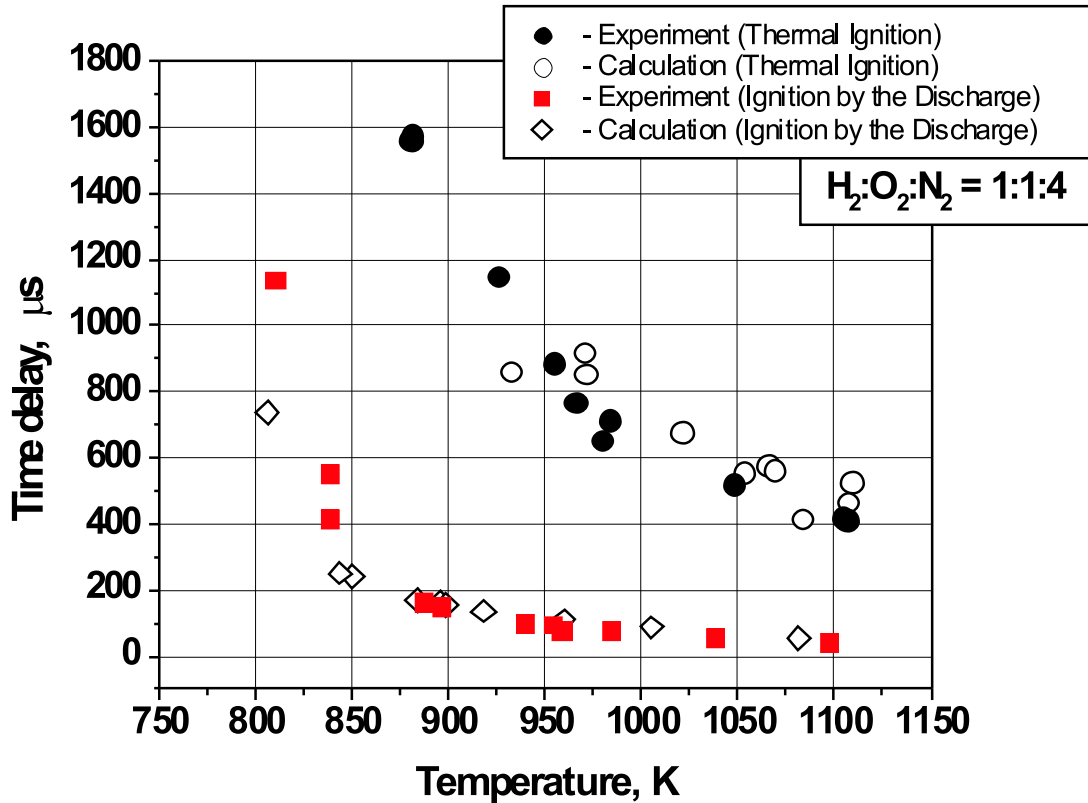


Figure 4.20: Comparison of the measured ignition delay time with calculated one. Mixture H_2 : O_2 : $\text{N}_2 = 0.167$: 0.167 : 0.666 . 1 – autoignition; 3 – with discharge; 2 – numerical simulation for autoignition, GRI-Mech 3.0, with gasdynamic correction; 4 – numerical simulation for the shock wave and the discharge action, BOLSIG + GRI-Mech 3.0, with gasdynamic correction.

It is obvious that the correlation between the measurements and the calculations is also good enough for the case of the discharge initiation of the ignition (Figures 4.20). The good agreement between the experiments and the simulations allows this kinetic scheme to be used for the estimation of the nanosecond discharge efficiency for the ignition of combustible mixtures.

4.4 Ignition delay time measurements in CH₄: O₂: N₂: Ar mixture

Table 4.9: Composition of the gas mixtures

CH ₄ ,%	O ₂ ,%	N ₂ ,%	Ar,%
1	4	15	80

The measured time delays of the ignition of the CH₄-Air-Ar mixture (Table 4.9) are shown in Figure 4.21. At $T = 1000$ K, the energy input in the discharge decreases the ignition delay time by a factor of 4.8, from 860 to 140 μ s. It should be noted that in this figure and in the next figures devoted to the experimentally measured ignition delay, the dashed line at 2 μ s means some conventional value, which actually gives the typical duration of the electrical noise from the discharge. If ignition delay is shorter, we can not resolve it in the present experiments; this is the lower limit of our measurements.

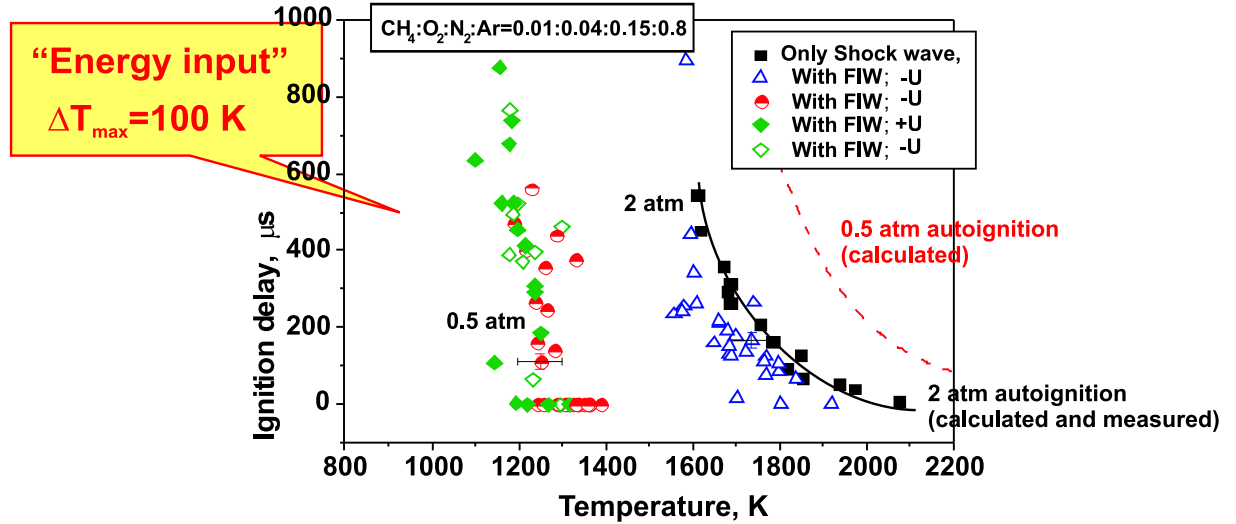


Figure 4.21: Measured ignition delay time *vs* gas temperature. Mixture CH₄: O₂: N₂: Ar = 1: 4: 15: 80. Pressure behind the reflected shock wave is indicated with numbers near appropriate curves. 1 – autoignition, 2 – with discharge, $W = 10^{-3}$ J/cm³; 3 – with discharge, $W = 3 \cdot 10^{-2}$ J/cm³; 4 – with discharge, $W = 5 \cdot 10^{-2}$ J/cm³.

We determined the dependence of ignition delay upon the temperature at fixed voltage $U = 160$ kV. The ignition delay time changes dramatically under the action of the discharge. We were able to provide the ignition of highly diluted methane-air mixture at a pressure of 0.3 atm and a temperature of 1100 K using a 0.05 J/cm³ energy release in the discharge. The figure also demonstrates a difference in the delay time in the case of ignition by the nanosecond discharge at different pressures behind the reflected shock wave. Curves at different pressure values were obtained by using different gases in the high pressure chamber. Regime 1 was obtained with He, which led to the highest velocity of the shock wave, and, consequently, to the highest temperature and density; regime 2 was obtained with dry air; and regime 3 was obtained with CO₂. The Table 4 gives

the gas parameters (pressure, temperature and density) behind the reflected shock wave for different experimental regimes. In experiments where driver gas is marked with †, a flow plate was used. The discharge development, at given parameters of the generator, is most efficient at gas densities of about of 10^{18} cm^{-3} . At this gas number density, the energy consumption in the discharge is maximal. A decrease of the pressure P_5 , and, consequently, of the number density of the particles from $\sim 10^{19}$ to 10^{18} cm^{-3} , leads to higher energy consumption, and, as a result, to a significant decrease in the ignition delay. It is this effect that explains three branches in the Figure 4.21.

In the case where we have relatively low gas number densities, we can expect to shift the ignition curve (the dependence of ignition delay time τ upon temperature) to as low of temperatures as possible. We carried out experiments with different mixtures, high pressure chamber gases, and diaphragms trying to reach the particle number densities behind the reflected shock wave, which would be the most efficient for the discharge development.

The Table 4.10 gives the gas parameters (pressure, temperature and density) behind the reflected shock wave for different experimental regimes. The discharge development, at given parameters of the generator, is most efficient at gas densities of about of 10^{18} cm^{-3} . At this gas number density, the energy consumption in the discharge is maximal. A decrease of the pressure P_5 , and, consequently, of the number density of the particles from $\sim 10^{19}$ to 10^{18} cm^{-3} , leads to higher energy consumption, and, as a result, to a significant decrease in the ignition delay.

Table 4.10: Parameters of the gas behind the reflected shock wave for CH₄-O₂-N₂-Ar mixture

Mixture	Driver gas	T_5 , K	P_5 , atm	$^*\tau_0$, μs	τ_+ , μs
CH4-air-Ar	He	2225	1.68	0	-
CH4-air-Ar	He	2075	1.67	8.9	-
CH4-air-Ar	He	1973	1.83	40.6	-
CH4-air-Ar	He	1938	2.05	50.9	-
CH4-air-Ar	He	1853	1.92	69.7	-
CH4-air-Ar	He	1849	2.04	97.8	-
CH4-air-Ar	He	1838	1.77	-	65.8
CH4-air-Ar	He	1816	2.10	94.8	-
CH4-air-Ar	He	1803	1.89	-	< 2
CH4-air-Ar	He	1799	1.83	-	83.1
CH4-air-Ar	He	1783	2.11	165.6	-
CH4-air-Ar	He	1770	1.96	-	123.7
CH4-air-Ar	He	1755	1.94	207.2	-
CH4-air-Ar	He	1736	1.73	-	165.7
CH4-air-Ar	He	1723	2.05	-	137.8
CH4-air-Ar	He	1700	2.12	-	177.2
CH4-air-Ar	He	1690	1.94	-	127
CH4-air-Ar	He	1687	2.21	262.5	-
CH4-air-Ar	He	1686	2.10	315.6	-
CH4-air-Ar	He	1684	2.15	-	129.5

Table 4.10: Parameters of the gas behind the reflected shock wave for CH₄-O₂-N₂-Ar mixture

Mixture	Driver gas	T_5 , K	P_5 , atm	$^*\tau_0$, μs	τ_+ , μs
CH4-air-Ar	He	1679	2.05	292.9	-
CH4-air-Ar	He	1671	2.12	361.5	-
CH4-air-Ar	He	1661	2.16	-	213.5
CH4-air-Ar	He	1661	2.26	-	215.5
CH4-air-Ar	He	1617	2.17	452.5	-
CH4-air-Ar	He	1610	1.95	547.9	-
CH4-air-Ar	He	1610	2.31	-	260.1
CH4-air-Ar	Air	1389	0.32	-	< 2
CH4-air-Ar	Air	1360	0.39	-	< 2
CH4-air-Ar	Air	1349	0.38	-	< 2
CH4-air-Ar	Air	1322	0.37	-	< 2
CH4-air-Ar	Air	1311	0.44	-	< 2
CH4-air-Ar	Air	1257	0.41	-	< 2
CH4-air-Ar	Air	1250	0.47	-	110.9
CH4-air-Ar	Air	1241	0.47	-	162.8
CH4-air-Ar	Air	1237	0.46	-	265.5
CH4-air-Ar	Air	1233	0.46	-	282.4
CH4-air-Ar	Air	1231	0.49	-	561
CH4-air-Ar	Air	1215	0.51	-	404.1
CH4-air-Ar	Air	1188	0.46	-	471.8
CH4-air-Ar	Air	1184	0.52	-	967.3
CH4-air-Ar	CO ₂	1195	0.28	-	< 2
CH4-air-Ar	CO ₂	1145	0.32	-	107.2
CH4-air-Ar	CO ₂	1099	0.35	-	636

* In the Table, τ_0 is a delay time for autoignition, τ_+ is a delay time in the case of ignition by nanosecond pulse of positive polarity with the amplitude of 160 kV, τ_- is a delay time in the case of ignition by nanosecond pulse of negative polarity with the amplitude of 160 kV.

In the case where we have relatively low gas number densities, we can expect to shift the ignition curve (the dependence of ignition delay time τ upon temperature) to as low of temperatures as possible. We carried out experiments with different mixtures, high pressure chamber gases, and diaphragms trying to reach the particle number densities behind the reflected shock wave, which would be the most efficient for the discharge development.

4.5 Gas discharge and ignition homogeneity measurements

ICCD camera PicoStar HR12 was used to obtain discharge and combustion images in a hot mixture with high temporal resolution. The wavelength sensitivity of the optical system

was 300-800 nm. We obtained integral in spectra images. The scheme of the camera synchronization is represented in Figure 4.22. The gate was 1 ns for nanosecond images of the discharge and 30 ms for microsecond images of the combustion. We measured the emission from the shock tube window 2 cm in diameter.

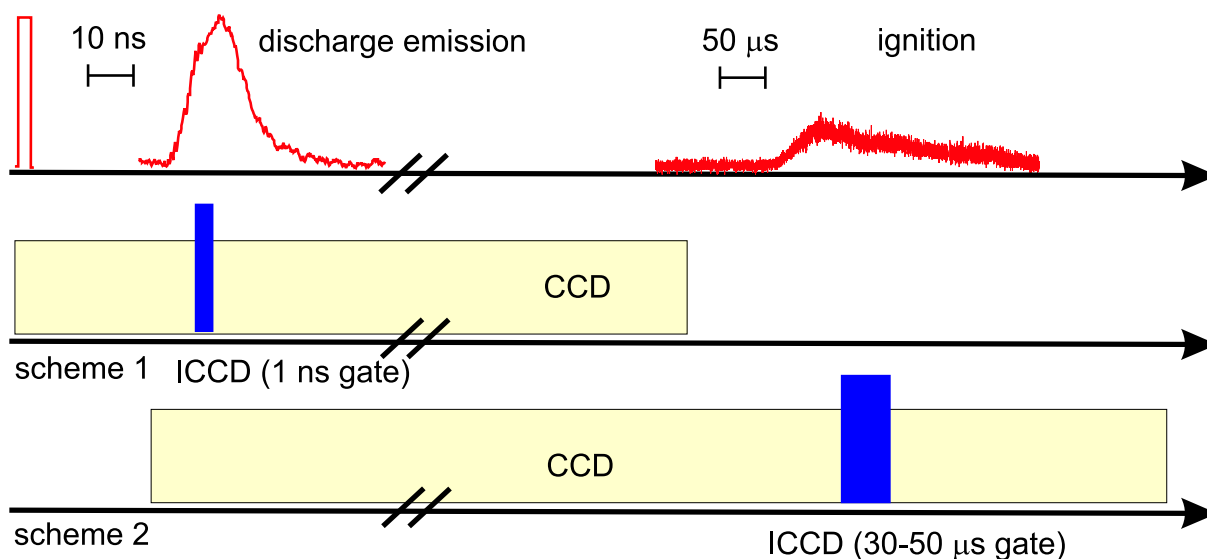


Figure 4.22: An example of a synchronization scheme for PicoStar Camera.

As an example, Figures 4.23 and 4.24 represent images of a nanosecond discharge and combustion at two different pressure and temperature values (indicated in the Figures) for the mixture $\text{CH}_4:\text{O}_2:\text{N}_2:\text{Ar}=1:4:15:80$. It is clear from the Figures that the higher pressure the less uniform the discharge. This leads to non-uniform combustion. At relatively low pressure both discharge and combustion processes develop uniformly in space.

Figure 4.25 represents the different experiments for emission field measurement. These images allow to analyze the reproducibility of the gas discharge in the form of fast ionization wave, and homogeneity of mixture ignition. It is clearly seen that discharge remains spatially-uniform up to pressures of about 2 atmospheres behind reflected shock wave. Ignition of the mixture is almost homogeneous. These experiments show the possibility of application of discharge in the fast ionization wave form to spatially-uniform mixture excitation and ignition.

4.6 Ignition of homological series of hydrocarbons.

The problem of the uniform ignition of a combustible mixture of gases is of crucial importance from both scientific and technological standpoints. The oxidization of a fuel proceeds via a chain mechanism, which is very fast. The delay time of ignition is limited by the rate at which active centers are produced, usually by thermal dissociation. For this reason, the total rate of reaction is, in fact, higher with artificial initiation of a chain. The easiest way to produce free radicals is to decompose the weakest bond of a molecule.¹⁴⁸

The two mechanisms by which a discharge can affect a gas should be taken into account when using a discharge to initiate combustion. For discharges resulting in the formation of

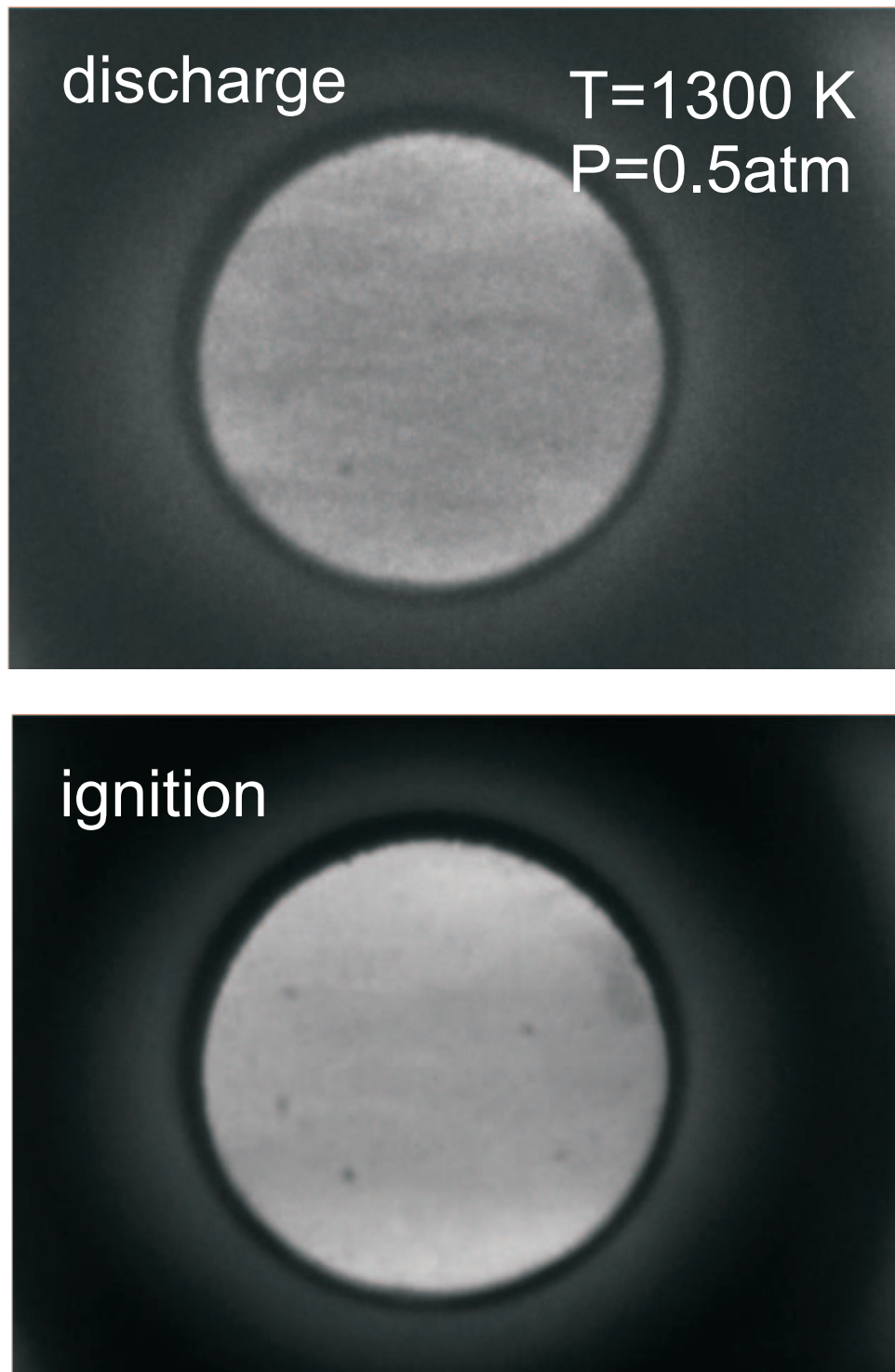


Figure 4.23: Image of a nanosecond discharge (gate 1 ns) and combustion (gate 30 mks) stages

an equilibrium (or nearly equilibrium) plasma (e.g., sparks and arcs), the main factor that reduces the delay time of ignition is local heating of gas and, accordingly, the increase in rate of thermal dissociation.^{103,149,150} In the case of a nonequilibrium plasma, the

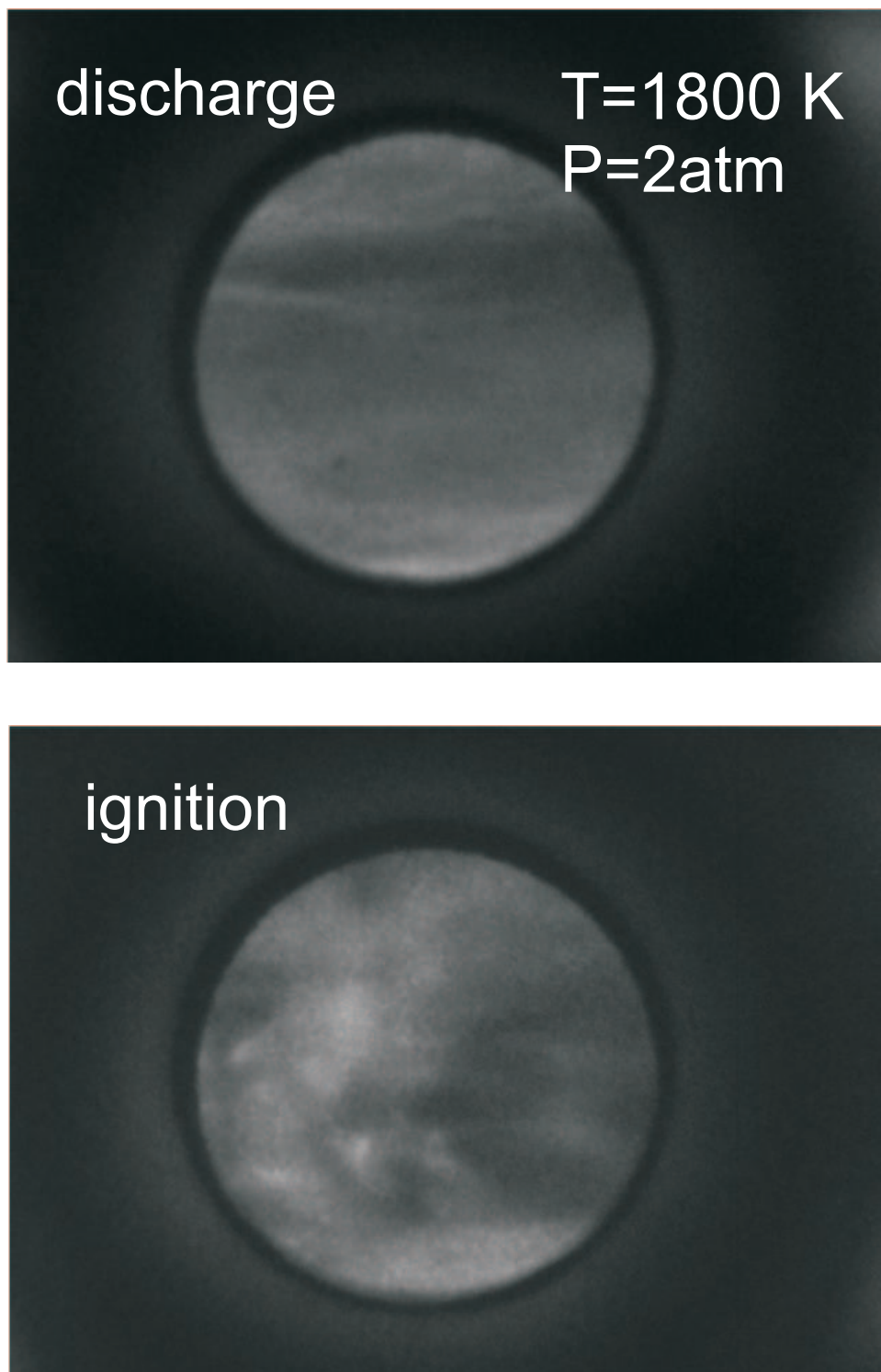
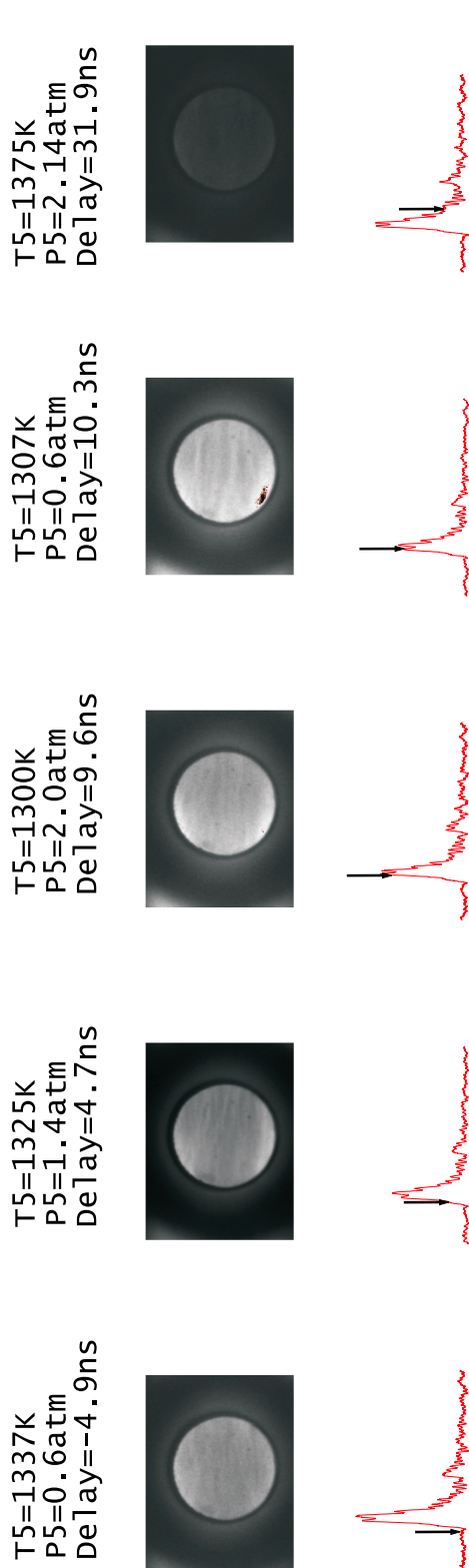


Figure 4.24: Image of a nanosecond discharge (gate 1 ns) and combustion (gate 30 mks) stages

main mechanism initiating chain reactions is dissociation and excitation of molecules by electron-impact. The question of the efficiency of using nonequilibrium plasmas still

Discharge Phase



Flame Phase

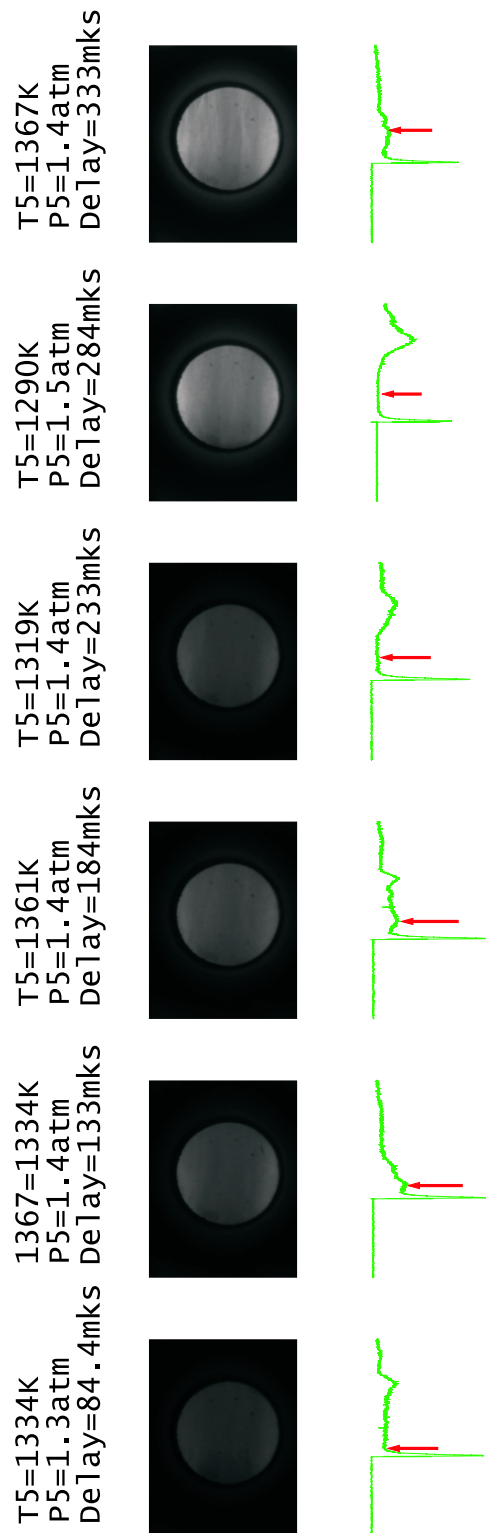


Figure 4.25: Image of a nanosecond discharge (gate 1 ns) and combustion (gate 30 mks) stages. Mixture $\text{CH}_4:\text{O}_2:\text{N}_2:\text{Ar}=1:4:15:80$

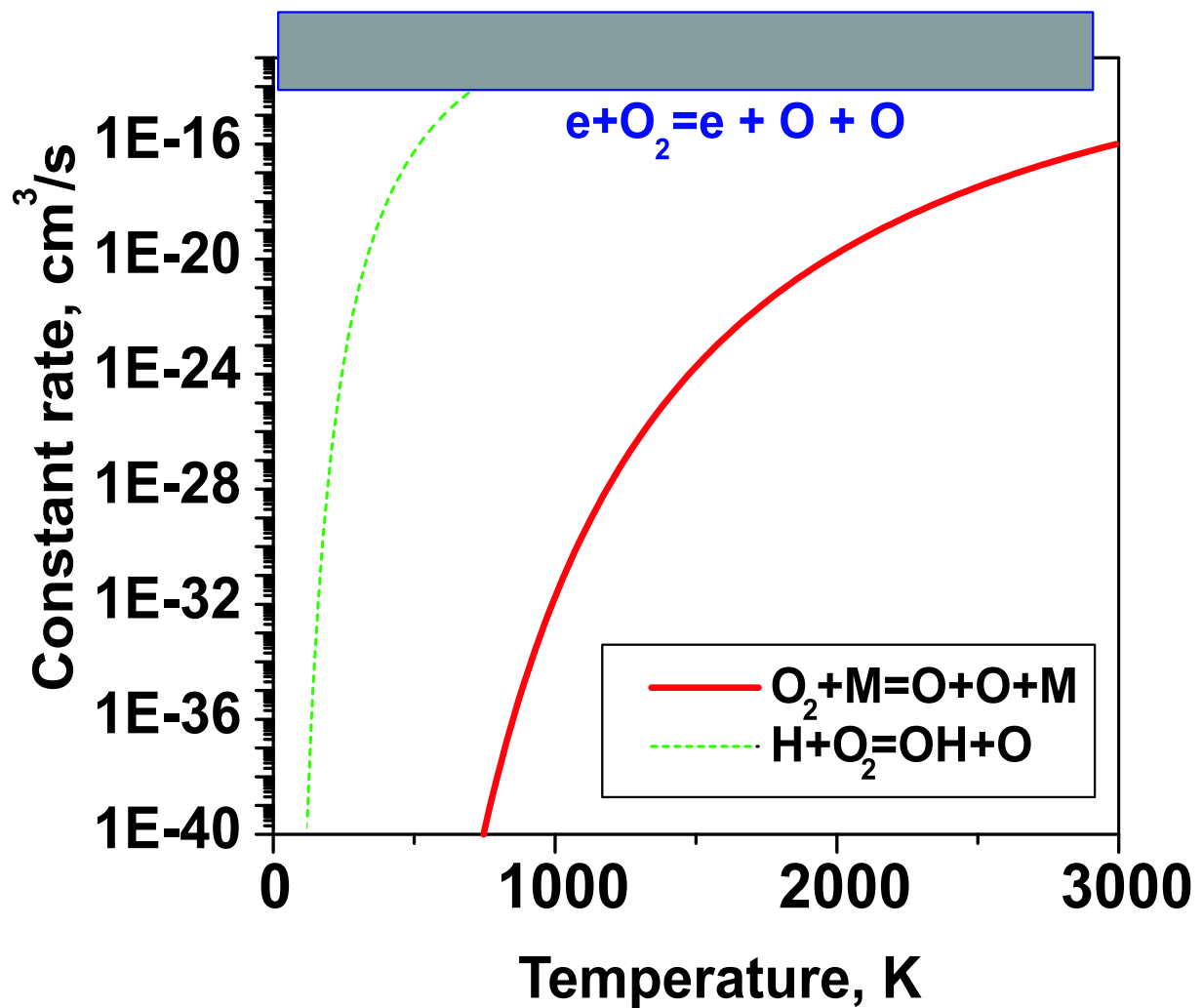


Figure 4.26: Comparison of typical reaction rates at different temperatures: solid line is a rate of reaction of thermal dissociation; dashed line is a rate of a typical reaction of chain prolongation; square in the top of a plot - typical rate of reaction of dissociation by an electron impact at electric field values typical for the discharge

remains open. On the one hand, even relatively small amounts of atoms and radicals ($\sim 10^{-5}$ – 10^{-3} of the total number of the gas particles) can shift equilibria in the system and initiate a chain reaction, so, it may be efficient. For example, Fig. 4.26 demonstrates the difference between reaction rates. From the figure it is evident that dissociation by electron impact in nonequilibrium plasma is much more efficient in comparison with the thermal dissociation which becomes significant at very high temperatures only.

Moreover, if mentioned concentration of active particles is produced uniformly over the entire volume of gas, the combustion will certainly be non-detonation in character. On the other hand, the problem of igniting a spatially uniform discharge in a large volume of gas with a relatively high initial density of neutral particles is technically complicated.

The ignition of mixtures of hydrogen+air and methane+air diluted with either argon or helium has been studied in our laboratory.¹¹³ The mixtures were ignited by a spatially uniform nanosecond discharge. The experiments and calculations showed that, for cer-

tain initial densities and temperatures, significant decreases (by 600 K) of the ignition temperature were observed. An advantage of high-voltage nanosecond discharges is that they almost instantaneously (in our experiments, over a time of a few nanoseconds) bridge the 20-cm-long discharge gap and then produce atoms and radicals, which are required to initiate spatially uniform combustion. The characteristic time during which energy is deposited in the gas can be increased to a few hundred nanoseconds and is limited by a transition of the discharge to an arc. It was also shown¹¹³ that the ignition delay time substantially depends on the discharge parameters and the density of gas.

A comprehensive study of the discharge parameters allows^{14,80} one to analyze the efficiency of the produced plasma as a generator of active particles. Present-day methods of recording high-voltage nanosecond pulses facilitate measurements of the current and voltage waveforms with a time resolution of several nanoseconds. The aim of this study was a detailed analysis of the electric parameters of the discharge and their influence on the efficiency of ignition, as well as the possibility of optimizing discharges used to ignite combustible mixtures.

This part of our work covers two questions: the change of the ignition delay from lower to higher hydrocarbons in a set of C1-C4; experiments to elucidate the role of dissociated and excited species in the ignition.

As a reference result, we considered data obtained for the methane – synthetic air stoichiometric mixture, diluted by argon. What is important that we came back to this mixture during 1.5 years with a gap of a half of a year. The results represented here is a summary of all these data, which confirms an excellent reproducibility of the results.

Table 1 presents the parameters measured behind the reflected shock wave for every experiment in CH₄-N₂-O₂-Ar mixture. The data are arranged in decreasing order of temperature T_5 . The energy input W is represented in the last column of the table. A plot of time delay of ignition versus temperature based on data from Table 1 and previous work¹¹³ is shown in Fig. 4.27. The operation time of the shock tube is indicated by the horizontal dash-dot line.

In addition to the experimental measurements, the dependencies of the autoignition time by the GRI-Mech 3.0⁴ mechanism simulated with the Chemkin 2.0 computer code for chemical kinetics are also shown. The computations were performed at a constant pressure. It can be seen that the simulation (symbols 4) and experimental (symbols 1) results are in good agreement for pressures of ~ 2 atm behind the reflected shock wave. Parameters for the autoignition at 0.5 atm were out of the operating range of our shock tube, and the results of calculations at $P_5=0.5$ atm are represented by a dashed line. With a discharge, both the ignition time and the minimum temperature needed for ignition decrease. At a pressure of 2 atm, the decrease in the ignition temperature is 100 K, whereas at a pressure of 0.5 atm, the ignition temperature decreases by 600 K. One of the aims of our detailed monitoring of the electric parameters of the discharge was to reveal a reason for such a discrepancy.

To analyze the effect of a nanosecond-discharge plasma on combustible mixtures in more detail, it is necessary to thoroughly examine the electric parameters of the discharge. The monitoring of the energy deposited in a gas is a common diagnostic method for studying repetitive nanosecond discharges at room temperature.^{90,94,151} The dependence of the energy deposited in the gas on the gas's density, $w(n)$, is usually dome-shaped. The maximum of $w(n)$ lies approximately in the same density range as the maximum of

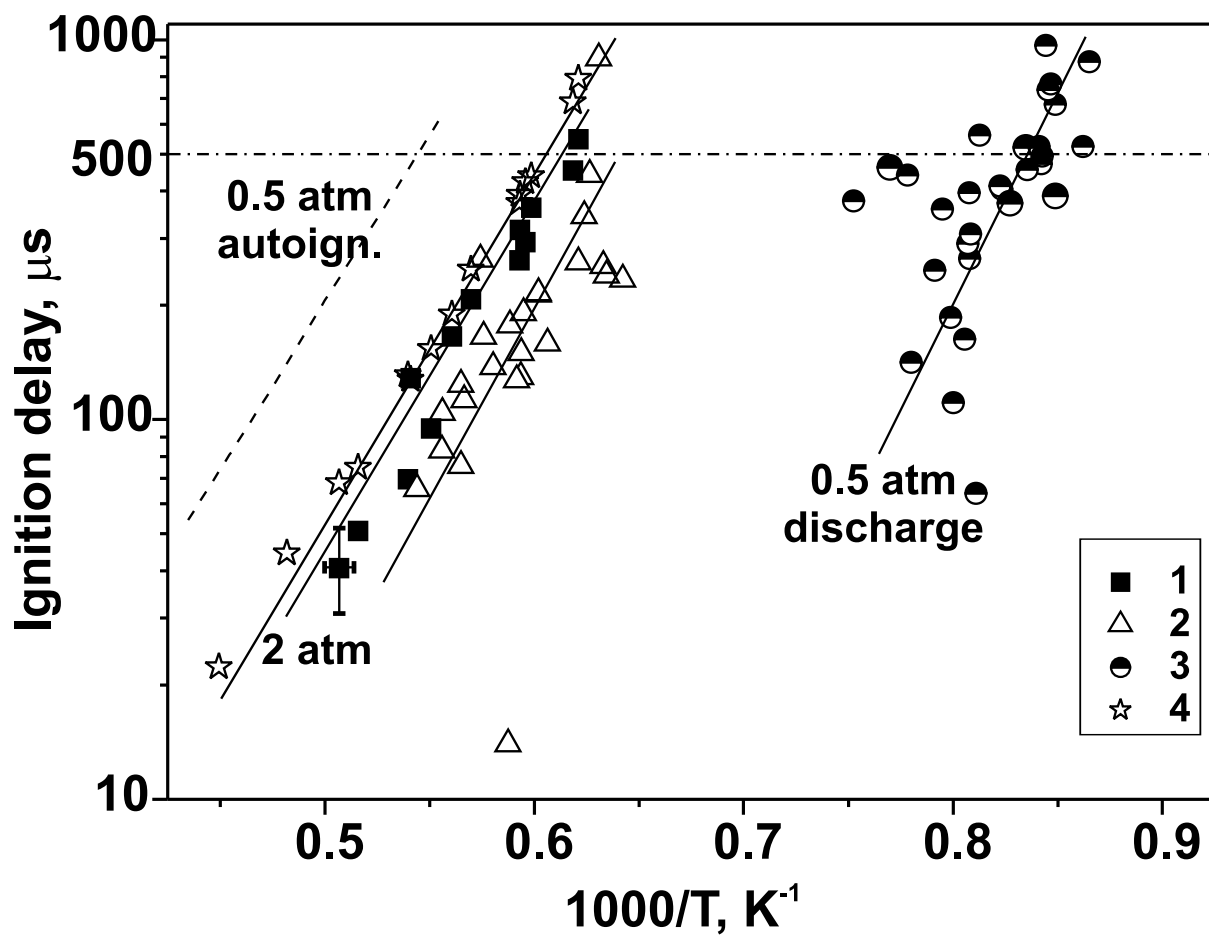


Figure 4.27: Ignition delay time *vs* temperature. Symbols: 1 — 2 atm, autoignition; 2 — 2 atm, ignition with discharge; 3 — 0.5 atm, ignition with discharge; dashed line — 0.5 atm, autoignition (calculated); 4 — 2 atm, autoignition (calculated).

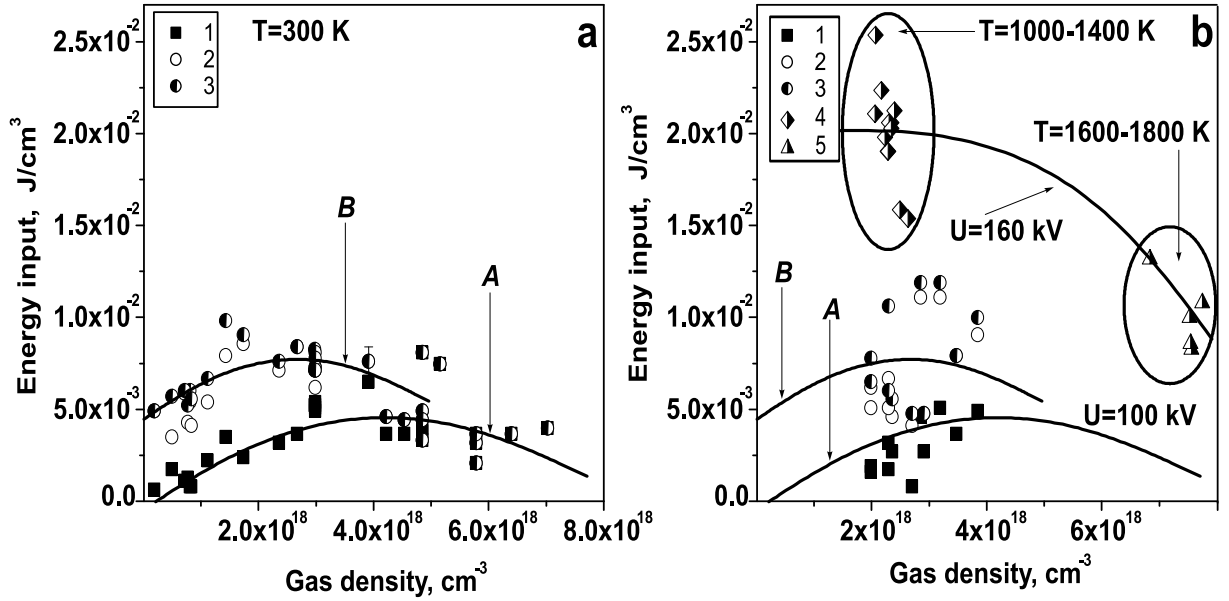


Figure 4.28: Energy deposited in the discharge: **a** — low temperature, **b** — high temperatures. Curves A and B are discussed in the text. Symbols: 1 — w_1 , $U = 100\text{ kV}$; 2 — $w_1 + w_2$, $U = 100\text{ kV}$; 3 — $w_1 + w_2 + w_3$, $U = 100\text{ kV}$; 4, 5 — $w_1 + w_2 + w_3$, $U = 160\text{ kV}$.

the discharge propagation velocity. So far, no measurements of energy deposition in a gas in a single-pulse nanosecond discharge at gas temperatures of $\sim 2000\text{ K}$ have been performed. Figure 4.28a plots the energy deposited in the gas in a single-pulse discharge versus the gas's density at a gas temperature of 300 K . The amplitude and duration of the high-voltage pulse are 100 kV and nearly 50 ns , respectively. In Fig. 4.28, the lower curve (A) shows the energy deposited during the first (main) pulse (w_1), and the upper curve (B) shows the total deposited energy, with allowance for all the subsequent reflections ($w_1 + w_2 + w_3$), and the symbols show the scatter of the w_1 , $w_1 + w_2$ and $w_1 + w_2 + w_3$. It can be seen that almost the entire energy is deposited during the main pulse and one subsequent reflection ($w_1 + w_2$). At a gas temperature of 300 K , the dependence of $w(n)$ has a shape typical for a discharge in the form of a repetitive fast ionization wave.¹⁴ The two lower curves in Fig. 4.28b follow the curves (A) and (B) measured at room temperature, whereas the symbols 1–3 show the energy deposited in the gas at $1000\text{--}1400\text{ K}$ with a high-voltage pulse amplitude of 100 kV . It can be seen that, in spite of a somewhat larger scatter in the experimental data, the energy deposited in the gas at room temperature and a temperature of $1000\text{--}1400\text{ K}$ is approximately the same. Thus, the temperature dependence of the total energy deposited in the gas changes only slightly, when the gas is heated to temperatures of a few thousand degrees. This circumstance allows one to extrapolate the experimental results obtained at room temperature to higher temperatures.

Figure 4.28 also plots the total energy deposited in the gas (with allowance for the main pulse and two reflections) versus gas density for a high-voltage pulse amplitude of 160 kV (symbols 4 and 5). One can see that a one-and-a-half increase in the voltage leads to a fourfold increase in the total energy deposition. We note that there are two separate groups of points marked with ovals. The left group corresponds to temperatures of $1000\text{--}1400\text{ K}$ and pressures behind the reflected shock wave of $\sim 0.5\text{ atm}$, whereas the right

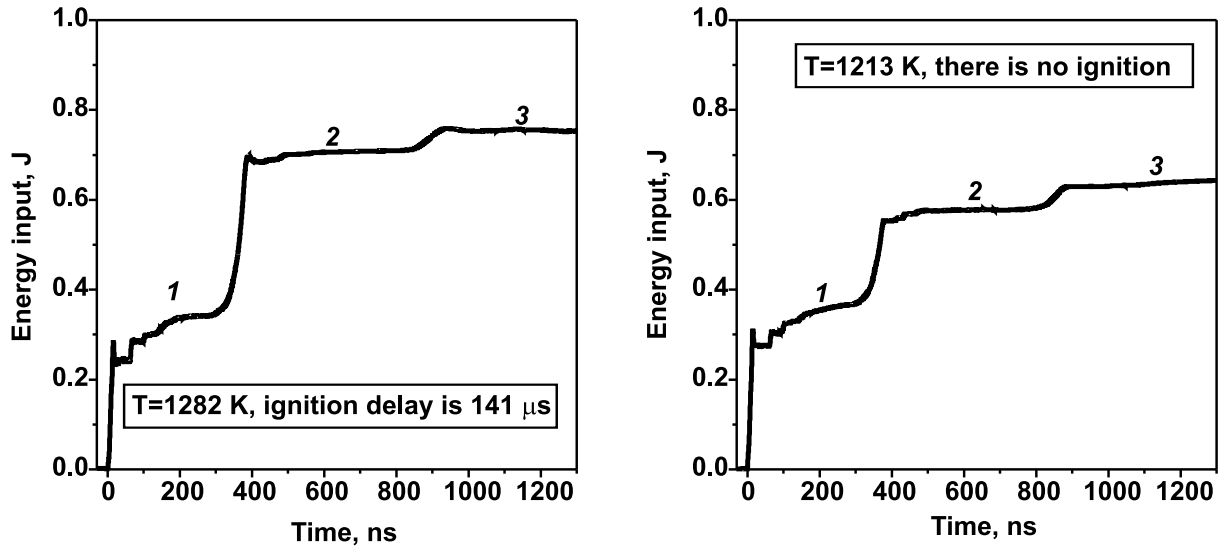


Figure 4.29: Energy input *vs* time. The plateau 1 corresponds to the energy W_1 , the plateau 2 — to the $W_1 + W_2$, the plateau 3 — to the $W_1 + W_2 + W_3$.

group corresponds to temperatures of 1600–1800 K and pressures of 2 atm. One may to interpolate the $w(n)$ dependence by a dome-shaped curve, as was done for measurements at $U=100$ kV. Let us consider two points taken from the left group. The time evolution of the deposited energy for these points are represented in Fig. 4.29. One can see that almost one-half of the energy (w_1) is deposited during the main pulse. In spite of the fact that the points in Figs 4.29a and 4.29b differ only slightly (by less than 10%) in the deposited energy, the ignition time amounts to 141 μs at a temperature of 1282 K, whereas, at a temperature of 1213 K, the mixture is not ignited at all. So, the absolute value of the deposited energy (though certainly being a characteristic of a gas discharge) does not reflect the kinetic features of the system and does not allow one to analyze the efficiency of the discharge as a plasmochemical source.

Returning to Fig. 4.28b, we note that, in the temperature range 1000–1400 K, the specific energy deposition changes by a factor of 5 (from 0.5×10^{-2} to 2.5×10^{-2} J/cm³) as the high-voltage pulse amplitude varies from 100 to 160 kV. At the same time, the temperature dependence of the ignition time, which involves all these points, is fairly smooth (see Fig. 4.27). The experimental data on the discharge current and voltage indicate that the amplitude of the high-voltage pulse only slightly affects the discharge's evolution in the gas density range under study.

At high pressures (~ 2 atm) and high (1600–1800 K) temperatures, the situation is quite different. Thorough analysis of the waveforms (Fig. 4.30) of the current, voltage, and emission intensity from short-lived states of molecular nitrogen ($\lambda = 337.1$ nm, $C^3\Pi_u(v' = 0) \rightarrow B^3\Pi_g(v'' = 0)$ transition) shows that the discharge evolves at low gas densities (2.3×10^{18} cm⁻³, 0.5 atm, 1000–1400 K) quite differently from that at high gas densities (7.5×10^{18} cm⁻³, 2 atm, 1600–1800 K). Indeed, at a pressure of 0.5 atm, the signals from the current gauge and photomultiplier are fairly intense. At a pressure of 2 atm, the current and emission intensity are relatively low, whereas the intense signal from the capacitance gauges indicates that the ionization region does not reach the low-voltage electrode. In this regime, the discharge develops as a corona from the high-voltage electrode and the atoms

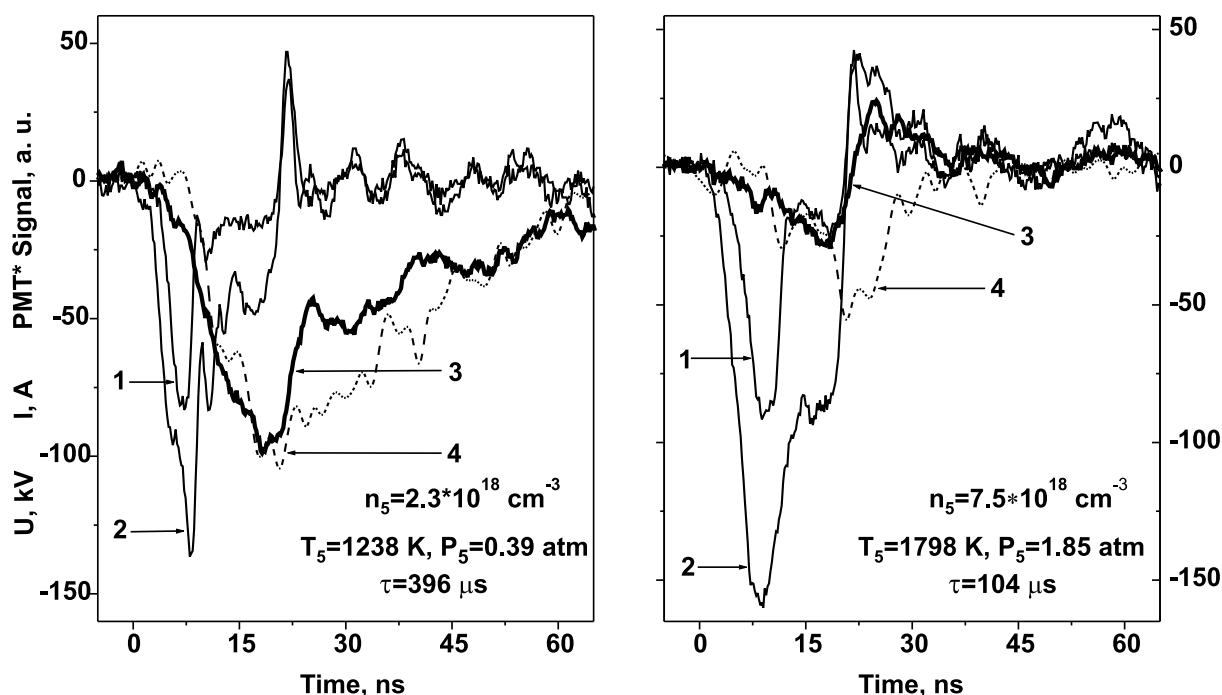


Figure 4.30: Typical waveforms of voltage (curves 1 and 2 are the signals from the different capacitive gauges), current (curve 3) and emission (curve 4).

and radicals are mainly produced in the electrode region. To increase the production rate of active particles, it is necessary to increase the output voltage of the Marx generator to a value sufficient for the discharge to close the gap.

The same experiments were performed for different hydrocarbons. Fig. 4.31 demonstrates dependence of ignition delay time for autoignition and ignition by nanosecond discharge for propane and butane containing mixtures. It is clearly seen that ignition delay is well-pronounced in both cases. Difference for C_4H_{10} is the most strong in a region of 1100–1200 K, while for C_3H_8 the difference is practically constant within a range of 1400–1600 K and comprises about of 200 K.

Fig. 4.32 demonstrates ignition delay for C3 and C4 – containing mixtures in $1000/T$ coordinates. Energy measurement have been performed for different mixtures. Detailed analysis of energy input in methane – containing mixture is analyzed above. Fig. 4.33 demonstrates energy input in a set of experiments with propane – containing mixture. It is obvious that the energy values are of the same order of magnitude as in methane-containing mixture.

4.7 Kinetics of C1-C5 hydrocarbons in gas mixtures for PAI

It is extremely important to understand the physical peculiarities of ignition and combustion supported by nonequilibrium plasma of gas discharges. Ignition and combustion, which are sustained by nonequilibrium plasma, are caused by interaction of a number of physical phenomena. In order to give an adequate description of PAI/PAC it is neces-

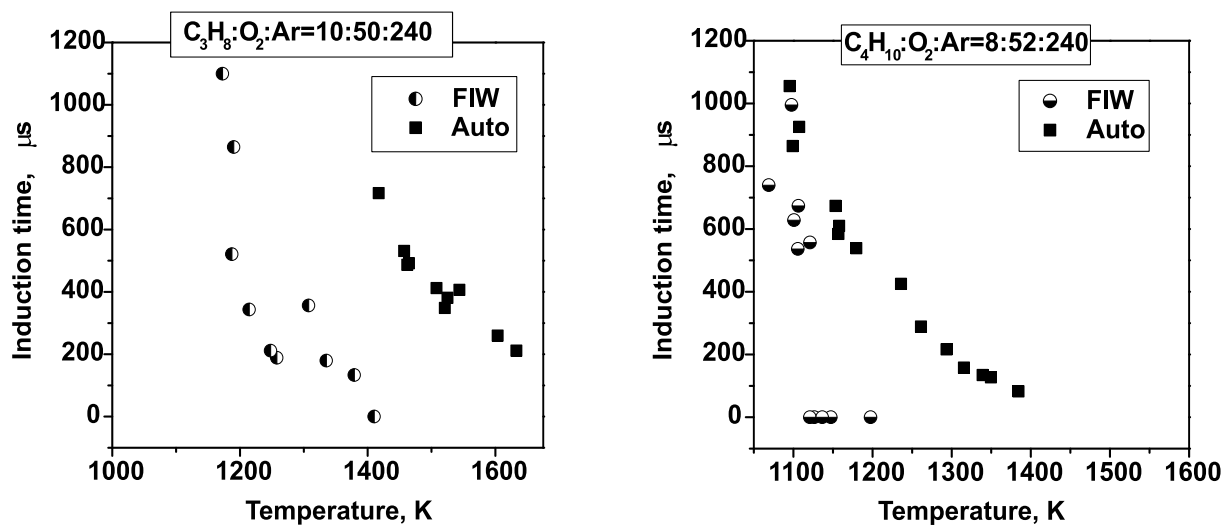


Figure 4.31: Ignition delay time *vs* temperature. **a** — propane – containing mixture, **b** — butane – containing mixture.

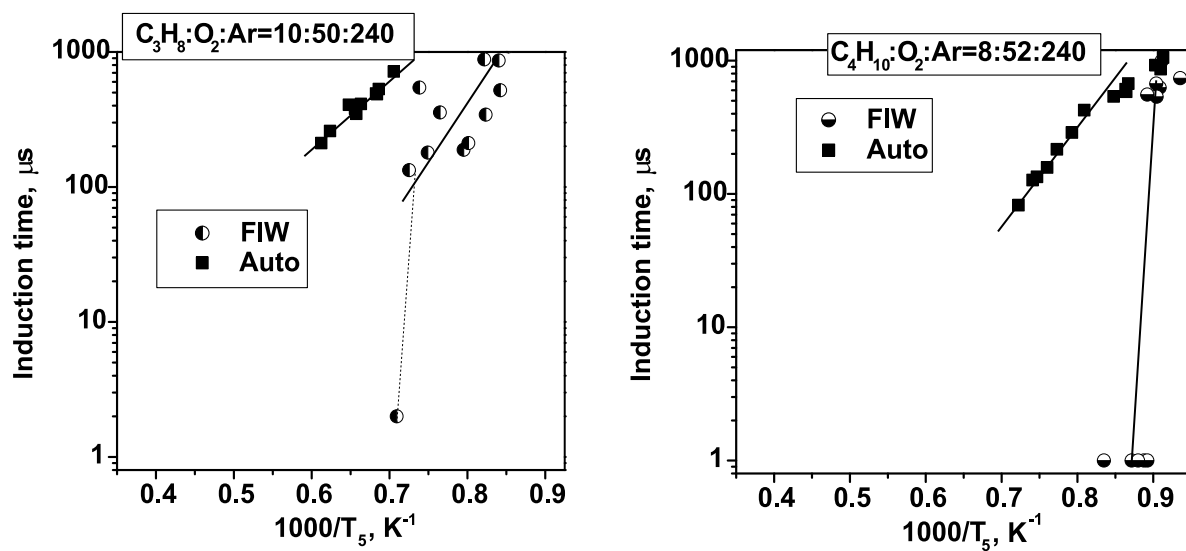


Figure 4.32: Ignition delay time *vs* temperature. **a** — propane – containing mixture, **b** — butane – containing mixture.

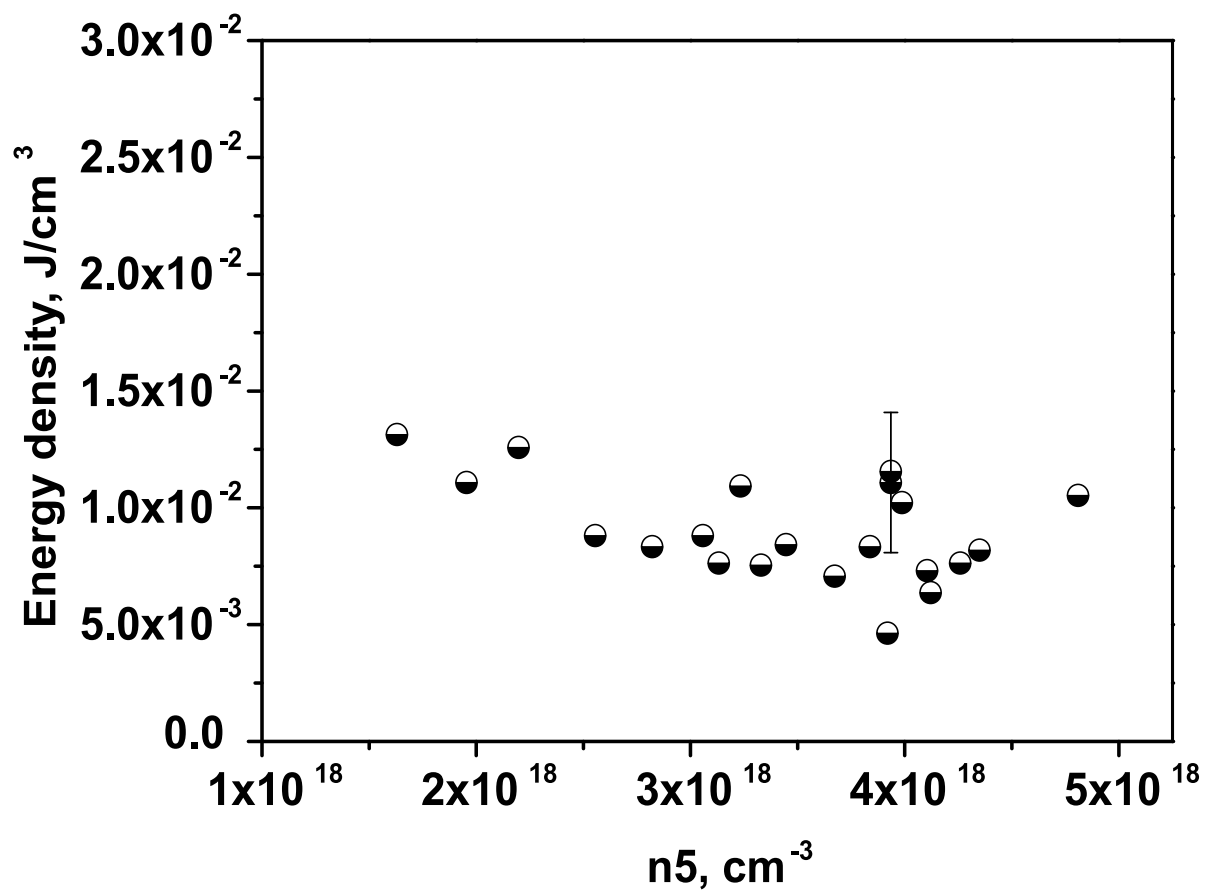


Figure 4.33: Energy input in a gas during nanosecond discharge action in dependence upon gas density behind the reflected shock wave.

sary to combine detailed knowledge in gas discharge physics and chemical kinetics, both high-temperature and that taking into account excited and charged particles.

Nowdays different schemes describing the kinetics of fuel–air mixtures at high temperatures are known. They include hundreds of species and thousands of reactions. A detailed sensitivity analysis is an inherent tool to analyze such schemes and even in “pure” combustion schemes a precise description of experimental data, especially with complex fuels, requires significant computational efforts. Discharge kinetics at low gas temperatures has been under investigation for decades.^{71,152}

There are different opinions concerning the interaction between nonequilibrium plasma and combustion. For discharges at low reduced electric fields, low-energy excitation, such as vibrational excitation or excitation of lower electronic states,¹⁵³ is dominant. So, paper¹⁵⁴ proposed a kinetic mechanism where electronically excited oxygen molecules in $a^1\Delta_g$ and $b^1\Sigma_g^+$ – states are the main components responsible for enhanced combustion efficiency. The authors reported that a possible excitation of these states by laser radiation at wavelengths 1.268 μm and 762 nm, respectively, can lead to ignition of $\text{CH}_4\text{:O}_2$ mixture at low temperature. Referring to experiments at high reduced electric fields, researchers insist on the leading role of high-energy electronic levels leading to dissociation. Here, dissociation may be caused by both a direct electronic impact and an interaction of molecules with electronically excited species, such as $\text{N}_2^* + \text{O}_2 = \text{N}_2 + \text{O} + \text{O}$.⁷¹

The other authors¹⁵⁵ analyzed the efficiency of O-atoms, dissociated by the discharge. Hydrogen–oxygen kinetics at 1 atm and different initial mixture temperatures was taken as a basis for calculations. A certain amount of oxygen atoms was artificially injected at the initial moment of a common high-temperature modelling of the ignition. Minimal density of O-atoms leading to ignition was determined. It was shown that at low temperatures the main effect leading to acceleration of ignition process, is fast gas heating due to recombination of radicals. Injection of O-atoms becomes to be more and more efficient starting from hundreds of K. The atoms cause not only heating but initiation of chemical chains, and this scenario is much more promising. The authors emphasized that gas discharge impact is not restricted by oxygen recombination. The nonequilibrium energy input into the gas leads to additional production of ions, as well as electronically and vibrationally excited species. The so-called “ion chains” and “energetic chains” are well-known in laser physics. They are exactly the chains where ions or excited species rather than radicals serve as intermediates. The presence of a few chain mechanisms in the system do not provide an additive result, inasmuch as chain processes are non-linear. On the other hand, these mechanisms have not been thoroughly investigated yet. For example, the experiments and the subsequent numerical calculations⁹⁵ revealed a plasma chemical chain branching mechanism multiplying the primary radicals generated in low-temperature hydrocarbon/air and CO/air plasmas. At the same time, the experiments in ambient temperature hydrocarbon–air and hydrocarbon–oxygen mixtures¹⁵⁶ demonstrated that the role of the discharge in low-temperature oxidation of different alkanes, starting from CH_4 to C_6H_{14} , can be reduced to the supplier of radicals, while further oxidation takes place via well-known low temperature oxidation mechanisms (see, for example, mechanism¹⁵⁷). Some authors claim¹⁵⁸ that ions are important for ignition kinetics. They demonstrated numerically that addition of 10^{-4} of NO^+ ions/electrons to $i\text{-C}_8\text{H}_{18}\text{:O}_2\text{:NO:Ar}=1.4\text{:}17.6\text{:}1\text{:}80$ mixture at the pressure 1 atm shifts the ignition delay time.

It is quite typical to numerically analyze the discharge effect on a combustible mixture by artificially injecting different radicals at the initial moment of calculations. Paper¹⁵⁹ investigated numerically the kinetic paths to radical-induced ignition of a methane–air mixture. They were able to obtain the ignition starting even from 300 K at 1 atm mixture pressure injecting CH_3 , CH_2 , CH and C ; there the radical densities were rather high reaching a few percent. The author concluded that this is the CH radical that is mostly important in initiating the chain and which is oxidized to HCO . They also remarked that CH_2 can act as a surrogate for CH as it reacts with H to produce CH , the role of C atoms was restricted to gas heating due to recombination with O_2 producing CO , and CH_3 was found to be relatively unimportant for ignition. The authors concluded that ignition by radicals can be a promising technique and that the researchers have to keep in mind that a real gas discharge gives different radical distributions depending upon the conditions of the experiment.

Paper¹⁶⁰ gave the calculations of the impact of radicals addition on the extinction limits of H_2 and CH_4 flames in a perfectly stirred reactor. They investigated the comparative effect of O , H , N , and NO_x additions and found that the difference between the effects caused by different radicals is very slight. They also reported that the extinction limits of both fuels were extended by adding the radicals, though the effect on the extinction limit was much smaller than that on the ignition limit. In case of low inlet temperature, where the radicals initially added to the mixture were quickly quenched *via* recombination reactions, the combustion enhancement effect was mainly due to the thermal effect by heat release via recombination of radicals. The effect of radical addition on the extinction limit was manifested vividly when the inlet temperature was considerably increased.

The experimental data testifying the increased efficiency of ignition/combustion under non-equilibrium plasma may rarely be considered as unambiguous. In this sense the experiments where, at least, some uncertainties are artificially excluded or where the authors compare the impact of different plasmas under the same experimental conditions are of great importance.

Ethylene oxidation by nanosecond discharge has been observed in paper.¹⁶¹ A high voltage (16 – 18 kV) nanosecond (20 – 30 ns duration) pulsed power with repetitive frequency up to 50 kHz was applied to the electrodes within a pressure range of 70–100 Torr. The discharge power was as low as 70 – 115 W, and the gas temperature was 100 – 300° C. It is important that the authors demonstrated flameless oxidation by plasma or ignition while increasing the energy input in the discharge during the same experiments. The authors concluded that (i) significant amounts of hydrocarbons can be oxidized by low temperature plasma chemical reactions before ignition is achieved, (ii) the detected plasma temperature rise is due to heat release during the net exothermic plasma chemical fuel oxidation process, and (iii) ignition occurs when the temperature rise due to heat generation in the plasma chemical oxidation process becomes sufficiently high. As the authors¹⁶¹ put this, the low-temperature plasma chemical fuel conversion and the resultant flow heating “open the door” to ignition.

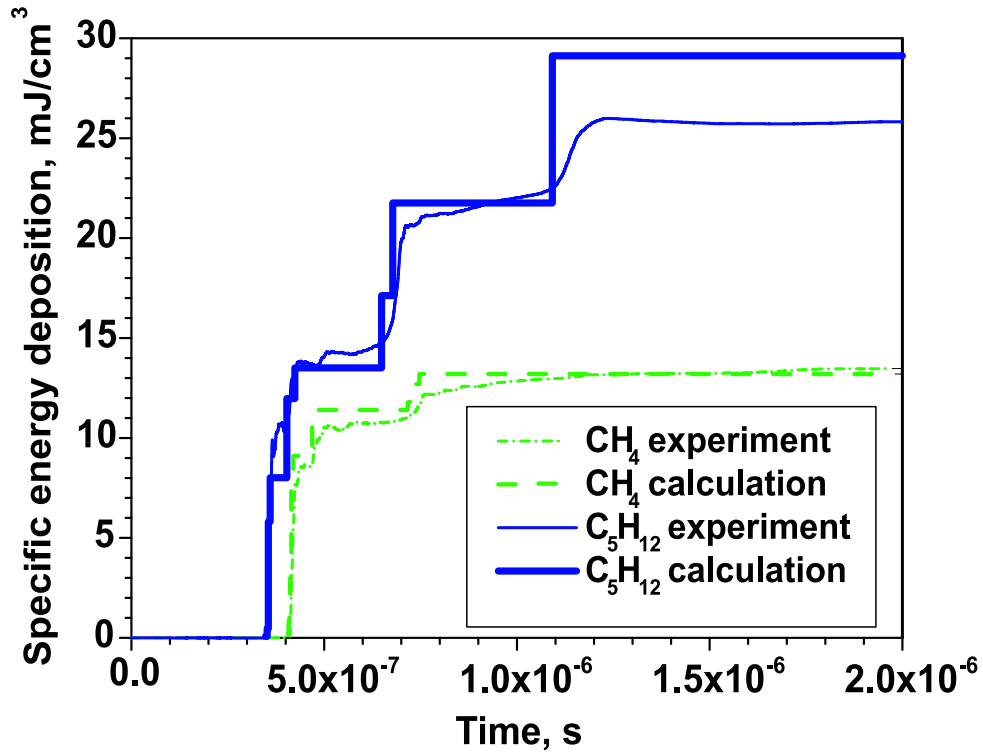


Figure 4.34: The evolution in time of the specific energy deposited in the Ar:O₂:CH₄ mixture at 1.1 atm and 1530 K and in the Ar:O₂:C₅H₁₂ mixture at 0.52 atm and 1390 K. Curves 1 correspond to calculation and curves 2 correspond to measurements.

4.7.1 Experimental analysis of the artificial ignition. mixtures with hydrocarbons

In this part we will consider the continuation of our previous work at the conditions where the impact of nanosecond pulsed discharge and ignition are separated in time. In 1996 it was proposed¹⁶² to use the shock wave technique, rather common for autoignition studies, to check the efficiency of ignition by nanosecond discharge. The calculations demonstrated that an operation near the autoignition temperature threshold gives an opportunity to quantitatively measure the shift of the ignition threshold. It was proposed to use a nanosecond pulsed discharge in the form of spatially uniform fast ionization wave to initiate ignition. Indeed, in this case a shock tube allows to obtain fixed pressure and temperature behind the reflected shock wave. Significantly diluted by monatomic gas, such as Ar or He, the flow will be quasi-one-dimensional, so, it is possible to use the 1D shock tube theory to determine the gas temperature T_5 , pressure P_5 and gas density n_5 behind the reflected shock wave. Here, the nanosecond discharge is spatially uniform up to the gas densities about 10^{19} cm^{-3} at high voltage amplitudes as high as tens and hundreds of kV. This means that the plasma is non-thermal in quite a large volume. Such experiments were carried out and reported in our papers.^{80,113,155}

A typical experimental setup is described elsewhere.¹¹³ In each experiment the delay time for autoignition was compared with the ignition delay time for ignition by a nanosecond discharge developed in the end-plate section of the shock tube. The section was made of dielectric material and the discharge developed between the end plate of

the shock tube and stainless steel part 20 cm apart. The shock tube had a rectangular cross-section of 25x25 mm. Eight optical windows were used to provide optical diagnostics. The ignition delay time was determined from a sharp increase of OH (306 nm) or CH (431 nm) emission. It is worth to mention here that CH emission and OH emission give similar ignition delay time. The system for monitoring the shock wave parameters included a system for measuring the velocities of the incident and reflected shock waves by means of the laser schlieren technique and a system for controlling initial pressure. The gas density (ρ_5), pressure (P_5), and temperature (T_5) behind the reflected shock wave were determined from the known initial gas mixture composition, the initial pressure, and the velocity of the incident shock wave, using conservation laws and assuming that relaxation was complete and chemical reactions frozen. Thermodynamic data were taken from.¹³⁸ Correction of such approach and of the calculation of T_5 has been checked by controlling IR emission of CO₂ additives (1 %) in specially prepared controlled mixtures. It has been shown that the ignition temperature determined from schlieren signals and from IR coincides reasonably for all the mixtures except the mixture with methane where systematical error can reach 50 K.

Table 4.11: Processes dominating production of atoms and radicals by gas discharge in Ar:CH₄ mixtures

Number	Reaction	Rate constant, cm ³ /s or cm ⁶ /s	Reference
Electron impact dissociation			
R1	$e + \text{O}_2 \rightarrow e + \text{O} + \text{O}$	$f(E/N)$	163
R2	$e + \text{CH}_4 \rightarrow e + \text{CH}_3 + \text{H}$	$f(E/N)$	164
Electron impact excitation			
R3	$e + \text{Ar} \rightarrow e + \text{Ar}^*$	$f(E/N)$	163
Electron impact ionization			
R4	$e + \text{Ar} \rightarrow 2e + \text{Ar}^+$	$f(E/N)$	163
R5	$e + \text{O}_2 \rightarrow 2e + \text{O}_2^+$	$f(E/N)$	163
R6	$e + \text{CH}_4 \rightarrow 2e + \text{CH}_4^+$	$f(E/N)$	164
Quenching of excited Ar atoms			
R7	$\text{Ar}^* + \text{O}_2 \rightarrow \text{Ar} + 2\text{O}$	$2 \cdot 10^{-10}$	165166
R8	$\text{Ar}^* + \text{CH}_4 \rightarrow \text{Ar} + \text{CH}_2 + 2\text{H}$	$3.25 \cdot 10^{-10}$	165166
R9	$\text{Ar}^* + \text{CH}_4 \rightarrow \text{Ar} + \text{CH} + \text{H} + \text{H}_2$	$5.833 \cdot 10^{-11}$	165166
R10	$\text{Ar}^* + \text{CH}_4 \rightarrow \text{Ar} + \text{CH}_3 + \text{H}$	$5.833 \cdot 10^{-11}$	165166
R11	$\text{Ar}^* + \text{CH}_4 \rightarrow \text{Ar} + \text{CH}_2 + \text{H}_2$	$5.833 \cdot 10^{-11}$	165166
Charge exchange			
R12	$\text{CH}_4^+ + \text{O}_2 \rightarrow \text{CH}_4 + \text{O}_2^+$	$5 \cdot 10^{-10}$	Estimate
R13	$\text{Ar}^+ + \text{O}_2 \rightarrow \text{Ar} + \text{O}_2^+$	$1 \cdot 10^{-10}$	112
R14	$\text{Ar}^+ + \text{CH}_4 \rightarrow \text{Ar} + \text{CH}_3^+ + \text{H}$	$1.056 \cdot 10^{-9}$	112
R15	$\text{Ar}^+ + \text{CH}_4 \rightarrow \text{Ar} + \text{CH}_2^+ + \text{H}_2$	$2.275 \cdot 10^{-10}$	112
Electron-ion recombination			
R16	$e + \text{O}_2^+ \rightarrow \text{O} + \text{O}$	$2 \cdot 10^{-7} \cdot (300/T_e)$	71
R17	$e + \text{CH}_4^+ \rightarrow \text{CH}_3 + \text{H}$	$1.75 \cdot 10^{-7} \cdot (300/T_e)^{0.5}$	109167
R18	$e + \text{CH}_4^+ \rightarrow \text{CH}_2 + 2\text{H}$	$1.75 \cdot 10^{-7} \cdot (300/T_e)^{0.5}$	109167
R19	$e + \text{CH}_3^+ \rightarrow \text{CH}_2 + \text{H}$	$7.75 \cdot 10^{-8} \cdot (300/T_e)^{0.5}$	168

R20	$e + \text{CH}_3^+ \rightarrow \text{CH} + 2\text{H}$	$2 \cdot 10^{-7} \cdot (300/T_e)^{0.4}$	168
R21	$e + \text{CH}_3^+ \rightarrow \text{CH} + \text{H}_2$	$1.95 \cdot 10^{-7} \cdot (300/T_e)^{0.5}$	168
R22	$e + \text{CH}_2^+ \rightarrow \text{CH} + \text{H}$	$1.60 \cdot 10^{-7} \cdot (300/T_e)^{0.6}$	168
R23	$e + \text{CH}_2^+ \rightarrow \text{C} + \text{H}_2$	$7.68 \cdot 10^{-8} \cdot (300/T_e)^{0.6}$	168
R24	$e + \text{CH}_2^+ \rightarrow \text{C} + 2\text{H}$	$4.03 \cdot 10^{-7} \cdot (300/T_e)^{0.6}$	168

The nanosecond discharge was initiated at the instant at which the reflected shock wave arrived at the observation point. High-voltage pulses were produced with a ten-stage GIN-9 Marx high-voltage generator. To enable the operation of the spark gap, the generator was filled with nitrogen at a pressure of 3 atm, which provided voltage amplitude in the range 100–160 kV at the high-voltage electrode. The duration of the pulse was about 40 ns, and 1–2 re-reflections were observed during 0.2 μs depending upon the parameters of the experiment.

The experiments were carried out with a set of stoichiometric mixtures $\text{C}_n\text{H}_{2n+2} : \text{O}_2$ (10%) diluted by Ar (90%) for hydrocarbons from CH_4 to C_5H_{12} . The temperature behind the reflected shock wave (T_5) varied from 950 to 2000 K, and the pressure (P_5) was 0.2 to 1.0 atm. In each experiment, we kept parameters T_5 and P_5 the same for autoignition and ignition by the discharge.

The main aim of the present paper was to calculate numerically the shift of the ignition delay time for hydrocarbon–oxygen mixtures numerically in the assumption that the main process which causes the ignition is productions of radicals in nanosecond discharge and in early afterglow, and to compare the results with experimental data.

4.7.2 Simulation of production of atoms and radicals

Numerical simulation of production of active particles in $\text{Ar}:_2\text{C}_n\text{H}_{2n+2}$ gaseous mixtures with a high-voltage nanosecond discharge was reduced (i) to the simulation of production of active particles (electrons, ions, excited particles, atoms and radicals) in a high electric field in the discharge and (ii) to the simulation of conversion of the active particles during plasma decay after the active phase of the discharge. Active particles under consideration were excited Ar atoms, O atoms, H atoms, radicals of hydrocarbon molecules, electrons and positive ions. Production of negative ions and complex positive ions (Ar_2^+ , O_4^+ , etc.) was neglected because of high (> 1000 K) gas temperatures in the discharge gap. At the end of plasma decay, only atoms and radicals were assumed to dominate the composition of active particles, whereas the existence of long-lived excited states was neglected.

The dominant mechanisms for formation of active particles by a high-voltage nanosecond discharge are similar in all gaseous mixtures considered. As an example, Table 4.11 shows the main reactions taken into account to simulate the production of active particles in the $\text{Ar}:\text{O}_2:\text{CH}_4$ mixture. Simulation of the processes during the discharge was carried out using electric fields measured in the discharge gap at every instant. Electron drift velocity and rate coefficients for electron impact dissociation (such as reactions (R1) and (R2) in Table 4.11), for electron impact excitation (reaction (R3)) and for electron impact ionization (such as reactions (R4) — (R6)) were calculated by solving the electron Boltzmann equation in the classical two-term approximation. When solving the Boltzmann equation, the input parameters were the electric field, number density of neutral particles, gas temperature and gas composition. We considered only electron collisions with atoms

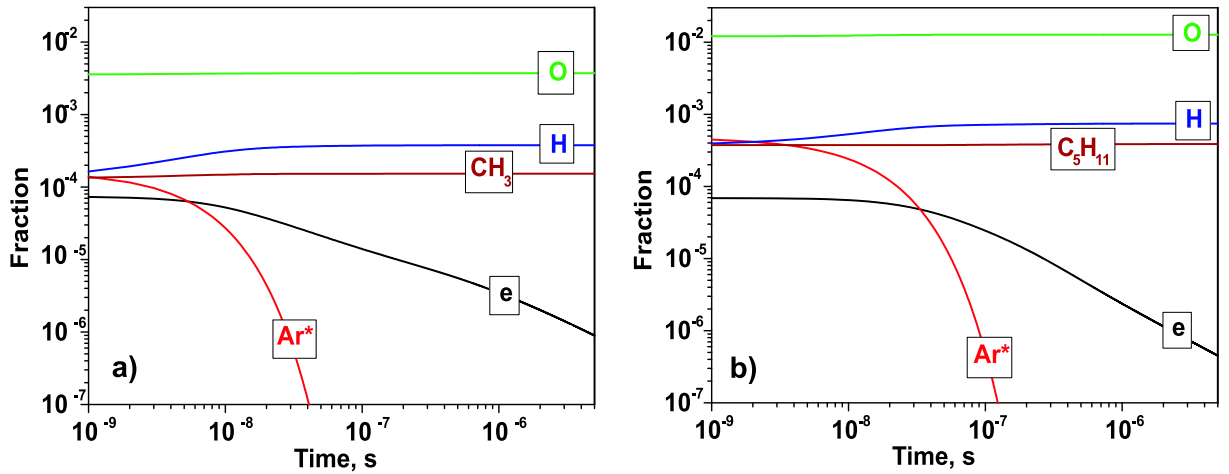


Figure 4.35: The evolution in time of the densities of dominant active species in the afterglow of the discharge in (a) the Ar:O₂:CH₄ mixture and (b) Ar:O₂:C₅H₁₂ mixture. The curves correspond to the same conditions as those in Fig.4.34.

and molecules of the dominant species in the gas mixtures. The effect of electron–electron collisions and collisions between electrons and new particles produced in the discharge was neglected because of small densities of these particles. For electron collisions with Ar, O₂, CH₄ and C₂H₆, we used the available in literature, self-consistent sets of cross sections, which allow a good agreement between calculations and measurements of transport and rate coefficients in the pure gases. Reliable and self-consistent data on electron cross sections for C₃H₈, C₄H₁₀ and C₅H₁₂ are not available. As a first approximation, in this simulation, it was assumed that these cross sections are similar to those for C₂H₆. In this approximation, the largest error for the calculated density of produced atoms and radicals is expected to be induced by the uncertainty in the rate of electron impact dissociation of hydrocarbon molecules during the discharge. However, it will be shown below that this effect is not important under the conditions considered.

The rate coefficients and transport coefficients calculated from the Boltzmann equation were used to simulate the evolution in time of the densities of active particles in a high electric field during the discharge. In this discharge phase, because of its short duration, the loss of active particles can be neglected. As a result, the evolution in time of the densities of these particles in this phase was analytically determined from the corresponding balance equations.

In the beginning of pulses of applied voltage (in the discharge front), there is generally a very short and high overshoot of the applied voltage that cannot be experimentally resolved. During the corresponding peak of the electric field in the discharge gap, according to approximate calculations, a noticeable density of charged particles is produced, whereas the production of neutral active particles is negligible. To take into account the production of electrons and ions in this, poorly known, phase, we considered the initial electron density in the beginning of the main pulses of applied voltage to be an adjusted parameter. This parameter was determined when calculating the evolution in time of the discharge current and adjusting it to corresponding measured data. As an example, Fig. 4.34 compares the calculated specific deposited energy and measured one for the Ar:O₂:CH₄ mixture at 1.1 atm and 1530 K and for the Ar:O₂:C₅H₁₂ mixture at 0.52 atm

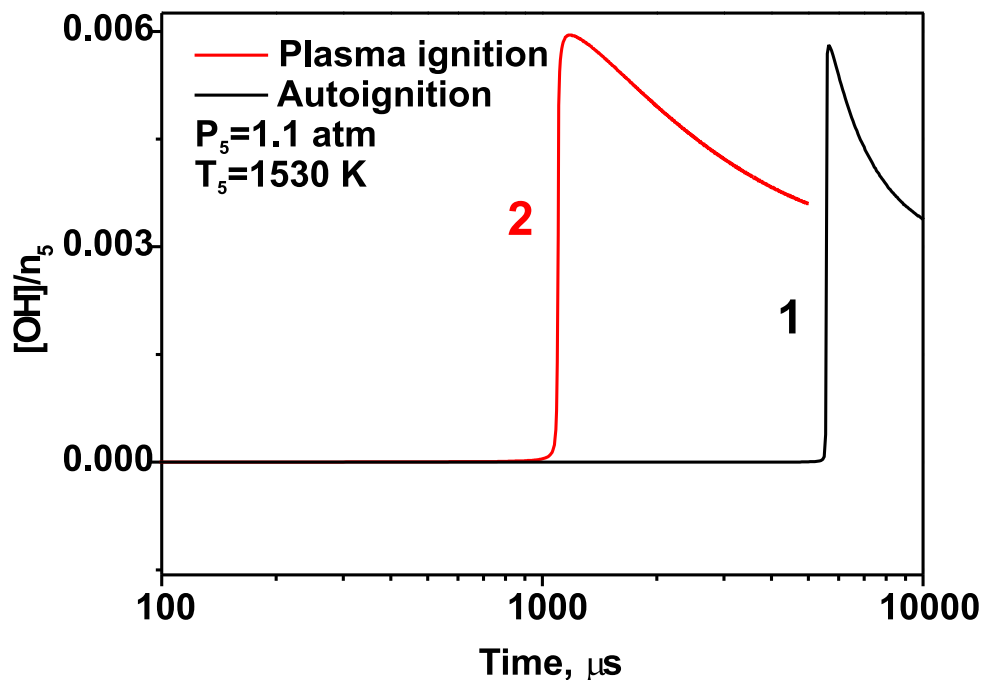


Figure 4.36: The evolution in time of the OH – density in the Ar:O₂:CH₄ mixture at 1.1 atm and 1530 K. Curve 1 corresponds to autoignition and curve 2 corresponds to ignition by injection of radicals.

and 1390 K. The theoretical curves were calculated from the calculated discharge currents and measured electric fields in the gap. The experimental curves were obtained directly from the measured electric field and discharge current. Let us note that typical values of the reduced electric field behind the discharge front are not higher than 150 Td.

In the experiments under consideration, the main pulse of applied voltage was generally followed by several smaller pulses. Production of active particles was simulated also in these additional discharge phases. As a rule, in this case production of atoms, radicals and excited neutral particles was noticeable, whereas production of electrons and ions was not important.

The evolution of the densities of active particles between and behind voltage pulses was simulated using a numerical solution of the balance equations. The rate coefficients for elementary processes were taken from literature or, if required, were estimated. In this phase, in a zero electric field charged particles were removed due to dissociative electron-ion recombination (such as reactions (R16) - (R24) in 4.11) producing an additional number of atoms and radicals. The last particles were also produced due to charge exchange of some positive ions on hydrocarbon molecules (such as reactions (R14) and (R15)) and due to quenching of excited Ar atoms by oxygen and hydrocarbon molecules (such as reactions (R7) — (R11)). In our kinetic model, in the end charged and excited particles were excluded from the consideration and the gas mixture consisted of initial neutral species and atoms and radicals produced during the discharge and in its afterglow. The densities of atoms and radicals were used further as input parameters for a computer program to simulate ignition in the mixtures under consideration.

Fig. 4.35 shows the evolution in time of the densities of dominant active species in the

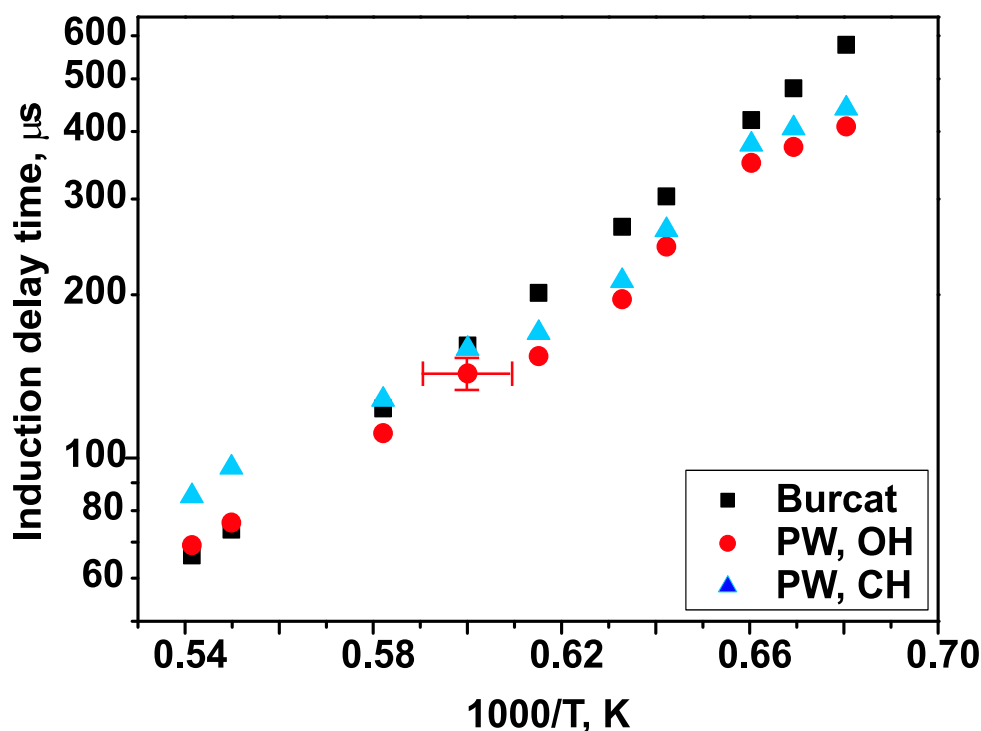


Figure 4.37: Comparison of autoignition delay time, experimentally determined from OH-emission at 306 nm (PW, OH), experimentally determined from CH-emission at 431 nm (PW, CH), and calculated in accordance with the formula given by Burcat¹⁶⁹.

afterglow of the discharge in the Ar:O₂:CH₄ mixture and Ar:O₂:C₅H₁₂ mixture. The curves correspond to the same conditions as those in Fig. 4.34. It is worth mentioning that the difference between energy input is defined by different gas density: for CH₄, gas number density is equal to $n = 5.2 \cdot 10^{18} \text{ cm}^{-3}$, while for C₅H₁₂ it is equal to $n = 2.7 \cdot 10^{18} \text{ cm}^{-3}$.

Similar calculations were made also for other mixtures with hydrocarbons. Under the conditions considered, O-atoms is the dominant active particle. The main mechanism for production of O atoms is electron impact dissociation of O₂ in a high electric field during the discharge. The production of atoms and radicals due to electron impact dissociation of hydrocarbon molecules is less important. De-excitation of Ar atoms increases density of H-atoms and radicals like CH₃ and C₅H₁₁ in early afterglow of the discharge (tens and hundreds of nanoseconds).

It is expected that the uncertainty in the cross section for electron impact dissociation of C₃H₈, C₄H₁₀ and C₅H₁₂ does not affect strongly the results of our calculations. To verify this, additional calculations were carried out with the cross sections of dissociation of these molecules increased by an order of magnitude. This decrease in the dissociation cross sections led to an increase in the densities of H atoms and radicals of hydrocarbon molecules by a factor of 6–7, whereas the density of O atoms decreased by tens percent. As a result, the total density of atoms and radicals increased in the mixtures with C₃H₈, C₄H₁₀ and C₅H₁₂ only by $\sim 10\%$. This does not affect noticeably the induction time in the mixtures considered; our calculations showed that this time is sensitive to the total density of atoms and radicals produced by the discharge and less sensitive to the composition of active particles. For example, we calculated ignition delay time in CH₄:O₂:Ar mixture

replacing CH_3 and H radicals by equivalent amount of O -atoms. As a result, we obtained difference for the ignition delay time within tens of microseconds for the regimes where the ignition delay itself is about of hundreds of microseconds.

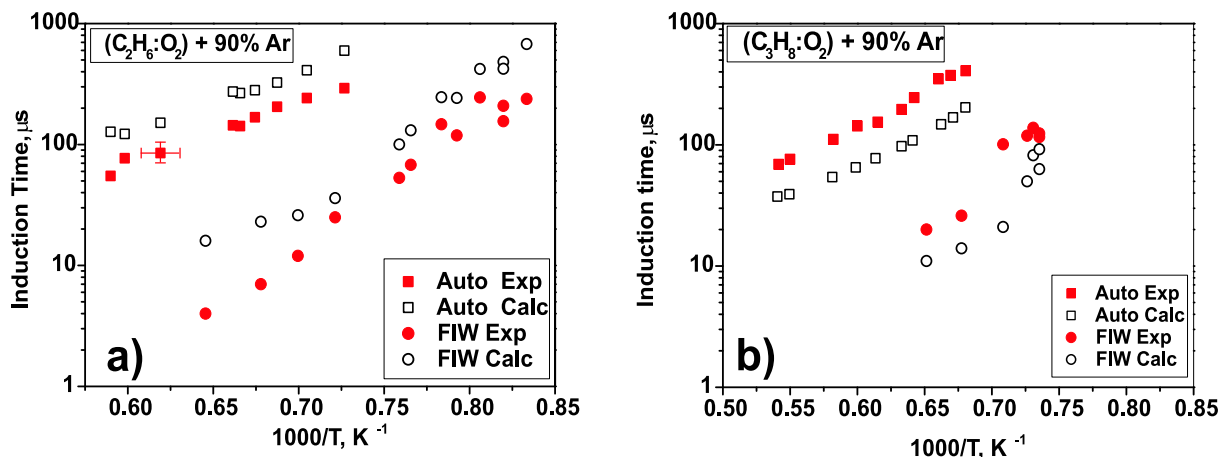


Figure 4.38: Autoignition (designated as “auto”) and ignition by nanosecond discharge in the form of fast ionization wave (designated as “FIW”) for C_2H_6 - and C_3H_8 -containing mixtures. Comparison of experiments and calculations.

4.7.3 Simulation of autoignition and artificial ignition. Comparison with the experiments

A zero-dimensional simulation of autoignition and artificial ignition by the discharge were performed at constant pressure using CHEMKIN code.¹⁷⁰ Autoignition was modelled using mechanism proposed by Tan¹⁷¹ for CH_4 - C_3H_8 containing mixtures, and mechanism used by Zhukov and Starikovskii¹⁷² (based on Westbrook mechanism¹⁷³) for C_4H_{10} and C_5H_{12} containing mixtures. These mechanisms were supplemented with the reactions of formation and quenching of OH radical in $A^2\Sigma$ state to compare the numerical and experimental results.

So, we assumed that the nonequilibrium plasma of a pulsed gas discharge may be considered as an instantaneous injection of dissociated species and radicals, as described above. In this case, we observe significant difference in time between ignition delays for the autoignition and ignition “by plasma”, i.e. by the injection of radicals. This can be easily seen from the Fig. 4.36, where two kinetic curves for OH - radicals are given for methane-oxygen mixture diluted with argon.

Let us note that we do not obtain a good correlation between absolute values of experimentally and numerically determined autoignition delay for methane-oxygen mixture: the calculated values are two times higher than the measured ones. To convince of the T_5 value, additional experiments have been conducted using IR-emission of asymmetric mode of CO_2 additives at $4.52\ \mu\text{m}$. These experiments have proved that the systematical error for methane-air mixture is not higher than 50 K. At the moment we believe that the discrepancy between experimentally and numerically obtained values for autoignition delay time can be explained by some impurities of the system, which was pumped not better than to 10^{-3} Torr, but this fact needs an additional examination.

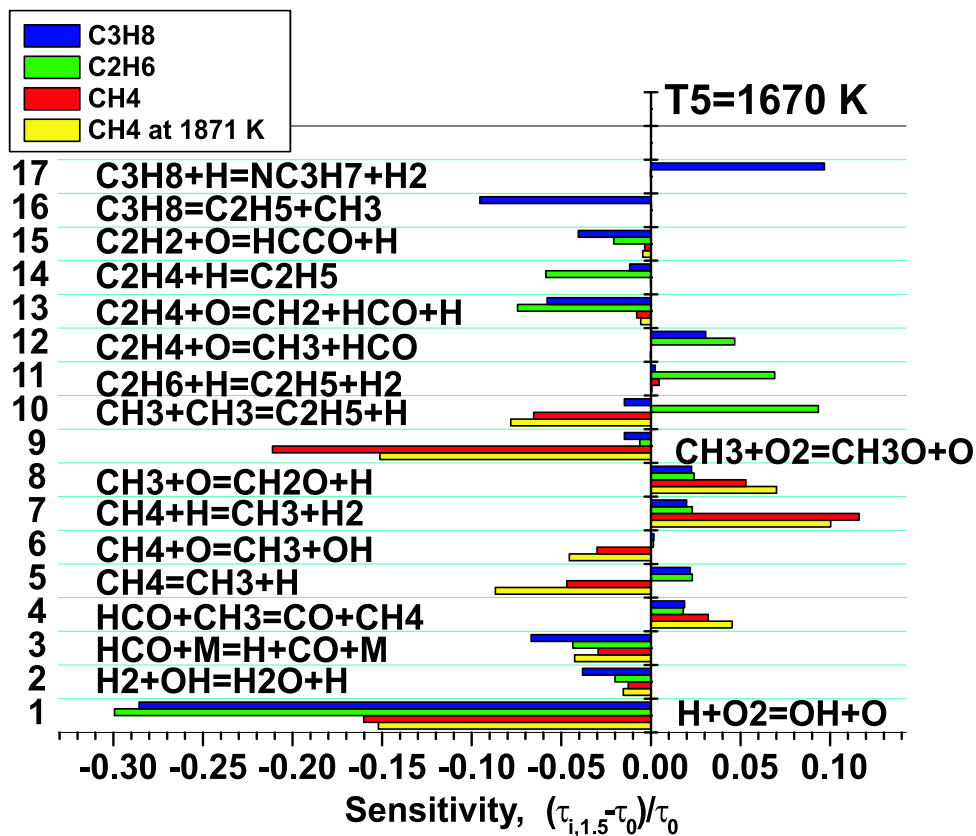


Figure 4.39: Comparison of sensitivity analysis of the kinetic scheme for CH₄ (red bars), C₂H₆ (green bars) and C₃H₈ (blue bars) – containing mixtures. Temperature $T_5 = 1670$ K. For comparison, another temperature for methane-containing mixture (1870 K) is given by yellow bars.

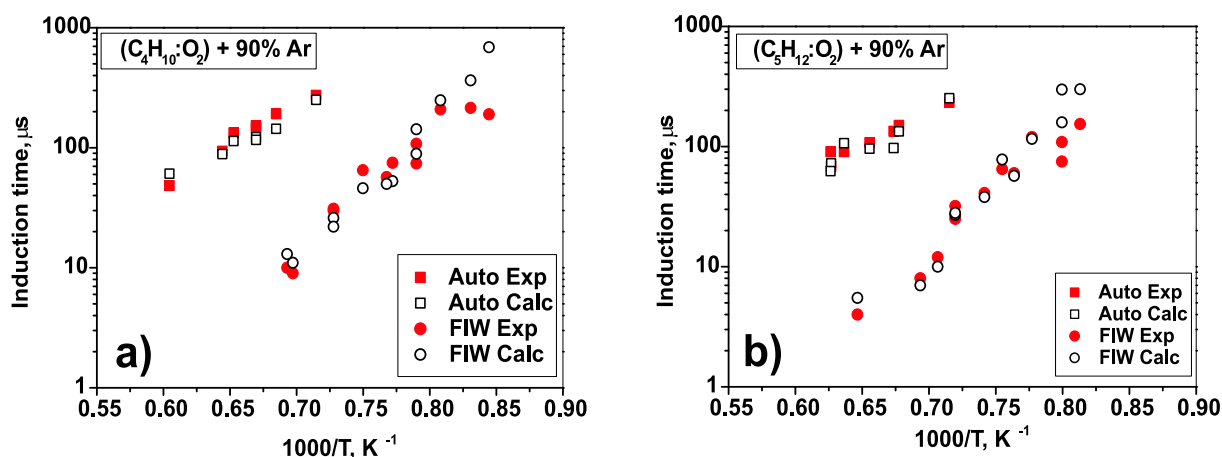


Figure 4.40: Autoignition (designated as “auto”) and ignition by nanosecond discharge in the form of fast ionization wave (designated as “FIW”) for C_4H_{10} - and C_5H_{12} -containing mixtures. Comparison of experiments and calculations.

All other calculations give reasonable correlation between measured and calculated values of the autoignition delay time. There the experimental data are in good agreement with the experimental data of other author. Fig. 4.37 proves this fact for propane-containing mixture. The same figure gives an impression about discrepancy between two ways of the determining of the ignition delay time. It is clearly seen that the ignition delay time determined from OH-emission at 306 nm as very similar to the ignition delay time determined from CH-emission at 431 nm, and that the difference between them is negligible comparing to the difference between the autoignition and ignition by the discharge.

The results of the calculations for ethane – propane containing mixtures are given in Fig. 4.38. Here it is worth mentioning that two different schemes for C1–C5 mixtures were used in the present paper. The reason of using Tan scheme¹⁷¹ for CH_4 – C_3H_8 containing mixtures was dictated by the fact that this mechanism gives the same relative position of autoignition curves for C1–C2–C3, as we have under our experimental conditions.

To understand peculiarities of the kinetic mechanism, we conducted the sensitivity analysis of the kinetic scheme. The analysis was made as follows: the rate constants of every reaction were in turn increased by a factor of 1.5 and the induction delay time was calculated separately for every case. The sensitivity coefficients were calculated as $(\tau_{1.5}^i - \tau)/\tau$, where τ is the induction delay time calculated with basic (unchanged) rate constants, $\tau_{1.5}^i$ is the induction delay time calculated at the i^{th} rate constant multiplied by 1.5. The results of the calculations for C1–C3 mixtures at the temperature $T_5 = 1670 \text{ K}$ are given in Fig. 4.39. The most important 17 reactions are indicated at the plot. It is clearly seen that for the conditions of our experiments there are reactions which are important in any mixture (like reactions (1), (4) or (8)), and there are reactions which are significant for methane-containing (reaction (9)) or ethane- and propane-containing mixtures only (reactions (11)–(17)). Yellow bars illustrate change of the role of different reactions with temperature increase.

Finally, Fig. 4.40 gives the comparison between experiments and calculations for C_4H_{10} - and C_5H_{12} -containing mixtures. Let us note that here we have quite reason-

able agreement both for autoignition and for the ignition by nanosecond discharge. These figures, together with experimental data and numerical results for other hydrocarbons, mean that under our experimental conditions, when the electric fields behind the discharge front are of the order of magnitude of 50–150 Td, we can describe the plasma assisted ignition assuming that the main governing factor accelerating the ignition is production of radicals, dissociated and electronically excited species by the discharge.

So, we have conducted experiments and numerical modelling of ignition of hydrocarbon-containing mixtures under the action of pulsed nanosecond discharge. The experiments were carried out with a set of stoichiometric mixtures $C_nH_{2n+2} : O_2$ (10%) diluted by Ar (90%) for hydrocarbons from CH_4 to C_5H_{12} . The temperature behind the reflected shock wave (T_5) varied from 950 to 2000 K, and the pressure (P_5) was 0.2 to 1.0 atm. For each set of experimental parameters, we compared the ignition by the discharge with autoignition.

Numerical modelling took into account both high-temperature kinetics of the ignition and production of atoms and radicals by a nanosecond discharge. At the first stage, we calculated energy branching in the discharge on the basis of experimentally determined electric field and energy input. Reactions responsible for the energy transfer from electronically excited buffer gas to molecules with subsequent production of atoms and radicals was included into kinetic scheme. At the second stage, we modelled high-temperature kinetics, taking into account atoms and radicals produced at the first step.

Comparison of the results of experiments and numerical modelling give a reasonable agreement and allow to conclude that, at our experimental conditions, the most important channel of the energy input is dissociation by an electron impact and production of electronically excited atoms and molecules. Additional production of atoms and radicals due to the quenching of electronically excited species in the nearest afterglow does not exceed factor of 2–3. These atoms and radicals (O, H, OH, C_nH_{2n-1} etc.) lead to the uniform in space ignition of gas mixtures at temperatures 500–200 K lower than the autoignition temperature.

Chapter 5

Experimental and Numerical Analysis of Efficiency of Different Species for Artificial Initiation of Ignition

5.1 Experimental study of the efficiency of excited atomic species for artificial ignition

The discharge produces a lot of species: electronically excited atoms and molecules, ionized particles, vibrationally excited components. The relative role of different species is under discussion now. In part, ion mechanism is proposed to explain efficiency of non-equilibrium plasma in combustion applications.¹⁷⁴ The role of radicals, such as OH, was discussed and investigated using emission spectroscopy and laser induced fluorescence (LIF) technique in different discharge systems,^{175, 176, 177}

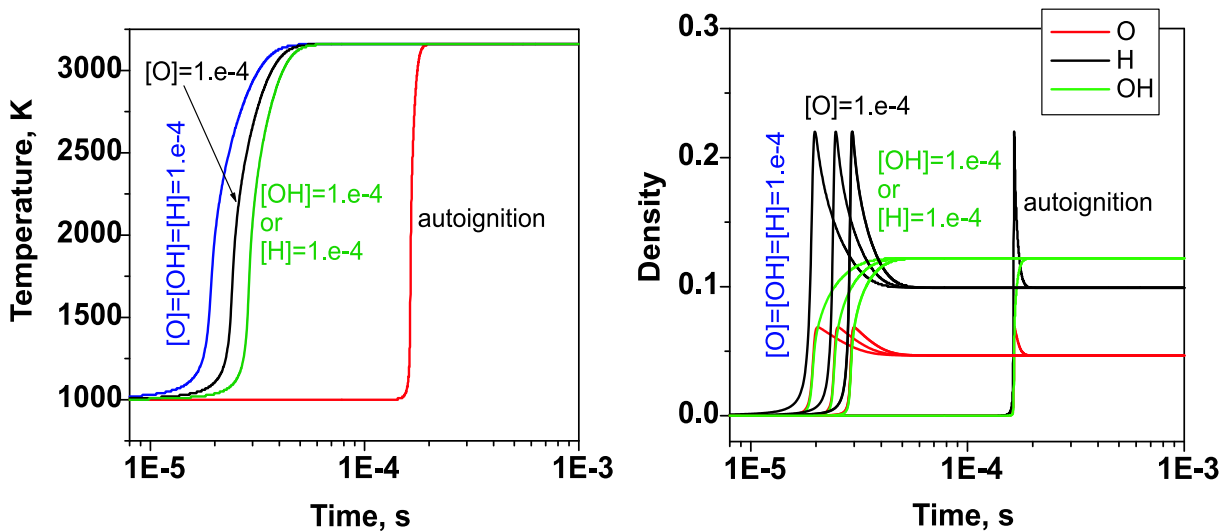


Figure 5.1: Influence of a small amount of different radicals on combustion kinetics, results of calculations. **a** — temperature behavior, **b** — density of different species (in fractions).

As it was mentioned already, even small additives of radicals may change significantly kinetics of the combustion. To illustrate this, we calculated temporal behavior of temperature and different radicals in hydrogen – oxygen stoichiometric mixture at pressure of 1 atm and temperature of 1000 K. The results of calculations are represented in Fig. 5.1.

We have demonstrated experimentally and by calculations (¹¹³¹⁷⁸) that nonequilibrium plasma of nanosecond discharge reduces the ignition delay time significantly (by a few orders of magnitude). Investigations were carried out for a set of combustible mixtures, where we used oxygen or air as an oxidizer and hydrogen or methane as a fuel. The very last work (¹⁷⁹) demonstrates the same effect for a set of hydrocarbons starting from methane up to pentane. The main advantage of a nanosecond discharge as an initiator of ignition is its uniformity and short time of production of active species. The uniformity of single – shot nanosecond discharge in gas volume 25x25x200 mm³ under the action of nanosecond high voltage discharge of 60-160 kV in amplitude and space uniformity of consequent combustion has been controlled in.⁸⁰ Short in comparison with typical ignition delays, time of active species production in a nanosecond discharge gives unique possibility for experimentalist to subdivide control of "action" on the system (the discharge) and "response" (ignition) in experiment. From the point of view of kinetics, high electric fields, which realizes in nanosecond high-voltage discharge, allow electrons to excite electronic states of atoms and molecules with relatively high thresholds and to dissociate species effectively. Maximal possible duration of a nanosecond discharge is restricted by its transfer to the arc form, when the main part of energy turns to gas heating and excitation of high-energy levels of atoms and molecules is not efficient any more. Typical time for such a transition is about of hundreds of nanoseconds. For example, an efficient production of H atoms in nanosecond discharge at ambient temperature for pulse duration of 480 ns has been demonstrated by two-photon absorption laser induced fluorescence in.¹⁸⁰

Coming back to the discussion about role of different species in the process of ignition, it is significant to note that the capabilities for control of influence of separate species are quite limited. First of all, this is numerical modelling with detailed analysis of different channels at different conditions of discharge and ignition. The problem here that even numerical model for separate kind of species (for example, ions¹⁷⁴) can be large and include huge amount of species and reactions with numerous links between them. Inclusion of additional class of species in calculations (let say, electronically excited atoms and molecules) leads to essential complication of the system. So, an experimental material, which allows to analyze the role of separate class of species at the ignition, is of great importance.

The experiments were carried out in the system described in details elsewhere (¹¹³⁸⁰). Our aim was to compare efficiency of ignition of a combustible mixture by nanosecond discharge and by technique which allows to excite separate class of species only. Experiments were carried out behind a reflected shock wave, as in classic experiments on the autoignition of gas mixtures.¹⁸¹

The experimental setup consisted of a shock tube with a discharge cell, a gas evacuation and supply system, a system for ignition with discharge, and a diagnostic system. The shock tube (25x25-mm square cross section) had a 1.6 m long working channel. The length of the high-pressure cell was 60 cm. There were two pairs of windows for optical diagnostics along the stainless-steel working channel. The last section of the low pressure cell (LPC)

of the shock tube was made from 40 mm thick plexiglas and had eight optical windows (quartz and MgF_2). The metal end plate of the tube served as a high-voltage electrode. Another electrode was the grounded steel section of the shock tube. The nanosecond discharge was initiated at the instant at which the reflected shock wave arrived to the observation point. High-voltage pulses were produced with a Marx type high voltage generator.

The diagnostic system consisted of a system for monitoring the shock wave parameters, a system for detecting ignition, and a system for monitoring the electric parameters of the nanosecond discharge. Velocity of a shock wave was measured by Schlieren system consisted of three He-Ne lasers and a set of photodiodes. The gas density, pressure and temperature behind the reflected shock wave were determined from the known initial gas mixture composition, the initial pressure, and the velocity of the incident shock wave. Ignition delay time was controlled using emission of OH emission at 306 nm in microsecond time scale. Simultaneously we controlled current through the discharge cell and voltage drop between high-voltage electrode and cross-section of measurement with nanosecond time resolution.

To act on a gas mixture selectively, we decided to excite gas by laser flash-photolysis. The diagnostic system used for ignition by the discharge, was modified as this presented in Fig. 5.2. A flash of UV-radiation of ArF excimer laser ("Center of Physical Devices" production, Troitsk, 193 nm) was organized behind the reflected shock wave instead of the nanosecond discharge. Laser output reached 0.2 J. The laser radiation was supplied to the dielectric section of the shock tube through the optical window perpendicularly to the shock tube axis in the same cross-section where we performed measurements in a case of the ignition by nanosecond discharge. Laser output had approximately rectangular shape with 5x21 mm dimensions and was controlled by special sensible paper. It reached optical window perpendicularly to its plane, so, we excited gas volume of 5x21x25 mm. A piezoelectric detector (PEM21) with 21 mm diameter of receiving site was used to determine energy input from laser radiation into the gas. It was installed behind the shock tube. Signal from PEM21 was controlled every time before the experiment, when the system was pumped up to 5×10^{-3} Torr and then during the experiment. During the pumping pipes were cooled with liquid nitrogen to avoid track amounts of oil in the system. These precautions were important to keep optics in a proper state: trace amount of oil leads to production of a thin film on windows under the action of laser UV radiation. Knowing spectral transmission of MgF_2 windows in this spectral range (were controlled by Varian Cary 50 Spectrophotometer) we calculated energy input into a gas. We organized experiment so, that energy input in the discharge and energy input from a laser were within one order of magnitude. We controlled initial gas pressure and shock wave velocity, and parameters behind the reflected shock wave were calculated as in the previous case. Ignition delay time was determined from the OH emission at 306 nm. The experiments were repeated with the same mixture for autoignition, discharge initiation of ignition and ArF flash-photolysis. Ignition delay times were compared for all cases.

To make these experiments, we chosen N_2O as a main absorbing component. Really, N_2O is known to be very efficient as an oxidant. On the other hand, it absorbs radiation at 193 nm better than molecular oxygen.

To demonstrate this, cross-sections of molecular oxygen and N_2O molecule are represented in the Fig. 5.3. So, experiments were performed in gas mixture $\text{N}_2\text{O}:\text{H}_2:\text{Ar} =$

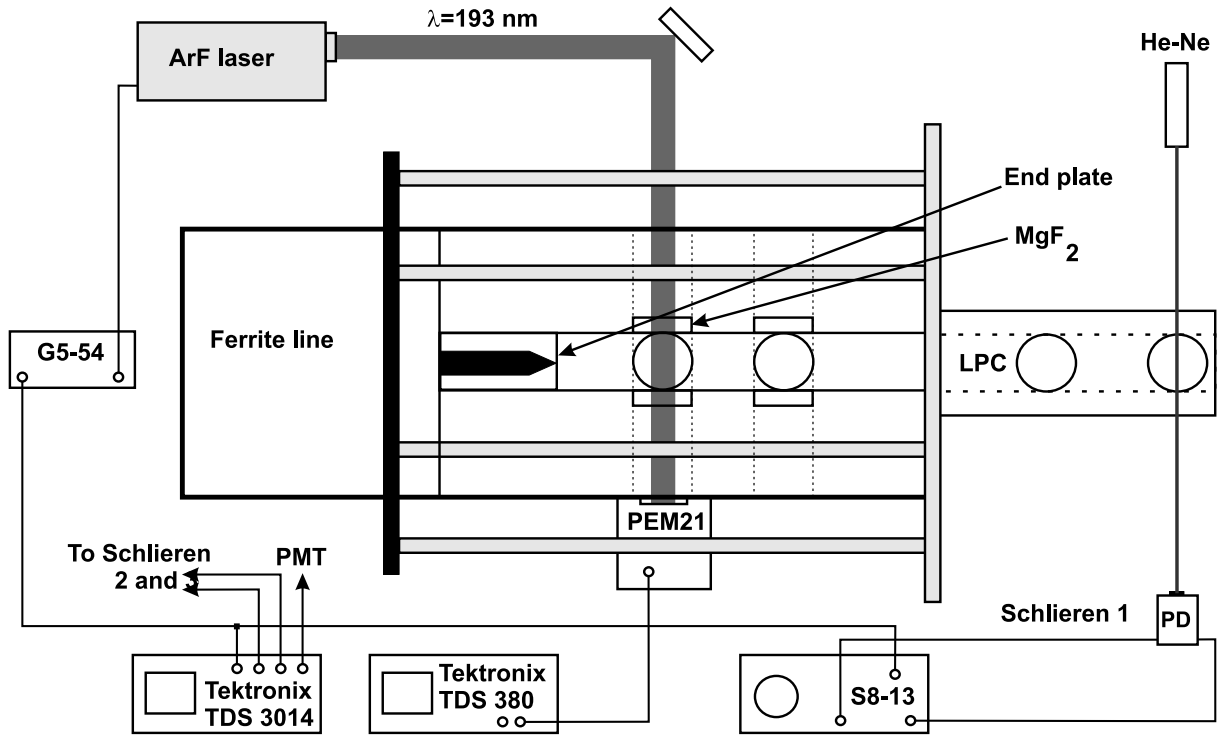


Figure 5.2: General view on experimental setup for study of shift of the ignition delay by ArF-photolysis.

1:1:8. In our earlier experiments 1% of CO_2 was added to a gas mixture for control of a gas temperature using emission in IR range of spectrum.

Typical energy input in a gas in experiments with flash-photolysis is demonstrated by a Fig. 5.4. The shape of a laser beam is quite uniform. It is represented in a right hand side of the figure. Energy value obtained by piezoelectric gauge was divided by volume $5 \times 20 \times 25$ mm, where 25 mm is a transverse size of a shock tube channel.

So, the experiments were performed in N_2O – containing gas mixtures diluted by argon. Hydrogen was taken as a fuel. We carried out special experiments to control linearity of absorption with increase of N_2O part in a gas mixture and to adjust discharge so that we obtained similar energy input into gas in experiments with discharge and with laser flash-photolysis.

Every time working with nanosecond discharge we obtained well-pronounced shift of the ignition delay time. It comprises up to 2 orders of magnitude (from hundreds of microseconds to units of microseconds) and leads to shift of a temperature threshold at fixed pressure up to 250 K. We were not able to obtain pronounced shift of ignition delay time in experiments with flash-photolysis even when we tried to increase N_2O part in gas mixture or focus laser radiation (with mixture containing 40% of N_2O) trying to get ignition in fixed point.

We have performed the most general analysis of possible situation. It is known that N_2O photolysis takes place via the reactions:



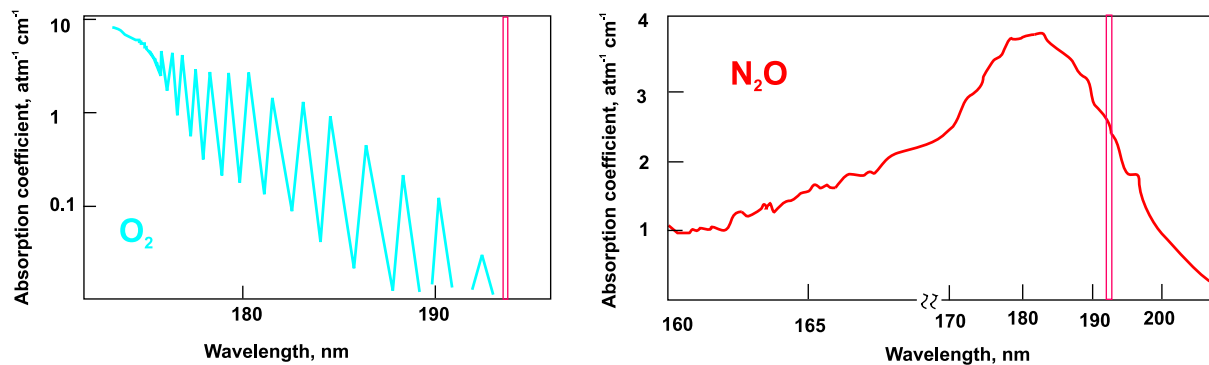


Figure 5.3: Cross-section of absorption: **a** — for molecular oxygen, **b** — for nitrous oxide. Region of ArF laser generation is marked with red vertical lines.

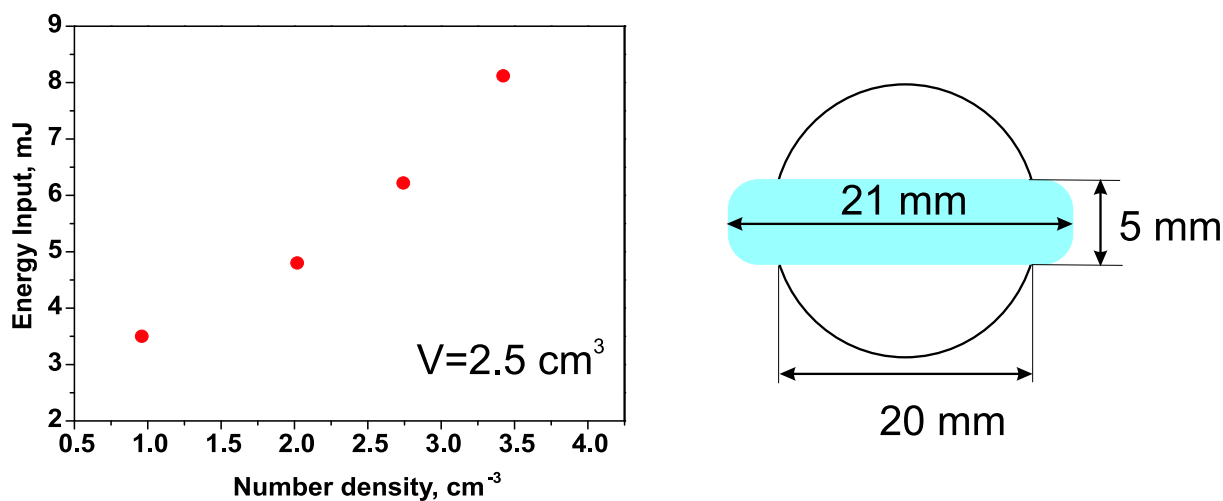


Figure 5.4: Typical energy input in experiments with laser flash-photolysis. A shape of a laser beam is on the right part of a figure.



at this weight of reaction (5.1) is 99%. $\text{O}(^1\text{D})$ is a metastable atom, its life time is 150 s, and usually it loses excitation in collisions with other species. It may destruct N_2O via the reactions



On the other hand, $\text{O}(^1\text{D})$ has to be active in chain initiation:



Sum of constant rates of reactions (5.3) and (5.4) is of the same order of magnitude that the constant rate of reaction (5.5). It seems that N_2O and $\text{O}(^1\text{D})$ mutual destruction in processes (5.3) and (5.4) leads to the blocking of possible mechanism of ignition acceleration. To check this, we performed experiments with oxygen-containing mixture (without N_2O) but obtained zero ignition delay shift because of small absorption cross-section at 193 nm.

Preliminary calculations, based on N_2O - H_2 - O_2 high temperature kinetic scheme¹⁸² with addition of reactions with $\text{O}(^1\text{D})$, confirmed important role of reactions (5.3) and (5.4). On the result of the calculations and analysis of kinetics it was proposed to take for experiments $\text{H}_2 - \text{O}_2$ mixture diluted with Ar, and to use N_2O as a supplier of $\text{O}(^1\text{D})$ atoms, not as oxidizer. The experiments with mixture with relatively high contain of H_2 and O_2 (30% and 10% respectively) led to detonation, so, we decided to stop at relatively low amount of molecular oxygen in a mixture ($\text{N}_2\text{O}:\text{O}_2:\text{H}_2:\text{Ar}=10:3:30:50$), and this set of experiments was successful.

The results of experiments and experimental parameters, such as pressure, temperature and gas density are summarized in the Table 5.1.

Table 5.1: Results of the experiments. Comparison of flash-photolysis and nanosecond discharge.

Mixture	Driver gas	T_5 , K	P_5 , atm	$n_5, 10^{18} \text{ cm}^{-3}$	$^*\tau_0$, μs	τ_{fl} , μs	τ_- , μs
$\text{N}_2\text{O}-\text{H}_2-\text{O}_2-\text{Ar}$	Air	949	0.49	3.80	656	-	-
$\text{N}_2\text{O}-\text{H}_2-\text{O}_2-\text{Ar}$	Air	971	0.49	3.71	551	-	-
$\text{N}_2\text{O}-\text{H}_2-\text{O}_2-\text{Ar}$	Air	998	0.44	3.25	463	-	-
$\text{N}_2\text{O}-\text{H}_2-\text{O}_2-\text{Ar}$	Air	1027	0.45	3.21	368	-	-
$\text{N}_2\text{O}-\text{H}_2-\text{O}_2-\text{Ar}$	Air	1168	0.24	1.50	175	-	-
$\text{N}_2\text{O}-\text{H}_2-\text{O}_2-\text{Ar}$	Air	1091	0.28	1.88	259	-	-
$\text{N}_2\text{O}-\text{H}_2-\text{O}_2-\text{Ar}$	Air	1125	0.26	1.69	218	-	-
$\text{N}_2\text{O}-\text{H}_2-\text{O}_2-\text{Ar}$	Air	1071	0.31	2.13	300	-	-
$\text{N}_2\text{O}-\text{H}_2-\text{O}_2-\text{Ar}$	Air	1064	0.35	2.44	306	-	-
$\text{N}_2\text{O}-\text{H}_2-\text{O}_2-\text{Ar}$	Air	1027	0.39	2.81	378	-	-
$\text{N}_2\text{O}-\text{H}_2-\text{O}_2-\text{Ar}$	Air	993	0.46	3.45	500	-	-

Table 5.1: Results of the experiments. Comparison of flash-photolysis and nanosecond discharge.

Mixture	Driver gas	T_5 , K	P_5 , atm	$n_5, 10^{18} \text{ cm}^{-3}$	$^*\tau_0, \mu\text{s}$	$\tau_{fl}, \mu\text{s}$	$\tau_-, \mu\text{s}$
N ₂ O-H ₂ -O ₂ -Ar	Air	1132	0.26	1.70	219	-	-
N ₂ O-H ₂ -O ₂ -Ar	Air	965	0.44	3.36	-	242	-
N ₂ O-H ₂ -O ₂ -Ar	Air	971	0.44	3.37	-	278	-
N ₂ O-H ₂ -O ₂ -Ar	Air	1021	0.46	3.34	-	235	-
N ₂ O-H ₂ -O ₂ -Ar	Air	1046	0.45	3.17	-	215	-
N ₂ O-H ₂ -O ₂ -Ar	Air	1077	0.41	2.79	-	190	-
N ₂ O-H ₂ -O ₂ -Ar	Air	1118	0.37	2.41	-	147	-
N ₂ O-H ₂ -O ₂ -Ar	Air	1176	0.32	2.02	-	126	-
N ₂ O-H ₂ -O ₂ -Ar	Air	955	0.49	3.74	-	288	-
N ₂ O-H ₂ -O ₂ -Ar	Air	924	0.51	4.02	-	309	-
N ₂ O-H ₂ -O ₂ -Ar	Air	909	0.54	4.39	-	367	-
N ₂ O-H ₂ -O ₂ -Ar	Air	905	0.59	4.78	-	344	-
N ₂ O-H ₂ -O ₂ -Ar	Air	890	0.62	5.09	-	416	-
N ₂ O-H ₂ -O ₂ -Ar	Air	877	0.69	5.77	-	561	-
N ₂ O-H ₂ -O ₂ -Ar	Air	1004	0.43	3.14	-	-	101
N ₂ O-H ₂ -O ₂ -Ar	Air	1040	0.39	2.80	-	-	92
N ₂ O-H ₂ -O ₂ -Ar	Air	1064	0.35	2.40	-	-	64
N ₂ O-H ₂ -O ₂ -Ar	Air	1091	0.31	2.07	-	-	54
N ₂ O-H ₂ -O ₂ -Ar	Air	976	0.51	3.82	-	-	177
N ₂ O-H ₂ -O ₂ -Ar	Air	929	0.53	4.23	-	-	246
N ₂ O-H ₂ -O ₂ -Ar	Air	909	0.56	4.53	-	-	261
N ₂ O-H ₂ -O ₂ -Ar	Air	900	0.60	4.91	-	-	296
N ₂ O-H ₂ -O ₂ -Ar	Air	877	0.62	5.19	-	-	506
N ₂ O-H ₂ -O ₂ -Ar	Air	877	0.67	5.57	-	-	523
N ₂ O-H ₂ -O ₂ -Ar	Air	868	0.68	5.77	-	-	698
N ₂ O-H ₂ -O ₂ -Ar	Air	970	0.45	3.37	-	-	139

* In the Table, τ_0 is a delay time for autoignition, τ_{fl} is a delay time in the case of ignition by nanosecond flash laser pulse, τ_- is a delay time in the case of ignition by nanosecond high-voltage pulse of negative polarity with the amplitude of 60 kV.

Fig. 5.5,a represents the results obtained with gas mixture N₂O:O₂:H₂:Ar = 10:3:30:50. The accuracy of ignition delay time determination is about of 2 μs . Energy input for experiments with nanosecond discharge and with flash-photolysis is represented in the Fig. 5.5,b. It is clearly seen that we work within an order of magnitude. Volumetric energy density is in a range of 1-5 mJ/cm³. The energy density decreases in discharge at constant amplitude of high-voltage pulse (we used 60 kV and 40 ns pulses) and increases in flash-photolysis with gas number density. As a result, we obtain well-pronounced shift in ignition delay time both in experiments with flash-photolysis and in experiments with nanosecond discharge. At low temperatures (that is, at high densities) efficiency of laser flash-photolysis is similar to the efficiency of a nanosecond discharge. At high temperatures and low densities the efficiency of discharge is higher. Data obtained will

be used for validation of numerical model to analyze in detail the role of excited species in the ignition.

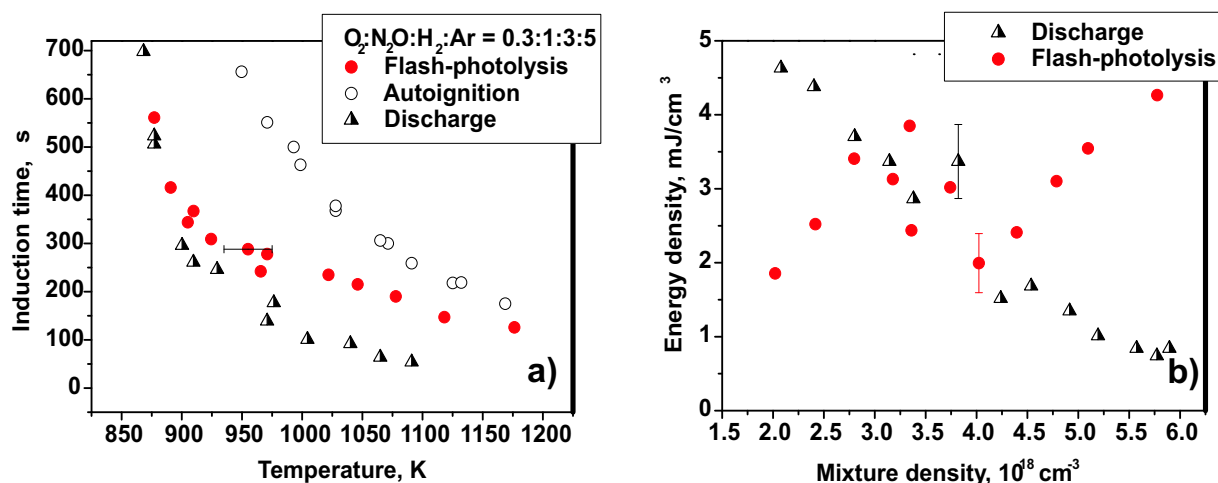


Figure 5.5: a — shift of ignition delay time. Experiments on autoignition, ignition by nanosecond discharge and ignition by ArF laser flash–photolysis. b — volumetric energy input in experiments with discharge and with flash-photolysis.

Thus, the experimental scheme for the analysis of efficiency of excited atomic species in mechanism of artificial ignition by nanosecond discharge has been proposed. Experiments were carried out in a set of fuel-containing mixture. Positive results were obtained for combustible mixture $N_2O:O_2:H_2:Ar = 10:3:30:50$. Ignition delay time was compared for autoignition, ignition by nanosecond discharge and ignition by laser flash-photolysis for the same experimental conditions.

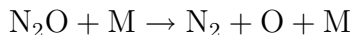
5.2 The development of kinetic model to describe the role of the excited species in ignition

The kinetics of N_2O -containing mixtures are of great interest because nitrous oxide is a reliable source of atomic oxygen in both the ground ($O(^3P)$) and excited ($O(^1D)$) states. N_2O is widely used as a source of atomic oxygen in kinetic experiments. For this reason, the kinetics of unimolecular decomposition of N_2O and following secondary reactions between nitrous oxide and atomic oxygen have been extensively investigated by numerous groups of researchers.

Experiments to determine reaction rate constants at high temperatures usually use shock tube technique. There the researchers use mixtures which are significantly (by 95—97%) diluted with monatomic inert gas.^{183,184} This fact makes it possible to appreciably simplify the interpretation of experimental data and reduce the number of processes for which the kinetic scheme is to be optimized.

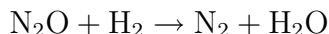
However, for combustion of fuel–air mixtures concentrations of chemically active components are not low. In this case, reactions and processes unimportant in diluted mixtures, come forward. These processes may cause a significant change of the kinetic characteristics of the system and call for thorough analysis.

We can refer to the reaction of unimolecular decomposition of nitrous oxide in an $\text{N}_2\text{O-H}_2\text{-Ar}$ system as an example :



The rate constant of this process is well studied for the case $\text{M} = \text{Ar}$ (see, for example, the review in¹⁸⁵), while no experimental data are available for $\text{M} = \text{H}_2$

The situation is similar situation for the process



which was first introduced in¹⁸⁶ in describing the results of the experiments in a weakly dilute mixture. There are no other data presently available for this reaction.

It was the main aim of this study to construct a kinetic scheme that would describe the kinetics of both lean and rich $\text{N}_2\text{O:O}_2\text{:H}_2$ mixtures.

In constructing this scheme, we used the results of our experiments in weakly dilute mixtures containing 50 to 80% argon, as well as the results of the experiments in highly dilute mixtures performed by one of the present authors^{185–187} and some experimental results of other authors.¹⁸⁸

5.2.1 Experiments in autoignition in N_2O -containing mixtures

The ignition delay time in N_2O -containing mixtures was measured in a square shock tube (ST) with the working part of 1.6 m long. The experiments were performed behind a reflected shock wave at a distance of 5 mm from the end plate. The thermodynamic parameters of the gas under investigation behind the reflected shock wave were determined using the ideal ST theory. During the experiments the special attention was given to the quality of the ST channel. The maximal size of steps and clearances when mounting windows and assembling ST sections did not exceed 0.05 mm. Two pairs of quartz windows of diameter $d = 25$ mm and two cross sections with four windows of diameter $d = 20$ mm in the side walls of the shock tube enabled us to perform optical diagnostics of the shock wave. Furtheron, we will refer to the cross section that is closest to the ST end plate as a diagnostic cross section. The incident shock wave velocity was determined using three laser schlieren gages located in series at three points spaced at 226 and 250 mm. The deceleration of shock wave in the ST channel was taken into account in the data processing. The mixtures to be investigated were prepared using high-purity gases O_2 (99.99%), H_2 (99.999%), Ar (99.998%) and N_2O of 98% purity. The accuracy of determination of gas mole fractions in the mixture was at least 0.0025 and was largely defined by the purity of N_2O and by the inleakage to a low-pressure chamber. Air was used as a driver gas. The working chamber and the high-pressure chamber were separated by a metallized lavsan (Russian equivalent of Dacron) diaphragm 12 μm thick that bursted at a pressure difference of $\Delta P \approx 3$ atm. In order to measure the ignition delay time, the emission of mixture was measured in the diagnostic cross section at a wavelength of 306.4 nm that corresponds to transition of the excited OH radical to the ground state ($A^2\Sigma \rightarrow X^2\Pi$). The delay time was determined as a time between the schlieren signal which corresponds to the coming of reflected shock wave to the diagnostic cross section and the point of intersection of the time axis with the leading front of emission. The point of intersection was determined tangentially to the curve constructed at the point of the maximum of signal

derivative. The optical system included a condenser which focused the image of window in the measuring cross section onto the slit of MDR-23 monochromator. The emission was then detected by a FEU-100 photomultiplier connected to the monochromator. A vertical 2x20 mm slit was installed on the window. The signals from the schlieren sensors and photomultiplier were delivered to the inputs of TDS 3014 Tektronix oscillograph (transmission band of 150 MHz).

The experiments were performed in mixtures of $O_2 : H_2 : N_2O : Ar = 3 : 30 : 10 : 50$ and $N_2O:H_2:Ar = 10:10:80$ in the range of initial temperature from 1000 to 1600 K and pressures from 0.1 to 0.5 atm. The data obtained in the series of experiments in mixture of $N_2O:H_2:O_2:Ar = 10:30:3:50$ are given in Tables (5.2). Table 5.3 contains the data on the autoignition of mixture $N_2O:H_2:Ar = 10:10:80$.

Table 5.2: Data on the autoignition in mixture $N_2O:H_2:O_2:Ar = 10:30:3:50$

T_5 , K	1278	1195	1244	1195	1172	1150	1107
P_5 , atm	0.14	0.21	0.17	0.17	0.20	0.23	0.36
τ , μs	190	222	228	235	254	261	268
T_5 , K	1165	1121	1094	1061	1068	1024	1007
P_5 , atm	0.22	0.26	0.28	0.37	0.30	0.37	0.39
τ , μs	273	288	305	365	366	482	521

Table 5.3: Data on the autoignition in mixture $N_2O:H_2:Ar = 10:10:80$

T_5 , K	1574	1461	1396	1328	1312	1288
P_5 , atm	0.22	0.29	0.36	0.39	0.40	0.47
τ , μs	94	146	203	287	339	422

5.2.2 Other kinetic experiments in N_2O -containing mixtures

Papers^{185–187} deal with the kinetics of reactions in highly dilute mixtures containing N_2O and H_2 . Paper¹⁸⁵ gives the results of the experimental investigation and numerical simulation of the reaction of unimolecular decomposition of N_2O . this paper is also presents a review of rate constants of unimolecular decomposition of N_2O . The experiments were performed behind a reflected shock wave in N_2O/Ar mixtures in the range of temperatures from 1780 to 2300 K and pressures from 2 to 20 atm. The IR emission of N_2O on a wavelength of 4.5 μm and absorption of N_2O in the UV range (250 nm), absorption of NO_2 on a wavelength of 434 nm, and recombination emission of $NO-O$ on a wavelength of 500 nm were monitored synchronously in each experiment. The experiments were performed in a pure mixture and in mixtures containing controlled additions of hydrogen on various levels, namely at 250, 1000 ppm, and 1%. As a result, the authors of¹⁸⁵ derived expressions for the rate constants of unimolecular decomposition of N_2O in the limit of high ($k^\infty = 1.7 \cdot 10^{11} \exp(-29000/T) s^{-1}$; $T = 1750 - 2000$ K; $\Delta \lg k^\infty = 0.15$) and low ($k^0 = 1.49 \cdot 10^{18} T^{-1} \exp(-29000/T) cm^3/(mole \cdot s)$; $T = 1500 - 5000$ K; $\Delta \lg k^0 = 0.05$ at $T = 1700 - 3500$ K, and $\Delta \lg k^0 = 0.15$ in the remaining range) pressures.

The NO yield in the range of temperatures from 1750 to 3300 K and pressures from 2.5 to 23 atm was measured in.¹⁸⁹ The authors¹⁸⁹ measured the IR emission of NO on a wavelength of 5.6 μm and absorption of NO in the UV range (235 nm) behind a reflected shock wave in the process of unimolecular decomposition of N_2O . The numerical simulation of the process of decomposition along with the analysis of the sensitivity of the parameters being measured to the variation of individual reaction rates, made it

possible to determine the rate constant of the reaction $\text{N}_2\text{O} + \text{O} \rightarrow \text{NO} + \text{NO}$ ($k = 9.0 \cdot 10^{13} \exp(-14085/T) \text{ cm}^3/(\text{mole}\cdot\text{s})$; $T = 1750 - 3300 \text{ K}$; $\Delta \lg k = 0.1$) as well as to give the upper estimations for the rate constants of reactions $\text{N}_2\text{O} + \text{O} \rightarrow \text{N}_2 + \text{O}_2$ and $\text{N}_2\text{O} + \text{NO} \rightarrow \text{NO}_2 + \text{N}_2$.

The measurements of NO_2 absorption in the visible range (434 nm) and of NO_2 chemiluminescent emission as a result of reaction $\text{NO} + \text{O} \rightarrow \text{NO}_2^* \rightarrow \text{NO}_2 + h\nu$ (wavelength of 500 nm) are discussed in greater detail in.¹⁹⁰ A detailed kinetic scheme with identification of the basic processes together with the analysis of kinetic data of other authors made it possible to determine the rates of reactions $\text{NO} + \text{O} + \text{M} \rightarrow \text{NO}_2 + \text{M}$ and $\text{NO}_2 + \text{O} \rightarrow \text{NO} + \text{O}_2$ in the range of temperatures from 1780 to 2300 K and pressures from 2 to 20 atm.

Numerical simulation of reactions in the $\text{N}_2\text{O}-\text{H}_2$ system with addition of different amounts of hydrogen is described in.¹⁸⁷ A kinetic scheme of 64 reactions describes the experimental data obtained previously for the range of temperatures from 1800 to 2700 K and pressures of ~ 10 atm. The recommendations of other authors are also analyzed. The results of analysis of sensitivity, along with the data on the absolute reaction rates, for the first time made it possible to measure the rate constant of reaction $\text{OH} + \text{O} \rightarrow \text{H} + \text{O}_2$ within this temperature range. The authors¹⁸⁷ give the value of $k = 5.1 \cdot 10^{12} \exp(375/T) \text{ cm}^3/(\text{mole}\cdot\text{s})$ for this rate constant in temperature range $T = 1800 - 2700 \text{ K}$ with accuracy $\Delta \lg k = 0.1$.

The experiment presented in¹⁸⁸ were performed behind a reflected shock wave in mixtures of (A) $\text{N}_2\text{O}:\text{H}_2:\text{Ar} = 2:1:97$, (B) $\text{N}_2\text{O}:\text{H}_2:\text{Ar} = 1:1:98$, and (C) $\text{N}_2\text{O}:\text{H}_2:\text{Ar} = 1:0.5:98.5$ in the temperature range $T_5=1400$ to 2000 K and at a pressure P_5 close to 2 atm. The authors of¹⁸⁸ demonstrated that the emission of OH on a wavelength of 306 nm is mainly defined by the processes $\text{H} + \text{O} + \text{M} = \text{OH}^* + \text{M}$ and $\text{N}_2\text{O} + \text{H} = \text{N}_2 + \text{OH}^*$. They determined the rate constant for the latter of these two reactions. The paper gives both the obtained temperature dependences of the ignition delay time and the oscillograms of OH emission. The authors determined the ignition delay time by the peak of the time dependence of OH emission.

In constructing the mechanism of kinetics in $\text{N}_2\text{O}-\text{H}_2$ mixtures, we will use three groups of experimental data. The data of two of these groups (the series of papers¹⁸⁵⁻¹⁸⁷ and the results of¹⁸⁸) describe the kinetics of lean mixtures. The maximal concentration of N_2O in these studies did not exceed 3%. The third group contains the data obtained in rich mixtures (10% N_2O and 10–30 % H_2) by the authors. The suggested kinetic scheme describes two curves experimentally obtained by the authors, seven dependencies experimentally obtained in the series of papers¹⁸⁵⁻¹⁸⁷ and two curves experimentally obtained by Hidaka et al.¹⁸⁸ This set of data makes it possible to construct a consistent mechanism of kinetics for a wide range of initial concentrations of N_2O and H_2 at high ($T > 1000 \text{ K}$) temperatures.

5.2.3 Analysis of basic reactions in $\text{N}_2\text{O}-\text{H}_2-\text{O}_2$ system. Description of numerical model and comparison of calculations and experiments.

There was performed a zero-dimensional simulation of ignition and of unimolecular decomposition of N_2O at constant pressure using CHEMKIN code.¹⁷⁰ The GRI 2.11 mechanism⁴ for the combustion of methane-air mixtures was used in the scheme as the basis

of hydrogen-oxygen kinetics. This mechanism was supplemented with the reactions of formation and quenching of OH radical in the $A^2\Sigma$ state (given in table as (OH(A)) to compare the numerical results with those of the experiments. These reactions are given in Table 5.4 (reactions 73—79).

Table 5.4: The kinetic scheme. The rate constants are given in the form $k = AT^\beta \exp(-E/RT)$; dimensions are in $\text{cm}^3/(\text{mole}\cdot\text{s})$.

N	Reaction	A	β	E	Ref
1	$\text{N}_2\text{O} + \text{H}_2 \rightleftharpoons \text{N}_2 + \text{H}_2\text{O}$	$2.10 \cdot 10^{14}$	0.0	32500.0	present paper ¹
2	$\text{N}_2\text{O} + \text{M} \rightleftharpoons \text{N}_2 + \text{O}_2 + \text{M}$	$1.7 \cdot 10^{11}$	0.0	59580.0	¹⁸⁷ , changed ²
2a	$\text{N}_2\text{O} + \text{M} \rightleftharpoons \text{N}_2 + \text{O}_2 + \text{M}$	$5.1 \cdot 10^{18}$	-1.12	59580.0	¹⁸⁷ , changed ³
3	$\text{N}_2\text{O} + \text{H} \rightleftharpoons \text{N}_2 + \text{OH}$	$2.0 \cdot 10^{14}$	0.0	15100.0	¹⁸⁷ , changed
4	$\text{OH} + \text{O} \rightleftharpoons \text{H} + \text{O}_2$	$4.51 \cdot 10^{14}$	-0.5	60.0	¹⁸⁷ , changed
5	$\text{N}_2\text{O} + \text{O} \rightleftharpoons 2\text{NO}$	$5.8 \cdot 10^{13}$	0.0	26000.0	¹⁸⁹ , changed
6	$\text{N}_2\text{O} + \text{O} \rightleftharpoons \text{N}_2 + \text{O}_2$	$5.0 \cdot 10^{12}$	0.0	27804.0	¹⁸⁹⁴
7	$\text{NO} + \text{O} + \text{M} \rightleftharpoons \text{NO}_2 + \text{M}$	$7.2 \cdot 10^{20}$	-1.8	0.0	¹⁸⁷ ⁵
8	$\text{NO}_2 + \text{O} \rightleftharpoons \text{NO} + \text{O}_2$	$6.0 \cdot 10^{12}$	0.0	0.0	¹⁸⁷
9	$\text{H}_2 + \text{O}_2 \rightleftharpoons \text{OH} + \text{OH}$	$3.9 \cdot 10^{14}$	0.0	43500.0	present paper ⁶
10	$\text{N}_2\text{O} + \text{OH} \rightleftharpoons \text{N}_2 + \text{HO}_2$	$6.3 \cdot 10^{11}$	0.0	9930.0	¹⁸⁷
11	$\text{NO}_2 + \text{M} \rightleftharpoons \text{NO} + \text{O} + \text{M}$	$7.6 \cdot 10^{16}$	-2.0	71583.0	¹⁸⁷⁷
12	$\text{NO}_2 + \text{NO}_2 \rightleftharpoons \text{NO}_3 + \text{NO}$	$2.7 \cdot 10^{14}$	0.0	36731.0	¹⁸⁷
13	$\text{NO}_2 + \text{NO}_2 \rightleftharpoons 2\text{NO} + \text{O}_2$	$2.0 \cdot 10^{12}$	0.0	27000.0	¹⁸⁷
14	$\text{NO}_3 + \text{M} \rightleftharpoons \text{NO}_2 + \text{O} + \text{M}$	$1.0 \cdot 10^{25}$	-2.0	49600.0	¹⁸⁷
15	$2 \text{O} + \text{M} \rightleftharpoons \text{O}_2 + \text{M}$	$1.2 \cdot 10^{17}$	-1.0	0.0	⁴⁸
16	$\text{O} + \text{H} + \text{M} \rightleftharpoons \text{OH} + \text{M}$	$5.0 \cdot 10^{17}$	-1.0	0.0	⁴⁹
17	$\text{O} + \text{H}_2 \rightleftharpoons \text{H} + \text{OH}$	$5.0 \cdot 10^4$	2.67	6290.0	⁴
18	$\text{O} + \text{HO}_2 \rightleftharpoons \text{OH} + \text{O}_2$	$2.0 \cdot 10^{13}$	0.0	0.0	⁴
19	$\text{O} + \text{H}_2\text{O}_2 \rightleftharpoons \text{OH} + \text{HO}_2$	$9.63 \cdot 10^6$	2.0	4000.0	⁴
20	$\text{H} + \text{O}_2 + \text{O}_2 \rightleftharpoons \text{HO}_2 + \text{O}_2$	$3.0 \cdot 10^{20}$	-1.72	0.0	⁴
21	$\text{H} + \text{O}_2 + \text{H}_2\text{O} \rightleftharpoons \text{HO}_2 + \text{H}_2\text{O}$	$9.38 \cdot 10^{18}$	-1.76	0.0	⁴
22	$\text{H} + \text{O}_2 + \text{N}_2 \rightleftharpoons \text{HO}_2 + \text{N}_2$	$3.75 \cdot 10^{20}$	-1.72	0.0	⁴
23	$\text{H} + \text{O}_2 + \text{Ar} \rightleftharpoons \text{HO}_2 + \text{Ar}$	$7.0 \cdot 10^{17}$	-0.8	0.0	⁴
24	$2\text{H} + \text{M} \rightleftharpoons \text{H}_2 + \text{M}$	$1.0 \cdot 10^{18}$	-1.0	0.0	⁴¹⁰
25	$2 \text{H} + \text{H}_2 \rightleftharpoons 2\text{H}_2$	$9.0 \cdot 10^{16}$	-0.6	0.0	⁴
26	$2 \text{H} + \text{H}_2\text{O} \rightleftharpoons \text{H}_2 + \text{H}_2\text{O}$	$6.0 \cdot 10^{19}$	-1.25	0.0	⁴
27	$\text{H} + \text{OH} + \text{M} \rightleftharpoons \text{H}_2\text{O} + \text{M}$	$2.2 \cdot 10^{22}$	-2.0	0.0	⁴¹¹
28	$\text{H} + \text{HO}_2 \rightleftharpoons \text{O} + \text{H}_2\text{O}$	$3.97 \cdot 10^{12}$	0.0	671.0	⁴
29	$\text{H} + \text{HO}_2 \rightleftharpoons \text{O}_2 + \text{H}_2$	$2.8 \cdot 10^{13}$	0.0	1068.0	⁴
30	$\text{H} + \text{HO}_2 \rightleftharpoons 2\text{OH}$	$1.34 \cdot 10^{14}$	0.0	635.0	⁴
31	$\text{H} + \text{H}_2\text{O}_2 \rightleftharpoons \text{HO}_2 + \text{H}_2$	$1.21 \cdot 10^7$	2.0	5200.0	⁴
32	$\text{H} + \text{H}_2\text{O}_2 \rightleftharpoons \text{OH} + \text{H}_2\text{O}$	$1.0 \cdot 10^{13}$	0.0	3600.0	⁴
33	$\text{OH} + \text{H}_2 \rightleftharpoons \text{H} + \text{H}_2\text{O}$	$2.16 \cdot 10^8$	1.51	3430.0	⁴
34	$2 \text{OH}(+\text{M}) \rightleftharpoons \text{H}_2\text{O}_2(+\text{M})$	$7.4 \cdot 10^{13}$	-0.37	0.0	⁴¹²
34b	$2 \text{OH}(+\text{M}) \rightleftharpoons \text{H}_2\text{O}_2(+\text{M})$	$2.3 \cdot 10^{18}$	-0.9	-1700.0	⁴¹³

¹see the text for explanations

²Efficiencies of collision partners: H_2 — 15.0, H_2O — 9.6; Ar — 1.0, N_2 — 1.74, N_2O — 6.9, O_2 — 1.3, NO — 3.0

³low pressure limit

⁴upper limit, estimation

⁵Efficiencies of collision partners: H_2 — 3.2, H_2O — 9.6; Ar — 1.0, N_2 — 1.6, N_2O — 7.0, O_2 — 1.3, NO — 2.8

⁶see the text for explanations

⁷Efficiencies of collision partners: H_2 — 3.2, H_2O — 9.6; Ar — 1.0, N_2 — 1.6, N_2O — 7.0, O_2 — 1.3, NO — 2.8

⁸Efficiencies of collision partners: H_2 — 2.4, H_2O — 15.4; Ar — 0.83

⁹Efficiencies of collision partners: H_2 — 2.0, H_2O — 6.0; Ar — 0.7

¹⁰Efficiencies of collision partners: Ar — 0.63

¹¹Efficiencies of collision partners: H_2 — 0.73, H_2O — 3.65; Ar — 0.38

¹²Efficiencies of collision partners: H_2 — 2.0, H_2O — 6.0; Ar — 0.7; Troe's parameters are 0.7346, 94.0, 1756.0, 5182.0.

¹³low pressure limit

Table 5.4: The kinetic scheme. The rate constants are given in the form $k = AT^\beta \exp(-E/RT)$; dimensions are in $\text{cm}^3/(\text{mole}\cdot\text{s})$.

N	Reaction	A	β	E	Ref
35	$2 \text{ OH} \rightleftharpoons \text{O} + \text{H}_2\text{O}$	$3.57 \cdot 10^4$	2.4	-2110.0	⁴
36	$\text{OH} + \text{HO}_2 \rightleftharpoons \text{O}_2 + \text{H}_2\text{O}$	$2.9 \cdot 10^{13}$	0.0	-500.0	⁴
37	$\text{OH} + \text{H}_2\text{O}_2 \rightleftharpoons \text{HO}_2 + \text{H}_2\text{O}$	$1.75 \cdot 10^{12}$	0.0	320.0	⁴
38	$\text{OH} + \text{H}_2\text{O}_2 \rightleftharpoons \text{HO}_2 + \text{H}_2\text{O}$	$5.8 \cdot 10^{14}$	0.0	9560.0	^{4,14}
39	$2 \text{ HO}_2 \rightleftharpoons \text{O}_2 + \text{H}_2\text{O}_2$	$1.3 \cdot 10^{11}$	0.0	-1630.0	⁴
40	$2 \text{ HO}_2 \rightleftharpoons \text{O}_2 + \text{H}_2\text{O}_2$	$4.2 \cdot 10^{14}$	0.0	12000.0	^{4,15}
41	$\text{N} + \text{NO} \rightleftharpoons \text{N}_2 + \text{O}$	$3.5 \cdot 10^{13}$	0.0	330.0	⁴
42	$\text{N} + \text{O}_2 \rightleftharpoons \text{NO} + \text{O}$	$2.65 \cdot 10^{12}$	0.0	6400.0	⁴
43	$\text{N} + \text{OH} \rightleftharpoons \text{NO} + \text{H}$	$7.33 \cdot 10^{13}$	0.0	1120.0	⁴
44	$\text{HO}_2 + \text{NO} \rightleftharpoons \text{NO}_2 + \text{OH}$	$2.11 \cdot 10^{12}$	0.0	-480.0	⁴
45	$\text{NO}_2 + \text{H} \rightleftharpoons \text{NO} + \text{OH}$	$1.32 \cdot 10^{14}$	0.0	360.0	⁴
46	$\text{NH} + \text{O} \rightleftharpoons \text{NO} + \text{H}$	$5.0 \cdot 10^{13}$	0.0	0.0	⁴
47	$\text{NH} + \text{H} \rightleftharpoons \text{N} + \text{H}_2$	$3.2 \cdot 10^{13}$	0.0	330.0	⁴
48	$\text{NH} + \text{OH} \rightleftharpoons \text{NHO} + \text{H}$	$2.0 \cdot 10^{13}$	0.0	0.0	⁴
49	$\text{NH} + \text{OH} \rightleftharpoons \text{N} + \text{H}_2\text{O}$	$2.0 \cdot 10^9$	1.2	0.0	⁴
50	$\text{NH} + \text{O}_2 \rightleftharpoons \text{HNO} + \text{O}$	$4.61 \cdot 10^5$	2.0	6500.0	⁴
51	$\text{NH} + \text{O}_2 \rightleftharpoons \text{NO} + \text{OH}$	$1.28 \cdot 10^6$	1.5	100.0	⁴
52	$\text{NH} + \text{N} \rightleftharpoons \text{N}_2 + \text{H}$	$1.5 \cdot 10^{13}$	0.0	0.0	⁴
53	$\text{NH} + \text{H}_2\text{O} \rightleftharpoons \text{HNO} + \text{H}_2$	$2.0 \cdot 10^{13}$	0.0	13850.0	⁴
54	$\text{NH} + \text{NO} \rightleftharpoons \text{N}_2 + \text{OH}$	$2.16 \cdot 10^{13}$	-0.23	0.0	⁴
55	$\text{NH} + \text{NO} \rightleftharpoons \text{N}_2\text{O} + \text{H}$	$4.16 \cdot 10^{14}$	-0.45	0.0	⁴
56	$\text{NH}_2 + \text{O} \rightleftharpoons \text{OH} + \text{NH}$	$7.0 \cdot 10^{12}$	0.0	0.0	⁴
57	$\text{NH}_2 + \text{O} \rightleftharpoons \text{H} + \text{HNO}$	$4.6 \cdot 10^{13}$	0.0	0.0	⁴
58	$\text{NH}_2 + \text{H} \rightleftharpoons \text{NH} + \text{H}_2$	$4.0 \cdot 10^{13}$	0.0	3650.0	⁴
59	$\text{NH}_2 + \text{OH} \rightleftharpoons \text{NH} + \text{H}_2\text{O}$	$9.0 \cdot 10^7$	1.5	-460.0	⁴
60	$\text{NNH} \rightleftharpoons \text{N}_2 + \text{H}$	$3.3 \cdot 10^8$	0.0	0.0	⁴
61	$\text{NNH} + \text{M} \rightleftharpoons \text{N}_2 + \text{H} + \text{M}$	$1.3 \cdot 10^{14}$	-0.11	4980.0	^{4,16}
62	$\text{NNH} + \text{O}_2 \rightleftharpoons \text{HO}_2 + \text{N}_2$	$5.0 \cdot 10^{12}$	0.0	0.0	⁴
63	$\text{NNH} + \text{O} \rightleftharpoons \text{OH} + \text{N}_2$	$2.5 \cdot 10^{13}$	0.0	0.0	⁴
64	$\text{NNH} + \text{O} \rightleftharpoons \text{NH} + \text{NO}$	$7.0 \cdot 10^{13}$	0.0	0.0	⁴
65	$\text{NNH} + \text{H} \rightleftharpoons \text{H}_2 + \text{N}_2$	$5.0 \cdot 10^{13}$	0.0	0.0	⁴
66	$\text{NNH} + \text{OH} \rightleftharpoons \text{H}_2\text{O} + \text{N}_2$	$2.0 \cdot 10^{13}$	0.0	0.0	⁴
67	$\text{H} + \text{NO} + \text{M} \rightleftharpoons \text{HNO} + \text{M}$	$8.95 \cdot 10^{19}$	-1.32	740.0	^{4,17}
68	$\text{HNO} + \text{O} \rightleftharpoons \text{NO} + \text{OH}$	$2.5 \cdot 10^{13}$	0.0	0.0	⁴
69	$\text{HNO} + \text{H} \rightleftharpoons \text{H}_2 + \text{NO}$	$4.5 \cdot 10^{11}$	0.72	660.0	⁴
70	$\text{HNO} + \text{OH} \rightleftharpoons \text{NO} + \text{H}_2\text{O}$	$1.3 \cdot 10^7$	1.9	-950.0	⁴
71	$\text{HNO} + \text{O}_2 \rightleftharpoons \text{HO}_2 + \text{NO}$	$1.0 \cdot 10^{13}$	0.0	13000.0	⁴
72	$\text{NH}_3 + \text{H} \rightleftharpoons \text{NH}_2 + \text{H}_2$	$5.4 \cdot 10^5$	2.4	9915.0	⁴
73	$\text{NH}_3 + \text{OH} \rightleftharpoons \text{NH}_2 + \text{H}_2\text{O}$	$5.0 \cdot 10^7$	1.6	955.0	⁴
74	$\text{NH}_3 + \text{O} \rightleftharpoons \text{NH}_2 + \text{OH}$	$9.4 \cdot 10^6$	1.94	6460.0	⁴
75	$\text{H} + \text{N}_2\text{O} \rightarrow \text{OH(A)} + \text{N}_2$	$1.1 \cdot 10^{14}$	0	50300	¹⁸⁸
76	$\text{H} + \text{O} + \text{Ar} \rightarrow \text{OH(A)} + \text{Ar}$	$1.2 \cdot 10^{13}$	0	6940	¹⁸⁸
77	$\text{OH(A)} + \text{H}_2 \rightarrow \text{OH} + \text{H}_2$	$2.71 \cdot 10^{14}$	0	0	¹⁹¹
78	$\text{OH(A)} + \text{O}_2 \rightarrow \text{OH} + \text{O}_2$	$9.03 \cdot 10^{13}$	0	0	¹⁹¹
79	$\text{OH(A)} + \text{H}_2\text{O} \rightarrow \text{OH} + \text{H}_2\text{O}$	$2.53 \cdot 10^{14}$	0	0	¹⁹¹
80	$\text{OH(A)} + \text{N}_2\text{O} \rightarrow \text{OH} + \text{N}_2\text{O}$	$2.83 \cdot 10^{14}$	0	0	¹⁹¹
81	$\text{OH(A)} + \text{N}_2 \rightarrow \text{OH} + \text{N}_2$	$6.02 \cdot 10^{12}$	0	0	¹⁹¹

The constants of several reactions defining the kinetics in a system containing H, N, and O atoms were taken from.^{187, 189} These reactions included reactions of interaction of N_2O with main radicals and the reaction of thermal decomposition of N_2O , but a part of the rate constants was corrected to fit the entire set of available experimental data. We will consider in more detail the changes made in the kinetic scheme in comparison with the scheme presented in^{185—, 187}

¹⁴ $k = k_{37} + k_{38}$

¹⁵ $k = k_{39} + k_{40}$

¹⁶Efficiencies of collision partners: H_2 — 2.0, H_2O — 6.0; Ar — 0.7

¹⁷Efficiencies of collision partners: H_2 — 2.0, H_2O — 6.0; Ar — 0.7

The preliminary analysis of the experimental data revealed that the process suggested by Hanson et al.¹⁸⁶



is of significant importance.

The ignition delay is highly sensitive to the rate constant of reaction (5.6) even for the rate constant values that are much lower than those of chain propagation or than the rate constants of high-temperature decomposition of N_2O , because it is reaction (5.6) that is responsible for the heating of mixture. The only known experimentally obtained evaluation of the rate constant of this reaction¹⁸⁶ is based on monitoring the kinetics of reaction $\text{NH}_2 + \text{NO}$. At this, reaction (5.6) was one of the numerous channels of the mechanism and the experimental data were relatively insensitive to the rate constant of the reaction. Experiments were performed in a mixture containing 2% NH_3 and 2% NO in argon. The rate constant for reaction (5.6) was estimated by the authors of¹⁸⁶ as $2 \cdot 10^{11} \text{T}^{0.5} \text{ cm}^3/(\text{mole} \cdot \text{s})$ in the temperature range from 1700 to 3000 K.

The importance of reaction (5.6) decreases rapidly with decreasing concentrations of N_2O and H_2 and becomes insignificant at hydrogen concentrations of less than 1%. Besides, the decomposition of N_2O becomes important in the N_2O – H_2 system at high temperatures:



This process is accompanied by a fast chain mechanism



which makes the interpretation of kinetic data much more difficult. Note that reactions (5.8) and (5.9) are important part in thermal decomposition of N_2O at almost any concentrations of H_2 starting with ~ 20 ppm.^{187,189} Treating the kinetics, one must further take into account the decomposition of N_2O by atomic oxygen:

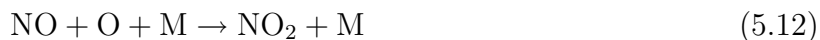


Note that, as was demonstrated in,¹⁸⁹ the channel which is alternative with respect to products



is much slower than reaction (5.10) and does not influence decomposition of N_2O at high temperatures. The production of molecular oxygen is related to the mechanism (5.8) — (5.9) and is attributed to the presence of microimpurity of hydrogen in the experiments.

At high pressures, the three-particle conversion of NO to NO₂ becomes important,



with subsequent reaction of NO₂ with atomic oxygen



At low temperature in hydrogen-free mixtures this channel is the main source of molecular oxygen during the decomposition of N₂O.

When molecular oxygen is added to the system (for example, N₂O:H₂:O₂:Ar mixture under our experimental conditions), there arises one more important channel of production of OH



which affects the rate of ignition of rich N₂O–H₂–O₂ mixtures at high temperatures.

We will analyse the role of every mentioned reaction.

Figure 5.6 gives the data presented in¹⁸⁵ on the rate of unimolecular decomposition of N₂O. The rate of decomposition was determined from direct measurements of the profile of N₂O concentration by the absorption of N₂O in the UV spectral range ($\lambda \approx 250$ nm) and emission of N₂O in the band of asymmetric mode ($\lambda = 4.5$ μm). The results produced by both methods agree with each another (see Fig. 5.6). When even 250 ppm hydrogen is added to the mixture, the observed rate of decomposition of N₂O increases significantly. This is related to the development of reaction by the chain mechanism (5.8) — (5.9). In this case, the effect of processes (5.6) and (5.7) is insignificant because of low concentration of hydrogen under given conditions. The observed rate of decomposition increases with the concentration of H₂. At [H₂]=1000 ppm, the rate is doubled compared to hydrogen-free mixture. The concentration being [H₂]=1%, the rate of decomposition of N₂O increases by a factor of four. Note that the mechanism (5.8) — (5.9) depends on the presence of atomic oxygen and, in principle, can increase the rate of decomposition of N₂O not more than to its double value. For this reason, the authors of¹⁸⁵ failed to explain the rate of decomposition in N₂O:H₂:Ar=3:1:96 mixture.

The implementation of process (5.6) makes it possible to fit the experimental data of¹⁸⁵ to the results of numerical simulation for all concentrations of hydrogen in the mixture (see Fig. 5.6). Thus, the displacement of the observed rate constant at adding of hydrogen is adequately described. Moreover, the change in temperature dependence, which is connected with partial replacement of reaction (5.7) by reaction (5.6) with a weaker temperature dependence, is clearly manifested.

The rate constant obtained for unimolecular decomposition of N₂O in the limit of low and high pressures may be approximated by the expressions (hereinafter, the rate constants are in [cm³/(mole·s)])

$$k_{5.7}^0 = 5.1 \cdot 10^{18} T^{-1.12} \exp\left(-\frac{59580}{RT}\right), \quad (5.15)$$

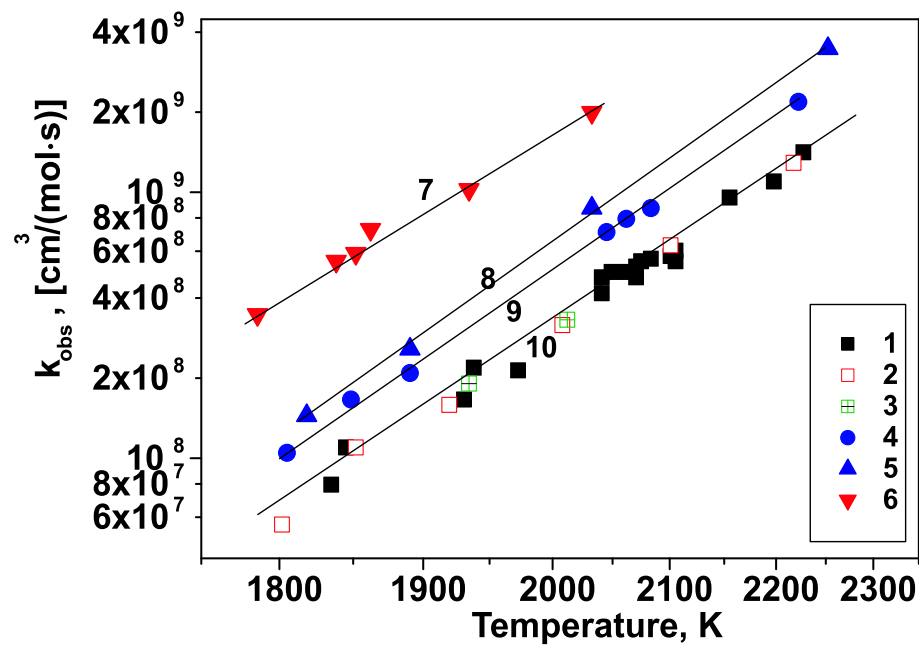


Figure 5.6: Comparison of experimental and calculation results for kinetics of N_2O -containing mixtures. Data on the observed rate constant of unimolecular decomposition. The experimental points are taken from¹⁸⁵: 1 — mixture of 3% N_2O +Ar, data on IR emission ($4.5 \mu\text{m}$); 2 — mixture of 3% N_2O +Ar, data on UV absorption (250 nm); 3 — mixture of 3% N_2O , data on IR emission ($2.9 \mu\text{m}$); 4 — mixture of 3% N_2O +250 ppm H_2 +Ar, data on IR emission ($4.5 \mu\text{m}$); 5 — mixture of 3% N_2O +1000 ppm H_2 +Ar, data on IR emission ($4.5 \mu\text{m}$); 6 — mixture of 3% N_2O +1% H_2 +Ar, data on IR emission ($4.5 \mu\text{m}$). Lines 7–10 give the results of the numerical model, proposed in the present paper.

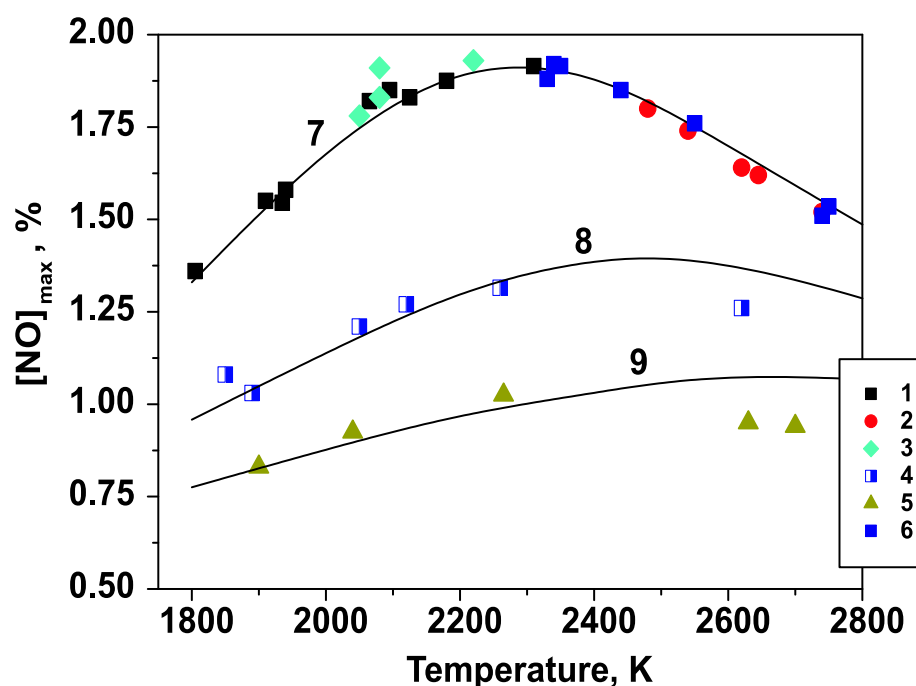


Figure 5.7: Comparison of the experimental and calculation results for the kinetics of N_2O -containing mixtures. The experimental data are borrowed from¹⁸⁹: 1 — mixture of 3% N_2O +Ar, data on IR emission, pressure $P = 11.5$ atm; 2 — mixture of 3% N_2O +Ar, data on IR emission, pressure $P = 8$ atm; 3 — mixture of 3% N_2O +Ar, data on UV absorption, pressure $P = 11.5$ atm; 4 — mixture of 3% N_2O +250 ppm H_2 +Ar, data on IR emission, pressure $P = 11.5$ atm; 5 — mixture of 3% N_2O +1000 ppm H_2 +Ar, data on IR emission, pressure $P = 11$ atm; 6 — mixture of 3% N_2O +Ar, data on IR emission, pressure $P = 8$ atm.

$$k_{5.7}^{\text{inf}} = 1.7 \cdot 10^{11} \exp \left(-\frac{59580}{RT} \right). \quad (5.16)$$

These values correlate with the data of¹⁸⁵ in the overlapping range and approximate most of the data of other authors in the range from 1000 to 4000 K.

The value obtained for the rate constant of reaction (5.6) is much lower than that given in¹⁸⁶ in the low-temperature region. The reaction accelerates with increasing temperature and the activation energy is approximately half of the activation energy of unimolecular decomposition of N₂O,

$$k_{5.6} = 2.1 \cdot 10^{14} \exp \left(-\frac{32500}{RT} \right), \quad (5.17)$$

Figure 5.7 gives the data on measurements of the absolute yield of NO under conditions of thermal decomposition of N₂O for different concentrations of hydrogen in the mixture. The measurements were performed by both UV absorption of NO in the γ -band ($\lambda=225$ nm) and IR emission ($\lambda = 5.3$ μm). A reference mixture containing 1% N₂O+Ar was taken for absolute calibration of the system. Both UV and IR measurements produced close results and provided a high accuracy in determining the concentration of NO after the decomposition of N₂O.

There is observed a good agreement between the measured and calculated values of NO yield within the entire range of parameters. The analysis of the dome-shaped NO-yield temperature dependence performed in¹⁸⁹ revealed that the decrease in the low-temperature region is related to the loss of atomic oxygen in processes (5.12) and (5.13). At high temperatures, the accelerating unimolecular decomposition of N₂O leads to an abrupt decrease in the N₂O concentration in the mixture and to a relative deceleration of reaction (5.10) whose temperature dependence is twice weaker than that of reactions (5.12) and (5.13).

The competition of reactions (5.10), (5.12), and (5.13) with unimolecular decomposition of N₂O + M \rightarrow N₂ + O + M completely defines the shape of the curve of NO yield in hydrogen-free mixtures. The results of the performed modelling confirm the inference of¹⁸⁹ that the ratio between rate constants of channels (5.10) and (5.11) at $T = 1000 - 2000$ K is $k_{5.10}/k_{5.11} > 20$.

The scheme presented here included the changed value of rate constant $k_{5.10}$:

$$k_{5.10} = 5.8 \cdot 10^{13} \exp \left(-\frac{26000}{RT} \right). \quad (5.18)$$

This expression differs from the approximation suggested in¹⁸⁷ by less than the value of the measurement error. However, it enables one to more accurately reproduce the behavior of the curve of NO yield (see Fig. 5.7).

As was noted above, the kinetics of mixtures containing less than 1% H₂ are almost independent of the choice of rate constants $k_{5.6}$ and $k_{5.7}$.

The decrease in the yield of nitrogen monoxide in mixtures with an addition of 250 and 1000 ppm of hydrogen is defined by the competition between channels (5.10) and (5.8)—(5.9). This fact enables one to clarify the rate constants of processes (5.8), (5.9) taking into account a weak impact made by reactions (5.6) and (5.7),

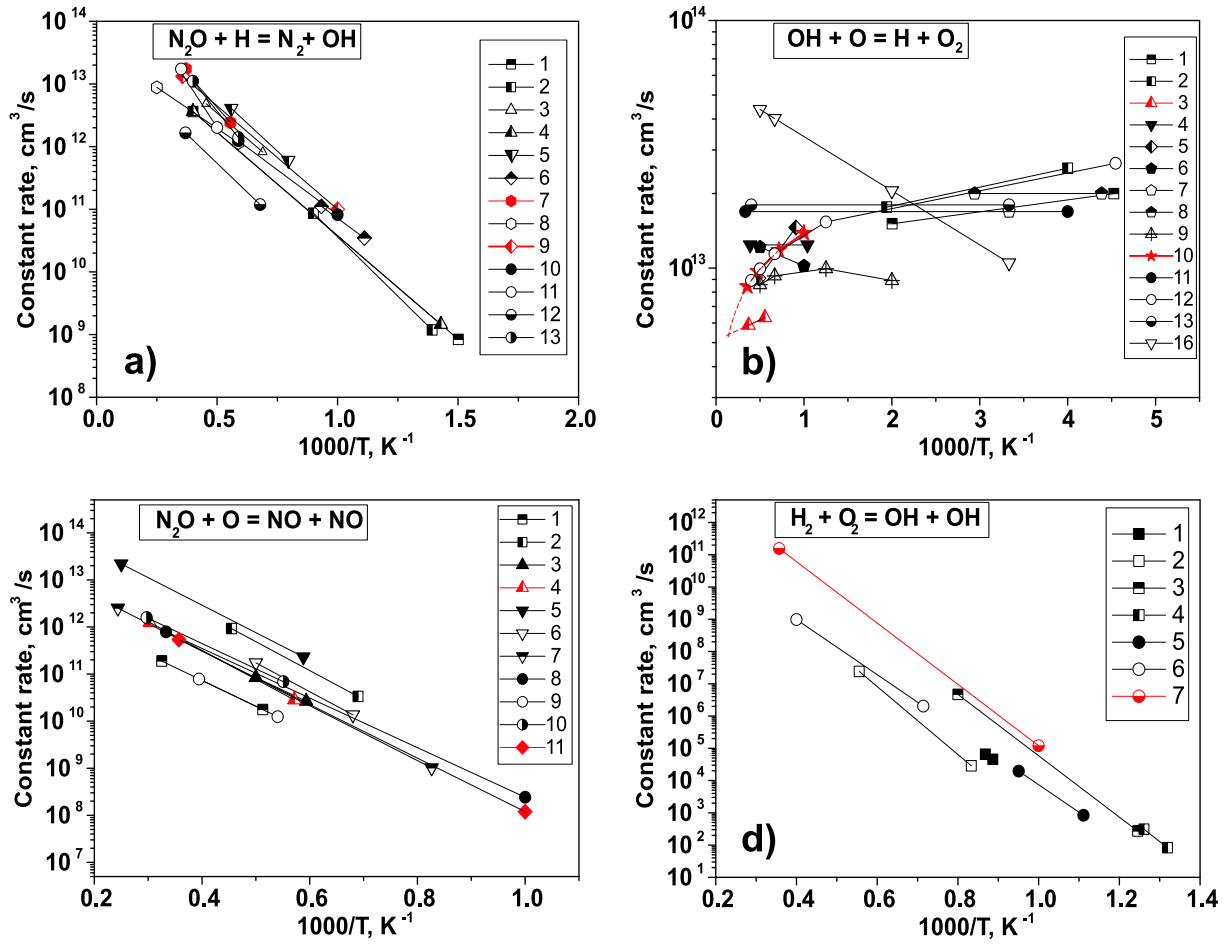


Figure 5.8: Review of reaction rate constants: a) — reaction $\text{N}_2\text{O} + \text{H} = \text{N}_2 + \text{OH}$. 1 $_{-193}$, 2 $_{-194}$, 3 $_{-195}$, 4 $_{-196}$, 5 $_{-197}$, 6 $_{-198}$, 7 $_{-187}$, 8 $_{-199}$, 9 — our data, 10 $_{-200}$, 11 $_{-201}$, 12 $_{-202}$, 13 $_{-203}$; b) — reaction $\text{OH} + \text{O} = \text{H} + \text{O}_2$. 1 $_{-204}$, 2 $_{-205}$, 3 $_{-187}$, 4 $_{-206}$, 5 $_{-207}$, 6 $_{-208}$, 7 $_{-209}$, 8 $_{-210}$, 9 $_{-211}$, 10 — our data, 11 $_{-212}$, 12 $_{-192}$, 13 $_{-213}$, 14 $_{-214}$; c) — reaction $\text{N}_2\text{O} + \text{O} = \text{NO} + \text{NO}$. 1 $_{-184}$, 2 $_{-195}$, 3 $_{-215}$, 4 $_{-189}$, 5 $_{-199}$, 6 $_{-216}$, 7 $_{-217}$, 8 $_{-218}$, 9 $_{-219}$, 10 $_{-220}$, 11 — our data; d) — reaction $\text{H}_2 + \text{O}_2 = \text{OH} + \text{OH}$. 1 $_{-221}$, 2 $_{-222}$, 3 $_{-223}$, 4 $_{-224}$, 5 $_{-225}$, 6 $_{-226}$, 7 — our data.

$$k_{5.8} = 2.0 \cdot 10^{14} \exp\left(-\frac{15100}{RT}\right), \quad (5.19)$$

$$k_{5.9} = 4.5 \cdot 10^{14} T^{-0.5} \exp\left(-\frac{60}{RT}\right). \quad (5.20)$$

The obtained value of the rate constant of reaction (5.8) agrees well with the value given in¹⁸⁷ in the overlapping temperature range and correlates with the numerous experimental data obtained for this reaction elsewhere (see the review in¹⁸⁷).

The value of the rate constant of reaction (5.9) lies slightly higher than the data of¹⁹⁰ and fits exactly the value given in,¹⁹² which is based on low-temperature data for this reaction and on the value of the rate constant of the inverse process at high temperatures.

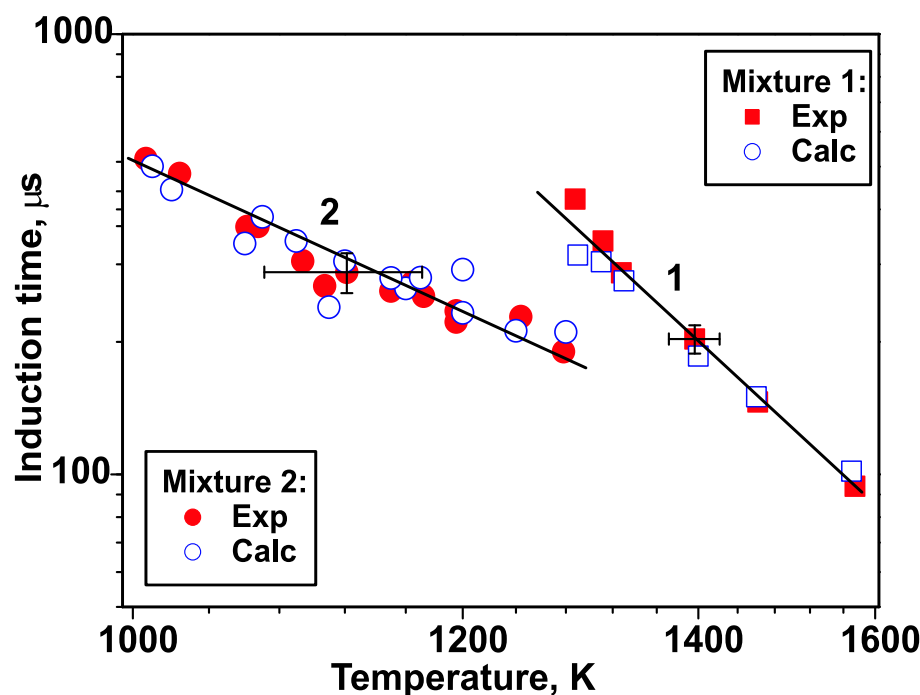


Figure 5.9: Comparison of the experimental and calculation results for the autoignition of N_2O -containing mixtures. Our experiments: 1 – $\text{H}_2 : \text{N}_2\text{O} : \text{Ar} = 10 : 10 : 80$ mixture, 2 — $\text{O}_2 : \text{H}_2 : \text{N}_2\text{O} : \text{Ar} = 3 : 30 : 10 : 50$ mixture.

The rate constants for the reactions $k_{5.8}$, $k_{5.9}$, and $k_{5.10}$ are illustrated by Figs. 5.8 a-c, respectively. The figures give the values obtained by other authors along with those suggested in the present paper. One can see good agreement with the main array of data for all of the reactions mentioned above.

Figure 5.9 gives the results of experiments in water-diluted mixtures containing N_2O , H_2 , and O_2 (the initial data for the experiments are as given in Tables 5.2—5.3). It also presents the results of the calculations. In all the calculations under our experimental conditions, the ignition delay time was determined by the point of intersection of the tangent to the emission of electronically excited $\text{OH}(A^2\Sigma)$ at the maximum of derivative with the abscissa, i.e., similarly with the experimental data. The figure demonstrates good agreement between the experimental and theoretical data for the entire investigated range of temperatures and pressures.

The selected numerical mechanism was further validated by comparing the results of the calculations with the experimental results of.¹⁸⁸ Comparison is given in Fig. 5.10. In these calculations, in accordance with the experiments,¹⁸⁸ we determined the ignition time by the maximum of emission of the $\text{OH}(A^2\Sigma)$ state as a function of time. The figure demonstrates good agreement between the experimental and theoretical data for the entire investigated range of parameters and lends support to the validity of choice of the kinetic scheme as a whole.

Note that the suggested scheme reproduces both the temperature dependence and the absolute values of the ignition delay time in different mixtures (Figs. 5.9 and 5.10).

We will enlarge on the experiments in weakly dilute mixtures (Fig. 5.9). Good agreement between the theory and the experiment was observed for both investigated mix-

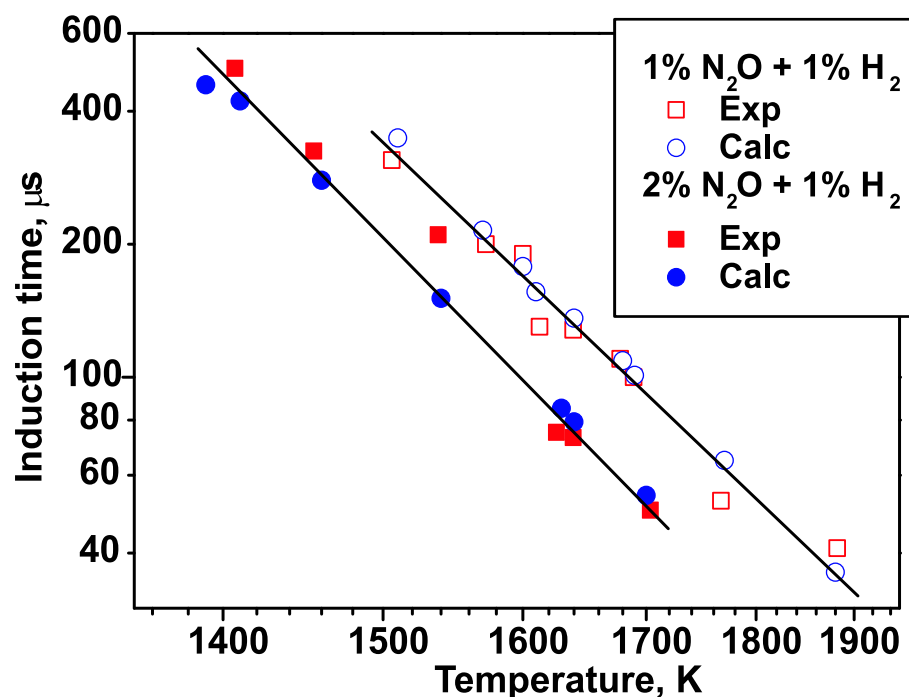


Figure 5.10: Comparison of the experimental and calculation results for the autoignition of N₂O-containing mixtures. The composition of mixtures is given in the figure. Argon is used as diluent gas. The experimental data are taken from¹⁸⁸; the calculations are performed on the basis of the kinetic scheme proposed in the present paper.

tures. For N₂O:H₂:Ar = 10:10:80 mixture in the temperature range of $T \sim 1500$ K, the unimolecular decomposition of N₂O becomes important (reaction (5.7)). The high value of activation energy of unimolecular decomposition enables one to single out this process against the background of reactions (5.6) and (5.14),

$$k_{5.7}(M = H_2) = (13 \pm 3)k_{5.7}(M = Ar). \quad (5.21)$$

Note that this is apparently the first experimentally obtained evaluation of the rate constant of unimolecular decomposition of N₂O in an atmosphere of hydrogen.

At lower temperatures, the behavior of the temperature dependence of the delay time for both mixtures is mainly defined by reaction (5.6). The results of the experiments in N₂O:H₂:Ar = 10:10:80 mixture demonstrate a more pronounced temperature dependence of the delay time in comparison with N₂O:H₂:O₂:Ar = 10:30:3:50 mixture. At the same time, the abrupt decrease in the ignition delay time in the case of transition to the second mixture cannot be explained by the increase in the hydrogen concentration alone. In this case, an important role is played by the addition of molecular oxygen which causes a significant acceleration of ignition in this temperature range.

Therefore, in the case of transition from one mixture to the other, there arises yet another process of low activation energy, which controls the ignition, in addition to reactions (5.7) and (5.6).

The rate constant of reaction (5.14) ($H_2 + O_2 \rightarrow OH + OH$) was measured in a number of studies;²²³ this reaction has a much lower activation energy than the reaction of unimolecular decomposition of N₂O. Simultaneous analysis of the kinetics of autoignition of

mixtures with and without addition of oxygen yields a possible value of the rate constant of this reaction based on our experimental data as

$$k_{5.14} = 3.9 \cdot 10^{14} \exp \left(-\frac{43500}{RT} \right). \quad (5.22)$$

This value is in adequate agreement with results of the previous studies though somewhat exceeding the value recommended by Azatyan et al.²²³ (see Fig. 5.8 d). It would be wise to note that proposed kinetic scheme describes adequately our recent experiments in H₂:O₂:Ar mixture.¹¹³

Thus, based on the results of shock-tube experiments on autoignition and unimolecular decay of mixtures containing N₂O, hydrogen, and oxygen and on the results of appropriate numerical calculation there has been suggested a mechanism which describes the kinetics of both highly dilute N₂O–H₂–O₂ mixtures and mixtures which are weakly diluted with inert gas at high ($T > 1000$ K) temperatures and moderate (up to several atmospheres) pressures.

The subdivision of the discharge action and ignition processes allows to subdivide the processes of injection of radicals / ions / excited species and their influence on the ignition process. From this point of view, a nanosecond volume discharge, at least not longer than a few hundreds of nanosecond, with its dominant excitation of high-energy degrees of freedom, is the optimal type of the discharge. To justify the mechanism of ignition by low-temperature plasma, it is necessary to trace in experiment behavior of temperature and main intermediates with a suitable temporal and spatial resolution. Model experimental systems, where the role of the certain component can be elucidated, are desirable. An example of such a system, allowing to test the role of O(¹D) in the ignition process and to compare discharge efficiency with the efficiency of radical injection, is proposed.

The kinetics of chemical transformation in N₂O–H₂–O₂–Ar mixtures have been studied in the temperature range from 1000 to 2700 K and pressures from 0.1 to 10 atm. A shock-tube experiment has been used to obtain data on the times of ignition delay in mixtures which are weakly diluted with inert gas (50 to 90% Ar). Based on the data obtained and the data of kinetic experiments in mixtures containing up to 97% Ar, a mechanism to describe the kinetics in the given system has been suggested. The values of rate constants of some chemical reactions involving N₂O, NO, and OH have been clarified.

Chapter 6

Mechanisms of Flames Control by Means of a Non-Equilibrium Low-Temperature Pulsed Nanosecond Barrier Discharge Plasma

6.1 Flame control by pulsed nanosecond barrier discharge

The effect of the electric field on a flame was first observed in 1814 by Brande,²²⁷ who discovered that the flame behavior changes substantially when the flame is placed between two electrodes. It was found that the influence of the electric field on the heat and mass transfer was so strong that both the flame and carbon soot began to move toward the negatively charged electrode. Thus, Brande was the first to affect the flame propagation velocity by applying an electric field. The review of the studies in this field can be found in the papers of Malinovsky²²⁸

Since that time, the interaction of electric fields and discharges with flames has been studied widely and extensively all over the world. The main idea of these investigations is flame stabilization,²²⁹ the production of the atoms, ions, and active radicals neutralizing hazardous wastes of heat power plants and chemical factories (NO_x , SO_2 , etc.),²³⁰ extending flammability limits, and increasing the flame luminosity. The determination of the basic mechanisms responsible for the combustion stability is also of great interest. It is known that unstable combustion of solid, liquid, or gaseous fuels in power plants manifests itself in a spontaneous onset of self-oscillating combustion regimes, which are accompanied by significant fluctuations of the thermal flux rate and pressure, as well as by mechanical vibrations (or even destruction) of the combustion chamber. Therefore, the problem of the effective combustion stability control is very pressing.

A separate field of research is the use of electric fields and discharges to affect the flame propagation velocity. By applying an electric field, one can decrease the flame propagation velocity along the channel and even extinguish the flame (as was shown by

Malinovsky as long ago as in 1924²³¹) or, on the contrary, accelerate the combustion rate by increasing the flame blow-off velocity.²³² This field of research holds great promise and is quite challenging for practical applications, such as aircraft engines, in which combustion should be as rapid and full as possible. More rapid combustion makes it possible to use more lean mixtures, which results in a decrease in the temperature of the combustion products and a reduction in the amount of the harmful NO_x impurities produced.

Discussion about the real mechanisms through which the electric field can affect the combustion rate has been lasted for many years. The problem of determining such mechanisms is particularly important because of the rapidly growing interest in the possibility of additionally controlling the flame dynamics with the help of a non-equilibrium plasma.

The simplest means for affecting a combustible mixture with an electric discharge is a pulsed arc, which occurs, for instance, in the spark plug of a IC engine. In this case, the discharge current density is high enough, the produced plasma is close to a thermally equilibrium state, and the fuel is ignited due to the heating of the mixture in a small-volume arc channel and the adjacent regions. The energy input on such an ignition can be rather high, and the ratio of the discharge energy to the gas chemical energy in the spark channel is much larger than unity. For this reason, this type of discharge is inapplicable for volume ignition because of the high energy consumption. However, it is volume (or nearly volume) ignition that is of greatest interest for applications with a high rate of energy release. The slow propagation of the flame front from the point of ignition limits this rate and does not allows one to use spark discharges in high-speed (including supersonic) gas flows.

Therefore, of especial interest in this field is to find such methods of flame control at which energy deposition in the gas is certainly insufficient to heat the mixture up to the temperature of spontaneous thermal ignition. That's why we will consider below discharges in which Joule heating is negligibly small in comparison with the chemical heat release and is distributed over the gas volume.

Flame is a low-temperature plasma with a mean particle energy of $\simeq 0.2$ eV. This plasma consists mainly of molecules and radicals, as well as electrons and positively charged ions produced by chemical or thermal ionization. Calculations of the equilibrium composition of the combustion products of a hydrocarbon–air mixture at atmospheric pressure and the temperature corresponding to the adiabatic equilibrium (higher than 2000 K) by Sakha equation give the electron density lower than 10^8 cm⁻³, whereas the total density of the molecules, radicals, and atoms is about 10^{18} cm⁻³. For this reason, the following two mechanisms (besides Joule heating) through which the electric field affects the flame characteristics are considered in the literature.

At low reduced fields (that are insufficient for the excitation of the mixture components (several hundred volts per centimeter at atmospheric pressure), the so-called "ionic wind" (the electric field–induced redistribution of the charged particles, as well as neutral atoms and molecules, which are set into motion due to the resonance charge-exchange processes, $\tilde{A} + A^+ \rightarrow \tilde{A}^+ + A$) plays a decisive role. It was shown in the monograph by Lawton and Weinberg,²³³ that the electric forces inside a flame can exceed the convective forces by more than two orders of magnitudes. This effect is especially pronounced in the case of slow diffusion flames, whose propagation velocities are much lower than those of premixed flames.²³⁴

At higher electric fields, the processes of gas excitation, dissociation, and ionization

by electron impacts become important. These processes lead to the appearance of new chemically active particles and additional interaction mechanisms that modify and accelerate the kinetics of the entire system. The electron energy should be high enough for the electronical and vibrational excitation of the molecules in this case; hence, this range of electric fields generally corresponds to the development of a gas discharge.

At present, it is commonly believed that almost all of the existing experimental data can be explained (at least qualitatively) by the ionic wind action. Most of the experiments are dealing with dc fields (high-frequency fields do not affect the combustion rate because the ions have no time to move out of their positions during the field period) in the typical "burner – ring" electrode geometry. The ring is placed at a certain distance (from a few millimeters to a few centimeters) above the burner rim, and the potential difference between the electrodes is several kilovolts. It is worth mention that there is a sense to talk just about the potential difference (rather than the electric field intensity) because, in such an electrode geometry, the field distribution is highly nonuniform. For example, a significant increase of flame blow-off velocity in the methane–air mixture (by a factor of 2.0–4.2) was observed when the nozzle was at a negative potential.²³⁵ The authors explain this result by (i) a change in the temperature distribution within a narrow nozzle region filled with unburned reactants, (ii) the slowing-down and stabilization of the effluent gas near the burner edge due to the ionic wind, and (iii) the intensification of the reaction due to heat transfer and the incoming of the combustion products into the region where the mixture has not burnt yet.

Unfortunately, in spite of the interesting results obtained, such a burner design has some drawbacks. In particular, the burner wall thickness, which determines the distance over which the flame is stabilized, plays an important role. Hence, it is problematic to use this method for flame stabilization in industrial burners. Moreover, because of a highly non-uniform electric field, the main voltage drop occurs at distances of several millimeters from the nozzle. Calculations show that, in this region, the electric field intensity is close to the breakdown field in air, which leads to the formation of a corona at the nozzle edge. Therefore, the change in the blow-off velocity is not related to the ionic wind action but is a consequence of the local energy deposition in a few points inside the flow where the ignition of the mixture occurs.

The influence of a corona discharge on the blow-off velocity of a methane–air flame was studied in detail by Bradley and Nasser.²³⁶ In that study, a voltage was applied between a spiral coil placed above the flame and four tapered points placed inside the nozzle. Bradley found the following three regimes of the electric field effect: (i) the ionic wind, which slightly increases the blow-off flow rate (by $\simeq 30\%$); (ii) a corona discharge, in which the flame is stabilized at the burner nozzle; and (iii) an unstabilized corona discharge with four inverted-flame cones. As in,²³⁵ the mixture was ignited at the cone vertexes (at each point); then, the flame propagated due to conventional mechanisms, such as heat transfer and diffusion. In this case, a significant (nearly twofold) increase in the flame propagation velocity was achieved. However, a further increase in the voltage (and, accordingly, the flame velocity) was impossible in this geometry because the corona discharge transformed into a spark mode. Moreover, only a fraction of the flow that was admixed to the cone was burnt out. As a result, combustion became incomplete, which led to a decrease in the burner power.

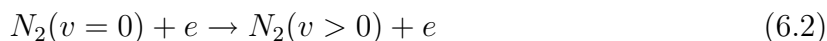
Both of the above studies dealt with edge effects that stemmed from the highly nonuni-

form electric field; consequently, practical implementation of the results obtained in those papers is rather problematic. In present study it will be shown experimentally that, in the above geometry, the increase in flame propagation velocity isn't related to the current running through the flame, so ionic wind role is negligible. Seemingly, the ionic wind is of limited utility as a means for increasing the combustion rate in premixed flames (a possible exception may be specific burners with a thick wall and small inner diameter of the nozzle).

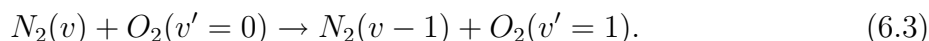
Some authors (see, e.g.,²³⁷) suppose that kinetics of the combustion processes can be affected by a relatively weak (1–2 kV/cm) alternating electric field and explain the change in the normal flame velocity by the acceleration of the reaction



This reaction is one of the most important in flame,²³⁸ and its rate substantially determines the oxidation rate of CO and the production of the OH radicals, which play a major role in the branching of the chain reaction of hydrocarbon combustion. An analysis of the experimental data²³⁹ shows that the effect of flame propagation velocity increase takes place at reduced electric fields E/N (where E is the electric field intensity and N is the density of molecules in a mixture) as low as 10 Td (1 Td = 10^{-17} V·cm²). The process



is likely to be the primary process of field influence on flame velocity. Then, a vibrationally excited nitrogen molecule can transfer the vibrational quanta to other mixture molecules (in particular, O₂ molecules) in the reaction



In the opinion of the author of,²³⁷ such a vibrational excitation of oxygen molecules can accelerate chemical reactions with their participation, including reaction (6.1), and, accordingly, the combustion process as a whole.

An indirect confirmation of this mechanism is the fact that an increase in the combustion rate was observed in CH₄/O₂/N₂ mixtures, whereas in CH₄/O₂/Ar mixtures this effect was much less pronounced, although the electron density was the same. Unfortunately, it is not yet quite clear to which extent this mechanism can accelerate reaction (6.1), because, in typical fuel–air mixtures, the rates of the relaxation and deactivation processes competing with the vibrational excitation of N₂ and O₂ are fairly high. Hence, further experimental study of such mechanisms is required to verify the above statements.

However, even without carrying out thorough investigations, one can assert that a reduced electric field of 10 Td is insufficient to enable the electron-impact excitation of higher ($v > 3$) vibrational levels (to saying nothing of electronic ones) of both nitrogen and oxygen. In addition, the discharges at such a low reduced electric field are not self-sustained. This reduces the efficiency of this type of discharge.

Nowadays it seems that the most challenging method for accelerating combustion is the non-equilibrium excitation of the gas mixture components, which allows one to affect the chemical reaction kinetics. To enable more efficient excitation of the electronic and vibrational degrees of freedom, one should use short-duration (nanosecond) pulses with a high reduced electric field.^{113,240} In pulsed discharges, the reduced electric field at the

front of an ionization wave (e.g., in the steamer head) attains hundreds of Td, whereas the electric field in the streamer channel is significantly lower and certainly insufficient for the production of active particles. The experiments of⁴⁰ demonstrated that it is the region with a strong field in the streamer head in which the active particles are mainly produced.

Employing a pulsed barrier discharge allows one to avoid the transition of a streamer discharge to a spark form, because the dielectric barrier limits the maximum charge transmitted through a channel. This type of discharge is non-equilibrium: the electron temperature is rather high (4–5 eV), whereas the translational temperature of the neutral gas is close to the temperature of the electrodes.⁴⁷ Thus, the gas is heated only slightly and the energy is mainly deposited in the vibrational and electronic (rather than translational) degrees of freedom of the gas molecules.

The aim of this study is to experimentally investigate the possibility of the premixed flames propagation control by means of pulsed nanosecond discharges that develop at high reduced electric fields and to find the main mechanisms for the discharge–flame interaction. The influence of gas excitation by a pulsed nanosecond atmospheric-pressure barrier discharge (with a high-voltage pulse amplitude up to 25 kV) on the characteristics of a premixed propane–air flame has been investigated within a wide range of the equivalence ratios (0.4–5). It is experimentally found that the flame blow-off velocity increases more than twice at a discharge energy input less than 1% of the burner power. The emission profiles of the OH, CH, and C₂ radicals along the flame are studied using emission spectroscopy. An efficient production of active radicals under the action of a barrier discharge has been observed. Based on the data obtained, the increase in the flame propagation velocity is explained by the production of atomic oxygen in a discharge due to the quenching of electronically excited molecular nitrogen N₂ and the electron-impact dissociation of molecular oxygen. A numerical model has been developed that qualitatively describes the influence of a barrier discharge on flame propagation.

6.1.1 Effect of the electric field configuration on the flame

We examined different electric field configurations to choose such that is optimum for determining the most efficient mechanisms for flame control and, at the same time, allows us to avoid excess electric energy losses and gas heating. The key requirements to the discharge section geometry are as follows:

- Taking into account that the energy deposition in the discharge is much lower than the burner power, it is necessary that the discharge affects the preflame zone, rather than the ignited mixture.
- The discharge should occupy the entire cross section of the nozzle. This enables a nearly uniform gas excitation and significantly facilitates the interpretation of the results obtained.

Early experiments were carried out using a metal nozzle with a rectangular cross section. The discharge operated either between two multipoint plates placed horizontally at a distance of 2–20 mm above the burner edge or between these plates, which were at the same potential, and the burner nozzle. However, this design had the following drawbacks:

- The discharge transformed into a spark form, which led to the sharp increase in the discharge energy and the heating of the mixture. A decrease in the amplitude of high-voltage pulses (their duration being kept constant) led to the transformation of the discharge into a pulsed corona; as a result, its effect on the flame significantly reduced.
- In the plate-to-plate geometry, the discharge mainly affected the high-temperature region (because the flame, in contrast to the preflame zone, already contained charged particles) and only slightly influenced the preflame zone. The electric field was asymmetric with respect to the nozzle axis. This hampered the interpretation of the experimental results and numerical simulation.
- In the plate–nozzle geometry, the discharge did not occupy the entire cross section of the nozzle and occurred in the boundary layers. As a result, the combustible mixture in the preflame zone remained practically unexcited.

Taking into account the results of these preliminary experiments, as well as the requirement that the high-voltage electrode should be located as close as possible to the mixture to be excited (the specific energy deposition decreases with distance from the electrode), we have modified the burner design.

The burner with barrier discharge

In the new burner, the metal nozzle was replaced with a rectangular glass nozzle, inside which a high-voltage electrode was placed. The low-voltage electrodes were positioned near the nozzle edge; in order to prevent a transition of the discharge into a spark form, they were set tightly into quartz tubes. On applying a voltage to the gap, a barrier discharge occurred, whose current was limited by the dielectric layers.

The specific feature of such construction is that it's allowed us to avoid a transition of the discharge into a spark form at high voltages and long pulse durations. By varying the vertical positions of the low-voltage electrodes, we found a discharge configuration that was optimum from the standpoint of increasing the flame blow-off velocity.

The scheme of the experimental facility and diagnostic system is shown in Fig. 6.1. The burner body was made of glass. The burner nozzle opening was a rectangle 30×2 mm in size. Thus, the flame base was fairly long, so that the flame geometry was almost plane-parallel. A multipoint brass plate with a cross section of 28×1 mm was placed inside the nozzle parallel to its walls and was used as a high-voltage electrode. The low-voltage electrodes were made of a copper foil, placed into quartz tubes (with an inner diameter of $d = 5$ mm and a wall thickness of about 2 mm) and mounted near the burner nozzle edge. The positions of the tubes with respect to the nozzle could be varied. The burner holder allowed us to vary the nozzle edge height with respect to the optical diagnostic system with an accuracy of 0.16 mm.

A pulsed voltage generator was designed by the rotating interrupter scheme. The high voltage pulses were fed through a transmission line made of a 40-m-long RK-50-24-13 cable. A calibrated back current shunt placed in the break of the braiding of the feeding coaxial cable at a distance of 20 m from the discharge section was used to control the parameters of the electric pulses. The amplitude of the incident voltage pulse was $U_{max} = 12$ kV, the pulse duration at a half-height was $\tau_{1/2} = 77$ ns, the rise time was

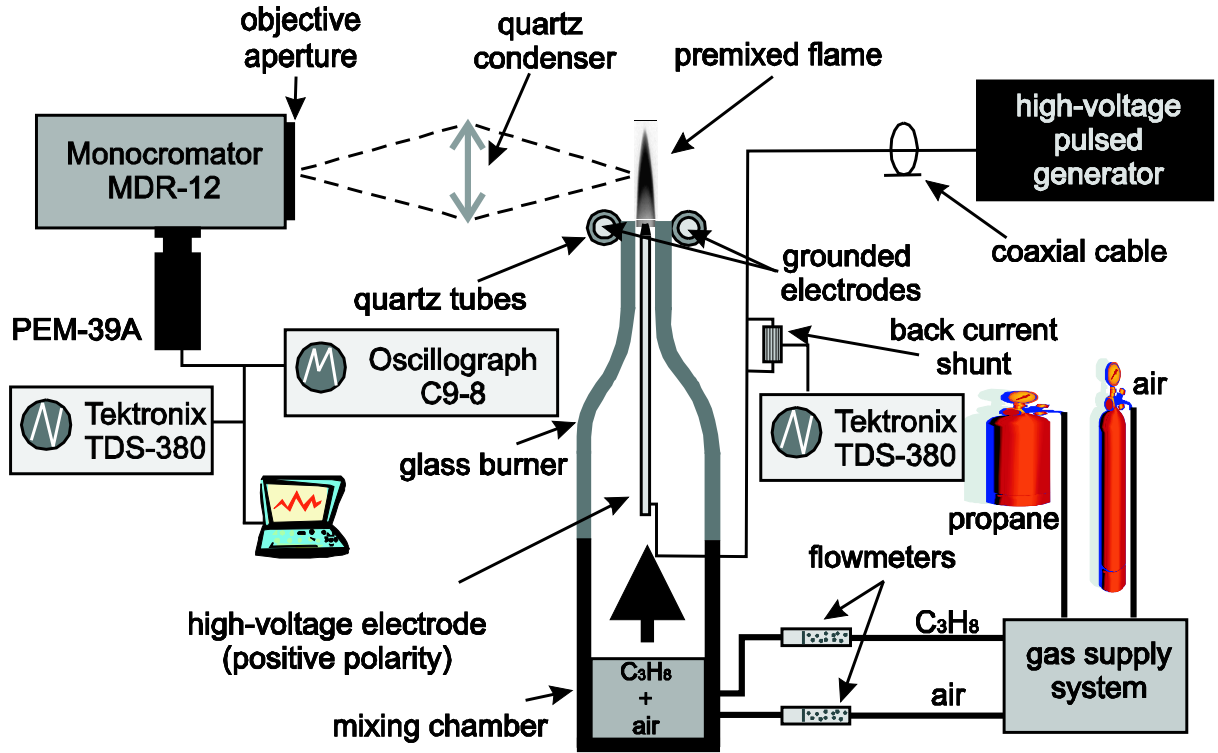


Figure 6.1: Experimental setup scheme.

$\tau_{inc} = 10$ ns, and the pulse repetition rate was $f = 1.2$ kHz. The pulsed voltage polarity could be varied. The design of the voltage supply also allowed us to apply a dc voltage of either polarity to the discharge gap. In the experiments, the waveforms of both the discharge current and voltage were recorded, which allowed us to determine the energy input in the discharge.

The gas supply system enabled the formation of a premixed propane-butane (volumetric ratio is 80%/20%)–air mixture in a wide range of equivalence ratios. To determine the gas-mixture flow rate, a volumetric rate for each mixture component was measured by flowmeters. Among the macroscopic parameters determining the efficiency with which the discharge acts on the flame (such as the flame shape, height, etc.), we chose the flame blow-off velocity, which is directly related to the normal flame propagation velocity and the rates of chemical reactions in flame.²⁴¹

The investigations of active particles production was performed by emission spectroscopy methods. The recording facility consisted of an FEU-39A photomultiplier (with a photocathode spectral range of $\lambda = 160\text{--}600$ nm) and an MDR-12-1 monochromator (with an operating range of $\lambda = 190\text{--}600$ nm and a linear dispersion of 2.4 nm/mm). To measure the absolute emission intensity, the optical system was calibrated using a standard emission source (a calibrated DDS-30 deuterium arc lamp emitting in the range 190–500 nm).

To determine the time-averaged characteristics of the flame and discharge emission, we used the regime of signal accumulation (the time constant was varied from 0.1 to 7.0 s). Thus, at a pulse repetition rate of 1.2 kHz, the emission characteristics were averaged over $10^2\text{--}10^3$ pulses, which enabled both a significant increase in the measurement accuracy

and the identification of the weak spectral bands and lines. When measuring the intensity profiles of the active-particle emission along the flame height, we used a slit with a 1-mm-high diaphragm and a quartz condenser, which enabled us to record the emission only from the flame region located at a given height.

The signals were recorded with the help of a Tektronix TDS-380 and an S9-8 digital oscilloscopes (with the 400- and 5-MHz bandwidths, respectively), an LA-70 analog-to-digital converter (with a sample rate of 100 kHz), and a PC.

6.1.2 Effect of the ionic wind on flame propagation

To determine the influence of the ionic wind on the flame blow-off velocity increase at a constant electric field (some authors, e.g.,²³⁵ report about fourfold increase), we used a conventional nozzle–ring electrode geometry. A negative dc voltage of up to 7 kV was applied to the high-voltage electrode located inside the nozzle. The height at which the ring (with a diameter of $d = 32$ mm) was located above the nozzle could be varied from 0 to 20 cm. The discharge current was measured with a microammeter. It is known that the ionic-wind effect increases with increasing current. Studying the dependence of the flame blow-off velocity on the current allowed us to determine the influence of the ionic wind on the processes occurring in the flame.

The circuit current depended upon the voltage and ring height above the burner. Generally, the current varied in the range from tens of microamperes to a few milliamperes (in the latter case, the energy input to the flame was comparable with the burner power). The experiments showed that the flame blow-off velocity increased appr. by a factor of 1.3. However, when the low-voltage electrode (ring) was absent and the discharge current was nearly zero, the effect also took place and was only slightly weaker than in the case with a ring (the flame blow-off velocity increased by a factor of 1.25). This can be explained by the development of both a low-current corona at the nozzle edge and plasmochemical processes in the adjacent region. Thus, the role of ionic wind in such kind of processes is worth to be doubted on.

Turning back to the results of,²³⁶ which were mentioned above, we can conclude that, even at moderate (1–2 kV) voltages, it is the corona arising at the sharp nozzle edges (rather than the ionic wind) that plays a major role in increasing the flame blow-off velocity. The current value reported in²³⁶ ($\simeq 100 \mu\text{A}$) also points to the development of a corona discharge - it's known that ionic wind characteristic current is appr. 10 times smaller.

Nevertheless, the ionic wind can significantly affect slow diffusion flames. In this case, the discharge current is usually less than $10 \mu\text{A}$ ²³⁴ and the change in the flame propagation regime is mainly related to the redistribution of charges in the flame region and the transfer of an additional momentum from the electric field to the gas flow. In slow diffusion flames, such a momentum can be comparable with the momentum of the initial gas flow and, depending on the polarity of the applied voltage, may either to stabilize the flame or, on the contrary, to cause the onset of flame oscillations.²³⁴

Flame propagation velocity increase under the excitation of a gas mixture by a pulsed high-voltage discharge

We have found (see Fig. 6.2) that the action of a barrier discharge on a flame leads to an increase in the flame propagation velocity.

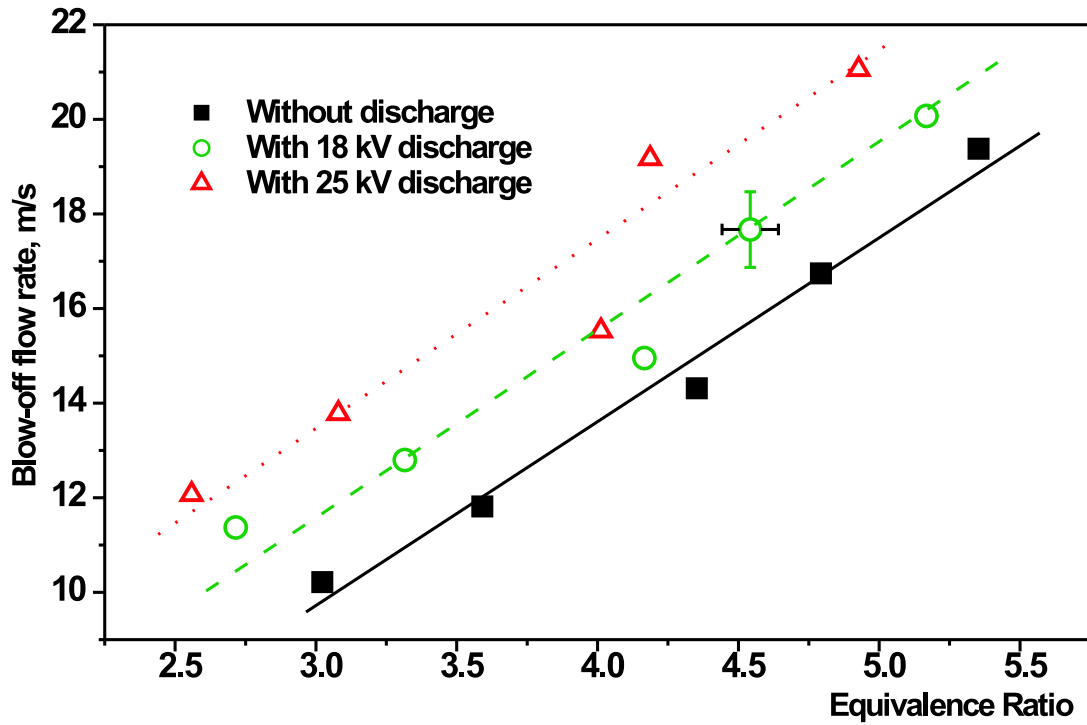


Figure 6.2: Flame propagation velocity increase depending on barrier discharge power.

The higher the discharge power, the higher the increase. (It should be noted, however, that, in all the regimes, the discharge power did not exceed 1% of the burner chemical power.) To find the type of discharge that is most efficient for controlling the flame propagation velocity in the given geometry, the following four versions of the high-voltage power supply were examined:

- a 25 kV dc voltage of positive polarity,
- a 25 kV dc voltage of negative polarity,
- a 25 kV pulsed voltage of positive polarity; and
- a 25 kV pulsed voltage of negative polarity.

A comparative analysis of these discharges and their effect on the blow-off velocity is presented in Fig. 6.3. From the standpoint of increasing the flame propagation velocity, a positive-polarity pulsed barrier discharge is the most efficient. The higher efficiency

of this discharge as compared to a negative-polarity barrier discharge stems from the fact that, at the same pulse voltages, a cathode-directed streamer develops faster and produces a larger number of active particles than an anode-directed one because of the different mechanisms for their propagation.⁴⁰ In the case of a dc discharge, the situation is opposite. At a negative polarity, the tapered electrode in a hot gas efficiently emits electrons, which leads to the formation of a dc corona with a high current density near the points. In the given geometry, a positive dc voltage only slightly affects the flame propagation velocity.

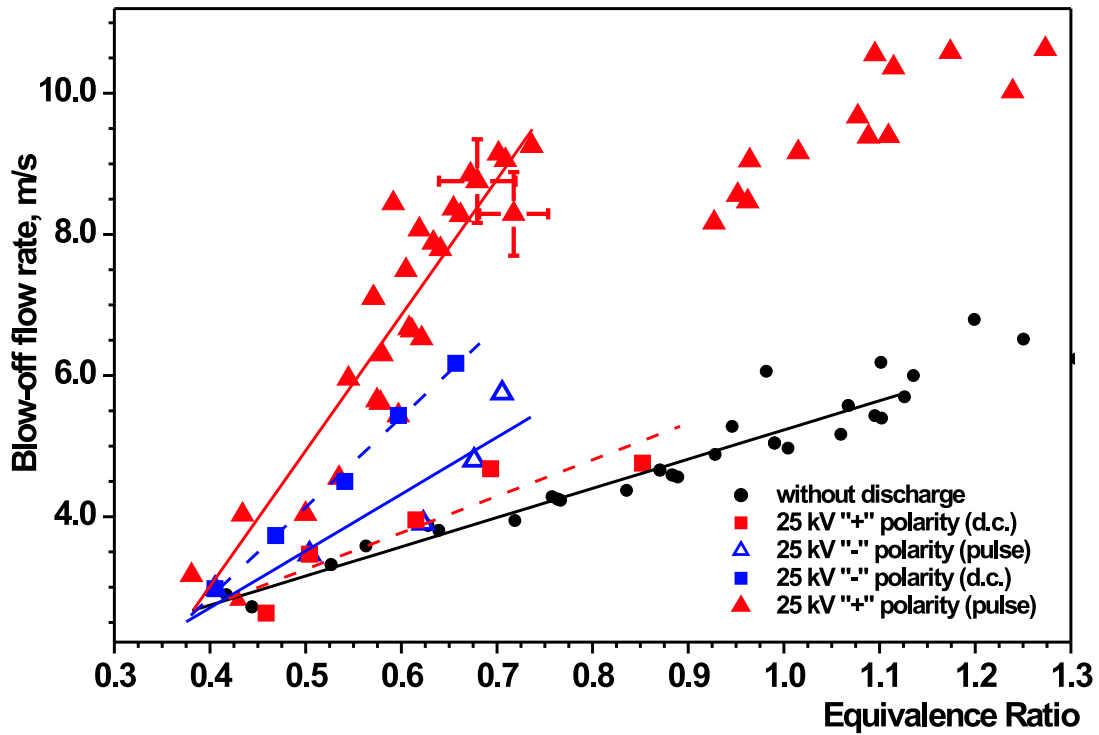


Figure 6.3: The comparative analysis of different discharges types influence on flame propagation velocity.

In the case of a positive-polarity pulsed discharge, which is the most efficient from the standpoint of increasing the flame propagation velocity, the change in the flame blow-off velocity is shown in Fig. 6.3 for a wider range of the equivalence ratios ϕ (the ratio of the fuel percentage in the mixture under study to the fuel percentage in a stoichiometric mixture). It can be seen that the effect of the discharge is strongest at $\phi=0.65-0.75$. In a system with a barrier discharge, the increase in the flame propagation velocity is higher than 100%.

If we increase the discharge frequency, we will obtain further flame blow-off velocity increase (Figure 6.4). The difference between excited and unexcited gas becomes more and more significant and for the pulse frequency $f = 6000$ Hz reaches 5 times for equivalence ratio of $\phi = 0.7$.

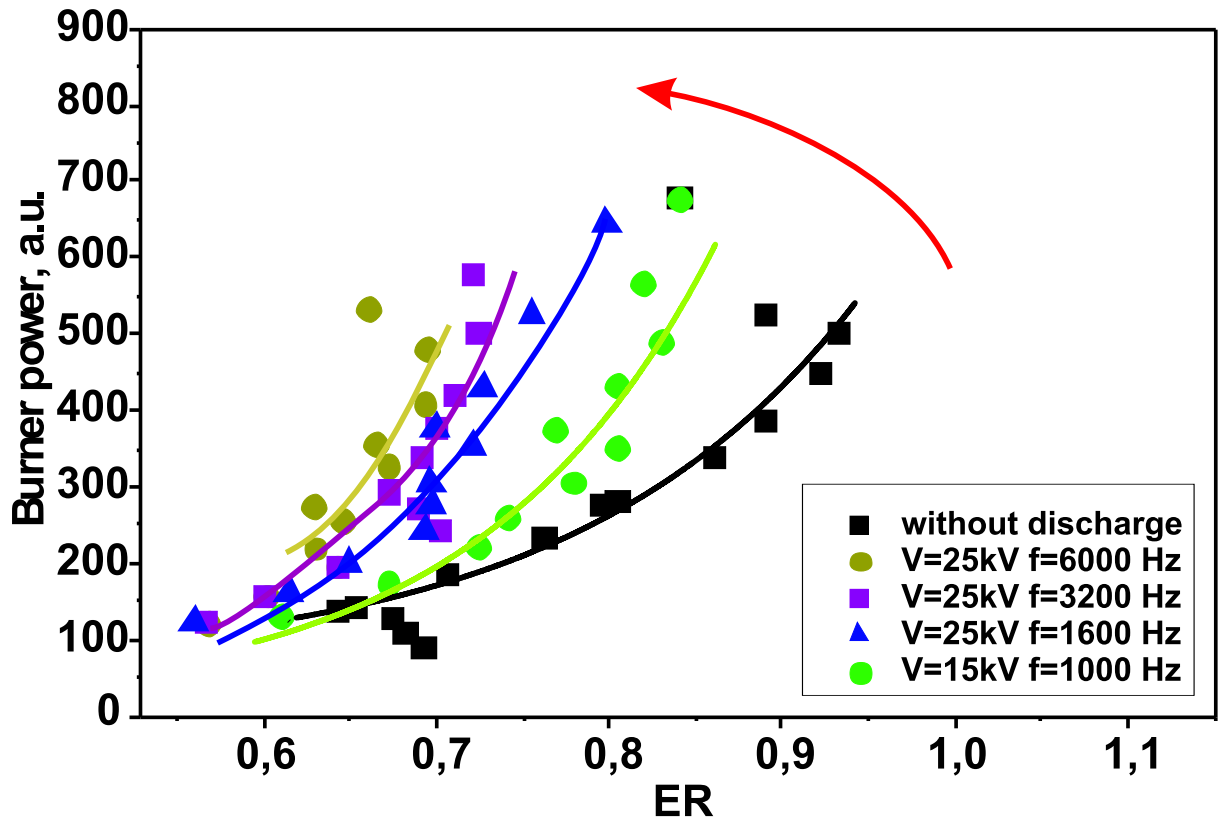


Figure 6.4: The comparative analysis of different discharge frequencies influence on flame propagation velocity.

It is possible to obtain the same flame blow-off velocities for different mixture composition using gas discharge for nonequilibrium excitation of the flow (Figure 6.5). Thus, it is possible to control the flame stability and burner power using lean mixtures with gas discharge flame stabilization. On the other hand, the low-frequency DBD practically does not influence on the flame (Figure 6.6).

To estimate the energy deposited in the fuel mixture, the waveforms of the discharge voltage and current were monitored with the help of a back-current shunt and a digital Tektronix TDS-3054 oscilloscope. The energy deposited in one pulse is appr. 8 mJ, which corresponds to an average power of 9W at a pulse repetition rate of 1200 Hz. This is less than 1% of the chemical energy released in the combustion of a propane–air mixture. For 50 Hz DBD common Current-Voltage Oscillogram technique was used (Figure 6.7).

Diagnostics of the chemically active components

To determine the intrinsic flame characteristics and to study the kinetics of the active particles capable of affecting the flame propagation velocity, the investigations of flame have been carried out using emission spectroscopy methods.¹³⁹

Figure 6.8 shows the emission spectrum from a barrier discharge in a $\phi = 1$ propane–air mixture at $U = 22$ kV and the flame emission spectra from a $\phi = 0.6$ propane–air mixture without a discharge and with a discharge at $U = 22$ kV. The lower region (near the burner edge) of the flame was projected by a quartz condenser onto the spectrograph

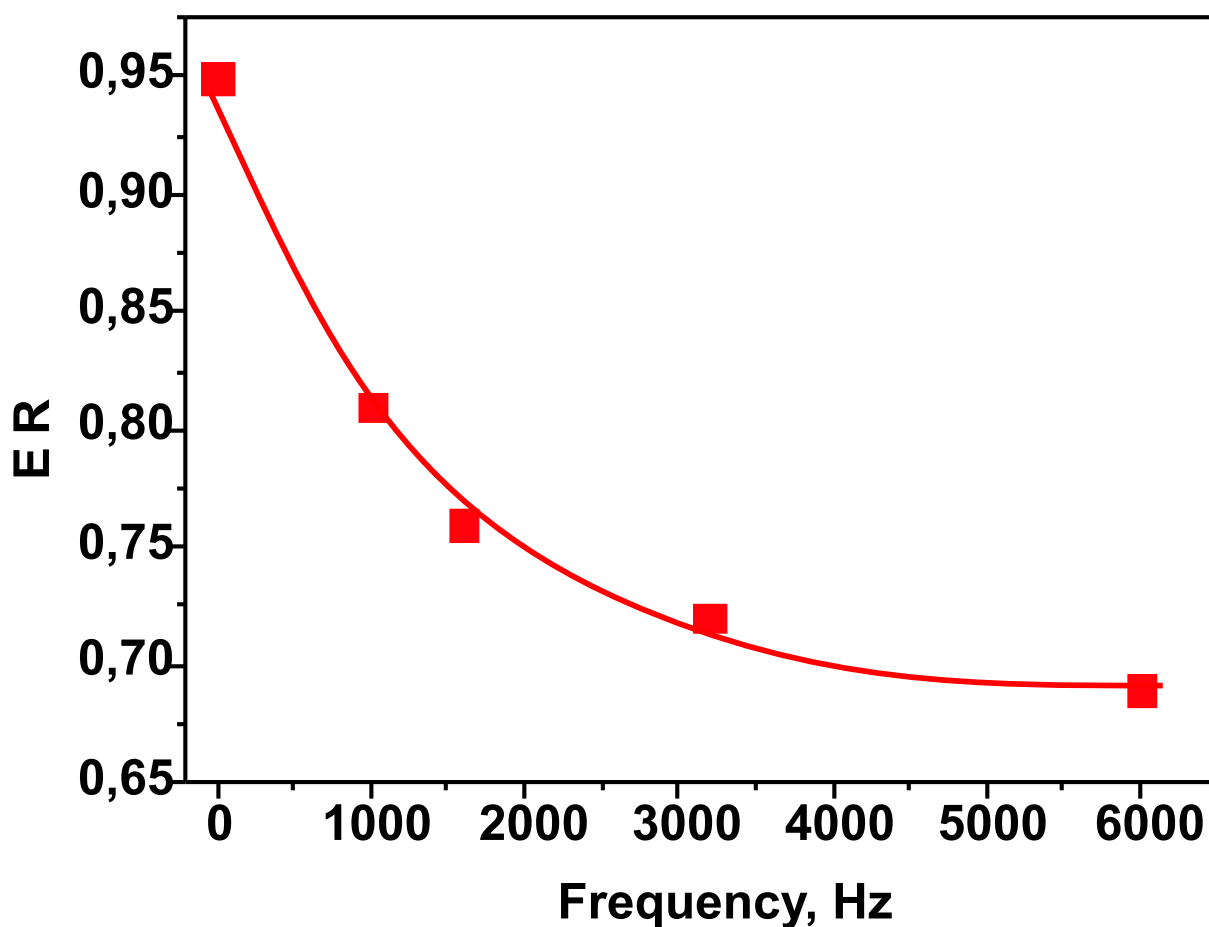


Figure 6.5: The comparative analysis of different discharge frequencies influence on flame propagation velocity.

slit. The spectra were recorded in the range 200–600 nm with slits providing a spectral resolution of 1.2 nm.

In the spectra of a barrier discharge, the molecular band of the second positive system of nitrogen (the transition $C^3\Pi_u \rightarrow B^3\Pi_g$) in the wavelength range 290–500 nm is well pronounced and much less intense γ bands of nitric oxide NO ($\lambda = 220\text{--}260$ nm), as well as the band corresponding to the transition $0 \rightarrow 0$ of the first negative system of nitrogen ion N_2^+ ($\lambda = 391.4$ nm), are also present. A comparison with⁴⁰ shows that the emission spectrum from a barrier discharge in a stoichiometric propane–air mixture is almost the same as that from an air discharge.

In the flame emission spectrum, there are molecular bands of CH, C_2 , NH, CN, and NO, as well as the $0 \rightarrow 0$ line of the $A^2\Sigma^+ \rightarrow X^2\Pi$ electronic transition of OH radical of the wavelength $\lambda = 306.4$ nm. In the presence of a discharge, the spectrum also contains the 294.5 nm line corresponding to the $3 \rightarrow 2$ vibrational transition. The OH radicals play an important role in combustion and are a major factor determining both the reaction rate and the flame propagation velocity.

The emission intensity profiles from C_2 ($\phi = 1$, $v = 3.75$ m/s, $\lambda = 517.8$ nm), CH ($\phi = 1$, $v = 3.75$ m/s, $\lambda = 431.5$ nm), and OH ($\phi = 1.3$, $v = 3$ m/s, $\lambda = 306.4$ nm) without a discharge and with a barrier discharge at $U = 20$ kV are shown in Figs. 6.9–

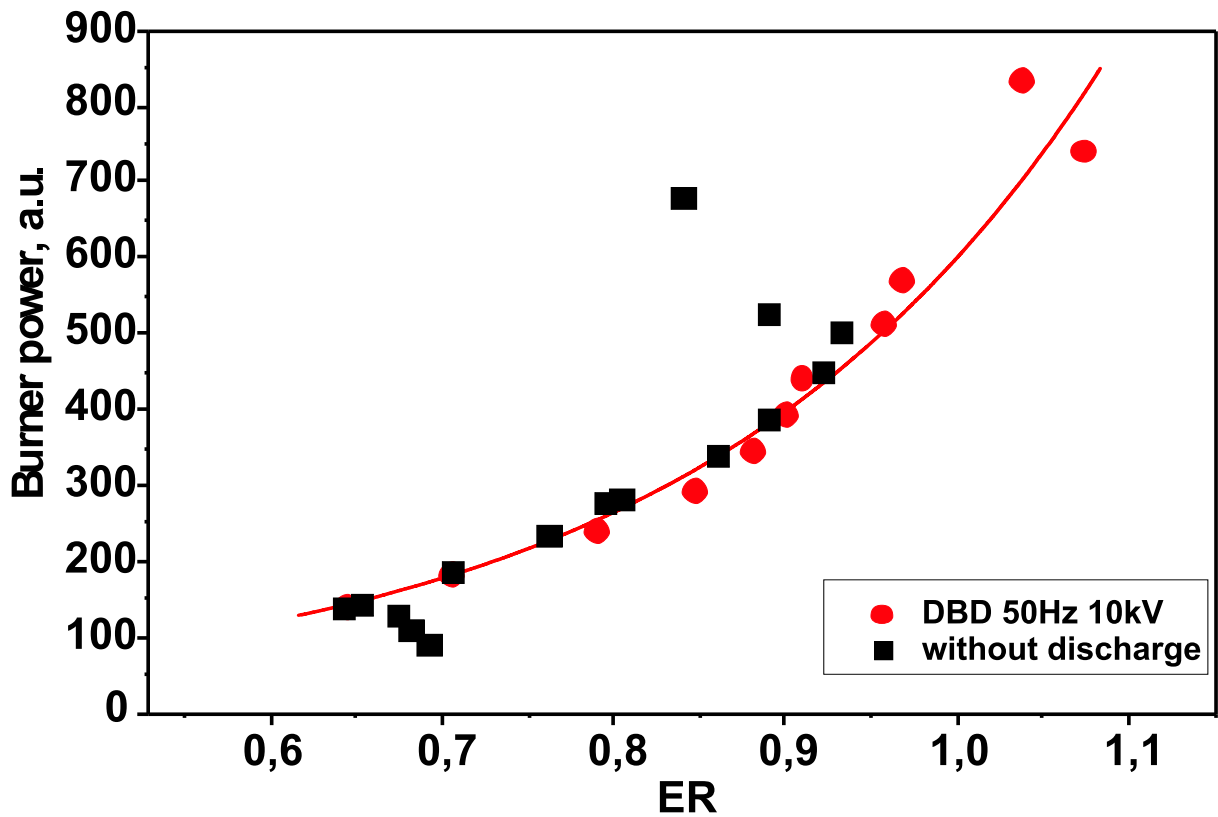


Figure 6.6: 50 Hz DBD influence on flame propagation velocity.

6.11. When recording these spectra, the slit with a width of 0.5 mm (a spectral resolution of 1.2 nm) was blinded with a rectangular aperture 1×1 mm in size. It can be seen that, in the presence of a barrier discharge, the peaks of the emission intensity from C_2 and CH increase, shift toward the nozzle, and become narrower. This indicates the intensification of the combustion process and the acceleration of the chemical reactions occurring in the flame. For the OH radical, besides the above change in the emission profile, applying a barrier discharge results in the appearance of the second emission maximum located in the discharge region, which reflects the production of this radical under the action of the discharge.

Such a behavior of the OH radical confirms once again its great importance for the flame propagation. Figure 6.12 shows the OH emission intensity versus the height above the burner edge in the presence of a discharge at $\phi = 0.6$ and different flow rates of the combustible mixture. It can be seen from this figure that the profile of the OH radical emission changes as the flow rate increases. For the sake of comparison, the dashed curve shows a similar dependence for the same value of the parameter ϕ but without a discharge. If time (instead of height) is plotted on the abscissa, then the discharge is seen to boost combustion, thus allowing the mixture to burn in the region where it cannot burn without a discharge. In fact, the dashed curve corresponds to the boundary of the combustion zone in the absence of a discharge.

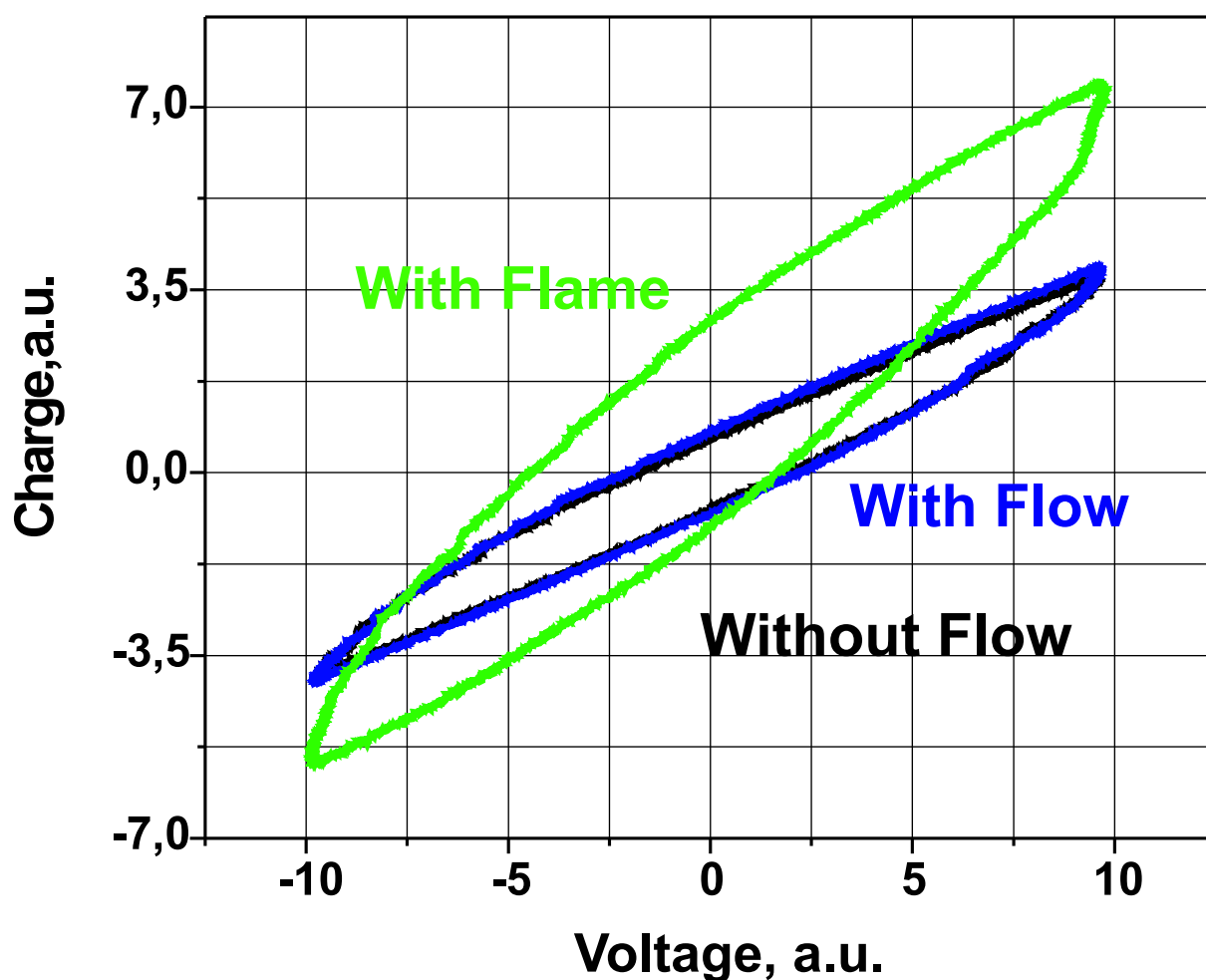


Figure 6.7: 50 Hz DBD energy measurements.

6.1.3 Excitation of particles in a flame

The emission from the flame zone in which the initial components are heated and decomposed, as well as from the region located above this zone, cannot be regarded as being in thermal equilibrium. Hence, to describe the flame emission spectrum, it is necessary to know not only the flame temperature and the densities of molecules in the ground state, but also the possible mechanisms for the excitation of their high-lying electronic states. In spite of extensive studies, these mechanisms have not yet been thoroughly investigated. Besides, it is necessary to take into account the quenching of the excited states in collisions with gas molecules. The probability of this quenching depends on both the mixture composition and the flame temperature. Pronounced spatial variations in the mixture composition and the flame temperature make such an analysis even more complicated.

Let us consider mechanisms for the production of the main excited radicals and active particles in a flame.²²⁹

1. **OH***. The excited OH* radicals are mainly produced in the combustion zone through the following chemical reaction:



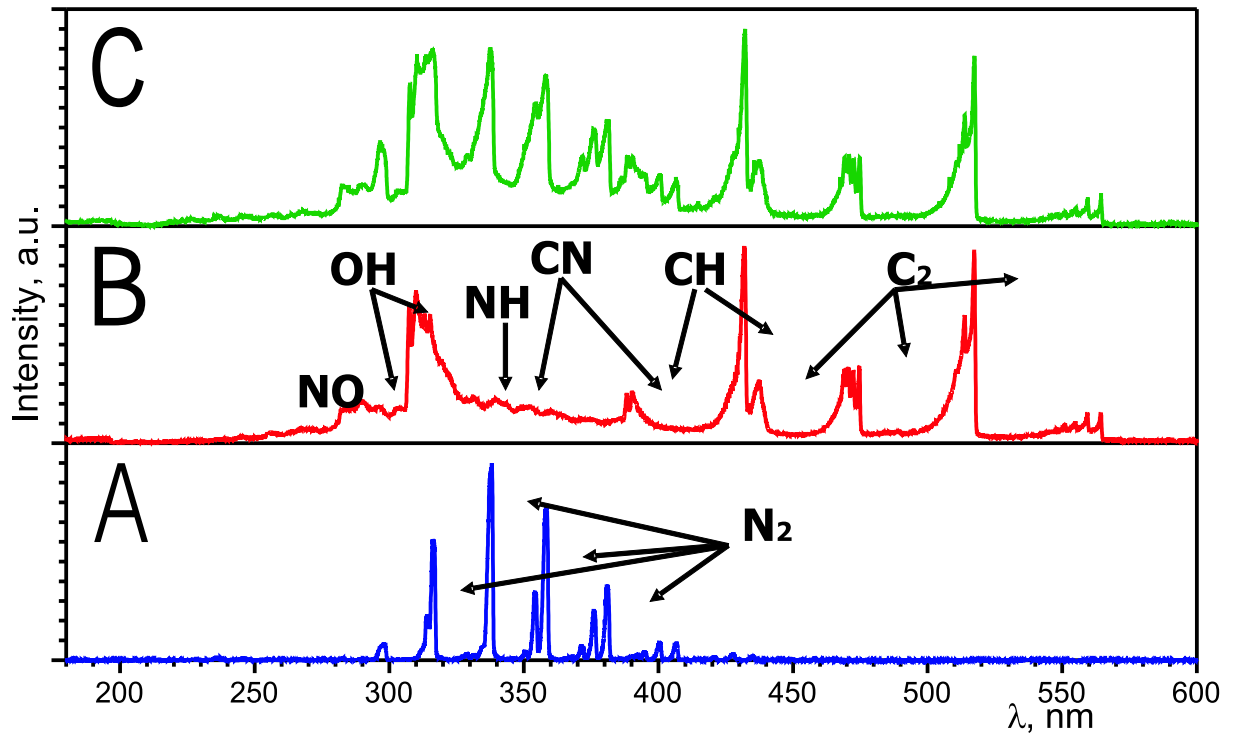
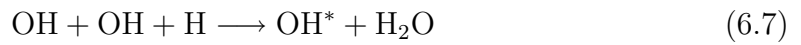


Figure 6.8: Emission spectra: A – barrier discharge in the propane-air mixture, $U=22$ kV, $\phi=1$; B – premixed propane-air flame, $\phi=0.6$; C – premixed propane-air flame with barrier discharge, $U=22$ kV, $\phi=0.6$. Flow velocity is 3 m/s.

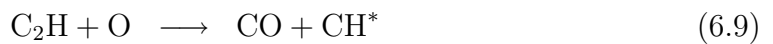
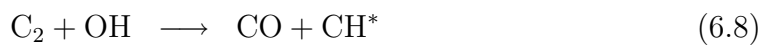
In hydrogen-air flames, there are other important mechanisms for the production of the electronically excited OH^* radicals:



Besides the above mechanisms, the OH radicals can be excited in the recombination reaction of two other particles, for example,



2. **CH^*** . The mechanism for the production of the excited CH^* radicals in a flame has long been the subject of controversy. A comparison of the CH^* emission in the flames of different gases shows that this radical is produced not due to the direct decay of an acetylene molecule C_2H_2 , but in alternative reactions. The fact that the peak of the CH^* emission intensity ($A^2\Delta$ or $B^2\Sigma$) is generally located in the flame above the peak of the C_2 emission intensity allows to suggest the following mechanisms for the production of CH^* from C_2 :²²⁹



These reactions are highly exothermic and the energy released in them is sufficient for the production of the $A^2\Delta$ and $B^2\Sigma$ states of CH^* .

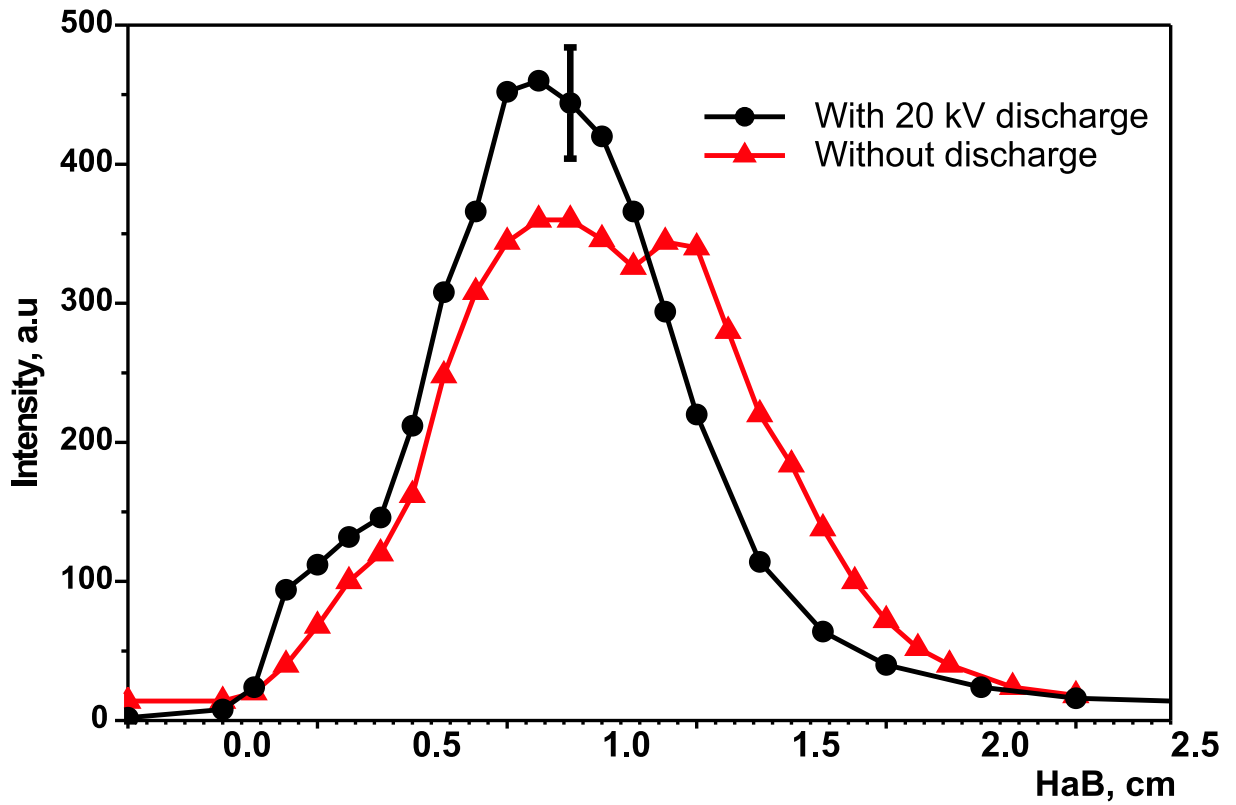


Figure 6.9: CH emission profile along flame height with and without barrier discharge, $\phi=1$, $\lambda=431.5$.

3. C_2^* . In most studies, the following reactions are considered to be responsible for the production of C_2^*



When a discharge acts on a flame, the main channel for the excitation of the high-lying electronic states of molecules and radicals is electron-impact excitation. To adequately calculate the rates of these processes in a strongly non-equilibrium low-temperature plasma, it is necessary to know the EEDF, which is determined by the reduced electric field in a discharge.

Determination of the reduced electric field in the discharge region

Generally, the electric field distribution in the discharge gap of a barrier discharge is non-uniform and quite complicated. The reduced electric field can roughly be estimated as $E/N = U/LN$, where U is the voltage between the electrodes and L is the gap length. Under our conditions, such an estimate gives $E/N \simeq 330$ Td.

An alternative method for determining the reduced electric field is to measure the ratio of the emission intensities of the following electronic-vibrational transitions of nitrogen:⁴⁰

- The transition $C^3\Pi_u, v = 0 \rightarrow B^3\Pi_g, v' = 0$ ($\lambda = 337.1$ nm) of the second positive system 2^+ .

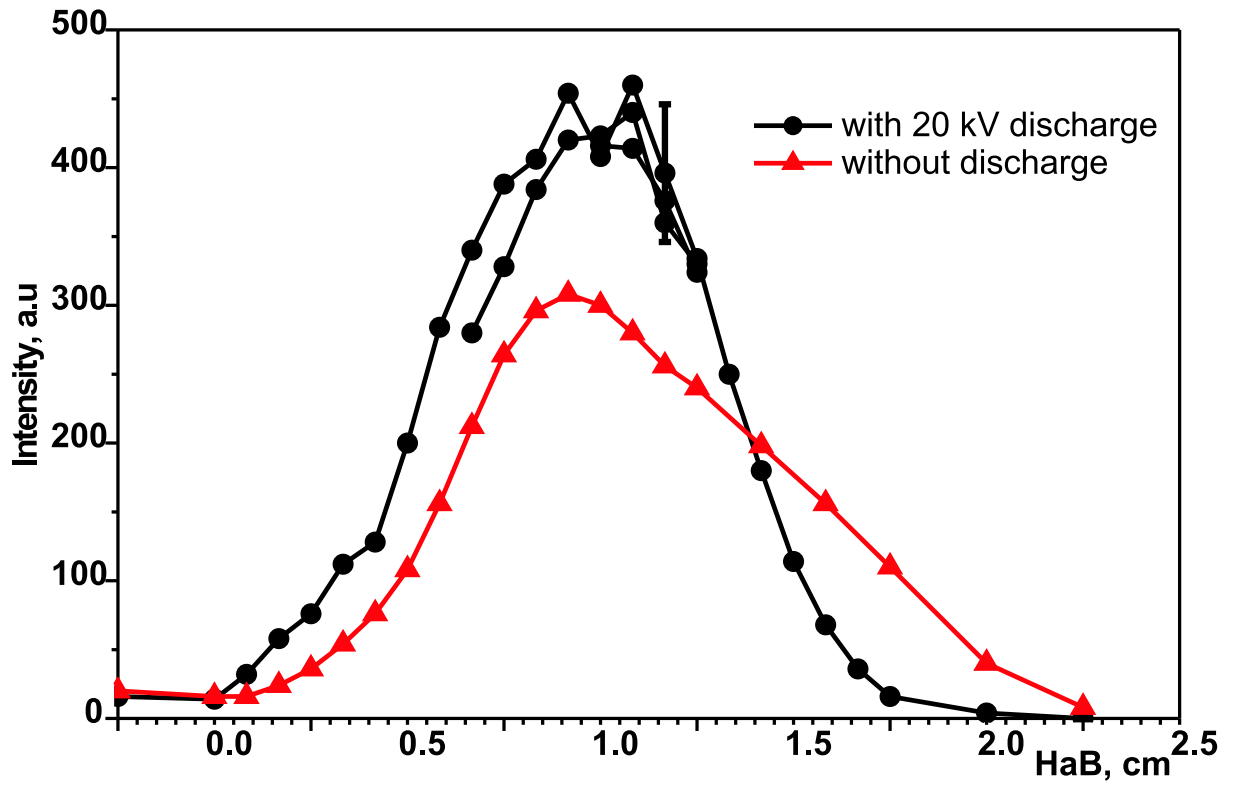


Figure 6.10: C_2 emission profile along flame height with and without barrier discharge, $\phi=1$, $\lambda=517.8$.

- The transition $B^2\Sigma_u^+, v = 0 \rightarrow X^2\Sigma_g^+, v' = 0$ ($\lambda = 391.4$ nm) of the first negative system 1^- .

Note that the emitting particles are mainly produced in the streamer head, where the electric field intensity is higher than that averaged over the gap. The intensity ratio measured in the present experiment is $I_{337.1}/I_{391.4} = 75/1$, which corresponds to a reduced electric field of 550–600 Td.⁴⁰ Thus, at an average field in the gap of 330 Td, the electric field in the region with the most intense production of active particles reaches 600 Td under our experimental conditions.

Numerical simulations of the flame propagation velocity change under the discharge influence

To find mechanisms responsible for the influence of a non-equilibrium discharge on the flame velocity, it is necessary to determine the role of plasmachemical processes in the discharge and the preflame zone. As was mentioned above, the flame propagation velocity depends on the rates of chemical reactions in the gas and, especially, in the preflame zone. Hence, the excitation of reactants can significantly affect the flame propagation velocity. In this study, we first calculate the production of active particles in the barrier discharge gap; then, the densities obtained are used as initial conditions for the one-dimensional task of flame propagation. After applying periodical high-voltage pulses, plasmachemical reactions in the flame can be divided into three spatially separated stages:

- (i) electron-impact excitation of molecules in a barrier discharge,

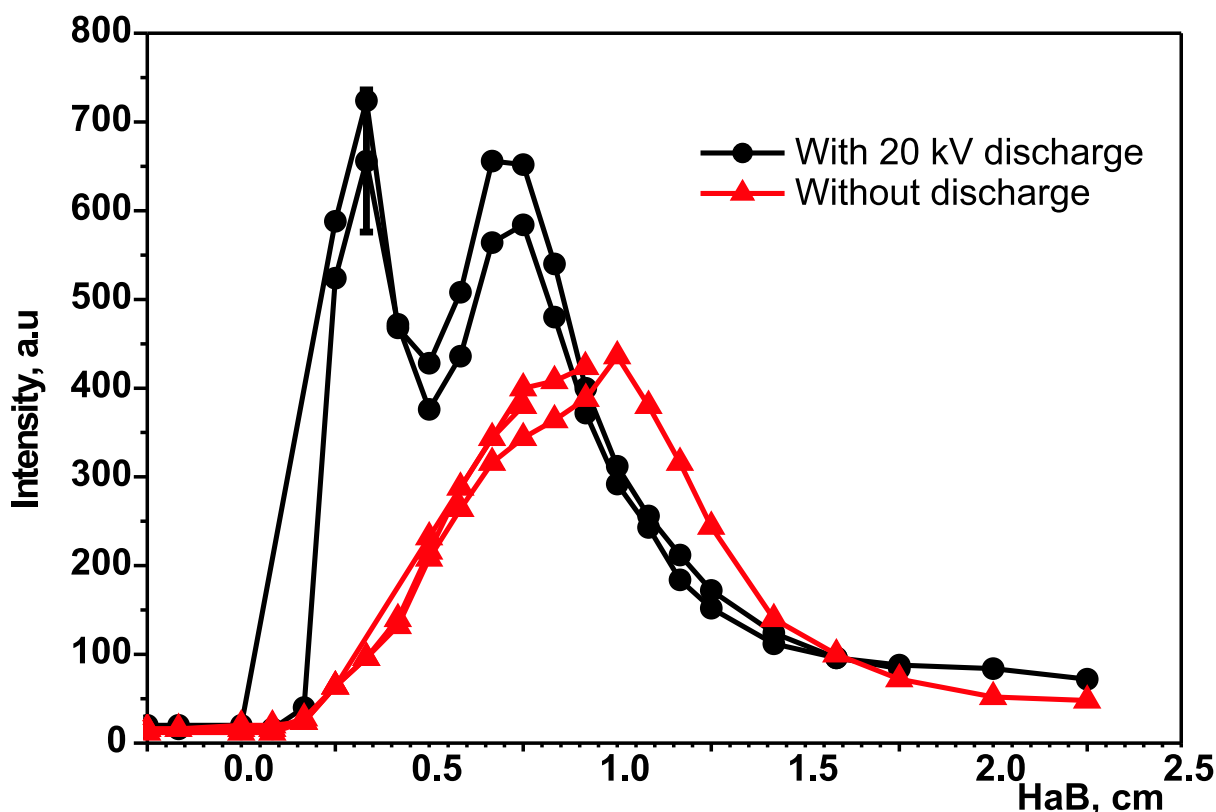


Figure 6.11: OH emission profile along flame height with and without barrier discharge, $\phi=1.3$, $\lambda=306.4$.

- (ii) kinetics of the excited states in the preflame zone, and
- (iii) flame propagation through the pre-excited mixture.

Obviously, these stages can partially overlap. In fact, it is necessary to take into consideration the level-by-level kinetics in a discharge, the influence of the vibrationally and electronically excited particles on combustion, and so on.²⁴² However, besides the difficulties related to the limited computational capability, most of the rate constants are poorly known. For this reason, the main aim of our study was to develop a qualitative model capable of explaining mechanisms through which flames can be controlled by non-equilibrium discharges.

Electron-impact excitation of molecules in a barrier discharge

In the first stage, the particles are excited by electron impact. After applying a $\simeq 75$ ns high-voltage pulse to the electrode, a streamer starts propagating from the electrode. In the streamer head, fast electrons with a mean energy of 5–6 eV are generated. In 5–10 ns, the streamer overlap the discharge gap. Generally, the active particles are produced only in the streamer head, which is quite small (~ 0.05 cm for typical voltages of 10–20 kV¹⁰¹). Below, we will consider the main processes that occur when the gas is excited by electron impact at electric fields intensity values characteristic of our experiments.

- Elastic collisions of electrons with molecules.

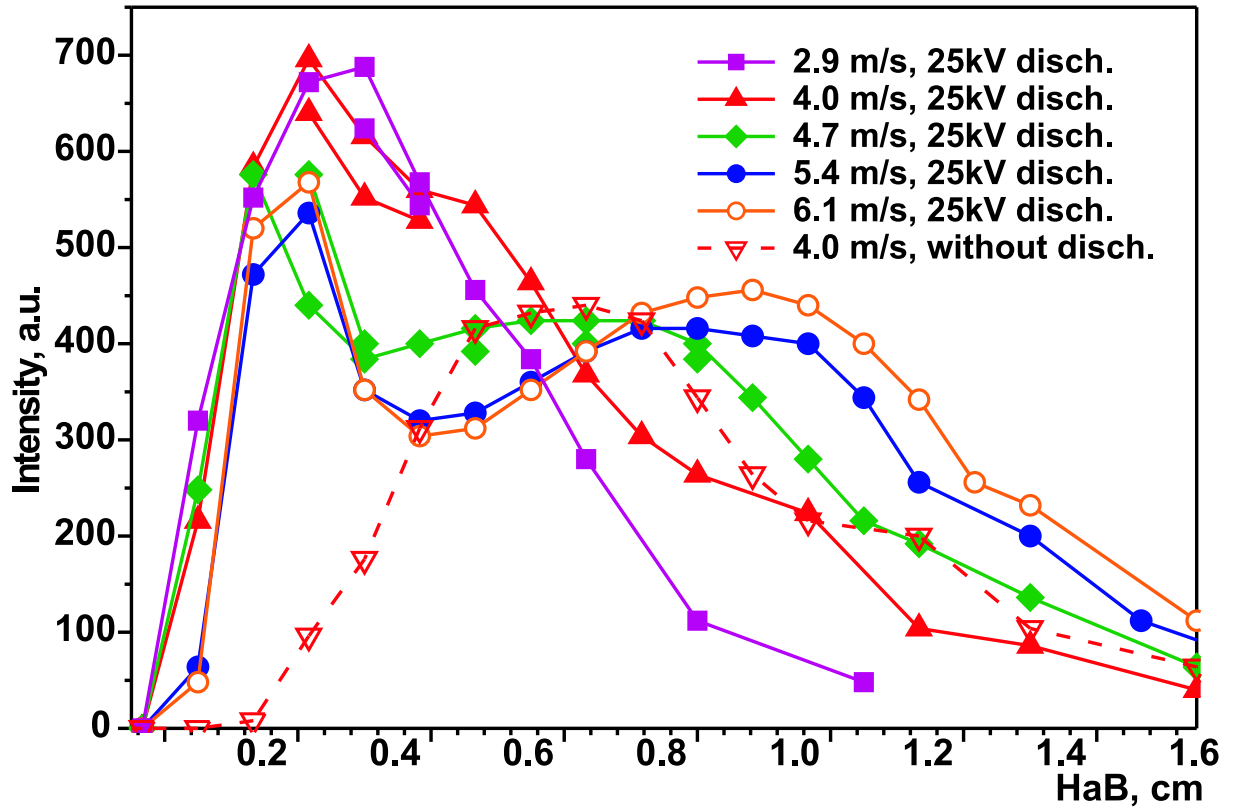
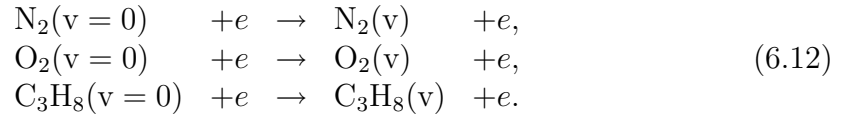
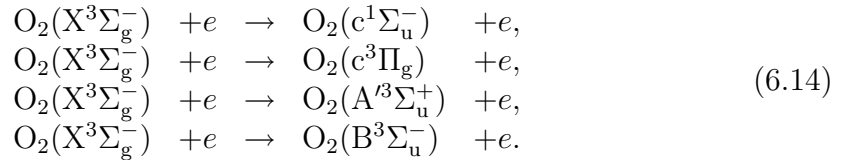
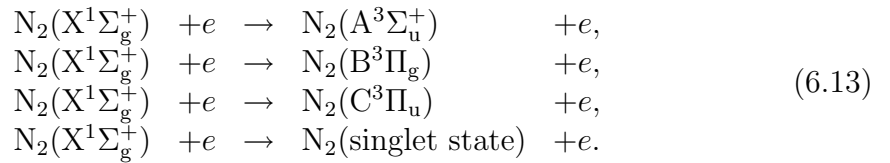


Figure 6.12: OH emission profile along flame height for different mixture consumptions, $\phi=0.6$, $\lambda=306.4$ nm.

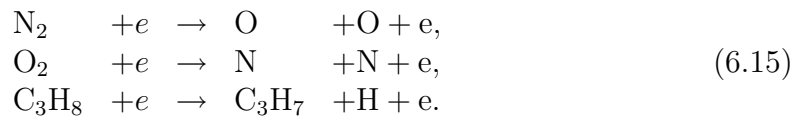
- Vibrational excitation of molecules:



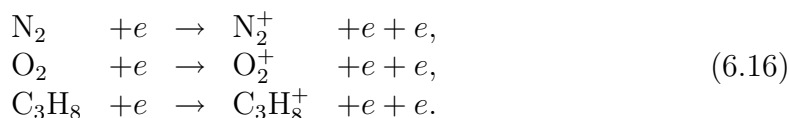
- Electronic excitation of molecular states:



- Molecules dissociation:



- Molecules ionization:

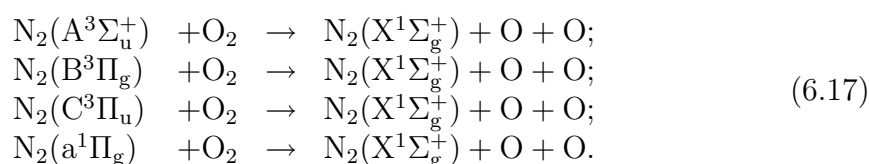


The distribution of the energy of a high-voltage pulse over the above processes in the range of electric fields of our interest (330–570 Td) was analyzed by solving of the Boltzmann equation in the two-term approximation. The results of this analysis are presented in Fig. 6.13. The main fraction of the pulse energy goes to the dissociation and electronic excitation of molecules (in particular, nitrogen molecules). At higher fields, it is also goes to the ionization of nitrogen molecules. After the end of the high-voltage pulse, the electric field intensity in the gap sharply drops, which leads to a rapid decrease in the electron energy in the channel.

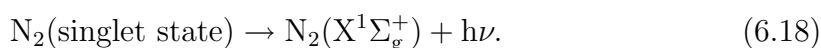
Kinetics of the excited states in the preflame zone

The second stage (which lasts for tens of microseconds) is characterized by intensive atomic–molecular reactions and the processes involving excited at previous stage particles. Let us consider most important of these processes.

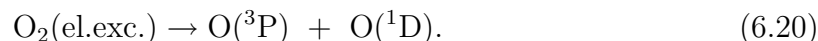
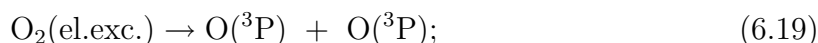
- Quenching of the electronically excited nitrogen molecules, which mainly proceeds through the following reactions:⁷¹



- Emission from most of the electronically excited singlet-states of nitrogen:



- Dissociation of oxygen molecule, which can proceed via its electronically excited states:



An oxygen atom in the $\text{O}(^1\text{D})$ state is produced from the electronically excited state $\text{O}_2(\text{B}^3\Sigma_u^-)$ (the excitation energy from the ground state is 8.4 eV), whereas process (6.19) goes mainly via the excited state $\text{A}^3\Sigma_u^+$ (with an excitation energy of 6.0 eV), though the states $\text{A}^3\Delta_u$ and $\text{c}^1\Sigma_u^-$ also contribute in this process. The number of oxygen atoms produced in reaction (6.20) is about three times higher than that produced in reactions (6.19).⁴⁷ As a result, about one-half of the produced atoms are in the $\text{O}(^1\text{D})$ state.

This explains the fact that, applying a barrier discharge to a flame results in the appearance of the 294.5-nm vibrational band (the $3 \rightarrow 2$ transition) in the emission

spectrum of OH radicals in addition to the 306.5-nm vibrational band (the $0 \rightarrow 0$ transition). Since the excited OH radicals are produced in part through the reaction $\text{H}_2 + \text{O}^+$, the change of the oxygen atomic state from $\text{O}(^3P)$ to $\text{O}(^1D)$ leads to the excitation of OH radicals into the $A^2\Sigma^+$ state with $v > 0$.

- Ionization of the mixture components (primarily, molecular nitrogen). At high reduced electric fields, this processes consumes a significant fraction of the energy of a high- voltage pulse (see Fig. 6.13).

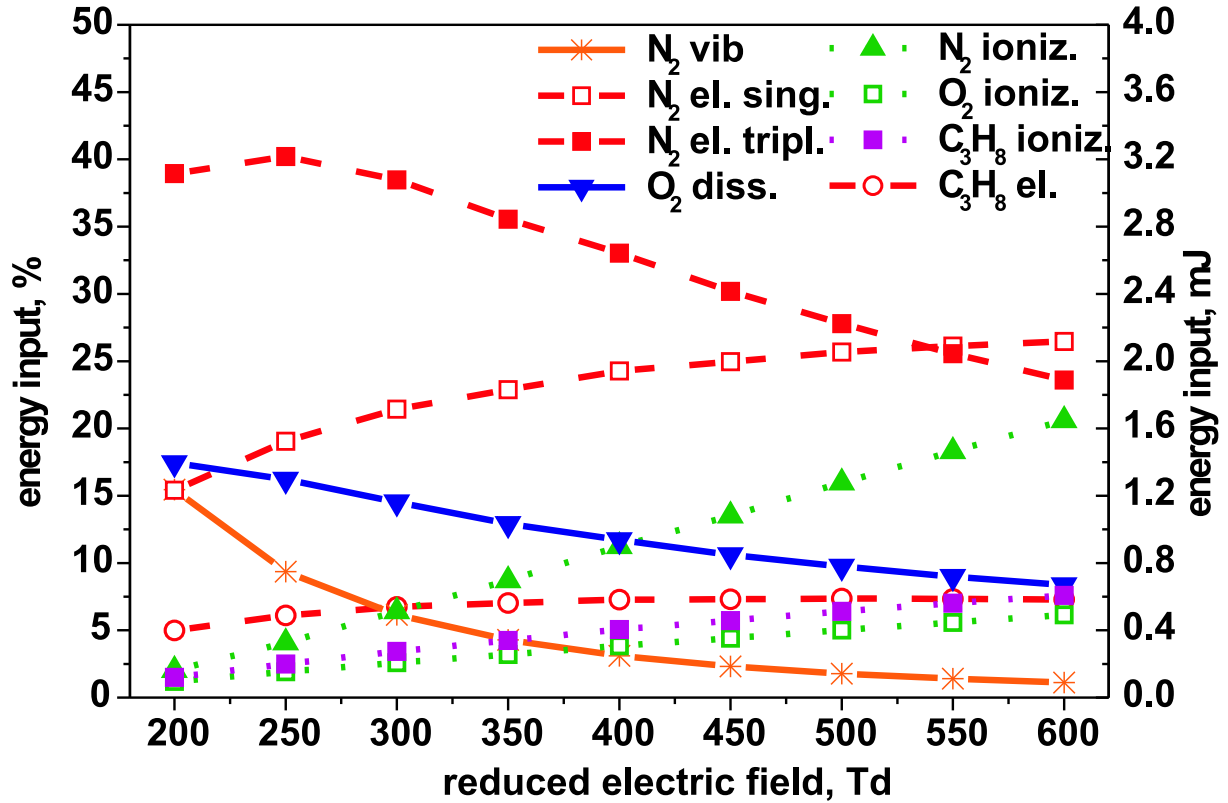
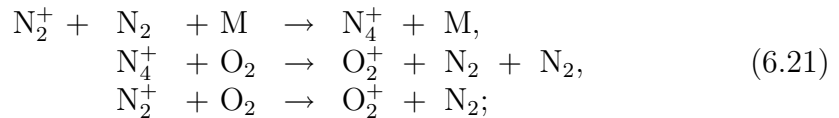


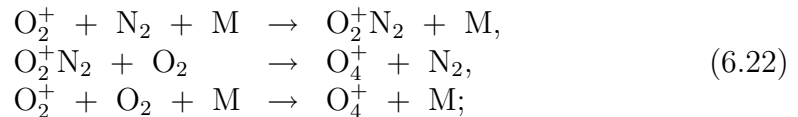
Figure 6.13: Impulse energy distribution to the processes taking part under the electron impact action in barrier discharge.

The main ions (namely, N_2^+ and O_2^+) are converted via the N_4^+ and O_4^+ ions into molecular oxygen O_2 through the following reactions:

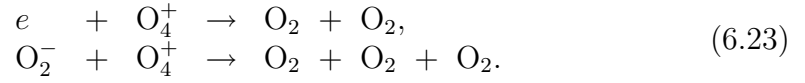
- N_2^+ to O_2^+ conversion (the typical time is a few nanoseconds):



- conversion of O_2^+ ion into O_4^+ (tens of nanoseconds):



– recombination of O_4^+ ion (a few microseconds):



- V-T relaxation of vibrationally-excited states of components, which is the main channel of gas heating.

Thus, during the characteristic gas-dynamic time of flame propagation (a few milliseconds), the electronic and vibrational excitation of the mixture components is either transferred to the translational degrees of freedom (which leads to the gas heating) or is spent on dissociation (mainly, of oxygen and hydrocarbons, because their dissociation energies are fairly low). Hence, the third stage—flame propagation through the excited mixture—can be treated as the combustion of a new mixture produced at the burner exit under the action of a barrier discharge (see table 6.1). Based on the distribution of the pulse energy over the processes of reactant excitation, we calculated the densities of the molecules, atoms, and radicals produced in the mixture under the action of a high-voltage pulse.

<u>Mixture component</u>	Without discharge	With discharge	
	<u>Concentration</u> (% in the mixture)	<u>Concentration</u> (% of the mixture)	<u>Concentration</u> (% of the in-al. comp-t.)
N ₂	76.8	76.8	100
O ₂	19.2	19.07	99.33
C ₃ H ₈	4.0	3.94	98.5
O	-	0.13	0.67
C ₂ H ₅	-	0.03	0.75
CH ₃	-	0.03	0.75

Table 6.1: Concentrations of mixture components before and after barrier discharge action.

It was assumed that, at the given discharge power, active particles are generated within the time interval equal to the pulse repetition period, in a rectangular volume with the base area equal to the nozzle area and the height equal to the distance passed by the gas during the pulse repetition period. A streamers flash starting from the high-voltage electrode is three-dimensional and occupies a finite gas volume (a few millimeters in height). At a high repetition rate of the high-voltage pulses, the discharge quasi-continuously excites the gas flow, which passes a distance of about 1 mm during the pulse repetition period.

It is seen that the concentration of atomic oxygen in the discharge region can be fairly high ($[O]/[O_2] = 0.7\%$), which leads to a substantial acceleration of combustion by a barrier discharge.

Flame propagation through the pre-excited mixture

One-dimensional simulations of the combustion and propagation of a premixed propane–air flame was performed using the Premix Chemkin-II package. Besides the chemical

reaction kinetics, the code also incorporates the diffusion of the mixture components, thermodiffusion, and heat transfer. The Konnov²⁴³ kinetic scheme was used.

The program allows us to change the initial temperature, initial mixture composition and the distance between burner edge and combustion zone. The results of simulations are presented in Figs. 6.14–6.16.

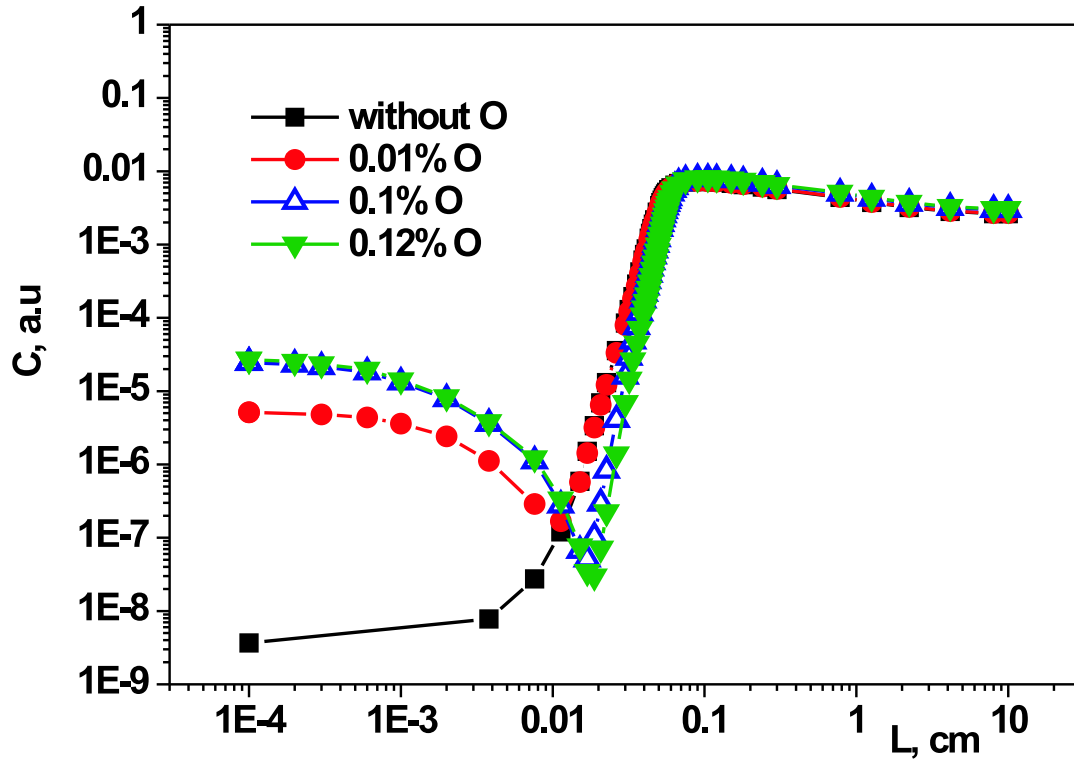
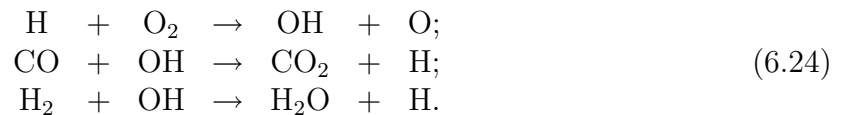


Figure 6.14: Calculated OH concentration profile along flame height for different initial oxygen concentration.

Figure 6.14 shows the variations in the height profile of the OH radical density. It can be seen that, as the initial density of oxygen atoms increases, the flame front (the region where the main reactions occur and heat is primarily released) narrows, which means that the combustion rate increases. The simulation results show that the main reactions that substantially affect the combustion rate are the following:



Atomic oxygen produced in the discharge zone near the nozzle edge participates in chain branching reactions. At low temperatures, the rate at which chain reactions are broken exceeds the formation rate of new chains and the initial O concentration is insufficient to ignite the mixture and sustain combustion. Hence, the efficiency of the discharge

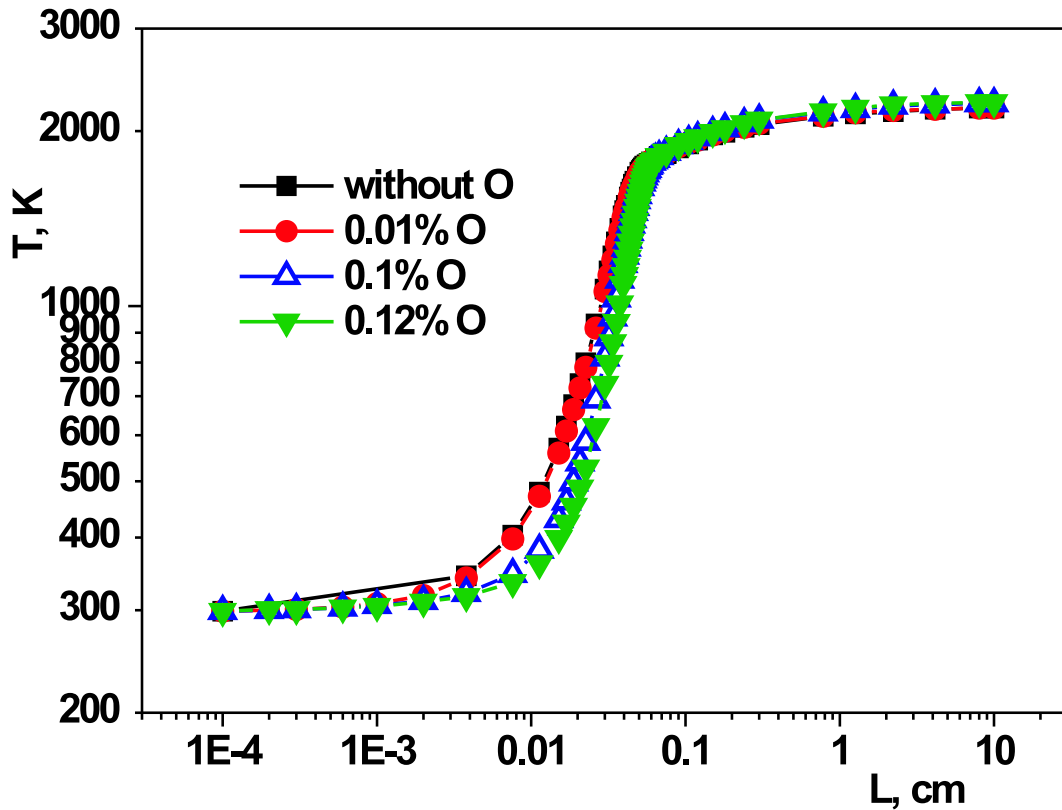


Figure 6.15: Calculated temperature profile along flame height for different initial oxygen concentration.

energy utilization is primarily determined by the temperature growth related to the heat flux from the region where the chemical energy released. The radicals created in the preheated flow give rise to significantly longer chains, which leads to an increase in the energy released in a single act of oxygen dissociation in the discharge. Thus, applying a discharge to the adjacent to the flame front region significantly increases the efficiency with which the flame can be controlled.

As the atomic oxygen concentration is increased above the critical value (0.12%), the flame propagation velocity predicted by the model tends to infinity. This result can be interpreted as the self-ignition of the mixture due to the development of chain reactions at the temperature equal to the gas temperature in the discharge zone. In this case, the flame propagation velocity formally becomes infinitely large, so that combustion is sustained at any outflow velocity of the mixture. However, to provide such a regime, it is necessary to keep the atomic oxygen concentration in the pre-flame zone at an overcritical level. As the flow velocity increases, the power of the discharge, in which atomic oxygen is produced, should also increase. In real experiments (where the generator power is finite), when the atomic oxygen concentration exceeds the critical value, the increase in the flame propagation velocity leads to a decrease in the concentrations of the active components;

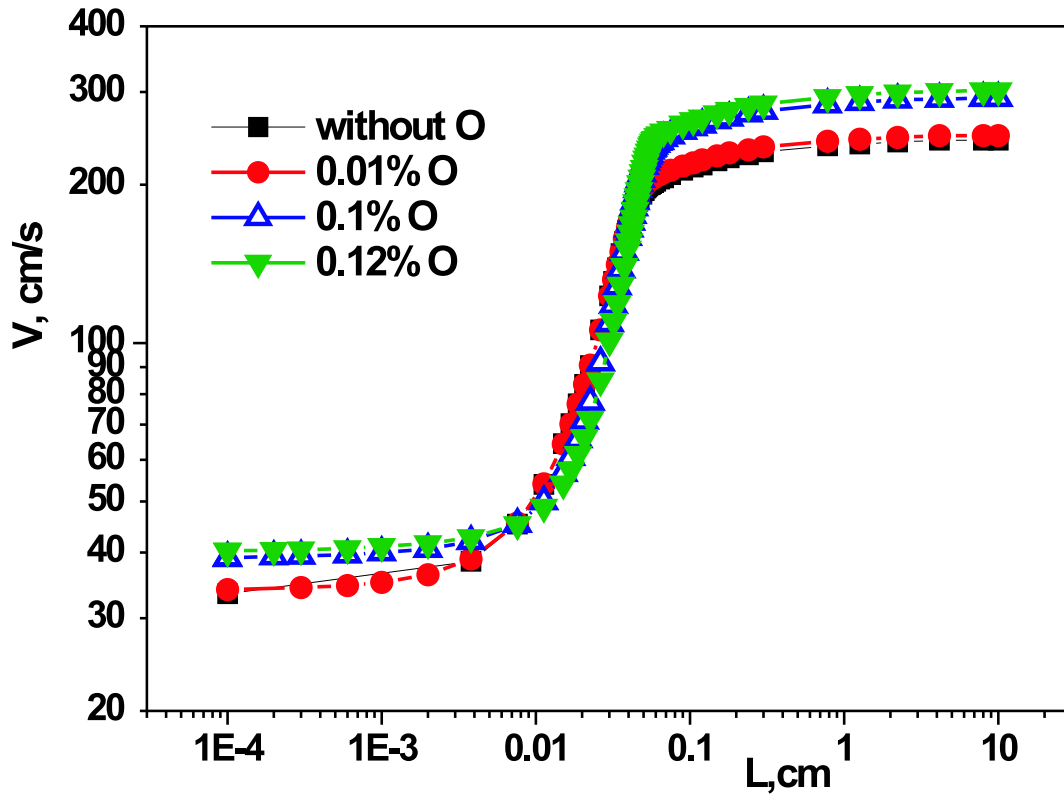


Figure 6.16: Calculated flame velocity profile along flame height for different initial oxygen concentration.

as a result, the flame propagation velocity stabilizes at a new (higher) level.

The concentration profiles of other active particles (O, CH, and others) behave similarly to the OH concentration profile. Figures 6.15–6.16 show the profiles of the temperature and velocity along the flame. The increase in the flame propagation velocity depends on the discharge power (the concentration of atomic oxygen); at a subcritical concentration of atomic oxygen (0.1%), it is about 20%.

6.2 Control of plasma-enhanced combustion using optical diagnostics

6.2.1 Role of a nanosecond pulse duration in combustion enhancement

Detailed description of the setup you can find in the previous section. We analyzed the efficiency of nanosecond discharge in plasma-enhanced combustion using different modifications of the burner. Three different quartz nozzles with rectangular cross-section, with 2.2, 2.5 and 4.3 mm in width and the same length of 30 mm, were used. Stainless steel 0.8 mm thick high-voltage electrode was placed inside the nozzle and the grounded electrodes were set tightly into quartz tubes and placed near the nozzle edges, parallel to them. To fix the point of streamer's start and the number of streamers as well, the high-voltage electrode has a number of pins on its upper edge. Three electrodes were used — with 8, 15 or 28 pins, so the number of streamers could be 16, 30 or 56 respectively. The nozzle and images of discharge and flame are presented in Fig. 6.17. On the left hand side a photo of discharge with flame in propane-air gas flow is represented. The flame blow-off point is clearly seen. On the right hand side nanosecond discharge without flame is represented. To measure the combustion rate increase, an emission spectroscopic system was used as well as flowmeters.

For investigation of bunch of parallel streamers and their interaction and influence on each other we used installation shown in fig. 6.18. To change amount of streamers, we changed the amount of initiating pins on electrode. The low-voltage electrode was protected by the dielectric barrier from quartz and frequency of following impulses was 1 kHz. Experiment were carried out in ambient air.

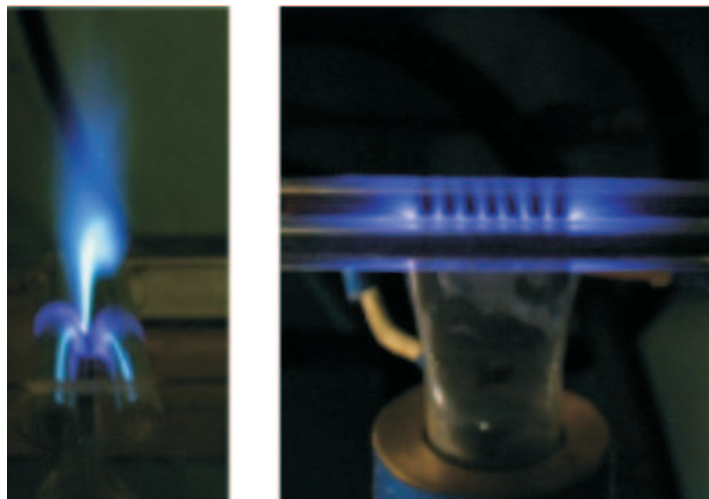


Figure 6.17: General view of the flame and discharge.

For the present work we used three different types of nanosecond pulses: with FWHM 7, 19 and 24 ns. The voltage on the discharge gap could be 14 kV or 22 kV, pulse polarity was positive. Pulse repetition rate could be varied within the range of 400-1000 Hz. For determining of spatial and temporal characteristics of a streamer the PicoStar HR12

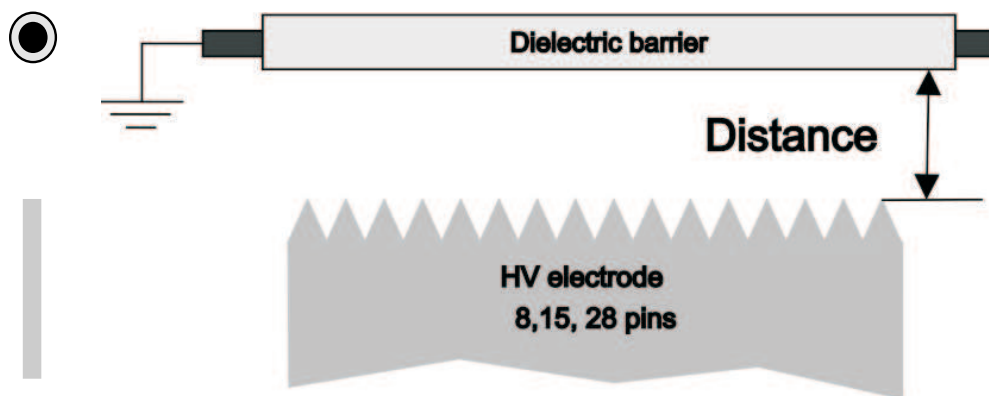


Figure 6.18: Set-up for investigations of bunch of streamers. Scheme of the electrodes.

camera (LaVision) with a spectral range of sensitivity 300–700 nm and time resolution up to 200 ps was used. Photos of streamer discharge were received in two modes of operation of the high-speed camera: integral and stroboscopic mode. When working in integral mode the amplifier of the high-speed camera was switching on simultaneously with coming of high-voltage pulse on electrode. Time of exposure was 50 ns and was longer than the duration of a high-voltage impulse. For working in stroboscopic mode, on the amplifier of the camera a triggering sine signal is set with frequency of 300 MHz, time of exposure of the camera's amplifier is set by the program and in our experiments it was 300 ps.

It was shown in,¹⁷⁵ that in processes of combustion acceleration and flame velocity increase the main role is played by active particles (such as O, H, OH), which are responsible for chain branching. These results are confirmed by experimental data. In particular, additional OH* production (in $A^2\Sigma$ – state) under discharge influence in methane–air and propane–air premixed flames was observed. The similarity of the results is the evidence of likeness between mechanisms of flame acceleration. This result is confirmed by numerical simulation as well. Combustion intensification shows itself in an emission peak shift and narrowing of area of growth of OH* concentration. The results for temperature – both experimental and calculated – was obtained and in a good agreement as well. Using spectroscopic data, we also can conclude that flame blow-off velocity increase is closely connected with combustion rate increase.

The formation of secondary OH* peak in the discharge zone corresponds with the statement that place where the active particles are put is important. It's useless to produce radicals in the reaction zone, where temperature is high enough and radical production in discharge is negligible with that one in chain reactions. On the other hand, if radicals are produced before reaction zone at a large distance, they probably recombine and just heat the gas for a few decades of K. So, an optimal place exists, where radical production is most effective in terms of flame blow-off increase.

A number of experiments were made to prove the correctness of the model of flame acceleration and kinetic scheme, suggested in the previous work.¹⁷⁵ It's worth to remind that, according to,¹⁷⁵ the main role is played by radicals, which appears under the non-equilibrium nanosecond discharge action. That's why it's very important to make

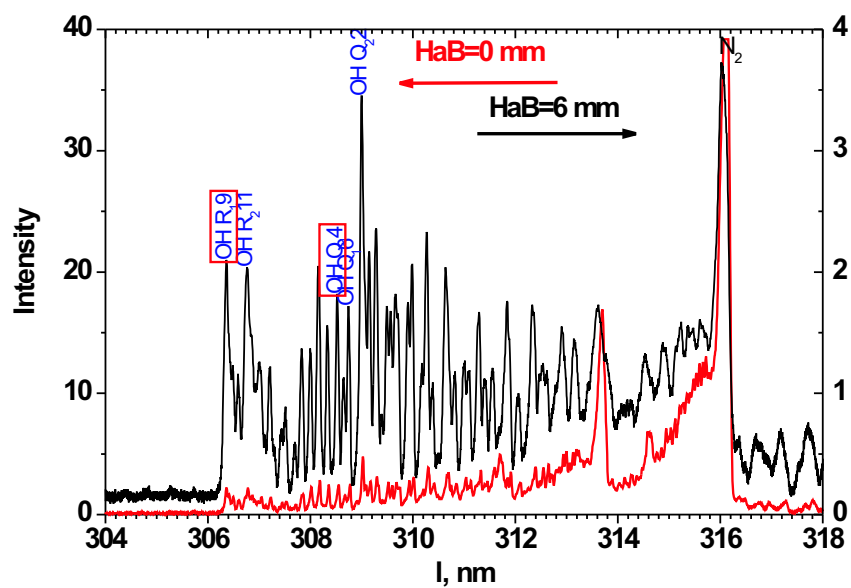


Figure 6.19: OH* spectra in methane-air flame under discharge action at HaB=0 mm and HaB=6 mm

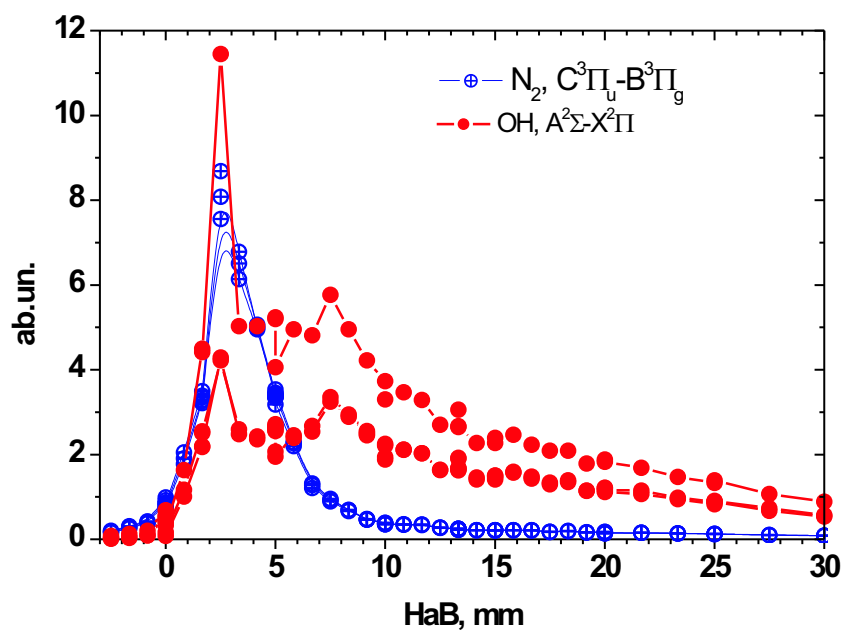


Figure 6.20: OH* and N2* profile along the HaB in methane-air flame

spectroscopic investigation of the flame itself and the flame under discharge action. In,¹⁷⁵ the profile of OH radical along the height above burner in propane-air flame was presented.

That result was based on the non-resolved spectrum ($\text{OH}(A^2\Sigma, v' = 0 \rightarrow X^2\Pi, v'' = 0)$) at 306.4 nm with quite a large apparatus function of monochromator (2.4 nm). This caused a question, is the first peak of the typical "two-humped" spectrum connected with N_2 production in the discharge (second positive system of nitrogen $C^3\Pi_u \rightarrow B^3\Pi_g$ has intense lines on the wavelengths of 315.9 nm ($1 \rightarrow 0$), 313.6 nm ($2 \rightarrow 1$) and 311.6 nm ($3 \rightarrow 2$))? In the present work, using CCD-line with signal accumulation mode, it became possible to obtain rotationally resolved spectrum of OH radical in methane-air flame. The spectra of OH* for two different heights (0 mm and 6 mm) above the burner are presented in fig.6.19. It's distinctly seen that in the region below 310-312 nm we can use any rotational line of OH* spectrum to build the dependence between OH* emission and height above burner (HaB). The result is presented in fig.6.20, and this figure confirms the previously obtained one for propane-air mixture as well as the importance of OH radical in flame and the similarity of kinetic processes, which lead to flame blow-off velocity increase, for the vast majority of premixed hydrocarbon-air flames. The results for methane-air flame blow-off velocity increase (fig.6.21) are in agreement with this theory.

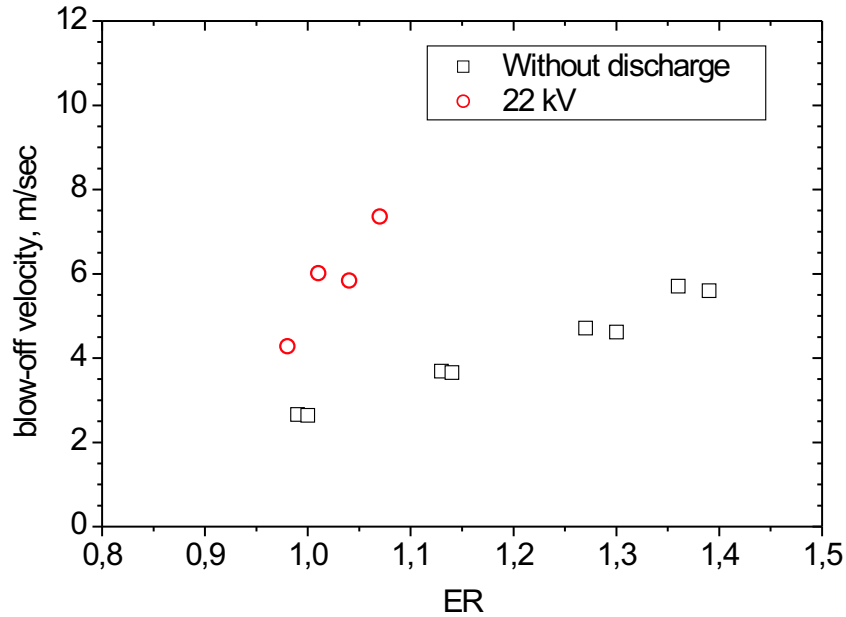


Figure 6.21: Methane-air flame blow-off velocity increase

Using OH rotationally resolved spectra, the rotational temperature was calculated. We used the ratio of $R_1(9)$ ($\lambda=306.3565$ nm) line and $Q_1(4)$ ($\lambda=308.3278$ nm) line. In the case of equilibrium flame, the rotational temperature, obtained in a such way, is close to the translational temperature (the radiative time of living of $A^2\Sigma$ level is 690 ns, and the typical time between particles collisions is about 30 ns, so the Boltzmann distribution of particles at rotational levels occurs before radiation). Experimental OH rotational temperature profiles along the height above burner in methane-air flame are presented in fig.6.22

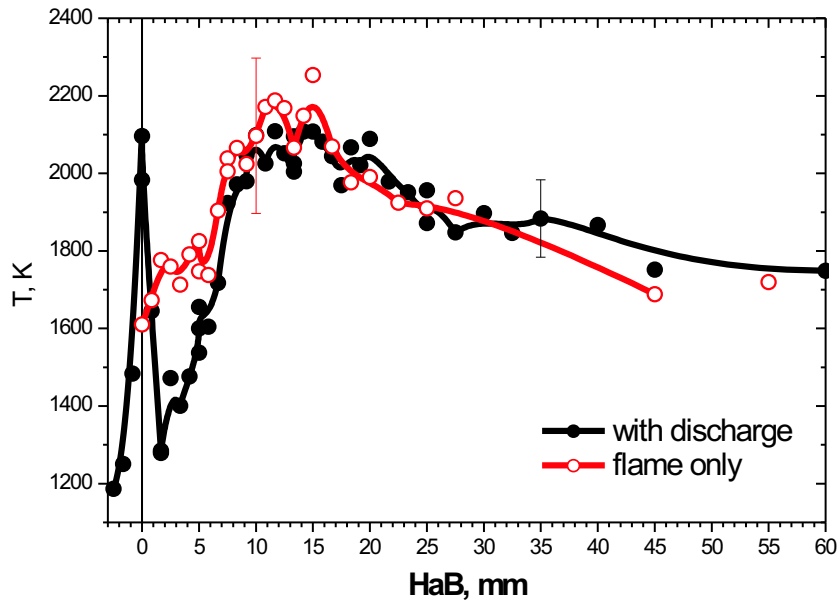


Figure 6.22: Experimental OH rotational temperature profile along the HaB in methane-air flame

The comparison of experimental profile with calculated one shows a good data agreement (compare with fig.6.15). The theoretical model is based on changing in initial mixture composition under the discharge action.

It worth mention that geometry of burner and discharge cell are of great importance. Electrodes, if placed near the burner, serve as additional stabilizers and allow to increase blow-off velocity even without discharge. The way of influence in this case is changes in flow pattern and heat-removing processes. Another mechanism for flame stabilizing is creation of zones with near-zero flow rate, where ignition occurs, and than flame moves upward the stream.

So, there are two types of discharge application in combustion tasks. The first is to ignite mixture in areas with low flow speed with combustion rate remaining constant, i.e., by heating, as in,¹⁷⁶ and the second is to increase combustion rate by uniform treatment of mixture in the discharge. We think that the second way is more perspective and that's why one should use relative flame velocity increase as the main parameter of discharge effectiveness, instead of absolute values of flow speed. We should compare the discharge power to relative burner power increase, taking into account that completeness of combustion could change.

Our results show that flame propagation velocity can be increased more than twice, depending on the way we organize discharge as well as discharge parameters (duration, pulse repetition rate, voltage etc) with energy input less then 0.5 % of the burner power. To verify the statement that our discharge doesn't heat the gas, we performed spectroscopic investigations and found that the widening of the lines of emission of molecular nitrogen corresponds to the additional heating about a few decades of K. Moreover, a

number of experiments with different high voltage electrodes – with 8 and 15 pins – has been done. Estimates show that the local overheating is greater for the case of 8 pins (16 streamers develop from the electrode), while the intensification ratio (we determine it as a blow-off rates ratio with and without discharge) is significantly greater in the case of 15 pins (that is in the case of 30 streamers). This fact is illustrated by Fig. 6.23.

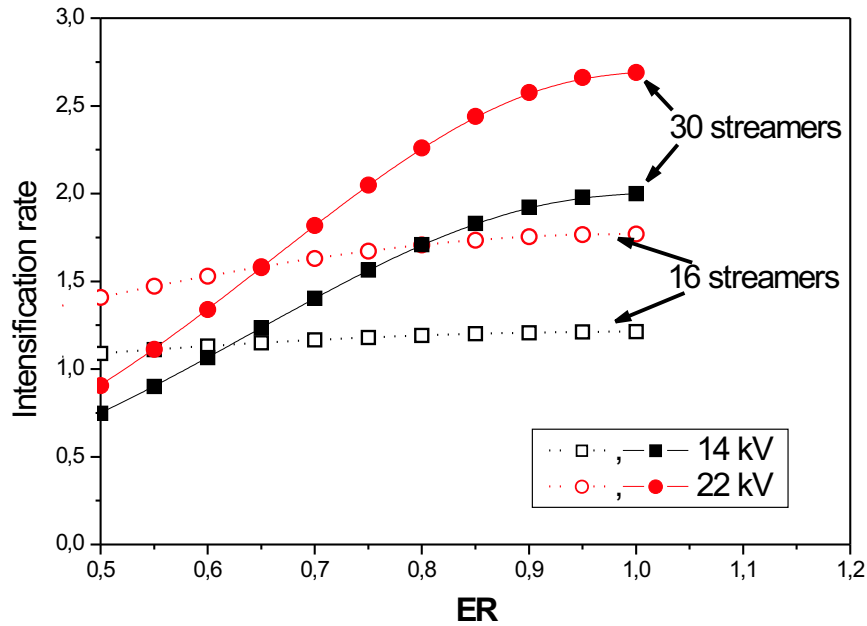


Figure 6.23: Intensification ratio for different number in pins at a high-voltage electrode and for different voltage amplitude.

Different pulse durations were investigated. It was found that with effect of flame blow-off velocity increase is significantly greater for the pulse length of 19 ns than for 7 ns (Fig. 6.24), and corresponds to energy input. But further pulse length increase results in shifting of the main zone of energy release out of the flow gap, so discharge doesn't influence on the mixture any more, concentrating near dielectric barrier. The investigation of discharge frequency influence on flame blow-off velocity showed that with frequency growth the effect significantly increases (Fig. 6.4) - we can sustain combustion with the same burner power using lean mixtures. Based on this result a conclusion could be drawn that with ER (equivalence ratio) reducing it's necessary to input larger amount of discharge energy to provide the same burner chemical power.

So, the effect of blow-off increase is explained by active particles production. The larger the number of active particles, up to some limit, the greater blow-off rate increase. To determine optimal discharge parameters, which give us maximum efficiency of radical production at minimum energy input, streamers development and their interaction were investigated. It was found that two different regimes of streamer propagation exist. When we use term "streamer", we mean a self-sustained cold discharge, with ion temperature close to room temperature. We want to underline this fact to exclude the hypothesis about thermal effect of the discharge. Using of barrier discharge allows to translate this

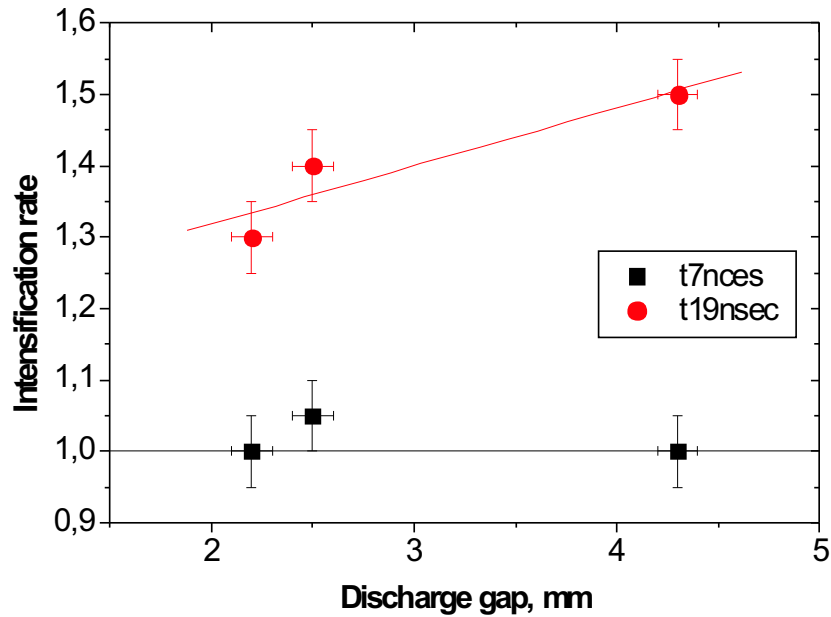


Figure 6.24: a) Intensification ratio for different number in pins at a high-voltage electrode and for different voltage amplitude; b) Intensification ratio for different high-voltage pulse duration.

technique of flame acceleration to the higher pressures. When the discharge gap is small enough, the reduced electric field exceeds breakdown field in the air both in the streamer head and in the channel, so active particles are produced inside the gap. At larger distances the main active particles production takes place only in the streamer head, so the effectiveness does not depend on the pulse duration. So, an optimal gap exists, where active particles production is maximal. This gap is depended on applied voltage. When gap is long enough, the streamer couldn't propagate and only a corona develops near the pin, so the larger part of the gap is not treated by the discharge. On the contrary, at short gaps values of reduced electric field exceed optimal.

The comparison of cathode-directed streamer and anode-directed streamer showed that the emission from the cathode-directed one is more intensive (see Fig. 6.25). It is known that the emission intensity is proportional to the density of excited species. This fact explains and confirms results obtained earlier in,¹⁷⁵ where flame blow-off increase was compared for both cases and it was found that the effect is greater for positive (cathode-directed) streamer. It's also seen quite well that anode-directed streamer doesn't branching. Starting from a certain number of pins, the number of streamer stops to grow and become fixed. So, streamers if situated near each other, strongly interfere. More detailed investigation of streamer properties and other results by this topic you can find in.²⁴⁴

An additional proof to the suggested theory and model of radical influence lies in the results of experiments with Ar/O₂/C₃H₈ mixture. According to this theory,¹⁷⁵ the main channel of active particles production (O, H, OH) in nitrogen/oxygen mixture is the

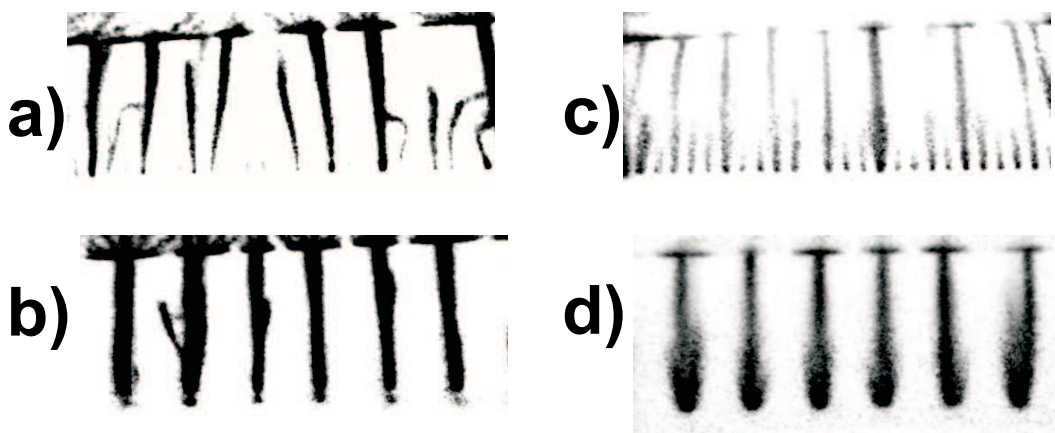


Figure 6.25: Images of streamers in the discharge gap. a — cathode-directed streamer, 28 pins, b — cathode-directed streamer, 8 pins, c — anode-directed streamer, 28 pins, d — anode-directed streamer, 8 pins.

following:

- Nitrogen excitation by electronic impact, with production of electronically-excited molecules.
- Kinetic of excited states, primarily quenching of excited nitrogen on oxygen molecules with atomic oxygen formation.
- Combustion of a new mixture with highly non-equilibrium radicals concentration and production of new radicals (OH).

So, in experiment we have changed the nitrogen in the mixture to argon in order to remove main channel of active particles formation and decelerate flame in comparison with $\text{N}_2/\text{O}_2/\text{C}_3\text{H}_8$ mixture. Indeed, the results of experiments showed that the phenomenon in argon mixture is much weaker. This is an evidence for our flame acceleration model.

Thus, the study of nanosecond barrier discharge influence on flame propagation and flame blow-off velocity was carried out. The following conclusions could be made: With energy input negligible in comparison with burner's chemical power, a double propane-air flame blow-off velocity increase was obtained. It was shown experimentally that results for methane-air flame are similar with propane-air one. The acceleration mechanisms are similar in both cases. Besides proper form of energy input, proper organization of discharge is of great importance. It was found that the effectiveness of plasma-assisted combustion depends on type of discharge, pulse duration, pulse repetition rate and other parameters, which are responsible for active particles production. Development of the streamer in different regimes was studied, optimal regimes were found. It was found that active particles (O and OH primarily), which are produced under the discharge action, play the most significant role in the effect of combustion acceleration. The model of flame acceleration, based on nitrogen quenching on oxygen molecules, with production of O and OH radicals, was confirmed by spectroscopic investigations and experiments with $\text{Ar}/\text{O}_2/\text{C}_3\text{H}_8$ mixture, where discharge influence is small because of the excluding of the main mechanism of active particles production — oxygen dissociation by excited nitrogen quenching.

6.3 Kinetic mechanisms of plasma-assisted combustion

The problem of finding mechanisms in the task of plasma-assisted combustion takes on special significance. The main idea of PAC studying is comparison of efficiency of different types of plasma for flame stabilization (especially lean mixtures at high velocities), lean mixtures combustion at low temperatures for NOx amount reduction etc. Practically in all the papers on this subject (see, for example, review²⁴⁵) such effects are achieved by active particles generation in plasma - by heating or in plasmochemical transformations. Now it's become obvious that for effective flame and combustion control it's necessary to understand mechanisms of plasma influence and the parameters range (pressures, initial temperatures) at which such mechanisms are most effective.

At present time several main mechanisms are suggested: rapid gas heating in the discharge, "active particles" production (O, H, CH_3) and "ion chains". Depending on that fact, which of these mechanisms is the main for specific task, we should choose the proper type of gas discharge. If the thermal heating is more effective, it worth using equilibrium plasma of arc and spark discharges with relatively low reduced electrical fields.

For example, this mechanism was realized in the paper.¹⁷⁶ In this work gas flow ignition was performed by nanosecond spark discharge in a recirculation zone. The main disadvantage of such technique is the existence of region with zero flow velocity and the fact that the flame propagation velocity from the small discharge channel toward unburned mixture remains the same in comparison with the system without discharge.

On the other hand, non-equilibrium influence with production of electronically-excited states of molecules (N_2, O_2) instead of direct gas heating has higher energy effectiveness, as was shown by calculations. The reason for this is initiation of chain reactions at low temperatures with additional energy release in chemical transformations. In this case, we should use barrier or streamer type of discharge with high reduced fields.

So, for effective flame and combustion control it is necessary to know which mechanism at certain conditions is dominant. Such knowledge will allow to predict optimal discharge type and parameters of burner. The problem of mechanism determining becomes even more complicated because of complex discharge action. At first, on discharge stage, "excited particles" are produced under electronical impact action - electronically and vibrationally excited molecules, ionized molecules, products of dissociation. Then these particles are transformed into more stable particles in ground states - typical times for these processes is approximately 100-500 ns. At last, these new particles - we suggest that they are O, H, CH_3 and other radicals - participate in chain reactions with typical times 1 μs (for 1000K, for 300K the typical time is 70 μs).

Along with these plasmochemical transformations with new particles production gas heating occurs in processes of vibrational and electronical relaxation, with typical times which are depend strongly on the initial temperature (from 1 μs at high temperatures - 1000K - to tens of milliseconds and room temperature). Such heating could be high not only in the case of an arc or spark discharge, where heating proceeds very fast in discharge channel during the tens of nanosecond, but even in the case of barrier discharge, for example, at high discharge frequencies. Such heating could be important when studying the mechanism of flame control and combustion acceleration.

To study the role of radicals in plasma-assisted combustion with nanosecond barrier

discharge experimental temporally resolved measurements of OH radical by LIF technique and temperature measurements by N₂ rotationally-resolved spectrum were performed in fuel-air gas flows. Calculations of chemical kinetics were performed, the results have confirmed that the main role in flame acceleration is played by radicals which are produced in discharge.

6.3.1 Temperature measurements

To determine the mechanism which is responsible for flame stabilization in our conditions (in previous reports we have written about significant increase in flame blow-off velocity for this type of the burner) we performed measurements of gas flows (air and propane-air) temperatures in the barrier discharge. As it was mentioned above, two main reasons exist: the first is thermal heating (or local overheating), and the second is direct production of excited particles in the discharge. To determine the possible value of gas overheating in our burner temperature measurements of gas flow through pulsed nanosecond discharge plasma.

The investigations were made for pulses of positive polarity (it provides greater effect), FWHM (full width at half magnitude) is 12 ns, pulse amplitude 7-12 kV, pulse repetition rate 1-10 kHz. The energy input into the flow was approximately 0.5 mJ per pulse. We used propane-air mixture with equivalence ratios 0.6-1.4, the flow velocity was 5 m/s. Spectroscopic diagnostic was performed using the CCD-array and monochromator. The discharge image was built on the input slit of monochromator with linear dispersion of 0.96 nm/mm, the slit width was 30 mkm. The parameters of CCD-array are following: pixel dimensions of 8x200 mkm, the number of elements is 3648, total array spectral length is 28 nm (30 mm real length).

The measurements were performed using rotationally-resolved 0-0 band of 2nd positive emission system of nitrogen molecule. In fig.6.26 the correspondence between experimental and calculated spectrum for T=400K is shown. The error of temperature determining is approximately 5K. Systematic error, which is due to uncertainties in spectroscopic system parameters as well as to the selection of the range of rotational numbers J, is greater and is near 20K, but such error provides only common shift for all experimental points.

The temperature measurements of air flow in pulse discharge have showed that at frequency 1 kHz (in this working regime the effect of flame blow-off acceleration is noticeable) the air is heated up to the 400-450 K, and the heating grows with further increase of frequency. Such additional heating is insufficient for propane-air mixture inflammation (the temperature of self-ignition is near 800K). Also the thesis about small heating is confirmed by the fact that even at low flow velocities (2 m/s) and at high discharge frequency the mixture ignition doesn't happen. These facts are illustrated with figures 6.27-6.28.

But the value of 100K of air heating exceed significantly theoretical prediction of temperature in the discharge channel. Estimation was performed basing on value of energy input into the mixture (which, in turn, was calculated with the aid of oscillograms of incident and reflected pulses and was find to be equal to 0.3-0.5 mJ/pulse for 10 kV amplitude). For streamer diameter value of 0.5 mm (see our previous reports) the heating should be approximately 10K. The reason for such difference from experimental value is the following: when dealing with low frequencies (1-2 kHz) it's necessary to

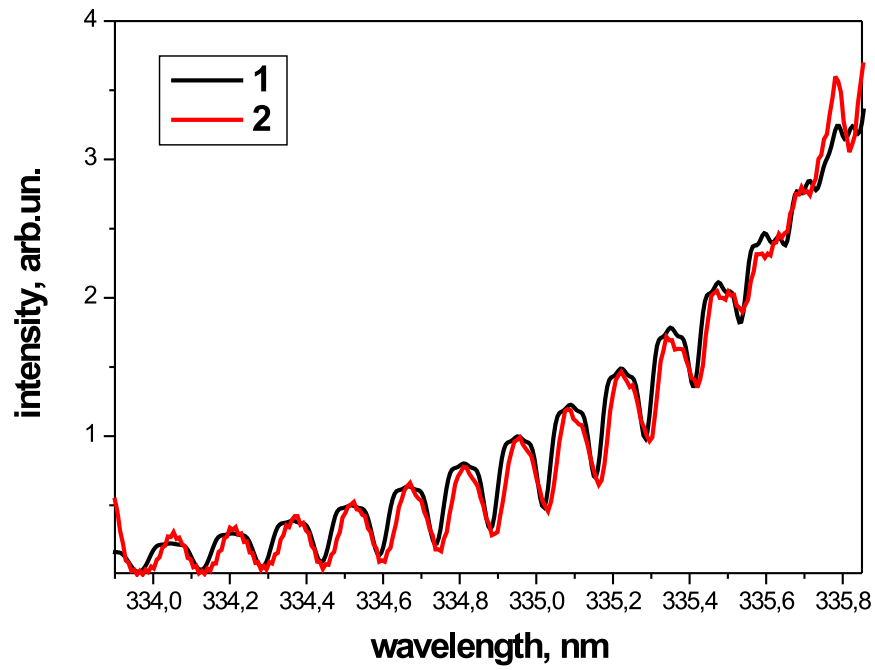


Figure 6.26: Experimental (1) and calculated (2) spectra for 2+ nitrogen system, 0-0 vibrational transition. T=400K.

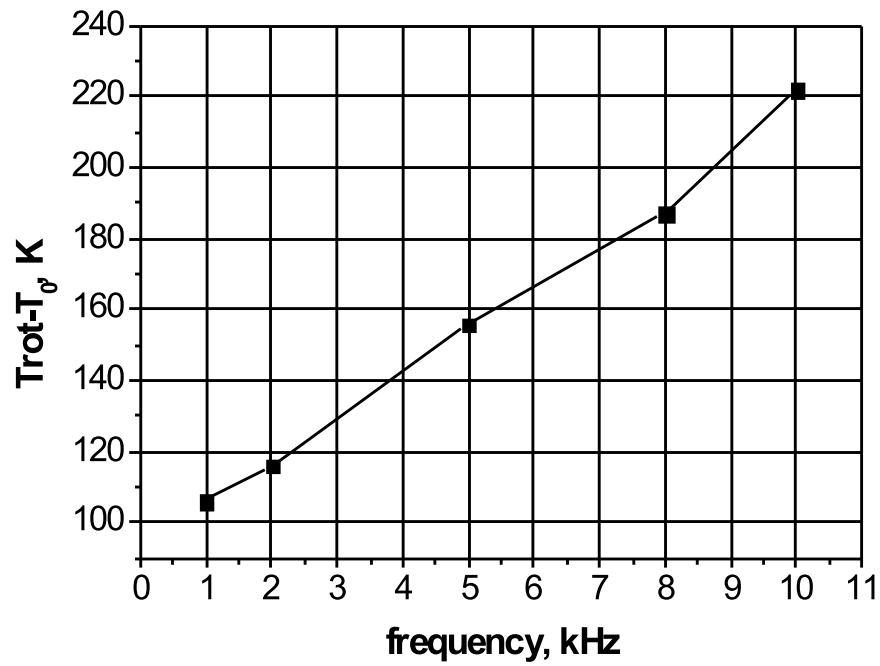


Figure 6.27: Air flow heating for different discharge frequencies.

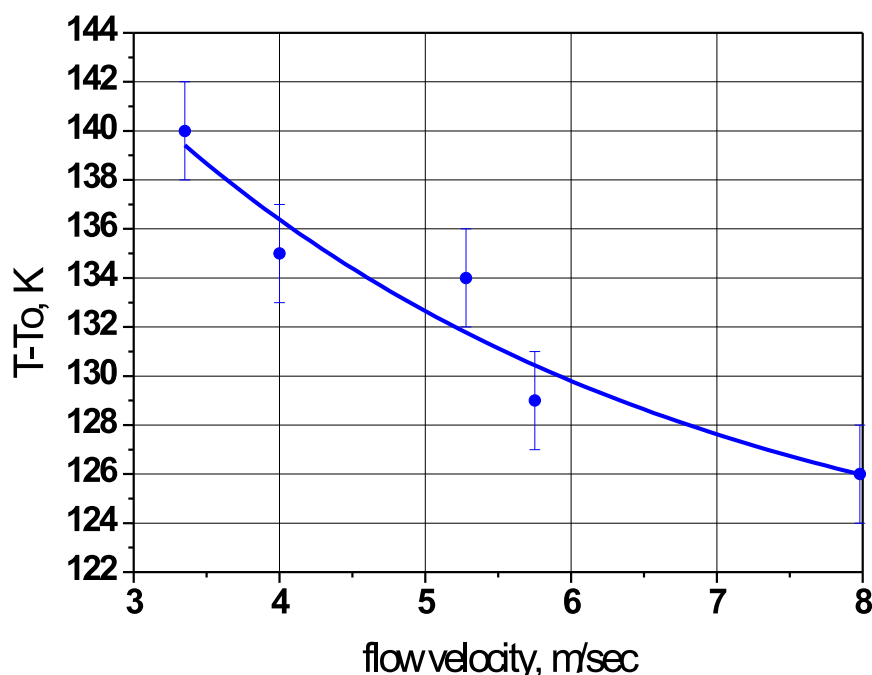


Figure 6.28: Air flow heating for different flow velocities.

accumulate discharge emission during 60-120 sec for precise temperature measurements. This time is enough for quartz tubes to be heated up to 100 K (quartz has very low thermal conductivity and the flow velocity near quartz tubes is near to zero). Fig.6.29, where temporal dynamics of flow temperature is presented, is the evidence for this explanation. Another way to show this is to analyze fig.6.27. It's distinctly seen that, if we linearly approximate points, the heating at 10 kHz frequency is 10 times higher than in the case of 1 kHz frequency and corresponds to 12K heating per pulse (flow velocity is 5 m/s).

The same measurements were performed for propane/air mixture of stoichiometric composition. Because the amount of propane in the mixture is quite small (4% at ER=1) as well as flow velocity increase, the experiments were performed in the following way. At first, air flow temperature was measured, then propane was added to the mixture and the measurements were repeated. Energy input was controlled by oscilloscope, and it was found that, despite of significant changes in N₂ second positive system emission intensity (it was much weaker with propane), the energy input was practically the same in both cases.

Temperature measurements have showed that gas heating in propane-air mixture is stronger than in the pure air. The additional (in comparison with air) heating grows with pulse repetition rate and pulse amplitude increase (fig.6.30,6.31). The value of such additional heating as great as the half of air flow heating. Also a tendency of additional heating increase with the growth of energy input is observed.

Now we'll try to explain the reason for additional heating in propane-air mixture. It's seems that in propane-air mixture additional energy release takes place (the discharge energy input is the same, and, according to the thermodynamical data, the gas heating

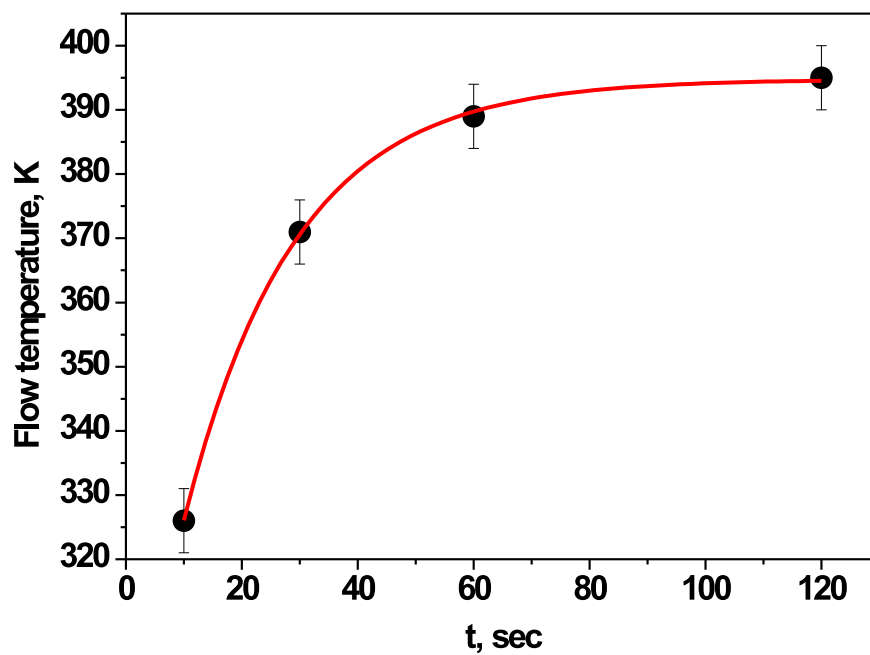


Figure 6.29: Temporal dynamic of gas flow temperature in dependence on time gap from discharge start.

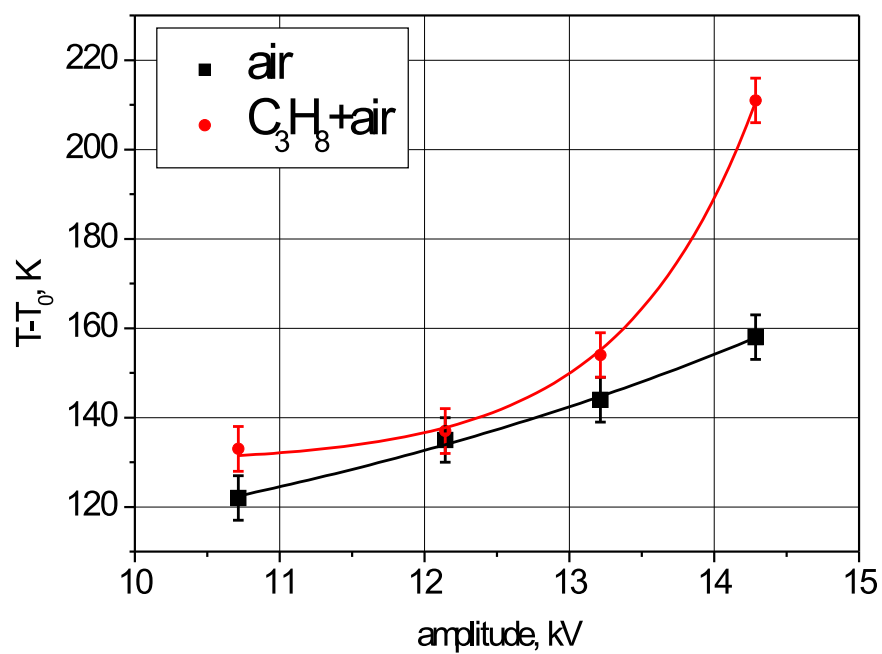


Figure 6.30: Comparison of air flow and propane-air flow (ER=1) heating for different pulse amplitudes.

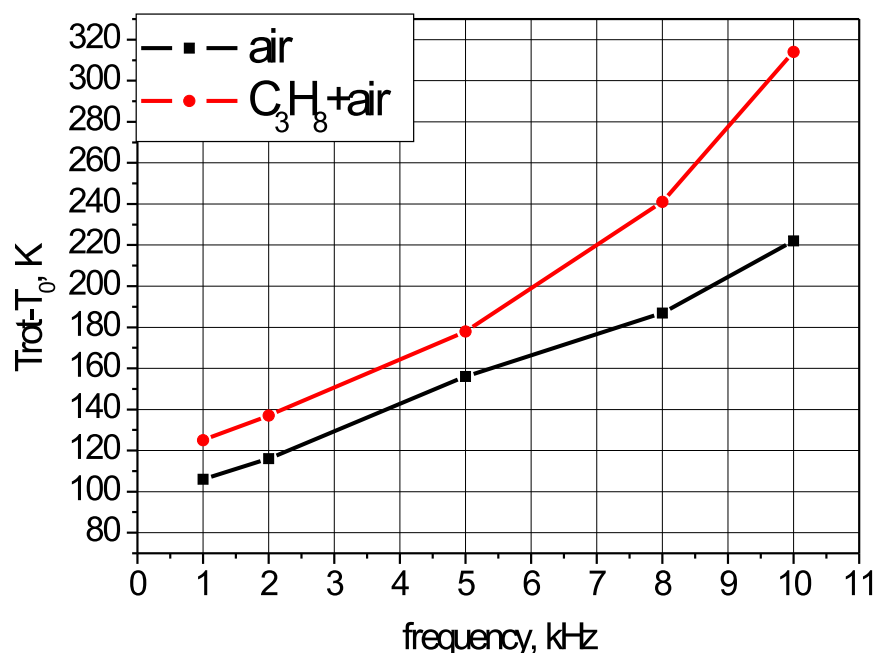


Figure 6.31: Comparison of air flow and propane-air flow (ER=1) heating for different pulse repetition rates.

should be higher in pure air - because of lower thermal capacity and flow velocity). It's quite logical to suggest that additional energy release occurs in chain reactions. But the results of calculations (which were performed in CHEMKIN package using GRI-Mech2.1 scheme) have showed that such additional heating even at initial temperature 500 K is very low and corresponds to 1-2 K at typical time 1 sec, which is much greater than typical time of our task – 1 ms (flow velocity 5 m/s, discharge zone 5 mm). Experiments with preheated mixture were performed in flow reactor, it was found, that such effect cannot be explained in terms of “thermal” initiation of chain reactions.

That's why we suggest mechanism based on O radical production in the discharge. In¹⁷⁵ it was shown that concentration of atomic oxygen could reach 1% after the discharge. We performed calculations using GRI-Mech 2.1 scheme for methane, and results have showed that in this case additional heating of the gas mixture in chains reaction is only 10 K greater than in the pure air. This result means that at large timescales and low temperatures there's no matter how to input energy into the mixture: into direct thermal heating or into atomic oxygen production.

But it's important to notice that in mixtures with fuel mechanism of O atoms recombination greatly differs from that one in mixture without fuel. In the pure air the main mechanisms of recombination are collisions with O₂ with ozone formation (at low temperatures up to 400 K) and direct recombination in reaction O+O+M→O₂+M. Typical time of these reaction is rather high (near 1 ms). On the other side, in fuel-air mixtures recombination proceeds via chain reactions with OH formation. Typical times of these reaction is significantly smaller, and they're reduced with temperature increase. The comparison

of temporal dynamic of temperature in both cases - with and without methane – is presented in fig.6.32. The situation differs for propane-containing mixtures (calculations were performed using the kinetic scheme suggested in.²⁴⁶ In this case the additional heating in chains reaction is significantly higher then for the methane-containing mixtures.

Fig.6.33 demonstrates the maximum of OH production in time versus initial mixture temperature: it's seen that with temperature increase reactions go faster and maximum of OH production reaches 1 μ s. This calculations were performed for the atomic oxygen in 3P state. But in experiments the O atoms could be produced in 1D state as well, and the amount of such excited atoms could be higher than concentration of 3P states (oxygen dissociation proceeds via excited nitrogen states with high term energy). On the same figure the data for O(1D) is presented as well, the typical rates of OH formation in this case higher.

So it's very important to take into account such excited oxygen atoms. In fig.6.34 calculations for propane-air mixture are presented. One can see that accounting of 1D states gives higher temperature increase and provide better correspondence with experimental data. The role of atomic hydrogen is negligible because the largest part of discharge energy goes to oxygen dissociation instead of propane dissociation because the oxygen concentration is 5 times higher. The comparison of experimental data and calculations with O1D for gas mixture heating in the air flow in the propane-air mixture is presented in fig.6.35.

Similar results for additional heating in fuel-containing mixtures at low pressures (hundreds of torrs) were obtained in,¹⁶¹ where additional heating in fuel-containing mixtures was equal to hundreds K. But it seems that such great value was obtained due to additional heating of initial mixture by heat transfer from the flame zone.

Thus we can conclude that additional heating in fuel-air mixtures occurs due to radicals production in the discharge. The main reasons for the temperature growth are the following. The first is additional energy release in chain reactions, and this effect is important at high temperatures (near the temperature of self-ignition). The second, which is more important at lower temperatures, is the difference in mechanisms of O atoms recombination in air and fuel-air mixture: recombination in air proceeds via O-O and O-O₂ collisions, while in fuel-containing mixtures recombination goes with OH radical formation - this process is much more faster. Because the residual time of mixture portion in the discharge zone is limited with flow velocity (near 1 ms), such energy release acceleration is very important in kinetic processes.

6.3.2 LIF diagnostic of OH radical in plasma-assisted flame

To prove the mechanism suggested above we performed measurements of OH radical using LIF technique. Experiments were performed in flames, where it's worth to expect formation of secondary OH peak.

For LIF diagnostics an optical system was assembled and adjusted. A pulsed Nd:YAG laser (Quantel) doubled at 530 nm with 1, 5 or 10 Hz repetition rate was used to pump a dye laser (Quantel, TDL 50). Solution of rhodamine 6G in ethanol was used to obtain laser radiation at 564 nm. This radiation was doubled in frequency using BBO crystal. Cylindrical lenses to transform laser beam into laser knife, picosecond ICCD-camera "La Vision Picostar HR 12" with interference filter and spectrograph with CCD-line for

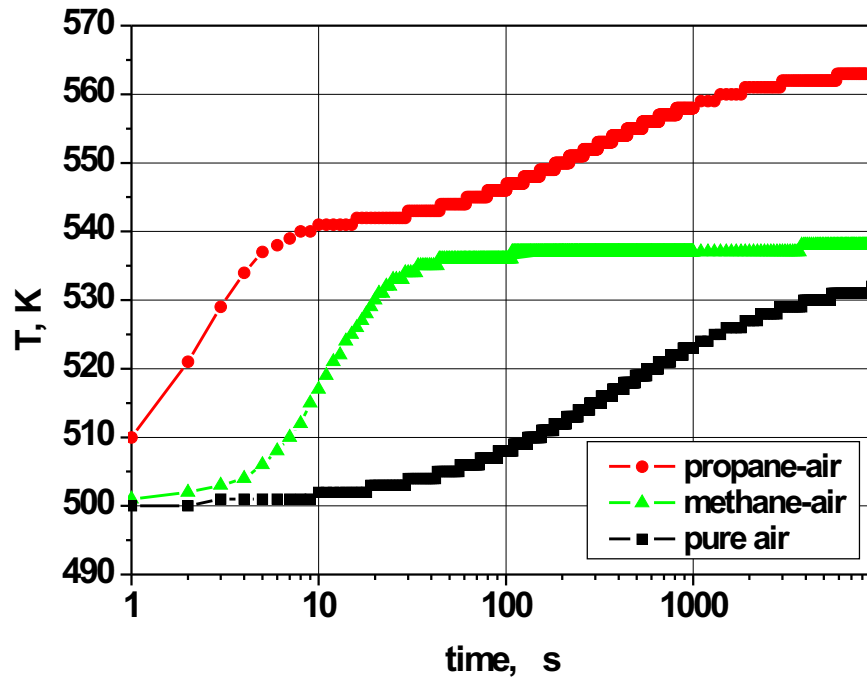


Figure 6.32: Comparison of heating dynamic for different gas mixtures. Initial temperature is 500K.

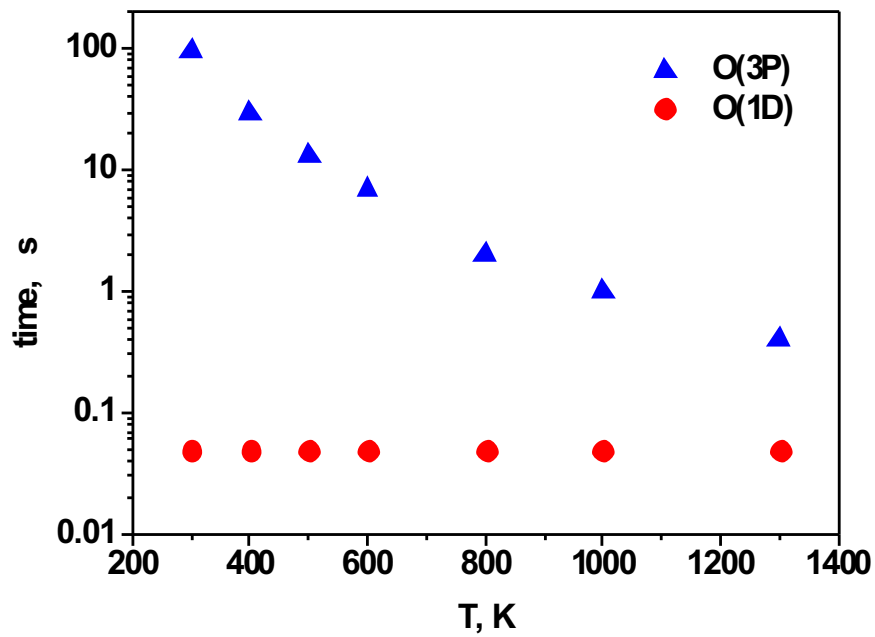


Figure 6.33: OH maximum in time versus gas initial temperature.

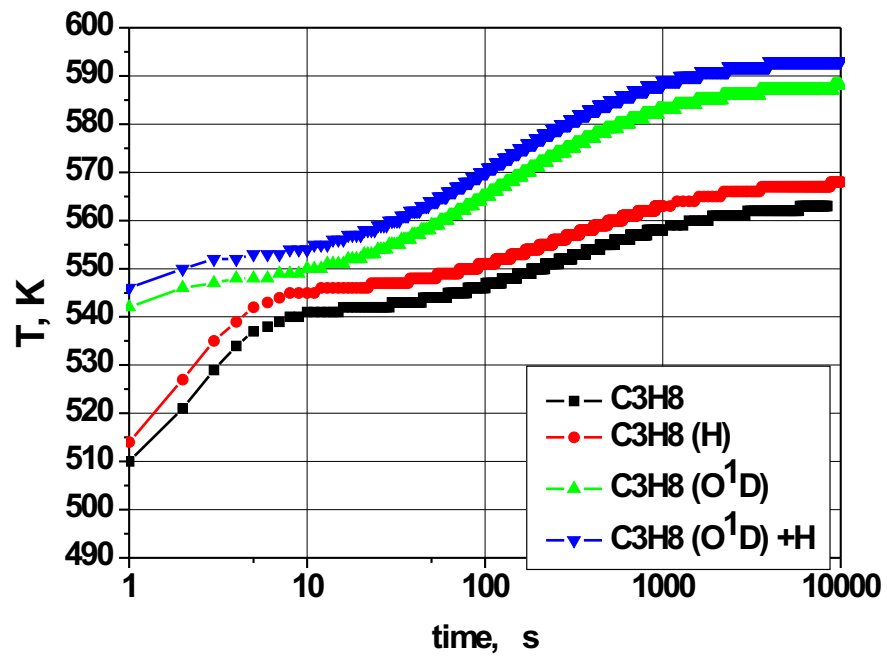


Figure 6.34: The calculation for heating dynamic with and without O(1D)

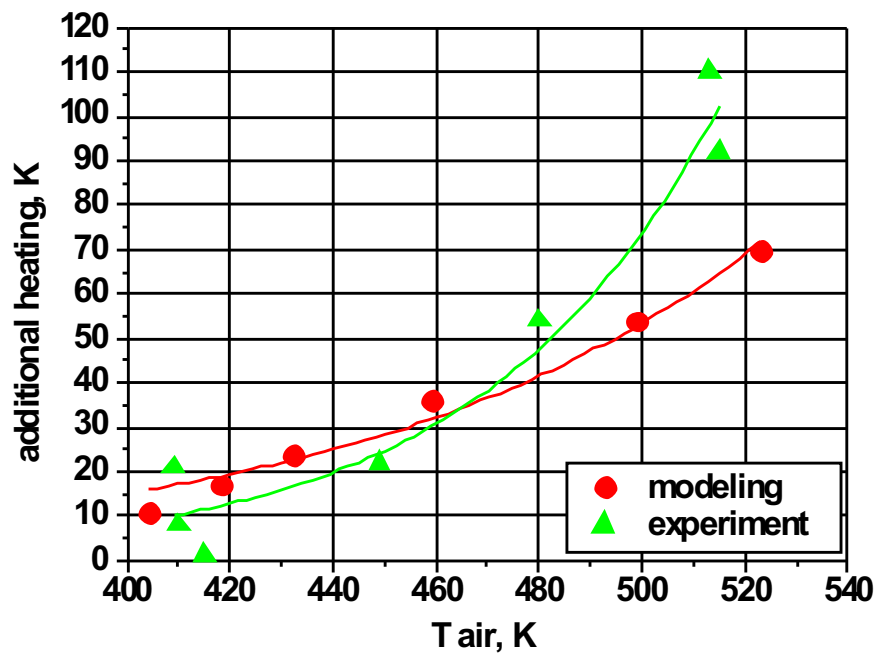


Figure 6.35: The comparison of experimental data and calculations with O1D for gas mixture heating in the air flow in the propane-air mixture

emission wavelength control. Nanosecond synchronization between laser and camera was performed using pulse generator G5-54. Experimental setup is represented in Fig. 6.36.

The laser pulse energy was 0.2 mJ at the wavelength 282.96 nm (which corresponds to Q1(6) line of $X^2\Pi$ ($v=0$) \rightarrow $A^2\Sigma$ ($v=1$) OH transition), laser pulse duration was 12 ns, laser jitter was 15 ns. Using CCD-line emission flame spectra was measured with 0.07 nm resolution. The spectrum of laser scattered radiation was used to control the excited line Q1(6), an example of the adjustment is represented in Fig. 6.37. The ICCD camera exposure was equal to 40 ns and was synchronized with laser. The height of laser knife was 4 cm, the width was 1 mm. The spatial resolution of our system was 0.12 mm, the accuracy of experiment better than 5%. We observe fluorescence perpendicular to the laser radiation through the quartz lens and interference filter (with maximum at 313.5 nm, FWHM 1.8 nm). For OH temporal behavior between voltage pulses we used system of external launching of laser by one of the intermediate outputs of high-voltage generator. This allowed us to perform LIF-measurements with synchronization with discharge up to 10 μ s.

We used two regimes of OH control in nanosecond discharge: non-synchronized, when the discharge operates at 1 kHz frequency and laser starts at 10 Hz synchronously with ICCD-camera, but at any point of the discharge or its afterglow. This means that we obtain some average picture of additional OH production due to the discharge. In a second regime the synchronization of the discharge and PLIF imaging was organized with the help of special delay system. We observed significant enhancement of OH production in early afterglow of the discharge, and OH decay between high-voltage pulses.

We controlled separately background from a laser without flame and discharge (it was zero in all investigated regimes), emission from flame without discharge, LIF image of flame without discharge, LIF of flame under the discharge and emission at the same regime. It was possible to extract different images from each other. We accumulated the signal during 90 s at laser repetitive frequency of 10 s. Fig. 6.38 represents results of non-synchronized LIF imaging of OH in the flame and in discharge + flame (discharge emission is extracted). Gate of CCD-camera during the experiment was equal to 30 ns. We were able to extract region of additional OH production by the discharge.

Using these experimental results we proved that there is a zone of additional OH production in the discharge (it is designated as “area 1” in the Fig. 6.39) and that the combustion under the discharge is more intensive (the emission drops faster — see “area 2” in the figure).

Fig. 6.40 gives an impression about OH (ground state) distribution in a regime when flame does not exist without the discharge. The most typical feature of this regime is the presence of bright spot with high OH density above the discharge zone. Thus, we were able to obtain planar LIF images of OH distribution in a ground state in the process of combustion assisted by plasma of nanosecond discharge. These results are very important for analysis of kinetics of plasma-assisted combustion.

The comparison of OH and OH* profiles (fig.6.41 along the flame height have showed that in flame without discharge the intensity maximum of OH* is situated closer to the burner than the intensity maximum of OH. Probably, this occurs because of different kinetic mechanisms of OH and OH* formation. In particular, excited OH can transform to OH in ground state, for example, in processes of collisional quenching, while the direct (non-chemical) excitation mechanism of OH in flame is absent. We compared emission

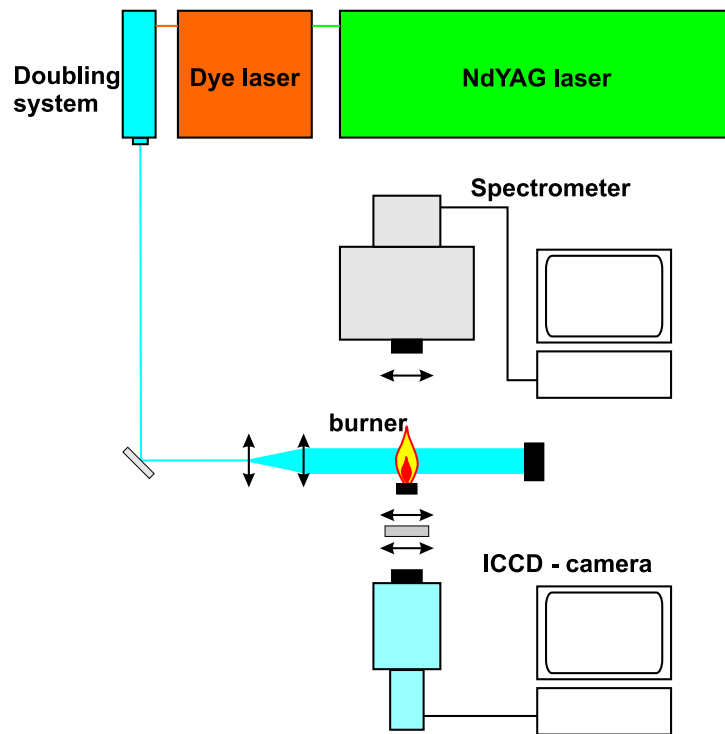


Figure 6.36: Scheme of experimental setup for planar laser-induced fluorescence measurements of OH distribution in flame and discharge.

intensity with and without discharge. It was found that when discharge is on the intensity maximum both for OH and OH* move toward the nozzle (fig.6.41). The largest shift of LIF-signal profile maximum was 5 mm (the distance between flame and nozzle was 15 mm). The flame regimes with flow velocities beyond blow-off limit (without discharge) were investigated, and it was found that presence of discharge results in formation of flame region with increased OH concentration near the unburned mixture. An analysis of intensity profiles have showed that data obtained using LIF-diagnostics are in agreement with emission spectroscopy data. Profile of concentration of OH in flame becomes narrower under the action of the discharge and moves toward the unburned mixture. This is the evidence of combustion acceleration. The OH concentration growth rate in flame front is increased too. It's seen that OH concentration grows near the burner nozzle in comparison with that one without discharge.

Then we have built the synchronization system which allowed to perform measurements with 10 μ s accuracy. With this system measurements were made for stable flame (with flow velocity lower than flame blow-off velocity without discharge). Unfortunately, no significant effect was found, just the difference between flame with discharge and flame without discharge.

Then we remembered that earlier¹⁷⁵ we have obtained the profiles of excited OH for different flow velocities (see fig.6.12). This graph demonstrates that the behavior of OH(A) depend strongly on gas flow velocity. It's distinctly seen that the typical two-humped picture appears only at high velocities, for example, beyond the blow-off limit. The first peak corresponds to OH production in the discharge, and the second corresponds to OH formation in combustion processes.

So, to provide spatial resolution of these two peaks, the experiment was performed with LIF measurements beyond the blow-off limit (flame cannot exist without discharge, but discharge cannot ignite this mixture). The results of these experiments are presented in fig.6.42. It's seen very well that near the burner nozzle formation of OH proceeds, similar to that one for OH(A). OH maximum corresponds to 1 μ s, this result coincide with calculations for OH dynamics which were performed above. Because of low temporal resolution we were unable to see OH formation at nanosecond time scale, but OH reduction is seen very good. OH dynamics and front wideness are presented in fig.6.43-fig.6.44. The changes in the front sharpness corresponds to flame "blow-off" - and only a new portion of O atoms, which are produced in a new pulse, tends the flame to return to the nozzle.

These results confirmed the theory about radical mechanism of flame stabilization by nanosecond barrier discharge.

6.3.3 LIF diagnostic of OH radical in streamer discharge and its afterglow

Now, when the role of active species is proved experimentally for PAC, it's necessary to build a kinetic scheme which allow to describe quantitatively processes of particles excitation in the discharge, kinetic of excited states and combustion kinetics within the time range 1ns–100mks. At present moment we are able to calculate the discharge stage with particles vibrational and electronical excitation and ionization for known reduced electrical field and kinetic stage at temperatures higher than ignition threshold, where reaction constants are known rather good.

The main problem is to perform quantitative calculations for the stage where excited states reacts at temperatures between 300-800K. This parameters range is extremely important for the task of plasma radical assisted ignition combustion because it's necessary to understand, how is the radical mechanism works: by heating in recombination or by heat release in chemical reactions. We have showed earlier that both mechanisms are important depending on the certain experiment parameters, but there were a lack of kinetic data to determine the relative effectiveness of these mechanisms precisely for different cases. At present moment there is no kinetic scheme which is capable to describe current experimental results of different groups of researches in this parameters region, especially for atmospheric and evaluated pressures, where discharge propagates in spatially and temporally non-uniform form. That's why we began experiments directed to obtain kinetic data of excited states reactions constants and radicals production and to build a kinetic scheme of processes in this parameters and time ranges.

To perform measurements a new setup was constructed. In the center of a circular ceramic nozzle with 5 cm in diameter a stainless steel needle was placed, which was one of the electrodes. The second electrode was placed into the quartz tube with one end soldered, so dielectric barrier discharge took place in this configuration. Typical distance between electrodes was 5 mm.

The methane-air mixture was supplied through the nozzle with the velocity 1 m/s. The preheating system allowed to change the gas mixture temperature within the range 300–800 K. The scheme of setup is presented in fig. 6.45. Measurements of dynamics of discharge development with nanosecond resolution were performed using ICCD camera synchronized with discharge of 5 Hz frequency and 20 kV amplitude, pulse length is 50 ns.

The integral photo of discharge you can find in the right part of figure fig 6.45. To measure OH radical concentration saturated laser-induced fluorescence technique was used with absolute calibration with the aid of flat laminar burner flame.

Preliminary experiments were conducted for different temperatures: from 300 K up to 620 K, the results are presented in dots in fig.6.46. The typical concentration of OH radical is 10^{14} cm^{-3} . The effective recombination constant of OH depending on the gas temperature is shown in fig. 6.47.

The calculations were performed for this experiments using the data for energy input from incident and reflected electrical pulses. GRI-Mech 2.1 scheme was used. The preliminary calculations have not showed even qualitative correspondence: on microsecond timescale the growth OH was observed in calculation. Because of this, the scheme was modernized and reaction with participating of O(1D) were added. The results for this calculations are presented in fig.6.46 with lines. There is a good correspondence for high temperature and poor one for low temperatures. This is the evidence that it's necessary to perform detailed measurements to build an accurate kinetic scheme to describe plasma-assisted ignition at intermediate temperatures.

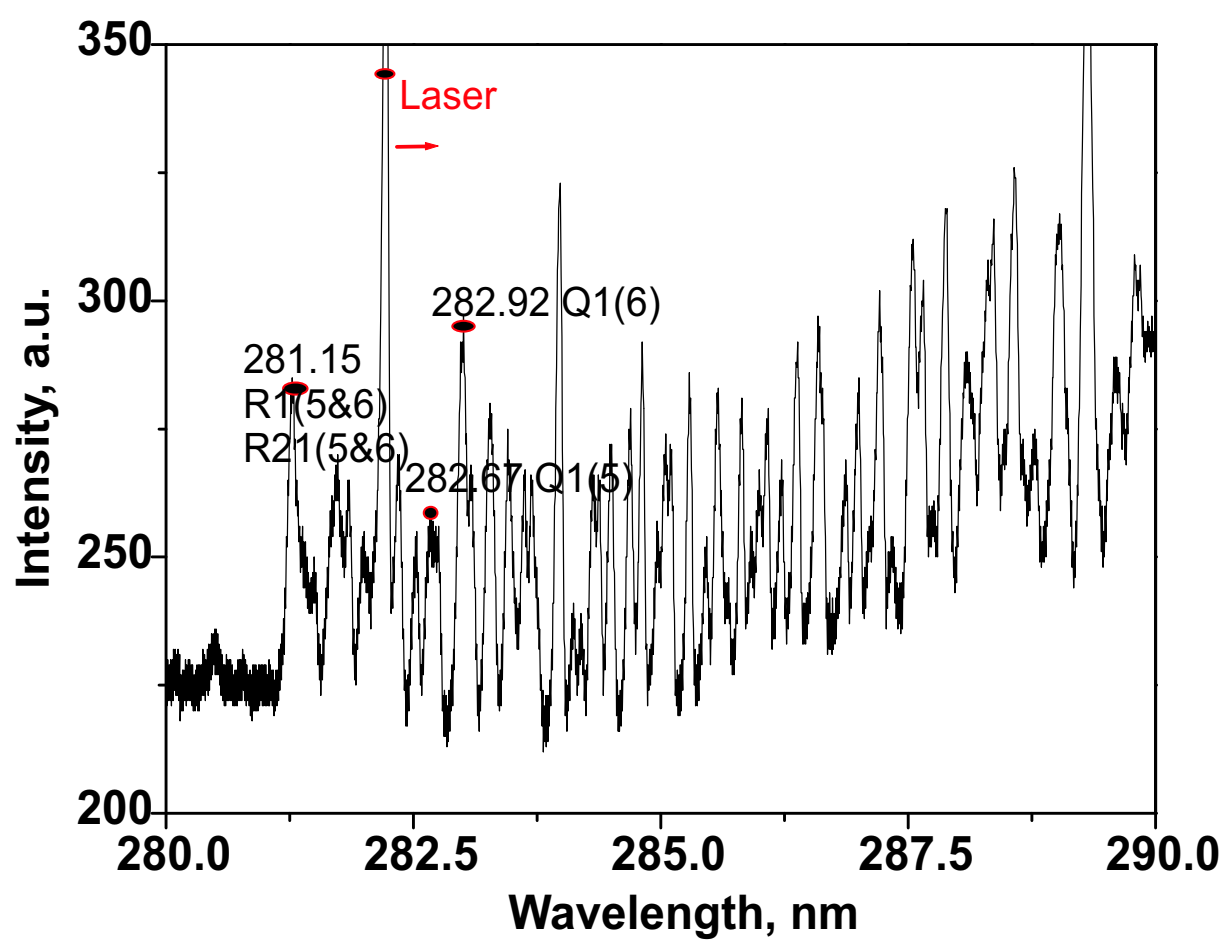
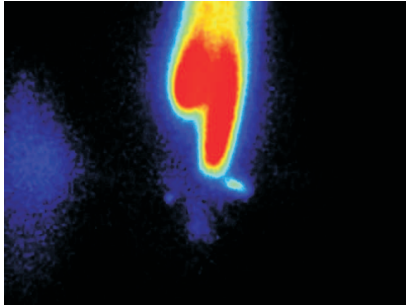
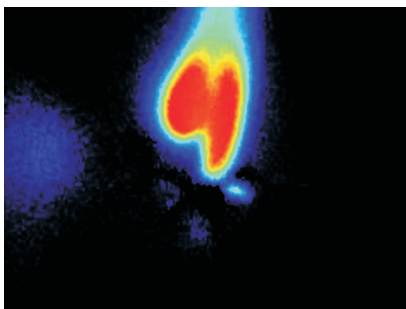


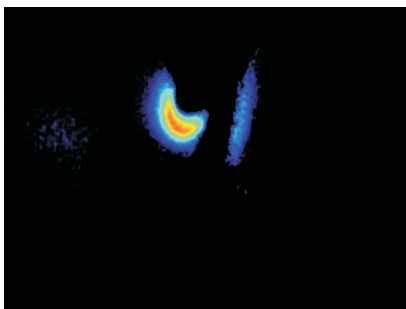
Figure 6.37: An example of OH emission from the burner together with laser scattered emission.



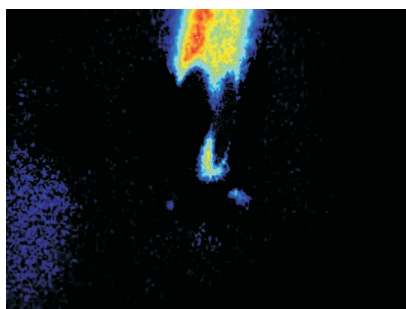
OH in a ground state.
Flame without discharge.



OH in a ground state.
Flame with discharge.



Additional OH production
in flame under
discharge action.



Excessive OH
production in flame.

Figure 6.38: An example of PLIF images. Analysis of additional OH production in nanosecond discharge and difference between OH in flame and in the discharge. $ER=1.07$. Air consumption is 470 l/h, propane consumption is 20 l/h, flow rate is 4 m/s.

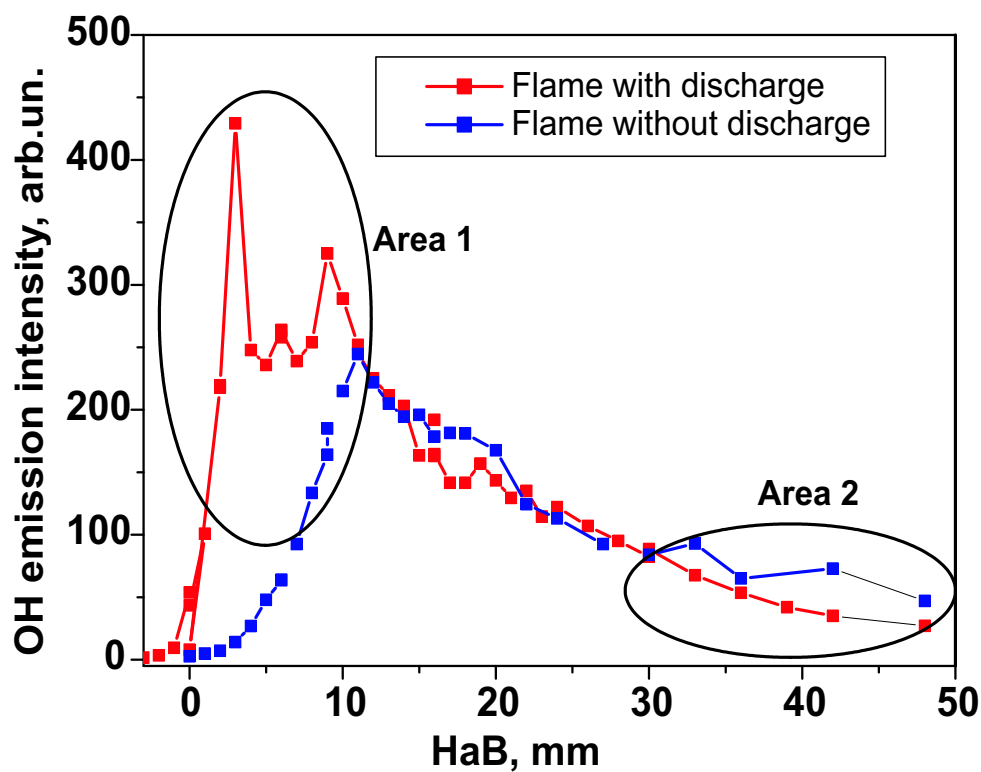


Figure 6.39: OH excited state emission at 306.4 nm with and without nanosecond discharge. HaB means “height above burner”.

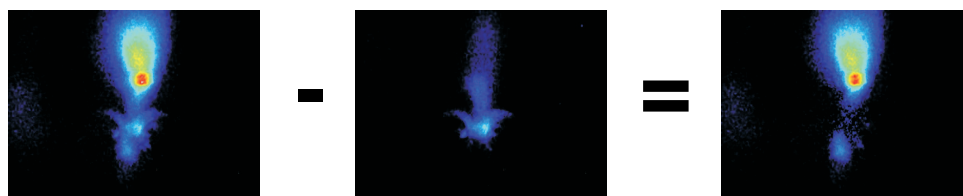


Figure 6.40: An example of PLIF images. $ER=0.93$. Figure demonstrates extraction of emission of the discharge. It was not possible physically to extract flame without discharge: this point is at higher velocity, that blow-off velocity without the discharge. Air consumption is 551 l/h, propane consumption is 20 l/h, flow rate is 4.7 m/s.

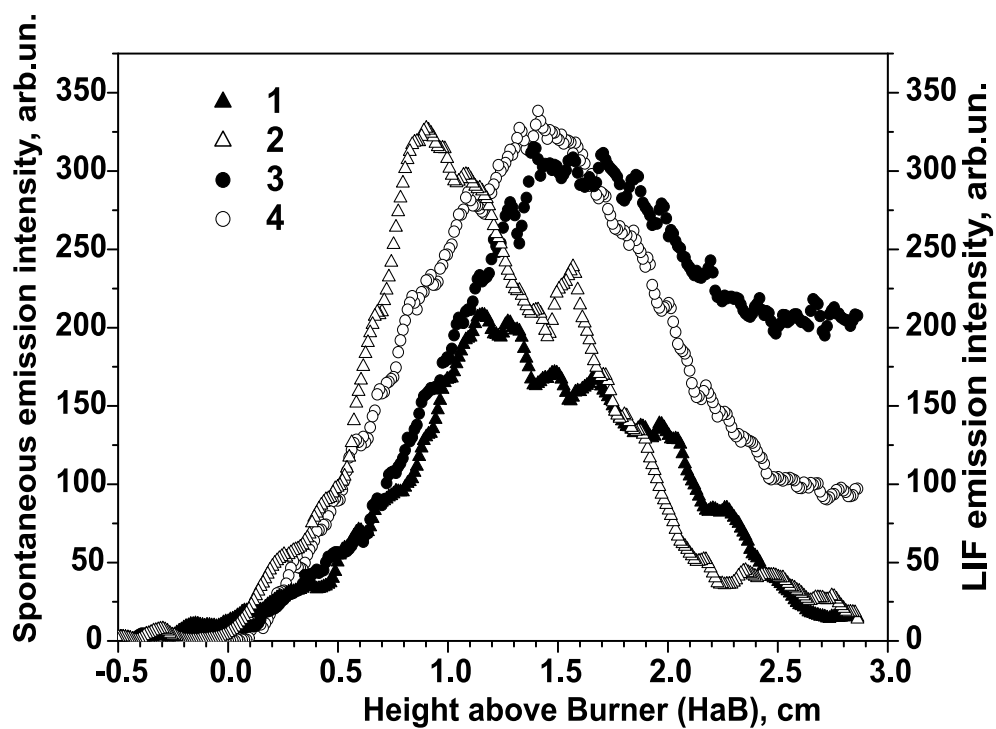


Figure 6.41: Profiles of spontaneous OH emission (1- in flame; 2 - in flame with discharge) and LIF signal, which corresponds to OH concentration (3- in flame, 4 - in flame with discharge).

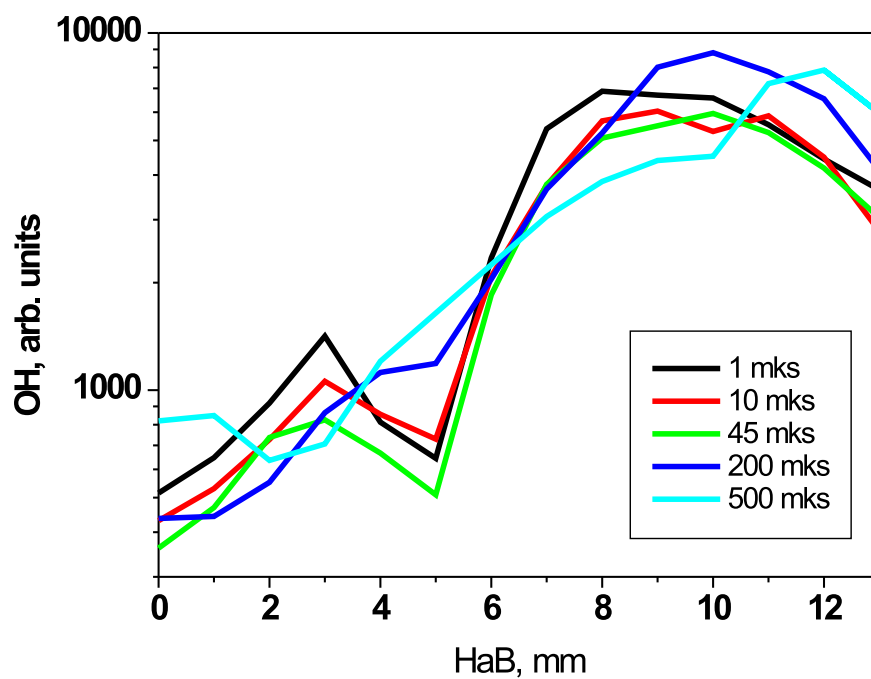


Figure 6.42: LIF OH profiles between two discharge pulses at different time moments

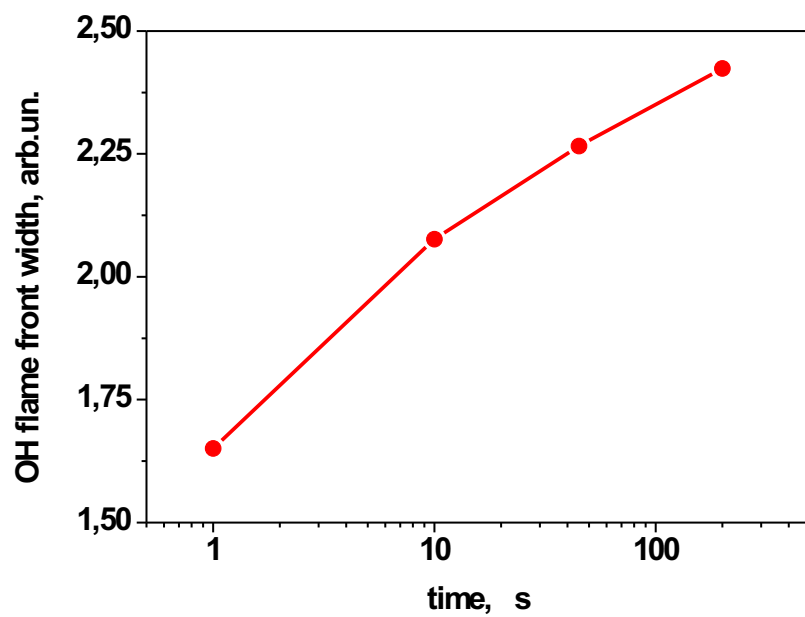


Figure 6.43: Temporal dynamics of flame front width between pulses

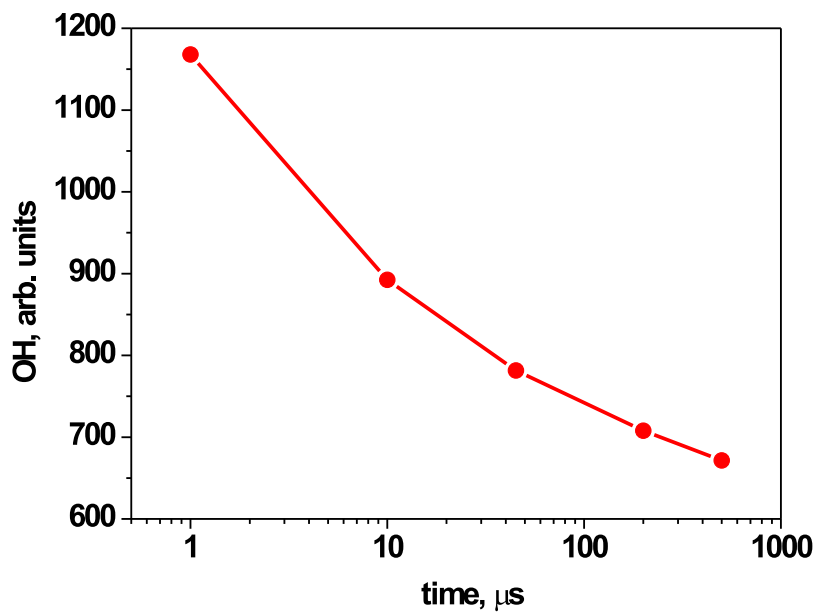


Figure 6.44: OH temporal dynamics between pulses at fixed distance from burner nozzle (1st maximum decrease)

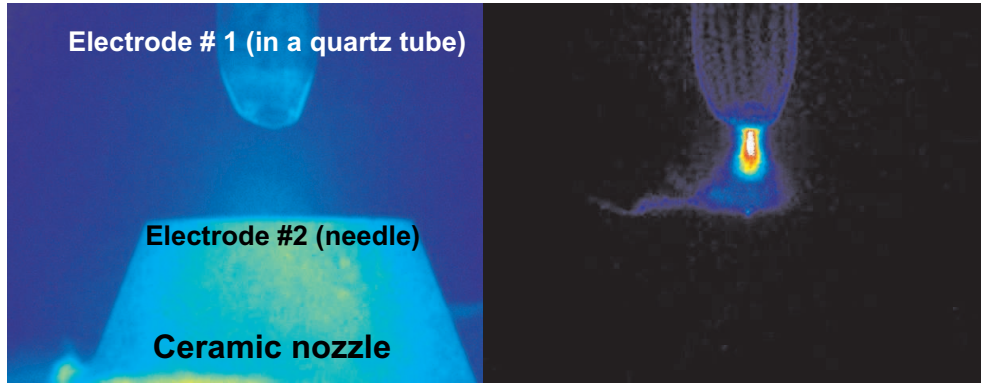


Figure 6.45: Scheme of experimental setup (left) and the integral picture of streamer discharge (right).

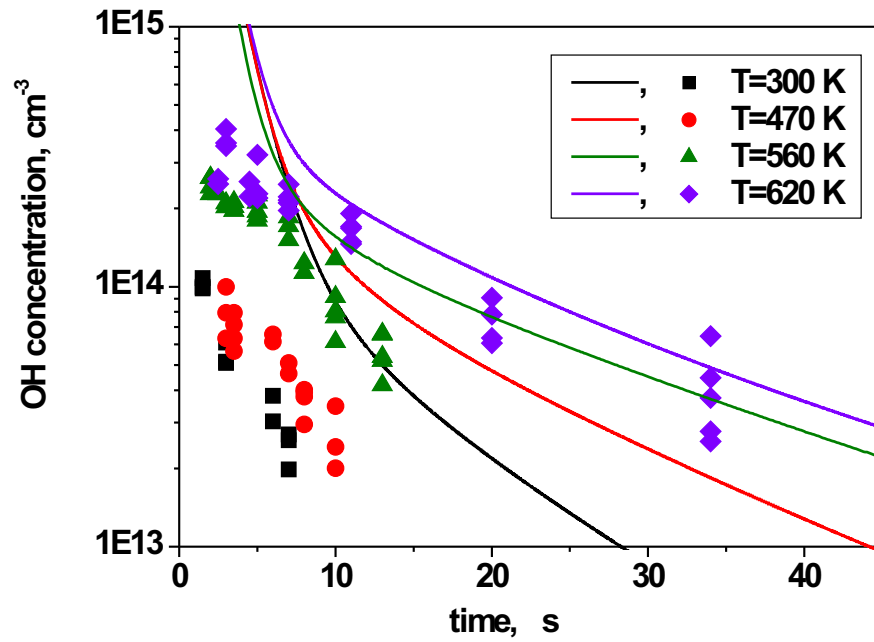


Figure 6.46: Experimental measurements of OH concentration in the streamer discharge afterglow (dots) and results of modelling using GRI-Mech2.1 scheme with O(1D) kinetics (lines).

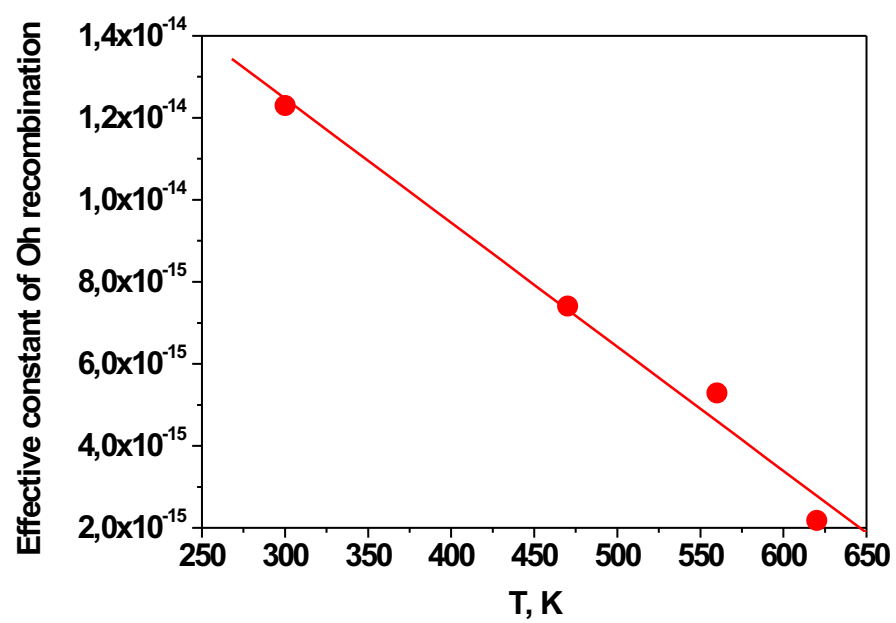


Figure 6.47: Effective recombination constant of OH depending on the gas temperature.

Chapter 7

Liquid Fuel Atomization Using Nanosecond Discharge

7.1 The aim of investigations

In many practically important combustion processes in the beginning a fuel is not in a gaseous phase but in liquid or solid phase, and than mixes and burns with gaseous oxidizer. These concerns jet engines, car engines, and diesel engines working on kerosene and gasoline. The burning of solid fuels occurs during coal combustion, wood combustion during forest fires etc. Important problem is also to perform household and industrial rubbish, or oil with low effective fuel content, which couldn't burn under common conditions.

These put additional problems in combustion description, connected with phase transitions and presences of phase boundaries. In addition to gas phase processes (chemical reactions, molecular transfer processes), it's necessary to take into account the similar processes in liquid and solid phases and at phases' boundaries. Also the flow is turbulent as a rule.

During liquid phase combustion some main stages could be distinguished. The first is the injection of fuel into the combustion chamber filled with oxidizer through the sprayer (mechanical, pneumatic, combined etc.) and further mixing of fuel drops with oxidizer. Inside the sprayer liquid breaks into small drops with aerosol production. The parameters of this aerosol determine the energy output of mixture combustion.

The second stage is fuel drop vaporization and gaseous mixture combustion. The smaller the drops, the more effective mixing occurs. There is no combustion of drop itself, only drop's vapour are burning. It's well-known that drop's combustion rate is proportional to the second power of drop's diameter (d^2 -law), so the initial drop size has the crucial meaning for combustion rate. With drop size decrease mixing time becomes shorter, thus the combustion proceeds faster. This fact allows, for example, to reduce the engine size, this is important in mobile engines. Usually the vaporization occurs due to thermal flux from the reaction zone. An additional vaporization could be maid by drop heating if we apply discharge to the mixing zone or by charging the drop using high values of reduced electric field in nanosecond discharge.

It was found earlier by the authors^{113-, 247} that nanosecond discharge could strongly influence on the ignition delay and combustion rate of gaseous mixtures. The main role is played by active particles (such as O, H, OH), which are responsible for chain branching.

These particles are additionally produced under the discharge action, primarily by excited nitrogen quenching on oxygen molecules, and followed by combustion intensification, which shows itself in an OH emission peak shift and narrowing of area of growth of radicals concentration. Thus, this is the reason to expect increase in the combustion rate of heterogeneous mixtures as well. The investigations of the streamer discharge showed that when the discharge gap is small enough, the reduced electric field exceeds breakdown field in the air both in the streamer head and in the channel, so active particles are produced inside the gap. At larger distances the main active particles production takes place only in the streamer head, so the effectiveness does not depend on the pulse duration. When gap is long enough, the streamer couldn't propagate and only a corona develops near the pin, so the larger part of the gap is not treated by the discharge and wasted. On the contrary, at short gaps production of radicals exceeds required one. Thus, when nanosecond discharge is using, combustion rate could significantly increase. But the effectiveness of plasma-assisted combustion depends on type of discharge, pulse duration, pulse repetition rate and other parameters, which are responsible for active particles production. Development of the streamer in different regimes was studied, optimal regimes were found. During experiments it was shown that nanosecond discharge could increase reaction rate and provide effective production of hydrogen from methane and water vapour mixture. The hydrogen output in a non-optimized discharge configuration is 10 times smaller than theoretically possible, but the principal possibility of influence on reaction rate with participation of water vapour was shown.²⁴⁷

It also was found in²⁴⁸⁻¹⁷⁵ that electric fields and discharges could strongly affect on the diffusion flame. Using the electric field, applied parallel to the gas flow, we can stabilize flame on the burner or cause self-sustained oscillations of the flame. The main mechanism lies in changing the diffusion coefficients between oxidizer and fuel under the ionic wind action, after which the combustion rate could increase.

Thus, using nanosecond discharge pulses in combination with high values of reduced electric fields, we can influence on combustion rate by radicals production. Using combination of nanosecond discharge with high values of electric field, we can avoid the using of dc high-voltage in the engine and possible breakdown. So, besides proper form of energy input, proper organization of discharge is of great importance. We are going to provide effective atomization using an optimal configuration of nanosecond discharge first and then move to mixing and combustion investigations, based on results obtained earlier.

7.2 Experimental setup

At present time the set-up for experimental study of fuel atomization is constructed. The main parts are high-pressure cylinder and a system of atomization with sprayer (fuel injector), diagnostic systems for pressure control, control of electrodynamical parameters and liquid drops parameters control. Overall view of experimental setup is presented in the figure 7.1.

Atomization system consists of high-pressure cylinder of 5 liters volume. Maximum pressure is 150 atm. The vessel is fixed near the optical table, where optical diagnostic is placed. The vessel's mounting elements allow to move vessel in three dimensions.

Sprayer was screwed onto the bottom orifice of this vessel. Sprayer was combined with electrode systems, but in some configurations we used external electrodes (steel ring or

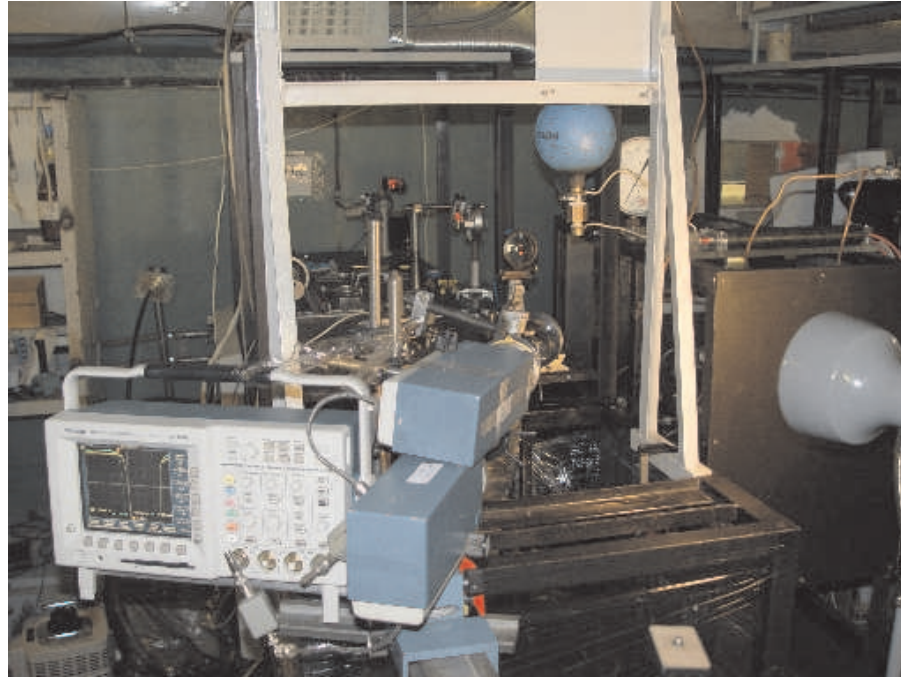


Figure 7.1: Overall view of experimental setup.

steel mesh or system of meshes). We used different sprayer configuration. It's well known that different sprayer configurations are exist: mechanical, pneumatic, combined etc., depending on the mechanism of liquid fragmentation. In SCRAMJETs a simple sprayers are typically used, without any additional ways of breaking up: aerated fuel (kerosene) at pressure 1-3 MPa yields through an orifice with typical dimension of 0.5-1.5 mm to combustion chamber. All geometries we used were made based on this idea; some of them are presented in fig. 7.2. In fig. 7.3 the shape of atomized liquid is presented for some sprayers. It's seen that the angle of cone of atomization was quite small, and only using external electrode it was possible to provide large cone's angle.

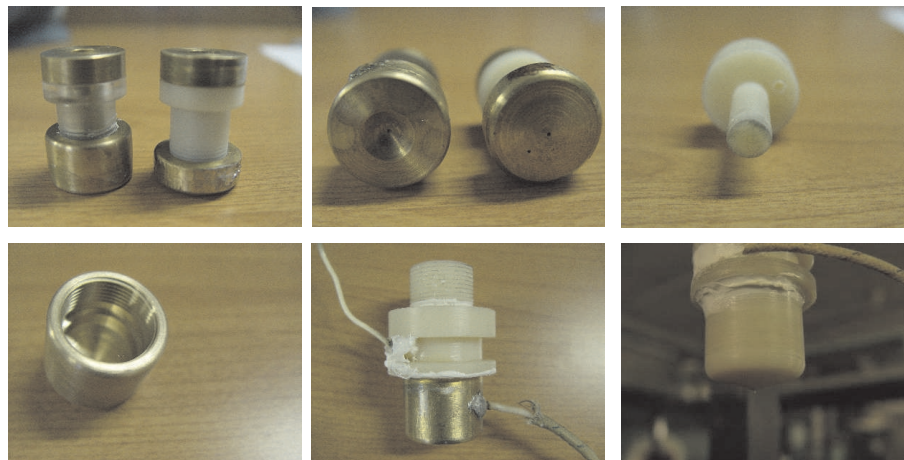


Figure 7.2: Different sprayers construction.

We assembled an optical setup for drops' parameters measurement based on phase-

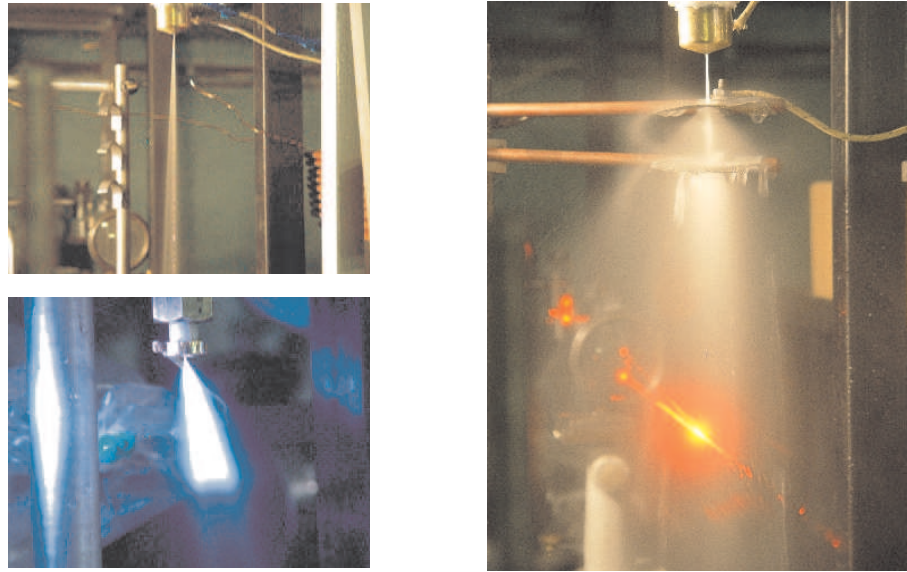


Figure 7.3: Atomization pattern for different configurations.

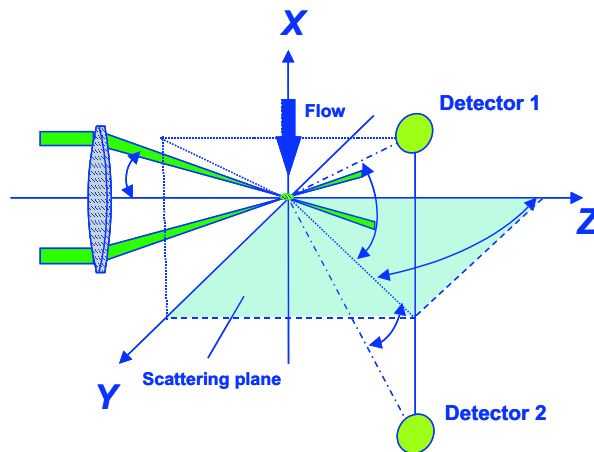


Figure 7.4: The principal scheme of PDA system

Doppler anemometry method - PDA. This system allows to measure drop size and velocity during atomization. . The range of drop parameters which could be measured by this system are: velocities up to 20 m/s, drop diameter from 10 up to 300 μm .

Main elements of PDA system (the principle scheme is presented in fig.7.4) are He-Ne laser (632 nm), system of laser beam splitting, focus system and 2 photosensors (we used PEM-100). After splitting two coherent beams obtained intersect in the region to be studied. When the drop crosses this area of interference, laser light reflects and scatters, depending on the system parameters. We can choose parameters which allow to work with only one, dominant mechanism. Then the light scattered is detected by two PEM, placed together at some angles. Analysis of interference picture obtained allows to determine drop size and velocity: velocity is proportional to the period of interference, and the size is proportional to phase shift between two channels. This value depends on setup geometry (distances and angles, laser wavelength) only. You can see typical oscillogram on fig. 7.5. We used two different nanosecond pulse generators as a source high-voltage

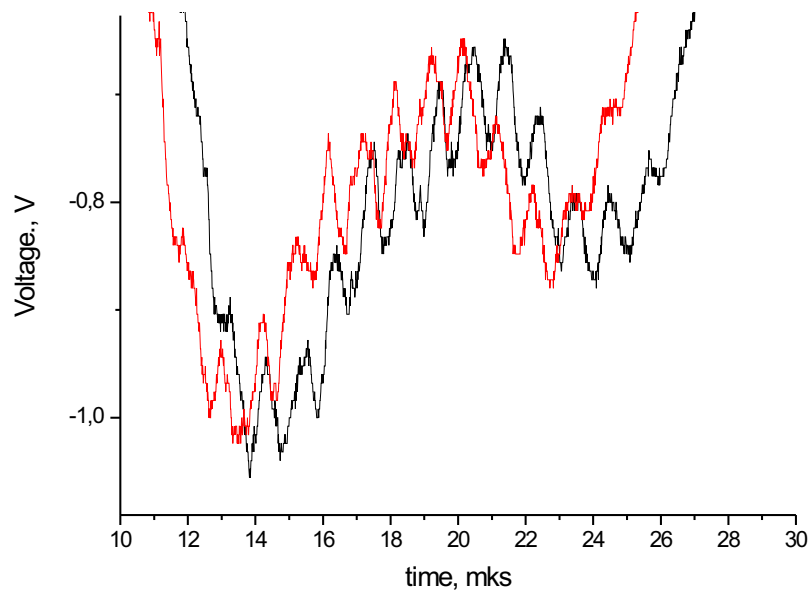


Figure 7.5: Typical oscillogrammes for drop's size and velocity determining.

pulses. The first is generator by FID Technology (Russia) (fig.7.6). This device provides short stable pulses, each one with 12 ns FWHM. The amplitude could be varied within the range of 5-15 kV, the frequency range was 1-100 kHz. Maximum output power is 3kW (if pulse is absorbed entirely). The generator has two outputs, with pulses of positive and negative polarity between central line and grounded cable armor. Thus, the maximum voltage drop between electrodes could reach 30 kV. The typical pulse form (both for incident and reflected pulse) is presented in figure 7.7.

The other generator is rotated-interrupter scheme generator (RISG), which was used in our previous experiments. This generator has fixed frequency of 5 kHz, and pulse form could be varied from pulse to pulse. The mean FWHM is approx. 40-60 ns, the form of pulse is dome (time of front rise is large, approx. 15-20 ns. Total power of this generator was also smaller then of previous one - approximately 0.5 kW, but the energy per pulse was greater. The advantage of this generator is the possibility to provide larger voltage drop between high-voltage electrode and grounded electrode (up to 30kV). This fact was important when we have worked with electrodes configuration which didn't allowed to provide high-voltage supply of different polarities on both electrodes due to constructive features.

During experiment liquid (we used water in our experiments as a test liquid to obtain preliminary results) has being pouring into the cylinder. After this, all vessel's orifices have being closed and the cylinder has being filled by air at high pressure and atomization started. The pressure range was 2 up to 100 atmospheres. During experiment oscillogrammes from optical system (which allows to obtain drop velocity and drop size) and time of atomization (liquid consumption) were measured as well as working pressure. We shoot a movie during atomization which allowed to determine angle of atomization cone.

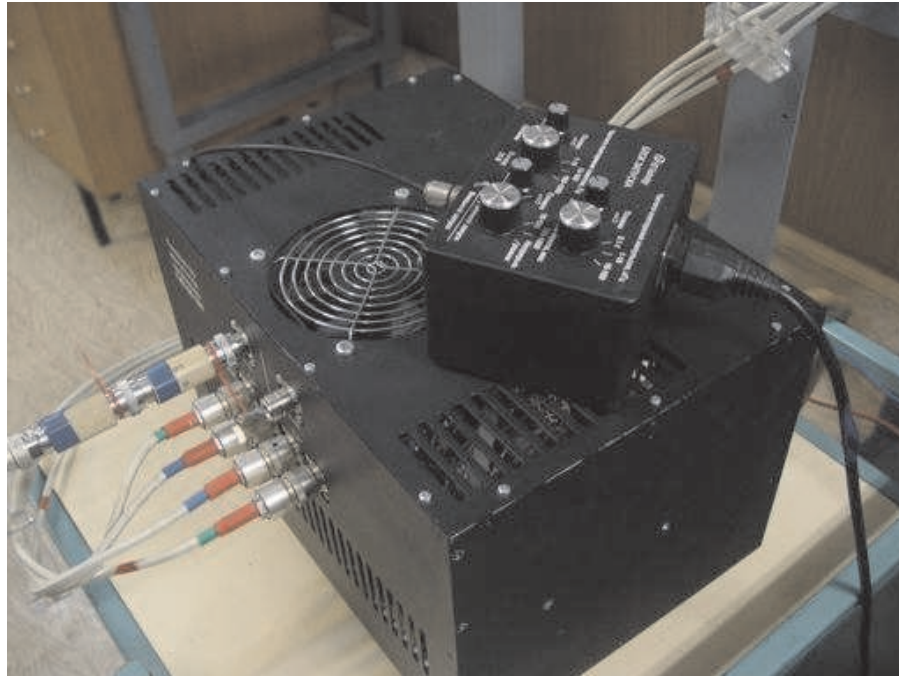


Figure 7.6: Generator by FID Technology (Russia).

7.3 The results of experiments

As it was mentioned above, the aim of this work was to obtain the influence of nanosecond pulsed discharge on liquid atomization. There are several main reasons why electric field or discharge can promote effective atomization:

- Discharge, if properly organized, could provide additional heating and vaporization. In this case, the discharge shows itself only in thermal effect.
- Discharge could provide local heating in the sprayer and increase local pressure. This allows to change atomization parameters.
- Discharge could charge drops or polarize it. In this case, drop's charge prevents them from coagulation.

Some other mechanisms of influence are also possible.

We have tested a number of different electrodes' configuration in the nozzle, some of them are presented in fig.7.8. The first configuration we used was the following. The sprayer consisted of three parts: two metallic electrodes (0.5 mm thick) and dielectric layer between them (1 mm thick), the sprayer diameter is 0.6 mm. Schematic view of this construction is presented in fig. 7.8. Discharge could develop through the water along dielectric surface. According to our hypothesis, breakdown, if happened, leads to pressure increase and changes in atomization pattern.

Analysis of atomization pattern has showed no difference between atomization with and without discharge (fig.7.9). It's seen that angle of atomization cone is the same. Nevertheless, in some cases it was found that when discharge is turned on, the atomization cone changes (fig.7.10). But this changing wasn't stable and probably was due to

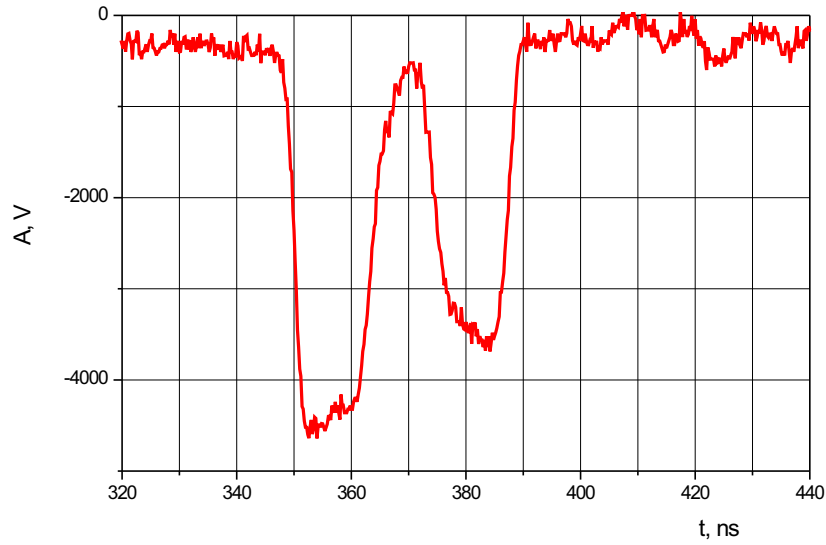


Figure 7.7: The typical pulse form (both for incident and reflected pulse)for FID generator.

dielectric structure deformation under discharge influence. Such deformations were the first drawback of this configuration. The second was a weak electric field produced by external electrode.

We have made a number of estimations to determine the possible discharge influence. The discharge energy is significantly greater than the energy of a flow (5-50 W for flow velocity 20-70 m/s). But the influence in terms of heating isn't so great. The maximum possible energy input per one pulse by our generator is 30 mJ. This energy allows to heat and vapourize appr. 10^{-5} grams of water (it worth mention that for kerosene this value is approximately one order of magnitude greater). So it's necessary to have a number of pulses through the same water portion for effective influence.

We have measured the dependence between pressure in the vessel and atomization time. It was found that only at relatively low pressures (up to 3 MPa) there is a strong linear dependence between these parameters. At higher pressures atomization time doesn't depend on the pressure. Thus it's possible that even if discharge produces additional pressure inside the sprayer, it doesn't provide changes in atomization pattern.

Third configuration implies using an external electrode. Previous experiments have showed that it's necessary to provide uniform discharge propagation instead of filamentary and try to influence on the area where liquid from sprayer have converted into drops. Different configurations were tested: with external ring inside and outside flow, with mesh and two meshes. Unfortunately, no effect was found primarily even in this case the discharge propagated through the air instead of water. Thus, the efficiency of influence was extremely low, even in case of two meshes (7.11).

In second configuration we have tried to eliminate all these problems (fig.7.8). An external electrode becomes a cone, and the central electrode was a thick needle placed in the center of sprayer. In this configuration external field was weak again – the electrode's cone angle was too big, but the dielectric layer was absent, so breakdown should develop

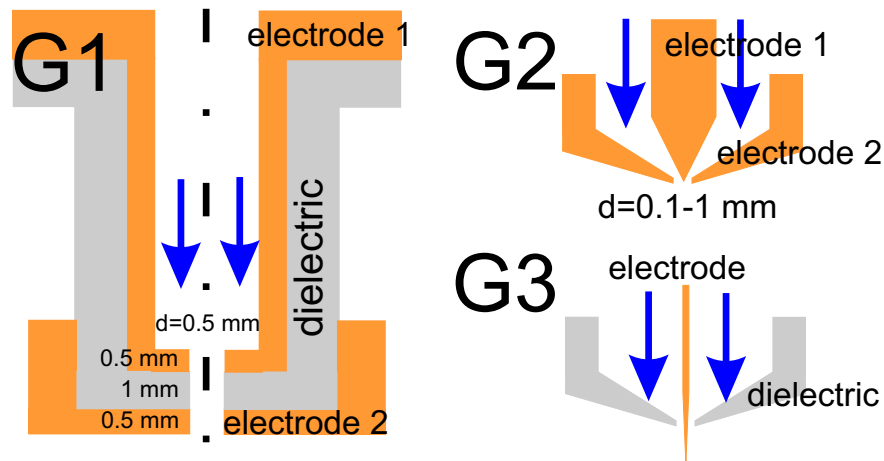


Figure 7.8: Different electrodes configurations inside the sprayer.

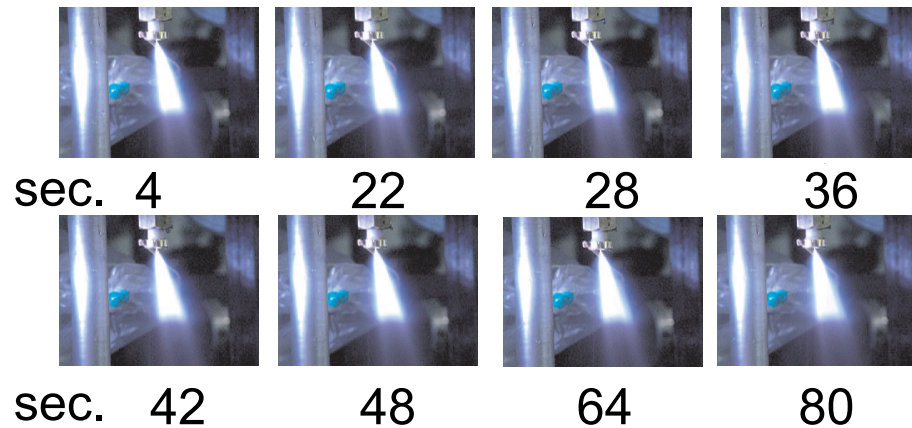


Figure 7.9: Cones comparison with (top) and without (bottom) discharge

through the water. Also a gap between electrodes was reduced - from 1 mm to 0.3 mm. This allowed to obtain breakdown at lower frequencies and amplitudes.

The influence of discharge was observed during the regime of strongly aerated liquid atomization, which happened at the end of atomization. During this stage, the cone's angle becomes significantly greater (because of additional air involved into atomization). The discharge showed itself in two ways: the optical density of the flow becomes lower and the atomization time decreases too (fig. 7.12-7.13).

The significant effect was found when we used electrodes configuration G2 with a thin needle placed in the sprayer as a central electrode, so the flow was effectively treated by the discharge, if breakdown occurred. Also a minimal gap between electrodes was reduced up to 0.1 mm to provide effective breakdown. Depending on the liquid consumption, breakdown occurred at some pulse frequency within the range 10-100 kHz. After this it was possible to reduce frequency significantly, and stable regime still remained (it's necessary to have larger amount of energy input to perform breakdown than to sustain it).



Figure 7.10: Changing in atomization cone under discharge influence

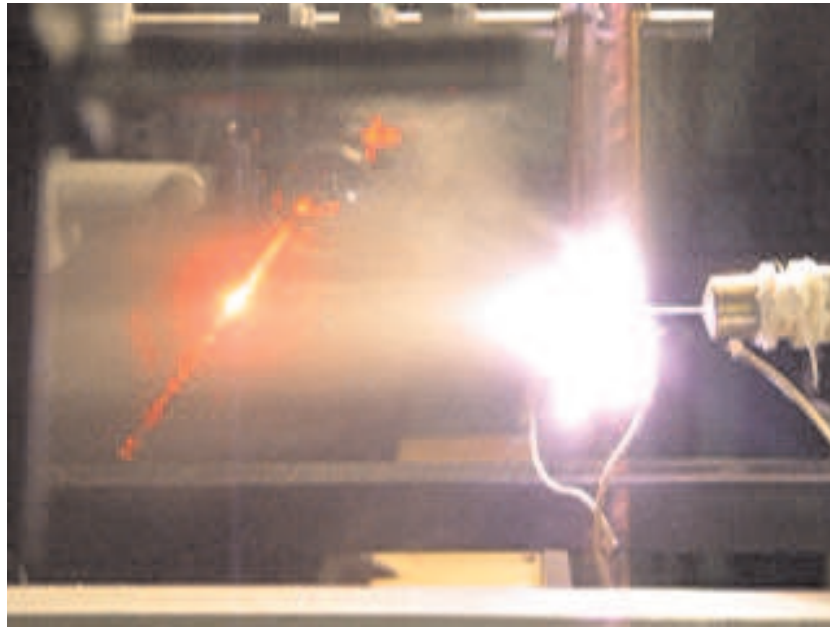


Figure 7.11: Discharge propagates through the air instead of water and plasma treatment is non-uniform.

In this operation mode a strong influence was obtained on the flow parameters. Without discharge no effective atomization occurred. Within pressure range up to 2 atmospheres a flow was broken up to the drops under the discharge action (fig.7.14). At low pressures the pressure value determines liquid consumption, that's why at pressures higher than critical one, depending on the frequency, the breakdown failed to set itself, and the influence of discharge had been diminishing.

The dependence of the liquid consumption versus vessel pressure is presented in figure 7.15. It's seen quite well that starting with some pressure, the consumption is determined only by sprayer configuration and doesn't depend on vessel pressure. For our task, it's necessary to increase energy input approximately 3 times for working in the regimes which are close to typical in aviation engines. Now it's possible to atomize flows with velocities up to 30 m/s (20 g/sec). The main mechanisms lies in liquid vapourization and pressure pulsations generation in the sprayer. It was measured that atomization time grows in the case of atomization under discharge influence approximately 15-20%.

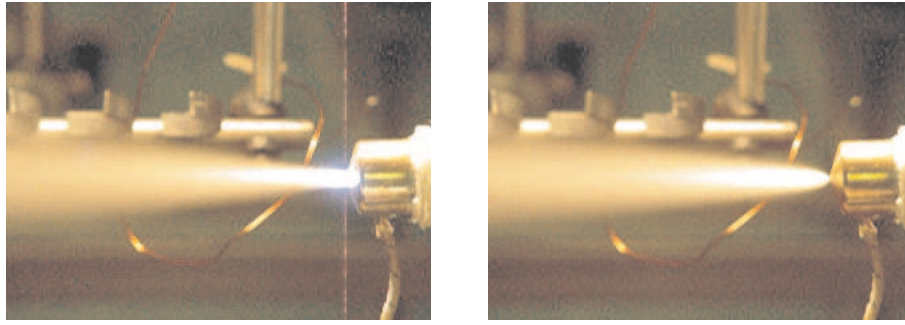


Figure 7.12: Changing in atomization cone of aerated liquid under discharge influence

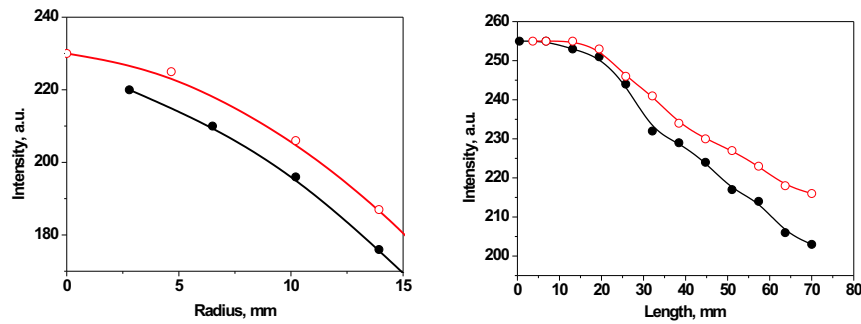


Figure 7.13: Emission profiles for atomization cone's length (right) and radius (left). Red unfilled circles - without discharge, black filled circles - with discharge

The influence of nanosecond discharge on liquid atomization was investigated in this paper. It was found that nanosecond pulsed discharge affects strongly on the liquid atomization. With liquid consumption up to 20 g/sec (and discharge power 3kW, which corresponds to 5% vapourization) it's possible to obtain atomization of a flow in the regimes where there is no atomization in absence of the discharge. It was found that main mechanism of influence lies in vapourization of water in the breakdown channel with further changes in flow pattern. The maximum liquid consumption for effective atomization is limited by the stable breakdown appearance.

Images of atomization are presented in fig.7.16-7.17. It's seen that drop size is quite large (1 mm) near atomization cone's edges, but small in the cone's center, where atomization is most effective. On the images it's distinctly seen that discharge strongly tubulate the water flow. Because our diagnostic system could work only at small water consumption (at low optical density, low drop's concentration) many experiments were conducted in regimes with small atomization pressure. In such regimes water jet doesn't atomized at all without discharge (see fig.7.18). Maybe, this technique could be applied on practice in these regimes, when it's impossible to ignite kerosene jet and it's necessary to atomize it before ignition.

Drops' sizes and velocities distribution were measured for different discharge frequencies. PDA system was focused at the cone's center, so typical size is quite small - smaller than big drops that flies at maximum angles. The results for different frequencies are presented in fig. 7.19- 7.20. One may see that with frequency increase drop's velocity

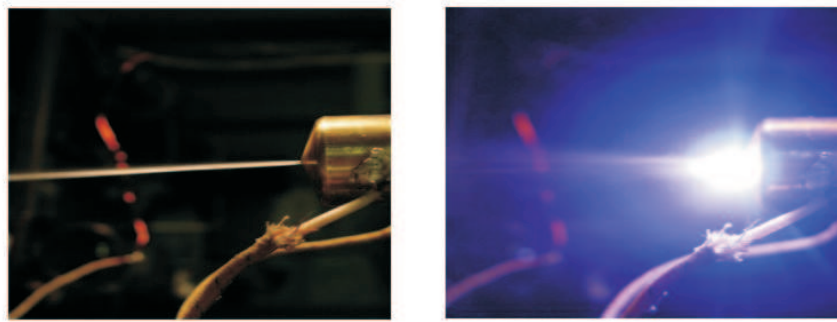


Figure 7.14: Atomization by discharge. Left - no atomization without discharge, right - atomization under discharge influence at same parameters.

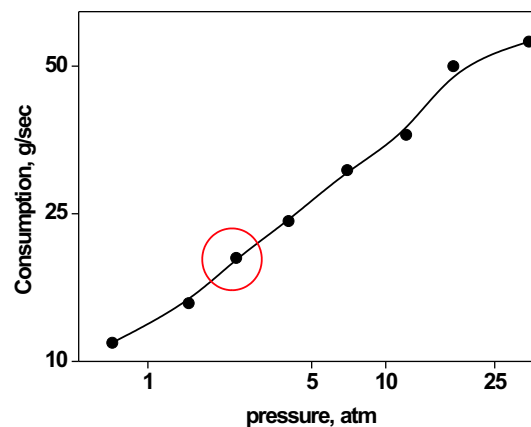


Figure 7.15: Dependence of consumption versus pressure. Red circle shows area where atomization by discharge is possible for our energy input.

significantly decreases (the channel section becomes more closed, water consumption reduces, stronger flow turbulization occurs) while the drops' size remains the same. For every curve approx. 200-300 measurements were made.

It worth mention that during experiment electrodes were evaporating significantly because of high current density. But the changes wasn't as great as they could be with dc arc or pulses with microsecond duration. That's why one should use should nanosecond pulses with high frequency for such purposes. The results obtained have showed with the help of pulsed nanosecond discharge combustion rate of heterogenous mixtures should increase because of effective atomization and effective production of active particles in nanosecond discharge, which are responsible for ignition delay time and flame propagation velocity.

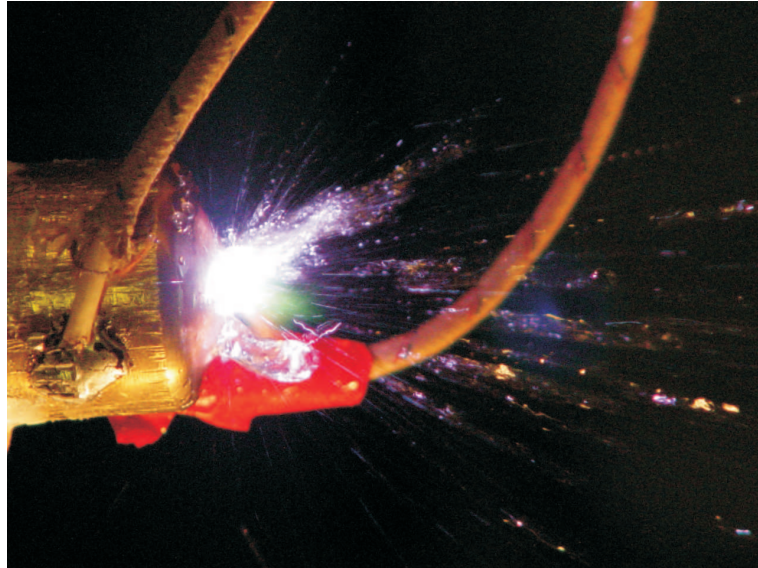


Figure 7.16: Pattern of atomization by discharge.

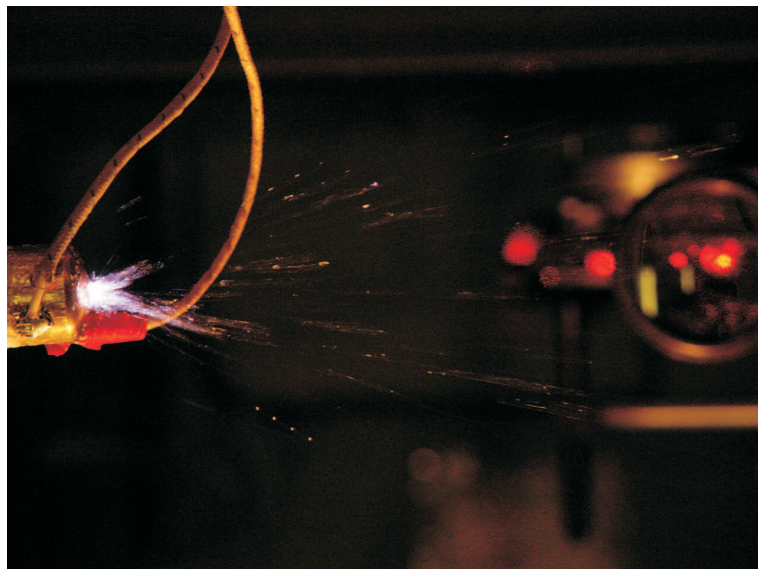


Figure 7.17: Pattern of atomization by discharge.

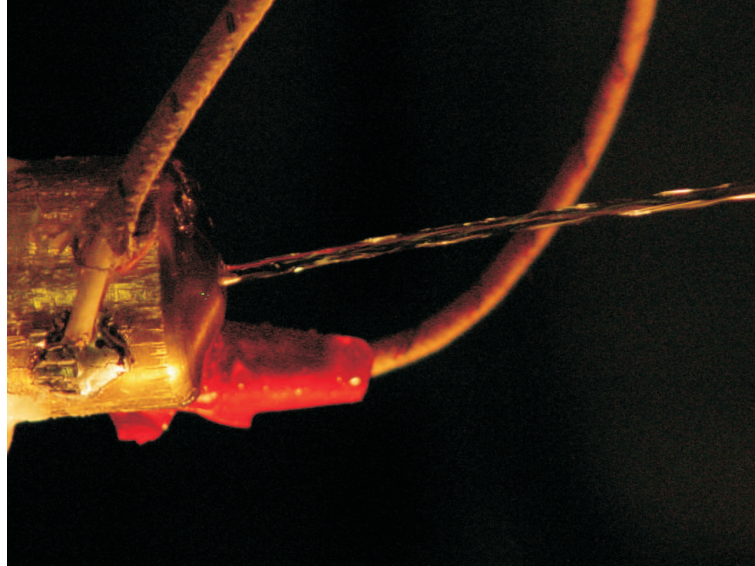


Figure 7.18: Water jet without discharge.

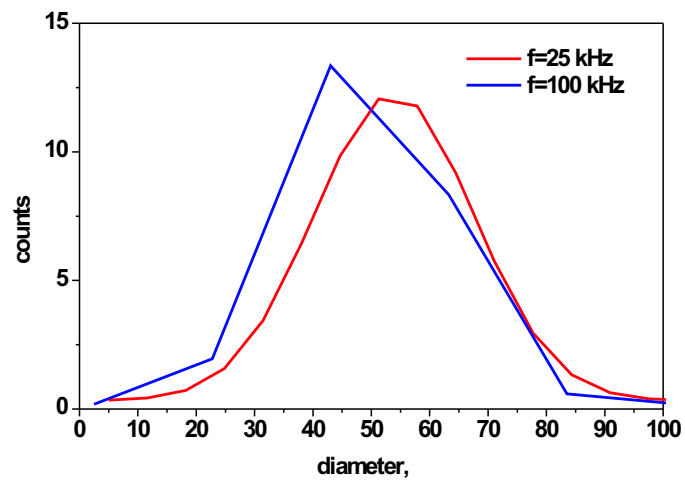


Figure 7.19: Drops' size distribution for different frequencies.

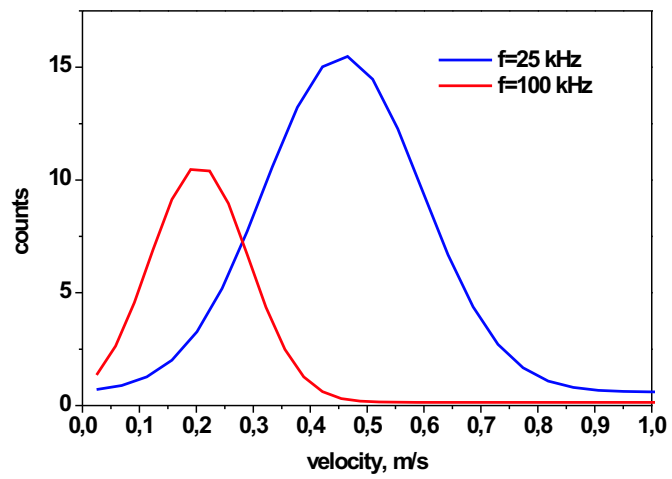


Figure 7.20: Drops' velocity distribution for different frequencies.

Chapter 8

Supersonic Hydrocarbon-Air Mixtures Ignition and Flame Control by Non-Equilibrium Low-Temperature Plasma.

8.1 Hypersonic air plasma flow

In experiments we used continuous operating vacuum tube (Fig. 8.1). Test chamber $\sim 0.5 \text{ m}^3$ in volume was connected by a valve of 350 mm in diameter with main vacuum chamber $\sim 6 \text{ m}^3$ in volume. The volume was pumped by four oil-vapor booster vacuum pumps BN-4500 with 4500 l/s productivity at a pressure of 10^{-2} Torr and by two parallel mechanical pumps VN-6G. The total pump rate was 18000 l/s at a pressure of 0.1 Torr. Additional rotary pump with a productivity of 5 l/s allowed to pump test chamber separately.

Hypersonic plasma flow was formed when work gas expanded from forevacuum chamber to test chamber through the conical nozzle. The rated regime corresponded to Mach number of $M = 8.2$. Pressure drop between forevacuum chamber and test chamber was adjusted by a special valve and comprised 20-40 Torr. This value was measured by an U-shape manometer. Gas flow was equal to $\sim 0.5 \text{ g/s}$. Pressure in a test chamber and in main chamber was measured by thermocouple gauges LG-2 and was equal $\sim 5 \cdot 10^{-3}$ Torr. Critical cross-section diameter of a nozzle was equal to 4 mm, and outer diameter was 80 mm. At our pressures it was necessary to take into account boundary layer, which is about of 12 mm in the outlet section of the nozzle. As a consequence, isentropic kernel of the flow was less than outlet cross-section and was about of $\sim 55 \text{ mm}$.

Cylindrical model was made from dielectric (caprolon) and was placed along the flow. Metallic plug was mounted along the axis of the cylinder, and high voltage of negative polarity was applied to the plug. There was hole in the middle of the plug connected to the Pitot tube, so that it was possible to control the pressure behind the shock wave. The length of dielectric cylinder was 150 mm and the diameter was 40 mm. Outer diameter of the steel plug was equal to 5 mm, and hole diameter was equal to 2 mm. The stable diffuse plasma was created by low-pressure aerodynamically stabilized DC discharge between nozzle and model in the supersonic test section.

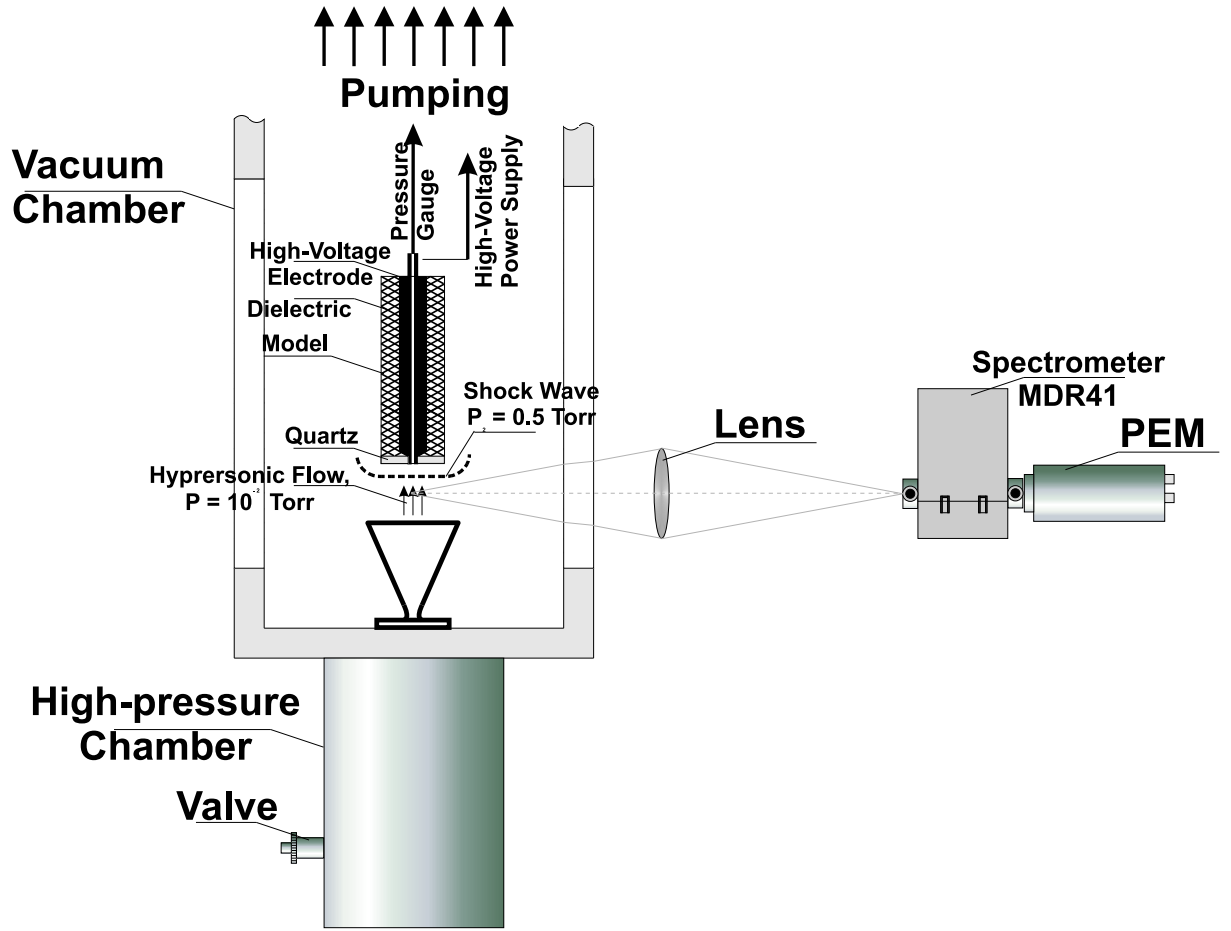


Figure 8.1: Hypersonic plasma flow diagnostics

8.1.1 Electron number density and mean energy in the flow

We have analyzed the first negative ($B^2\Sigma_u^+ \rightarrow X^2\Sigma_g^+$) and second positive ($C^3\Pi_u \rightarrow B^3\Pi_g$) systems spectra in near-ultraviolet region. On the Figure 8.2 the absolute intensity of 0-0 transitions of 2^+ and 1^- systems are shown. Model is at $x = 0$. Line represents the approximate position of shock wave.

It is well-known that absolute measurements of two different bands emission allow to restore electron energy and electron number density in the discharge using appropriate electron energy distribution function.²⁴⁹

Mean energy and electron concentration were obtained from measured intensity fields of transitions from $N_2(C^3\Pi_u, \nu = 0)$ and $N_2^+(B^2\Sigma_g^+, \nu = 0)$ levels (Figure 8.3). We assume

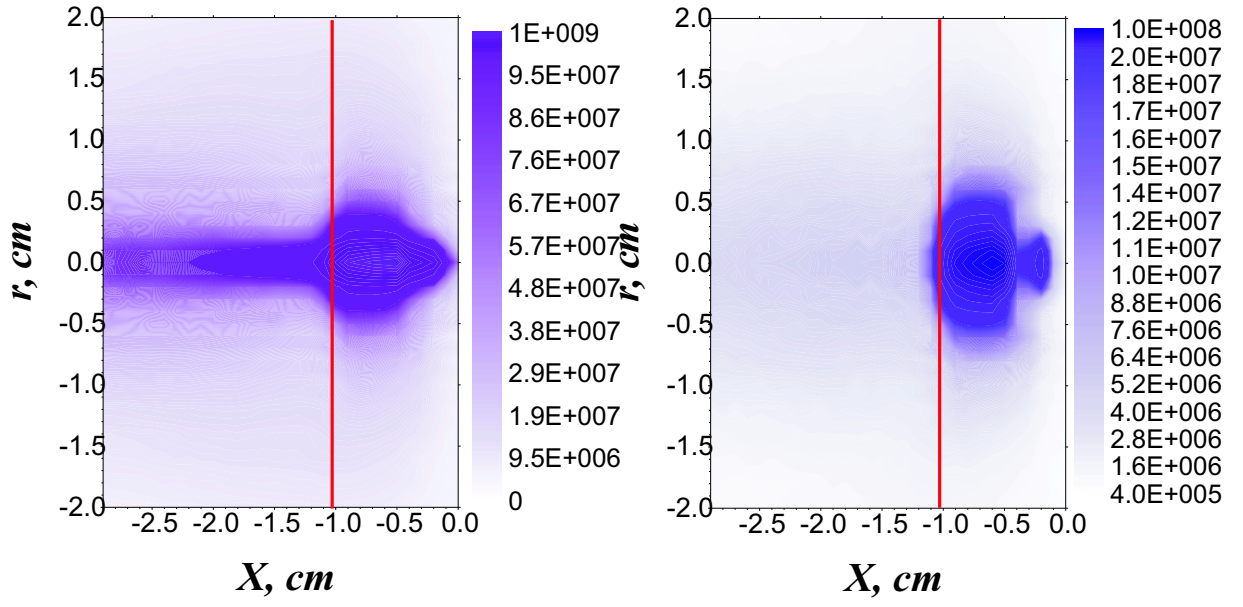


Figure 8.2: The absolute intensity of 0 – 0 transitions of 1^- (left) and 2^+ (right) systems, $1/\text{s cm}^3$

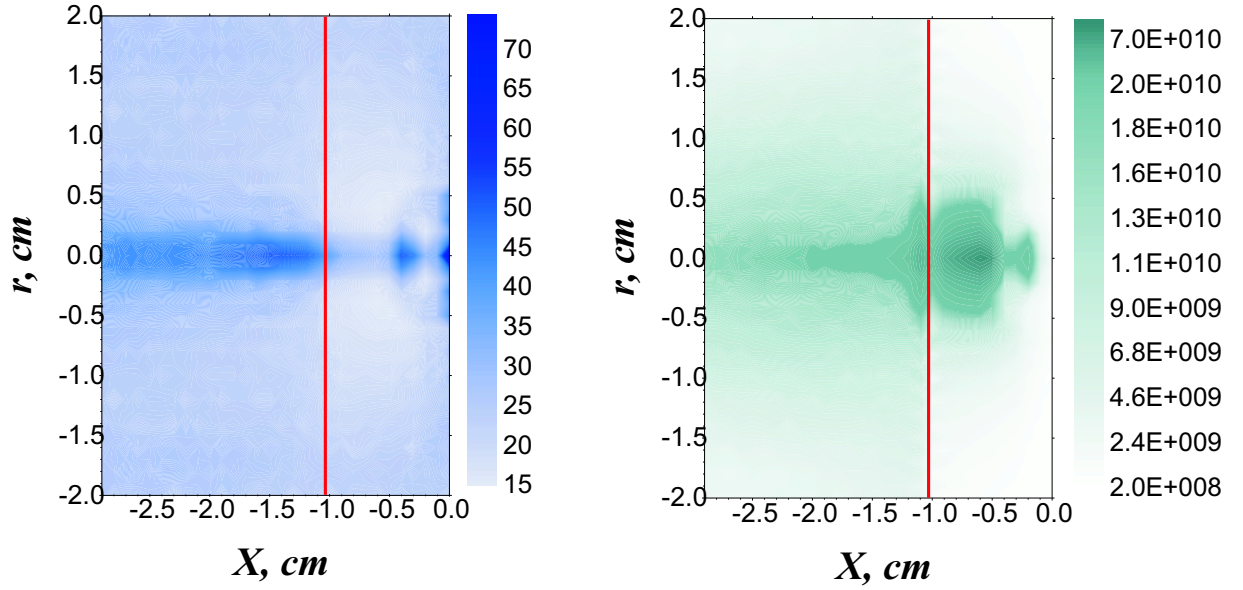


Figure 8.3: Electron energy distribution, eV (left) and electron number density distribution, cm^{-3} (right)

that electron energy distribution function was close to Maxwellian

negligible influence on the flow properties. Cross-sections for excitation of upper levels of 2^+ and 1^- systems were taken from²⁵⁰ and,²⁵¹ correspondingly.

8.1.2 Gas flow rotational temperature measurements

To analyze rotational temperature of the gas distribution in the flow we used technique of a temperature determination from resolved vibrational spectra of first negative system of molecular nitrogen.²⁵² The approach allows to determine rotational population of a ground electron-vibrational state of molecular nitrogen and to calculate efficient population temperature.

For our experimental conditions efficient temperature of population for vibrational states of ground electronic-vibrational state of molecular nitrogen is equal to translational gas temperature. So, it is possible to determine gas temperature before the shock wave and behind it (Fig. 8.4). On the Fig. 8.4 measured spectra were shown. Gas temperature before the shock for low discharge power (5 Wt) is about 20 ± 5 K, and for gas temperature behind shock $T = 300 \pm 30$ K. These values are in good correlation with the data calculated from nozzle theory. Figure 8.5 represents the temperature variation along the flow axis.

Dependence of the gas temperature from discharge power before and behind (Figure 8.5) shock wave. At the discharge power of about 70 Wt the temperature before the shock increases on 20%, and behind the shock — on 10%.

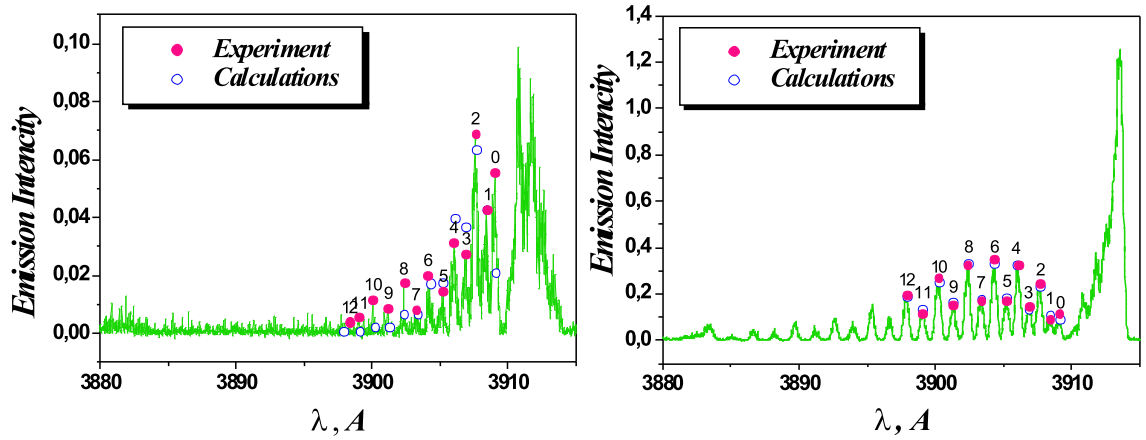


Figure 8.4: Rotational Temperature Measurements Using N_2 First Negative System Emission. $M = 8.2$. $T = 19$ K (left), $T = 295$ K (right)

8.2 Modelling of the energy exchange processes in the flow

The non-equilibrium hypersonic flow around the cylinder was investigated numerically. 2D axially-symmetric calculations of the flow were performed. We analyzed regimes with independent variation of vibrational temperature in the hypersonic flow. MacCormack

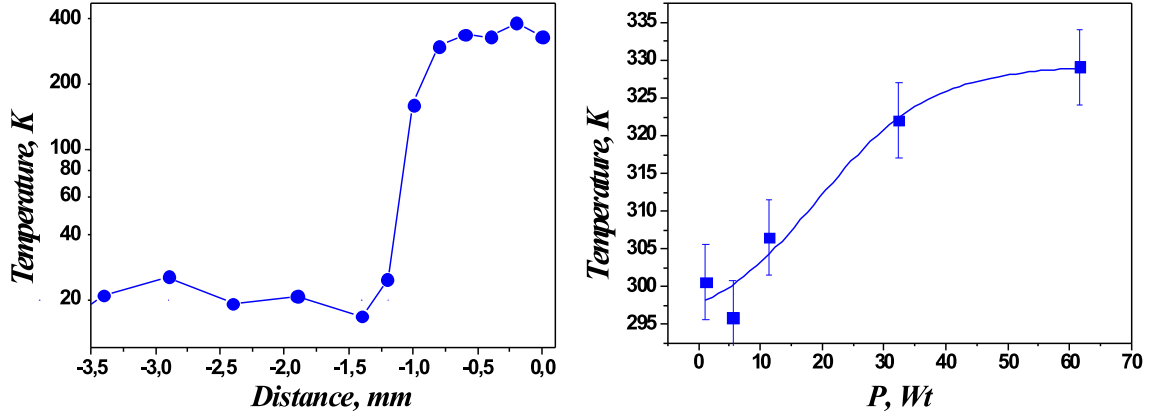


Figure 8.5: Temperature variation along the flow axis (left). Gas rotational temperature vs discharge power behind shock wave (right). Air. $M = 8.2$

scheme with FCT correction was used for solving the components, mass, momentum and energy conserve equations. Vibrational excitation and energy exchange in N_2O_2 plasma flow were taken into account.

Figure 8.6 shows results of calculations with vibrational temperature equal to the translational one (A), and $T_{vib} = 1800, 1900$ and 2000 K, respectively. We assume dissociation degree to be in equilibrium with vibrational temperature of the gas. It is clearly seen that energy release behind the shock wave leads to the flow field change.

Relaxation of vibrational excitation takes place in the process (8.1)

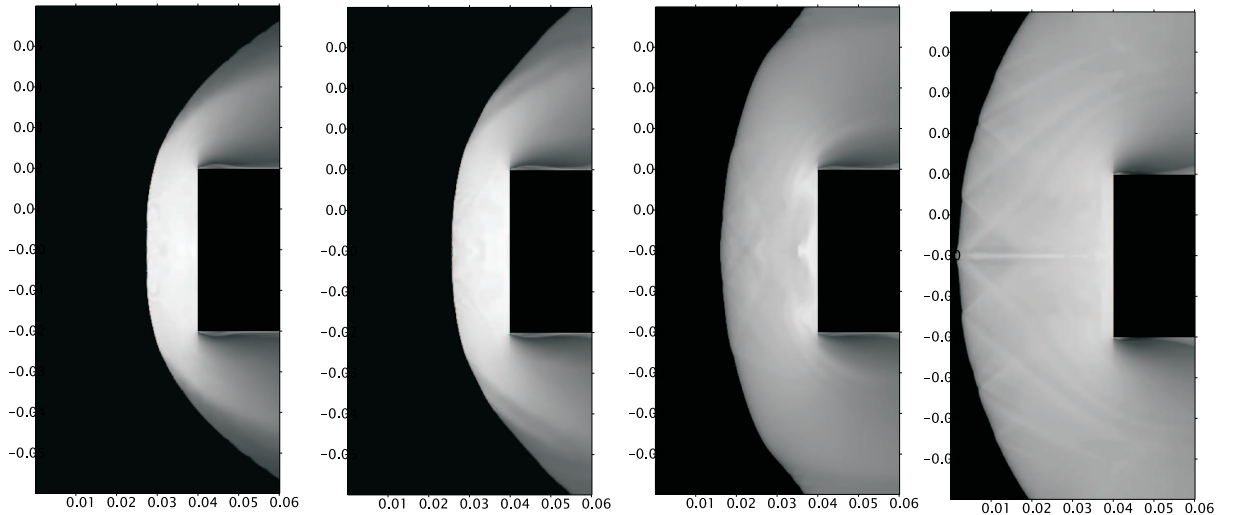


Figure 8.6: Numerical Model of Hypersonic Plasma Flow. Air. $M = 8.2$. $T_{tr} = 21$ K. $T_{vib} = 21, 1800, 1900$ and 2000 K, correspondingly.

Calculations show the decrease the nitrogen vibrational relaxation rate with atomic

oxygen concentration decrease. On the other hand, the atomic oxygen concentration is controlled by the vibrational temperature of O_2 and depends on the vibrational temperature of nitrogen. So, some specific type of back-coupling with vibrational energy exchange participation in the system is formed. Rate of relaxation is dramatically decreases with excitation level decrease (Fig. 8.7).

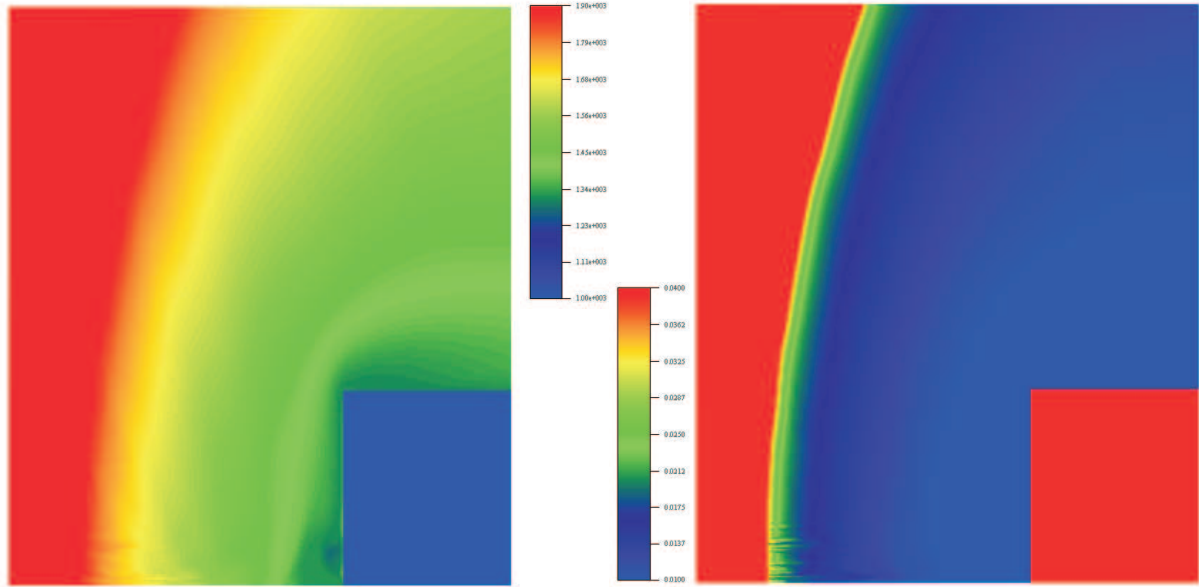


Figure 8.7: Nitrogen vibrational energy and atomic oxygen distribution in the flow

8.3 Reacting plasma hypersonic flow

Hypersonic plasma propane-air flow was formed by conical nozzle. The flow regime corresponded to Mach number of $= 8$. Gas flow was equal to ~ 0.2 g/s. The pre-chamber was equipped with heater which allows us to heat the gas before the expansion in the nozzle up to 700 K. Gas temperature in the pre-chamber was measured by thermocouple gauges (Figure 8.8).

Cylindrical model was made from glass and was placed along the flow axis. The stable diffuse plasma was created by low-pressure aerodynamically stabilized DC discharge between nozzle and high-voltage electrode in the supersonic test section. Behind the reflected shock wave we have the region of excited gas flow with translational temperature equal to the gas temperature in the pre-chamber. So, we can adjust translational temperature and excitation of the internal degrees of freedom of the gas separately. Mean electron energy in this type of the discharge is rather high and gas excitation includes ionization, electronic states, vibrational states, dissociation (Figure 8.9).

Spatial distribution of different molecular bands emission was shown on the Figure 8.10 for low-current discharge conditions, similar to those of Figure 8.9. Zone of gas relaxation and chemical reactions (emission peak of CH radical) is clearly seen on the figure.

Figure 8.11 shows the high-current (~ 20 mA, 1 kV) discharge regime. This regime corresponds to the conditions analyzed in the first part of the paper. The discharge

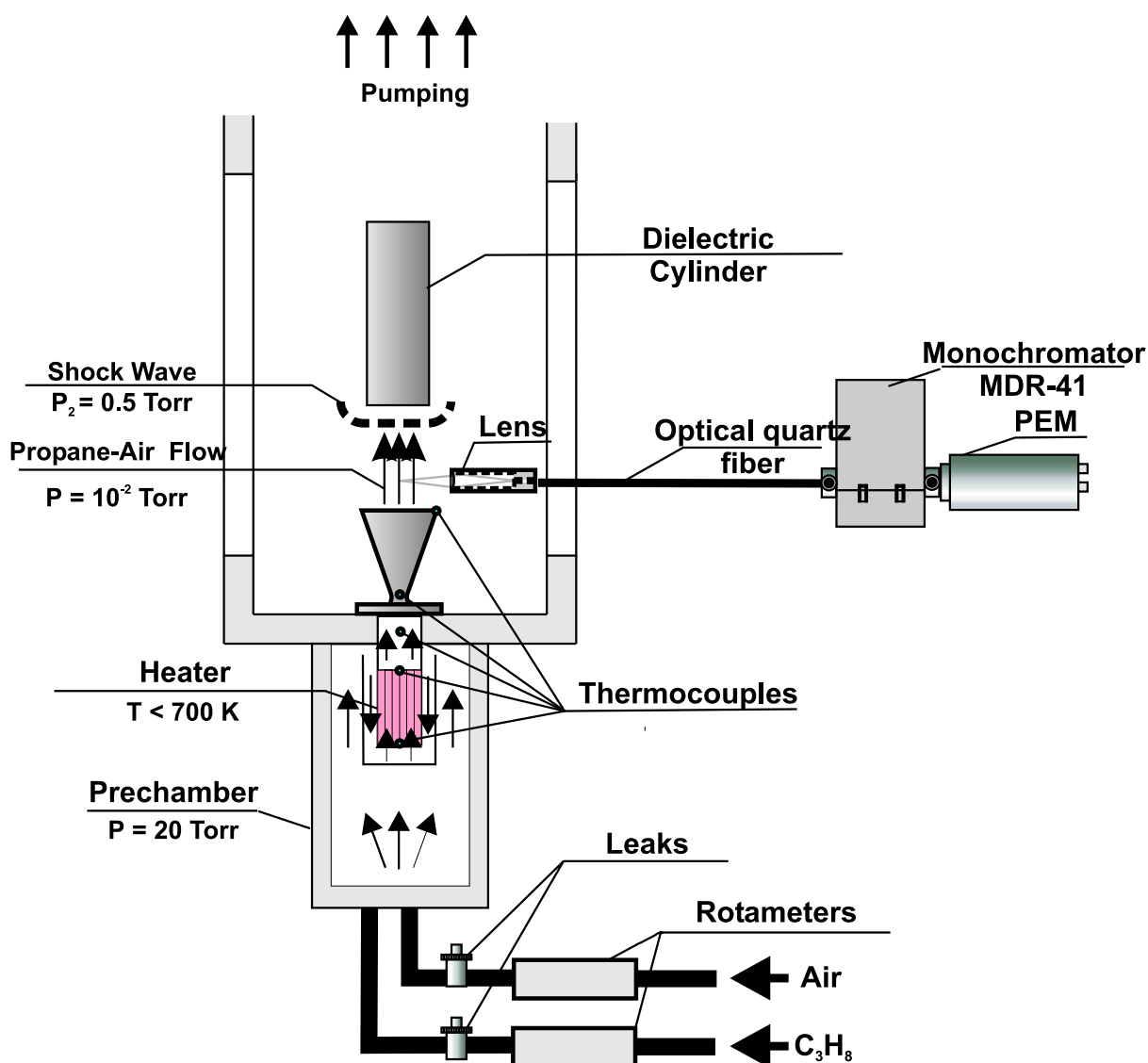


Figure 8.8: Nozzle with pre-heated gas flow

provides very strong gas excitation and almost no heating. Peak of CH-emission becomes extremely strong and comparable with the emission from nitrogen lines. Maxima of the emission intensities shift from each other. Maximum of CH-emission corresponds to the region near the shock wave front, while the maximum of N_2 intensity corresponds to the near-electrode region. The emission of CH-radical rapidly drops down due to fast chemical reactions in this regime near the shock wave front (Figure 8.11). Thus, we have demonstrated the chemical reactions and ignition zone stabilization in the cold flow by high-voltage gas discharge.

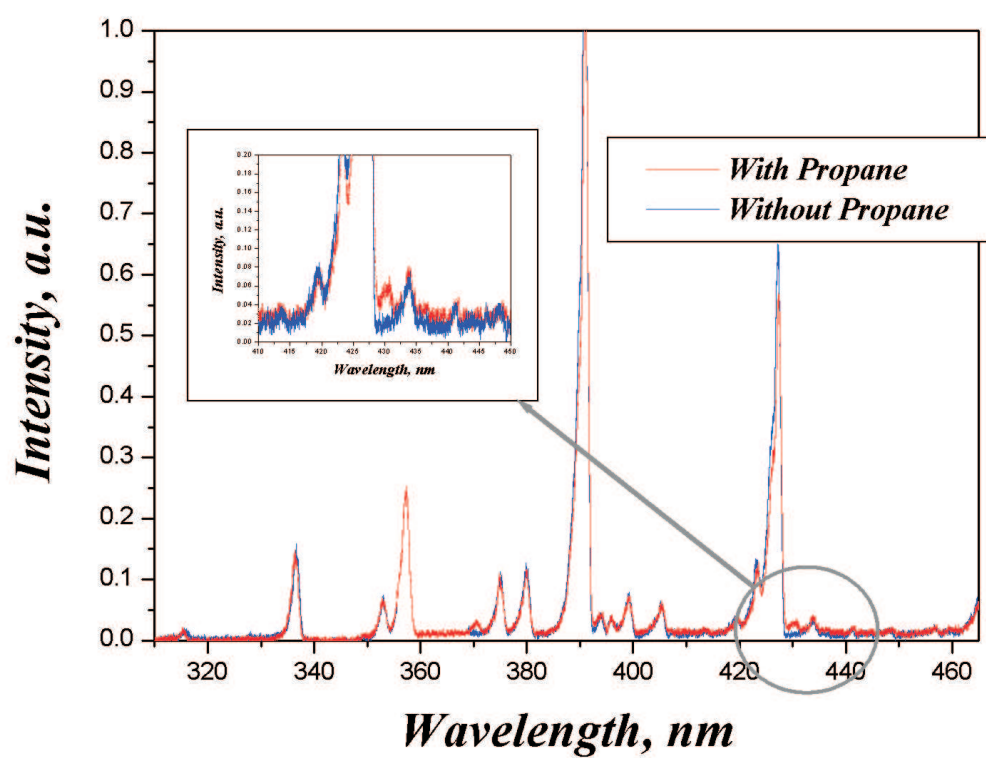


Figure 8.9: Emission spectra of the hypersonic propane-air flow excited by high-voltage gas discharge

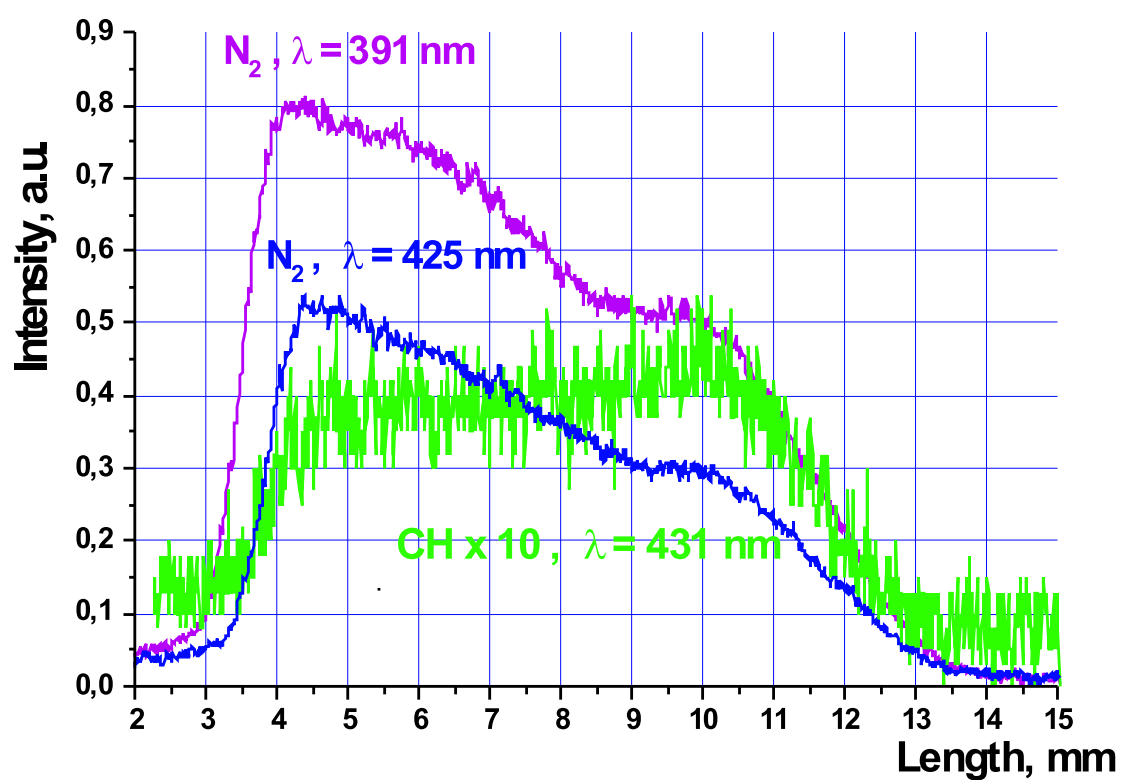


Figure 8.10: Spatial distribution of the emission in propane-air flow. Ring electrode

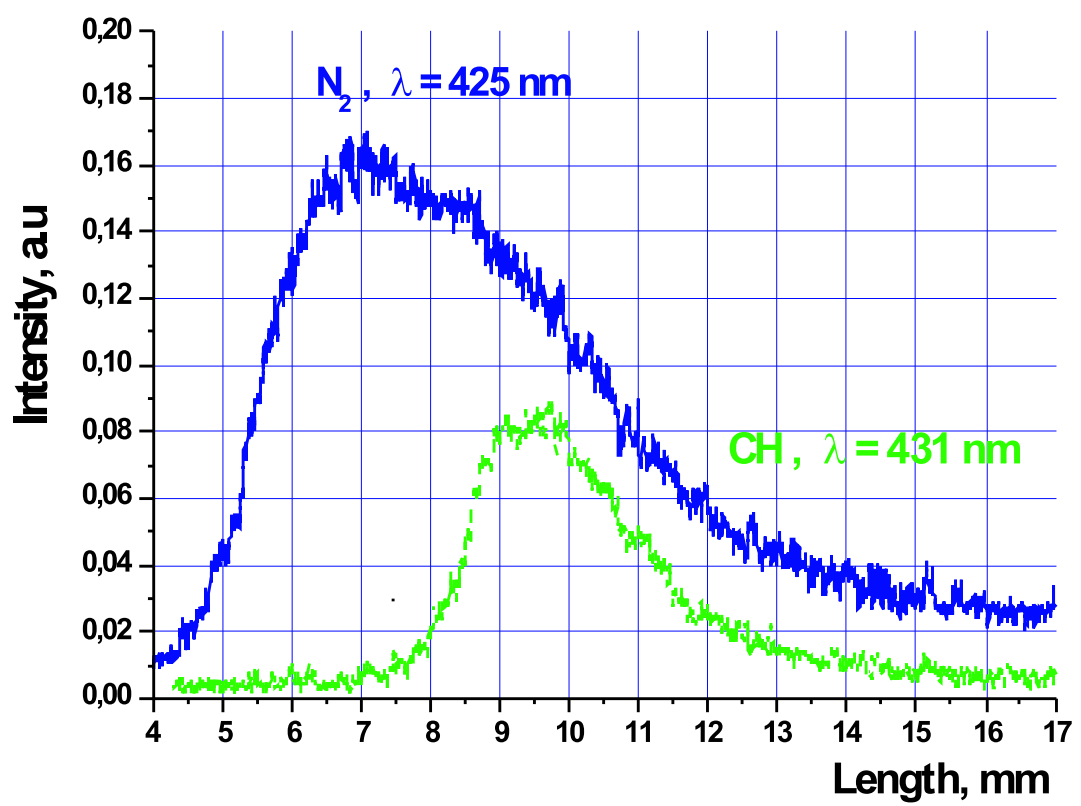


Figure 8.11: Spatial distribution of the emission in propane-air flow. Point electrode

Chapter 9

Detonation Initiation by High-Voltage Pulsed Discharges

The goal of this part of work is the reduction of the deflagration to detonation transition (DDT) length and time in smooth detonation tubes under minimum energy of initiation. The DDT length and time are crucial parameters for pulsed detonation engines (PDE) applications. Thus, it is necessary to find an effective means for detonation initiation.

For direct detonation initiation a considerable energy deposition into the mixture is required. For stoichiometric propane-air mixture, experiments yield minimum initiation energy of 0.08 kg in TNT equivalent or 300 kJ for spherical detonation.²⁵³ When initiated in a tube by a lower energy source, the DDT may occur at the distance of several tens of tube diameters away from the initiation point. The most common method of reducing the DDT length is application of various types of obstacles, which disturb the flow and increase the flame velocity.²⁵⁴⁻²⁵⁹ A modification of this method is application of a two-chamber initiating system, where the mixture is ignited in the first chamber, whereas detonation wave is initiated in the second chamber by hot turbulent jets.²⁵⁷⁻²⁶⁰ In this case, the acceleration of the flame front depends on its own speed and power. If the initial flame front velocity is low, turbulization and consequent acceleration of the flame are weak. Usually, the initial flame front is weak, so this method is not the most effective. This concept was realized experimentally;²⁶⁰ C-J detonation mode was obtained at 2 m in a 15 cm diameter tube with regularly spaced obstacles in a $C_3H_8 + 5O_2 + 15N_2$ mixture at 1 bar. The use of a precombustion chamber for turbulent flame ejection allowed to decrease the DDT time from 24 to 14 ms, but at the same time no effect on the DDT length was found.

Coherent ignition technique was used for detonation initiation in other works.²⁶¹ In the experiments, the mixture was ignited by a set of spark plugs installed along the detonation tube. Different delay times for each spark plug were chosen in order to obtain maximum flame front acceleration. The DDT length of 0.6-0.7 m was achieved in propane-air mixture at 1 bar. This technique allowed to reach detonation initiation energy of 1.68 MJ/m², which is less in comparison to the initiation by TNT,²⁵³ but is still higher than for the case of non-equilibrium plasma igniters.

In Ref.,²⁶² it was found that the critical energy of initiation by a spark decreases as the power density of the initiating source increases. A number of scientific groups carried out investigations of ignition by non-equilibrium corona discharges.^{263,264} The experiments

were performed for ethylene-air, propane-air,²⁶³ and methane-air²⁶⁴ mixtures. The authors applied a pulsed nanosecond discharge with duration of 50 ns. They performed a comparison of ignition delay times under ignition by the corona and by a conventional spark discharge with the same energy. The ignition delay times were shorter by a factor of 3–5 under ignition by a pulsed corona discharge.

Nanosecond discharge in the form of a fast ionization wave (FIW) as a source of ignition has a set of advantages:^{113,265} high spatial uniformity, high efficiency of formation of reactive species, high power, and coherence, that is, simultaneous excitation of the mixture in a bulk volume. A theoretical study of application of nanosecond discharge was performed by Starikovskii.²⁶⁵ It was confirmed that formation of a strong shock wave from compression waves arises if the typical time of chemical energy release is shorter than the time of gas-dynamic processes under the selected initial conditions and mixture composition. It was also shown that the length and the time of DDT are shorter under fast energy release and low temperatures.

Non-equilibrium nanosecond discharge is also promising for detonation initiation from the point of view of Zeldovich's gradient mechanism. In a medium with an induction time gradient, the DDT is obtained at shorter distances. It has been shown²⁶⁵ that a fast ionization wave allows to produce active species in a bulk volume. If a proper geometry and parameters of the discharge device are chosen, this may lead to formation of the required induction time gradient.

In the current work, two setups have been assembled to study detonation initiation. In the first, the mixture was ignited by a distributed high-voltage non-equilibrium nanosecond discharge, which excited the mixture in a bulk volume across the tube cross-section. In the second, the mixture was ignited by a localized high-voltage microsecond spark discharge. The discharge energies and the geometries of the discharge sections in these cases were comparable, which allowed us to compare the efficiencies of different detonation initiation means.

9.1 Detonation initiation by non-equilibrium nanosecond discharge

9.1.1 Experimental setup

The experimental setup used for study of detonation initiation by a high-voltage nanosecond discharge is described in detail in our previous works.^{266,267} The experiments were carried out in a detonation tube with inner diameter of 140 mm. The discharge was initiated by a 60 ns long high-voltage pulse with 12 ns rise time. Voltage amplitude ranged from 4 to 70 kV, the corresponding energy input range – from 70 mJ to 14 J. The discharge section was a distributed electrode system consisting of 131 discharge cell placed over the cross-section of the tube. The pulse parameters were registered by a back-current shunt and a capacitive gauge. Flame propagation velocity was registered by 5 IR sensors installed along the detonation tube. Simultaneously, shock wave propagation velocity was measured by 2 schlieren sensors.

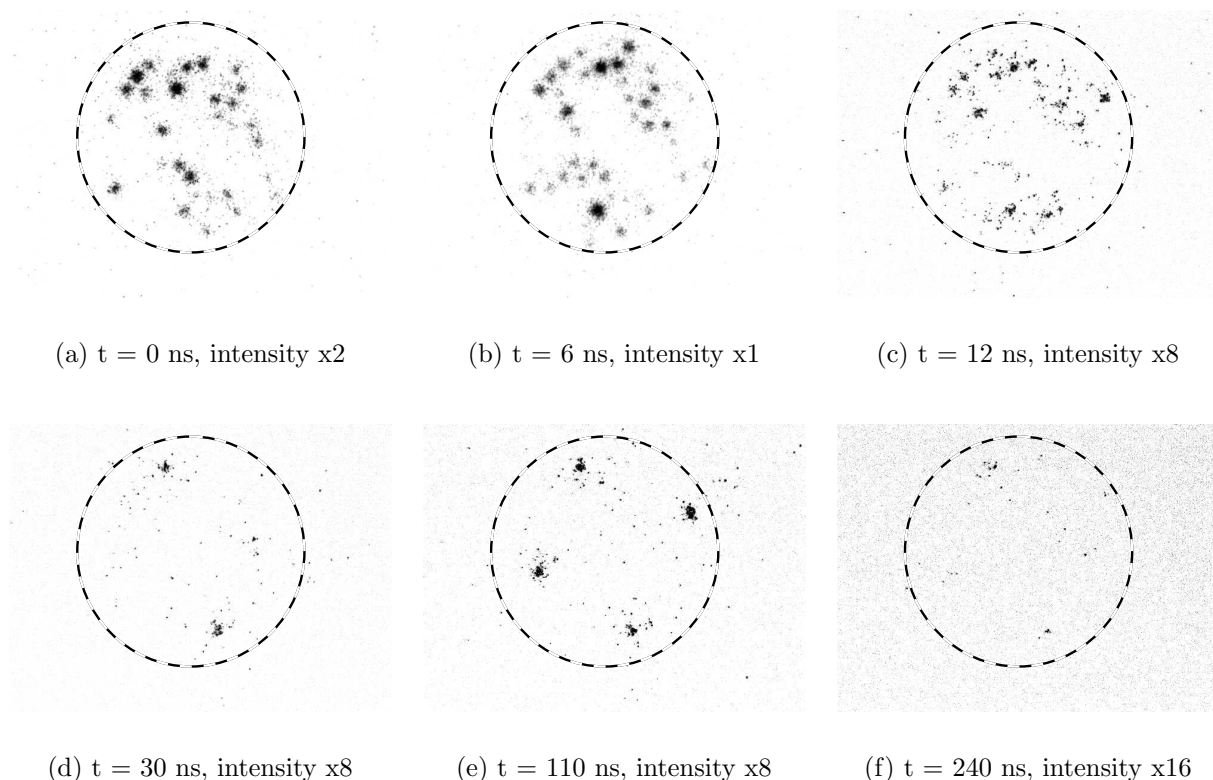


Figure 9.1: Negative images of a nanosecond discharge development in air at 0.33 bar at different moments in time. Dashed line corresponds to the edge of the discharge chamber. Camera gate 3 ns. Time was counted off from the moment when back-current shunt signal reached half of the maximum value.

9.1.2 Nanosecond discharge development

The discharge development was studied with an ICCD camera (LaVision Picostar 12HR) with nanosecond temporal resolution. The main contribution to the intensity of discharge radiation was made by nitrogen emission line at 337 nm. A series of images for the discharge development in air at 0.33 bar is presented in figure 9.1. Dark dots in the images correspond to the radiation of single discharge cells. The discharge had three temporal stages. During the first stage (0–15 ns), emission intensity rose steeply, reaching its maximum value. The emission at this stage was distributed quasihomogeneously over the discharge section. During the second stage (15–50 ns), the intensity decreased sharply. The third stage ($t > 200$ ns) was the afterglow stage, when the emission was localized within 1–2 discharge cells. Emission intensity of each subsequent stage decreased by about an order of magnitude comparing to the preceding one.

9.1.3 Results of detonation initiation experiments

The experiments in detonation initiation were carried out in different stoichiometric mixtures: $\text{C}_3\text{H}_8 + 5\text{O}_2 + x\text{N}_2$ ($0 \leq x \leq 4$), $\text{C}_3\text{H}_8/\text{C}_4\text{H}_{10} + 5\text{O}_2 + x\text{N}_2$ ($0 \leq x \leq 10$), $0.5\text{C}_6\text{H}_{14} + 4.5\text{O}_2 + x\text{N}_2$ ($0 \leq x \leq 3$), and $\text{C}_3\text{H}_8/\text{C}_4\text{H}_{10} + \text{air}$. Initial pressure values varied from 0.15 to 1 bar. In the experiments, flame front velocity, shock wave velocity, and ignition delay

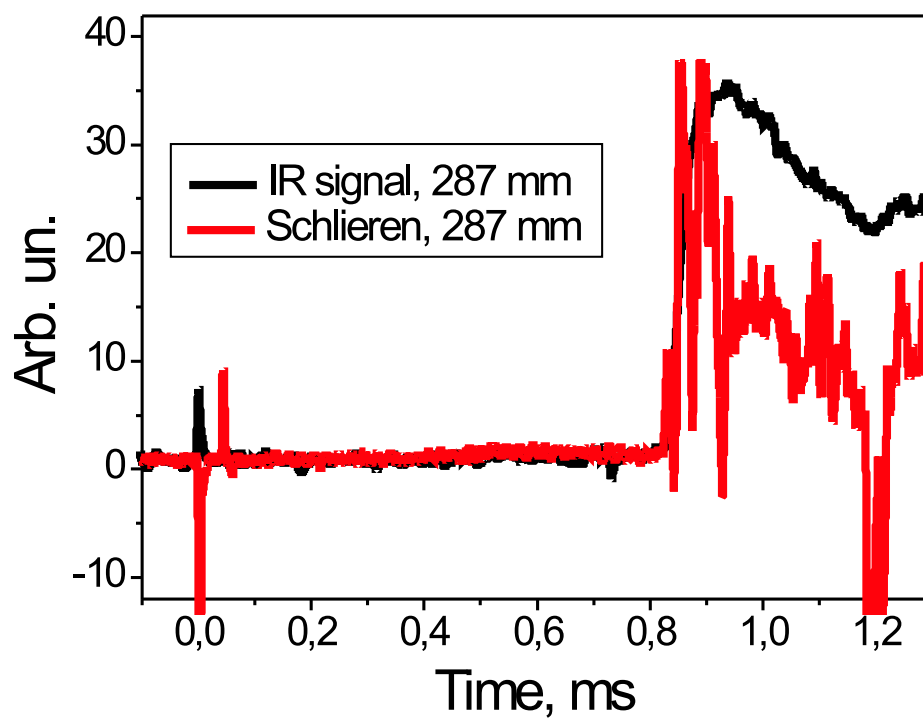


Figure 9.2: Responses of IR sensor (black line) and Schlieren sensor (red line) in the same cross-section 287 mm away from the discharge chamber. $0.5\text{C}_6\text{H}_{14} + 4.5\text{O}_2 + 3\text{N}_2$ at 0.76 bar. Detonation.

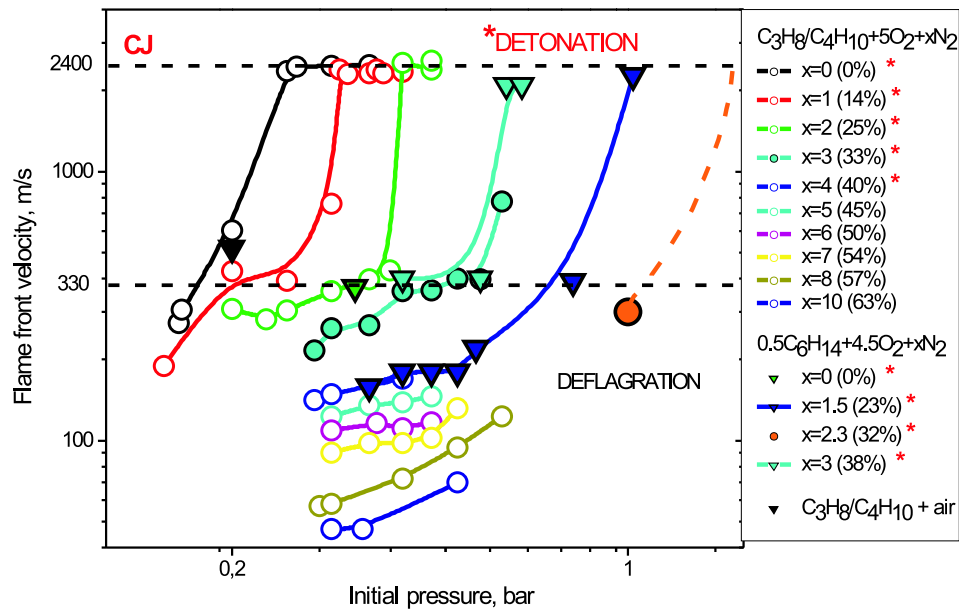


Figure 9.3: Flame front velocity dependence upon initial mixture pressure for different mixture compositions under ignition by a nanosecond discharge. C-J velocity is 2400 m/s for propane/butane mixtures (circles) and 2100 m/s for hexane mixtures (triangles).

times were measured simultaneously with initial mixture pressure, nitrogen dilution level, and nanosecond pulse parameters. The comparison of shock wave velocities obtained with schlieren sensors and flame front velocities obtained with IR sensors (see figure 9.2) showed that the velocities coincided in all supersonic propagation modes. This proved the possibility to use IR emission diagnostics for DDT study and allowed us to compare the velocity values obtained with the IR sensors with those obtained with the pressure transducers in the supersonic modes.

Under the current experimental conditions, three modes of flame propagation were observed: deflagration, with subsonic velocities of propagation, transient detonation, with supersonic velocities and high values of flame front acceleration along the tube, and Chapman-Jouguet (C-J) detonation. C-J velocity for all propane/butane mixtures under study was appr. 2400 m/s, whereas for all hexane mixtures it was appr. 2100 m/s. The results of these experiments are presented in figure 9.3 in terms of the dependences of flame front propagation velocity 400 mm (~ 3 calibers) away from the discharge chamber upon initial mixture pressure, for different mixture compositions. Velocity values of ~ 2400 m/s for propane/butane mixtures and ~ 2100 m/s for hexane mixtures correspond to the experiments where C-J detonation were obtained. Relative velocity measurement error was the greatest for deflagration mode; nevertheless, its absolute value did not exceed 20 m/s.

At higher nitrogen dilution levels or at lower pressures, a deflagration mode was observed. In this mode, the flame front propagated with almost constant velocity of 50 to 300 m/s, gradually accelerating. Under lower nitrogen dilution levels or at higher pressures C-J detonation was observed. The measured velocity of flame front propagation corresponded to the calculated value.

In a small range of pressures between deflagration and C-J detonation, a nonstationary mode of transient detonation was observed. The velocities in this mode ranged from sonic speed in fresh mixture (~ 300 m/s) to almost C-J velocity (~ 2400 m/s). Transient detonation mode was characterized by strong flame front acceleration along the tube ($\sim 3 \cdot 10^6$ m/s²) and strong dependence of velocity upon initial pressure.

The DDT was observed 400 mm away from the discharge chamber or closer in all mixtures with nitrogen dilution level up to 38%. The energy input in these cases did not exceed 3 J. For undiluted stoichiometric propane-oxygen mixture the DDT length and time amounted to, respectively, 130 mm and 0.6 ms, under energy input of 70 mJ. This value of energy input corresponded to 4 J/m² of energy per unit cross-section. In $0.5\text{C}_6\text{H}_{14} + 4.5\text{O}_2 + 3\text{N}_2$ mixture (38% N₂), the DDT length under energy input of 3 J at initial pressure of 1 bar was 300 mm, the DDT time was 0.6 ms. It is also seen from figure 9.3, that flame front velocities in propane/butane and hexane mixtures are the same for mixtures with the same values of nitrogen dilution, for which the combustion heat values are also close.

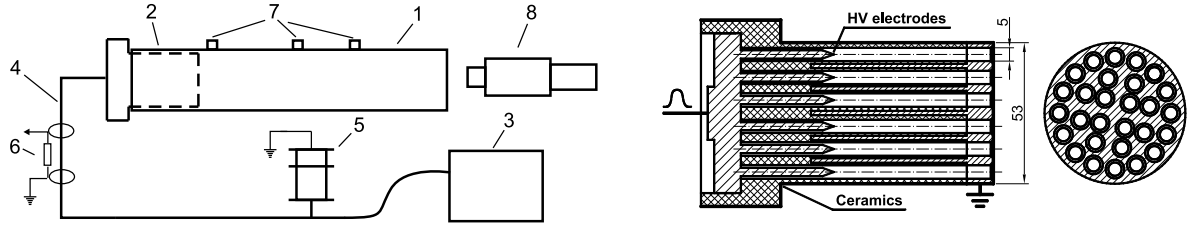
9.2 Detonation initiation by microsecond spark discharge

9.2.1 Experimental setup

For comparison between detonation initiation and flame propagation modes under different initiation conditions a new setup has been assembled. The setup scheme is presented in figure 9.4a. The inner diameter and the length of the detonation tube (1) were 53 and 1000 mm, respectively. The discharge chamber (2) was mounted to one end of the tube. The geometry of the discharge chamber pictured in figure 9.4b was analogous to the one used for nanosecond detonation initiation and discussed in section 9.1.1 and Refs. 266,267. The high-voltage electrode was a distributed electrode system consisting of 28 pins separated from each other and from the ground electrode by a ceramic insulator. Each pin formed a discharge cell with interelectrode gap of 50 mm. The DC power supply (3) charged the feeding line (4) up to a voltage of 37 kV. A high-voltage pulse was formed on the electrode when the feeding line had been grounded by the thyatron (5). The pulse parameters were registered by the back-current shunt (6).

For shock and detonation waves velocity measurement piezoelectric pressure transducers (7) were used. The transducers were installed in the sidewalls of the tube at the distances of 3, 363, and 873 mm from the discharge chamber. A typical oscillogram of the pressure transducers signals is presented in figure 9.5. In this case the DDT took place between the 1st and the 2nd transducers. The error in pressure wave velocity measurement was determined mainly by the signal rise time. In detonation mode, the error value was insignificant due to the steepness of the shock wave front, whereas for deflagration modes the error could reach ~ 20 m/s.

Pulse parameters were the following: amplitude – 37 kV, width – 1–3 μ s, rise time – ~ 100 ns. The rise time was determined by thyatron switching time. The energy input in this case was limited by the energy stored in the feeding line, which was equal to 14 J. The actual energy input value was not measured in the experiments. Images of discharge



(a) Principal scheme of the setup: 1 – detonation tube, 2 – discharge chamber, 3 – DC power supply, 4 – high-voltage feeding line, $Z = 17 \text{ Ohm}$, 5 – thyatron, 6 – back-current shunt, 7 – piezoelectric pressure transducers, 8 – ICCD camera with picosecond nanosecond resolution.

(b) Discharge chamber (2) consisting of 28 discharge cells: chamber diameter – 53 mm, discharge cell diameter – 5 mm, discharge cell length – 95 mm, interelectrode gap – 50 mm.

Figure 9.4: The setup for detonation initiation with microsecond spark discharge.

development were taken through the end of the detonation tube with an ICCD camera (8) with picosecond temporal resolution (LaVision Picostar 12HR). Radiation in the spectral range of 300–800 nm was registered in the experiments.

9.2.2 Microsecond discharge development

The discharge development was studied with the ICCD camera for this electrode configuration and pulse parameters. Temporal dependence of discharge emission integrated over the cross-section was registered under the same conditions by a photoelectric multiplier (PEM). This temporal dependence is presented in figure 9.6 for discharge development in air at 1 torr. The corresponding spatially resolved ICCD images of the discharge are presented in figure 9.7. Time is counted off from the moment of electrical pulse reaching the electrode. It is seen that the discharge development occurred in a large portion of discharge cells not sooner than 80 ns after the pulse had reached the electrode. Due to the long rise time of the high-voltage pulse, the overvoltage on the discharge gap was not as high as in the case of the nanosecond discharge, which led to a streamer discharge formation. The streamers then reached the low-voltage electrode closing the discharge gap. Because of the scattering of the streamers properties there was one high-conducting channel, which was where the main portion of the discharge current passed. This led to the channel overheating and spark formation. As it is seen from the ICCD images, the spark could last for several microseconds, though the emission intensity was not high enough for the PEM to detect it.

At air pressure of 1 bar the discharge developed essentially differently. Temporal dependence of discharge emission registered by the PEM together with the back-current shunt signal and ICCD images of the discharge are presented in figures 9.8 and 9.9, respectively. In images (a) and (b) of figure 9.9, the streamer phase of discharge development at 1 bar is presented. The intensity of emission at this stage was extremely low. Unlike in the case of discharge development at low pressure, the discharge localization and spark formation due to ionization instability occurred sooner than $\sim 50 \text{ ns}$ after the pulse had reached the electrode. The spark stage of discharge development is presented in images

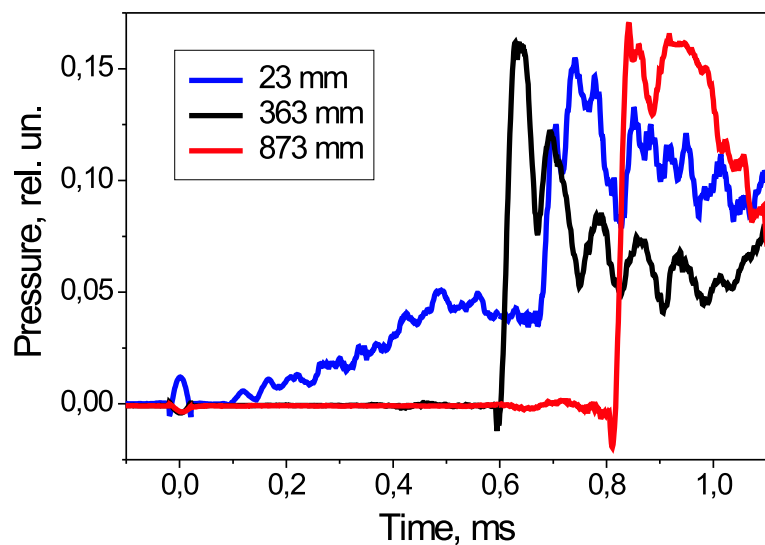


Figure 9.5: A typical oscillogram of the pressure transducers signals. The distance from the discharge section is shown in the figure for every transducer. Initial mixture pressure 0.6 bar. Mixture: $\text{C}_3\text{H}_8/\text{C}_4\text{H}_{10} + 5\text{O}_2$. Detonation, shock wave velocity 2350 m/s measured between transducers 2 and 3. C-J velocity for the given mixture ~ 2400 m/s.

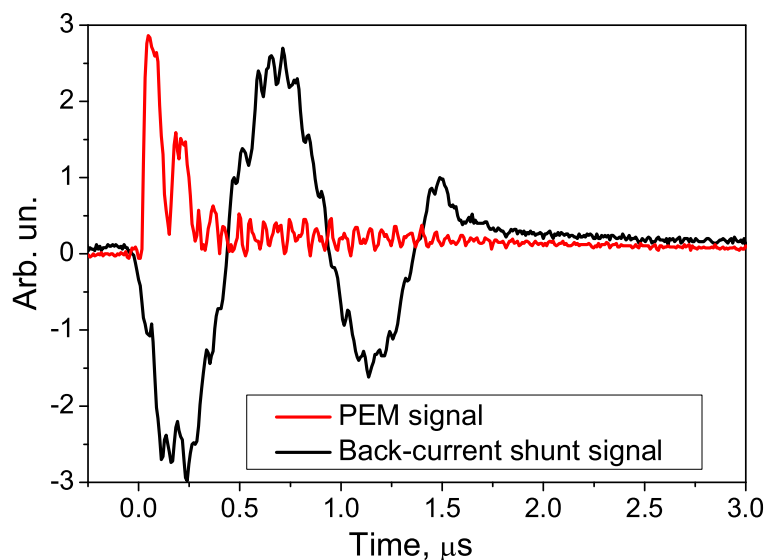


Figure 9.6: PEM signal (red line), proportional to emission intensity, and back-current shunt signal (black line). Air, 1 torr.

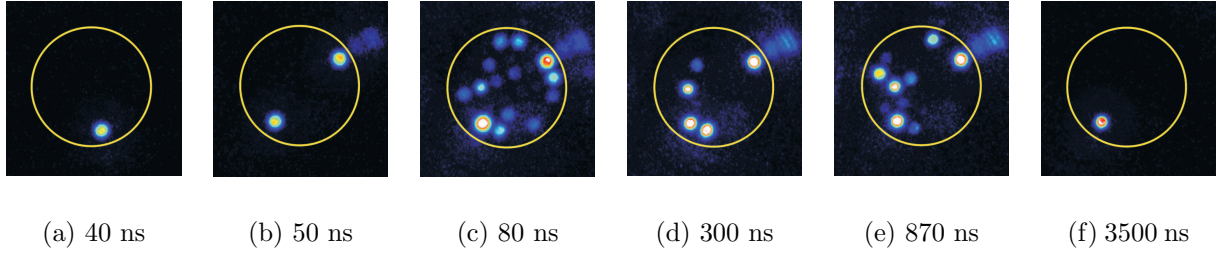


Figure 9.7: Images of the microsecond discharge development in air at 1 torr at different moments in time. Yellow line corresponds to the edge of the discharge chamber. Camera gate 1 ns.

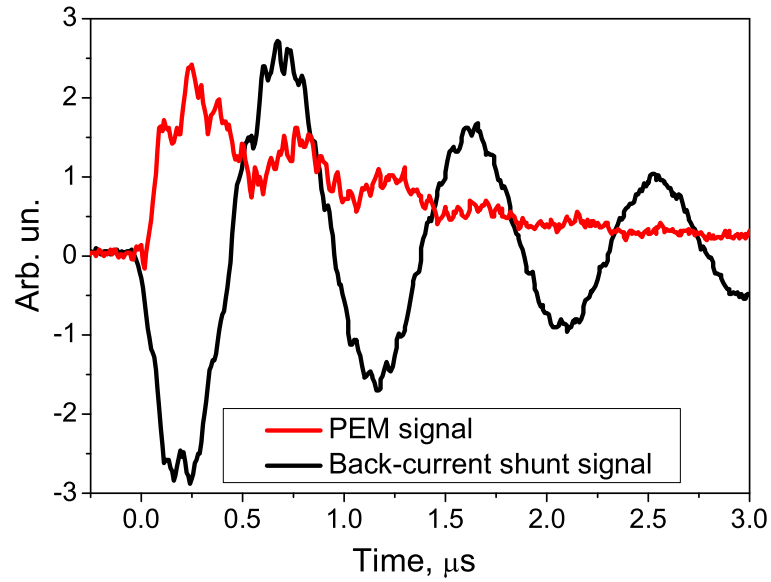


Figure 9.8: PEM signal (red line), proportional to emission intensity, and back-current shunt signal (black line). Air, 1 bar.

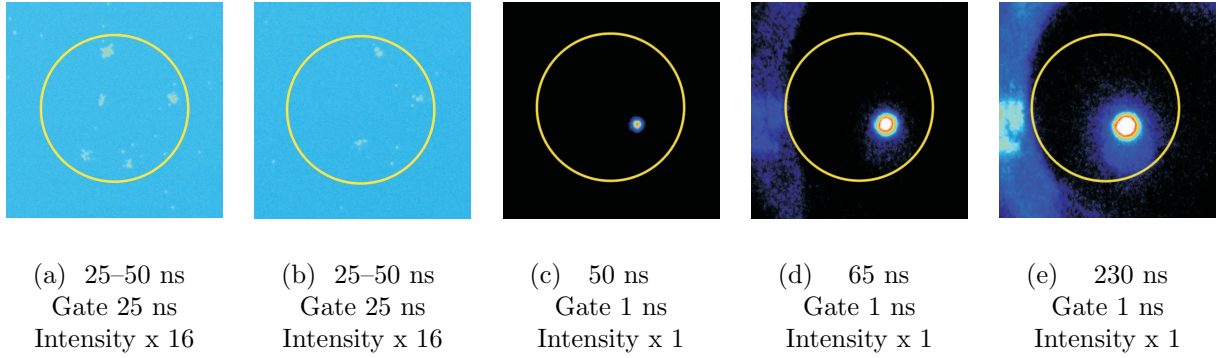


Figure 9.9: Images of the microsecond discharge development in air at 1 bar at different moments in time. Yellow line corresponds to the edge of the discharge chamber.

(c), (d), and (e). It was these stages when most of the pulse energy consumption occurred. Homogeneous discharge phase was not observed at all in most of the discharge cells. Such discharge development pattern is a result of relatively long pulse rise time (~ 100 ns).

9.2.3 Results of detonation initiation experiments

Experiments on detonation initiation by a high-voltage microsecond discharge were carried out in two propane/butane mixtures ($\text{C}_3\text{H}_8/\text{C}_4\text{H}_{10} + 5\text{O}_2 + x\text{N}_2$ with $x=0$ and $x=4$) at initial pressures up to 1 bar. The mode of flame propagation was determined by shock wave velocity measured with pressure transducers. As has been shown in section 9.1.3, flame front velocity coincides with shock wave velocity in all supersonic modes of propagation. The results of these experiments are presented in figure 9.10 (solid lines, solid symbols) in terms of the dependences of shock wave velocity 600 mm away from the discharge chamber upon initial mixture pressure, for different mixture compositions. The results are presented in comparison with the ones in the same mixtures obtained under initiation by a nanosecond discharge and described in section 9.1.3 (dashed lines and hollow symbols of the same color). It needs to be noted that these results are only to be compared in the region of supersonic propagation velocities.

The same modes of flame propagation were observed in these experiments: deflagration, transient detonation, and C-J detonation. For the undiluted mixture (red lines), detonation was observed at 0.6 bar of initial pressure under initiation by a microsecond spark, whereas in the case of initiation by a non-equilibrium nanosecond discharge the DDT was obtained at essentially lower pressure of 0.25 bar. For the mixture with nitrogen dilution level $x=4$, detonation was only observed under nanosecond initiation. In the case of microsecond spark initiation, at maximum initial pressure of 1 bar transient detonation mode with flame front velocity of ~ 1000 m/s was observed. This indicates essentially higher efficiency of a distributed quasihomogeneous non-equilibrium discharge as a detonation initiator.

Simultaneously in the same experiments, mixture ignition was studied by measurement of ignition delay time dependence upon initial mixture pressure and nitrogen dilution level. Ignition delay time was determined from the delay between discharge initiation and the onset of signal of the first pressure transducer located 23 mm away from the discharge chamber. This ignition delay time dependence in various mixtures is presented in fig-

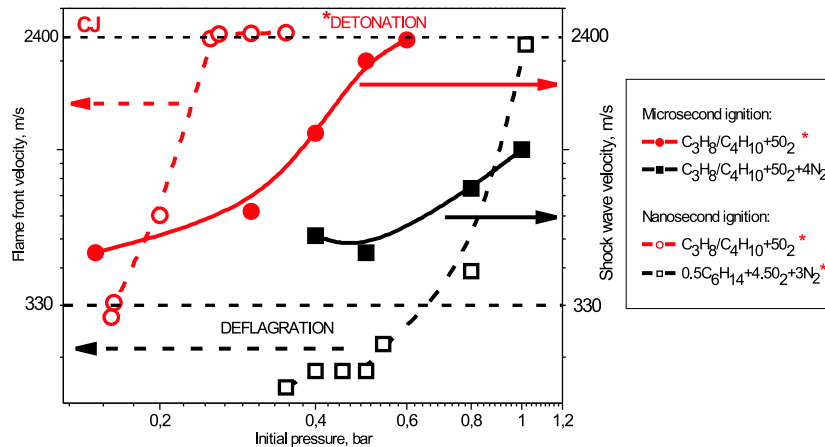


Figure 9.10: Flame front velocity dependence upon initial mixture pressure for different mixture compositions. Solid lines and solid symbols for microsecond initiation, dashed lines and hollow symbols for nanosecond initiation. Same colors correspond to the same mixtures.

ure 9.11. The results for ignition by a microsecond spark discharge are represented by red symbols. Green symbols correspond to ignition by a non-equilibrium quasihomogeneous nanosecond discharge in the first experimental setup described in section 9.1.1. The latter results are described in detail in Refs.^{266,267} It is seen that in log-log scale the dependences are straight lines, the slopes being different for different ignition types. Noteworthy is that the values of ignition delay times are substantially lower for the microsecond ignition in all the mixtures at initial pressures up to ~ 0.5 bar.

9.3 Results discussion

Experiments on detonation initiation by a high-voltage nanosecond discharge in detonation tube with 140 mm diameter showed that as nitrogen dilution level increased (mixtures with $x \geq 3$ in figure 9.3) the DDT at the distance of 400 mm from the discharge chamber occurred at increasingly higher initial pressures (0.4 bar and higher). In stoichiometric propane/butane–oxygen mixture diluted with nitrogen, the minimal initial pressure for the DDT to be observed increased from 0.31 to 0.4 bar when nitrogen concentration in the mixture increased from 14% to 25%, whereas at nitrogen concentration of 33% the minimal initial pressure amounted to 0.61 bar. When the dilution reached 38% the DDT was only observed at the initial pressure of 1 bar. The dependence of flame front velocity upon initial pressure in the region of nonstationary transient detonation became less steep: for weakly diluted mixtures (with nitrogen concentration below 33%) transient mode was observed in a ~ 0.05 bar wide range of initial pressures, whereas in the mixture with 40% of nitrogen, transient mode was observed at various initial pressures from 0.6 to 1 bar.

At the same time, the typical flame front acceleration decreased substantially as nitrogen concentration increased. In $C_3H_8/C_4H_{10} + 5O_2 + N_2$ mixture, the acceleration reached $\sim 3 \cdot 10^6$ m/s² at initial pressure of 0.3 bar, whereas it amounted to only $\sim 4 \cdot 10^5$

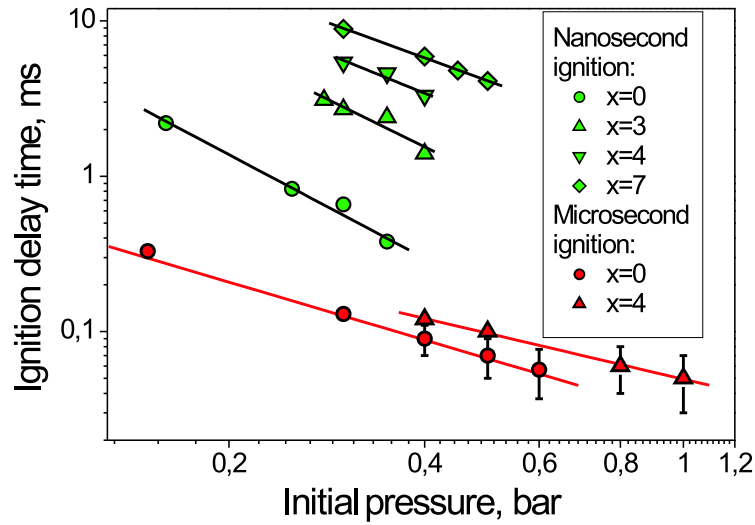


Figure 9.11: Ignition delay time dependence upon initial pressure in $\text{C}_3\text{H}_8/\text{C}_4\text{H}_{10} + 5\text{O}_2 + x\text{N}_2$ mixtures for various nitrogen dilution levels. Green symbols for nanosecond ignition,^{266,267} red symbols for microsecond ignition.

m/s^2 in $0.5\text{C}_6\text{H}_{14} + 4.5\text{O}_2 + 3\text{N}_2$ mixture at initial pressure of 0.8 bar. Low value of flame front acceleration leads to a longer transient mode and, thus, to the increase of the DDT length. This is also related to the less steep dependence of flame front velocity upon initial pressure in transient mode. Since in transient detonation mode the pressure wave is a shock wave propagating in front of the flame, the dependence of flame front acceleration and velocity upon initial pressure is remarkably steeper in this mode than in deflagration.

For comparison between detonation initiation efficiency by a distributed nanosecond and a localized microsecond discharge, experiments were carried out in a detonation tube with discharge chamber of analogous geometry. The tube diameters were different: 140 mm for the case of nanosecond initiation and 53 mm for the case of microsecond initiation. The comparison was made for the mixtures with detonation cell size substantially smaller than both tube diameters: detonation cell size for $\text{C}_3\text{H}_8 + 5\text{O}_2$ mixture at 0.25 bar is 3.8 mm, for $\text{C}_3\text{H}_8 + 5\text{O}_2 + 4\text{N}_2$ at 1 bar – 4.0 mm, and for $0.5\text{C}_6\text{H}_{14} + 4.5\text{O}_2 + 3\text{N}_2$ at 0.4 bar – 6.3 mm.²⁶⁸ This allowed us to consider the conditions of detonation wave propagation to be equivalent for the two detonation tubes. The results of the comparison, presented in figure 9.10 and discussed in section 9.2.3, indicate that the efficiency of detonation initiation in the setup with nanosecond ignition is remarkably higher.

The conditions of detonation initiation in the two setups differ mostly in the temporal and spatial shape of the discharge. The discharge chamber geometry itself influences detonation initiation and propagation to a lesser extent, since the tube diameters exceed detonation cell sizes greatly in all cases, and the single cell size diameter is 5 mm for both discharge chambers. Nevertheless, the discharge chamber geometry together with the high-voltage pulse shape governs the discharge temporal and spatial shape.

The ICCD imaging with nanosecond temporal resolution showed that the discharge

developed quite differently in the two setups. It is seen from figure 9.1, that during the early stages ($t \leq 50$ ns) the nanosecond discharge was distributed over the cross-section of the chamber, filling a larger portion of the cells. During the later stages, the intensity fell sharply. This indicated that most of the energy was deposited during the first 50 ns of the discharge development, in agreement with the temporal shape of the electrical pulse.

In the setup with nanosecond ignition under typical values of voltage amplitude (~ 10 – 70 kV), voltage rise time (> 1 kV/ns), and pressure (0.1 – 1 bar), gas ionization and dissociation occur during very short times in the volume of each discharge cell. The typical times of these processes are shorter than the typical gas-dynamic times. At the same time, a relatively low portion of energy is deposited into translational degrees of freedom. Instead, active radicals are produced in the discharge with their generation rate being governed by the reduced electric field value. The radical concentration gradient, responsible for Zeldovich's gradient mechanism realization, is formed beside the high-voltage electrode in the non-uniform electric field. Originating at the tips of the pin-like electrode, the combustion wave propagates along the discharge cell, being intensified by the gradient mechanism. The simultaneous exit of the combustion waves from the discharge cells into the detonation tube leads to rapid the formation of the detonation wave. An experimentally observed onset of detonation at a distance of less than one tube caliber at an initial pressure of 0.25 bar confirms the high efficiency of detonation initiation by the non-equilibrium plasma of the high-voltage nanosecond discharge.

In the setup with microsecond ignition, the discharge development begins at the reduced electrical field values close to the breakdown value, due to the long rise time of several hundreds of nanoseconds. Since high values of overvoltage can not be reached, the breakdown develops in the form of a streamer discharge, which transforms into a localized spark discharge within ~ 1 μ s. In this case, a considerable portion of energy is deposited into heating of the gas. It is noteworthy that ignition efficiency of a microsecond discharge is significantly higher: ignition delay times for this kind of ignition are lower than those in the same mixtures for nanosecond ignition (see figure 9.11). However, rapid ignition in a single cell does not lead to effective shock wave formation and acceleration and, thus, is not an effective means for detonation initiation.

Chapter 10

Conclusions

During this project the following tasks have been performed and the following conclusions can be done.

- A review was made which discusses different types of the discharges applied for plasma assisted ignition and combustion. Special attention to experimental and theoretical analysis of some plasma parameters was given, such as reduced electric field, electron density and energy branching for different gas discharges. Streamers, pulsed nanosecond discharges, dielectric barrier discharges, radio frequency discharges, atmospheric pressure glow discharges are considered.
- Detailed measurements of the parameters of a streamer flash development in the air for the pressure range 90-1300 Torr have been carried out in the plane-to-plane geometry for 20-42 kV positive and negative polarity nanosecond pulses. A numerical model, which successfully predicts such streamer parameters as current, velocity of propagation, and streamer's head diameter in a wide range of pressures and voltages has been developed.

New results have been obtained for spatial control of discharge uniformity at different experimental conditions. LaVision ICCD camera with picosecond resolution was used to obtain discharge images with a gate of 1 ns and subnanosecond delay between frames. We controlled the process of the uniform discharge development from a tip of conical electrode for different pressures and polarities. Development of the discharge in plane-to-plane geometry was investigated for different repetition rates of the pulses.

New technique for the control of electron density with a lower limit of measurements 10^{11} cm^{-3} and temporal resolution up to 100 ns has been adjusted and tested. The technique is based on microwave I/Q interferometry at 94 GHz frequency. The experiments demonstrated the efficiency of the technique in experiments with discharge in repetitive regime. Good correlation between experimental data for electron density obtained from electric current measurements and from microwave interferometry has been demonstrated.

- The decay of electron density in the afterglow of a nanosecond pulsed discharge has been investigated for room temperature and for high temperatures (1500–3000 K). The experiments were carried out in N_2 , O_2 , CO_2 , $\text{N}_2 : \text{O}_2 = 4 : 1$, and water vapor

for a gas temperature $T=295$ K and high voltage pulse of positive polarity with the amplitude $U=11$ kV. Different repetition rates of pulses were tested. The initial electron density practically does not depend upon a gas mixture composition. It is equal to $(1-3) \cdot 10^{12} \text{ cm}^{-3}$ within the pressure range of 1–10 Torr. The plasma decay time decreases with pressure, and corresponds to a few microseconds for N_2 , O_2 , CO_2 , $\text{N}_2 : \text{O}_2 = 4 : 1$. Maximal recombination time ($\tau \approx 1.7 \text{ } \mu\text{s}$, $p=2.5$ Torr, $T=295$ K) and initial electron density ($n_0 \approx 2.2 \cdot 10^{12} \text{ cm}^{-3}$) have been observed for synthetic air. For water vapor, the recombination time is significantly lower. The kinetic schemes were proposed for pure gases. Their verification has been made using experimental data. The experiments in a high-temperature range were carried out for $\text{CO}_2:\text{O}_2:\text{N}_2$ mixture with different admixtures of water vapor. It can be concluded from the experiments that water addition decreases significantly the plasma decay time. Typical decay time during high temperature experiments was equal to a few microseconds, and the electron density drops by an order of magnitude during 10 microseconds. Preliminary numerical modelling has been made, the results demonstrate a reasonable agreement with the experiments.

- The decay of electron density in the afterglow of a nanosecond pulsed discharge has been investigated for ambient temperature and for high temperature range (1500–3000 K). The experiments were carried out in N_2 , O_2 , CO_2 , $\text{N}_2 : \text{O}_2 = 4 : 1$, and water vapor for a gas temperature $T=295$ K, and for positive polarity high voltage pulse with the amplitude $U=11$ kV. Different repetitive frequencies were tested. The initial electron density practically does not depend upon a gas mixture composition. It is equal to $(1-3) \cdot 10^{12} \text{ cm}^{-3}$ in a pressure range 1–10 Torr. Plasma decay time decrease with pressure, and lies within a few microseconds for N_2 , O_2 , CO_2 , $\text{N}_2 : \text{O}_2 = 4 : 1$. Maximal recombination time ($\tau \approx 1.7 \text{ } \mu\text{s}$, $p=2.5$ Torr, $T=295$ K) and initial electron density ($n_0 \approx 2.2 \cdot 10^{12} \text{ cm}^{-3}$) have been observed for synthetic air. For water vapor, the recombination time is significantly lower. The kinetic schemes were proposed for pure gases. Their verification has been made with the use of experimental data. Experiments for high-temperature range were carried out for $\text{CO}_2:\text{O}_2:\text{N}_2$ mixture with different admixtures of water vapor. It follows from the experiments that water addition decreases significantly the decay time. Typical decay time in high temperature experiments is equal to a few microseconds, and the electron density drops by an order of magnitude during 10 microseconds. Preliminary numerical modelling has been made. The results demonstrate a reasonable agreement with the experiments.
- The experimental investigation of processes of alkanes slow oxidation has been performed. We have investigated kinetics of alkanes oxidation from methane to decane in stoichiometric and lean mixtures with oxygen and air at room temperature under the action of uniform high-voltage nanosecond discharge without gas flow. Also we have investigated experimentally kinetics of $\text{C}_2\text{H}_5\text{OH}$, CH_3COCH_3 , C_2H_2 in their mixtures with oxygen and $\text{CO}:\text{O}_2$ mixtures with small controlled additives of water vapour.

The discharge was initiated with repetition rate 40 Hz in the discharge screened tube with 5 cm diameter and 20 cm length. The pulses polarity was negative, with 10 kV amplitude and 25 ns duration. Mixtures' initial pressures were varied

within 0.8-11 Torr range with the step of 0.8 Torr. The discharge current, electrical field and energy input have been measured with nanosecond time resolution. Emission intensities of the molecular bands such as $\text{NO}(A^2\Sigma \rightarrow X^2\Pi, \delta v = 3)$, $\text{N}_2(C^3\Pi, v' = 1 \rightarrow B^3\Pi, v'' = 7)$, $\text{N}_2(B^3\Pi, v' = 6 \rightarrow A^3\Sigma, v'' = 3)$, $\text{N}_2^+(B^2\Sigma, v' = 0 \rightarrow X^2\Sigma, v'' = 2)$, $\text{CO}_2^+(B^2\Sigma \rightarrow X^2\Pi, \delta v = 0)$, $\text{CH}(A^2\Delta, v' = 0 \rightarrow X^2\Pi, v'' = 0)$, $\text{OH}(A^2\Sigma, v' = 0 \rightarrow X^2\Pi, v'' = 0)$, $\text{CO}(B^1\Sigma, v' = 0 \rightarrow A^1\Pi, v'' = 2)$ have been measured in integral regime (integration time was 2.2 s) and with nanosecond resolution. Methane concentration was measured by absorption of He-Ne laser emission in integral regime. On the base of optical measurements time of the full oxidation of the alkanes was determined.

On the base of experimental data the kinetic scheme was proposed to describe nanosecond discharge action on hydrocarbon-containing mixtures. It was demonstrated that it is possible to describe experimentally obtained dependencies of the oxidation time *vs* gas pressure for different mixtures. The main radicals responsible for oxidation are $\text{O}(^1\text{D})$ and OH . Equal time of oxidation for a set of heavy hydrocarbons is explained by negative reverse back-coupling through stable intermediates, such as H_2O_2 and CO . A good correlation between calculations based on these assumption and experimental data was found.

- An analysis of the ignition of H_2 -containing mixtures at high temperatures under the action of a nanosecond high-voltage discharge has been performed numerically and experimentally for a wide range of parameters. A comparison of the equilibrium and nonequilibrium excitation was performed. The model constructed supports the conclusion that nonequilibrium excitation is much more effective than the equilibrium one for ignition control. In particular, the ignition threshold shift in H_2 -Air mixture is about 300 K under the discharge action with the equivalent energy input of 15 K.
- The numerical analysis of ignition efficiency allowed to perform experimental investigations of the initiation of the ignition by nanosecond discharge at high temperatures. A novel experimental scheme for the investigation of ignition delay at high temperatures under the action of a high-voltage nanosecond discharge has been developed. Electrical parameters on a nanosecond time scale and the ignition processes on a microsecond time scale were investigated. Ignition delays for different mixtures, gas pressures and temperatures were obtained experimentally. The dependence of the ignition delay upon temperature, high voltage pulse amplitude, and the energy release into the discharge was determined experimentally for $\text{H}_2\text{-O}_2$ and $\text{H}_2\text{-air}$ mixtures diluted with argon or helium. ICCD camera PicoStar HR12 was used to obtain the discharge images in a hot mixture with high temporal resolution. The wavelength sensitivity of the optical system was 300-800 nm. The homogeneity of the discharge development and the ignition initiation was shown up to the pressure of 2 atmospheres under the discharge excitation. Obtained data were compared with the results of numerical calculations.
- We have conducted the experiments and numerical modelling of the ignition of hydrocarbon-containing mixtures under the action of pulsed nanosecond discharge. The experiments were carried out with a set of stoichiometric mixtures $\text{C}_n\text{H}_{2n+2} : \text{O}_2$

(10%) diluted by Ar (90%) for hydrocarbons from CH_4 to C_5H_{12} . The temperature behind the reflected shock wave (T_5) varied from 950 to 2000 K, and the pressure (P_5) was 0.2 to 1.0 atm. For each set of experimental parameters we have compared the ignition by the discharge with autoignition.

A numerical model has been built which takes into account both high-temperature kinetics of the ignition and production of atoms and radicals by a nanosecond discharge. At the first stage, we calculated energy branching in the discharge on the basis of experimentally determined electric field and energy input. Reactions responsible for the energy transfer from electronically excited buffer gas to molecules with subsequent production of atoms and radicals was included into kinetic scheme. At the second stage, we modelled high-temperature kinetics, taking into account atoms and radicals produced at the first step.

Comparison of the results of experiments and numerical modelling gives a reasonable agreement and allows to conclude that, at our experimental conditions, the most important channel of the energy input is dissociation by an electron impact and production of electronically excited atoms and molecules. Additional production of atoms and radicals due to the quenching of electronically excited species in the nearest afterglow does not exceed factor of 2–3. These atoms and radicals (O, H, OH, $\text{C}_n\text{H}_{2n-1}$ etc.) lead to the uniform in space ignition of gas mixtures at temperatures 500–200 K lower than the autoignition temperature.

- To elucidate the main channels which are responsible for the ignition under the action of a nanosecond discharge, and separate the role of dissociated species, in part, the role of electronically excited atoms $\text{O}(^1\text{D})$, we performed a set of experiments with specially prepared mixtures of N_2O with hydrogen, diluted by argon. The experiments were carried out behind a reflected shock wave. A radiation of pulsed ArF laser was used instead of the discharge to provoke the ignition. Comparison of ignition by the discharge and by laser flash-photolysis for the same experimental conditions and for gas mixture of special composition has been made.

The kinetics of chemical transformations in $\text{N}_2\text{O}-\text{H}_2-\text{O}_2-\text{Ar}$ mixtures have been studied in the temperature range from 1000 to 2700 K and pressures from 0.1 to 10 atm. A shock-tube experiment has been used to obtain data on ignition delay time in mixtures which are diluted with the noble gas (50 to 90% Ar). Based on the data obtained and the data of kinetic experiments in mixtures containing up to 97% Ar, a mechanism to describe the kinetics in the given system has been suggested.

- The influence of gas excitation by a pulsed nanosecond atmospheric-pressure barrier discharge (with a high-voltage pulse amplitude up to 25 kV, pulse repetition rate up to 10 kHz, pulse duration is 5–70 ns) on the characteristics of a premixed propane–air and methane–air flames has been investigated within a wide range of the equivalence ratios (0.4–5). It was experimentally found that the flame blow-off velocity increases more than twice with the discharge energy input 0.1% of the burner's chemical power. The emission profiles of the OH, CH, and C_2 radicals along the flame were studied using emission spectroscopy. An efficient production of active radicals under the action of a barrier discharge has been observed. Based on the data obtained, the increase in the flame propagation velocity is explained by the production of

atomic oxygen in a discharge due to the quenching of electronically excited molecular nitrogen N_2 and the electron-impact dissociation of molecular oxygen. A numerical model has been developed that qualitatively describes the influence of a barrier discharge on flame propagation.

It was shown experimentally that results for methane-air flame are similar with propane-air one. The acceleration mechanisms are similar in both cases. Besides proper form of energy input, proper organization of discharge is of great importance. The main characteristics of successful energy input, in this case, is the maximum value of the ratio of flame blow-off velocity with discharge to that one without the discharge (instead of maximum possible flow speed), and the minimal ratio between discharge energy input and chemical power of a burner. The comparison of the effectiveness of plasma-assisted combustion for different types of the discharge, different pulse durations, pulse repetition rates and other parameters, which are responsible for active particles production, was performed. Development of the streamer in different regimes was studied, optimal regimes were found.

It was found that active particles (O and OH primarily), which are produced under the discharge action, play the most significant role in the effect of combustion acceleration. The model of flame acceleration, based on nitrogen quenching on oxygen molecules, with production of O and OH radicals, was confirmed by spectroscopic investigations. Detailed results concerning OH emission and blow-off velocities are represented. For barrier discharge, which was proved to be efficient for flame control, dependence of flame blow-off velocity from pulse amplitude and pulse repetition rate was found.

- To prove the suggested mechanism which is responsible for a flame stabilization by the nanosecond barrier discharge we performed measurements of the gas flows (air and propane-air) temperatures in the barrier discharge. The measurements were performed using rotationally-resolved 0-0 band of 2nd positive emission system of a nitrogen molecule. It was found that gas heating in a propane-air mixture is stronger than in a pure air. Basing on the results of numerical modelling we can conclude that additional heating in propane-air mixtures occurs due to atomic oxygen production in the discharge, and the direct thermal heating by the discharge is insufficient to promote a combustion. The main reasons for the temperature growth are the following. The first is an additional energy release in chain reactions, and this effect is important at high temperatures (near the temperature of self-ignition). The second, which is more important at lower temperatures, is the difference in mechanisms of O atoms recombination in air and propane-air: recombination in air proceeds via O-O and O-O₂ collisions, while in propane-containing mixtures the recombination goes with OH radical formation – this process is much more faster. Because the residual time of a mixture portion in the discharge zone is limited by the flow velocity (near 1 ms), such energy release acceleration is important in kinetic processes. The modelling of gas heating was performed with taking into account O(1D) which is produced in the discharge, good correlation between experimental data and calculations was performed.
- A set-up to study the liquid fuel atomization under the influence of pulsed nanosecond discharge was designed and assembled. The effect of discharge influence was

observed during the regime of strongly aerated liquid atomization. Two differences could be mentioned: the optical density of the flow was reduced with the discharge as well as the atomization time. Regimes and electrodes' geometry were found when nanosecond pulsed discharge affects strongly the liquid atomization. With liquid consumption up to 20 g/sec (and discharge power 3kW, which corresponds to 5% vapourization) it's possible to obtain atomization of a flow in the regimes where there is no atomization in the absence of the discharge. It was found that the main mechanism of the discharge influence lies in vapourization of liquid in the breakdown channel with further changes in flow pattern. The maximum liquid consumption for effective atomization is limited by the stable breakdown appearance.

- The study of propane-air plasma in the hypersonic flow was performed. The flow regime corresponded to Mach number of 8, gas flow was equal to 0.2 g/s. The pre-chamber was equipped with heater which allowed us to heat the gas up to 700 K before its expansion into the nozzle. The stable diffuse plasma was created by low-pressure aerodynamically stabilized DC discharge between nozzle and high-voltage electrode. Mean electron energy in this type of discharge is rather high and gas excitation includes ionization, dissociation, excitation of electronic and vibrational states, so discharge provides almost no direct heating. Spatial distribution of the different molecular bands emission was measured. The region of gas relaxation and chemical reactions (emission peak of CH radical) was determined. Maximum of CH emission corresponds to the region near the shock wave front, while the maximum of emission intensity of nitrogen molecule corresponds to the near-electrode region. The emission of CH radical rapidly drops down due to fast chemical reactions near the shock wave front in this regime. Thus, we have demonstrated the chemical reactions initiation and ignition zone stabilization in the cold flow by high-voltage gas discharge.
- Two installations have been assembled to experimentally study detonation initiation by high-voltage nanosecond and microsecond discharges. Images of the discharge development were taken by an ICCD camera with nanosecond temporal resolution in both cases. The nanosecond pulsed discharge developed quasihomogeneously over the discharge chamber cross-section within the first 50 ns effectively ionizing and dissociating the mixture in a bulk volume. The microsecond discharge developed into a localized spark discharge after 50 ns at atmospheric pressure.

Under initiation by the distributed nanosecond discharge in a 140 mm diameter smooth detonation tube, a successful DDT was observed at 3 calibers from the discharge chamber in all the $C_3H_8/C_4H_{10}+5O_2+xN_2$ mixtures with N_2 concentration up to 38%. The energy input did not exceed 3 J, the DDT time was less than 1 ms. Under initiation by the localized microsecond discharge in a 53 mm diameter smooth detonation tube, the DDT was observed at higher initial pressures for the same mixtures as compared to the nanosecond ignition. Thus, higher efficiency of detonation initiation by the nanosecond discharge comparing to the microsecond spark discharge has been demonstrated. At the same time, the ignition delay times under the microsecond excitation in all mixtures under study were significantly lower as compared to the nanosecond ignition, due to the local nature of energy deposit in the microsecond discharge.

Thus, a method for detonation initiation has been developed which allows to decrease the DDT length in smooth tubes to several calibers due to the non-equilibrium mixture excitation in a bulk volume. The simultaneous mixture ignition in a large number of discharge cells together with Zeldovich's gradient mechanism leads to the rapid formation of a detonation wave.

Basing on the results obtained, two new projects were proposed and supported by EOARD. The first is "Kinetics in Gas Mixtures for Problem of Plasma Assisted Combustion" (RUP1-1513-MO-06). The aim of this project is to analyze efficiency of different species in plasma activation of fuel for PAI/PAC problem. Experiments will be performed using the same type of discharge, but for different gas temperatures: series of the experiments will be made near the autoignition threshold, and another series of experiments will be made at ambient gas temperature. We will study reduction of ignition delay at relatively high temperatures, extracting the main species and processes responsible for the ignition. We will analyze kinetics of oxidation in case of experiments at ambient temperature. We will construct kinetic schemes for both cases and will compare them with available kinetic schemes for oxidation and ignition.

As a result of the project we anticipate experimental data concerning production of radicals, electronically excited species, dissociated species and gas temperature dynamics under the plasma assisted ignition and combustion. Kinetic scheme will be built to describe plasma assisted oxidation at low temperatures as well as at the temperatures near the autoignition threshold.

The second project is "Deflagration-To-Detonation Transition Control By Nanosecond Gas Discharges" (RUP1-1512-MO-06) The goal of this project is the investigation of detonation-to-deflagration transition in hydrocarbon-air mixtures and possibility to control this process by non-equilibrium gas discharge plasma. The main problem for deflagration-to-detonation process control is the length of detonation wave formation. DDT length depends on the initial mixture composition, the initiation energy distribution and geometry of the chamber. In this project we propose to use non-equilibrium gas discharge plasma for preliminary gas excitation and for the reduction of the chemical induction time in the mixture. The synchronization of the ignition of different parts of the gas using gas discharge excitation may lead to sufficient reduction of the DDT length and improvement the efficiency of the process.

The ignition dynamics under the action of nanosecond discharge (up to 300 kV voltage, up to 3 atm initial gas pressure, $T = 300$ K) will be investigated under non-equilibrium plasma excitation conditions. The main processes responsible for the ignition initiation and control will be determined. The reduction of DDT length due to gradient mechanism will be experimentally investigated and numerical model of the process will be constructed for hydrocarbon-air mixtures. We propose the experimental investigations of the flame control using the electric discharge. Strong electric field causes the pulsed discharge development and the non-equilibrium plasma production and start of chain chemical processes. We suggest the experimental investigation of deflagration-to-detonation transition and it's control with the help of electric discharge through Zeldovich's gradient mechanism. The influence of the discharge parameters on characteristic time and length of deflagration-to-detonation transition in hydrocarbon-air mixtures will be investigated. Also a laboratory-scale discharge cell installation will be constructed.

Bibliography

- [1] Cheng, R.K. and Oppenheim, A.K. *Combust. Flame* 58:125, (1984).
- [2] Frenklach, M. and Bornside, D.E. *Combust. Flame* 56:1, (1984).
- [3] Burcat, A., Crossley, R.W., and Scheller, K. *Combust. Flame* 18:115, (1972).
- [4] Smith, G.P., Golden, D.M., Frenklach, M. et al.
http://www.me.berkeley.edu/gri_mec
- [5] Starikovskaia S.M., Starikovskii A.Yu., Zatsenpin D.V. , 27th (Int.) Symposium on Combustion. Boulder. 1998. WIP Abstracts. P.4.
- [6] Morris R.A., Viggiano A.A., Arnold S.T., Maurice L.Q., Sutton E.A. , 27th (Int.) Symposium on Combustion. Boulder. 1998. WIP Abstracts. P.343.
- [7] Morsy, M.H., Ko, Y.S., Chuhg, S.H., Cho, P. *Combust. Flame* 125:724, (2001).
- [8] Phuoc, T.X., White, F.P. *Combust. Flame* 119:203, (1999).
- [9] Phuoc, T.X. *Optics Commun.* 175:419, (2000).
- [10] Ma, J.X., Alexander, D.R., Poulain D.E. *Combust. Flame* 112:492, (1998).
- [11] Thiele, M., Warnatz, J., Maas, U. *Combust. Theory Modelling* 4:413, (2000).
- [12] Thiele, M., Warnatz, J., Dreizler, A., Lindenmaier, S., Schieβl, R., Maas, U., Grant, A., Ewart, P. *Combust. Flame* 128:74, (2002).
- [13] Takita, K., Uemoto, T., Sato, T., Ju., Y., Masuya, G., Ohwaki, K. *Journ. of Propulsion and Power* 16:227, (2000).
- [14] Starikovskaia, S.M., Anikin, N.B., Pancheshnyi, S.V., Zatsenpin, D.V., Starikovskii, A.Yu. *Plasma Sources Sci. Technol.* 10:344 (2001).
- [15] Raizer Yu P 1991 *Gas discharge physics* (New York: Springer)
- [16] Gleizes A , Gonzalez J J and Freton P 2005 Thermal plasma modelling *J. Phys. D: Appl. Phys.* **38** R153–R183
- [17] Khmara D, Kolesnichenko Yu Modeling of microwave filament origination *44th AIAA Aerospace Sciences Meeting and Exhibit* (Reno, Nevada, USA, 9—12 January 2006) AIAA—2006—794

- [18] Gallimberti I 1972 A computer model for streamer propagation *J. Phys. D: Appl. Phys.* **5** 2179—89
- [19] Hartmann G and Gallimberti I 1975 The influence of metastable molecules on the streamer progression *J. Phys. D: Appl. Phys.* **8** 670—80
- [20] Dhali S K and Williams P F 1985 Numerical simulations of streamer propagation in nitrogen at atmospheric pressure *Phys. Rev. A* **31** 1219—21
- [21] Kunhardt E E and Tseng Y 1988 Development of an electron avalanche and its transition into streamers *Phys. Rev. A.* **38** 1410—21
- [22] Gaivoronskii A S and Razhanskii I M 1986 Numerical model of the development of cathode-directed streamer in air gaps with non-uniform field *Zhurnal Tekhnicheskoi Fiziki* **56** 1110—6
- [23] Morrow R Lowke J J 1997 Streamer propagation in air *J. Phys. D: Appl. Phys.* **30** 614—27
- [24] Vitello P A , Penetrante B M and Bardsley J N 1994 Simulation of negative-streamer dynamics in nitrogen *Phys. Rev. E* **49** 5574—98
- [25] Babaeva N Yu and Naidis G V 1996 Simulation of positive streamers in air in weak uniform electric fields *Phys. Lett. A.* **215** 187—90
- [26] Babaeva N Yu and Naidis G V 2002 Simulation of stepped propagation of positive streamers in SF₆ *J. Phys. D: Appl. Phys.* **35** 132--6
- [27] Pancheshnyi S V and Starikovskii A Yu 2003 Two-dimensional numerical modelling of the cathode-directed streamer development in a long gap at high voltage *J. Phys. D: Appl. Phys.* **36** 2683—91
- [28] Tardiveau P, Marode E and Agneray A 2002 Tracking an individual streamer branch among others in a pulsed induced discharge *J. Phys. D: Appl. Phys.* **35** 2823--9
- [29] van Veldhuizen E M and Rutgers W R 2002 Pulsed positive corona streamer propagation and branching *J. Phys. D: Appl. Phys.* **35** 2169—79
- [30] Arrayas M, Ebert U, Hundsdorfer W 2002 Spontaneous branching of anode-directed streamers between planar electrodes. *Phys. Rev. Lett.* **88** N 17 174502—(1—4)
- [31] Kulikovskiy A A 2000 The role of photoionization in positive streamer dynamics *J. Phys. D: Appl. Phys.* **33** 1514—24
- [32] Tardiveau P, Marode E, Agneray A and Cheaib M 2001 Pressure effects on the development of an electric discharge in non-uniform fields *J. Phys. D: Appl. Phys.* **34** 1690--1696
- [33] Pancheshnyi S, Nudnova M, Starikovskii A 2005 Development of a cathode-directed streamer discharge in air at different pressures: experiment and comparison with direct numerical simulation *Phys. Rev. E* **71** 016407 (1—12)

- [34] Nudnova M M, Pancheshnyi S V, Starikovskii A Yu Nonequilibrium plasma formation by high-voltage pulsed nanosecond gas discharge at different pressures *42nd AIAA Aerospace Sciences Meeting and Exhibit* (Reno, Nevada, USA, 5–8 January 2004) AIAA—2004—0353
- [35] Group of Prof. Gundersen M 2005 (private communication)
- [36] Allen N L, Ghaffar A 1995 The variation with temperature of positive streamer properties in air *J. Phys. D: Appl. Phys.* **28** 338–43
- [37] Hidaka K, Kouno T and Hayashi I 1989 Simultaneous measurement of two orthogonal components of electric field using a Pockels device *Rev. Sci. Instrum.* **60**(7) 1252
- [38] Paris P, Aints M, Laan M and Valk F 2004 Measurement of intensity ratio of nitrogen bands as a function of field strength *J. Phys. D: Appl. Phys.* **37** 1179–84
- [39] Paris P, Aints M, Valk F, Plank T, Haljaste A, Kozlov K V and Wagner H–E 2005 Intensity ratio of spectral bands of nitrogen as a measure of electric field strength in plasmas *J. Phys. D: Appl. Phys.* **38** 3894–9
- [40] Pancheshnyi S V, Sobakin S V, Starikovskaya S M and Starikovskii A Yu 2000 Discharge dynamics and the production of active particles in a cathode-directed streamer *Plasma Phys. Rep.* **26**(12) 1054–65
- [41] Ono R and Oda T 2002 Dynamics and density estimation of hydroxyl radicals in a pulsed corona discharge *J. Phys. D: Appl. Phys.* **35** 2133–8
- [42] Ono R and Oda T 2002 NO formation in a pulsed spark discharge in N₂/O₂/Ar mixture at atmospheric pressure *J. Phys. D: Appl. Phys.* **35** 543–8
- [43] Filippov Yu V 1959 Electrosynthesis of ozone *Vestnik MGY, seria Khimia* N 4, 153 (*In Russian*)
- [44] Bersis D and Katakis D 1964 Surfa effects in the production of ozone in the silent discharge *J. Chem. Phys.* **40**(7) 1997
- [45] Carlins J J and Clark R G 1982 Ozone generation by corona discharge *Handbook of ozone technology and applications* **1**(2) 41
- [46] Eliasson B, Hirth M, Kogelschatz U 1987 Ozone synthesis from oxygen in dielectric barrier discharges *J. Phys. D: Appl. Phys.* **20** 1421–37
- [47] Samoilovich V G, Gibalov V I, Kozlov K V 1989 *Physical chemistry of barrier discharge* (Moscow: Moscow State Univ. Publ.) (*In Russian*) 176 p.
- [48] Bagirov M A, Nuraliev N E and Kurbanov M A 1972 Investigation of discharge in air gap with dielectric and technique for determination of number of partial discharges *Journ. Techn. Phys.* **43**(3) 629 (*In Russian*)
- [49] Bagirov M A, Burziev K S and Kurbanov M A 1979 Investigation of energetic parameters of discharge in air between electrodes covered by dielectric at low pressures *Journ. Techn. Phys.* **49**(2) 339 (*In Russian*)

- [50] Tanaka M, Yagi S and Tabata N 1982 Observations of silent discharge in air, oxygen and nitrogen by super-high sensitivity camera Journ. of the Inst. of Electrical Engineers of Japan **102A(10)** 533
- [51] Liu S and Neiger M 2001 Excitation of dielectric barrier discharges by unipolar submicrosecond square pulses *J. Phys. D: Appl. Phys.* **34** 1632–8
- [52] Jidenko N, Petit M and Borra1 J P 2006 Electrical characterization of microdischarges produced by dielectric barrier discharge in dry air at atmospheric pressure *J. Phys. D: Appl. Phys.* **39** 281–93
- [53] Kozlov K V, Wagner H-E, Brandenburg R and Michel P 2001 Spatio-temporally resolved spectroscopic diagnostics of the barrier discharge in air at atmospheric pressure *J. Phys. D: Appl. Phys.* **34** 3164–76
- [54] Kline L E 1974 Calculations of discharge initiation in overvolted parallel-plane gaps *J. Appl. Phys.* **45(5)** 2046
- [55] Kline L E 1975 Effect of negative ions on current growth and ionizing wave propagation in air *J. Appl. Phys.* **46(5)** 1994
- [56] Stefanovic I, Bibinov N K, Deryugin A A, Vinogradov I P, Napartovich A P and Wiesemann K 2001 Kinetics of ozone and nitric oxides in dielectric barrier discharges in O_2/NO_x and $N_2/O_2/NO_x$ mixtures *Plasma Sources Sci. Technol.* **10** 406–16
- [57] Lukas C, Spaan M, Schulz-von der Gathen V, Thomson M, Wegst R, Doebele H F and Neiger M 2001 Dielectric barrier discharges with steep voltage rise: mapping of atomic nitrogen in single filaments measured by laser-induced fluorescence spectroscopy . *Plasma Sources Sci. Technol.* **10** 445–50
- [58] Ono R, Yamashita Y, Takezawa K and Oda T 2005 Behaviour of atomic oxygen in a pulsed dielectric barrier discharge measured by laser-induced fluorescence *J. Phys. D: Appl. Phys.* **38** 2812–16
- [59] Bibinov N K, Fateev A A and Wiesemann K 2001 Variations of the gas temperature in He/ N_2 barrier discharges. *Plasma Sources Sci. Technol.* **10** 579–88
- [60] Williamson J M, Bletzinger P and Ganguly B N 2004 Gas temperature determination in a N_2/Ar dielectric barrier discharge by diode-laser absorption spectroscopy and resolved plasma emission *J. Phys. D: Appl. Phys.* **37** 1658–63
- [61] Baeva M, Dogan A, Ehlbeck J, Pott A and Uhlenbusch J 1999 CARS diagnostic and modelling of a dielectric barrier discharge *Plasma Chem. and Plasma Proc.* **19** 445–66
- [62] Hosselet L M L F 1973 Increased efficiency of ozone production by electric discharges *Electrochim. Acta* **18** 1033
- [63] Georghiou G E , Papadakis A P, Morrow R and Metaxas A C 2005 Numerical modelling of atmospheric pressure gas discharges leading to plasma production. *J. Phys. D: Appl. Phys.* **38** R303–R328

- [64] Kanazava S, Kogoma M, Moriwaki T and Okazaki S 1998 Stable glow plasma at atmospheric pressure *J. Phys. D: Appl. Phys.* **21** 838—40
- [65] Yokoyama T, Kogoma M, Moriwaki T and Okazaki S 1990 The mechanism of the stabilisation of glow plasma at atmospheric pressure *J. Phys. D: Appl. Phys.* **23** 1125—8
- [66] Okazaki S, Kogoma M, Uehara M and Kimura Y 1993 Appearance of stable glow discharge in air, argon, oxygen and nitrogen at atmospheric pressure using a 50 Hz source *J. Phys. D Appl. Phys.* **26** 889—92
- [67] Kekez M M, Barrault M R and Craggs J D 1970 Spark channel formation *J. Phys. D: Appl. Phys.* **3** 1886—96
- [68] Gherardi N, Gouda G, Gat E, Ricard A and Massines F. 2000 Transition from glow silent discharge to micro-discharges in nitrogen gas *Plasma Sources Sci. Technol.* **9** 340--6.
- [69] Navratil Z, Brandenburg R, Trunec D, Brablec A, St'ahel P, Wagner H-E and Kopecky Z 2006 Comparative study of diffuse barrier discharges in neon and helium *Plasma Sources Sci. Technol.* **15** 8--17
- [70] Brandenburg R, Maiorov V A, Golubovskii Yu B, Wagner H-E, Behnke J and Behnke J F 2005 Diffuse barrier discharges in nitrogen with small admixtures of oxygen: discharge mechanism and transition to the filamentary regime *J. Phys. D: Appl. Phys.* **38** 2187--97
- [71] Kossyi I A, Kostinsky A Yu, Matveyev A A and Silakov V P 1992 Kinetic scheme of the non-equilibrium discharge in nitrogenoxygen mixtures *Plasma Sources Sci. Technol.* **1** 207--20
- [72] Trunec D, Navratil Z, Stahel P, Zajickova L, Bursikova V and Cech J 2004 Deposition of thin organosilicon polymer films in atmospheric pressure glow discharge *J. Phys. D: Appl. Phys.* **37** 2112--20
- [73] Guimond S, Radu I, Czeremuszkina G, Carlsson D J and Wertheimer M R 2002 Biaxially Oriented Polypropylene (BOPP) Surface Modification by Nitrogen Atmospheric Pressure Glow Discharge (APGD) and by Air Corona *Plasmas and Polymers* **7(1)** 71—88
- [74] *Proceedings of the XVth International Conference on Gas Discharges and their Applications* (Toulouse, France, 5—10 September 2004) Vol. 1.
- [75] Staack D, Farouk B, Gutsol A and A. Fridman 2005 Characterization of a dc atmospheric pressure normal glow discharge *Plasma Sources Sci. Technol.* **14** 700—711
- [76] Fan H Y 1939 *Phys. Rev.* **55** 769
- [77] Yu L, Laux C O, Packan D M and Kruger C H 2002 Direct-current glow discharges in atmospheric pressure air plasmas *J. Appl. Phys.* **91** 2678

- [78] Yalin A P, Laux C O, Kruger C H and Zare R N. 2002 Spatial profiles of N_2^+ concentration in an atmospheric pressure nitrogen glow discharge *Plasma Sources Sci. Technol.* **11** 248–53
- [79] Laux C O, Spence T G, Kruger C H and Zare R N 2003 Optical diagnostics of atmospheric pressure air plasmas *Plasma Sources Sci. Technol.* **12** 125–38
- [80] Starikovskaia S M, Kukaev E N, Kuksin A Yu, Nudnova M M and Starikovskii A Yu 2004 Analysis of the spatial uniformity of the combustion of a gaseous mixture initiated by a nanosecond discharge. *Comb. and Flame* **139** 177–87
- [81] Korolev Yu D, Mesiats G A 1991 *Physics of pulsed gas breakdown* (Moscow: Nayka Publ.) (*In Russian*)
- [82] Allen K R and Phillips K 1963 *Electrical Rev.* **173** 779
- [83] Thomson J J 1893 *Recent researches in electricity and magnetism*. (Oxford, Clarendon), P. 115.
- [84] Babich L P, Loiko T V, Tsykerman V A 1990 High voltage nanosecond discharge in dense gases at high overvoltages developing in the regime of electrons running away *Physics – Uspekhi* **49** 49
- [85] Babich L P 2003 *High-Energy Phenomena in Electric Discharges in Dense Gases*. (ISTC Science and Technology Series, Vol. 2. Arlington, Virginia: Futurepast.)
- [86] Vasilyak L M, Kostyuchenko S V, Kudryavtsev N N, Filyugin I V 1994 High-speed ionization wave s at an electric breakdown *Physics – Uspekhi* **163** 263
- [87] Anikin N B, Marchenko N (private communication)
- [88] Starikovskaia S M, Starikovskii A Yu, Zatsepin D V 1998 Development of a spatially uniform fast ionization wave in a large discharges volume *J.Phys.D.: Appl.Phys.* **31** 1118–1124.
- [89] Repev A G and Repin P B 2006 Dynamics of the optical emission from a high-voltage diffuse discharge in a rod-plane electrode system in atmospheric-pressure air *Plasma Physics Reports* **32** 72–8
- [90] Krasnochub A V and Vasilyak L M 2006 Dependence of the energy deposition of a fast ionization wave on the impedance of a discharge gap *J. Phys. D: Appl. Phys.* **34** 1678–82
- [91] Anikin N B, Pancheshnyi S V, Starikovskaia S M and Starikovskii A Yu 1998 Break-down development at high overvoltage: electric field, electronic levels excitation and electron density *J.Phys.D.: Appl.Phys.* **31** 826–33
- [92] Pancheshnyi S V, Starikovskaia S M and Starikovskii A Yu 1999 Population of nitrogen molecule electron states and structure of the fast ionization wave *J.Phys.D.: Appl.Phys.* **32** 2219–27

- [93] N B Anikin, S M Starikovskaia and A Yu Starikovskii 2002 Polarity effect of applied pulse voltage on the development of uniform nanosecond gas breakdown *J. Phys. D: Appl. Phys.* **35** 2785–94
- [94] Anikin N.B., Starikovskaia S.M. and Starikovskii A.Yu. *J. Phys. D: Appl. Phys.* 2001. V. 34 P. 177.
- [95] Chintala N, Bao A, Lou G and Adamovich I V (available online 7 November 2005) Measurements of combustion efficiency in nonequilibrium RF plasma-ignited flows *Comb. and Flame* 2006, in press
- [96] Raizer Yu P, Shneider M N, Yatsenko N A 1995 *Radio-Frequency Capacitive Discharges* New York: CRC Press
- [97] Leonov A B, Yarantsev D A, Napartovich A P and Kochetov I V Plasma-assisted ignition and flameholding in high-speed flow. *44th AIAA Aerospace Sciences Meeting and Exhibit* (Reno, Nevada, USA, 9–12 January 2006) AIAA 2006–563.
- [98] Kolesnichenko Yu F, Brovkin V G, Afanas'ev S A and Khmara D V Interaction of High-Power MW with DC, RF, SHF and Laser Created Plasmas *43rd AIAA Aerospace Sciences Meeting and Exhibit* (Reno, Nevada, USA, 10–13 January 2005) AIAA–2005–0405.
- [99] E.M. Van Veldhuizen (ed) *Electrical Discharges for Environmental Purposes: Fundamentals and Applications* (New York: Nova Science) ISBN 1-56072-743-8, 1999.
- [100] A.V. Krasnochub, M.M.Nudnova, A.Yu.Starikovskii *Cathode-Directed Streamer Development In Air At Different Pressures.* // 43-rd AIAA Aerospace Sciences Meeting and Exhibit, 2005. Reno, Nevada, USA, paper AIAA 2005-1196, 2005.
- [101] S.V. Pancheshnyi, S.M. Starikovskaia, A.Yu. Starikovskii *Role of Photoionization Processes in Propagation of Cathode-Directed Streamer* // *J.Phys.D.: Appl.Phys.* 34 (2001) 105.
- [102] M.B. Zheleznyak, A.Kh. Mnatsakanyan, S.V. Sizykh. *Photoionization of Nitrogen–Oxygen Mixtures by Emission from a Gas Discharge* // *Teplofiz. Vys. Temp.*, 20 (1982) 423.
- [103] Polak L.S., Ovsyannikov D.I., Slovetskii D.I. and Vurzel F.B. *Theoretical and Applied Plasmachemistry.* // Nauka, Moscow, 1975.
- [104] Zanner F.J. and Bertram L.A. *IEEE Trans. Plasma Sci.* 11 (1983) 32.
- [105] Boeuf J.P. *J. Phys. D: Appl. Phys.* 36 (2003) 53.
- [106] Hollenstein Ch. *Plasma Phys. Control. Fusion*, 42 (2000) 93.
- [107] M.A. Heald and C.B. Warrton, *Plasma diagnostics with microwaves*, John Wiley&Sons, New York, 1965.
- [108] B M Smirnov 1983 *Complex ions* M.: Nauka

- [109] J B A Mitchell 1990 *Phys. Rep.* **186** 215
- [110] R Johnsen 1993 *J.Chem.Phys.* **98** 5390
- [111] Aleksandrov N.L., Konchakov A.M., Shackin L.V., Shashkov V.M. "Dissociative and triple electron-ion recombination in a CO₂ gas discharge plasma". Plasma Physics, 1986.
- [112] McEwan M J, Phillips L F 1975 *Chemistry of the atmosphere* (Edward Arnold Publ.)
- [113] Bozhenkov S A, Starikovskaia S M, Starikovskii A Yu 2003 Nanosecond gas discharge ignition of H₂ – and CH₄ – containing mixtures. *Comb. and Flame* **133** 133-146
- [114] Asinovskii E. I., Vasiluyak L.M., Kirillin A.V., Markovets V.V.// High temperature. 1975. V. 13. p.195.
- [115] Anikin N.B., Starikovskaia S.M., Starikovskii A.Yu.// High Temperature. 1998. V. 36. p. 992.
- [116] Korolev U.D., Mesiats G.A., Field-emission and explosive processes in gas discharge. Novosibirsk: "Nauka", 1982.
- [117] Farley D.R., Cattolica R.J.// Chem. Phys. Lett. 1997. V. 274. P. 445.
- [118] Kuznetsova L.A, Kuzmenko N.E., Kuziakov Yu. Ya., Plastinin Yu.A. Transition probabilities of diatomic molecules. Moscow.: "Nauka", 1980.
- [119] Herzberg G., Electronic spectra and structure of multiatomic molecules. Moscow: "Mir", 1969.
- [120] Morgan, W.L. Kinema software and Boeuf, J.-P., Pitchford, L.C. *The Siglo Database, CPAT and Kinema Software* <http://www.siglo-kinema.com>.
- [121] David R Bates // J. Phys. B: At. Mol. Opt. Phys. W (1991) 695-701.
- [122] W. B. DeMore, C. J. Howard, S. P. Sander, A. R. Ravishankara, D. M. Golden, C. E. Kolb, R. F. Hampson, M. J. Molina, M. J. Kurylo // JPL Publication 97-4, "Chemical Kinetics and Photochemical Data for Use in Stratospheric Modeling Evaluation" N 12, January 15, 1997.
- [123] Hayashi M., "Electron collision cross sections determined from beam and swarm data by Boltzmann analysis" in "Nonequilibrium Processes in Partially Ionized Gases," eds. M. Capitelli and J.N. Bardsley (Plenum Press, New York, 1990)
- [124] Zatsepin, D.V., Starikovskaia, S.M., Starikovskii, A.Yu. *Chem. Phys. Rep.* 20:66 (2001).
- [125] Aleksandrov, N.L., Son, E.E. in: *Smirnov, B.M.(ed.), Chemistry of Plasma* Moscow, Atomizdat Press, 1980, V.7, p.35
- [126] Gordeev, O.A., Hmara, D.V., IX Conference on Gas Discharge Physics. Ryazan, 1998, p.91.

- [127] Itikawa Y. , Atomic Data and Nuclear Data Tables. 1974, v.14, No1.
- [128] Galtsev V.E. et al. , Preprint IAE-3156, Moscow. 1979
- [129] Erwin D.A., Kunc J.A. , IEEE Transact. On Plasma Science. 1983. v.11. No4. p.266.
- [130] Hake R.D., Phelps A.V. , Phys. Rev. 1967. v.158. No1. p.70.
- [131] Islamov R. Sh., Kochetov I. V., Pevgov V. G. , Preprint FIAN, No 169. Moscow, FIAN. 1977
- [132] Itikawa Y. , J. Phys. Chem. Ref. Data. 1989. v.18. No1. p.23.
- [133] Rapp D., Briglia D.D. , J. Chem. Phys. 1965. v.43. No5. p.1480.
- [134] Rapp D., Englander-Golden P. , J. Chem. Phys. 1965. v.43. No5. p.1464.
- [135] Rapp D., Englander-Golden P., Briglia D.D. , J. Chem. Phys. 1965. v.42. p.4081.
- [136] Konnov, A.A., Proceedings of the Combustion Institute, Vol.28, The Combustion Institute, Pittsburg, 2000, p.317.
- [137] Bhaskaran, K.A., Roth, P. *Progress in Energy and Combustion Science* 28:151 (2002).
- [138] Glushko, V.P. (Ed.), Thermodynamical properties of individual species, M: Nauka, 1978.
- [139] Starikovskaia, S.M., Anikin, N.B., Pancheshnyi, S.V., Starikovskii, A.Yu. In: *Selected Research Papers on Spectroscopy of Nonequilibrium Plasma at Elevated Pressures*. (Ochkin, V.N., ed.) *Proc. of SPIE* 4460:63 (2002).
- [140] Schulz G.J. // Phys. Rev. 1964. v.135. A938.
- [141] Boness M.J.W., Schulz G.J. // Phys. Rev. 1973. v.A8. p.2883.
- [142] Cartwright D.C. // Phys.Rev. A. 1977. v.16. No3.
- [143] Itikawa Y. // J. Phys. Chem. Ref. Data. 1986. v.15. No3. p.985.
- [144] Spence D., Burrow P.D. // J.Phys.B. 1979. v.12. L.179.
- [145] Winters H.F. // J.Chem.Phys. 1966. v.44. p.1472.
- [146] Zipf E.C. // Planet Space Sci. 1978. v.26. p.449.
- [147] Onda K. // J. Phys. Soc. Japan. 1985. v.54. No12. p.4544.
- [148] N.N. Semenov, Nobel Lecture, December 11, 1956
<http://www.nobel.se/chemistry/laureates/>.
- [149] D.A. Eichenberger and W.L. Roberts, *Combust. Flame* 118 (1999) 469.

- [150] E. C. Samano, W. E. Carr, M. Seidl, and Brian S. Lee, Review of Scientific Instruments **64** (10) (1993) 2746–2752.
- [151] S.M. Starikovskaia, Plasma Physics Rep. **21** (1995) 541–547.
- [152] Slovetenskii D I 1980. *Mechanisms of Chemical Reactions in Nonequilibrium Plasma* (Moscow: Nauka) (*In Russian*)
- [153] Lukhovitskii B I, Starik A M and Titova N S 2005 Activation of chain processes in combustible mixtures by laser excitation of molecular vibrations of reactants *Combustion, Explosion, and Shock Waves* **41** 386–94
- [154] Starik A M and Titova N S Possibility of initiation of combustion of CH₄–O₂ (Air) mixtures with laser induced excitation of O₂ molecules 2005 *Combustion, Explosion, and Shock Waves* **40** 499–510
- [155] Starikovskaia S M, Anikin N B, Kosarev I N, Popov N A and Starikovskii A Yu Analysis of ignition by nonequilibrium sources. Ignition of homological series of hydrocarbons by volume nanosecond discharge *44th AIAA Aerospace Sciences Meeting and Exhibit* (Reno, Nevada, USA, 9–12 January 2006) AIAA—2006—616
- [156] Anikin N B, Starikovskaia S M and Starikovskii A Yu 2004 Study of the oxidation of alkanes in their mixtures with oxygen and air under the action of a pulsed volume nanosecond discharge *Plasma Phys. Rep.* **30** 1028–42
- [157] von Elbe G, Lewis B 1942 *J.Chem.Phys.* **10** 366–93
- [158] Williams S, Popovic S, Vuskovic L, Carter C, Jacobson L, Kuo S, Bivolaru D, Corera S, Kahandawala M and Sidhu S Model and igniter development for plasma assisted combustion *42nd AIAA Aerospace Sciences Meeting and Exhibit* (Reno, Nevada, USA, 5–8 January 2004) AIAA—2004—1012
- [159] Campbell C S and Egolfopoulos F N 2005 Kinetic paths to radical-induced ignition of methane/air mixtures *Comb. Sci. Technol.* **177** 2275–98
- [160] Takita K and Ju Y Effect of radical addition on extinction limits of H₂ and CH₄ Flames *44th AIAA Aerospace Sciences Meeting and Exhibit* (Reno, Nevada, USA, 9–12 January 2006) AIAA—2006—1209
- [161] Lou G, Bao A, Nishihara M, Keshav S, Utkin Y G and Adamovich I V Ignition of premixed hydrocarbon–air flows by repetitively pulsed, nanosecond pulse duration introduction plasma *41st AIAA Aerospace Sciences Meeting and Exhibit* (Reno, Nevada, USA, 9–12 January 2003) AIAA—2006—1215
- [162] Kof L M, Starikovskii A Yu Oxygen–hydrogen mixtures ignition under the high-voltage ionization wave conditions at high temperatures *26th Int. Symposium on Combustion. Abstracts of Work-in-Progress Papers* (Napoli, 1996, the Combustion Institute Publ.) P.406.
- [163] Hagelaar G J M and Pitchford L C 2005 *Plasma Source Sci. Technol.* **14** 722–33 and <http://www.siglo-kinema.com/> BOLSIG

- [164] Hayashi M, 1987 *Swarm studies and inelastic electron-molecule collisions* (L.C. Pitchford, ed., New York, Springer) 167—87
- [165] Smirnov B M 1982 *Excited atoms* (Moscow, Energoizdat)
- [166] Zhiglinskii A G, ed. 1994 *Handbook on rate coefficients for elementary processes with atoms, ions, electrons and photons* (St-Petersburg University Press)
- [167] Bates D R 1986 *Astrophys. J.* **306** L45
- [168] <http://www.udfa.net> The UMIST Database for Astrochemistry
- [169] Burcat A, Scheller K, Lifshitz A 1971 Shock-tube Investigation of Comparative Ignition Delay Times for C1—C5 alkanes. *Comb. Flame* **16** 29
- [170] Kee R J, Miller J A and Jefferson T H 1980 *Report No. SAND 80-8003, Sandia National Laboratory, Livermore, CA*
- [171] Tan Y, Dagaut P, Cathonnet M, Boetther J C 1994 Oxidation and Ignition of Methane-Propane and Methane-Ethane-Propane Mixtures: Experiments and Modelling. *Combust. Sci. Technol.* **103** 133
- [172] Zhukov V P 2004 Autoignition of Saturated Hydrocarbons at High Pressures and Initiation of Detonation by Nanosecond Discharge PhD Thesis, Moscow Institute of Physics and Technology
- [173] Curran H J, Gaffuri P, Pitz W J, Westbrook C K 1998 A Comprehensive Modlling Study of n-Heptane Oxidation *Combustion and Flame* **114** 149–77
- [174] Carter C.D., Williams S., Lee L.C., Sidhu S., Graham J. AIAA Paper 2003-0703. 41st Aero-space meeting and Exhibit. 6-9 Jan 2003, Reno, Nevada, USA.
- [175] E.I. Mintoussov, S.V. Pancheshnyi, A.Yu. Starikovskii. AIAA paper 2004-1013. 42nd Aerospace meeting and Exhibit. 5-8 Jan 2004, Reno, Nevada, USA.
- [176] D. Galley, G. Pilla, D. Lacoste, S. Ducruix, F. Lacas, D. Veynante and C.O. Laux. AIAA paper 2005-1193. 43rd Aerospace meeting and Exhibit. Jan 2005, Reno, Nevada, USA.
- [177] Packan D., Grisch F., Attal-Tretout B., AIAA paper 2004-0983. 42nd Aerospace meeting and Exhibit. 5-8 Jan 2004, Reno, Nevada, USA.
- [178] Starikovskii A.Yu. Combustion, Explosion and Shock Waves, V.39, 2003, p.619.
- [179] Kosarev I.N., Starikovskaia S.M., Starikovskii A.Yu. 15th International Conference on MHD Energy Conversion and 6th International Workshop on Magnetoplasma Aerodynamics. Moscow, May 24-27, 2005, V.1, p.335.
- [180] Parish J.W., Ganguly B.N. AIAA paper. 42nd Aero-space meeting and Exhibit. 5-8 Jan 2004, Reno, Nevada, USA.
- [181] Schott G.L., Kinsey J.L. *J. Chem. Phys.* V. 29, 1958, p.1177.

- [182] Zuev A.P., Starikovskii A.Yu. *Khimicheskaya Fizika*, V.10, 1991, p.347.
- [183] Zaslonko I S, Losev S A, Mozzhukhin E V, Mukoseev Yu K 1980 *Kinetika i kataliz* **21** 311 (In Russian)
- [184] Dean A M 1976 Shock Tube Studies of the N₂O/Ar and N₂O/H₂/Ar Systems *Int. J. Chem. Kinet.* **8** 459
- [185] Zuev A P and Starikovskii A Yu 1992 Reactions involving nitrogen oxides. Unimolecular N₂O decomposition *Sov. J. Chem. Phys.* **10(1)** 80—99
- [186] Roose T R, Hanson R K, Kruger C H 1978 Decomposition of NO in the Presence of NH₃. *Proc. Int. Symp. Shock Tubes Waves* Vol.11, 245—53
- [187] Zuev A P and Starikovskii A Yu 1992 Reactions in the N₂O—H₂ system at high temperatures *Sov. J. Chem. Phys.* **10(3)** 520—40
- [188] Hidaka Y, Takuma H and Suga M 1985 Shock-tube study of the rate constant for excited OH*(²Σ⁺) formation in the N₂O—H₂ reaction *J. Phys. Chem.* **89** 4093—5
- [189] Zuev A P and Starikovskii A Yu 1991 Nitrogen oxide involving reactions at high temperatures. Reactions of N₂O with O. *Khimicheskaya fizika. Transl: Sov. J. Chem. Phys.* **10(2)** 179—189
- [190] Zuev A P and Starikovskii A Yu 1991 Nitrogen oxide involving reactions at high temperatures. Reactions NO + O + M → NO₂ + M. *Khimicheskaya fizika. Transl: Sov. J. Chem. Phys.* **10(2)** 190—199
- [191] Fairchild P W, Smith G, and Crolesey D R 1983 Collisional Quenching of A²Σ⁺ OH at Elevated Temperatures *J Chem Phys* **79(4)** 1795—807
- [192] Tsang W, Hampson R F 1986 Chemical kinetic data base for combustion chemistry. Part I. Methane and related compounds *J. Phys. Chem. Ref. Data* **15** 1087
- [193] Baldwin R R, Gethin A, Walker R W 1973 Reaction of Hydrogen Atoms with Nitrous Oxide *J. Chem. Soc. Faraday Trans.* **69** 352
- [194] Albers E A, Hoyermann K, Schacke H, Schmatjko K J, Wagner H Gg, Wolfrum J 1975 Absolute Rate Coefficients for the Reaction of H—Atoms with N₂O and Some Reactions of CN Radicals *Symp. Int. Combust. Proc.* **15** 765
- [195] Hidaka Y, Takuma H, Suga M 1985 Shock-tube studies of N₂O decomposition and N₂O—H₂ reaction *Bull. Chem. Soc. Jpn.* **58** 2911
- [196] Walker R W 1973 Comments on “An Assessment of Rate Data for High-Temperature System” *Symp. Int. Combust. Proc.* **14** 117
- [197] Fenimore C P, Jones G W 1959 Rate of reaction in hydrogen, nitrous oxide and in some other flames *J. Phys. Chem.* **63** 1154
- [198] Dixon-Lewis G, Sutton M M, Williams A 1965 The reaction of hydrogen atoms with nitrous oxide *J. Chem. Soc.* 5724

- [199] Henrici H, Bauer S H 1969 Kinetics of the nitrous oxide-hydrogen reaction *J. Chem. Phys.* **50** 1333
- [200] Balakhnine V P, Vandooren J, Van Tiggelen P J 1977 Reaction Mechanism and Rate Constants in Lean Hydrogen–Nitrous Oxide Flames *Combust. Flame* **28** 165
- [201] Dean A M, Steiner D C, Wange E E 1978 A Shock Tube Study of the $\text{H}_2/\text{O}_2/\text{CO}/\text{Ar}$ and $\text{H}_2/\text{N}_2\text{O}/\text{CO}/\text{Ar}$ Systems: Measurements of the Rate Constant for $\text{H} + \text{N}_2\text{O} = \text{N}_2 + \text{OH}$ *Combust. Flame* **32** 73
- [202] Glass G P, Quay R B 1979 Measurement of High Temperature Rate Constants Using a Discharge Flow Shock Tube *J. Phys. Chem.* **83** 30
- [203] Dean A M, Johnson R L, Steiner D C 1980 Shock–Tube Studies of Formaldehyde Oxidation *Combust. Flame* **37** 41
- [204] Lewis R S, Watson R T 1980 Temperature Dependence of the Reaction $\text{O}(^3\text{P}) + \text{OH} = \text{O}_2 + \text{H}$ *J. Phys. Chem.* **84** 3495
- [205] Howard M J, Smith I W M 1981 Direct Rate Measurements on the Reactions $\text{N} + \text{OH} = \text{NO} + \text{H}$ and $\text{O} + \text{OH} = \text{O}_2 + \text{H}$ from 250 to 515 K *J. Chem. Soc. Faraday Trans.* **77** 997
- [206] Pirraglia A N, Michael J V, Sutherland J W, Klemm R B 1989 A flash photolysis–shock tube kinetic study of the H atom reaction with O_2 : $\text{H} + \text{O}_2 = \text{OH} + \text{O}$ ($962\text{ K} < T < 1705\text{ K}$) and $\text{H} + \text{O}_2 + \text{Ar} = \text{HO}_2 + \text{Ar}$ ($746\text{ K} < T < 987\text{ K}$) *J. Phys. Chem.* **93** 282
- [207] Shin K S, Michael J V 1991 Rate constants for the reactions $\text{H} + \text{O}_2 = \text{OH} + \text{O}$ and $\text{D} + \text{O}_2 = \text{OD} + \text{O}$ over the temperature range 1085–2278 K by the laser photolysis–shock tube technique *J. Chem. Phys.* **95** 262–273
- [208] Baulch D L, Cobos C J, Cox R A, Esser C, Frank P, Just Th, Kerr J A, Pilling M J, Troe J, Walker R W Warnatz J 1992 Evaluated kinetic data for combustion modelling *J. Phys. Chem. Ref. Data* **21** 411–429
- [209] Kurzius S C, Boudart M 1968 Kinetics of the branching step in the hydrogen–oxygen reaction *Combust. Flame* **12** 477–491
- [210] Westenberg A A, DeHaas N, Roscoe J M 1970 Radical reactions in an electron spin resonance cavity homogeneous reactor *J. Phys. Chem.* **74** 3431–3438
- [211] Klimo V, Bittererova M, Biskupic S, Urban J, Micov M 1993 Temperature dependences in the $\text{O} + \text{OH} = \text{O}_2 + \text{H}$ reaction. Quasiclassical trajectory calculation *Collect. Czech. Chem. Commun.* **58** 234–243
- [212] Cobos C J, Hippler H, Troe J 1985 High–pressure falloff curves and specific rate constants for the reactions $\text{H} + \text{O}_2 = \text{HO}_2 = \text{HO} + \text{O}$ *J. Phys. Chem.* **89** 342
- [213] Warnatz J 1984 Rate coefficients in the C/H/O system "Combustion Chemistry", ed. W.C.Gardiner,Jr. Springer-Verlag,NY, 197

- [214] Kaufman F, Del Greco F P 1963 Fast reactions of OH radicals *Symp. Int. Combust. Proc.* **9** 659
- [215] Sulzmann K G P, Kline J M, Penner S S 1980 Shock–Tube Studies of N₂O–Decomposition *Symp. Int. Shock Tubes Waves Proc.* **12** 465
- [216] Fenimore C P, Jones G W 1962 Rate of the reaction, O + N₂O = 2NO *Symp. Int. Combust. Proc.* **8** 127—133
- [217] Tsang W, Herron J T 1991 Chemical kinetic data base for propellant combustion. I. Reactions involving NO, NO₂, HNO, HNO₂, HCN and N₂O *J. Phys. Chem. Ref. Data* **20** 609—663
- [218] Soloukhin R I 1972 Thermal Decompositin Kinetics of N₂O in Shock Waves *Dokl. Phys. Chem.* **207** 912
- [219] Baber S C, Dean A M 1975 N₂O Dissociation behind Reflected Shock Waves *Int. J. Chem. Kinet.* **7** 381
- [220] Monat J P, Hanson R K, Kruger C H 1977 Kinetics of Nitrous Oxide Decomposition *Combust. Sci. Technol.* **16** 21
- [221] Belles F E, Brabbs T A 1971 Experimental Verification of Effects of Turbulent Boundary Layers on Chemical–Kinetic Measurements in a Shock Tube *Symp. Int. Combust. Proc.* **13** 165
- [222] Jachimowski C J, Houghton W M 1971 Shock–Tube Study of the Initiation Process in the Hydrogen–Oxygen Reaction *Combust. Flame* **17** 25
- [223] Azatyan V V, Aleksandrov E N, Troshin A F 1975 Chain Initiation Rate in the Reactions of Hydrogen and Deuterium with Oxygen *Kinetika i kataliz* **16** 306
- [224] Semenov N 1945 On the constants of the reactions H + O₂ = OH + O and H₂ + O₂ = 2OH *Acta Physicochim. U.R.S.S.* **20** 292
- [225] Balakhnin V P, Gershenzon Yu M, Kondrat'ev V N, Nalbandyan A B 1966 A quantitative study of the mechanism of hydrogen combustion close to the lower explosion limit *Dokl. Phys. Chem.* **170** 659
- [226] Ripley D L, Gardner W C, Jr. 1966 Shock–tube study of the hydrogen-oxygen reaction. II. Role of exchange initiation *J. Chem. Phys.* **44** 2285
- [227] W.T. Brande, Phil. Trans. Roy. Soc., 104, 1814, 51.
- [228] A.E. Malinovsky, Sotsialisticheskaya Rekonstruktsia i Razvitie (Socialistic Reconstruction and Development), Moscow, **7**, 1934, 24.
- [229] A.B. Fialkov, Prog.Energy Combust.Sci., **23**, 1997, 399-528.
- [230] C.H. Berman, R.J. Grill, and H.F. Calcote, NO_x reduction in flames stabilized by an electric field, ASME Fossil Combs. Symposium, 1991, 3rd Energy-Sources Technology Conference, Houston, TX.

- [231] A.E. Malinovsky, J.Chem.Phys., Paris, **21**, 1924, 469.
- [232] H.F. Calcote, Effect of dc Electric Field on Burner Flame, Princeton University, Project Squid Technical Report, 1946.
- [233] J. Lawton and F. Weinberg, Electrical Aspects of Combustion, Clarendon Press, Oxford, 1969.
- [234] E.I. Mintoussov, S.V. Pancheshnyi, A.Yu. Starikovskii, 17th International Symposium on Gas Kinetics, Essen, Germany, 2002, CP24.
- [235] H.F. Calcote, C.H. Berman, ASME Fossil Fuels Combustion Symposium PD, **25**, 1989, 25-31.
- [236] D. Bradley, S.H. Nasser, Combust. Flame, **55**, 1984, 53-58.
- [237] Yu.N. Shebeko, FGV (*in russian*), **18**, 4, 1982, 48-51.
- [238] Combustion Chemistry, ed. W. Gardiner-Jr, Moscow, Mir, 1988.
- [239] G.P.Tewari, J.R.Wilson, Combust. Flame, **24**, 2, 1975, 159-167.
- [240] N.B. Anikin, E.I. Mintoussov, S.V. Pancheshnyi, D.V. Roupassov, V.E. Sych, A.Yu. Starikovskii, 41st AIAA Aerospace Sciences Meeting and Exhibit, AIAA Paper, 2003, AIAA-2003-1053.
- [241] Ya.B. Zeldovich, G.I. Barenblatt, Mathematical Theory of Combustion and Explosion, Nauka, Moscow, 1980.
- [242] S.M. Starikovskaia, A.Yu. Starikovskii, D.V. Zatspein, Combust. Theory Modelling, **5**, 2001, 97-129.
- [243] Konnov, A. Detailed Reaction Mechanism for Small Hydrocarbons Combustion. <http://homepages.vub.ac.be/~akonnov/>
- [244] A.V. Krasnochub, E.I. Mintoussov, M.M. Nudnova, A.Yu. Starikovskii Interference between streamers in bunch of streamers. XXVIIth ICPIG, Eindhoven, the Netherlands, June 2005.
- [245] Starikovskaia S.M. 2006 Plasma Assisted Ignition and Combustion *J. Phys. D: Appl. Phys.* **39** 265-299
- [246] Zhukov V.P., Sechenov V.A., Starikovskii A.Yu. *Comb. Flame*, 2004, **136**, 257-259
- [247] S.M.Starikovskaia, I.N.Kosarev, A.V.Krasnochub, E.I.Mintoussov, A.Yu.Starikovskii AIAA paper 2005-1195
- [248] V.N Dashevsky, B.S. Fialkov. FGV, 1993, 29,105.
- [249] Pancheshnyi S.V., Starikovskaia S.M., Starikovskii A.Yu. *Chemical Physics Letters* **294**, 523 (1998)
- [250] Skubenich V.V., Zapesochnyi I.P. *High Energy Chemistry* **9**, 387 (1975)

- [251] Borst W.L., Zipf E.C. *Phys.Rev.A* **1**, 834 (1970)
- [252] Shukhin G.I., Sharafutdinov R.G. *J.Tech.Phys.* **53**, 333 (1983)
- [253] Bull D.C., Elsworth J.E., Hooper G, "Initiation of spherical detonation in hydrocarbon/air mixtures", *Acta Astron.*, 5, 997–1008, 1977.
- [254] Schultz, E. Wintenberger, and J.E. Shepherd, "Investigation of deflagration to detonation transition for application to pulse detonation engine ignition systems", *Proceedings of the 16th JANNAF Propulsion Symposium*, Chemical Propulsion Information Agency, 1999.
- [255] Brown C.J., Thomas G.O., *Shock Waves*, 10 (2000) 23–32.
- [256] R. Sorin, R. Zitoun, D. Desbordes, "Optimisation of the Deflagration to Detonation Transition: Reduction of Length and Time of Transition", *19th Int. Colloq. on Dynamics of Explosions and Reactive Systems (ICDERS)*, July 27th – August 1st, 2003 in Hakone Prince Hotel, Hakone, Kanagawa, Japan.
- [257] Jackson S. I., and Shepherd J. E., *38th AIAA/ASME/SAE/ASEE Joint Propulsion Conference and Exhibit*, July 7-10, 2002, Indianapolis, USA , AIAA 2002–2627.
- [258] Shepherd J.E., Austin J.M., Chao T., Pintgen F., Wintenberger E., Jackson S., and Cooper M., "Detonation initiation and propagation", *Proceedings of the 15th ONR Propulsion Conference*, Washington DC, August 2002
- [259] Smirnov N.N., and Nikitin V.F., *Combustion, Explosion, and Shock Waves*, 40 (2004) 186–199.
- [260] Higgins A.J., Pinard P., Yoshinaka A.S., Lee J.H.S., *High-speed deflagration and detonation: fundamentals and control*, edited by Roy G., Frolov S., Netzer D., Borisov A., Moscow, Elex-KM Publ., 2001. p. 45-62.
- [261] Frolov S.M., Basevich V.Ya., Aksenov V.S., *J. Propul. Power*, 2003; 19(4): 573-80.
- [262] Lee J.H., Knystautas R. and Guirao C.M., *Proceedings of the 15th Symp (Int) on Combustion*, The Combustion Institute, Pittsburgh, 1974, p. 53.
- [263] Wang F., Jiang C., Kuthi A., et al., "Transient Plasma Ignition of Hydrocarbon-Air Mixtures in Pulse Detonation Engines", 42nd AIAA Aerospace Sciences Meeting and Exhibit, Reno, NV, Jan 5 8, 2004. AIAA Paper 2004–834.
- [264] Liu J.B., Ronney P.D. and Gundersen M.A., "Premixed flame ignition by transient plasma discharges", *Proceedings of The Twenty-Ninth International Symposium on Combustion*, Sapporo, Japan, July 21-26, 2002.
- [265] Kukaev E.N., Tsyganov D.L., Zhukov V.P., Starikovskaia S.M., Starikovskii A.Yu., "Deflagration-to-Detonation Control by Non-Equilibrium Gas Discharges and its Applications for Pulsed Detonation Engine", 42nd AIAA Aerospace Sciences Meeting and Exhibit, Reno, Nevada, 2004.

- [266] Zhukov V.P., Starikovskii A.Yu., "Effect of a Nanosecond Gas Discharge on Deflagration to Detonation Transition", *Combustion, Explosion, and Shock Waves*, Vol. 42, N2, pp. 195-204, 2006.
- [267] Zhukov V.P., Rakitin A.E., Starikovskii A.Yu., "Initiation of detonation by Nanosecond Gas Discharge", 44th AIAA Aerospace Sciences Meeting and Exhibit, 9-12 Jan., Reno, Nevada, USA, paper AIAA 2006-952, 2006.
- [268] California Institute of Technology. http://www.galcit.caltech.edu/detn_db/html/db_125.html.

List of Figures

2.1	Example of still (left) and streak (right) images of a streamer emission ²⁸	16
2.2	CCD photos of a plane-protrusion discharge in air using the semiconductor switch. The applied voltage is (a) 9 kV, (b) and (c) 10kV,(d)(g) 12.5 kV and (h) 15 kV. The optical gate is (a)-(e) 5 μ s, and (f)-(h) 50 μ s. ²⁹	17
2.3	Photograph of streamer heads of a point-wire discharge in air taken with the ICCD with 0.8 ns gate. A pulse of 25 kV with a rise time of 20 ns is applied. The photo is taken 31 ns after the start of the pulse. Discharge gap is 25 mm, plane-to-plane geometry ²⁹	18
2.4	ICCD images of streamer in air at different pressures. Interelectrode gap is 30 mm, high voltage amplitude is 20 kV, and pulse duration is 25 ns. According to ³⁴	19
2.5	The effect of temperature on streamer propagation ³⁶ . Numbers indicate the number of superimposed shots: a) T=290 K and b) T=373 K. The applied electric field was 500 kV m ⁻¹ ; with pulse voltage 4.25 kV and gap length 15 cm.	20
2.6	Reduced electric field in the streamer head <i>vs.</i> the distance from the high-voltage electrode for the interelectrode distance equal to 24 mm ⁴⁰	21
2.7	(a) Distribution of OH radicals at 5 μ s observed by the two-dimensional LIF and (b) spontaneous emission of a positive discharge in H ₂ O(2.4%):N ₂ mixture ⁴¹ . Each image is obtained at a different discharge pulse. The white line represents the needle electrode. Discharge gap is 16 mm.	22
2.8	Short-time-exposure photographs of a filamentary DBD (anode, top; cathode, bottom) from a single voltage pulse (800 ns exposure time, N ₂ , 3 l/min, 1 atm, interelectrode distance 1.7 mm, repetition rate 2000 Hz ⁵¹	23
2.9	(a) Voltage and instantaneous current, (b) single current pulse and (c) series of current pulses, typical for DBD-discharge ⁵²	24
2.10	(a) Electrode arrangement with the indicated range of axial scanning and a typical example of the oscillograms of voltage and current; (b) Determined distributions of electric field and electron density. The positions of the tips of the electrodes indicated by the arrows on the left ⁵³	25
2.11	Density distribution of atomic nitrogen in a DBD at 950 mbar, containing 90% N ₂ and 10% O ₂ ; 8 kV voltage; positive dielectric (DE+); 2 μ s after discharge initiation. Light colours correspond to low densities, dark colours to high densities ⁵⁷	26
2.12	Typical 10 ns exposure time photographs of a 4 mm gas gap during (a) an APGD ($V = 11$ kV) and (b) a filamentary discharge ($V = 14$ kV) ⁶⁸	28

2.13	DC glow discharge in air (1.4 kV/cm, 200 mA). Interelectrode distance is 3.5 cm ⁷⁹	29
2.14	Image of the glow discharge in atmospheric pressure hydrogen. Positive column and negative glow are visible; standing striations are visible in the positive column ⁷⁵	31
2.15	Regions of breakdown development per different mechanisms depending upon overvoltage in air ¹⁴	32
2.16	Subsequent ICCD images of nanosecond discharge in air. ICCD gate is equal to 1 ns, time moments from the discharge start are indicated ⁸⁷ . High voltage electrode is on the left hand side.	34
2.17	Temporal evolution of electric field, $N_2(C^3\Pi_u, v'=0)$ and $N_2^+(B^2\Sigma_u^+, v'=0)$ level densities and electron concentration in nitrogen at a distance 20 cm from the high-voltage electrode. Electric field represented with a solid line is determined from the electrical measurements; represented by symbols – from the spectroscopy. Nitrogen, $P = 4$ Torr, $U = -15.5$ kV ¹⁴	35
2.18	Fraction of energy contribution per pulse into inner degrees of freedom for various gases: (a) air (curves 1-4 correspond to N_2 ; 5 and 6 to O_2); (b) nitrogen; (c) hydrogen. Numbers designate: 1 and 5, ionization; 2 and 6, excitation of electronic terms; 3, dissociation; 4, excitation of vibration levels; 7, excitation of rotation levels ⁹⁴	36
2.19	Experimental setup for streamer discharge investigations.	40
2.20	Voltage and anode current measurements. 30 mm. Air.	41
2.21	Velocity dependence on the voltage. $U = 24$ kV. Discharge gap is 30 mm. Air. Cathode directed streamer. Dots are experimental results, curves are numerical modeling.	42
2.22	Current dependence on the Pressure. $U = 24$ kV. Discharge gap is 30 mm. Air. Cathode directed streamer. Dots are experimental results, curve is numerical modeling.	43
2.23	Calculated emission (A) and electric field (B) distributions. $U = 24$ kV. Discharge gap is 30 mm. Air. Cathode directed streamer.	43
2.24	Comparison of the measured and calculated streamer channel diameter. $U = 24$ kV. Discharge gap is 30 mm. Air. Cathode directed streamer.	44
2.25	Voltage applied and image of the streamer in the stroboscopic mode.	45
2.26	Emission distribution in the streamer head. Camera gate is 300 ps.	45
2.27	Streamer channel electrodynamic diameter. $U = 30$ kV, Air.	46
2.28	ICCD image of multi-channel flash for different pressures and voltages. Discharge gap is 30 mm. Air.	47
2.29	Electric field distribution in the gap ($lg(E/n)$). Four additional "conical branches" are added.	48
2.30	Dependence of the streamer velocity from number of branches. 30 mm. Air.	49
2.31	Dependence of the streamer current from number of branches. 30 mm. Air.	49
2.32	FIW front velocity upon pressure at a point $x=20$ cm from the high-voltage electrode for different gases. $U = -13.5$ kV, pulse duration is 25 ns, pulse front duration is 3 ns, $f = 40$ Hz, discharge tube diameter is 1.8 cm, tube length is 60 cm.	51

2.33	Energy contributed into gas in the first pair of pulses W_I and the energy, taking into consideration one reflection W_{II} in oxygen. $U = -15$ kV, pulse duration is 20 ns, pulse front duration is 8 ns, $f = 82$ Hz, discharge tube diameter is 4.7 cm, tube length is 20 cm.	52
2.34	The imaging of nanosecond discharge propagation in long tube for different polarities of a high-voltage pulse. $U = \pm 13.5$ kV, pulse duration is 25 ns, pulse front duration is 3 ns, $f = 40$ Hz. Discharge tube diameter is 18 mm; interelectrode distance is 60 cm.	53
2.35	The imaging of nanosecond discharge propagation in tubes of different diameters. Positive polarity, $U = +13.5$ kV, pulse duration is 25 ns, pulse front duration is 3 ns, $f = 40$ Hz. Discharge tube diameter is 18 mm; interelectrode distance is 60 cm.	54
2.36	Emission image from a nanosecond discharge taken by LaVision ICCD camera. Camera gate is equal to 1 ns. Air, +5 kV pulse amplitude and 12 ns pulse duration. a) – 0.6 Torr; b) – 20 Torr.	55
2.37	Electric field and electron density: typical temporal behavior. $U = -13.5$ kV, $x = 20$ cm from the cathode. Hydrogen pressure is pointed in the figure. Nitrogen pressure is equal 4 Torr.	56
2.38	Photo of a microwave interferometer installed near the discharge tube. Microwave lens and a part of waveguide are clearly seen.	57
2.39	Scheme of the interferometer and examples of preliminary experimental data.	58
2.40	Electron density at different pressures. Pulse amplitude is equal to 13.5 kV, pulse duration is 12 ns.	59
2.41	Experimental setup: 1 — discharge cell, 2,3 — electrodes, 4 — optical window (CaF_2), 5 — high voltage generator, 6 — back current shunt, 7 — oscilloscope Tektronix TDS-380, 8 — microwave interferometer, 9 — waveguide, 10 — angled reflector, 11 — oscilloscope Tektronix TDS-3054.	61
2.42	Oscillogrammes obtained by microwave technique in N_2 , $p = 1, 3, 6, 9$ Torr, $T = 295$ K, $U = 11$ kV in cable, positive polarity.	62
2.43	Electron density profiles in N_2 , $p = 1-3.5$ Torr, $T = 295$ K, $U = 11$ kV, positive polarity.	64
2.44	Electron density profiles in N_2 , $p = 4-9$ Torr, $T = 295$ K, $U = 11$ kV, positive polarity.	65
2.45	Electron density profiles in N_2 , $p = 1-10$ Torr, $T = 295$ K, $U = 11$ kV, positive polarity.	66
2.46	Electron density profile in N_2 , $p = 2.5$ Torr, $T = 295$ K, $U = 11$ kV, positive polarity.	66
2.47	Oscillogrammes obtained by microwave technique in O_2 , $p = 1, 3, 6, 9$ Torr, $T = 295$ K, $U = 11$ kV, positive polarity.	67
2.48	Electron density profiles in O_2 , $p = 1-3.5$ Torr, $T = 295$ K, $U = 11$ kV, positive polarity.	68
2.49	Electron density profiles in O_2 , $p = 4-9$ Torr, $T = 295$ K, $U = 11$ kV, positive polarity.	69
2.50	Electron density profiles in O_2 , $p = 1-10$ Torr, $T = 295$ K, $U = 11$ kV, positive polarity.	70

2.51	Electron density profile in O_2 , $p = 2.5$ Torr, $T = 295$ K, $U = 11$ kV, positive polarity.	70
2.52	Oscillogrammes obtained by microwave technique in CO_2 , $p = 1, 3, 6, 9$ Torr, $T = 295$ K, $U = 11$ kV, positive polarity.	71
2.53	Electron density profiles in CO_2 , $p = 1-3.5$ Torr, $T = 295$ K, $U = 11$ kV, positive polarity.	72
2.54	Electron density profiles in CO_2 , $p = 4-9$ Torr, $T = 295$ K, $U = 11$ kV, positive polarity.	73
2.55	Electron density profiles in CO_2 , $p = 1-10$ Torr, $T = 295$ K, $U = 11$ kV, positive polarity.	74
2.56	Electron density profile in CO_2 , $p = 2.5$ Torr, $T = 295$ K, $U = 11$ kV, positive polarity.	74
2.57	Oscillogrammes obtained by microwave technique in $N_2 : O_2 = 4 : 1$, $p = 1, 3, 6, 9$ Torr, $T = 295$ K, $U = 11$ kV, positive polarity.	75
2.58	Electron density profiles in $N_2 : O_2 = 4 : 1$, $p = 1-3.5$ Torr, $T = 295$ K, $U = 11$ kV, positive polarity.	76
2.59	Electron density profiles in $N_2 : O_2 = 4 : 1$, $p = 4-9$ Torr, $T = 295$ K, $U = 11$ kV, positive polarity.	77
2.60	Electron density profiles in $N_2 : O_2 = 4 : 1$, $p = 1-10$ Torr, $T = 295$ K, $U = 11$ kV, positive polarity.	78
2.61	Electron density profile in $N_2 : O_2 = 4 : 1$, $p = 2.5$ Torr, $T = 295$ K, $U = 11$ kV, positive polarity.	78
2.62	Oscillogrammes obtained by microwave technique in H_2O , $p = 1, 2.5, 3.5, 4$ Torr, $T = 295$ K, $U = 11$ kV, positive polarity.	79
2.63	Electron density profiles in H_2O , $p = 1-3.5$ Torr, $T = 295$ K, $U = 11$ kV, positive polarity.	80
2.64	Electron density profiles in H_2O , $p = 1-4$ Torr, $T = 295$ K, $U = 11$ kV, positive polarity.	81
2.65	Electron density profile in H_2O , $p = 2.5$ Torr, $T = 295$ K, $U = 11$ kV, positive polarity.	81
2.66	Pulse electrodynamics in the Water vapor. $p = 4$ Torr, $T = 295$ K, $U = 11$ kV, positive polarity.	82
2.67	Electron density kinetic curve. Comparison of experiments (blue curves) and calculations (green curves). $T = 300$ K, N_2	84
2.68	Electron density kinetic curve. Comparison of experiments (blue curves) and calculations (green curves). $T = 300$ K, O_2	88
2.69	Electron density kinetic curve. Comparison of experiments (blue curves) and calculations (green curves). $T = 300$ K, CO_2	89
2.70	Electron density kinetic curve. Comparison of experiments (blue curves) and calculations (green curves). $T = 300$ K, H_2O	92
2.71	Scheme of the experimental setup. Abbreviations: A — cross-section of measurement, DC — discharge cell, EP — end plate, HPC — high pressure cell, HVG — high voltage generator, ShT — shock tube, PD — photodiode, PEC — photoelectric cell.	94

2.72	Results of high-temperature experiments (curves with the experimental noise) and their comparison with preliminary calculations (smooth curves). Gas mixture $\text{CO}_2:\text{O}_2:\text{N}_2=9:5:86$ with different admixtures of water.	95
3.1	Experimental setup: 1 - discharge cell, 2,3 - electrodes, 4 - optical window (CaF_2), 5 - high-voltage generator, 6 - back current shunt, 7 - capacitive gauge, 8 - monochromator, 9 - photomultiplier FEU-100, 10 - oscilloscopes S9-8 and TDS-380, 11 - computer, 12 - power supplies, 13 - He-Ne laser ($\lambda = 3.3922\mu\text{m}$), 14 - photodetector Pb-Se.	99
3.2	Characteristics measured by the current shunt: a) - the oscillogram of the current in the cable, b) - the current through the high voltage electrode, c) - the high-voltage electrode potential. The initial pressure of the mixture CH_4+air is 1.5 torr.	100
3.3	Electrodynamics characteristics in the first high voltage pulse represented for three different pressures — 1.51, 6.05 and 18 torr. Potential distributions $U(t)$ are represented in sections $x = 0.0, 3.6, 7.2, 10.8, 14.4, 18.0$ cm. Distributions of reduced electric fields $E(t)/p$, currents $J(t)$, volumetric power densities $W(t)$ averaged over the intervals are represented for the intervals 0.0–3.6, 3.6–7.2, 7.2–10.8, 10.8–14.4 and 14.4–18.0 cm. Curves are enumerated from 1 to 6 for the potential and from 1 to 6 for other values consequently. Arrows in figures show directions of curves shifts with the consequent change from the 1-st to the 6-th section for voltage and from the 1-st to 5-th interval for other values. The mixture is the products of the oxidation of CH_4 in the methane–air stoichiometric mixture.	106
3.4	Distributions of the potential in the first high-voltage pulse for the pressure 0.76 torr in sections $x = 0.0, 3.6, 7.2, 10.8, 14.4, 18.0$ cm, which are enumerated from 1 to 6 consequently. The mixture is products of oxidation of CH_4 in the stoichiometric mixture with air.	107
3.5	The energy input in the discharge for the first and the second pulses in the processed methane-air mixture in dependence on the initial pressure of the mixture.	110
3.6	The sum of the energy input in the first and the second high-voltage pulses: a) in the initial mixture, b) in the mixture transformed by the discharge.	111
3.7	Spectrum of the discharge emission a) — in pure methane and b) — in the processed methane-oxygen mixture. The pressure is 4 torr.	112
3.8	Timeresolved intensities of the emission on the wavelength $\lambda = 430$ nm in the initial (CH_4+O_2) and the corresponded processed mixtures. The initial pressure is 3.78 torr.	113
3.9	Integral over time emission intensities of transitions $\text{CH}(A^2\Delta \rightarrow X^2\Pi)$, $\text{CO}(B^1\Sigma \rightarrow A^1\Pi)$, $\text{OH}(A^2\Sigma \rightarrow X^2\Pi)$ and methane concentration, measured by the absorption of the He-Ne laser emission on the wavelength $\lambda = 3.3922\mu\text{m}$, in the discharge. The initial pressure of the mixture CH_4+O_2 is 7.56 torr.	115
3.10	Integral over time emission intensities of transitions $\text{CH}(A^2\Delta \rightarrow X^2\Pi)$, $\text{CO}(B^1\Sigma \rightarrow A^1\Pi)$, $\text{CO}_2^+(B^2\Sigma \rightarrow X^2\Pi)$ and $\text{OH}(A^2\Sigma \rightarrow X^2\Pi)$ in the discharge. The initial pressure of the mixture $\text{C}_2\text{H}_6+\text{O}_2$ is 7.56 torr.	116

3.11	Dependencies of alkanes full oxidation times on initial pressures of stoichiometric mixtures, obtained from $\text{CH}(A^2\Delta \rightarrow X^2\Pi)$, $\text{CO}(B^1\Sigma \rightarrow A^1\Pi)$, $\text{CO}_2^+(B^2\Sigma \rightarrow X^2\Pi)$, $\text{OH}(A^2\Sigma \rightarrow X^2\Pi)$ bands emissions.	117
3.12	Dependencies of alkanes full oxidation times on initial pressures of stoichiometric mixtures, obtained from $\text{CO}(B^1\Sigma \rightarrow A^1\Pi)$ band emission. The data for the stoichiometric mixtures of oxygen with alkanes from ethane to hexane are denoted as "C2-C6+O2", and data for the stoichiometric mixtures of oxygen with alkanes from ethane to hexane are denoted as "C5-C6+air" (see table 1 and 4).	119
3.13	The sum of the energy input in the first and the second high-voltage pulses: a) in the initial mixture, b) in the mixture transformed by the discharge. .	120
3.14	Integral over time emission intensities of transition $\text{CO}(B^1\Sigma \rightarrow A^1\Pi)$ in the discharge. The initial pressures of the mixtures are 1.51 torr for a), 5.29 torr for b) and 9.83 Torr for c).	121
3.15	Time of full oxidation obtained from $\text{CO}(B^1\Sigma \rightarrow A^1\Pi)$ band emission - a) and time of $\text{CO}(B^1\Sigma \rightarrow A^1\Pi)$ band emission maximum versus initial pressure of butane with oxygen lean mixtures.	122
3.16	Intensity of $\text{OH}(A^2\Sigma \rightarrow X^2\Pi)$ band emission in the processed mixture of decane with oxygen versus time of mixing. The unit emission intensity level coincides to the emission intensity of $\text{OH}(A^2\Sigma \rightarrow X^2\Pi)$ in butane-oxygen stoichiometric mixture. The initial pressure of the mixture $\text{C}_{10}\text{H}_{22}+\text{O}_2$ is 4 torr.	123
3.17	Intensities of $\text{OH}(A^2\Sigma \rightarrow X^2\Pi)$ band emission in mixtures of oxygen with different alkanes.	124
3.18	Integral over time emission intensities of transitions $\text{CO}_2^+(B^2\Sigma \rightarrow X^2\Pi)$ (290 nm), $\text{OH}(A^2\Sigma \rightarrow X^2\Pi)$ (306 nm), $\text{CO}_2^+(A^2\Pi \rightarrow X^2\Pi)$ (330 nm) in the discharge versus the equivalence ratio of the mixture. All points corresponded to the decane mixture are demonstrated at 0.1 equivalence ratio point.	125
3.19	Energy input for butane and decane mixtures with oxygen. Equivalence ratio of the butane mixture is 0.1 and one of the decane mixture is 0.12 ± 0.01 . .	127
3.20	Time intervals between instants of discharge beginning and $\text{CO}(B^1\Sigma \rightarrow A^1\Pi)$ emission maximum — a) and instants of full oxidation — b).	128
3.21	Energy branching in the discharge (stoichiometric mixture $\text{C}_2\text{H}_6-\text{O}_2$). In the figure a) detailed energy branching is shown. Curves are designate percentage of energy directed on: 1) elastic collisions, 2) vibrational collisions (both $\text{C}_2\text{H}_5\text{OH}$ and O_2), 3) singlet molecular oxygen (both states), 4) dissociative attachment (C_2H_6 and O_2), 5) C_2H_6 dissociation, 6) O_2 dissociation, 7) C_2H_6 ionization, 8) O_2 ionization. Vertical lines show measured experimentally reduced electric field values, which are corresponded to maximum power in the discharge. In the figure b) summary energy branching is shown. Curves are designate percentage of energy directed on: 1) total (C_2H_6 and O_2) dissociation, 2) total (C_2H_6 and O_2) ionization, 3) total dissociation + 0.7 total ionization, 4) total dissociation + total ionization.	129

3.22	Energy branching in the discharge (mixture $\text{CO}_2:\text{H}_2\text{O}=2:3$). In the figure a) detailed energy branching is shown. Curves are designate percentage of energy directed on: 1) elastic collisions, 2 vibrational collisions (both CO_2 and H_2O), 3) singlet molecular oxygen (both states), 4) dissociative attachment (CO_2 and H_2O), 5) CO_2 dissociation, 6) H_2O dissociation, 7) H_2O ionization, 8) CO_2 ionization. Vertical lines show measured experimentally reduced electric field values, which are corresponded to maximum power in the discharge. In the figure b) summary energy branching is shown. Curves are designate percentage of energy directed on: 1) total (CO_2 and H_2O) dissociation, 2) total (CO_2 and H_2O) ionization, 3) total dissociation + 0.7 total ionization, 4) total dissociation + total ionization.	130
3.23	The calculated parts of the molecules during oxidation process of $\text{C}_2\text{H}_5\text{OH}$ and C_2H_6 in stoichiometric mixtures with oxygen. The initial pressure of the mixture is 6.8 torr. Dissociation degrees are corresponded to the 70% of the measured experimentally energy input in the discharge.	134
3.24	The calculated parts of the molecules during oxidation process of CH_4 in stoichiometric mixture with oxygen. The initial pressure of the mixture is 6.8 torr. Dissociation degrees are corresponded to the 70% of the measured experimentally energy input in the discharge.	135
3.25	The calculated and measured oxidation times of C_2H_6 , CH_4 , H_2 , $\text{C}_2\text{H}_5\text{OH}$ molecules during oxidation process in stoichiometric mixtures with oxygen. Dissociation degrees are corresponded to the 70% (with single exception of turquoise curve which corresponded to the case when 90% of energy input is pointed to the dissociation) of the measured experimentally energy input in the discharge.	136
3.26	The calculated parts of C_2H_6 molecules during oxidation process in the stoichiometric mixture with oxygen. The initial pressure of the mixture is 3.78 torr. Dissociation degrees correspond to the 70% of the measured experimentally energy input in the discharge.	137
3.27	The calculated parts of C_2H_6 molecules during oxidation process in the stoichiometric mixture with oxygen. The initial pressure of the mixture is 3.78 torr. Dissociation degrees correspond to the 70% of the measured experimentally energy input in the discharge. Dissociation degrees of C_2H_6 and O_2 are varied.	138
3.28	The calculated parts of C_2H_6 molecules during oxidation process in the stoichiometric mixture with oxygen. The initial pressure of the mixture is 3.78 torr. Dissociation degrees correspond to the 70% of the measured experimentally energy input. Dissociation channels are changed or switched off in a following ways: 1) all dissociation channels are in accordance with table 3.9, 2) O_2 dissociates to ground state O-atoms only, 3) dissociation of water is switched off, 4) O_2 dissociates to ground state O-atoms only and dissociation of water is switched off, 5) dissociation of ethane is switched off, 6) dissociation of oxygen is switched off.	139
3.29	Oxidation time determined by $\text{CO}(B^1\Sigma \rightarrow A^1\Pi)$ transition intensity. C2-C6 and C5-C6 denote $\text{C}_2\text{H}_6\text{-C}_6\text{H}_{14}$ and $\text{C}_5\text{H}_{12}\text{-C}_6\text{H}_{14}$ correspondingly. These series of alkanes have practically the same oxidation times.	140

3.30	Oxidation times of acetylene determined from $\text{CO}(B^1\Sigma \rightarrow A^1\Pi)$ emission intensity in the different equivalence ratio mixtures. The equivalence ratio of the mixture changes from 1 to 0.2.	142
3.31	Oxidation times of acetylene determined from $\text{CO}(B^1\Sigma \rightarrow A^1\Pi)$ and $\text{CH}(A^2\Delta \rightarrow X^2\Pi)$ emission intensities.	145
3.32	Emission intensities of $\text{OH}(A^2\Sigma \rightarrow X^2\Pi)$, $\text{CO}(B^1\Sigma \rightarrow A^1\Pi)$, $\text{CO}_2^+(B^2\Sigma \rightarrow X^2\Pi)$, $\text{CH}(A^2\Delta \rightarrow X^2\Pi)$ bands. Initial pressure of ethane-oxygen stoichiometric mixture is 6.8 torr.	145
3.33	Emission intensities of $\text{OH}(A^2\Sigma \rightarrow X^2\Pi)$, $\text{CO}(B^1\Sigma \rightarrow A^1\Pi)$, $\text{CO}_2^+(B^2\Sigma \rightarrow X^2\Pi)$, $\text{CH}(A^2\Delta \rightarrow X^2\Pi)$ bands. Initial pressure of acetylene-oxygen stoichiometric mixture is 6.8 torr.	146
3.34	$\text{CO}(B^1\Sigma \rightarrow A^1\Pi)$ emission intensity after 160 s from instant, when the discharge is switched on, versus the mixture initial pressure. Mixtures are CO-O_2 stoichiometric with small addition of water vapor.	148
3.35	Minimum values of $\text{CO}(B^1\Sigma \rightarrow A^1\Pi)$ emission intensity time derivative, when the discharge is switched on, versus the mixture initial pressure. Mixtures are CO-O_2 stoichiometric with small addition of water vapor.	149
4.1	Calculated ignition delay time <i>vs</i> initial gas temperature. H_2 : O_2 : $\text{N}_2 = 29.6$: 14.8 : 55.6 mixture. $P = 1$ atm. Non-equilibrium excitation. $E/N=300$ Td. Different curves correspond to different energy consumption: $1 - 0 \text{ J/cm}^3$ (autoignition); $2 - 4 \cdot 10^{-4} \text{ J/cm}^3$; $3 - 4 \cdot 10^{-3} \text{ J/cm}^3$; $4 - 4 \cdot 10^{-2} \text{ J/cm}^3$; $5 - 4 \cdot 10^{-1} \text{ J/cm}^3$	160
4.2	Calculated ignition delay time <i>vs</i> initial gas temperature. CH_4 : O_2 : $\text{N}_2 = 9.4$: 18.8 : 71.8 mixture. $P = 1$ atm. Non-equilibrium excitation. $E/N=300$ Td. Different curves correspond to different energy consumption: $1 - 0 \text{ J/cm}^3$ (autoignition); $2 - 10^{-3} \text{ J/cm}^3$; $3 - 10^{-2} \text{ J/cm}^3$; $4 - 10^{-1} \text{ J/cm}^3$; $5 - 4 \cdot 10^{-1} \text{ J/cm}^3$	161
4.3	Calculated ignition delay time <i>vs</i> initial gas temperature for thermal and nonequilibrium plasma excitation. H_2 : O_2 : $\text{N}_2 = 29.6$: 14.8 : 55.6 mixture. $P = 1$ atm. Total energy release $W = 4 \times 10^{-3} \text{ J/cm}^3$. Reduced electric field is $E/N=300$ Td. $1 -$ autoignition; $2 -$ equilibrium excitation; $3 -$ nonequilibrium excitation.	162
4.4	Calculated ignition delay time <i>vs</i> energy input for thermal and nonequilibrium plasma excitation. H_2 : O_2 : $\text{N}_2 = 29.6$: 14.8 : 55.6 mixture. $P = 1$ atm; $T_0 = 1000 \text{ K}$; $E/N=300$ Td. $1 -$ autoignition (corresponds to zero energy input); $2 -$ equilibrium excitation; $3 -$ nonequilibrium excitation ($E/N = 300 \text{ Td}$, $t = 40 \text{ ns}$).	163
4.5	Calculated ignition delay time <i>vs</i> reduced electric field. H_2 : O_2 : $\text{N}_2 = 29.6$: 14.8 : 55.6 mixture. $P = 1$ atm; $T_0 = 1000 \text{ K}$. Energy release is $W = 4 \times 10^{-3} \text{ J/cm}^3$; $t = 40 \text{ ns}$	164
4.6	Scheme of the experimental setup.	165
4.7	Typical behavior of synchronized signals from the N 3 schlieren gauge, synchronogenerator and photomultiplier at different amplitudes of high-voltage pulse. Mixture H_2 : O_2 : N_2 : $\text{Ar} = 6$: 3 : 11 : 80	167

4.8	Typical voltage on the electrode (1), voltage (2) and current (3) at the observation point.	168
4.9	LaVision ICCD camera PicoStar HR12 used in experiments for analysis of homogeneity of the discharge development and ignition initiation	169
4.10	Densities behind the reflected shock wave, realized in different mixtures, <i>vs</i> temperature. 1 – mixture H ₂ : O ₂ : Ar = 12: 6: 82, high pressure gas is air; 2,3 – mixture H ₂ : O ₂ : Ar = 12: 6: 82, high pressure gas is CO ₂ , in the case of curve 3 special flow plate was used to decrease shock wave velocity; 4 – mixture H ₂ : O ₂ : He = 12: 6: 82, high pressure gas is He, experiments with flow plate. Dashed circle corresponds to a region of densities where discharge development is optimal.	175
4.11	Measured ignition delay <i>vs</i> gas temperature for different voltage polarity. 1,2 – Mixture H ₂ : O ₂ : Ar = 12: 6: 82; 3,4 – Mixture H ₂ : O ₂ : He = 12: 6: 82. 1,3 – positive polarity of the electric pulse; 2,4 – negative polarity. <i>U</i> = 160 kV.	176
4.12	Comparison of the measured ignition delay time with calculated one. Mixture H ₂ : O ₂ : Ar = 12: 6: 82. 1 – autoignition, high pressure gas is CO ₂ ; 2 – with discharge, high pressure gas is CO ₂ ; 3 – autoignition, high pressure gas is air; 4 – with discharge, high pressure gas is air; 5 – numerical simulation for autoignition, GRI-Mech 3.0; 6 – numerical simulation for the shock wave and the discharge action, BOLSIG + GRI-Mech 3.0.	177
4.13	Measured ignition delay time <i>vs</i> gas temperature. Mixture H ₂ : O ₂ : N ₂ : Ar = 6: 3: 11: 80. 1 – autoignition, 2 – with nanosecond discharge. <i>U</i> = 160 kV.	180
4.14	Velocity of the incident shock wave. H ₂ -O ₂ -N ₂ = 16.7 : 16.7 : 66.6 mixture.	182
4.15	Gas density behind the reflected shock wave. H ₂ -O ₂ -N ₂ = 16.7 : 16.7 : 66.6 mixture.	183
4.16	Energy of the discharge for different gas densities. H ₂ -O ₂ -N ₂ = 16.7 : 16.7 : 66.6 mixture.	184
4.17	Pressure behind the reflected shock wave. H ₂ -O ₂ -N ₂ = 16.7 : 16.7 : 66.6 mixture.	185
4.18	Comparison of the measured ignition delay time with calculated one. Mixture H ₂ : O ₂ : N ₂ = 0.167: 0.167: 0.666. 1 – autoignition; 3 – with discharge; 2 – numerical simulation for autoignition, GRI-Mech 3.0, no gasdynamic correction; 4 – numerical simulation for the shock wave and the discharge action, BOLSIG + GRI-Mech 3.0, no gasdynamic correction. Log scale.	186
4.19	Gas Dynamic Fields. H ₂ -O ₂ -N ₂ = 16.7 : 16.7 : 66.6 mixture. 1 – pressure field; 2 – <i>v_x</i> velocity field; 3 – temperature field; 4 – pressure gradients picture; 5 – temperature gradients picture. Incident shock wave velocity 900 m/s. <i>p</i> ₀ = 10 Torr	188
4.20	Comparison of the measured ignition delay time with calculated one. Mixture H ₂ : O ₂ : N ₂ = 0.167: 0.167: 0.666. 1 – autoignition; 3 – with discharge; 2 – numerical simulation for autoignition, GRI-Mech 3.0, with gasdynamic correction; 4 – numerical simulation for the shock wave and the discharge action, BOLSIG + GRI-Mech 3.0, with gasdynamic correction.	190

4.21	Measured ignition delay time <i>vs</i> gas temperature. Mixture CH ₄ : O ₂ : N ₂ : Ar = 1: 4: 15: 80. Pressure behind the reflected shock wave is indicated with numbers near appropriate curves. 1 – autoignition, 2 – with discharge, $W = 10^{-3}$ J/cm ³ ; 3 – with discharge, $W = 3 \cdot 10^{-2}$ J/cm ³ ; 4 – with discharge, $W = 5 \cdot 10^{-2}$ J/cm ³	191
4.22	An example of a synchronization scheme for PicoStar Camera.	194
4.23	Image of a nanosecond discharge (gate 1 ns) and combustion (gate 30 mks) stages	195
4.24	Image of a nanosecond discharge (gate 1 ns) and combustion (gate 30 mks) stages	196
4.25	Image of a nanosecond discharge (gate 1 ns) and combustion (gate 30 mks) stages. Mixture CH ₄ :O ₂ :N ₂ :Ar=1:4:15:80	197
4.26	Comparison of typical reaction rates at different temperatures: solid line is a rate of reaction of thermal dissociation; dashed line is a rate of a typical reaction of chain prolongation; square in the top of a plot - typical rate of reaction of dissociation by an electron impact at electric field values typical for the discharge	198
4.27	Ignition delay time <i>vs</i> temperature. Symbols: 1 — 2 atm, autoignition; 2 — 2 atm, ignition with discharge; 3 — 0.5 atm, ignition with discharge; dashed line — 0.5 atm, autoignition (calculated); 4 — 2 atm, autoignition (calculated).	200
4.28	Energy deposited in the discharge: a — low temperature, b — high temperatures. Curves <i>A</i> and <i>B</i> are discussed in the text. Symbols: 1 — w_1 , $U = 100$ kV; 2 — $w_1 + w_2$, $U = 100$ kV; 3 — $w_1 + w_2 + w_3$, $U = 100$ kV; 4, 5 — $w_1 + w_2 + w_3$, $U = 160$ kV.	201
4.29	Energy input <i>vs</i> time. The plateau 1 corresponds to the energy W_1 , the plateau 2 — to the $W_1 + W_2$, the plateau 3 — to the $W_1 + W_2 + W_3$	202
4.30	Typical waveforms of voltage (curves 1 and 2 are the signals from the different capacitive gauges), current (curve 3) and emission (curve 4). . . .	203
4.31	Ignition delay time <i>vs</i> temperature. a — propane – containing mixture, b — butane – containing mixture.	204
4.32	Ignition delay time <i>vs</i> temperature. a — propane – containing mixture, b — butane – containing mixture.	204
4.33	Energy input in a gas during nanosecond discharge action in dependence upon gas density behind the reflected shock wave.	205
4.34	The evolution in time of the specific energy deposited in the Ar:O ₂ :CH ₄ mixture at 1.1 atm and 1530 K and in the Ar:O ₂ :C ₅ H ₁₂ mixture at 0.52 atm and 1390 K. Curves 1 correspond to calculation and curves 2 correspond to measurements.	208
4.35	The evolution in time of the densities of dominant active species in the afterglow of the discharge in (a) the Ar:O ₂ :CH ₄ mixture and (b) Ar:O ₂ :C ₅ H ₁₂ mixture. The curves correspond to the same conditions as those in Fig.4.34.	211
4.36	The evolution in time of the OH – density in the Ar:O ₂ :CH ₄ mixture at 1.1 atm and 1530 K. Curve 1 corresponds to autoignition and curve 2 corresponds to ignition by injection of radicals.	212

4.37	Comparison of autoignition delay time, experimentally determined from OH-emission at 306 nm (PW, OH), experimentally determined from CH-emission at 431 nm (PW, CH), and calculated in accordance with the formula given by Burcat ¹⁶⁹	213
4.38	Autoignition (designated as “auto”) and ignition by nanosecond discharge in the form of fast ionization wave (designated as “FIW”) for C ₂ H ₆ - and C ₃ H ₈ -containing mixtures. Comparison of experiments and calculations. .	214
4.39	Comparison of sensitivity analysis of the kinetic scheme for CH ₄ (red bars), C ₂ H ₆ (green bars) and C ₃ H ₈ (blue bars) – containing mixtures. Temperature $T_5 = 1670$ K. For comparison, another temperature for methane-containing mixture (1870 K) is given by yellow bars.	215
4.40	Autoignition (designated as “auto”) and ignition by nanosecond discharge in the form of fast ionization wave (designated as “FIW”) for C ₄ H ₁₀ - and C ₅ H ₁₂ -containing mixtures. Comparison of experiments and calculations. .	216
5.1	Influence of a small amount of different radicals on combustion kinetics, results of calculations. a — temperature behavior, b — density of different species (in fractions).	218
5.2	General view on experimental setup for study of shift of the ignition delay by ArF-photolysis.	221
5.3	Cross-section of absorption: a — for molecular oxygen, b — for nitrous oxide. Region of ArF laser generation is marked with red vertical lines. . .	222
5.4	Typical energy input in experiments with laser flash-photolysis. A shape of a laser beam is on the right part of a figure.	222
5.5	a — shift of ignition delay time. Experiments on autoignition, ignition by nanosecond discharge and ignition by ArF laser flash-photolysis. b — volumetric energy input in experiments with discharge and with flash-photolysis.	225
5.6	Comparison of experimental and calculation results for kinetics of N ₂ O-containing mixtures. Data on the observed rate constant of unimolecular decomposition. The experimental points are taken from ¹⁸⁵ : 1 — mixture of 3% N ₂ O+Ar, data on IR emission (4.5 μ m); 2 — mixture of 3% N ₂ O+Ar, data on UV absorption (250 nm); 3 — mixture of 3% N ₂ O, data on IR emission (2.9 μ m); 4 — mixture of 3% N ₂ O+250 ppm H ₂ +Ar, data on IR emission (4.5 μ m); 5 — mixture of 3% N ₂ O+1000 ppm H ₂ +Ar, data on IR emission (4.5 μ m); 6 — mixture of 3% N ₂ O+1% H ₂ +Ar, data on IR emission (4.5 μ m). Lines 7–10 give the results of the numerical model, proposed in the present paper.	233

5.7	Comparison of the experimental and calculation results for the kinetics of N_2O -containing mixtures. The experimental data are borrowed from ¹⁸⁹ : 1 — mixture of 3% N_2O +Ar, data on IR emission, pressure $P = 11.5$ atm; 2 — mixture of 3% N_2O +Ar, data on IR emission, pressure $P = 8$ atm; 3 — mixture of 3% N_2O +Ar, data on UV absorption, pressure $P = 11.5$ atm; 4 — mixture of 3% N_2O +250 ppm H_2 +Ar, data on IR emission, pressure $P = 11.5$ atm; 5 — mixture of 3% N_2O +1000 ppm H_2 +Ar, data on IR emission, pressure $P = 11$ atm; 6 — mixture of 3% N_2O +Ar, data on IR emission, pressure $P = 8$ atm.	234
5.8	Review of reaction rate constants: a) — reaction $\text{N}_2\text{O} + \text{H} = \text{N}_2 + \text{OH}$. 1 — ¹⁹³ , 2 — ¹⁹⁴ , 3 — ¹⁹⁵ , 4 — ¹⁹⁶ , 5 — ¹⁹⁷ , 6 — ¹⁹⁸ , 7 — ¹⁸⁷ , 8 — ¹⁹⁹ , 9 — our data, 10 — ²⁰⁰ , 11 — ²⁰¹ , 12 — ²⁰² , 13 — ²⁰³ ; b) — reaction $\text{OH} + \text{O} = \text{H} + \text{O}_2$. 1 — ²⁰⁴ , 2 — ²⁰⁵ , 3 — ¹⁸⁷ , 4 — ²⁰⁶ , 5 — ²⁰⁷ , 6 — ²⁰⁸ , 7 — ²⁰⁹ , 8 — ²¹⁰ , 9 — ²¹¹ , 10 — our data, 11 — ²¹² , 12 — ¹⁹² , 13 — ²¹³ , 14 — ²¹⁴ ; c) — reaction $\text{N}_2\text{O} + \text{O} = \text{NO} + \text{NO}$. 1 — ¹⁸⁴ , 2 — ¹⁹⁵ , 3 — ²¹⁵ , 4 — ¹⁸⁹ , 5 — ¹⁹⁹ , 6 — ²¹⁶ , 7 — ²¹⁷ , 8 — ²¹⁸ , 9 — ²¹⁹ , 10 — ²²⁰ , 11 — our data; d) — reaction $\text{H}_2 + \text{O}_2 = \text{OH} + \text{OH}$. 1 — ²²¹ , 2 — ²²² , 3 — ²²³ , 4 — ²²⁴ , 5 — ²²⁵ , 6 — ²²⁶ , 7 — our data.	236
5.9	Comparison of the experimental and calculation results for the autoignition of N_2O -containing mixtures. Our experiments: 1 — $\text{H}_2 : \text{N}_2\text{O} : \text{Ar} = 10 : 10 : 80$ mixture, 2 — $\text{O}_2 : \text{H}_2 : \text{N}_2\text{O} : \text{Ar} = 3 : 30 : 10 : 50$ mixture.	237
5.10	Comparison of the experimental and calculation results for the autoignition of N_2O -containing mixtures. The composition of mixtures is given in the figure. Argon is used as diluent gas. The experimental data are taken from ¹⁸⁸ ; the calculations are performed on the basis of the kinetic scheme proposed in the present paper.	238
6.1	Experimental setup scheme.	246
6.2	Flame propagation velocity increase depending on barrier discharge power.	248
6.3	The comparative analysis of different discharges types influence on flame propagation velocity.	249
6.4	The comparative analysis of different discharge frequencies influence on flame propagation velocity.	250
6.5	The comparative analysis of different discharge frequencies influence on flame propagation velocity.	251
6.6	50 Hz DBD influence on flame propagation velocity.	252
6.7	50 Hz DBD energy measurements.	253
6.8	Emission spectra: A — barrier discharge in the propane-air mixture, $U=22$ kV, $\phi=1$; B — premixed propane-air flame, $\phi=0.6$; C — premixed propane-air flame with barrier discharge, $U=22$ kV, $\phi=0.6$. Flow velocity is 3 m/s.	254
6.9	CH emission profile along flame height with and without barrier discharge, $\phi=1$, $\lambda=431.5$	255
6.10	C_2 emission profile along flame height with and without barrier discharge, $\phi=1$, $\lambda=517.8$	256
6.11	OH emission profile along flame height with and without barrier discharge, $\phi=1.3$, $\lambda=306.4$	257

6.12	OH emission profile along flame height for different mixture consumptions, $\phi=0.6$, $\lambda=306.4$ nm.	258
6.13	Impulse energy distribution to the processes taking part under the electron impact action in barrier discharge.	260
6.14	Calculated OH concentration profile along flame height for different initial oxygen concentration.	262
6.15	Calculated temperature profile along flame height for different initial oxygen concentration.	263
6.16	Calculated flame velocity profile along flame height for different initial oxygen concentration.	264
6.17	General view of the flame and discharge.	265
6.18	Set-up for investigations of bunch of streamers. Scheme of the electrodes. .	266
6.19	OH* spectra in methane-air flame under discharge action at HaB=0 mm and HaB=6 mm	267
6.20	OH* and N2* profile along the HaB in methane-air flame	267
6.21	Methane-air flame blow-off velocity increase	268
6.22	Experimental OH rotational temperature profile along the HaB in methane-air flame	269
6.23	Intensification ratio for different number in pins at a high-voltage electrode and for different voltage amplitude.	270
6.24	a) Intensification ratio for different number in pins at a high-voltage electrode and for different voltage amplitude; b) Intensification ratio for different high-voltage pulse duration.	271
6.25	Images of streamers in the discharge gap. a — cathode-directed streamer, 28 pins, b – cathode-directed streamer, 8 pins, c — anode-directed streamer, 28 pins, d– anode-directed streamer, 8 pins.	272
6.26	Experimental (1) and calculated (2) spectra for 2+ nitrogen system, 0-0 vibrational transition. T=400K.	275
6.27	Air flow heating for different discharge frequencies.	275
6.28	Air flow heating for different flow velocities.	276
6.29	Temporal dynamic of gas flow temperature in dependence on time gap from discharge start.	277
6.30	Comparison of air flow and propane-air flow (ER=1) heating for different pulse amplitudes.	277
6.31	Comparison of air flow and propane-air flow (ER=1) heating for different pulse repetition rates.	278
6.32	Comparison of heating dynamic for different gas mixtures. Initial temperature is 500K.	280
6.33	OH maximum in time versus gas initial temperature.	280
6.34	The calculation for heating dynamic with and without O(1D)	281
6.35	The comparison of experimental data and calculations with O1D for gas mixture heating in the air flow in the propane-air mixture	281
6.36	Scheme of experimental setup for planar laser-induced fluorescence measurements of OH distribution in flame and discharge.	283
6.37	An example of OH emission from the burner together with laser scattered emission.	286

6.38	An example of PLIF images. Analysis of additional OH production in nanosecond discharge and difference between OH in flame and in the discharge. ER=1.07. Air consumption is 470 l/h, propane consumption is 20 l/h, flow rate is 4 m/s.	287
6.39	OH excited state emission at 306.4 nm with and without nanosecond discharge. HaB means "height above burner".	288
6.40	An example of PLIF images. ER=0.93. Figure demonstrates extraction of emission of the discharge. It was not possible physically to extract flame without discharge: this point is at higher velocity, that blow-off velocity without the discharge. Air consumption is 551 l/h, propane consumption is 20 l/h, flow rate is 4.7 m/s.	288
6.41	Profiles of spontaneous OH emission (1- in flame; 2 - in flame with discharge) and LIF signal, which corresponds to OH concentration (3- in flame, 4 - in flame with discharge).	289
6.42	LIF OH profiles between two discharge pulses at different time moments .	289
6.43	Temporal dynamics of flame front width between pulses	290
6.44	OH temporal dynamics between pulses at fixed distance from burner nozzle (1st maximum decrease)	290
6.45	Scheme of experimental setup (left) and the integral picture of streamer discharge (right).	291
6.46	Experimental measurements of OH concentration in the streamer discharge afterglow (dots) and results of modelling using GRI-Mech2.1 scheme with O(1D) kinetics (lines).	291
6.47	Effective recombination constant of OH depending on the gas temperature.	292
7.1	Overall view of experimental setup.	295
7.2	Different sprayers construction.	295
7.3	Atomization pattern for different configurations.	296
7.4	The principal scheme of PDA system	296
7.5	Typical oscillogrammes for drop's size and velocity determining.	297
7.6	Generator by FID Technology (Russia).	298
7.7	The typical pulse form (both for incident and reflected pulse)for FID generator.	299
7.8	Different electrodes configurations inside the sprayer.	300
7.9	Cones comparison with (top) and without (bottom) discharge	300
7.10	Changing in atomization cone under discharge influence	301
7.11	Discharge propagates through the air instead of water and plasma treatment is non-uniform.	301
7.12	Changing in atomization cone of aerated liquid under discharge influence .	302
7.13	Emission profiles for atomization cone's length (right) and radius (left). Red unfilled circles - without discharge, black filled circles - with discharge	302
7.14	Atomization by discharge. Left - no atomization without discharge, right - atomization under discharge influence at same parameters.	303
7.15	Dependence of consumption versus pressure. Red circle shows area where atomization by discharge is possible for our energy input.	303
7.16	Pattern of atomization by discharge.	304

7.17	Pattern of atomization by discharge.	304
7.18	Water jet without discharge.	305
7.19	Drops' size distribution for different frequencies.	305
7.20	Drops' velocity distribution for different frequencies.	306
8.1	Hypersonic plasma flow diagnostics	308
8.2	The absolute intensity of 0–0 transitions of 1^- (left) and 2^+ (right) systems, $1/s\ cm^3$	309
8.3	Electron energy distribution, eV (left) and electron number density distribution, cm^{-3} (right)	309
8.4	Rotational Temperature Measurements Using N_2 First Negative System Emission. $M = 8.2$. $T = 19\ K$ (left), $T = 295\ K$ (right)	310
8.5	Temperature variation along the flow axis (left). Gas rotational temperature vs discharge power behind shock wave (right). Air. $M = 8.2$	311
8.6	Numerical Model of Hypersonic Plasma Flow. Air. $M = 8.2$. $T_{tr} = 21\ K$. $T_{vib} = 21, 1800, 1900$ and $2000\ K$, correspondingly.	311
8.7	Nitrogen vibrational energy and atomic oxygen distribution in the flow	312
8.8	Nozzle with pre-heated gas flow	313
8.9	Emission spectra of the hypersonic propane-air flow excited by high-voltage gas discharge	314
8.10	Spatial distribution of the emission in propane-air flow. Ring electrode	315
8.11	Spatial distribution of the emission in propane-air flow. Point electrode	316
9.1	Negative images of a nanosecond discharge development in air at 0.33 bar at different moments in time. Dashed line corresponds to the edge of the discharge chamber. Camera gate 3 ns. Time was counted off from the moment when back-current shunt signal reached half of the maximum value.	319
9.2	Responses of IR sensor (black line) and Schlieren sensor (red line) in the same cross-section 287 mm away from the discharge chamber. $0.5C_6H_{14} + 4.5O_2 + 3N_2$ at 0.76 bar. Detonation.	320
9.3	Flame front velocity dependence upon initial mixture pressure for different mixture compositions under ignition by a nanosecond discharge. C-J velocity is 2400 m/s for propane/butane mixtures (circles) and 2100 m/s for hexane mixtures (triangles).	321
9.4	The setup for detonation initiation with microsecond spark discharge.	323
9.5	A typical oscillogram of the pressure transducers signals. The distance from the discharge section is shown in the figure for every transducer. Initial mixture pressure 0.6 bar. Mixture: $C_3H_8/C_4H_{10} + 5O_2$. Detonation, shock wave velocity 2350 m/s measured between transducers 2 and 3. C-J velocity for the given mixture $\sim 2400\ m/s$	324
9.6	PEM signal (red line), proportional to emission intensity, and back-current shunt signal (black line). Air, 1 torr.	324
9.7	Images of the microsecond discharge development in air at 1 torr at different moments in time. Yellow line corresponds to the edge of the discharge chamber. Camera gate 1 ns.	325
9.8	PEM signal (red line), proportional to emission intensity, and back-current shunt signal (black line). Air, 1 bar.	325

9.9	Images of the microsecond discharge development in air at 1 bar at different moments in time. Yellow line corresponds to the edge of the discharge chamber.	326
9.10	Flame front velocity dependence upon initial mixture pressure for different mixture compositions. Solid lines and solid symbols for microsecond initiation, dashed lines and hollow symbols for nanosecond initiation. Same colors correspond to the same mixtures.	327
9.11	Ignition delay time dependence upon initial pressure in $C_3H_8/C_4H_{10} + 5O_2 + xN_2$ mixtures for various nitrogen dilution levels. Green symbols for nanosecond ignition, ^{266,267} red symbols for microsecond ignition.	328

List of Tables

2.1	Measured and estimated discharge parameters in APG discharge in air at 0.4 and 10 mA discharge currents. Data are taken from ⁷⁵	30
2.2	A summary table of the parameters of plasmas used for PAI/PAC	39
3.1	Investigated mixture.	97
3.2	Transitions, controlled in all mixtures.	104
3.3	Transitions, controlled in air mixtures.	104
3.4	Times of full oxidation of alkanes τ_{ox} in s, obtained from emission intensity of the emission $\text{CO}(B^1\Sigma \rightarrow A^1\Pi)$ transition, represented in dependence of initial pressure mixture.	118
3.5	Equivalence ratio.	126
3.6	Stable molecules ionization potential, affinity to proton and R-H bond strength.	131
3.7	Main loss processes of $\text{H}^+(\text{H}_2\text{O})_n$ ions.	131
3.8	Kinetics of $\text{H}^+(\text{H}_2\text{O})_n$ ions. Temperature is 300 K. Electron density is $2 \cdot 10^{12} \text{ cm}^{-3}$.	132
3.9	Stable molecules dissociation channels.	133
3.10	Investigated mixture.	141
3.11	Kinetics of C_2H radical in acetylene-oxygen mixtures.	143
3.12	Kinetics of OH radical in acetylene-oxygen mixtures.	144
3.13	Kinetics of C_2H_6 oxidation.	147
3.14	Kinetics of CO oxidation in the discharge.	150
4.1	Excitation of H_2 by electron impact. ΔE is a threshold of the process.	158
4.2	Excitation of O_2 by electron impact. ΔE is a threshold of the process.	159
4.3	Composition of the gas mixtures.	165
4.4	Parameters of the gas mixtures behind the reflected shock wave.	172
4.4	Parameters of the gas mixtures behind the reflected shock wave.	173
4.4	Parameters of the gas mixtures behind the reflected shock wave.	174
4.5	Composition of the gas mixtures.	178
4.6	Parameters of the gas behind the reflected shock wave for $\text{H}_2\text{-O}_2\text{-N}_2\text{-Ar} = 6 : 3 : 11 : 80$ mixture.	178
4.6	Parameters of the gas behind the reflected shock wave for $\text{H}_2\text{-O}_2\text{-N}_2\text{-Ar} = 6 : 3 : 11 : 80$ mixture.	179
4.7	Parameters of the gas behind the reflected shock wave for $\text{H}_2\text{-O}_2\text{-N}_2 = 16.7 : 16.7 : 66.6$ mixture.	181
4.8	Excitation of N_2 by electron impact. ΔE is a threshold of the process.	189
4.9	Composition of the gas mixtures	191

4.10	Parameters of the gas behind the reflected shock wave for CH ₄ -O ₂ -N ₂ -Ar mixture	192
4.10	Parameters of the gas behind the reflected shock wave for CH ₄ -O ₂ -N ₂ -Ar mixture	193
4.11	Processes dominating production of atoms and radicals by gas discharge in Ar: ₂ :CH ₄ mixtures	209
5.1	Results of the experiments. Comparison of flash-photolysis and nanosecond discharge.	223
5.1	Results of the experiments. Comparison of flash-photolysis and nanosecond discharge.	224
5.2	Data on the autoignition in mixture N ₂ O:H ₂ :O ₂ :Ar = 10:30:3:50	227
5.3	Data on the autoignition in mixture N ₂ O:H ₂ :Ar = 10:10:80	227
5.4	The kinetic scheme. The rate constants are given in the form $k = AT^\beta \exp(-E/RT)$; dimensions are in cm ³ /(mole·s).	229
5.4	The kinetic scheme. The rate constants are given in the form $k = AT^\beta \exp(-E/RT)$; dimensions are in cm ³ /(mole·s).	230
6.1	Concentrations of mixture components before and after barrier discharge action.	261